Sustainable dewatering of microalgae by centrifugation using Image 4-focus and MATLAB edge detection

Anyanwu, Ruth; Nisar, Fawwad; Rodriguez, Cristina; Durrant, Andrew; Olabi, Abdul-Ghani

Published: 08/05/2018

Document Version
Publisher's PDF, also known as Version of record

UWS UNIVERSITY OF THE WEST of SCOTLAND

Institute of Engineering and Energy Technologies

RENEWABLE AND SUSTAINABLE ENERGY DEVELOPMENTS BEYOND 2030

VOLUME 2

SEEP CONFERENCE 2018

University of the West of Scotland, Paisley Campus
Tuesday 8-Friday 11 May 2018

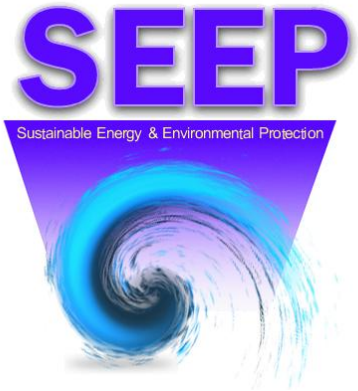

Renewable and Sustainable Energy Developments Beyond 2030

VOLUME 2

Proceedings of the 11th International Conference on Sustainable Energy & Environmental Protection

EDITED BY:

Prof Abdul Ghani Olabi

University of the West of Scotland

School of Engineering & Computing

Institute of Engineering & Energy Technologies

"Renewable and Sustainable Energy Developments Beyond 2030

VOLUME 2"

First Published in 2018
by
University of the West of Scotland
High Street, Paisley, PA1 2BE
UK

ISBN: 978-1-903978-61-0

Table of Contents

Biomass and Biofuels

Solar Energy

GREEN SYNTHESIS USING NATURAL OXIDANTS FUNCTIONALIZATION OF ACTIVATED CARBON FROM PUMPKIN PEELS FOR DECOLOURIZATION OF HAZARDOUS DYES IN WASTEWATER

Jamshaid Rashid*[1], Fakhra Tehreem[1], Adeela Rehman[2]

1. Catalysis for Environment and Energy Laboratory, Department of Environmental Sciences, Quaid-i-Azam University, 45320 Islamabad, Pakistan (E-mail: jrashid@qau.edu.pk ; hani_cnccc@yahoo.com)
2. Department of Chemistry, Inha University, South Korea (Email: adeelarehman00@gmail.com)

ABSTRACT

A green synthesis approach was adapted for synthesis of a low cost adsorbent using pumpkin peels which served as a precursor for activated carbon production, and their modification with commercial and natural beet root extracts. Effects of the production variables like functionalization agents and carbonization temperature were studied to determine their effects on adsorption capacity (qe). Functional groups, crystalline nature and surface morphology of adsorbent were analysed by using Fourier Transformed Infra-Red spectroscopy, X-ray Diffraction Spectroscopy and Scanning Electron Microscopy. The influence of the variables including dye concentration, pH of the solution, temperature and adsorbent dose on adsorption capacity of the adsorbent was assessed. Optimal conditions under which the synthesized adsorbent exhibited highest adsorption capacity and percentage removal were obtained when activation temperature was 250°C and impregnation agent was beet root extract. The kinetics analysis of the experimental data revealed that adsorption followed pseudo second order kinetic model with highest correlation coefficient value of 0.999. The equilibrium data was tested by using Freundlich and Langmuir isotherm model. For both isotherms, the characteristic parameters were determined and the adsorption behaviour was found to fit well with the Langmuir isotherm model indicating monolayer adsorption with maximum adsorption capacity of 185.1 mg/g for MB. The study demonstrated strong potential of synthesized activated carbon, to be used as an effective adsorbent for the removal of cationic dyes from wastewater.

Keywords: Activated Carbon, Green Synthesis, Methylene Blue, Degradation Kinetics

1 INTRODUCTION

Dyes are mainly utilized in industries especially in textile industry; however large quantity of dyes are also used for dyeing several materials, such as leather, petroleum products, paper, plastics and food [1]. Textile industry utilizes almost 56% of the total world dye manufactured per annum [2]. Textile industry releases approximately 280,000 tons of textile dyes in industrial runoff globally. Dyes are molecularly very stable, very difficult to degrade and are not only aesthetically displeasing but also toxic to aquatic life by decreasing sunlight penetration into the water reducing photosynthetic activity of the systems. Dyes have carcinogenic and mutagenic effect to both aquatic fauna and human beings [3]. Therefore, it is very important to treat dyes from waste water runoff. Several dye removal technologies are available including adsorption, coagulation and flocculation, biological treatment, advanced oxidation processes, photocatalytic process etc. Above all the techniques mentioned Adsorption process is the most versatile and widely used color removing technique. The process is simple to design, convenient and can be easily operated. Activated carbon (AC) adsorbent is technically easier to use and it is economically favorable as well. AC is a widely used adsorbent due to its large surface area, high degree of surface reactivity, high adsorption capacity and micro porous structure [4]. AC can be prepared from materials which possess high carbon content and low inorganics [5]. AC can be prepared by two main processes: (1) Carbonization of the precursor at high temperature and (2) modification of the carbonized char surface by either physical or chemical activation. The demand for AC is increasing day by day, due to its applicability in various fields such as purification and separation in many industrial processes including medicinal use, gas storage, pollutant and odor removal, gas separation, catalysis, pharmaceuticals, as electrode materials in electrochemical devices and in the wastewater treatment [6].Commercial activated carbons are considered expensive since they are produced from non-renewable and relatively expensive precursors like the ACs prepared from wood or coal [2]. Enhancement of the price of activated carbon results in economic difficulties for developing countries like Pakistan. The development of low cost alternate adsorbent is needed, which should have equivalent adsorption capacity as the commercial activated carbon possess. For this purpose, agricultural solid waste is being used as an adsorbent by carbonization and surface modification to increase its efficiency.

The objectives of this work were to study the adsorption performance of Pumpkin peels: an agricultural waste: as an adsorbent for the remove of methylene blue (MB) dye from wastewater. Effect of carbonization temperature and modifying agents for the preparation of optimal AC were investigated, the physicochemical properties of the as prepared AC were obtained by using scanning electron microscopy (SEM), Fourier transform infrared spectroscopy (FT-IR), Brunaur- Emmett- Teller (BET) surface area and point of zero charge (pHpzc). The effect of sorption parameters (initial dye concentration, adsorbent dose, pH and temperature) along with the sorption isotherms and kinetics were then discussed.

2 MATERIALS AND METHODS

The preparation circumstances and the properties of the precursor material are very important in preparing the AC. Pumpkin was obtained from market, washed thoroughly with deionized water to take off impurities prior to cutting. Peels were separated from pulp and seeds and placed under the sun from 8 am to 7 pm for 30 days in the month of May and then dried in drying oven 100 ^{o}C for 18 hrs, ground and sieved to get even particle size. Thermal treatment in a closed muffle furnace at a temperature of 250 ^{o}C, 350 ^{o}C, 450 ^{o}C, and 550 ^{o}C for 1 hr and named as AC_{250}, AC_{350}, AC_{450}, AC_{550} according to the carbonization temperature. The activated carbon obtained after carbonization at 250 ^{o}C was further treated with Citric acid, Nitric acid and Oxalic acid [7]. For oxalic acid treatment the AC_{250} was mixed with 0.5 mol.L^{-1} oxalic acid at a ratio of 10 ml oxalic acid to 1 g of AC_{250} and equilibrated at 28°C for 6 days. It was named as OAC [8]. Beet juice was prepared by blending 50 g beet root in 100 mL deionized water 3 thrice (10 min each). The mixture of juice and pulp was separated by using filter paper to obtain beet root extract. For activation of AC_{250} with beetroot extract 2 g of it was mixed with 6mL beet root juice at 100 ^{o}C for 60 min [9]. The as prepared Activated carbon was named as BAC.

2.1 Characterization of the Adsorbent:

Surface morphology of the prepared adsorbent was obtained by using SEM (Hitachi S 4800) at an operating voltage of 25 kV. The sample was coated with platinum and copper for effective imaging before being charged. The crystallographic nature of the adsorbent was identified by qualitative X-ray powder diffractometry (XRD) performed on (Model) using copper radiation (Cu Kα, λ 1.5nm) at 45 kV and 40 mA over the 2θ range 20-80. To determine the presence of functional groups, Fourier Transform Infrared Spectroscopy (FTIR) was obtained by FTIR spectrophotometer Bruker, Tensor 27. The spectrum was examined in the wave number range of 4000 - 400 cm^{-1}.

2.2 Point of zero charge:

pH_{zpc} is the pH on which surface of adsorbent is neutral. Surface of adsorbent is positively charged below pH_{zpc} and negatively charged when pH of the solution is above pH_{zpc}. Adsorbent point of zero charge was determined by preparing 0.1 molar solution of KCl dividing it in 5 beakers equally and adjusting pH at 2-9 respectively. After adjusting pH 0.01 g of adsorbent was added in each beaker and left for 24 h. After 24 h change in pH was determined and graph was plotted against initial and final pH to determine point of zero charge.

2.3 Adsorption performance:

The basic dye, MB (Type: cationic dye, chemical formula: $C_{16}H_{18}ClN_3S$, Molecular Weight: 319.85 g mol $^{-1}$, λ max: 665 nm) was used as adsorbates. Stock dye solutions (1000 mg.L^{-1}) were prepared by dissolving 1 g of dye in 1 L of deionized water. Further dilutions were made from the stock solution for adsorption studies. For adsorption study, a constant mass of BAC (1 g.L^{-1}) was added into 200 mL conical flask and mixed with 100 mL of dye solution with varying initial concentration of dye from 50 to 200 mg.L^{-1}, pH (3, 5, 7, 9), adsorbent dose (0.5, 1, 1.5 g.L^{-1}) and temperature (30 ^{o}C, 40^{o}C and 50 ^{o}C). The dye adsorbent solution was shaken in an orbital shaker for approximately 3 h and samples were taken after each adsorption experiment and were filtered through 0.45 µm syringe filters. The remaining of MB concentrations was detected by using UV-Visible Spectrophotometer (UV 3000) at a wavelength of 665 nm. The adsorption capacity of the adsorbent and percentage removal of dye was calculated by using eq. 1 and eq. 2 respectively.

$$q_e = (C_o - C_e / M) \times V \quad (1)$$

$$\%age\ removal = (C_o - C_e / C_e) \times 100 \quad (2)$$

Where Ce and Co are the equilibrium and initial concentration of the solute in mg/L, V is the volume of adsorbate solution in L and M is the mass of adsorbent in g.

3 RESULTS AND DISCUSSION

3.1 Characterizations

3.1.1 Scanning Electron microscopy (SEM)

The scanning electron micrographs of modified adsorbents show high pore volume, well distributed pore structure, different size of pores, uneven and rough surface morphology (**Fig. 1**). The heterogeneous character of BAC could possibly help in the adsorption of dye molecules. The white particles aggregated on the surface of the adsorbent may be un-reacted carbon particles or some impurities added during synthesis [10]. The pores size on the adsorbent was calculated from the SEM images which were greater than 72 nm, and according to IUPAC recommendation these pores are classified as macro-pores. The clearly visible macro-pores help easy mobility and diffusion of large sized and large number of dye molecules into the pore of the adsorbent similarly facilitate dye molecule adsorption onto the surface of the adsorbent [11]. Cellulose and lignin are the main components present in pumpkin peel which act as available sites for the adsorption of dye molecules.

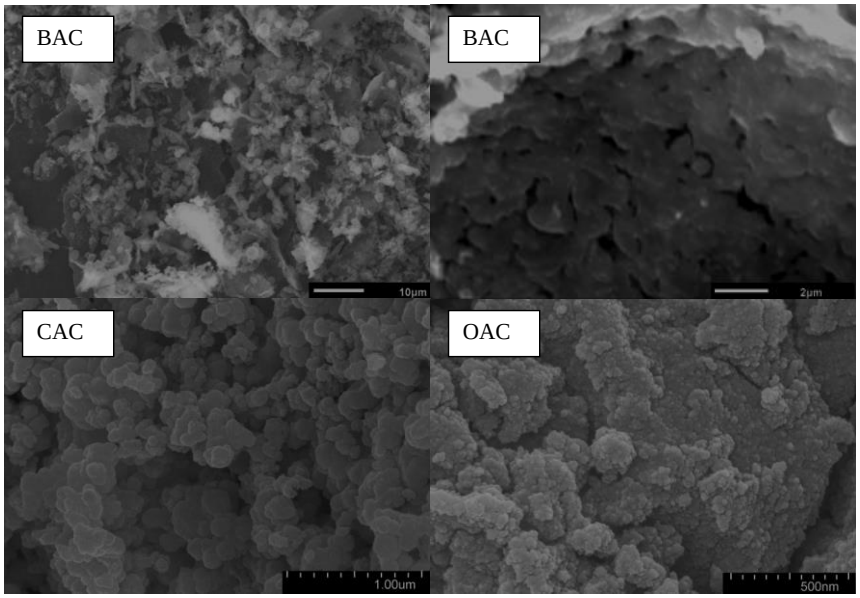

Figure1: Figure1: SEM images of modified adsorbents

3.1.2. X-Ray Diffraction spectroscopy (XRD) analysis

Figure 2 depicts the XRD pattern of BAC and NAC. The figure shows broad amorphous peak in the entire studied BAC and NAC, and did not show any well-defined diffraction peak of crystalline carbon thus reveals the heterogeneity and amorphous nature of the sample [12].

3.1.3. Fourier transforms infrared spectroscopy (FTIR) analysis

FTIR were applied on activated carbon prepared from pumpkin peels at different carbonization temperature i.e., 250^{o}C (AC_{250}), 350^{o}C (AC_{350}), 450^{o}C (AC_{450}), 550^{o}C (AC_{550}) to find out the functional groups. The FTIR spectrum was recorded and noted in 4000cm^{-1}- 400cm^{-1} wave number range. The existence of variety of functional groups in AC_{250} as compared to AC_{350}, AC_{450}, and AC_{550}, suggests its adsorption capacity may be higher than rest of the ACs. **Fig. 3** shows the FTIR spectra of CAC, NAC, OAC, BAC and AC250. CAC contained functional groups, includes 3434 cm^{-1} (bonded -OH groups), 1800 to 2100 cm^{-1} (C=C bending of alkyne), 2200 cm^{-1} (C≡N of nitrites) 1630 cm^{-1} (C=O stretching or Aromatic C=C, C=O), 750cm^{-1} (aliphatic C-H deformation) (Chen et al., 2003). The main functional groups identified in NAC contain 3436 cm^{-1}(–OH stretching), 2175 cm^{-1} (C≡N), 1690 cm^{-1} (N-H stretching of Amide), 1383 cm $^{-1}$ (NO_3 stretching), 1300 cm^{-1} (C-H bending) [7]. OAC contained the main functional groups at 3400 cm^{-1}(–OH group), 1601 cm^{-1} (C=C stretching of alkene), 1301 cm^{-1} and 700 cm^{-1} (C-H bending and C-H out of plane deformation respectively) [8]. The characteristic absorption bands of BAC were at 1300 cm $^{-1}$ (C-O of Alcohol, ether, ester, carboxylic acid and anhydride), 1375 cm^{-1} (C-H bending of CH_3), 1600 cm^{-1} (C=C of Aromatics),

3423 cm^{-1} (-OH group of akdehyde, ketone, carboxylic acid), 2100-2250 cm^{-1} (C≡C of Alkyne), 780 cm^{-1} (-CH deformation in cellulose) and 650 cm^{-1} (-NH deformation) [13].

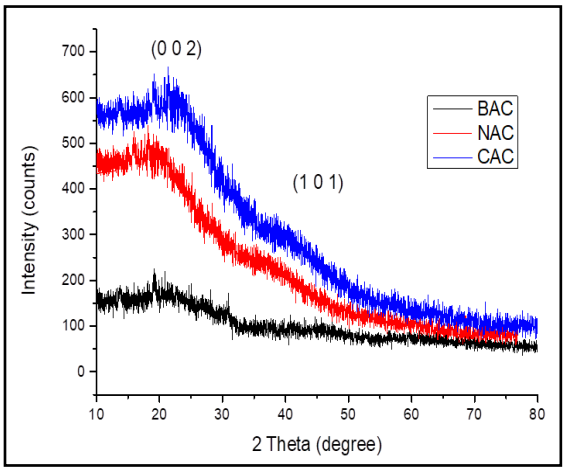

Figure 2: XRD Spectra of BAC and NAC

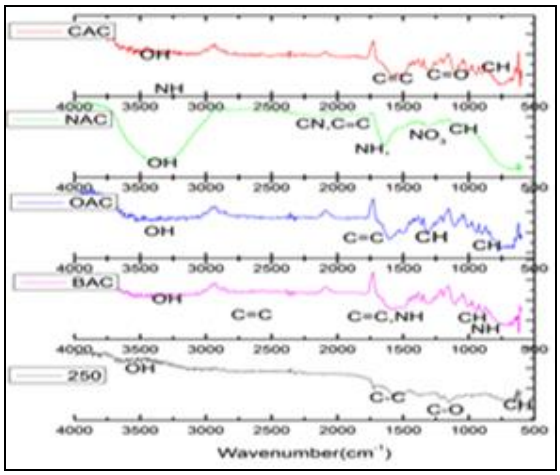

Figure 3: FTIR spectra of ACs after activation

3.1.4. Nitrogen physisorption and surface area determination

The surface area measurement of as prepared material through nitrogen adsorption–desorption at 77K are shown in **Fig.** 4. The isotherm shows Type IV behaviour as classified by IUPAC system. This shows the incomplete reversibility and desorption plot lying above the adsorption isotherm with the hysteresis existing between them attributed to the presence of slit shaped pores. Furthermore, pore size distribution measurements were conducted by nonlocal density functional theory (NLDFT) and it reveals the presence of large number of mesopores and/or macropores. The BET specific surface area comes out to be 3.6 m^2g^{-1} with 0.22 cm^3 g^{-1} total pore volume. The micropore volume was 0.01 cm^3 g^{-1}, determined by the Dubinin-Radushkevich (D-R) equation.

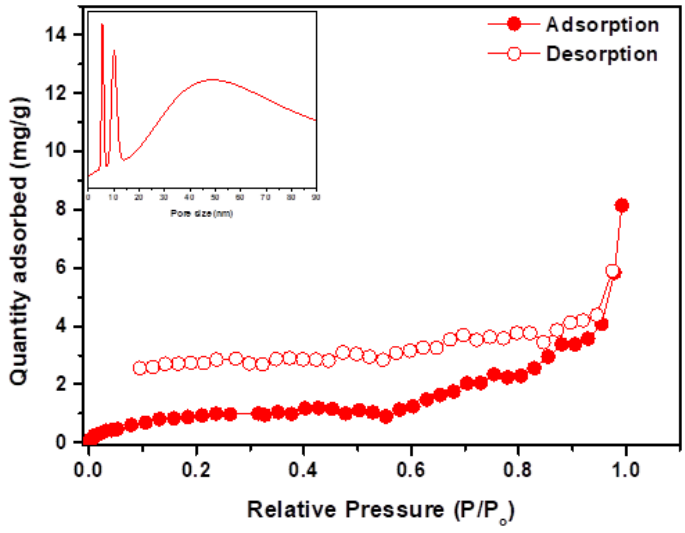

Figure 4: Nitrogen-adsorption-desorption of BAC; inset is the pore size distribution by NLDFT.

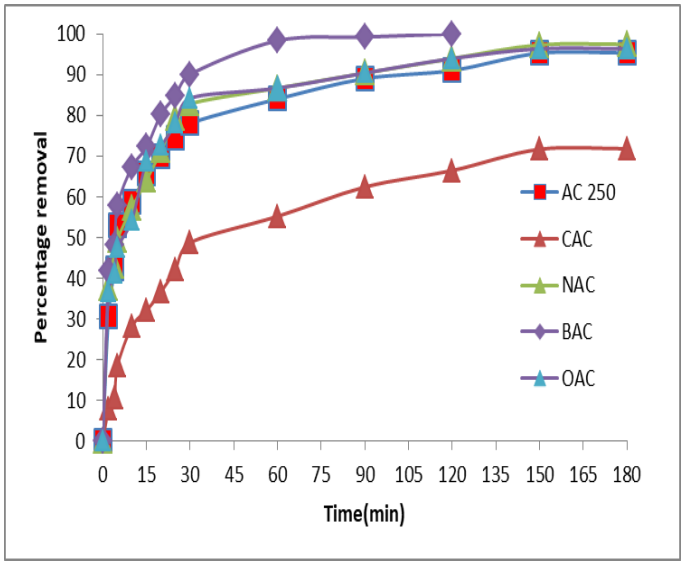

Figure 5: MB removal efficiency of Modified AC_{250}

3.2 Effect of activation with Acids vs Natural Beet root Extract:

In order to obtain optimal activated carbon AC 250 was modified with Citric acid, Nitric Acid, Oxalic acid and Beet root extract. **Fig. 5** revealed that BAC has the highest adsorption capacity of 100.6 mg/g which may be due to the increased number of functional groups attached during modification with beetroot extract. However in case of CAC the adsorption capacity is even lower than AC250 which was recorded as 71.7 mg/g because citric acid has small molecular size that can easily penetrate the pores of adsorbent thus reduce its surface areas by blockage of the pores [14]. In case of NAC and OAC there is no significant difference shown in the adsorption capacity as compared to AC 250.

3.3 Adsorbent endurance tests

The BAC adsorbent was exposed to a wide regiment of activity tests including solution pH, catalyst dosage and temperature. Adsorption of dye was greatly affected by the initial concentrations of the dye. **Fig. 6** shows the adsorption capacity of the adsorbent. It can be observed that maximum adsorption capacity of 162.34 $mg.g^{-1}$ was attained when initial dye concentration was 200 $mg.L^{-1}$ while minimum adsorption capacity of 83.51 $mg.g^{-1}$ has been noticed at initial dye concentration of 50 $mg.L^{-1}$ which may be due to increased mass transfer occur at high initial concentration. Increase in the driving force that is the initial concentration of MB is responsible for increased adsorption capacity [15]. Desorption is very important process for recovery and reuse of exhausted adsorbent since reusability of a used adsorbent is one of the most significant factors for resource conservation and economic stand point. The desorption value was calculated as 62%. The adsorption performance of BAC gradually decreased with increasing regeneration cycles. As observed in **Fig. 7** the removal percentage of 200 $mg.L^{-1}$ BAC was reduced from 49% to 35.5% after 3 cycles. These results indicated that adsorption efficiency of BAC adsorbent decreased after third cycle by only15% and a significant amount of qe value is retained after three cycles even at a very high concentration of 200 $mg.L^{-1}$.

3.4 Adsorption Isotherm modelling:

Adsorption can be described by a number of isotherms. At different concentration and temperature, the adsorption isotherms were analysed by keeping other experimental parameters constant. Freundlich and the Langmuir isotherm models were applied to the equilibrium data for analyzing the isotherm modelling.

Freundlich isotherm: $$\ln q_e = \ln K_f + (1/n_f)\ln C_e \quad (3)$$

Langmuir isotherm: $$C_e/q_e = (C_e/q_m) + (1/bq_m) \quad (4)$$

The experimental results advocate that dye removal by BAC was enhanced at higher temperatures. The regression co-efficient values of a linear plots at all three examined temperatures were found in better agreement with Langmuir isotherm model the qe values calculated from Langmuir model were in close agreement with the experimental results suggesting that the surface of the adsorbent is energetically homogeneous and a monolayer interaction between MB and BAC has taken place.

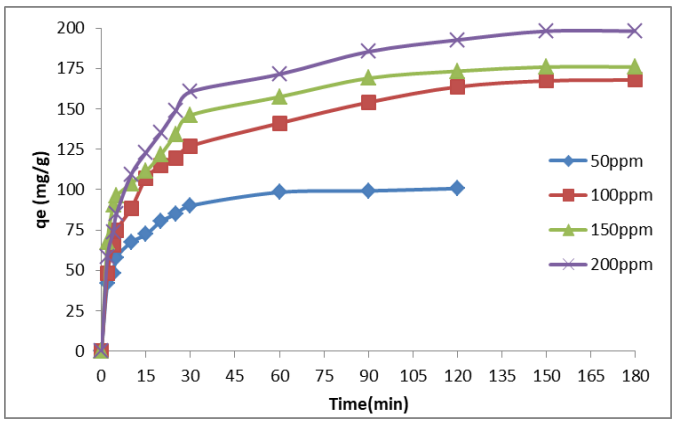

Figure 6: Initial dye concentration

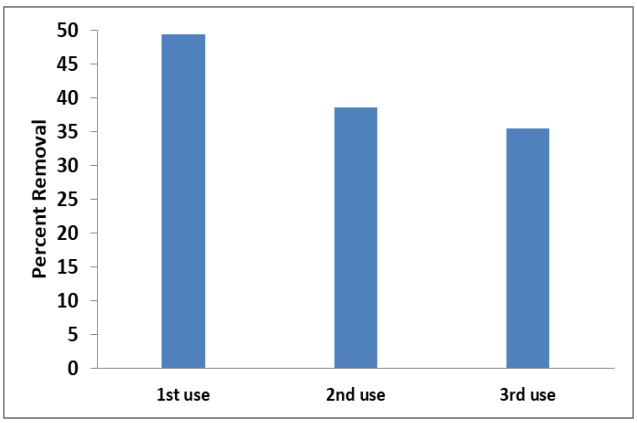

Figure 6: Adsorbent reuse effect on adsorption

3.5 Adsorption Kinetics:

To describe the adsorption process of MB on BAC, the pseudo first order and pseudo second order kinetics model were used [13, 16]. The pseudo-first-order and pseudo-second-order kinetic model equations are expressed as:

$$\log(q_e - q_t) = \log q_e - (k_1 t/2.303) \quad (5)$$

$$t/q_t = (1/k_2 q_e^2) + t/q_e \quad (6)$$

The values obtained for these kinetic models for operational parameters i.e. carbonization temperature, increasing initial concentration of the dye, adsorbent dose, pH and temperature are presented in table 2. The equation of pseudo 1st order (log (qe -qt) vs t) and 2nd order kinetics (t/qt vs t) were plotted and from the finding, it is obvious that the data followed pseudo 2nd order kinetics as the regression correlation coefficients of pseudo-second-order kinetic model were expressively higher as compared to the pseudo-first-order kinetic model. It can also be found that with the increasing in initial concentration of MB the qe

calculated values increased and were very close to the experimental qe values; ascribed to the fact that at higher MB concentration there would be competition for the surface sorption sites of the adsorbent.

4 CONCLUSION

The main purpose of this research was to use agricultural waste efficiently for the MB removal by adsorption process. For this purpose pumpkin peels were used with a little modification in its physical and chemical structure. Adsorption study exhibited that the best dosage was 0.5g and it was enough in aqueous solution to remove a significant amount of dye. The uptake of MB was maximum in basic condition rather than in acidic condition. Data of adsorption equilibrium revealed that the process is endothermic and best explained by the Langmuir isotherm model and obeyed pseudo-second order kinetics. Thus, it was concluded that Pumpkin peel is an advantageous, cheap, effective and eco-friendly adsorbent for the treatment of wastewater. As it is a waste product, it removes the issue of waste management as well. This study can help in future to treat hazardous pollutants discharged from pharmaceutical and other industries with the use of pumpkin peel adsorbent.

ACKNOWLEDGEMENTS

The authors would like to acknowledge the QAU, University Research Fund 2015-16 to fund this research.

REFERENCES

C. Djilani, Adsorption of dyes on activated carbon prepared from apricot stones and commercial activated carbon, Journal of the Taiwan Institute of Chemical Engineers. Vol. 53, pp. 112–121, 2015.

R. Subramaniam, Novel adsorbent from agricultural waste (cashew nut shell) for methylene blue dye removal: optimization by response surface methodology, Water Resources and Industry. Vol. 11, pp. 64–70, 2015.

B. Karagozoglu, The adsorption of basic dye (Astrazon Blue FGRL) from aqueous solutions on to sepiolite, fly ash and apricot shell activated carbon: Kinetic and equilibrium studies, Journal of Hazardous Materials. Vol. 147, pp. 297–306, 2007.

F. Kaouah, Preparation and characterization of activated carbon from wild olive cores (oleaster) by H_3PO_4 for the removal of basic red 46. Journal of Cleaner Production. 54: 296-306, 2013.

A. Adegoke and O.S Bello, Dye sequestration using agricultural wastes as adsorbents, Water Resources and Industry. Vol. 12, pp. 8–24, 2015

A. Ceyhan, Surface and porous characterization of activated carbon prepared from pyrolysis of biomass by two-stage procedure at low activation temperature and it's the adsorption of iodine, Journal of Analytical and Applied Pyrolysis. Vol. 104, pp. 378-383, 2013.

N. Soudani, Influence of Nitric Acid Concentration on Characteristics of Olive Stone Based Activated Carbon, Chinese Journal of Chemical Engineering. Vol. 21, pp. 1425-1430, 2013.

G. Jiang, Mechanism of lead immobilization by oxalic acid-activated phosphate rocks. Journal of Environmental Sciences. Vol. 24, pp. 919–925, 2012.

C. Djilani, Adsorption of dyes on activated carbon prepared from apricot stones and commercial activated carbon. Journal of the Taiwan Institute of Chemical Engineers. Vol. 53, pp. 112–121, 2012.

F. Kallel, Sorption and desorption characteristics for the removal of a toxic dye, methylene blue from aqueous solution by a low cost agricultural by-product, Journal of Molecular Liquids. Vol. 219, pp. 279–288, 2016.

L. Borah, Adsorption of methylene blue and eosin yellow using porous carbon prepared from tea waste: Adsorption equilibrium, kinetics and thermodynamics study, Journal of Environmental Chemical Engineering. Vol. 3, pp. 1018–1028, 2015.

S. Fan, Biochar prepared from co-pyrolysis of municipal sewage sludge and team waste for the adsorption of methylene blue from aqueous solutions: Kinetics, isotherm, thermodynamic and mechanism, Journal of Molecular Liquids. Vol. 220, pp. 432–441, 2015.

J. P. Chen, Surface modification of a granular activated carbon by citric acid for enhancement of copper adsorption, Carbon. Vol. 41, pp. 1979–1986, 2003.

A. Kumar, Removal of methylene blue and phenol onto prepared activated carbon from Fox nutshell by chemical activation in batch and fixed-bed column, Journal of Cleaner Production. Vol. 137, pp. 1246-1253, 2016.

R. Y. Liu, Biomass-derived highly porous functional carbon fabricated by using a free-standing template for efficient removal of methylene blue, Bio resource Technology. Vol. 154, pp. 138–147, 2014.

An integration approach of anaerobic digestion and fermentation process to produce high-value bio-based products and multiple bio-products

R. Alrefai, A. M. Alrefai, K.Y. Benyounis and j. Stokes

School of Mechanical and Manufacturing Engineering, Dublin City University, Ireland; alrefai.raid2@mail.dcu.ie

ABSTRACT

The attentions towards the renewable energy are increasing at a fast pace, due to the expected depletion of conventional fuel and the major impacts associated with it on the global environment. Anaerobic digestion is a biological conversion process which has proved its effectiveness in converting various types of biomass into biogas. Where, this biogas is a promising alternative for natural gas. Despite all advantages and the significant effectiveness of AD, it could contribute in major issues if it is applied at large scale as the amount of digestates which would be generated are quite high. In economic point of view, AD has became not economically feasible due to the high production cost and the volatile of conventional fuel price indexes. In order to limit these issues, many researchers have investigated an integration approach. This approach has the potential to increase the economic feasibility of AD through producing multiple bio-products simultaneously in addition to the biogas and biodiesel. It can offer an optimal solution as well for both bio-fuel production and waste management. As it is a new approach, the scientific literatures on it are relatively few. However, this paper discuss an integration approach of anaerobic digestion and fungal fermentation for producing multiple products such as; biogas, biodiesel and multiple by-products with low waste generated. The integration approach has taken its shape recently but more investigations on it are greatly advised.

Keywords: Renewable energy; Anaerobic digestion; Biodiesel; Integration approach.

1 INTRODUCTION

According to the recent projections of the world population, there will be an increase in the population in the coming decades. This increase would be associated with an increase in the world energy demands. Consequently, more depletion of energy sources and more major negative impacts of non renewable energy on the global environment are expected. For minimizing the effects of the projected increase in world energy demand, more investigations on the renewable energy are crucially needed to be good alternative for non-renewable energy. Biomass is renewable, sustainable and clean resource of energy that has numerous benefits, locally and globally [1-4]. As well known, lignocellulosic materials are available everywhere in low and stable costs. It is mainly waste materials that are containing in abundance of carbohydrates and non–competitive with food chain [5, 6]. Biomass as an energy resource, requires conversion process to be used as a bio-fuel. AD is one of the most effective biological conversion process of biomass into bio-fuel. It breaks down organic matter by microorganism and enzymes in an oxygen-free environment to produce biogas. Generally, the final output products of AD process are biogas and digesates. Where, the biogas can be directly used in several applications or upgraded and either injected into gas grid or used as a transportation fuel in compressed natural gas motor vehicles. While, the digestate generated usually comes in liquid streams and can be further separated. It contains the remained nutrients in which did not digested in the digestion process such as; ammonium and phosphates. Liquid stream has the potential to be used in agriculture as a bio-fertilizer and others while, solid stream can be composted, used for dairy bedding or applied directly to cropland. It can be also used in making of high-value bio-based products through biorefinery concepts i.e. biodiesel [7-11]. The production of lignocellulosic biodiesel includes five stages, are: pre-treatment, carbohydrate saccharification, aerobic fungal fermentation, lipid extraction and transesterification. Where, pre-treatment is the most important steps as the all following steps are highly depending on its results [12, 13]. Moreover, although biogas is a promising, sustainable and renewable energy substitute, the sustainable development of AD process primarily depends on the ability to deal with the excessive digestate produced. As an improper handling of the digestate would contribute in serious environmental issues. Due to that and to fully utilize the digestate and convert it into useful bio-based products, the attentions towards the development of new bio-refining processes have recently increased. Several studies have focused on developing an integrated system including AD and fermentation process to convert various feedstock into bio-fuel and high-value bio-based products [14-16].

Successful application of such a system could greatly results in the double benefit of producing renewable energy while adopting a zero waste approach. However, the proposed work aims to present an overview of integration approach of AD and fermentation process to produce biogas, biodiesel and multiple bioproducts such as: livestock food, fertilizer, glycerine in which they can be utilized in various applications and end up with zero waste.

2 BIO-DIESEL

Biodiesel is a promising liquid bio-fuel would play a significant role in providing the energy requirements for transportation. Thus, many scientists and researchers have focused recently more on the efficiency and emissions of the biodiesel engine. According to a study on biodiesel engine performances and emissions [17], using of biodiesel may result in considerable drop in particulate matter, hydro-carbon and carbon monoxide emissions and increase in nitrogen oxides due to the higher amount of oxygen content in biodiesel comparing to conventional diesel. It may result also in reduction in engine power because of the reduction in calorific value of biodiesel compared to conventional diesel. The study has concluded that, the blends of biodiesel with low percentage of petroleum diesel can help in controlling air pollution and easing the pressure on scarce resources without influencing on engine power and economy. In comparison to bio-ethanol as a liquid bio-fuel, biodiesel stands at present in lower position than bio-ethanol because of several factors such as; lower environmental sustainability of raw materials it is obtained from, not as good as bio-ethanol in mitigation of GHG emissions, higher production cost and less favourable future evolution [18-22].

3 ANAEROBIC DIGESTION

AD has proved its significant performance in converting a wide variety of biomasses such as: edible food (1st biofuel generation), LCB's and wastes (2nd generation) and seaweeds (3rd generation). However, the final products of AD are the biogas and digestate [23]. The next subsection overviewing these products.

3.1 AD Products

AD biogas is a promising biofuel. It contributes in bringing about environmental benefits globally. It is composed of different gases in different amounts. Its composition is varied depending on several factors such as feedstock types, digestion systems, temperature, retention time, etc. It is quite similar to landfill gas composition but vary from the natural gas. In comparison to natural gas, the calorific value of typical biogas (60% CH_4 and 40% CO_2) ranges from 5.5 to 6.5 kWh m^{-3}, while the calorific value of typical natural gas ranges from 5.8 to 7.8 kWh m^{-3}. Thus, biogas has the potential to be a significant alternative to natural gas and can be used in all natural gas appliances. However, biogas is able to be used in different applications, such as; heating, CHP and fuel cell or used as chemical feedstock or may be fuel for vehicles [24-27]. On the other hand, the biogas contains small traces of different impurities such as; H_2S, NH_3, O_2 and N_2. Due to that and to avoid corrosion and mechanical wear of appliance as well, biogas must be upgraded prior using it [28]. There are number of technologies available nowadays for scrubbing contaminants and upgrading gas to the required gas quality (e.g. carbon dioxide removal, hydrogen sulphide removal and Siloxanes removal technology) [24]. This final product is practically similar to a large extent to the natural gas. It can be blended as bio-natural gas or sold separately [29]. Additionally, digestate is the other AD product. N, P and K are the three main nutrients which conventional fertilizer are typically contained. The content of digestate from one or more of these nutrients make it a substitute for the conventional fertilizer. As aforementioned, digestate is produced in liquid form and can be used as it is or separated into liquid and solid digestate and use each of them separately. The amount of dry matter in both types are different. Usually, liquid digestate contains less than 15% dry matter, while the solid digestate contains more than 15%. The digestion process used and the composition of ingestates are important factors in determining the quality of the digestate. pH level, macro-element content (such as; N, P and K), micro-element content (such as; copper, zinc) and organic matter content of digestate are another factors to verify the quality and stability of the digestate [30]. A study in 2015 [16] has claimed that, anaerobic microbes can only convert approximately 40–60% of carbon into methane in AD of animal manure. However, utilizing the nutrients and lignocellulosic materials in the digestate is critical to significantly improve the efficiency of AD technology and produce multiple products such as: value-added chemical and fuel products from organic wastes [7-11].

4 INTEGRATION OF AD AND AEROBIC FUNGAL FERMENTATION PROCESS

The bio-refinery concept is quite similar to conventional petroleum refinery. It involves making full use of biomass. Where, the input of the process is only the biomass. While, the output can be feed, food, biomaterials and bio-fuel. In other word, the bio-refinery concept is a facility that integrates biomass conversion processes and equipments to produce feed, food, biomaterials, bio-fuel, etc. [11]. Moreover, A study in 2014 [16] was carried out to produce lignocellulosic biogas and biodiesel through an integration approach of AD and aerobic fungal fermentation. Generally, the study has concerned on developing an integrated system including AD and aerobic fungal fermentation in order to convert corn stover, animal manure and food wastes into microbial lipids for production of biodiesel. Figure 1, below illustrates the integration process of producing biogas and biodiesel. In the production of biogas, the main feedstock was animal manure and a small amount of food wastes which was used to balance nutrient to enhance AD performance. While, in the production of biodiesel, AD fibre was used as the main feedstock for fermentation stage. Corn stover as an agro-industrial wastes were used as a solid support, carbon source and nutrient source in the solid state fermentation process. Large amount of agro-industrial wastes are basically composed of cellulose, hemicelluloses and lignin and being called lignocellulose biomass. Stalk, leaves, husk, shell, peel, etc. are some types of agro-Industrial wastes. They are mainly contain of water and rich in sugar, minerals and protein which have made them suitable environment for the development of microorganisms, basically fungal strains, which are able to rapidly grow in these wastes. Due to that, they should not be considered as "waste" but lignocellulose raw material for other industrial processes. In the study, the combined hydrolysis of corn stover and AD fibre were accomplished by enzymatic hydrolysis of the combined slurry. This integrated process has ended up with producing of 1L of biodiesel and 1.9 kg CH_4 from (12.8 kg dry dairy manure, 3.1 kg dry food wastes and 12.2 kg dry corn stover) with a positive net energy of 57 MJ. The study has concluded that, combined hydrolysis of alkali treated AD fibres and acid treated corn stover is technically feasible for converting agricultural residues into mono-sugars without neutralization and detoxification [16, 31].

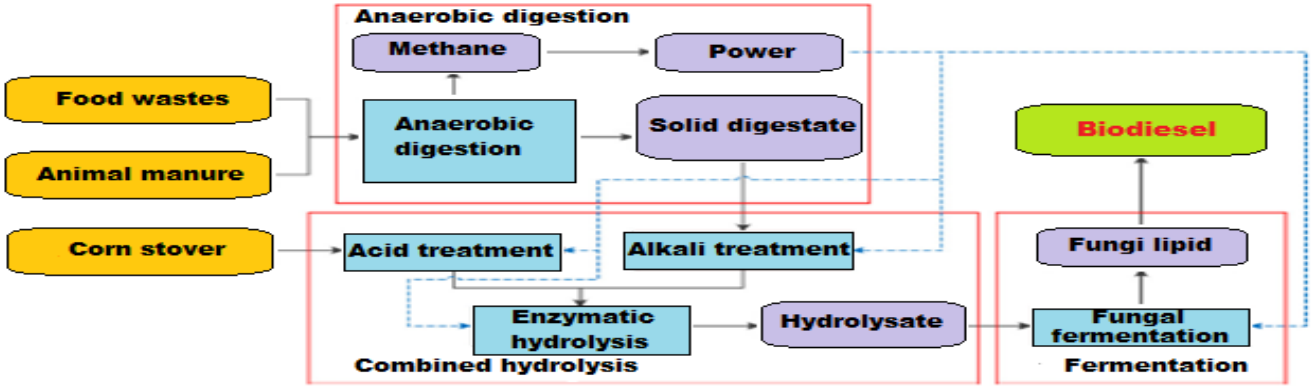

Figure 1. Flowchart of the integration process [16].

Furthermore, the biodiesel production process has begun by separating AD effluent into two streams: nitrogen and phosphorus- rich liquid digesate and fiber- rich solid digestate. Commercial screw press separator with 2mm screen was used to do so. After that, dilute alkali pretreatment was applied to treat the AD fibre at specific condition (temperature ^{o}C, time hr and NaOH %). While, corn stover was pre-treated at certain condition as well (temperature ^{o}C, time hr and sulphuric acid concentration %) by dilute acid pre-treatment. Total solid concentration of the two pre-treated slurries were then adjusted and thoroughly mixed at a ratio of 1:1 (wt/wt) to form combined slurry. For carrying out the enzymatic hydrolysis at certain condition (temperature ^{o}C, rotate speed rpm), an enzyme mixture was applied on the combined slurry in a shaking incubator. In order to separate the liquid hydrolysate from the residual solids, the hydrolysate was centrifuged. For sugar analysis, about 5 ml of the liquid hydrolysate was taken and filtered through a 0.22 µm polyethersulfone membrane filter. The remaining liquid hydrolysate were being used then for fungal lipid fermentation. Beyond that, the right oleaginous microorganism should be carefully selected to be used in accumulation of lipid on the hydrolysate. Where, microorganism which include bacteria, fungi, yeast, mold and microalgae that can accumulate lipids up to 20% or more of their dry weight are considered as oleaginous microorganism. Fungal lipid accumulation was then fulfilled in erlenmeyer flask with an amount of medium. Before being sterilized at specific temperature and time, certain percentage of NaOH was applied to the fermentation medium to adjust the pH level. The fermentation medium was inoculated with a % (vol/vol) seed and cultivated for particular days at

certain temperature on a rotary shaker with an agitation speed (rpm). Fungal biomass was collected by filtration and washing twice with distilled water over a filter paper. To obtain a consistent weight, cell mass was determined by drying at certain temp. Dried mycelia were ground in a mortar and used for lipid extraction. Total lipid was lastly determined gravimetrically [16]. However, several previous studies have confirmed that AD fibre has the potential to provide the same performance as a feedstock for both bio-ethanol and biodiesel productions. Of course, that would greatly contributes in expanding the potential application of AD solid digestate and improving the economical benefits of AD process [7, 16, 32]. Zhong, Y. et al. [33] have revealed that, although AD consumes a high proportions of organic matter in the waste, AD digestate still contains a significant amount of nutrients as well as lignocellulosic substances. This study has mainly aimed to develop an integrated system that the biogas produced is later used to power fungal fermentation and convert the existed carbon source, nutrients and water in the digestate into bio-fuel precursor-lipid. That would help in developing a fresh-water-free and energy-positive process to simultaneously utilize both solid and liquid digestate in the accumulation of fungal lipid for biodiesel production. The integrated system contains two unit operation, which are, AD and digestate utilization. Digestate utilization includes five main stages, are; digestate pretreatment, enzymatic hydrolysis for mono-sugar release, over-liming detoxification and lastly fungal fermentation for lipid accumulation. In order to release mono-sugar, the mixture of solid and liquid digestate was pre-treated at certain conditions and hydrolyzed, by alkali and enzyme respectively. In the pretreatment process, liquid digestate was used as the processing water. After releasing of mono-sugar, over-liming detoxification was applied to prepare the hydrolysate for fungal fermentation. The results have indicated that, the studied integrated system has the potential to offer optimal solutions for bio-fuel production and waste management and the fresh-water-free and energy-positive process was significantly developed to utilize solid and liquid digestate to the accumulate fungal lipid and subsequently produce biodiesel.

5 THE IMPORTANCE OF THE PRETREATMENT OF BIOMASS

Pretreatment methods are mainly classified into: physical (mechanical) such as; milling, beating, ultrasonic and collision plate pretreatment, chemical (e.g. alkaline and acid pretreatment), and biological (e.g. fungal pretreatment). Various types of pretreatment methods have been extensively investigated on the pretreatment of different types of biomass. The effectiveness of the different pretreatment methods on the biomass from even the same pretreatment group are varied from each others. For instance, a study in 2015 [34] has compared between three different mechanical pretreatment methods, are; microwave, milling and beating methods on different species of Irish seaweeds. The study has concluded that, the greatest performance in terms of methane production was achieved when beating pretreatment was applied. Whilst, the other two methods have negatively affected the digestion process. Beating pretreatment as relatively a new mechanical method was first introduced by the biomass research team in Dublin City University in 2011 based on employing Hollander beater device. This method has proved its performance in pretreatment of only few biomasses such as; seaweed, maize silage, fresh grass and potato wastes, but it is not yet widely applied. However, pretreatment is the most important step in the biomass conversion process as it has a major influence on all the other steps in the process. The optimum goal of the pretreatment process is to enhance the enzymatic hydrolysis of carbohydrates (cellulose and hemicellulose) therefore increasing the overall bioconversion efficiency for production of sugars. According to some previous studies, Alkaline pretreatment is one of the most viable process options, mainly due to its significant pretreatment effect and relatively simple process scheme. Alkaline pretreatment has a principal feature that, it selectively takes off lignin without degrading carbohydrates, and increases porosity and surface area, thereby improving enzymatic hydrolysis. Furthermore, in an integrated approach of AD and fermentation process, pretreatment plays a crucial role because the design of the subsequent saccharification and fermentation processes highly depending on the result of the pretreatment step. Thus, the following criteria should be considered for selecting the most effective and appropriate pretreatment methods: should require low capital and operational costs, require minimum size reduction of the biomass, toxic compounds produced under the pretreatment conditions should be minimum, etc. However, pretreatment method should be carefully selected and implemented prior to the combined hydrolysis of agro-industrial wastes and AD fibre which is carried out by enzymatic hydrolysis of the combined slurry [13, 35-37].

6 DISCUSSION

As previously mentioned, there will be a number of issues associated with AD when it is applied extensively. These issues have made the investment in AD less attractive and not economically feasible. These issues are categorized into operational, economical and environmental issues. Generally, there are number of operational factors must be considered in advance to be avoided. These factors can result in a failure or poor in the operational stability of the system such as: inadequate operational management, lack of process control, external disturbances, and others. In addition, personnel qualifications is considered another operational factor should be taken into account to professionally monitor and control the system. Economically, as the biogas is the single main product of AD, the production of AD biogas can be not economically competitive with its counterparts due to: 1. the amount of energy consumed in AD process especially, the energy consumed in the pretreatment and digestion and, 2. the fluctuation of fossil fuel price indexes. The production of more bioproducts could be a significant solution for increasing the economical viability of AD. While, the environmental issues lie in the accumulation and the improper handling of the huge amount of digestate which can lead to serious environmental issues. Practically, there are some ways to overcome the environmental issues, one of these ways is to utilize the digestate in other applications. As aforementioned, anaerobic microbes can convert only from 40 to 60 % of carbon into methane. AD digestate contains significant quantity of nutrients and lignocellulose materials which has not been digested in the digestion process. Thus, making a use of the digestate to produce biofuel or bioproducts would greatly contribute in overcoming the AD economical and environmental issues. On the other hand, as the digestate still contain undigested materials, it is required to be pretreated. Pretreatment step is the most important step as the other following steps in the biomass conversion processes are relying on its results. Thus, pretreatment method must be selected based on the aforementioned criteria in section 5. However, the integration approach corresponds to the refinery concept. It is incorporating conversion processes to produce multiple bioproducts. Many integration approaches of the biomass conversion processes have confirmed their potentials in previous studies. This approach could help in making a full use of byproducts and biomass, increasing the economical profit, minimizing the wastes, producing biofuel and high-value bio-based products simultaneously and improve the industrial values of the production of biofuels. Regarding to the production of biodiesel, various studies have proved the capability of the residual biomass to be used as animal feed or feedstock for AD. The glycerine extracted from biodiesel production process can be considered as byproducts and used further in different applications i.e.; soap making. While, the digestate can be used as a biofertilizer or soil amendment in agricultural applications. However, much attentions have been paid recently towards the development of integrated approaches as it can be a significant and radical solutions for AD issues. But, more studies are still required to exploit more biomass other than the conventional ones in order to discover and produce more byproducts and bioproducts. The successful application of the integration approach on the non-conventional biomass would certainly contribute in making AD prosper and the investment in it much more attractive. A substantial positive changes will be clearly noted when this system proves its effectiveness and capability to prosper.

7 CONCLUSION

Biodiesel is a promising liquid biofuel. Integration approach of producing biofuel, bioproducts and high-value bio-based products from AD fibre is a new approach. Investigation the effectiveness of more pretreatment methods on AD fibre prior to the enzymatic hydrolysis are strongly needed for further studies. That can be accomplished by comparing the pretreatment methods which have been applied in previous studies with other methods. However, scientific literatures on the production of lignocellulosic biodiesel through integration system are relatively low. An integration approach has the potential to offer optimal solutions for biofuel production and waste management. But, to end up with better integration system, more investigations regarding to several aspects such as; feedstocks used, pretreatment technique, economic analysis, agro-industrial waste applied and others are highly required.

ACKNOWLEDGEMENTS

The authors gratefully acknowledge Saudi Cultural Bureau for funded the study and Dublin City University for providing the appropriate environment and an easy access to enormous number of scientific publications.

REFERENCES

[1] Department of Eco. and Soc. Affair., World population prospects: the 2015 revision. UN, New York, 2015.

[2] Goswami, D. Yogi, Kreith, F., *Energy Efficiency and Renewable Energy Handbook*, CRC press, 2015.
[3] Saxena, R.C., Adhikari, D.K. and Goyal, H.B., Biomass-based energy fuel through biochemical routes: A review, *Renewable and sustainable energy reviews*, Vol. 13, pp. 168-170, 2007.
[4] Katuwal, H. and Bohara, Ak., Biogas: A promising renewable technology and its impact on rural households in Nepal. *Renewable and sustainable energy reviews*, Vol. 13, pp. 2668-2674, 2009
[5] Zabed, H., et al., Fuel ethanol production from lignocellulosic biomass: An overview on feedstocks and technological approaches, *Renewable and Sustainable Energy Reviews*, Vol. 66, pp. 751-774, 2016.
[6] Zhao, J. and Xia, L., Ethanol production from corn stover hemicellulosic hydrolysate using immobilized recombinant yeast cells, *Biochemical Engineering*, Vol. 49: pp. 28–32, 2010.
[7] Teater, C., et al., Assessing solid digestate from anaerobic digestion as feedstock for ethanol production, *Bioresource Technology*, Vol. 102, pp. 1856–1862, 2011.
[8] Yue, Z., et al., sustainable pathway of cellulosic ethanol production integrating anaerobic digestion with biorefining, *Biotechnology and Bioengergy*, Vol. 105, pp. 1031–1039, 2010.
[9] Pandey, A., et al., *Industrial Biorefineries and White Biotechnology*, Elsevier, 2015.
[10] Van Den Hende, S., Laurent, C. and Bégué, M., Anaerobic digestion of microalgal bacterial flocs from a raceway pond treating aquaculture wastewater: need for a biorefinery, *Bioresource. Technology*, Vol. 196, pp. 184–193, 2015.
[11] Sawatdeenarunat, C., et al., Review; Anaerobic biorefinery: Current status, challenges, and opportunities. Bioresource Technology, Vol. 215, pp. 304-313, 2016.
[12] Ruan, Z., et al., Co-hydrolysis of lignocellulosic biomass for microbial lipid accumulation, *Biotechnology Bioengineering*, Vol. 110, pp. 1039–1049, 2013
[13] Agustini, L., et al., Isolation and characterization of cellulase-and xylanase-producing microbes isolated from tropical forests in Java and Sumatra, *International Journal Environment Bioengergy*, Vol. Vol. 3, pp. 154–167, 2012
[14] Wang, D., et al., Enhancing ethanol production from thermophilic and mesophilic solid digestate using ozone combined with aqueous ammonia pretreatment, *Bioresource Technology*, Vol. 207, pp. 52-58, 2016.
[15] Dahlin, J., Herbes, C. and Nelles, M., Biogas digestate marketing: qualitative insights into the supply side, *Resources, Conservation and Recycling*, Vol. 104, pp. 152–161, 2015.
[16] Zhong, Y., et al., A self-sustaining advanced lignocellulosic biofuel production by integration of anaerobic digestion and aerobic fungal fermentation, *Bioresource Technology*, Vol. 179, pp. 173-179, 2015.
[17] Jinlin, X., Tony, E. G. and Alan, C. H., Effect of biodiesel on engine performances and emissions, *Renewable and sustainable energy reviews*, Vol. 15, pp. 1098-1116, 2011.
[18] Mussatto, S.I., et al., Technological trends, global market, and challenges of bio-ethanol production, *Biotechnology Advances*, Vol. 28, pp. 817–830, 2010.
[19] Demirbas, A., Progress and recent trends in biofuels, *Progress in Energy and Combustion Science*, Vol. 33, pp. 1-18, 2007.
[20] Demirbas, A., Biofuels securing the planet's future energy needs, *Energy Conversion and Management*, Vol. 50, pp. 2239-2249, 2009.
[21] Balat, M. and Balat, H., Recent trends in global production and utilization of bioethanol fuel, *Applied Energy*, Vol. 86, pp. 2273–2282, 2009.
[22] Demirbas, A., Competitive liquid biofuels from biomass, *Applied Energy*, Vol. 88, pp. 17–28, 2011.
[23] Al Seadi, T., Good practice in quality management of AD residues from biogas production. Report made for the International Energy Agency, 2001.
[24] Fabien, M., An Introduction to the Anaerobic Digestion of Organic Waste. pp. 17-38, 2003.
[25] Jensen, J. K. and Jensen, A. B., Danish bioenergy for the world, *Proc. Conf. On First world conference and exhibition on biomass for energy and industry*, Sevilla, 2000.
[26] Zorn, S., Biogas, Available online at www.folkecenter.dk/mediafiles/folkecenter/pdf/biogas-upgrading-corrected.pdf. Accessed in March, 2017.
[27] Yukawa, H., Vertes, A. A. and Blaschek, H. P., *Biomass to biofuels: Strategies for global industries*, Wiley, 2010.
[28] Khanal, S. K., Surampalli, R. Y., Zhang, T. C., Lamsal, B. P.,Tyagi, R. D. and Kao, C. M., *Bioengergy and biofuel from biowastes and biomass*, Reston, 2010
[29] Browne, J., et al., Assessing the cost of biofuel production with increasing penetration of the transport fuel market: A case study of gaseous biomethane in Ireland, *Renewable and Sustainable Energy Reviews*, Vol. 15, pp. 4537-4547, 2011.
[30] Kumar, S., *Biogas*, In Tech., 2012.
[31] Show, K-Y. and Guo, X., *Industrial Waste*, InTech., 2012.
[32] Mohan, S.V., et al., Ecologically engineered system (EES) designed to integrate floating, emergent and submerged macrophytes for the treatment of domestic sewage and acid rich fermented-distillery wastewater: evaluation of long term performance, *Bioresource Technology*, Vol. 10, pp. 3363–3370, 2010.
[33] Zhong, Y., et al., Fungal fermentation on anaerobic digestate for lipidbased biofuel production, *Biotechnology for Biofuels*, Vol. 9, pp. 1-11, 2016.
[34] Montingelli, M., Development & application of a mechanical pretreatment to increase the biogas produced from Irish macroalgal biomass, DCU, Ireland, 2015.
[35] Mosier, N., et al., Features of promising technologies for pretreatment of lignocellulosic biomass, *Bioresource Technology*, Vol. 96, pp. 673–686, 2005.
[36] Alvira, P., Tomás-Pejó, E., Ballesteros, M. J. and Negro, M. J., Pretreatment technologic for an efficient bioethanol production process based on enzymatic hydrolysis: a review, *Bioresource Technology*, Vol. 101, pp. 4851–4861, 2010.
[37] Yang, B. and Wyman, C.E., Pretreatment: the key to unlocking low-cost cellulosic ethanol, *Biofuels Bioproducts & Biorefiniery*, Vol. 2, pp. 26-40, 2008.

MODELING OF COMPLEX MASS AND HEAT TRANSFER TRANSITIONAL PROCESSES OF DISPERSED WATER DROPLETS IN WET GAS FLOW IN THE FRAMEWORK OF HEAT UTILIZATION TECHNOLOGIES FOR BIOFUEL COMBUSTION AND FLUE GAS REMOVAL

G. Miliauskas [1], M. Maziukienė[1], H. Jouhara[2] and R. Poškas[1,3]

1. Department of Thermal and Nuclear Energy, Faculty of Mechanical Engineering and Design, Kaunas University of Technology, Kaunas, Lithuania; email: gintautas.miliauskas@ktu.lt
2. College of Engineering, Design and Physical Sciences, Institute of Energy Futures, Brunel University London, UK; email: Hussam.Jouhara@brunel.ac.uk
3. Nuclear Engineering Laboratory, Lithuanian Energy Institute, Kaunas, Lithuania; email: Robertas.Poskas@lei.lt

ABSTRACT

This paper presents an analysis of complex processes on water droplet heat and mass transfer in a sequential cycle of condensing, transitional evaporation and equilibrium evaporation regimes of phase change on the surface of droplets. The change in the regimes is connected to the dynamics of the surface temperature of a heated droplet. The dynamics are defined according to a numerical iterative scheme which is based on the heat flow balance on the droplet surface. The scheme combines energy flows of external heat transfer and phase change as well as internal heat transfer in a droplet. The role of the droplet slipping in the flue gas and of the factors of the radiation flow absorbed in the flue gas within the interaction of complex transitional transfer processes was defined based on the results of the numerical investigation in the cycle of the phase change of water droplets performed in the conditions typical for biofuel furnaces and heat utilization technologies for flue gas removal.

Keywords: water droplets, heat and mass transfer, condensation and transitional evaporation regimes of phase change, numerical modeling

1 INTRODUCTION

Heat and mass transfer processes in liquid droplets are the basis for a number of energy and industrial technologies [1-3]. Understanding the thermal hydrodynamical processes of water droplets and their control is essential in order to optimize existing liquid dispersion technologies and to develop modern, more efficient ones. The issue here is that complex transfer processes in two-phase droplets and gas flows happen under conditions of intensive interaction. The level of the interaction intensity is determined by a number of factors, and the most important are the following: the influence of the Stefan's hydrodynamic flow on the convective heating and evaporation of droplets, the influence of water droplet slipping in the flow on the external heat transfer and on the forced liquid circulation within the droplets, and the spectral nature of radiation. The optical spectral effects of light on the surface of droplets define the intensity of the radiation flow absorption in a semi-transparent liquid. Spectral radiation models [4-8] allow the evaluation of the radiation input in the energy state of semi-transparent droplets. A proper knowledge of water spectral characteristics leads to a successful application of these models when defining radiation absorption in water droplets [9, 10]. In heat transfer and phase change thermal technologies, the variety of process conditions requires a systematic view in order to define the regularities of process interaction. For this purpose, the heat and mass transfer analysis of dispersed liquid droplets is a convenient tool in the regime cycle of consistently changing phase transitions. In the general case, the phase change cycle of water droplets dispersed in a wet gas flow will consist of condensation, transitional evaporation, and equilibrium evaporation regimes. The heating of droplets in the condensation regime is very intensive. In the transitional evaporation regime, the droplets are heated to a thermal state that ensures equilibrium evaporation. When such a state is reached, all heat is used for the water evaporation. The equilibrium evaporation regime of a droplet plays an important role in technologies based on liquid evaporation, and thus has been thoroughly investigated [11]. The transitional evaporation regime of a droplet has been widely investigated in fuel dispersion technologies [12]. This study has numerically modeled the transitional phase change of water droplets in a wet gas flow in the case of complex heating by

radiation and convection. The determination of droplet heat transfer boundary conditions helps to retain the aspects of water dispersion in a biofuel furnace and of the utilization of waste heat from the flue gas in a condensing shell and tube heat exchanger.

2 METHODOLOGY

Water dispersion can be used to regulate the biofuel combustion process in a furnace, to clean solid particles from the flue gas as well as to cool and wet it so that the process in a condensing shell and tube heat exchanger can be effective. In contact type condensing shell and tube heat exchangers, heat is recovered from the flue gas by condensing water vapor directly onto the dispersed water droplets. For such a technology, it is usually necessary to control the droplet heating to the dew point temperature and to use a transitional heat exchanger, the operation of which is usually burdened by condensate polluted with biofuel ash particles. In such types of condensing shell and tube heat exchangers, the vapor is condensed while the biofuel flue gas is flowing through the pipes, and thus the fluid flowing at the outside of the pipes receives heat through the wall. This technology requires optimal vapor condensation. Vapor condensation is a very complex process because of thermo-hydro-dynamical interaction processes between the polluted flue gas and the condensate's film. In order to improve those processes, water is dispersed additionally over the stack of the pipes. In these cases, consideration should be given to the heating of the dispersed water droplets and transitional phase change processes taking place at their surface. A complex analysis of droplet external and internal heat transfer and of phase change processes at the droplets' surfaces is necessary for the determination of the interaction between the dispersed water and the biofuel flue gas energy. R^+ and R^- radii relatively determine the external and internal surface of spherical droplets. In the case of complex heating, the total heat flux is determined by radiation and convective components, $q_\Sigma^+ = q_r^+ + q_c^+$ and $q_\Sigma^- = q_r^- + q_c^-$, respectively. In condensation $\tau \equiv 0 \div \tau_{co}$, transitional evaporation $\tau \equiv \tau_{co} \div \tau_{tf}$, and equilibrium evaporation $\tau \equiv \tau_{tf} \div \tau_f$, the relation of the heat fluxes at the surface of a droplet is:

$$\begin{aligned} q_\Sigma^-(\tau) &= q_\Sigma^+(\tau) + q_f^+(\tau), \text{ when } \tau \equiv 0 \text{ to } \tau_{co}, \\ q_\Sigma^-(\tau) &= q_\Sigma^+(\tau) - q_f^+(\tau), \text{ when } \tau \equiv \tau_{co} \text{ to } \tau_{tf}, \\ q_\Sigma^-(\tau) &= q_f^+(\tau) - q_\Sigma^+(\tau), \text{ when } \tau \equiv \tau_{tf} \text{ to } \tau_f. \end{aligned} \tag{1}$$

The magnitude of the total heat flux at the surface of the droplets determines the intensity of the complex external heating. The magnitude of the heat flux determines the energy intensity of the phase change at the droplet surface. The density of the total heat flux at the droplet surface internal side determines the heating intensity in the water droplets. In the condensation regime, the whole of the heat flux passed onto the droplet surface heats the water, while in the transitional evaporation regime it is only the part of the heat flux that is excluded from the evaporation process. In the equilibrium evaporation regime, the water is evaporated by the heat from the external heat transfer; the change in the enthalpy of cooling droplets may also take place in the process. Spectral light absorption indicators for water are finite [9]; therefore, it is assumed that water droplets do not absorb radiation through their surface and $q_r^- \approx q_r^+$. The external heat transfer convective flux of a droplet is described according to the model [13], where additionally the universal Spalding heat transfer B_T equation is adopted to phase change regimes according to the methodology in [14]:

$$q_c^+ = \left[\frac{\lambda_{vg}}{R} \frac{\ln(1+B_T)}{B_T} + \frac{\lambda_{vg}}{2R} \frac{0.552\,\mathrm{Re}^{1/2}\,\mathrm{Pr}^{1/3}}{(1+B_T)^{0.7}} \right] (T_g - T_R), \quad B_T = \frac{c_{p,vg}(T_g - T_R)}{L} \left(1 + \frac{q_c^-}{q_c^+} \right). \tag{2}$$

To describe the heat flux of phase change, the analytical model [15] for vapour flux density is applied:

$$q_f^+ = m_v^+ L, \; m_v^+ = \frac{D_{vg}\mu_v}{T_{vg,R} R_\mu R} p \left[p_{v,R} - p_{v.\infty} + \frac{\mu_v}{\mu_{vg}} \left(\ln \frac{p - p_{v.\infty}}{p - p_{v.R}} - p_{v,R} + p_{v.\infty} \right) \right]. \tag{3}$$

The convective component of the total heat flux in a droplet is defined according to the modified Fourier's law:

$$q_c^-(\tau) = -\lambda_{l,ef}\, grad T_{r \equiv R^-}, \tag{4}$$

where the effective thermal conduction coefficient $\lambda_{l,ef} \equiv \lambda_l k_c^-$ is used to take into account the influence of water circulation on heat transfer within the droplet according to the methodology in [13]. In equation (4), the

temperature field gradient is defined by conductivity and radiation in a semi-transparent spherical droplet for the case described by the transcendental system of differential and integral equations:

$$\rho_l c_p \frac{\partial T}{\partial \tau} = \frac{1}{r^2}\frac{\partial}{\partial r}\left(\lambda_l \frac{\partial T}{\partial r} - q_r\right), \tag{5}$$

$$q_r = \int_0^{\infty}\int_0^{\pi}\int_0^{2\pi} I_\omega \sin\Theta\cos\Theta d\Theta d\varphi d\omega,\ \ \frac{\partial I_\omega}{\partial s} = \chi_\omega\left[n_\omega^2 I_{\omega 0} - I_\omega\right],\ \ \chi_\omega = 4\pi k_\omega\omega,\ \ \bar{n}_\omega = n_\omega - ik_\omega. \tag{6}$$

The equation system (1–6) can be solved only using an iterative method, so that unambiguous conditions for the equations (5, 6) can be formulated with regard to the yet unknown functions of the droplet surface temperature and spectral radiation intensity at the internal surface of the droplet $I_{\omega R}(\tau)$:

$$R(\tau\equiv 0) = T_{l,0};\ T_l(\tau\equiv 0) = T_{l,0};\ \ T(r\equiv R^-,\tau) = T_R(\tau);\ I_\omega(r\equiv R^-,\tau) = I_{\omega,R^-}(\tau),\ \ \partial T(r\equiv 0,\tau)/\partial r = 0. \tag{7}$$

A combined analytical-numerical method is applied to solve the system (5-7). Analytically, the transfer cases (5) and (7) as well as (6) and (7) are analyzed independently. In the first case, the function of the local radiation flux $q_r(r,\tau)$ is assumed to be defined, and in the second case, the function describing the non-stationary temperature field in a droplet $T(r,\tau)$ is assumed to be defined. Using the auxiliary function $\vartheta(r,\tau) = r[T(r,\tau) - T_R(\tau)]$, the (5) and (6) system is transformed into the Dirichlet heat transfer case with the defined source function [6], and the temperature field gradient in the expression (4) is described by an infinite line of integral equations:

$$\left.\frac{\partial T}{\partial r}\right|_{r\equiv R^-} = \frac{2\pi}{R^2}\sum_{n=1}^{\infty} n\int_o^{\tau}\left[\frac{R}{n\pi}\frac{dT_R}{d\tau} - \frac{1}{c_{p,l}\rho_l}\int_0^R q_r\cdot\left(\sin\frac{n\pi r}{R} - \frac{n\pi r}{R}\cos\frac{n\pi r}{R}\right)dr\right]\exp\left[-a\left(\frac{n\pi}{R}\right)^2(\tau-\tau_*)\right]d\tau_*. \tag{8}$$

In the case of the defined radial function $T(r)$ describing the temperature field in a droplet, the function of the local radiation flux $q_r(r)$ in equation (8) is calculated using the [6] methodology that takes into account spectral light effects at both sides of the droplet surface, droplet radiation, and external source radiation when the external source is assumed to be a black body with a biofuel flue gas temperature.

The dynamics of the droplet movement in the gas flow and the change in the droplets' mass and volume are defined by the following equations:

$$\frac{dw_l(\tau)}{d\tau} = \frac{3}{8}\frac{C_l(\tau)}{R(\tau)}\frac{\rho_g(\tau)}{\rho_l(\tau)}\frac{w_g(\tau)-w_l(\tau)}{\left[w_g(\tau)-w_l(\tau)\right]^{-1}},\qquad \frac{dM_l(\tau)}{d\tau} \equiv \frac{4\pi}{3}\frac{d\left[\rho_{l,m}(\tau)R^3(\tau)\right]}{d\tau} = -g_v = -4\pi R^2(\tau)m_v^+(\tau). \tag{9}$$

In respect of the time function $T_R(\tau)$ of the droplet surface temperature, the system of the algebraical and integral equations (1–4, 7–9) is solved numerically according to the iterative scheme using the fastest descending method. In order to form the numerical scheme, the non-dimensional coordinates for radius $\bar{r} = r/R(\tau)$ and time $\bar{\tau} = \tau/\tau_{co}$ are introduced (if there is no condensation regime, then $\bar{\tau} = \tau/\tau_{tf}$). The coordinates ensure that the droplet radius equals 1 ($\bar{r}(R,\tau)=1$), and that the duration of the first phase change regime is also 1. Variation steps of the radial and time coordinates are defined as:

$$\Delta\bar{\tau} = \frac{1}{I-1},\ \ \Delta\bar{r} = \frac{1}{J-1},\ \ \sum_{i=2}^{I}\left(\bar{t}_i - \bar{t}_{i-1}\right) = 1,\ \ \sum_{j=2}^{J}\left(\bar{r}_j - \bar{r}_{j-1}\right) = 1. \tag{10}$$

For every time step starting with the second one – $\tau_i = \tau_i + \Delta\bar{\tau}\cdot\tau_{co}$, the iterative $it \subset 1\div IT$ cycle proceeds to define the instantaneous temperature $T_{R,i} \equiv T_{R,i,IT}$ of the droplet surface. The droplet surface temperature $T_{R,i,it=IT}$ attributed to the final iteration must ensure that the calculated heat fluxes would fulfill the condition of the expression (1) with a maximum error of five hundredths of a percent.

The droplet heat and mass transfer parameters $R_{i,it}$, , $q_{c,it}^+$, $q_{c,it}^-$ and $T_{i,j,it}$ that are necessary for an it iteration however are not yet defined; they are used from $it-1$ iteration calculated parameters $P_{i,it} \equiv P_{i,it-1}$. The mesh $I = 21,\ J = 41$ is used in the numerical modeling; the radiation spectrum is gradually divided into $M-1=100$ parts according to the wave number $\omega \equiv 10^3$ to $1.25\cdot 10^6$, and the (8) expression retains $\infty \equiv N = 121$. For the surface temperature $T_{R,i,IT}$, all instantaneous P_i parameters of the droplet heat and mass transfer are calculated.

3 RESULTS

In Figures 1-3 the biofuel flue gas is defined by the velocity $w_g = 15\,\text{m/s}$, the temperature T_g and humidity of $\bar{p}_v \equiv p_v / p = 0.2$ when $p = 0.1\,\text{MPa}$. The dispersion of the $T_l = 306\,\text{K}$ temperature water is defined by the dispersion of droplets $2R\cdot \equiv 25;\ 50; 100 \text{ and } 200\,\mu\text{m}$ and their initial velocity $w_l = 65\,\text{m/s}$. The relative water flow rate is assumed to be $G_l / G_g \to 0$, and therefore the air flow parameters in time are invariable.

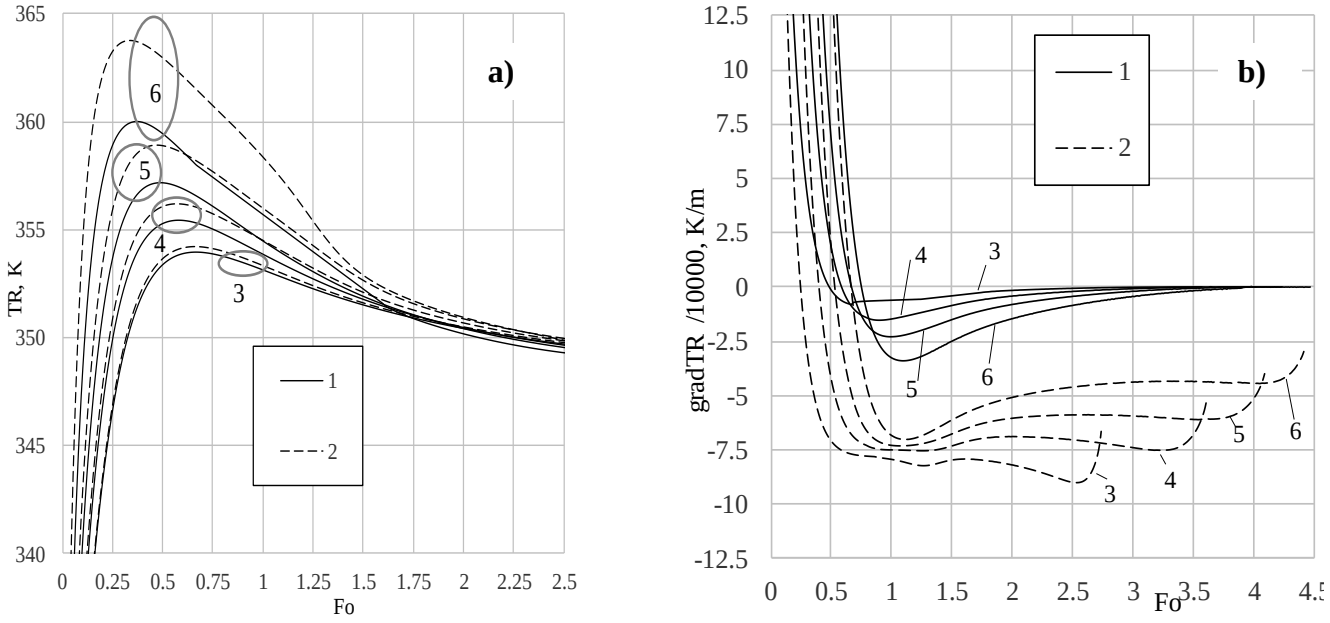

Fig. 1. The influence of the water droplet size on their surface heating at high temperature $T_g = 1073\,\text{K}$ and in air of $\bar{p}_v = 0.2$ humidity (a) and on the gradient variation in the temperature field within the droplets (b) in the case of convective (1) and complex (2) heating. $R_0 \times 10^6, \text{m}$: (3) 25, (4) 50, (5) 100, (6) 250; $T_{l,0} = 303\,\text{K}$; $w_{l,0} = 65\,\text{m/s}$; $w_g = 15\,\text{m/s}$.

The droplet heating is defined by the Reynolds criterion $\text{Re} = 2R\rho_g \left| w_l - w_g \right| / \gamma_{vg}$ and by the radiation source parameter $\bar{T}_{sr} = T_{sr} / T_g$: in the case of convective heating it is $\bar{T}_{sr} = 0$, and in the case of complex heating it is $\bar{T}_{sr} = 1$. The results have been analyzed in the time scale of the Fourier criterion $\text{Fo} = \left(a_0 / R_0^2\right) \cdot \tau$ where the individual multiplier $a(T_l = 278\,K) / R_0^2$ ensures a more convenient graphical $P(\text{Fo})$ interpretation of time functions $P(\tau)$ for droplets of different sizes [14]. The most important factors are droplet slipping in the air flow and radiation absorption within the droplets (Fig. 2). The droplet slipping defines the intensity of the external convective heating. The slipping significantly influences the transitional phase change regime because the droplet slipping slows down quickly due to resistance forces (Fig. 2a). In the case of bigger droplets, the convective heat transfer was of a higher intensity, although the initial slipping velocity was the same. The local radiation flow in the droplets depends on their dispersity (Fig. 2b).

The most essential changes in the radiation dispersion were observed at the final stage of the equilibrium evaporation due to the smaller droplets. The big droplets absorb the radiation intensively at the surface layers of the water. In the smaller droplets, optical effects at the internal surface have a greater influence, and thus the absorption within these droplets is clearly non-linear. It is interesting that the suitable conditions for the radiation to join the water evaporation process form only in the transitional evaporation regime when the negative temperature gradient field forms within the droplets (Fig. 1 b). Then a part of the radiation absorbed by the internal heat convection starts moving towards the droplet surface and it completely disappears during the equilibrium evaporation. The factors of slipping and radiation absorption define the parameters of droplet phase change (Fig. 3). The droplets grow due to condensation and water expansion (Fig. 3 a). At the beginning of the evaporation, the droplets still are growing, but when the evaporation dominates against the expansion, the droplets start to decrease. At a high temperature, the condensation is weak, the vapor flow becomes smaller

and soon gains the zero value. In the transitional regime it grows quickly, and during the equilibrium evaporation, it gradually becomes smaller again (Fig. 3 b).

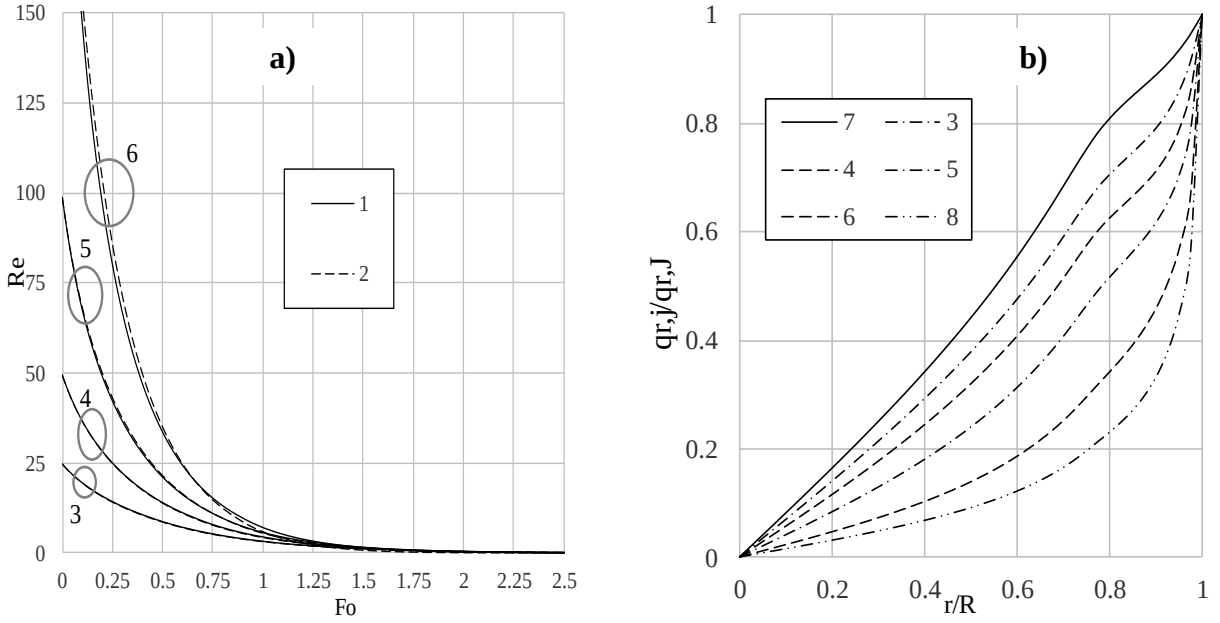

Fig. 2. Variation of the Reynolds number (a) and the local radiation flux in the droplets (b). $R_0 \times 10^6$, m: (7) 10, (8) 500; $q_{r,J}$, kW/m^2: (3)53.78, (4), 63.64, (5) 71.31, (6) 77.93, (7) 39.77, (8) 81.19; other as in Fig.1.

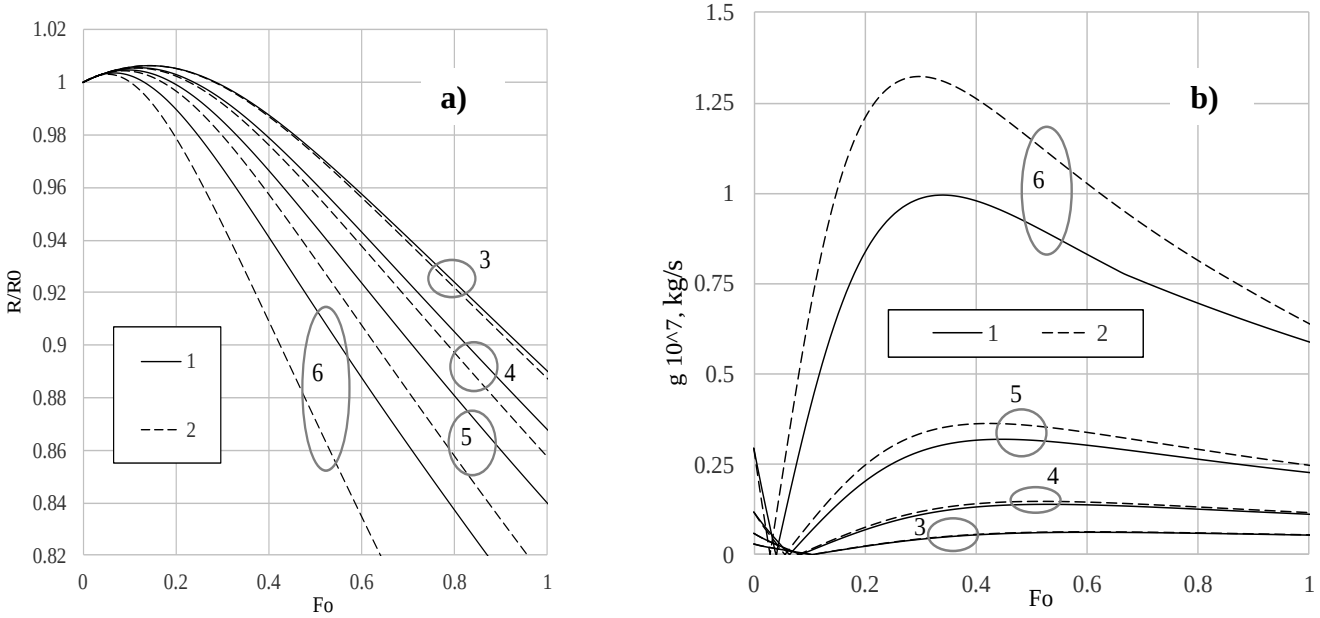

Fig. 3. Variation of droplet radius (a) and vapor flow (b). Boundary conditions as in Fig. 1.

4 CONCLUSIONS

The regularities of the phase change regimes of the water droplets dispersed in a wet gas flow are defined by the temperature and humidity of the gas as well as the droplet dispersity and their heating process. When water is dispersed into the high temperature flue gas of a biofuel furnace, the heating of the droplets is defined by radiation and droplet slipping factors. During the recovery process of waste heat from the flue gas, the flue gas temperature before the shell and tube heat exchangers is much lower than in the boiler furnace, yet the humidity is the same. For this reason, the thermal state of the equilibrium evaporation of the dispersed droplets is defined by the humidity of the flue gas, and the condensation regime duration becomes longer in the regime of transitional phase change. A higher slipping velocity of droplets means more intensive heating; however, the water circulation in the droplets is more intensive due to friction forces, and thus heat removal to the centre of the droplet intensifies and the surface layer heating slows down. This gives the necessary conditions for the

duration of the condensation regime to become longer, which is convenient talking about the increased efficiency of the utilization of phase change heat from the biofuel flue gas.

NOMENCLATURE

B_T is the Spalding transfer parameter; C_l is the droplet drag coefficient; *D* the mass diffusivity, m^2/s; *Fo* is the Fourier number; *g* is the vapor mass flux, kg/s; I_ω is the spectral intensity of radiation, W/(m steer); k_c is the effective conductivity parameter; k_ω is the spectral index of absorption; *L* is the latent heat of evaporation, J/kg; *m* is the vapor mass flux density, $kg/(m^2s)$; *M* is mass, kg; n_ω is the spectral index of refraction; $\bar{n}_\omega$ is the complex's spectral index of refraction; *Nu* is the Nusselt number; *p* is pressure, Pa; *P* is the symbol of free parameter in heat-mass transfer; *Re* is the Reynolds number; *Pr* is the Prandtl number; *q* is heat flux, W/m^2; *r* is a radial coordinate, m; *R* is the radius of a droplet, m; R_μ is the universal gas constant J/(kmol K); *T* is temperature, K; vapor mass flux, kg/s; *w* is velocity, m/s; **Greek symbols:** *a* is thermal diffusivity, m^2/s; μ is molecular mass, kg/kmol; λ is thermal conductivity, W/(m K); ρ is density, kg/m^3; τ is time, s; γ is dynamics viscosity, Pa s; θ is the angle between the opposite direction of the normal to the surface and the incident beam, rad; φ is the azimuthal angle, rad; χ_ω is the spectral coefficient of absorption, m^{-1};. **Subscripts**: *c* means "convective"; *f* means "phase change"; *g* means "gas"; *i* is the time index in a digital scheme; *it* means "number of iteration"; *I* means "index of control time"; *j* means "index of radial coordinate"; *J* means "index of droplet surface"; *co* means "condensation"; *l* means "liquid"; *m* means "mass average"; *tf* means "transit phase transformation regime"; *r* means "radiation"; *R* means "droplet surface"; *sr* means "radiation source"; *v* means "vapour"; *vg* means "vapor-gas mixture"; ω means "spectral"; Σ means "total"; 0 means "initial state"; ∞ means "far from a droplet"; + means "external side of a droplet surface"; - means "internal side of a droplet surface".

REFERENCES

[1] A Abdel-Salam A. H., Simmson J. C., State-of-the-art in liquid desiccant air conditioning equipment and systems, *Renewable and Sustainable Energy Reviews*, Vol 58, pp. 1152-1183, 2016.
[2] Bucklin J. M., Mitigation of industrial hazards by water spray curtains, *Journal of Loss Prevention in the Process Industries*, Vol. 50, pp. 91-100, 2017.
[3] Paepe W., Carrero M., Bram S., Contino F., Parente A., Waste heat recovery optimization in micro gas turbine applications using advanced humidified gas turbine cycle concepts, *Applied Energy*, Vol. 207, pp. 218-229, 2017.
[4] P. L. C. Lage, C. M. Hackenberg, R. H. Rangel, Nonideal Vaporization of Dilating Binary Droplets with Radiation Absorption**,** *Combustion and Flame*, Vol. 101, pp. 36–44, 1995.
[5] L. A Dombrovsky, S. S Sazhin, E. M. Sazhina, G. Feng, M. R. Heikal, M. E. A. Bardsley, Heating and evaporation of semi-transparent diesel fuel droplets in the presence of thermal radiation, *Fuel*, Vol. 80, pp. 1535–1544, 2001.
[6] G. Miliauskas, Regularities of unsteady radiative-conductive heat transfer in evaporating semi-transparent liquid droplets, *International Journal of Heat and Mass Transfe*r, Vol. 44, pp. 785–798, 2001.
[7] C. C. Tseng, R. Viskanta, Enhancement of water droplet evaporation by radiation absorption, *Fire Safety Journal*, Vol. 41, pp. 236-247, 2006.
[8]. M. Q. Brewster, Regularities of unsteady radiative-conductive heat transfer in evaporating semi-transparent liquid droplets, *International Journal of Heat and Mass Transfe*r, Vol. 44, pp. 785–798, 2015
[9] G. M. Hale, M. R Query, Optical constants of water in the 200-nm to 200-nm wavelength region, *Applied Optics*, Vol. 12, pp. 555–562, 1973.
[10] G. M. Hale, M. R Query, A.N. Rusk, D. Williams, Influence of temperature on the spectrum of water, *J. Opt. Soc. Am.*, Vol. 62, pp. 1103–1108, 1972.
[11] W. A. Sirignano, Fluid Dynamics and Transport of Droplets and Sprays, *Cambridge University Press*, p. 311, 1999.
[12] S. S. Sahin, Droplets and Sprays, *Springer*, p. 352, 2014.
[13] B. Abramzon, W. A. Sirignano, Droplet vaporization model for spray combustion calculations, *International Journal of Heat and Mass Transfer*, Vol 32, pp 1605-1618, 1989.
[14] Miliauskas G., Maziukiene M., Ramanauskas V., Puida E., The defining factors of the phase change cycle of water droplets that are warming in humid gas, *International Journal of Heat and Mass Transfer*, Vol 113, pp 683-703, 1917.
[15] A. V. Kuzikovskij, Dynamics of spherical particle powerful optical field, *Izv. VUZ Fizika*, Vol. 5, pp. 89–94, 1970.

DETERMINING HIGH PROTEIN CONCENTRATION YIELD FROM BAKER'S YEAST HOMOGENIZATION WITH PRESSURE, TEMPERATURE, NUMBER OF CYCLES AND DILUTION RATIOS AS UNDERLYING PARAMETERS

Leonard E. N. Ekpeni[1], Brian Corcoran[2], Joseph Stokes[3], Abdul G. Olabi[4]

1. School of Mechanical and Manufacturing Engineering, Dublin City University, Dublin 9, Ireland. email: Leonard.ekpeni3@mail.dcu.ie
2. School of Mechanical and Manufacturing Engineering, Dublin City University, Collins Avenue, Dublin 9, Ireland. email: Brian.Corcoran@dcu.ie
3. School of Graduate Studies, Dublin City University, Dublin 9, Ireland. email: Joseph.t.Stokes@dcu.ie
4. School of Engineering, University of the West of Scotland, Paisley Campus, Paisley, PA1 2BE, Scotland, UK. email: Abdul.Olabi@uws.ac.uk

ABSTRACT

Recent studies have shown improvement in the use of Baker's yeast in medicine and other branches of sciences including engineering and this cannot be underestimated due to its pivotal role in the developmental needs of human existence. Commercial *Saccharomyces cerevisiae,* a strain of yeasts otherwise known as Baker's yeast has without a doubt seen huge growth in the market of industrial yeasts because of the need of the strain affording better performance or requiring use in new applications. These strains of yeast importance are because of the higher contents of protein contained in it and improving on this protein content requires liberating this substrate through the disruption of the cell wall using the mechanical means of the high-pressure homogenizer (HPH). This will require being disrupted at high enough pressure (30 - 90 MPa) over several cycles (passes) to have the innermost content to be fully liberated and at some temperature conditions with dilution ratios for optimum yield of protein concentration. This research work, therefore analyze and consider these parameters for a highly-improved protein concentration yield after fully homogenized.

Keywords: Yeast strain; Protein concentration; *Saccharomyces cerevisiae;* Substrate; HPH

1. INTRODUCTION

By and large, baker's yeast (*Saccharomyces cerevisiae*) is now seen as one of the fastest growing organism to offset other microorganisms and lignocellulosic materials for energy production. This is due to its highly protein concentration rate that increases with its high gassing power. Saccharomyces cerevisiae another name for Baker's yeast is considered as one of the widely industrially used microorganisms in microbial production of proteins, chemicals and metabolites [1]. Nandy & Srivastava [1] further explained that this is because genetic manipulation of S. cerevisiae is relatively easy and established with large collection of genetic tools compared to other microorganisms. The current energy need requires more feasible source for energy development and improvement to continually meet the needs of the growing and teaming population of the world. Baker's yeast as other biomass substrates for bioenergy production, have set that standard. For example, Bioethanol; a household name of energy product mostly used as biofuel worldwide has been asserted by Azhar *et al.* [2] to have significantly contributed to the reduction of crude oil consumption and environmental pollution. As detailed, it can be produced from various types of feedstocks such as sucrose, starch, lignocellulosic and algal biomass through fermentation process by microorganisms. In comparison with other biomass substrates including lignocellulosic materials and marine products, Saccharomyces cerevisiae is regarded as the common microbes of fermenting wide range of sugars [2]. It is therefore seen now as a great source of energy production just as in other microbial products whose cell produces

high protein contents required for bioenergy production [3].
This as explained, Baker's yeast (*Saccharomyces cerevisiae*) has become a favourite production organism in industrial biotechnology and a suitable chassis in synthetic biology throughout the last decade Klein et al. [4]. Other than its use in the production of bioethanol a case study in the consideration as biomass substrate for energy production, its strains can be used in the production of compounds such as recombinant proteins, butanols, isprenoids and polyketides, as well as lactic and succinic acid through genetically engineered strains in large number [5 – 7]. This Nielsen et al. [8] also extensively discussed that the metabolic engineering of yeast result in the production of fuels and chemicals, and hence offers many advantages as a platform cell factory for such production. On the other hand, Ref [9] evaluated yeast and considered it as the workhouse in the current biofuel industry due to its use in the production of ethanol. Therefore, to determine high protein concentration yield from baker's yeast homogenization will requires pressure, temperature, number of cycles and dilution ratios being considered as parameters in this research for a highly improved protein concentration yield.

2. BAKER'S YEAST IMPORTANCE

Hinchliffe & Kenny [10] explained that many of the advances in gene-expression technology have been stimulated by the desire to produce high-value proteins of therapeutic and commercial potential. It is known as an old name in terms of its importance in the production of so many other products such as pharmaceuticals, food, medical and now, energy. This therefore makes Saccharomyces cerevisiae as yeast traditionally most exploited commercially product serving as substrate requiring further use for mankind. [11] further discussed in their paper with S. cerevisiae and certain other species being developed to produce biofuels from cellulosic materials and potentially other substrates and as a result, will have importance in the generation of new sources of energy. Energy now becoming the greatest obstacle required for development economically in terms of growth in the current 21st Century because of the growing demand for the ever-increasing population worldwide. This is therefore necessary developing alternative energy source whose production are affordable and as such will not interfere with the society negatively in anyway. Based on the above, the development will be required to compensate the present energy need via reducing the environmental concerns owed to pollution and global warming [12]. Baker's yeast as a biomass source has shown to be on top gear towards energy production like other lignocellulosic and biomass materials. Ekpeni et al. [13] found and analyzed biomass as the greatest challenge in its use for energy production and development due to its sustenance which has competed favourably well when compared to other renewable energy sources (RES) and which in fact, is topmost amongst the (RES). For example, lignocellulosic biomass is considered the most important future resource for biofuels and chemicals especially as the world is poised toward a carbohydrate economy as detailed by Mathew et al. [14]. The diversity in baker's yeast for energy production has taken dominance in the search for more alternative ways for energy improvement. These as known, have been on the increase from year to year. Azhar et al. [2] worked it out that more than 2500 yeast species were published by 2005 and it is of the assumption that only 1% of yeast species is currently known which represents approximately 1500 species. Though the total numbers of yeast species on earth are expected to reach 150,000 as detailed Barriga et al. [15].
This research work therefore analyze and consider these parameters; Pressure, Temperature, Number of cycles (Passes) and Dilution ratios for a highly-improved protein concentration yield after fully homogenized through optimization using the design of experiment (DoE). The mathematical model was represented, and the developed mathematical models were tested for adequacy via the analysis of variance (ANOVA) and other adequacy measures. The relationships between the yeast homogenizing parameters and the response; protein concentration was also identified.

3. DISRUPTION PROCEDURES

Previous works and researches on baker's yeast homogenization [3, 16-18] have shown the disruption processes and procedures required in the extraction and emulsification of protein from baker's yeast cell wall through constricting prepared soluble baker's yeast via the exit point of high-pressure homogenizer. This is in fact the first step required in the cell wall breaking down process for the liberation of the inner content of protein concentration. In an energy producing terms, Wenger et al.

[19] studies showed that intracellular proteins expressed in yeast, through small-scale cell breakage methods as capable of disrupting the rigid cell wall. This needed to match the protein release and contaminant profile of full-scale methods like homogenization thereby enabling representative studies of subsequent downstream operations being performed. To achieve this, a pre-treatment phase is generally necessary in the breakdown of the cell wall for the liberation of protein within the biomass and which in this case is considered as the mechanical means of high-pressure homogenizer (Figure 1). Other mechanical means though not of interest in this research are Ultrasound and Bead mill. The non-mechanical means employed in the recovery of intracellular products are Enzymatic, Electrical, Physical and Chemical ways [20]. The mechanical methods are shown to be non-specific as their efficiency is higher and application broader in comparison to other methods [21]. For baker's yeast and other microbial to be fully liberated of their inner contents (intracellular products), homogenizing parameters of the working substrates needs to be considered and be fully understood so as to be able to critically analyse the process [3, 16-18] For this research, the high-pressure homogenizer series GYB40-10S 2 stages Homogenizing Valves is employed as in (Figure 1) and the working parameters; Temperature (°C), Pressure (MPa), Number of Cycles (Passes) and Dilution Ratio as categorical factor were all considered. The main functionalities of the HPH will need to be fully studied to know about the working principles of the parts employed in the emulsification of biomass substrate that is being homogenized. These are the valve seat, impact ring and the valve head in operation as detailed in (Figure 2).

Figure 1: GYB40-10S 2 stage Homogenizer

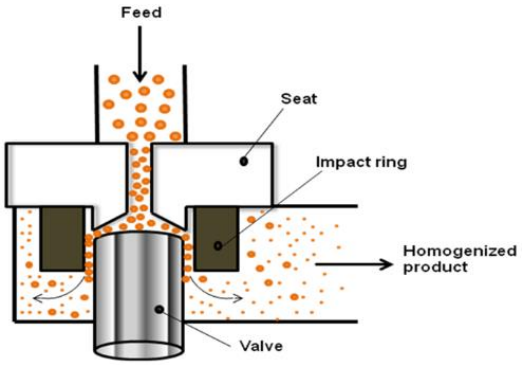

Figure 2: HPH parts during cell disruption [22]

4. MATERIALS AND METHODS

The experiments were conducted using the high-pressure homogenizer (HPH) shown in (Figure 1) and the materials and methods are as detailed in previous papers [3, 16-18] including the buffer solution which was prepared accordingly with the same rates and volumes. These are also indicated. The significant change is the constituents of the filtrate after
centrifugation the homogenized for 60 minutes and at 13,000 rev/mins wherein the samples
have been diluted in the ratio of the homogenized solution against the buffer solution as 10:90, 20:80 and 30:70 respectively. The diluted ratios in solutions were treated with protein reagent and then tested for protein concentration yields using the spectrophotometer. The procedures are as detailed in previous papers as mentioned. For the experimental and homogenization process, refer to [3, 16-18].

5. RESULTS AND DISCUSSION

Table 1: RSM showing design level and coded values against process variables.

Variables	Code	Unit	Limits Coded/actual		
			-1	0	+1
Pressure	A	MPa	30	60	90
No of Cycles	B	-	1	3	5
Temp.	C	°C	30	40	50
Ratio	D	-	10:90	20:80	30:70

Design of experiment with four factors has been applied here using the Box Behnken Design (BBD). 4 factors; temperature, pressure, number of cycles, and ratio (as categorical factor) as well as a response of protein concentration were analysed with 51 runs of experiments as seen in Table 2. While Table 1, shows the Response Surface Methodology (RSM) which is an experimental technique invented to find the optimal response within specified ranges of the factors. The generated equation as shown in equation (1) is aimed for optimizing single or multiple responses and for this work, it is considered for optimizing a single response of 'Protein Concentration Yield'.

Table 2: Design matrix with values

		Factor 1	Factor 2	Factor 3	Factor 4
Exp. No.	Run Order	A: Pressure	B: No. of cycles	C: Temp	D: Ratio
		MPa	-	(°C)	
1	13	30	1	40	10:90
2	18	90	1	40	10:90
3	23	30	5	40	10:90
4	10	90	5	40	10:90
5	5	30	3	30	10:90
6	48	90	3	30	10:90
7	45	30	3	50	10:90
8	36	90	3	50	10:90
9	11	60	1	30	10:90
10	42	60	5	30	10:90
11	49	60	1	50	10:90
12	12	60	5	50	10:90
13	9	60	3	40	10:90
39	38	30	3	30	30:70
40	22	90	3	30	30:70
41	15	30	3	50	30:70
42	19	90	3	50	30:70
43	41	60	1	30	30:70
44	26	60	5	30	30:70
45	7	60	1	50	30:70
46	39	60	5	50	30:70
47	14	60	3	40	30:70
48	46	60	3	40	30:70
49	33	60	3	40	30:70
50	50	60	3	40	30:70
51	17	60	3	40	30:70

5.1 Mathematical Model Developed for the Disruption Baker's Yeast Cell Wall

The fit summary output indicates that for the response, the quadratic model is statistically recommended for further analysis as they have the maximum predicted and adjusted R^2 as 0.567 and 0.666 respectively [2] The test of significance of the regression models, the test for significance on individual coefficients and the lack of fit test performed using the same statistical package for the response. Through selecting the step-wise regression method, the insignificant model terms can be automatically eliminated. The resulting ANOVA table for the quadratic model outline the analysis of variance for the response and illustrate the significant model terms (Table 3). This also show the other adequacy measures R^2, adjusted R^2 and predicted R^2. The entire adequacy measures are close to 1, which are in reasonable agreement and therefore indicate adequate models [23]. The adequate precision (15.552) compares the range of the predicted value at the design points to the average prediction error. In this case, the values of adequate precision ratios are dramatically greater than 4. An adequate precision ratio above 4 indicates that the model is adequate [23]. An adequate model means that the reduced model has successfully passed all the required statistical tests and can be used to predict the responses or to optimize the process and so on. The final mathematical model linked to the response with regards to the coded factors and actual factors as determined by the software are respectively equations (2) , (3),

(4) and (5) respectively. The actual factor equations are (3), (4) and (5) are representing the 10:90, 20:80 and 30:70 dilution ratios of homogenized yeast to buffer solution so achieved. The categoric factor (Ratio) has no implied order which means settings of a categorical factor are discrete and has no intrinsic order [17-18, 24].

Table 3: ANOVA Table for Protein Concentration reduced quadratic model (30 - 50° C)

Source	Sum of Squares	DF	Mean Square	F Value	Prob > F	
Model	4.184	8	0.523	13.435	< 0.0001	Significant
A-Pressure	1.629	1	1.629	41.855	< 0.0001	
B-No. of cycles	0.298	1	0.298	7.655	0.0084	
C-Temp	0.045	1	0.045	1.166	0.2865	
D-Ratio	0.474	2	0.237	6.091	0.0048	
A^2	0.669	1	0.669	17.174	0.0002	
B^2	0.168	1	0.168	4.309	0.0441	
C^2	0.885	1	0.885	22.741	< 0.0001	
Residual	1.635	42	0.039			
Lack of Fit	1.418	30	0.047	2.621	0.0400	Not Significant
Pure Error	0.216	12	0.018			
Cor Total	5.819	50				
$R^2 = 0.719$			Pred $R^2 = 0.567$			
Adj $R^2 = 0.666$			Adeq Precision = 15.552			

$$Y = b_o + \sum b_i \chi_i + \sum b_{ii} \chi_{ii}^2 + \sum b_{ij} \chi_i \chi_j \qquad (1)$$

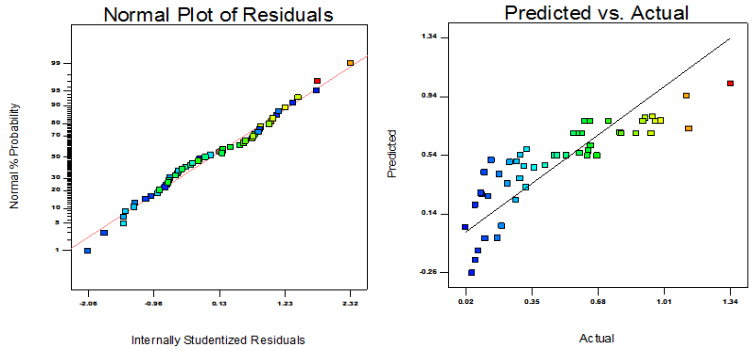

Figure 4: Scatter diagrams of normal plot of residuals (a) and predicted vs. Actual

Final Equation in Terms of Coded Factors:

*Protein Conc. = 0.665483871 + 0.260551075 * A + 0.111424731 * B + 0.043481183 * C - 0.127672359 * D[1] + 0.022327641 * D[2] - 0.230053763 * A^2 + 0.115241935 * B^2 - 0.264731183 * C^2* (2)

Final Equation in Terms of Actual Factors:

Ratio 10:90;

*Protein Conc. = -5.07097209 + 0.0039358871 * Pressure - 0.117150538* No. of cycles + 0.216133065 * Temperature - 0.000255615 *Pressure^2 + 0.028810484* No. of cycles^2 – 0.002647312 * Temperature^2* (3)

Ratio 20:80;

*Protein Conc. = -5.07097209 + 0.0039358871 * Pressure - 0.117150538* No. of cycles + 0.216133065 * Temperature - 0.000255615*Pressure^2 +0.028810484* No. of cycles^2 – 0.002647312 * Temperature^2* (4)

Ratio 30:70;

*Protein Conc. = -4.987955013 + 0.0039358871 * Pressure - 0.117150538* No. of cycles + 0.216133065 * Temperature - 0.000255615*Pressure^2 +0.028810484* No. of cycles^2 – 0.002647312 * Temperature^2* (5)

5.1.1 Process parameters Effect on the Responses - Protein Concentration

The perturbation plots Figure 5 (a, b and c) for the protein concentration yield from the 30 - 50 degrees temperature range is illustrated. The perturbation plot helped in comparing the effect of all the factors

at a particular point in the design space. Temperature has shown to be effective in protein concentration yield in the three plots. The reason for this change, have been accounted to the temperature effect of the biomass substrate before being homogenized. Pressure effect was negligible as well as that of temperature and because the substrate has been treated under heat to raise the temperature, passing it through the HPH over number of cycles say, 3 would have entirely broken down the cell wall of the yeast substrate. Considering the categorical factor of ratio in this study, protein concentration yield has been seen to be of highest yield at the ratio 30:70 when compared to other ratios of 10:90 and 20:80. Invariably, it therefore means that as the ratio increase, the yield in protein concentration also increases at the same rate as pressure rises but, in this case, here, only number of cycles has taken the incremental rate in the protein concentration yield. This can be seen at Figure 5(c) showing the highest of yield in protein concentration as against the other two

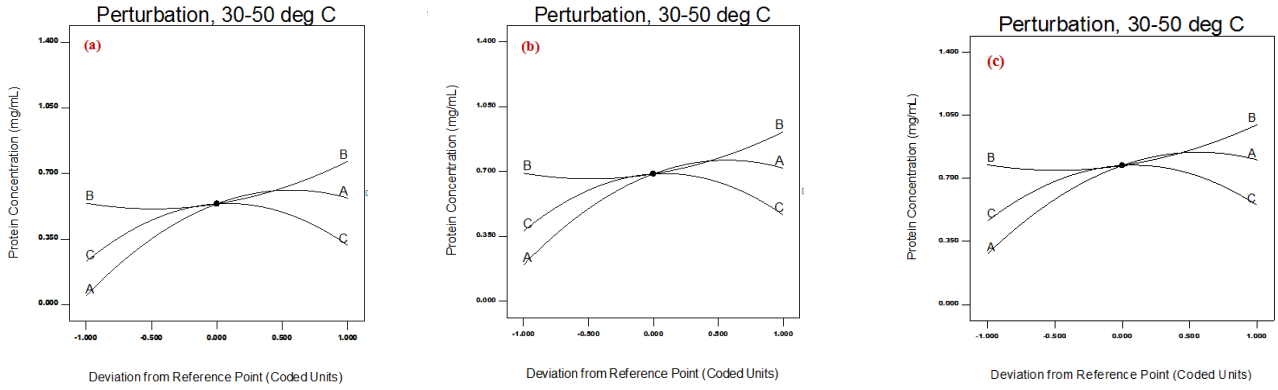

Figure 5: Perturbation plot showing pressure increasing with the number of cycles as yeast is homogenized

6. CONCLUSION

Experimental results show a great potential of the novel protein improvement through yeast use and cell wall breakage in HPH and as analysed using the design expert (DOE). The following points have therefore been achieved.

- The homogenization process carried out using the 2-Stage HPH GYB40-10S to obtain set results of the four factors (Temperature, Pressure, Number of cycles as well as ratio as categorical factor) and one response (Protein Concentration) using the *Design Expert*
- Rise in Protein yield as the dilution ratio increases from 10:90 to 30:70.
- The four factors temperature, pressure, number of cycles and ratio as categorical factors considered showed effect in the resultant protein yield.
- Ratio 30:70 showed highest yield of protein concentration
- Finally, the high-pressure homogenizer is seen as one of the best way of disrupting microbial product for high protein yield.

ACKNOWLEDGMENTS

The author gratefully thanks the organiser of the conference for the opportunity given to showcase the work.

REFERENCES

[1] Nandy, S. K., & Srivastava, R. K. (2018). A review on sustainable yeast biotechnological processes and applications. *Microbiological Research*, *207*, 83-90.

[2] Azhar, S. H. M., Abdulla, R., Jambo, S. A., Marbawi, H., Gansau, J. A., Faik, A. A. M., & Rodrigues, K. F. (2017). Yeasts in sustainable bioethanol production: A review. *Biochemistry and biophysics reports*, *10*, 52-61.

[3] Ekpeni, L. E. N., Benyounis, K. Y., Stokes, J., & Olabi, A. G. (2016). Improving and optimizing protein concentration yield from homogenized baker's yeast at different ratios of buffer solution. *International Journal of Hydrogen Energy*, *41*(37), 16415-16427.

[4] Klein, M., Islam, Z. U., Knudsen, P. B., Carrillo, M., Swinnen, S., Workman, M., & Nevoigt, E. (2016). The expression of glycerol facilitators from various yeast species improves growth on glycerol of Saccharomyces cerevisiae. *Metabolic Engineering Communications, 3*, 252-257.
[5] Hong, K.K., & Nielsen, J., 2012. Metabolic engineering of Saccharomyces cerevisiae: a key cell factory platform for future biorefineries. Cell. Mol. Life Sci. 69, 2671–2690.
[6] Nevoigt, E., 2008. Progress in metabolic engineering of Saccharomyces cerevisiae. Microbiol Mol. Biol. Rev. 72, 379–412.
[7] Borodina, I., & Nielsen, J., 2014. Advances in metabolic engineering of yeast Saccharomyces cerevisiae for production of chemicals. Biotechnol. J. 9, 609–620.
[8] Nielsen, J., Larsson, C., van Maris, A., & Pronk, J. (2013). Metabolic engineering of yeast for prodn. of fuels and chemicals. *Current opinion in biotechnology*, *24*(3), 398-404.
[9] Coyle W., (2010). Next-Generation Biofuels.
[10] Hinchliffe, E., & Kenny, E. (1993). Yeast as a vehicle for the expression of heterologous genes. In *The Yeasts (Second Edition)* (pp. 325-356).
[11] Johnson, E. A., & Echavarri-Erasun, C. (2010). Yeast biotechnology. In *The Yeasts (Fifth Edition)* (pp. 21-44).
[12] Divya, D., Gopinath, L. R., & Christy, P.M. (2015). A review on current aspects and diverse prospects for enhancing biogas production in sustainable means. *Rene. & Sust. Energy Reviews, 42*, 690-699.
[13] Ekpeni, L. E. N., Benyounis, K. Y., Nkem-Ekpeni, F., Stokes, J., & Olabi, A. G. (2014). Energy diversity through renewable energy source (RES)–a case study of biomass. *Energy Procedia, 61*, 1740-1747.
[14] Mathew, A. K., Abraham, A., Mallapureddy, K. K., & Sukumaran, R. K. (2018). Lignocellulosic Biorefinery Wastes, or Resources? In *Waste Biorefinery* (pp.267-297).
[15] Barriga, E. J. C., Libkind, D., Briones, A. I., Iranzo, J. U., Portero, P., Roberts, I., ... & Rosa, C. A. (2011). Yeasts biodiversity and its significance: case studies in natural and human-related environments, ex situ preservation, applications and challenges. In *Changing Diversity in Changing Environment*. InTech.
[16] Ekpeni, L. E. N., Nkem-Ekpeni, F. F., Benyounis, K. Y., Aboderheeba, A. K., Stokes, J., & Olabi, A. G. (2014). Yeast: a potential biomass substrate for the production of cleaner energy (Biogas). *Energy Procedia*, *61*, 1718-1731.
[17] Ekpeni, L. E. N., Benyounis, K. Y., Nkem-Ekpeni, F. F., Stokes, J., & Olabi, A. G. (2015). Underlying factors to consider in improving energy yield from biomass source through yeast use on high-pressure homogenizer (hph). *Energy, 81*, 74-83.
[18] Ekpeni, L. E. N. (2015). *Investigation and disruption of baker's yeast/chlorella vulgaris in high-pressure homogenizer (HPH) to improve cost-effective protein yield* (Doctoral dissertation, Dublin City University).
[19] Wenger, M. D., DePhillips, P. & Bracewell, D. G. (2008). A Microscale Yeast Cell Disruption Technique for Integrated Process Development Strategies. American Chemical Society and American Institute of Chemical Engineers Biotechnol. Prog., 24 (3): 606 – 614.
[20] Liu, D., Ding, L., Sun, J., Boussetta, N., & Vorobiev, E. (2016). Yeast cell disruption strategies for recovery of intracellular bio-active compounds—A review. *Innovative Food Science & Emerging Technol*, *36*, 181-192.
[21] Donsì, F., Ferrari, G., Lenza, E., and Maresca, P. (2009) Main factors regulating microbial inactivation by high-pressure homogenization: operating parameters and scale of operation, Chem Eng Sci, 64 (3), pp. 520–532
[22] HPH principle during operation. Available at http://nptel.ac.in/courses/102103045/module5/lec28/7.html (Accessed April 21st, 2018)
[23] Benyounis, K. Y., Olabi, A. G., Hashmi, M. S. J. (2008) Multi-response optimization of CO_2 laser-welding process of austenitic stainless steel. Optics & Laser Technology 40 (1) (76–87)
[24] Categorical Factor in statistical analysis https://stats.idre.ucla.edu/other/mult-pkg/whatstat/what-is-the-difference-between-categorical-ordinal-and-interval-variables/ (Accessed 19th April, 2018)

INTEGRATION OF GREENHOUSE AGRICULTURE TO THE ENERGY INFRASTRUCTURE AS AN ALIMENTARY SOLUTION

J. Farfan*[1], A. Poleva[1] and Ch. Breyer[1]

1. Lappeenranta University of Technology (LUT), School of Energy Systems, Skinnarilankatu 34, 53850, Lappeenranta, Finland. *Corresponding author; Javier.Farfan.Orozco@lut.fi

ABSTRACT

There is an evident food, water and energy crisis worldwide, up to a quarter of the global population has no reliable access to either or any of these basic supplies. Research is being carried out towards sustainable and comprehensive energy transitions. Separately, research in food production and food access is being done. However, not much research is being carried out that considers the integration of all parts into a system capable of providing the human basic needs of energy and food. Integrating greenhouses with energy production facilities provides an opportunity for a symbiotic relation where both systems benefit. Results show that using only 5% of the currently deployed biomass, utility photovoltaic and waste-to-energy for the proposed scenarios, a total of 31.3 million m^2 of greenhouses can be powered globally. Through cost savings in energy transmission, distribution and taxation, the system can reduce over 50% of the energy cost for greenhouse operation. Additionally, the CO_2 emissions of biomass or waste incineration power plants can be captured and used to increase the yield of the greenhouses by up to 30%. Moreover, the integrated system remains zero waste and net zero emissions, thus complying with the environmental targets of the COP21 Paris agreement.

Keywords: Renewable energy, food production, sustainability, energy-water-food nexus

1 INTRODUCTION

There is an evident food, water and energy crisis worldwide, up to a quarter of the global population has no reliable access to either or any of these basic supplies [1–3]. Research is conducted towards sustainable and comprehensive energy transitions (including water demand) [4–7], and separately, on food production and food access [8–11]. However, research considering the integration of all parts into a system capable of providing energy and food, is still limited. Integrating food production sites, such as greenhouses, to energy production facilities provides an opportunity for a symbiotic relation where both systems benefit of each other, thus producing food, generating energy, and reducing water consumption, while also cutting costs and improving quality of the combined services.

Currently, agriculture occupies 40% of the land not covered by ice [12] and uses 70% of the water consumed by humans [13, 14]. However, traditional agriculture is not possible everywhere on the globe. Areas of the world with extreme water scarcity (such as North Africa and Middle East), land scarcity (such as Japan and South Korea), and weather impairment (Canada, Nordic countries, Russia) are either unavailable for crops or with limited potential and/or limited timeframes for agricultural use. At the same time, water and food scarcity are current global issues, which further stresses the need of more efficient agricultural practices. Greenhouse agriculture has been well established for decades [15]. Greenhouses add to agriculture the capacity of producing higher yields and extend the agricultural season. At the same time, the water requirements are reduced by around 90% [16], the need for chemical fertilizers could be substituted by more sustainable organic fertilizers [17] and, depending the type of greenhouse, the need for pesticides can be eliminated [18]. However, the disadvantages of greenhouse agriculture come at the price of much higher energy cost, of up to 70-150 times the energy per m^2 [16] compared to traditional agriculture. It is the much higher energy requirement of greenhouse agriculture that tends to drive costs above compared to the goods produced by traditional agriculture.

2 PROPOSED SOLUTION

The core concept of the solution is based on the idea that by joining power utilities with greenhouse agriculture, it is possible to avoid the energy costs related to taxation, transmission and distribution, so the significantly higher energy demand can be dramatically reduced in cost. For example, only 44% of the electricity cost compared to end-consumer price worldwide is the generation cost [19]. Additionally, locally produced goods are exempt of import/export taxes and significantly reduced transportation costs. The significantly lower energy cost could tip the balance towards greenhouse-produced goods, thus turning agriculture towards a more sustainable future. To achieve this, the problem has been separated into three scenarios with a proposed solution for each; (1) Extreme Cold Weather, (2) Water Scarcity and (3) Land Scarcity, and assumptions are made also for each scenario. From the greenhouse side, an energy demand of 1321 kWh/(m^2·a), of which 80% is heating, ventilation and air conditioning (HVAC) and 20% is lighting, as estimated from Barbosa et al. [16].

2.1. Extreme Cold Weather

For extreme weather, the geographical regions targeted by the system are, for example, the boreal forest dominating the landscape of the Nordic countries, Canada and Russia. From the agricultural point of view, it is characterised by short agricultural seasons but otherwise availability of water, land and sustainable biomass (wood and forest residues). To tackle the scenario, a system is tailored as shown in Figure 1.

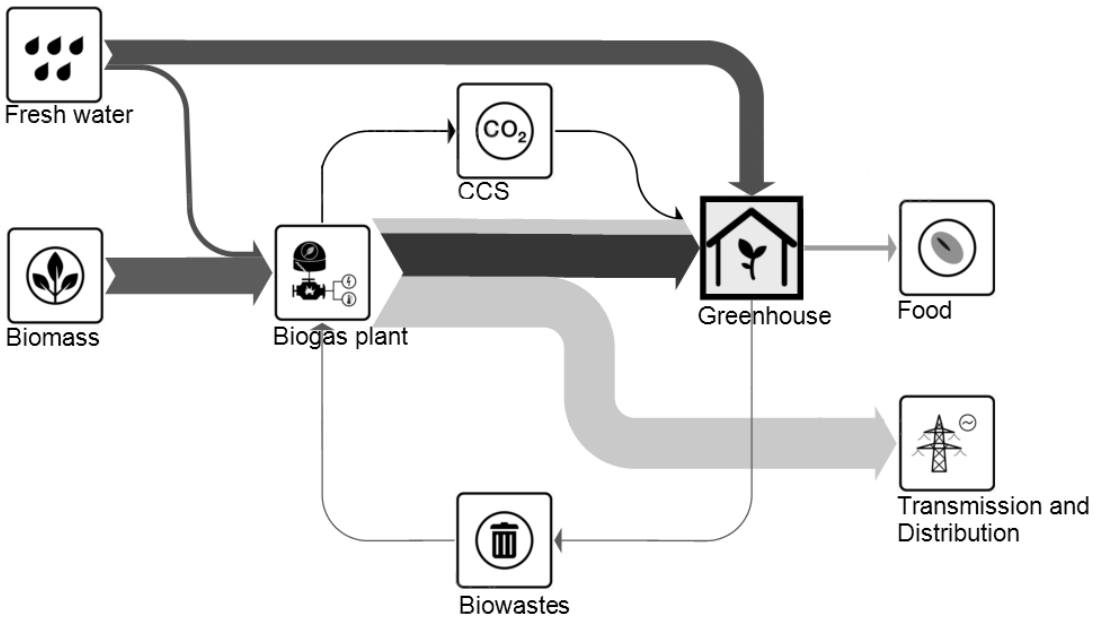

Figure 1: System proposed for locations of extreme cold weather.

The system consists of an integrated gasification combine cycle turbine (IGCC) coupled with carbon capture at the exhaust gas. The waste heat from the power plant as well as part of its output electric and heating power can be dedicated and directly connected to a nearby greenhouse. Additionally, the captured CO_2 from the power plant can be utilised to enrich the soil and air of the greenhouse to increase the greenhouse yield by up to an additional 60% [20], while the biowaste produced by the greenhouse can then be fed as fuel back to the IGCC. Assuming a sustainable source of biomass used for the power plant the system would be carbon neutral. In a comprehensive fully renewable-based energy system, biomass and other flexible energy sources are used for balancing the system, resulting in low full load hours per year [5, 7]. Coupling greenhouse agriculture to the IGCC would increase the utilisation rate of the power plant. Since in this scenario, the largest part (up to 80%) of the greenhouse demand can be covered by the excess heat, even at 5% operation some electricity can be then used grid under baseline operation.

2.2. Water Scarcity

The water scarcity scenario focuses on world's geographical areas where water conservation is mandatory, and traditional agriculture is not feasible or limited to short rain seasons, such as North Africa, the Persian

Gulf, etc. The geographic regions targeted by this scenario often have good solar irradiation and wind profiles. These locations focus on the benefit of significantly lower need of water, of 10% compared to traditional agriculture. Particularly if the water is provided by means of desalination, the cost savings of using less water provide further benefit.
Therefore, the proposed system is based on solar photovoltaic (PV) and wind turbines as energy source, with batteries to balance the system as shown in Figure 2. CO_2 capture directly from air or point sources (such as cement plants, industrial zones, etc.) could be coupled to the system to enhance the production yield in the same as described in the previous scenario.

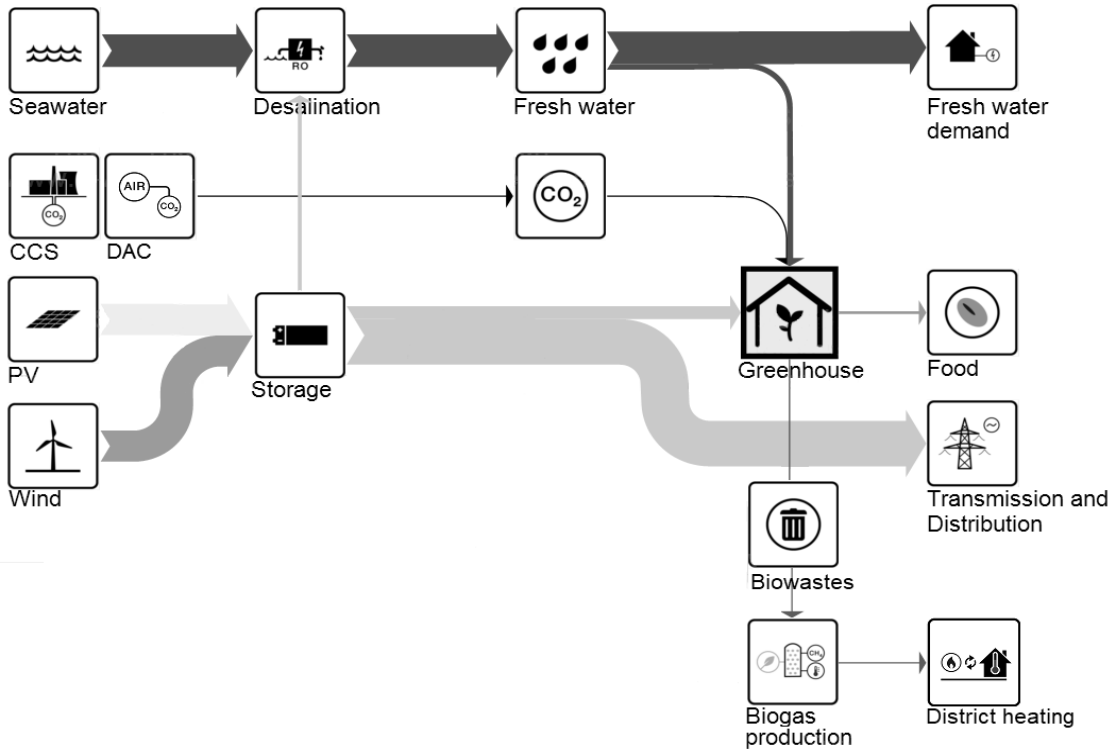

Figure 2: Power plant and greenhouse model for the water scarcity scenario.

2.3. Land Scarcity

The land scarcity scenario focuses on geographic regions of the world that are overly densely populated and/or that have very limited available area for agriculture, for example, islands or isolated nations such as Japan, Taiwan, South Korea, Qatar, etc. The regions targeted by this scenario are often characterised by having very high demand of energy, water and food. At the same time, such places are known to produce large amounts of solid waste, as well as waste heat from municipal heating or other sources.
This scenario exploits better the ability of greenhouse agriculture to produce higher yield over area compared to traditional agriculture. Furthermore, greenhouses and hydroponic plantations can be adapted to metropolitan settings, on the roof of buildings, or even underground, as they can operate on artificial lighting alone (as they often do in boreal regions). The CO_2 required to enhance the yield of the greenhouses could be captured directly from air or from nearby carbon point sources like industry or biomass or waste power plants. Water can be either extracted from a fresh water source or desalinated from the ocean. Similar to Scenario 1, a large part (up to 80%) of the greenhouse demand can be covered by the excess heat, even at 5% operation some excess electricity can be then sold to the grid-based electricity system under base generation operation.

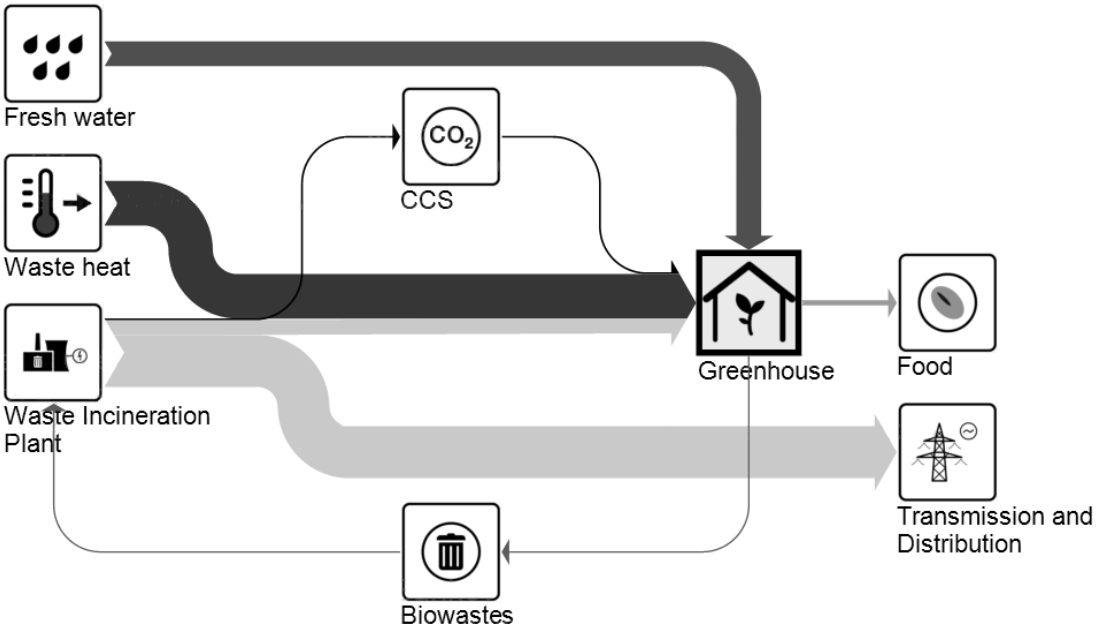

Figure 3: Power plant and greenhouse model proposed for the land scarcity scenario.

3. RESULTS AND CONCLUSIONS

For purposes of this work, the available installed capacities worldwide according to Farfan and Breyer [21], were used to estimate the currently available biomass, utility-scale solar PV and waste-to-energy capacities worldwide. An assumption was made to dedicate only 5% of the generated energy from the available capacities to power greenhouses. For biomass and waste-to-energy, 8000 hours of operation at 5% capacity (or 400 full load hours) were assumed to power greenhouse installations. In the case of utility-scale solar PV, the dedicated capacity of 5% was also assumed, while the full load hours have been extracted from [22], [23], and [24] for every specific region. The geographical regions are defined according to Breyer et al. [5], [25]. For every region, the installed capacities of biomass, waste-to-energy and utility-scale solar PV were taken into account, meaning that within a geographical region, the proposed scenarios can coexist. However, the installed capacities globally vastly follow the behaviour assumed by each scenario, where boreal forest regions have high biomass and waste to energy capacities but low to zero installed utility-scale solar PV capacities. The total powered greenhouse area is shown in Figure 4.

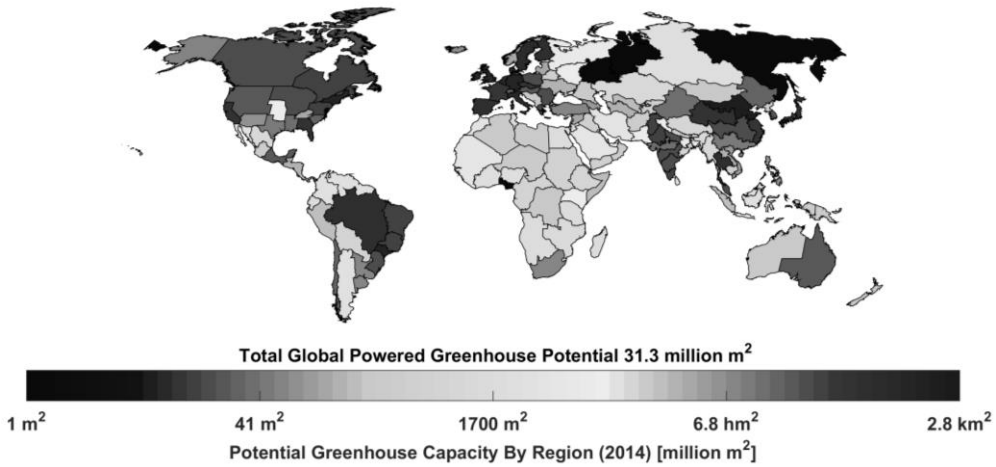

Figure 4: Global potential of powered greenhouse areas (in m^2) by adding the potential of all scenarios in each region by using only 5% of dedicated capacities.

Figure 4 shows the potential of applying the proposed scenarios to the currently installed capacities, according to each location. The map colour scale is logarithmic and shows several interesting findings.

Countries like Finland, Sweden, UK and Canada, which are net importers of vegetables, can host 0.78 million m^2, 1.14 million m^2, 1.45 million m^2 and 0.7 million m^2 of powered greenhouse area respectively. Only in Finland, according to the rates of greenhouse vegetable production [26], if used solely for cucumber production, it would result in 50,888 tons per year, or close to 10 tons of cucumber per person per year in Finland (that is before considering the carbon enrichment increase in yield), but of course, an optimal mix of vegetables should be planned. Highly populated locations such as Japan, South Korea and China could host 1.9 million m^2, 1.4 million m^2 and 4.73 million m^2 of powered greenhouse area respectively, providing a significant amount of food for places of very high demand. Europe in total could host over 10.8 million m^2 of powered greenhouse area, while the American continent could host over 5.7 million m^2 in the North America and 3.80 million m^2 in South America, for a total of over 31.3 million m^2 of greenhouses globally. In contrast, the Food and Agriculture Organization of the United Nations [27] reported that 4050 million m^2 of greenhouses are currently installed in Europe. Given the relatively small capacity (5%) dedicated to greenhouses, the increment in whole-year operational greenhouses is small, but of significance. Moreover, the map shows only the potential based on the installed capacities of with reference of 2014, but not the potential of the geographical regions according to their resources to host greenhouse and power capacities in the future.

Future work

Expansion on the potential of power plants and greenhouse according to the local weather, resource availability (further than the currently deployed capacities), and demand based on population maps. In addition, more detailed and accurate models for each of the scenarios are under work. Projections can then be created for further scenarios for years 2030 and 2050.

AKNOWLEDGEMENTS

The authors would like to thank the Lappeenranta University of Technology for providing the place and means to conduct the research, as well as the Research Foundation at Lappeenranta University of Technology (TUKISÄÄTIÖ) for sponsoring the participation to the conference.

REFERENCES

[1] FAO, IFAD, UNICEF, WFP & WHO, *The State of Food Security and Nutrition in the World*. 2017. [Online] Available: http://www.fao.org/state-of-food-security-nutrition/en/.

[2] WHO/UNICEF, "Progress on Drinking Water, Sanitation and Hygiene: 2017 Update and SDG Baseline," 2017.

[3] IEA, "Energy Access Outlook 2017," *Energy Procedia*, vol. 94, no. March, p. 144, 2017.

[4] U. Caldera, D. Bogdanov, and C. Breyer, "Local cost of seawater RO desalination based on solar PV and wind energy: A global estimate," *Desalination*, vol. 385, pp. 207–216, 2016.

[5] C. Breyer *et al.*, "Solar photovoltaics demand for the global energy transition in the power sector," *Prog. Photovoltaics Res. Appl.*, pp. 1–19, 2017.

[6] M. Z. Jacobson *et al.*, "100% Clean and Renewable Wind, Water, and Sunlight All-Sector Energy Roadmaps for 139 Countries of the World," *Joule*, vol. 1, no. 1, pp. 108–121, 2017.

[7] M. Ram *et al.*, "Global Energy System based on 100% Renewable Energy - Power Sector," Study by Lappeenranta University of Technology and Energy Watch Group, Lappeenranta, Berlin, 2017. [Online] Available: http://bit.ly/2hU4Bn9

[8] H. Azadi, S. Schoonbeek, H. Mahmoudi, B. Derudder, P. De Maeyer, and F. Witlox, "Organic agriculture and sustainable food production system: Main potentials," *Agric. Ecosyst. & Environ.*, vol. 144, no. 1, pp. 92–94, 2011.

[9] C. Galanakis, Ed., *Sustainable Food Systems from Agriculture to Industry: Improving Production and Processing*, 1st ed. Academic Press, 2018.

[10] F. H. Besthorn, "Vertical Farming: Social Work and Sustainable Urban Agriculture in an Age of Global Food Crises," *Aust. Soc. Work*, vol. 66, no. 2, pp. 187–203, 2013.

[11] P. Smith and P. J. Gregory, "Climate change and sustainable food production.," *Proc. Nutr. Soc.*, vol. 72, no. 1, pp. 21–8, 2013.

[12] N. Ramankutty, A. T. Evan, C. Monfreda, and J. A. Foley, "Farming the planet: 1. Geographic

distribution of global agricultural lands in the year 2000," *Global Biogeochem. Cycles*, vol. 22, no. 1, 2008.
[13] World Wide Fund for Nature (WWF), "Agricultural water use and river basin conservation," *Living Waters - Conserv. Source Life*, pp. 1–40, 2003.
[14] United Nations Educational Scientific and Cultural Organization (UNESCO), *Water in a changing world. The United Nations World Water Development Report 2 (WWDR2). World Water Assessment Programme (WWAP).* 2009.
[15] M. H. Jensen and A. J. Malter, *Protected Agriculture: A Global Review*. Washington, DC: World Bank Publications, 1995.
[16] G. L. Barbosa *et al.*, "Comparison of land, water, and energy requirements of lettuce grown using hydroponic vs. Conventional agricultural methods," *Int. J. Environ. Res. Public Health*, vol. 12, no. 6, pp. 6879–6891, 2015.
[17] M. Kacira, M. Jensen, T. Ribie, S. Tollefson, and G. Giacomelli, "Use resources wisely: waste management and organic liquid fertilizer use in greenhouse production system," 2017, pp. 541–548.
[18] J. C. Van Lenteren, "A greenhouse without pesticides: Fact or fantasy?," *Crop Protection*, vol. 19, no. 6. pp. 375–384, 2000.
[19] Statista. The Statistic Portal, "Breakdown of electricity prices worldwide, as of 2016," 2018. [Online]. Available: https://www.statista.com/statistics/571657/price-breakdown-of-electricity-globally/. [Accessed: 09-Mar-2018].
[20] E. Nederhoff, "Carbon Dioxide Enrichment. Fuels and Figures," *Pract. hydroponics greenhouses*, vol. May/June, pp. 50–59, 2004.
[21] J. Farfan and C. Breyer, "Structural changes of global power generation capacity towards sustainability and the risk of stranded investments supported by a sustainability indicator," *Journal of Cleaner Production*, vol. 141. pp. 370–384, 2017.
[22] P. W. Stackhouse and C. H. Whitlock, "Surface meteorology and Solar Energy (SSE) release 6.0," *Earth Science Enterprise Program, National Aeronautic and Space Administration (NASA)*, 2008. [Online]. Available: http://eosweb.larc.nasa.gov/sse/.
[23] Stackhouse, P. W and Whitlock, C. H., "Surface meteorology and solar energy (SSE) release 6.0 Methodology, NASA SSE 6.0," 2009. [Online]. Available: http://eosweb.larc.nasa.gov/sse/documents/SSE6Methodology.pdf .
[24] D. Stetter, "Enhancement of the REMix energy system model: Global renewable energy potentials , optimized power plant siting and scenario validation," 2012.
[25] C. Breyer *et al.*, "On the role of solar photovoltaics in global energy transition scenarios," *Prog. Photovoltaics Res. Appl.*, vol. 25, no. 8, pp. 727–745, 2017.
[26] Luke. Natural Resources Institute Finland, "Horticultural Statistics," 2013. [Online]. Available: http://stat.luke.fi/en/horticultural-statistics-2010_en-0. [Accessed: 09-Mar-2018].
[27] Food and Agriculture Organization of the United Nations (FAO), "Good Agricultural Practices for greenhouse vegetable production in the South East European countries. Principles for sustainable intensification of smallholder farms," *FAO plant Prod. Prot. Pap.*, vol. 230, 2017.

A HYBRID-MODEL TO DEBOTTLENECK THE COMMERCIALIZATION OF PALM OIL BIOMASS VALUE-ADDED PRODUCTS IN MALAYSIA

S.L. Ngan[1], P. Yatim[2], and H.L. Lam[1]

1. Department of Chemical and Environmental Engineering, Faculty of Engineering, University of Nottingham Malaysia Campus, Jalan Broga, 43500 Semenyih, Selangor Darul Ehsan, Malaysia; email: kebx6nsl@nottingham.edu.my; honloong.lam@nottingham.edu.my
2. Graduate School of Business, Universiti Kebangsaan Malaysa 43600 UKM, Bangi Selangor, Malaysia; email: puan@ukm.edu.my

ABSTRACT

The economic importance of "waste-to-wealth" concept has gained increased recognition within the economic policy arena in Malaysia as the country attempts to transition towards green growth. Policy frameworks have been established and implemented to promote and support green growth which includes the utilization of oil palm biomass for production of various value-added products. However, the biomass industry and the conversion of under-utilized oil palm biomass to value-added bio-products remain under-developed. Lack of understanding of risks associated with the biomass industry is often cited as one of the reasons for the industry's slow growth. Not only the industry players are facing business, operational and financial risks which commonly found in other industries, but they are also exposed to regulatory, supply chain, technology, and environmental and social risks. Therefore, it is imperative that these risk factors are identified and evaluated in a comprehensive manner so that industry players can address these risks and put in place risk management and mitigation mechanisms. In this study, Fuzzy Analytic Network Process (FANP), and Decision Making Trial and Evaluation Laboratory (DEMATEL) are employed to develop a hybrid model to assess risk factors typically found in biomass industry, and to evaluate risk mitigation strategies to debottleneck the commercialization of biomass value added products in Malaysia.

Keywords: Palm oil biomass, Fuzzy Analytic Network Process, DEMATEL, commercialization

1 INTRODUCTION

Malaysia, as the second world largest exporter of the oil and fat after neighbouring country, Indonesia produce about 20 million tonnes of crude palm oil per annum [1]. The palm oil biomass, such as oil palm trunk, oil palm frond, empty fruit bunches (EFB), palm oil mill effluent (POME), palm kernel shell (PKS), palm pressed fibre (PPF) and decanter cake are expected to reach 100 million dry tonnes by 2020 [2]. At current stage, most of the palm oil biomass are still engaging with low utilization value process in downstream activities. For instances, oil palm frond and trunk are mostly left in the field or pre-process (i.e., mulched) and returned to the field as fertilizer. EFB, PKS generated in the palm oil mill and biorefinery are transformed into pellets for power generation. It is estimated by fully capitalise the palm biomass for high value-added downstream activities could contribute additional 30 billion to the country's gross national income (GNI). Recognizing its potential, the government has stepped up its efforts to promote sustainable utilization of oil palm biomass. Biomass Industry Strategic Action Plan is introduced in 2012 as a joint effort of Malaysia with European Union to help small and medium enterprises (SMEs) in Malaysia to exploit biomass resources for high-value utilization [3]. National Biomass Strategy 2020 (2013) that introduce a series of strategy to exploit biomass for commercial opportunities. Furthermore, fiscal incentives such as tax rebate and tax exemptions are also offered to the new entrant to the industry. Financing scheme is also introduced in 2010 to provides financing aid for the user and producer of green technology project, inclusive biomass industry, wherein the government will provide 60 % of guarantee and subsidy 2 % of the total interest rate imposed on the total financing amount. Despite various actions and initiatives have been taken, the growth of the biomass industry in Malaysia is still relatively slow. Literature, anecdotal evidence and businesses have identified that one of the factors contribute to the slow diffusion of the industry is due to the high-risk profile of the industry. Biomass industry is a multidiscipline industry and thus associated with wide range of expertise and stakeholders. Yatim et al. (2017) [4] identify that the industry does not only associated with financial, operation, technology risk as any other industry, it also exposes to five main risk categories, namely technology, financing, supply chain, regulatory, and environmental and social. Risk is generally defined as the product of probability of occurrences of risk event multiple with its impact or

consequences. As biomass industry is a relatively new industry, there is still the lack of historical data to aid the estimation of the probability and impacts. Moreover, risk is exerting in both tangible and intangible as well as can be quantitative and qualitative event. Thus, in this work, Fuzzy Analytic Network Process (FANP) and Decision Making Trial and Evaluation Laboratory (DEMATEL) are adopted to develop a hybrid model to assess and prioritize risks to design the most effective debottlenecking solution.

2 BACKGROUND

Fuzzy Analytics Network Process (ANP) is a combination of fuzzy set theory and Analytics Network Process. Analytic Network Process is the generic form of Analytic Hierarchy Process (AHP) that developed by Saaty in the late 1980s [5]. ANP overcomes the constraint of AHP on unidirectional (i.e., top-to-bottom) problem structure to include feedback dependence and inner dependence in deriving the final composite priority through supermatrix approach. However, there have been increasing argument on the crisp value of the Saaty's traditional 9-point fundamental scale in elicit judgement on pairwise comparison questions. It is claimed that human judgement can be vague and ambiguity in time and not feasible to be fully represented with single crisp value [6]. Thus, fuzzy membership function has often integrating with ANP on better representation of judgement with inclusion of the confidence level of domain in giving judgement. Fuzzy membership function is represented by a vector <l, m, u> wherein l is the lower bound of the judgement, m is the modal value and u is the upper level. The range of upper bound and lower bound (i.e., u-l) indicates the confidence interval of the domain in giving judgement, wherein huge gap signifies the domain is less certain about the judgements given and vice versa. Fuzzy set theory was first introduced by Zadeh (1965) to overcome the constraints of high uncertainty due to incomplete or insufficient information [7]. Its application is wide extended to multiple field and industry ever since including in multiple criteria decision-making area to include uncertainties in the judgement given by domain. FANP is a powerful for multiple criteria decision making as it offer high flexibility in problem structuring. It enables a clear indication of dominance relationship between clusters, as well as inner relationship of elements in each cluster in fulfilling the overall goal.

On the other hand, Decision Making Trial and Evaluation Laboratory (DEMATEL) is first introduced by the Geneva Research Centre in 1972 [8]. The main function of DEMATEL is to analyse the relationship of multiple elements in a complex system to determine the causal and dependency relationship based on expert knowledges. Its ability to analyse and visualize the relationship in matrices or digraph have attracted high attention in recent year in investigating and intertwined complex problems in various field, inclusive but not limited to business arena, research field and etc. By recognizing and categorizing the variables into cause and effect factors, it enhances the decision making for optimal selection of the strategy to tackle the issues. The proposed model that integrating FANP and DEMATEL does not offers solution that solely based on the degree of dominance relation of the variables, but also synchronized with the causal and effect relationship in prioritizing risk. The outcome provides a comprehensive picture for the industry players to design the mitigation strategy that is most effective in managing the risk associated with the biomass industry. Meanwhile, policy makers can also utilize the information to put in place supports and mechanisms to reduce the risk barriers more effectively and efficiently to spur up the overall growth of the industry.

3 METHODOLOGY

The proposed methodology consists of five main steps with the detailed explanation as follows:

Step 1: Literature review are performed to identify the risks associated biomass industry. Focus group discussion that consists of 8 to 15 participants is conducted to validate the findings from literature review and get extra inputs that are more relevant to Malaysia context. The focus group participants comprised of a good mixed of biomass industry stakeholders, including industry players, researchers, capital providers and policy makers to encourage discussion on the opportunity and challenges faced by different stakeholders in the biomass industry.

Step 2: The information gathered from stakeholders is then structured into a hierarchical model as shown in Figure 1. The hierarchical model consists of 3 levels, with the top level as the goal, to prioritize the risks for debottlenecking, followed by level 2, risk categories and level 3, risk events. The details for the identified risk events are described in Table 1. Arrows are used to represent the relationship of elements and level clusters associated in the model. Downward arrows (i) and (ii) show the direct dependency of the element(s)

in the lower level with respect to the element(s) in upper level. Self-looping arrow (iii) indicates the inner dependency of the element with itself and other element(s) within the same level cluster. Self-looping arrow (iv) indicates the interdependency of element(s) with the other element(s) within the same level cluster. Feedback control loop arrows (v) and (vi) connecting all the element(s) back to the controlling element of the model, which is the goal. The purpose of feedback control loop is to ensure that the whole model is strongly connected to avoid judgements that are non-relevance to the purpose of study [6].

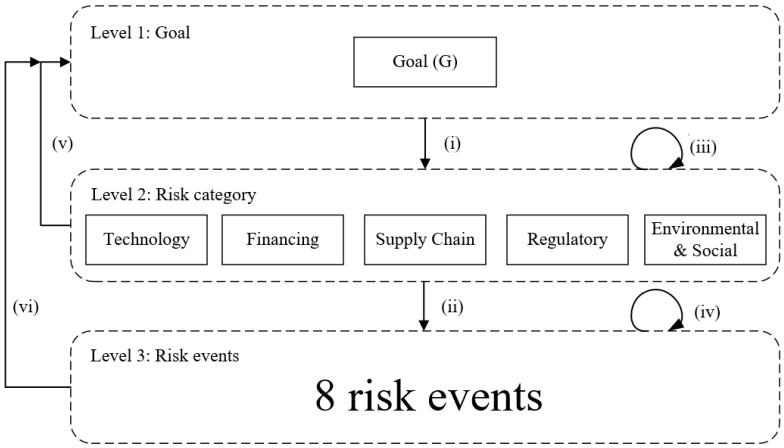

Figure 1: Diagraph of the hierarchical network model

Table 1. The description of the risk events in level 3

Code	Description
R1	Long pay back periods
R2	High upfront capital
R3	Inconsistent feedstock supply
R4	Lack of information to assess the performance of biomass project
R5	High logistics cost
R6	Lack of resources and capability to scale up to industrial level
R7	Lack of technical and safety standards for biomass plant
R8	Unclear regulations and policies related to biomass industry

Step 3: Elicit judgement from experts on the degree of the dominance relationship and intensity of influence power and being influenced through pairwise comparison questionnaires. Linguistics scale is adopted in this work to compare the relative dominance relationship of elements and clusters. The description of the linguistics scale with its correspond value is presented in Table 2. The questionnaire is divided into two parts. The first section comprises of inputs for FANP to assess: (a) direct dependence of level 2 with respect to level 1; (b) direct dependence of level 3 element(s) with respect level 2 element(s); (c) inner dependence of element(s) in level 2. The second section consists of questions for DEMATEL to determine (d) the interdependence of the element(s) in level 3 and to identify (e) causal and effect factor on the element(s) in level 3.

Table 2. Fuzzy scale for pairwise comparative judgement and measurement scale for DEMATEL

Linguistic scale	Lower bound (l_{ij})	Modal value (m_{ij})	Upper bound (u_{ij})
Equally	1.0	1.0	1.0
Slightly more	1.2	2.0	3.2
Moderately more	1.5	3.0	5.6
Strongly more	3.0	5.0	7.9
Very strongly more	6.0	8.0	9.5

Linguistic scale	Value
No influence	0
Very low influence	1
Low influence	2
High influence	3
Very high influence	4

Step 4: Derive the priority vectors and matrix to populate the initial supermatrix. The mathematic operation for both FANP and DEMATEL are associated with matrix, with procedures as described in the following. The fuzzy judgements from the first section (i.e. inputs for FANP) of pairwise comparison questionnaire are populated to form reciprocal matrix (i.e., $\hat{A}$)) as the following:

$$\hat{A} = \begin{bmatrix} \langle 1,1,1 \rangle & \hat{a}_{12} & \cdots & \hat{a}_{1n} \\ \hat{a}_{21} & \langle 1,1,1 \rangle & \cdots & \hat{a}_{2n} \\ \vdots & \vdots & \ddots & \vdots \\ \hat{a}_{n1} & \hat{a}_{n1} & \cdots & \langle 1,1,1 \rangle \end{bmatrix} \text{where } \hat{a}_{ij} = \langle l_{ij}, m_{ij}, u_{ij} \rangle \; ; \hat{a}_{ji} = \langle \frac{1}{u_{ij}}, \frac{1}{m_{ij}}, \frac{1}{l_{ij}} \rangle \quad (1)$$

Geometric mean method is used to aggregate the judgements of multiple experts on the same pairwise comparison judgement prior forming the reciprocal matrix [9]. Every relationship as indicated with arrow (i), (ii) and (iii) consists of its own matrices. The priority vector representing the final priority of the said relationship is derived with the non-linear programming (NLP) calibrated by Promentilla et al. (2015) [10] as follows:

Maximize λ (2a)

s.t.:

$$(m_{ij} - l_{ij})\lambda w_j - w_i + l_{ij} w_j \leq 0, \forall i = 1, \dots, n-1; j = i+1, \dots, n \quad (2b)$$

$$(u_{ij} - m_{ij})\lambda w_j - w_i + u_{ij} w_j \leq 0, \forall i = 1, \dots, n-1; j = i+1, \dots, n \quad (2c)$$

$$(m_{ij} - l_{ij})\lambda w_i - w_j + l_{ji} w_i \leq 0, \forall j = j, \dots, n-1; i = j+1, \dots, n \quad (2d)$$

$$(u_{ji} - m_{ji})\lambda w_i - w_j + u_{ji} w_i \leq 0, \forall j = 1, \dots, n-1; j = j+1, \dots, n \quad (2e)$$

$$\sum_{i=1}^{n} w_i = 1 \quad (2f)$$

$$w_i > 1, \forall i = 1, \dots, n \quad (2g)$$

where in λ is the overall degree of satisfaction of the judgements and a measure of consistency. λ value is suggested to be within 0.0 and 1.0, which 1.0 indicates that the judgements achieve perfect consistency while 0.0 indicates that the judgements only satisfy at its boundary. In the event that λ appeared to be negative-value, it is suggested for the respective experts to revisit his/her judgements as some of the judgements are conflicting with each other.

The judgements for DEMATEL questions are populated to form direct relation matrix (*D*). Varying with the FANP matrices which is reciprocal, *D* is a square matrix that indicates the intensity of the influence power of the row element *i* with respect to column elements *j*. The diagonal value for *D* (i.e., when *i=j*) is equal to zero, as it is assumed that an element has no influence upon itself [11]. *D* is then normalized by divided with the largest value of its row to form direct relation matrix (*M*). All the possible interacting of the elements in M is then captured to derive total relation matrix as illustrated by following equation:

$$T = M + M^2 + M^3 + \cdots + M^n \approx M(I - M)^{-1}, \quad \text{when } n \to \infty \quad (3)$$

where *M* is the normalized direct relation matrix and *I* is an identity matrix.

Next, calculate the sum of row (R_i) and column (C_i) of the T, where R_i indicates the overall influence power of row's element, while (C_i) indicates the intensity of column's element being influenced by other elements. The sum of row and column (i.e., $R_i + C_i$) shows the degree of prominence of the element *i* in the overall cluster. Meanwhile, ($R_i - C_i$) indicates the net effects of the element *i* in the system. Element with a positive value for ($r_i - c_i$) is classified as cause factor while element with a negative value for ($r_i - c_i$) is categorized as effect factor. The overall prominence level and cause and effect relationship can be illustrated by plotting a digraph with ($R_i + C_i$) against ($R_i - C_i$). The total relation matrix is normalized by the largest value of its column prior populated to the supermatrix.

Step 5: The priority vectors derived from FANP method and total relation matrix derived from DEMATEL method (i.e., shaded in grey in Figure 2) are act as entry into the initial supermatrix with the order as illustrated in Figure 2. The supermatrix is multiple by itself until the values are converged. The final priority weightage for the model is presented in the last column of the matrix in Figure 2 (i.e., highlighted in yellow).

$$S = \begin{pmatrix} 1 & e^T \text{ (v)} & e^T \text{ (vi)} \\ w_{21} \text{ (i)} & w_{22} \text{ (iii)} & 0 \\ 0 & w_{32} \text{ (ii)} & T \text{ (iv)} \end{pmatrix}$$

Note:

w_k - FANP priority vectors

T - DEMATEL total relation matrices

	Goal	TC	FN	SP	RG	ES	R1	R2	R3	R4	R5	R6	R7	R8	final value
Goal	1.00	1.00	1.00	1.00	1.00	1.00	1.00	1.00	1.00	1.00	1.00	1.00	1.00	1.00	**1.0000**
TC	0.22	1.00	0.50	0.37	0.29	0.27	0.00	0.00	0.00	0.00	0.00	0.00	0.00	0.00	**0.2396**
FN	0.32	0.41	1.00	0.34	0.19	0.25	0.00	0.00	0.00	0.00	0.00	0.00	0.00	0.00	**0.2994**
SP	0.17	0.29	0.28	1.00	0.29	0.28	0.00	0.00	0.00	0.00	0.00	0.00	0.00	0.00	**0.1849**
RG	0.14	0.14	0.12	0.14	1.00	0.19	0.00	0.00	0.00	0.00	0.00	0.00	0.00	0.00	**0.1335**
ES	0.15	0.16	0.10	0.15	0.23	1.00	0.00	0.00	0.00	0.00	0.00	0.00	0.00	0.00	**0.1425**
R1	0.00	0.03	0.19	0.03	0.12	0.05	0.56	0.70	0.56	0.50	0.53	0.60	0.17	0.20	**0.0930**
R2	0.00	0.14	0.23	0.08	0.17	0.03	1.00	0.65	0.83	0.45	0.77	0.79	0.16	0.22	**0.1157**
R3	0.00	0.07	0.17	0.30	0.09	0.16	0.80	0.47	0.57	0.66	0.98	0.39	0.25	0.45	**0.1105**
R4	0.00	0.14	0.14	0.12	0.11	0.19	0.97	0.79	0.66	0.55	0.58	0.89	0.94	0.78	**0.1555**
R5	0.00	0.08	0.09	0.19	0.05	0.12	0.85	0.48	1.00	0.38	0.53	0.35	0.13	0.19	**0.0913**
R6	0.00	0.27	0.03	0.05	0.13	0.07	0.97	1.00	0.96	0.66	1.00	0.68	0.26	0.50	**0.1442**
R7	0.00	0.18	0.08	0.12	0.17	0.20	0.51	0.45	0.82	0.88	0.60	0.68	0.41	1.00	**0.1391**
R8	0.00	0.09	0.07	0.11	0.16	0.18	0.57	0.64	0.68	1.00	0.49	1.00	1.00	0.43	**0.1507**

Figure 2: The initial supermatrix with the final priority weightages

The summary of procedures for the proposed methodology is illustrated in Figure 3.

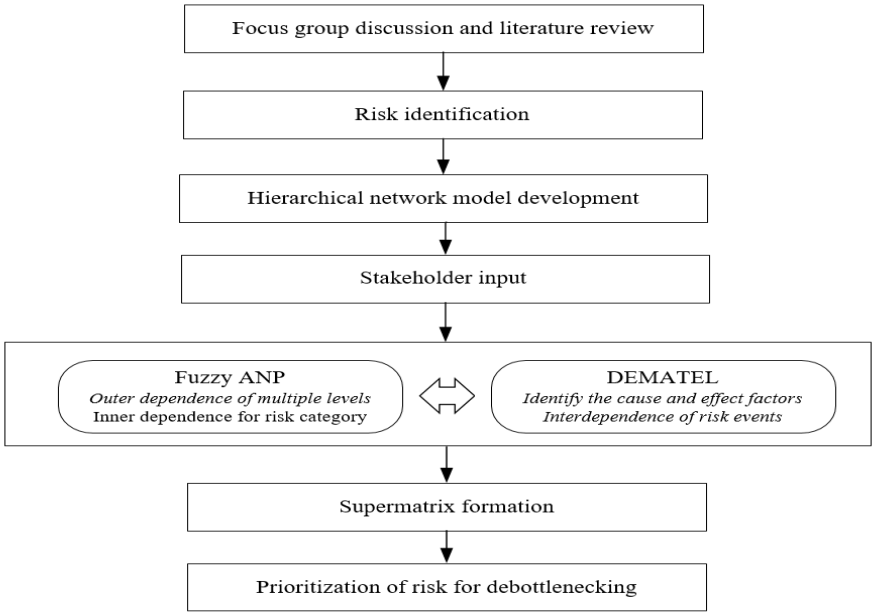

Figure 3: Methodology flow chart

4 RESULT AND RECOMMENDATIONS

Based on the final priority weightage, financing risk (29.94 %) appeared to be the most prominent risk category in hindering the overall development of the biomass industry, followed by the technology risk (23.96 %), supply chain risk (18.49 %), environmental and social risk (14.25 %) and regulatory risk (13.35 %). Biomass project often associated with high upfront cost, which set a high barrier to enter the industry. It is challenging for the industry players to receive financing or investment from capital providers to start-up the project, particularly for small and medium enterprises (SMEs) that are lack with liquidity and assets to serve as guarantee on the total financing amount. At current stage, the technology associated with high-value added conversion is still extremely expensive and yet to achieve cost reduction with production at economic-of-scale. Lack of the commercialize viable technology and uncertain of long-term performance of the technology intensify the technology risk.

Taking into the causal and effect of risk events in deriving the final priority weightage for the 8 risk events, "R4 Lack of information to assess the performance of biomass project" (15.55 %) ranked the first to be debottlenecked the commercialization of biomass value added products in Malaysia, followed with "R8

Unclear regulations and policies related to biomass industry" (15.07 %) and "R6 Lack of resources and capability to scale up to industrial level" (14.42 %). It is suggested for the government to initiate a centralized data system that congregate all the information related to biomass industry, inclusive but not limited to the price of the supply and demand, technology and process available, supports and incentives offered to the industry stakeholders and rules and regulation associated with the industry. Furthermore, clear, consistent and adequate regulatory framework with supporting policies are also necessary to provide essential information for the industry players to understand the industry as a whole and take advantage on the supports and incentives offered by government to manage the respective risks.

5 CONCLUSION AND FUTURE WORKS

The paper proposed a novel methodology for the assessment and prioritization of the risk associated with Malaysia biomass industry. The hybrid model that integrating FANP and DEMATEL provides a systematic and transparent way to identify, analyse and evaluate the correlation between elements and clusters and pinpoint the causal and effect factors in the model. The results provide a reference for the industry stakeholders to design risk management plan that directly tackle prominence and causal risk, to achieve the maximum output with minimum input. Future work will be focus on extending the model to produce a comprehensive risk profile for the biomass industry in Malaysia. Extra risk events can be added to current model to provides more dimension on the risks associated with the industry. An extra level of mitigation strategy can also be added to select the most effective strategy. Case study will be developed to validate the effectiveness of the risk mitigation strategy on hedge, transfer and reduce risks associated with the biomass industry in Malaysia.

ACKNOWLEDGEMENTS

The authors would like to thank Long Term Research Grant Scheme (LRGS Code: LRGS/2013/UKM-UKM/PT/06) from Ministry of Higher Education (MOHE), Malaysia, Universiti Kebangsaan Malaysia (UKM) and University of Nottingham Malaysia Campus for the funding of this research.

REFERENCES

[1] MPOB (Malaysia Palm Oil Board), Monthly production of Oil Palm Products 2016 & 2017, bepi.mpob.gov.my/index.php/en/statistics/production/177-production-2017/791-production-of-oil-palm-products-2017.html. (accessed on 22.2.2018)

[2] AIM (Agensi Inovasi Malaysia), National Biomass Stretegy 2020, nbs2020.gov.my/, 2013. (accessed on 17.03.2018)

[3] MIGHT, Malaysian biomass industry action plan 2020: Driving SMEs towards sustainable future. Selangor, Malaysia, 2013

[4] P. Yatim, S. L. Ngan, H. L. Lam, A. C. Er, Overview of the key risks in the pioneering stage of the Malaysian biomass industry, *Clean Technologies and Environmental Policy*, Vol. 19, pp. 1825 – 1839, 2017

[5] T. L. Saaty, M. Takizawa, Dependence and independence: From linear hierarchies to nonlinear networks, *European Journal of Operational Research*, Vol. 26, pp. 229 – 237, 1986.

[6] A. B. P. Promentilla, T. Furuichi, K. Ishii, N. Tanikawa, A fuzzy analytic network process for multi-criteria evaluation of contaminated site remedial countermeasures, *Journal of Environmental Management*, Vol. 88, pp. 479 – 495, 2008.

[7] L. Zadeh, Fuzzy sets, *Information Control*, Vol. 8, pp. 338 – 353, 1965.

[8] A. Gabus and E. Fontela, World Problems, An invitation to Further Thought within The Framework of DEMATEL, Battelle Geneva Research Centre, Geneva, Switzerland, 1972.

[9] A. H. Orbecido, A. B. Beltran, R. A. J. Malenab, K. I. D. Miñano, M. A. B. Promentilla, Optimal selection of aerobic biological treatment for a petroleum refinery plant, *Chemical Engineering Transactions*, Vol. 52, pp. 643 – 648, 2016.

[10] M. A. B. Promentilla, K. B. Aviso, R. R. Tan, A fuzzy analytic hierarchy process (FAHP) approach for optimal selection of low-carbon energy technologies, *Chemical Engineering Transactions*, Vol. 45, pp. 829 – 834, 2015.

[11] S. L. Si, X. Y. You, H. C. Liu, P. Zhang, DEMATEL Technique: A systematic Review of the State-of-the-Art Literature on Methodologies and Applications, *Mathematical Problems in Engineering*, pp. 1 – 26, 2018.

BIOOXYGENATES CROSS-COUPLING FOR FUEL COMPONENTS PRODUCTION

A.V. Chistyakov[1], P.A. Zharova[1], M.V. Tsodikov[1], S.A. Nikolaev[2]

1. Topchiev Institute of Petrochemical Synthesis RAS, Russia; email: chistyakov@ips.ac.ru
2. Moscow State University, Russia; email: serge2000@rambler.ru

ABSTRACT

C-C bond formation is a pivotal method to construct complex molecules from some simple substrates, with the electrophilic alkylation of a given starting material being one of the most useful procedures. The straightforward routes to the creation of a variety of alcohols having intricate structures through alkylation of simple alcohols remain very unusual. Previously we found that during heterogeneously catalyzed conversion of ethanol with iso-propanol 2-pentanol formed with the yield equal to 35 wt.%. The general co-products were 1-butanol, 1-hexanol and 1-octanol that are valuable chemicals itself. Here we propose a heterogeneously catalytic route to convert such fermentation products as ethanol, acetone, 2-propanol and 1-butanol obtained from a variety of renewable carbohydrate sources into precursors for petrol, diesel and jet fuels. One of the work features is the use of heterometallic precursors, containing different pairs of metals closer to a distance less than the sum of their covalent radii, for supported catalysts creation.

Keywords: bioalcohols, heterogeneous catalysis

1 INTRODUCTION

Natural biological routes to produce alcohols (ethanol and n-butanol) from carbohydrates have been known for more than 100 years, and these compounds have been produced in fermentations at high titres (100 and 15 g l21, respectively) and at yields near their theoretical maxima. These low-molecular-mass compounds are primarily suitable as additives or in certain situations (for example, E100 flex fuel vehicles) as alternatives to petrol. Advances in metabolic engineering have enabled the biological production of several higher-molecular mass jet and diesel fuel compounds from carbohydrates, but until now these processes have suffered from low titres and yields [1-3].

The use of biomass as raw material for the synthesis of fuels and chemicals is nowadays a major challenge because of the scarcity of fossil fuels and the global climate change concerns. Although from a thermodynamic point of view, the use of biomass for satisfying the needs of fuels and chemicals is reliable [4], many technological limitations burden this possibility. Only a very minor fraction of this biomass (triglycerides, sugars and starches) can be selectively transformed into fuels (biodiesel) or chemicals (mainly ethanol), whereas most of the biomass components (cellulose, lignin) are not easy to transform into valuable organic molecules. Cost of the treatments of the whole biomass (such as pyrolysis or acid/enzymatic hydrolysis) lead to the formation of low-rank organic molecules of low molecular weight and high oxygen/carbon ratio. In this way, bioethanol is obtained in the fermentation of sugars and starches; chemicals such as acetone, acetic acid, phenols, furfural and other light oxygenates are released during the fast pyrolysis of biomass feedstock [5], and large amount of oxidized derivatives of the sugars (such as furfural, hydroxymethylfurfural, glucuronic acid) are formed during the acid hydrolysis of wooden feedstocks [6]. The transformation of molecules of low molecular weight into larger molecules must involve the formation of new carbon–carbon bonds [7]. C-C bonds formation is a pivotal method to construct complex molecules from some simple substrates, with the electrophilic alkylation of a given starting material being one of the most useful procedures [8]. Alcohols are one of the most basic and important organic materials owing to their wide variety of uses in industrial and laboratory chemistry.

The classic β-alkylation of a secondary alcohol leading to a higher alcohol usually requires tedious processes producing a lot of waste: oxidation, alkylation and reduction, which cause some disadvantages in the atom economic [9] and environmental [10] points of view. Thus any new strategy for the catalytic direct β-alkylation of secondary alcohols to create higher alcohols would be highly desirable, all the more so if it is an environmentally benign route with high atom efficiency [11].

The scope of the present work is to study the effect of Cu and Pd supported on γ-Al_2O_3 on selectivity and catalytic activity in bioalcohols cross-coupling reaction. Previously, we found that during heterogeneously catalyzed conversion of ethanol with isopropanol 2-pentanol formed with the yield equal to 35 wt.% [12].

The general co-products were 1-butanol, 1-hexanol and 1-octanol that are valuable chemicals itself. Here we propose a heterogeneously catalytic route to convert such fermentation products as ethanol, acetone, 2-propanol and 1-butanol obtained from a variety of renewable carbohydrate sources into precursors for petrol, diesel and jet fuels. One of the work features is the use of heterometallic precursors, containing different pairs of metals closer to a distance less than the sum of their covalent radii, for supported catalysts creation.

2 EXPERIMENTAL

As a catalyst we used 0.1wt.%Pd-0.12wt.%Cu/γ-Al_2O_3 system. Analytical grade ethanol, isopropanol and 1-butanol were used without further purification. Catalytic experiments were carried out in a 45 mL high pressure Parr autoclave equipped with magnetic stirring. The reactor was loaded with the catalyst (typically 4.5 g). The catalyst testing procedure was as follows: the reactor with catalyst was loaded with equal volumes of ethanol (25 ml) or ethanol and isopropanol (typically 13 ml of each alcohol) or with 25 ml of mixture containing 60 vol.% 1-butanol, 30 vol.% acetone and 10 vol.% ethanol, closed and flushed with inert gas (Ar). The reactor was heated up to 275°C with a heating rate of 20°C/min. The reaction was carried out for 5 h. Then, the reactor was cooled down and analysis of the reaction mixture was performed.

Qualitative and quantitative analysis of the C_1–C_5 hydrocarbon gases was performed by gas chromatography (GC) with a Kristall-4000M chromatograph (carrier gas: He, column: HP-PLOT/Al_2O_3, 50 m × 0.32 mm; flame ionization detector). GC analyses of CO, CO_2 and H_2 were performed with a Kristall-4000 chromatograph (carrier gas: Ar, column: SKT, 1.5 m × 4 mm; thermal conductivity detector). The qualitative composition of the liquid organic products was carried out by gas-liquid chromatography coupled to a mass spectrometry (GLC-MS) using a MSD 6973 - and an Autowt.-150 spectrometer - (EI = 70 eV, columns: HP-5MS, 50 m × 0.32 mm and CPSil-5, 25 m × 0.15 mm). The quantitative content of the organic compounds was determined by GLC using a Varian 3600 chromatograph (carrier gas: He, column: Chromtec SE-30, 25 m × 0.25 mm detector: flame ionization detector).

3 RESULTS AND DISCUSSION

As it considered ethanol and acetone-butanol-ethanol (ABE) mixture might be a prospective bio-derived source for chemicals and fuels in future [13, 14]. First, we tested the activity of Pd-Cu catalyst for self-condensation of ethanol to 1-butanol and higher molecule alcohols (Scheme 1). 1-butanol is known to be an effective additive to gasoline [15], so the efficiency of the catalyst was evaluated as the selectivity of 1-butanol formation and the conversion of ethanol.

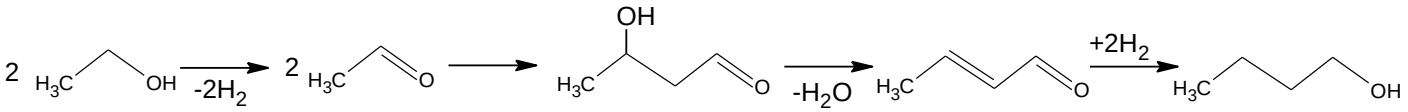

Scheme 1. Ethanol self-condensation pathways.

The catalyst showed the highest yield of condensation product such as 1-butanol with selectivity of 65.6 % at 56.3 % conversion of ethanol (Figure 1). An important aspect of any catalytic process is the lifetime of the catalyst that was investigated with series of consecutive experiments. During the first 20 hours being on stream the catalyst changes its activity and selectivity very markedly. After that, an insignificant (not more than 10%) decrease in the conversion of ethanol and an increase (no more than 10%) of the selectivity of the formation of 1-butanol is observed until 70 hours. The selectivity of the formation of 1-octanol and 1-hexanol remains constant. After 70 hours of operation of the catalyst, the reduction in the degree of conversion of ethanol becomes more pronounced, and the dynamics of increasing selectivity of 1-butanol formation slows down.

During the self-condensation reaction of ethanol, water forms. The results of the study of the effect of water content in ethanol on the selectivity of the reaction are shown in Figure 2. It is shown that when using absolute ethanol, its conversion is significantly increased, while the selectivity to 1-butanol remains practically constant. The selectivity of formation of 1-hexanol and 1-octanol decreases in proportion to the increase in water content. It is likely that a significant reduction in the degree of conversion of ethanol with increasing water concentration in the reaction zone is due to competitive chemisorption of water and ethanol at identical active sites. Perhaps the water molecules form tightly bound surface compounds with the catalyst, thereby blocking the active sites from the molecules of the alcohol.

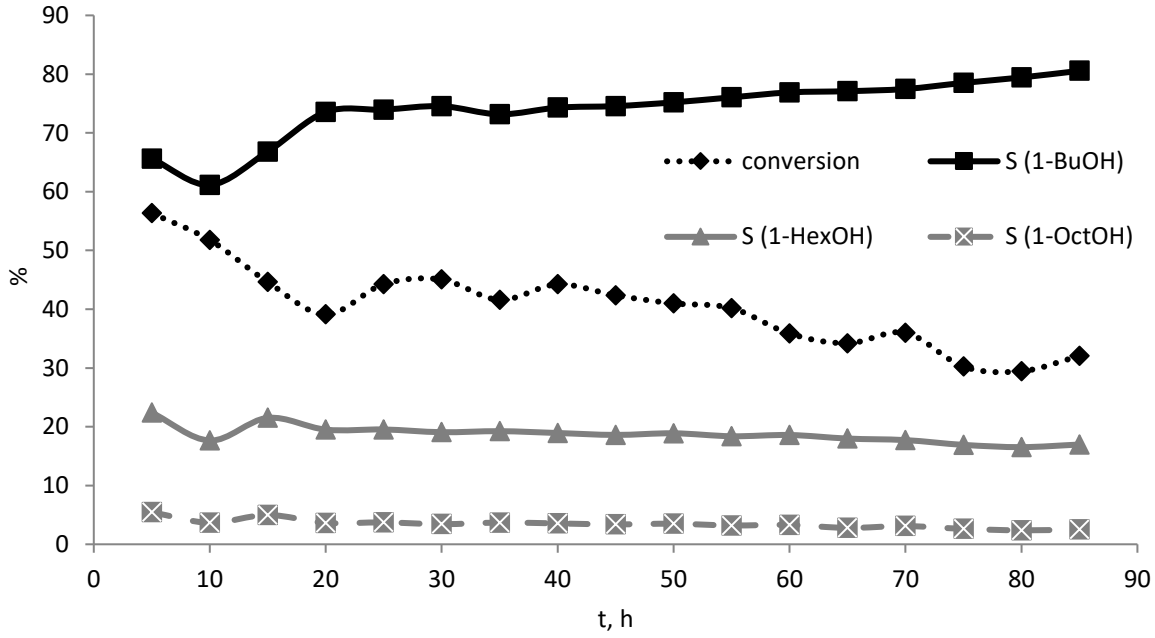

Figure 1. Dynamics of 1-butanol (S(1-BuOH)), 1-hexanol (S-(1HexOH)), 1-octanol (S(1-OctOH)) selectivity and ethanol conversion changes during stability experiments.

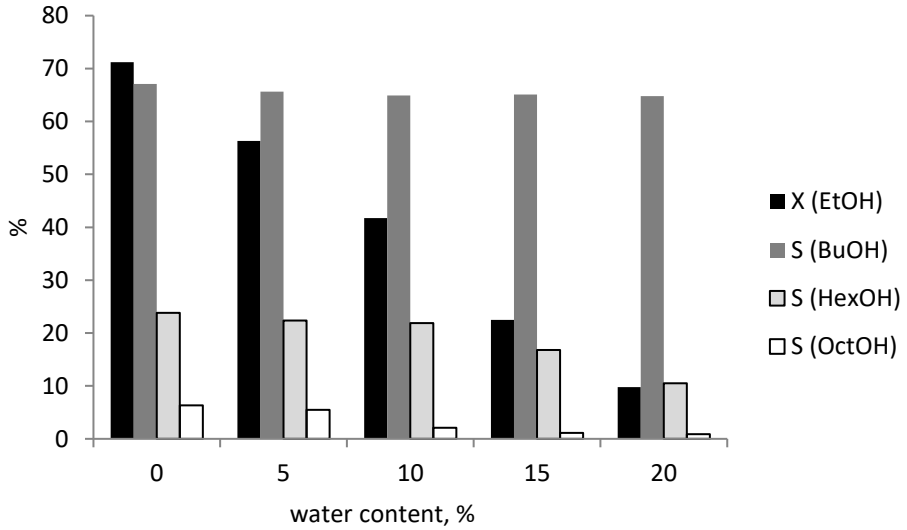

Figure 2. Water content effect on the self-condensation of ethanol reaction parameters.

To evaluate regularities of ABE mixture conversion first we tested ethanol and acetone mixture conversion and 1-butanol and acetone mixture conversion. Ethanol and 1-butanol do not react under the reaction conditions with each other. Products composition of 50 vol.% ethanol and 50 vol.% acetone mixture conversion are presented in Figure 3. Conversion of both reagents was approximately 50%. The first step of the reaction is dehydrogenation of ethanol to acetaldehyde followed by β-alkylation of acetone with acetaldehyde (Scheme 2). Products analysis indicates that acetone partially reduces to isopropanol. That is undesirable process, that probably may be inhibited with catalyst composition tuning. The main products of alkylation of acetone with ethanol are 2-pentanon and 2-pentanol (Scheme 3, product A). The content of 4-heptanol (Scheme 3, product C) is 4.5 times smaller than one of 2-pentanol and 2-pentanon. That phenomenon indicates that predominantly only one condensation step take place.

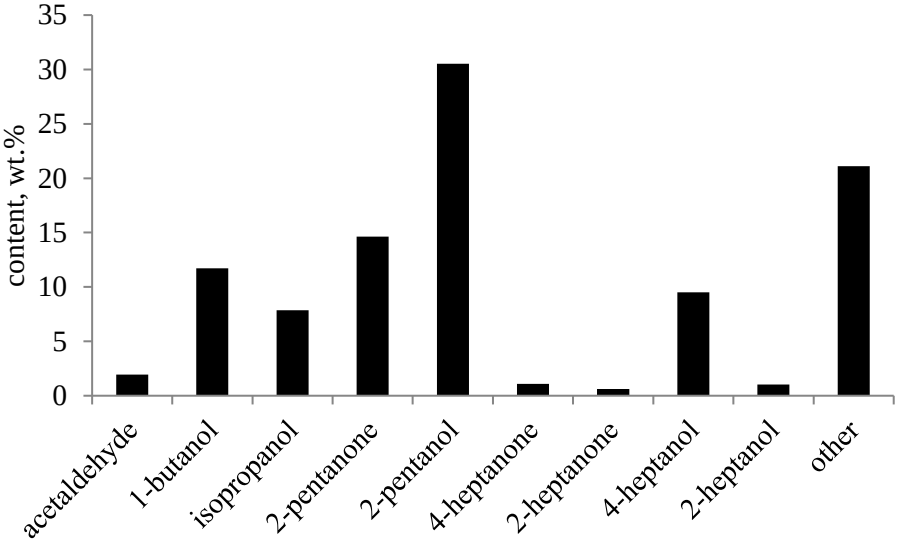

Figure 3. Products composition of 50 vol.% ethanol and 50 vol.% acetone mixture conversion

The composition of the products of the co-conversion of 1-butanol and acetone is shown in Figure 4. It is seen from the figure that 4-heptanone dominates in the reaction products (Scheme 3, product B1), which indicates the high intensity of the stage of monoalkylation of acetone with 1-butanol. It should be noted that part of the acetone is converted to isopropanol, undergoing hydrogenation with hydrogen formed during the dehydrogenation of 1-butanol (Scheme 2). The yield of doublalkylation products is lower than monoalkylated, but their content is approximately 20%. The main reaction products are ketones. The yield of alcohols is much lower. The high content of ketones in reaction products suggests that their composition is potentially promising for the preparation of C_{12}-C_{18} compounds, however, it is necessary to increase the condensing capacity of the catalyst.

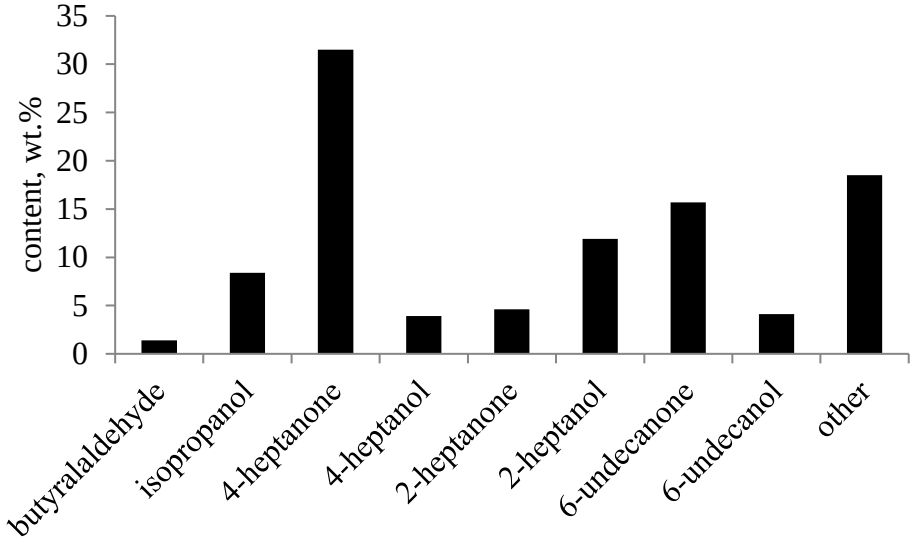

Figure 4. Products composition of 50 vol.% 1-butanol and 50 vol.% acetone mixture conversion

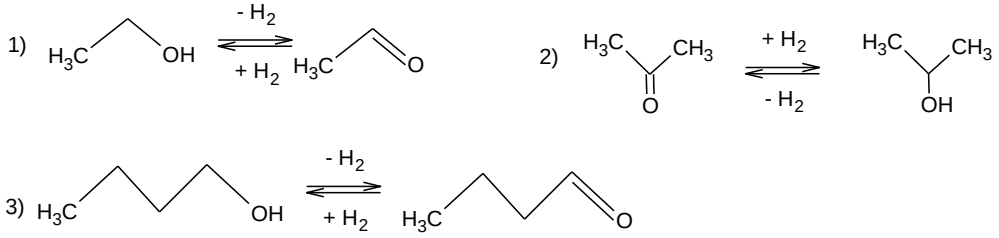

Scheme 2. The first step of the reaction dehydrogenation of alcohols 1) and 3). Undesirable reaction of acetone hydrogenation 3).

The composition of the products of the ABE mixture conversion is shown in Figure 5. In reaction products, ketones are observed up to three consecutive alkylation steps. Thus, the intensity of the condensation stage increases with increasing amount of initial reagents. We explored the mechanism of the reaction by following the reaction progress (Scheme 3). Monoalkylation of acetone with 1-butanol and ethanol produces 2-pentanone and 2-heptanone. These species underwent further reaction to form double-alkylated products. No aldehydes were observed during the reaction, suggesting that the aldehyde intermediates were present in very low concentrations and reacted rapidly with acetone and other ketones. Hence, the formation of Guerbet products was minimized, and acetone alkylation predominated.

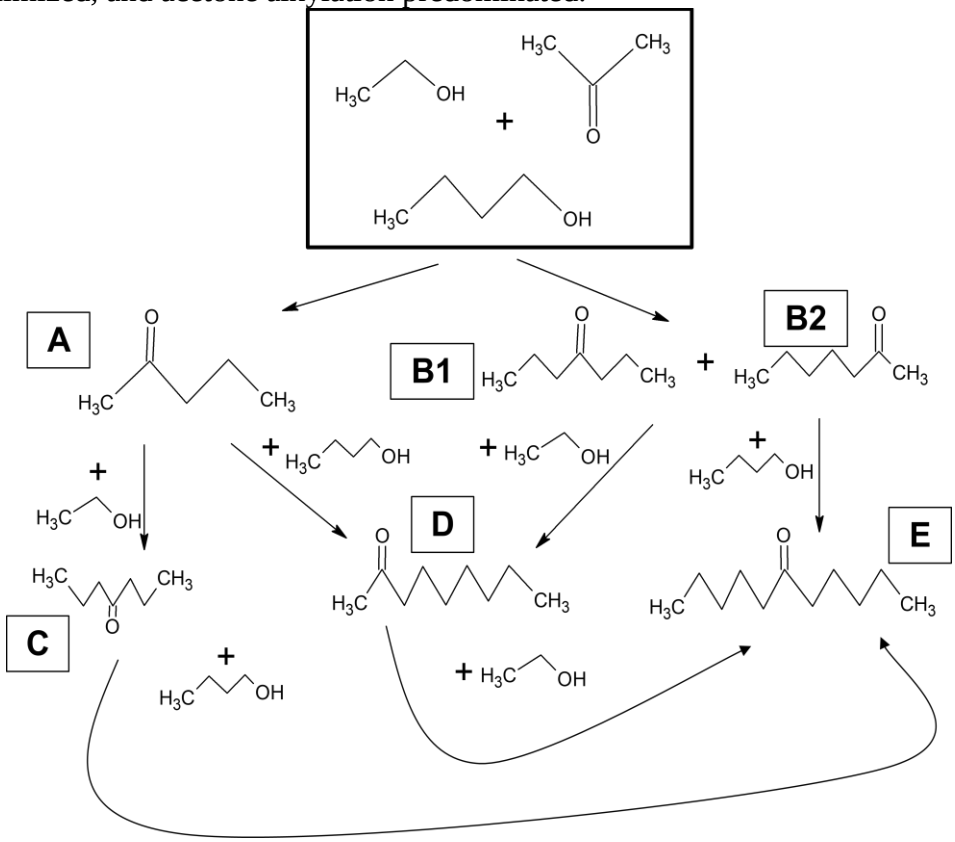

Scheme 3. A general pathways of ABE fermentation mixture conversion.

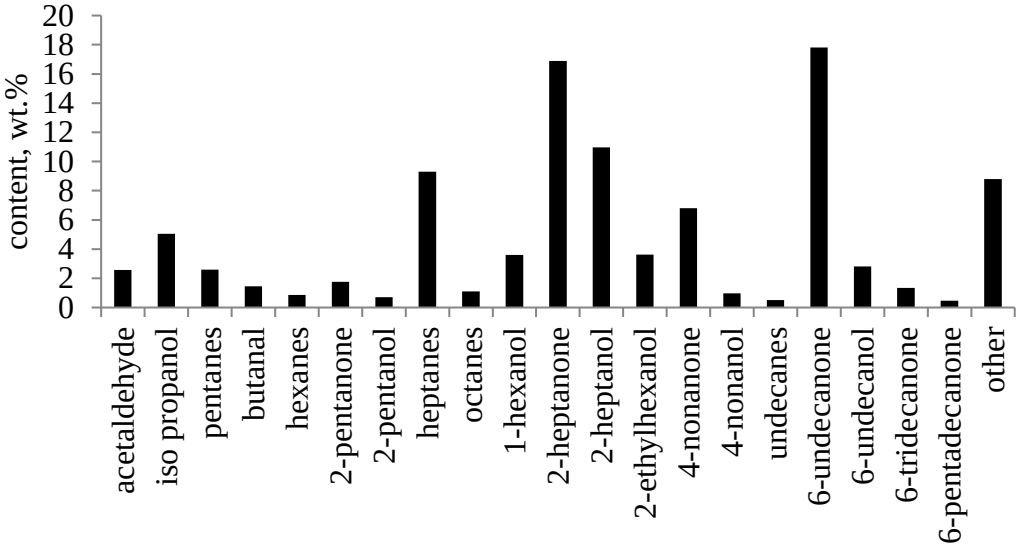

Figure 5. Products distribution of ABE mixture conversion.

The alcohols (1-butanol and ethanol) are dehydrogenated by the catalyst, generating the reactive aldehydes and hydrogen. At this stage the aldehydes undergo either a self-aldol reaction to form the Guerbet product precursor, or an aldol reaction with acetone. Under the conditions employed here, condensation with acetone

seems to be favoured, because acetone is present at much higher concentrations than the transient aldehydes. Subsequent dehydration of the aldol product under the reaction conditions furnishes α, β-unsaturated ketones that undergo hydrogenation with the hydrogen generated in the first step. Completing the same cycle with monoalkylated products affords the expected double alkylation products. The relative ease of attack by the unsubstituted versus the substituted a-carbon of the monoalkylated products leads primarily to unbranched products. This combination of kinetic controls on the alkylation reaction therefore enables the conversion of a mixture of renewable metabolites into a well-defined range of ketone products.
Thus, the principal possibility of obtaining high-molecular alcohols and ketones from ABE mixture is shown. The products obtained can be additives to gasoline, or be hydroisomerized to produce branched alkanes, which are the main components of motor fuels.

ACKNOWLEDGEMENTS

This work was done as part of TIPS RAS State Plan.

REFERENCES

[1] E.J. Steen, Y. Kang, G. Bokinsky, Z. Hu, A. Schirmer, A. McClure, S.B. del Cardayre, J.D. Keasling, Microbial production of fatty-acid-derived fuels and chemicals from plant biomass, *Nature*, Vol. 463, pp. 559–562, 2010.
[2] C. Wang, S.H. Yoon, H.J. Jang, Y.R. Chung, J.Y. Kim, E.S. Choi, S.W. Kim., Metabolic engineering of Escherichia coli for a-farnesene production, *Metabolic Engeneering*, Vol. 13, pp. 648–655, 2011.
[3] P.P. Peralta-Yahya, M. Ouellet, R. Chan, A. Mukhopadhyay, J.D. Keasling, T.S. Lee, Identification and microbial production of a terpene based advanced biofuel, *Nature Commun.*, Vol. 2, pp. 483-491, 2011.
[4] D. Tichit, D Lutic, B. Coq, R. Durand, R. Teissier, The aldol condensation of acetaldehyde and heptanal on hydrotalcite-type catalysts, *J. Catal*., Vol. 219, pp. 167-175, 2003.
[5] A. Pandey, *Handbook of Plant-Based Biofuels*, Taylor & Francis, Boca Raton, FL, 2009.
[6] E.L. Kunkes, D.A. Simonetti, R.M. West, J.C. Serrano-Ruiz, C.A. Gartner, J.A.Dumesic, Catalytic conversion of biomass to monofunctional hydrocarbons and targeted liquid-fuel classes, *Science*, Vol. 322, pp. 417-421, 2008.
[7] S. Ordóñez, E. Díaz, M. León, L. Faba, Hydrotalcite-derived mixed oxides as catalysts for different C–C bond formation reactions from bioorganic materials, *Catalysis Today*, Vol. 167, pp. 71-76, 2011.
[8] S.L. Schreiber, Target-oriented and diversity-oriented organic synthesis in drug discovery, *Science*, Vol. 287, pp. 1964-1969, 2000.
[9] R.A. Sheldon, Atom efficiency and catalysis in organic synthesis, *Pure Appl. Chem.*, Vol. 72, pp. 1233–1246, 2000.
[10] J. F. Jenck, F. Agterberg, M. J. Droescher, Products and processes for a sustainable chemical industry: a review of achievements and prospects, *Green Chem*., Vol. 6, pp. 544–556, 2004.
[11] J. Yang, X. Liu, D.-L. Meng, H.-Y. Chen, Z.-H. Zong, T.-T. Feng, K. Sun, Efficient iron-catalyzed direct b-alkylation of secondary alcohols with primary alcohols, *Adv. Synth. Catal.*, Vol. 354, pp. 328 – 334, 2012.
[12] A.V. Chistyakov, P.A. Zharova, S.A. Nikolaev, M.V. Tsodikov, Direct Au-Ni/Al_2O_3catalysed cross-condensation of ethanol with isopropanol into pentanol-2, *Catalysis Today*, Vol. 279, pp. 124–132, 2017.
[13] B.K. Tiwari and D.J. Troy, *Seaweed Sustainability*, Elsevier, 2015.
[14] J. Comwien, N. Boonvithaya, W. Chulaluksananukul, C. Glinwong, Direct production of butanol and ethanol from cane sugar factory wastewater and cellulosic ethanol pilot plant wastewater by clostridium beijerinckii CG1, *Energy Procedia*, Vol. 79, pp. 556 – 561, 2015.
[15] M. Uyttebroek, W. Van Hecke, K. Vanbroekhoven, Sustainability metrics of 1-butanol, *Catalysis Today*, Vol. 239, pp 7-10, 2015.

TECHNICAL PERFORMANCE AND ITS INFLUENCING FACTORS OF BIOENERGY FOR HEAT AND POWER

X. Li[1], L.W. Ma[1], Z. Li[1], W.D. Ni[1]

1. State Key Laboratory of Power Systems, Department of Energy and Power Engineering, Tsinghua-BP Clean Energy Research & Education Center, Tsinghua-Rio Tinto Research Center of Resource, Energy and Sustainable Development, Tsinghua University, Beijing, China; email: malinwei@tsinghua.edu.cn

ABSTRACT

China's total amount of bioenergy resources is close to 322 Mt oil equivalent, but most of them are abandoned or inefficiently utilized. Considering the urgent needs for low-carbon heat and power supply, it is of importance to further deploy advanced technologies to efficiently use these resources. However, various bioenergy technologies have different technical performance, and the performance is strongly associated with regional conditions of resources, engineering and policies. This manuscript compared typical case studies in various countries on biomass solid densified fuels, biomass power and biogas projects to comprehensively evaluate their technical performance. According to the technical stages from raw material, energy conversion to end use, we identified key influencing factors of the technical performance from perspectives of energy, environment and economy. The results indicated that raw material type, fuel forming method and production scale are main factors for biomass solid densified fuels. Raw material type, fuel pretreatment place and power generation mode greatly affect the technical performance of biomass power. The main factors for biogas projects are raw material type and utilization model of products. In general, the key point to improve the technical performance is to develop a comprehensive utilization approach suitable for local resource conditions of bioenergy.

Keywords: Technical performance, Biomass solid densified fuels, Biomass power, Biogas projects

1 INTRODUCTION

Bioenergy comes from the solar energy stored in biomass in the form of chemical energy. Bioenergy resources mainly include forest resources, agricultural resources, livestock manure, municipal solid waste, sewage sludge and others [1]. Compared with other kinds of renewable energy, the raw materials of bioenergy are relatively easy to collect and store [2].

Driven by the pressure of carbon emission reduction and environmental protection, the development of bioenergy and other kinds of renewable energy becomes an important issue. In China, there are large amounts of various bioenergy resources, especially agricultural and forestry residues. However, bioenergy utilization has met a series of problems, such as low resource utilization rate, immature bioenergy technologies and small industrial scale (see **Chapter 2**). These problems are related with the technical performance of various bioenergy technologies, and the performance is strongly associated with regional conditions, including local resources, engineering and policies. Therefore, it is deserved to further evaluate the technical performance of various bioenergy technologies according to regional specifications.

In this manuscript, we attempt to objectively evaluate and analyze the technical performance of bioenergy technologies based on specific cases. First, we reviewed the resource amount, utilization status and relevant literatures on technical performance (**Chapter 2**). Second, we select three main bioenergy technologies in the field of heat and power, including biomass solid densified fuels, biomass power and biogas projects (**Chapter 3-5** respectively). Based on typical cases in different countries, we conclude the key factors influencing the life-cycle technical performance from perspectives of energy, environment and economy. Finally, some conclusions and suggestions are given in **Chapter 6**.

2 LITERATURE REVIEW

The total amount of bioenergy resources in China is 322 Mt oil equivalent. In 2015, Crop straws, residues of forestry and livestock manure occupied 93% of the total amount [3], which belong to waste and are abundant in rural areas in China. However, the utilization of bioenergy resources still faces several problems in the following aspects:

(1) **Large amount of waste and low utilization efficiency**: In 2013, the consumption amount of bioenergy was 23.10 Mt oil equivalent, which only accounted for 0.9% of the total energy consumption in

China. From the aspect of power, the electricity produced by biomass was 42 billion kWh, which only occupied 0.8% of the total amount of electricity. In rural areas of China, most of the biomass is used in the traditional way of direct combustion, such as cooking and heating fuels with low utilization efficiency [4]. With the development of economy and change of energy structure, people in rural areas are more likely to choose commercial energy, such as coals, electricity and liquefied petroleum gas [5]. Such a way of energy consumption causes a number of abandoned agricultural and forestry residues. On-site burning of crop straws not only causes severe air pollution, but also wastes local bioenergy resources [6].

(2) **New types of bioenergy technologies lack large-scale applications**: Bioenergy utilization is still at the early stage in China. Compared with other developed countries, bioenergy technologies for heat and power need to be strengthened considering local conditions, commercial exploitation and scale utilization.

a. Biomass solid densified fuels: In China, the enterprises are scattered and lack uniform industrial and product standards. In contrast, biomass briquette industry is developing rapidly in Sweden, which benefits from available raw materials, a reasonable tax system and an extensive regional heating network [7].

b. Biomass power: Biomass-fired power industry is mature in European countries, such as straw-fired power technology in Denmark. Though China attached great importance to developing biomass power, few breakthroughs have been made in key technical procedures. Therefore, the main technologies and equipment still mainly rely on import [8].

c. Biogas projects: Biogas technology is developed in Germany. The products grow from combined heat and power to vehicle fuels as well as household fuels by network transmission. China has some demonstration projects in this field. However, it is necessary to optimize the stages of raw material collection, fermentation technology and product promotion and reduce the cost of a project [9].

From the above, the promotion and optimization are key points to develop bioenergy technologies, and technical performance of energy, environment and economy is the core issue. What's more, the development of bioenergy technology is in close contact with comprehensive utilization of local resources. Therefore, it is essential to know the reasons for their differences in specific cases. This manuscript aims at different cases of biomass solid densified fuels, biomass power and biogas projects, comparing their technical performance of energy, environment and economy and excavating their influencing factors.

3 BIOMASS SOLID DENSIFIED FUELS

Biomass solid densified fuels are processed from loose biomass at a certain temperature and under a certain pressure. They have the advantages of high heat value, high density and regular forms [10].

3.1 Technical Stages

The main technical stages of biomass solid densified fuels are shown in Figure 1.

Figure 1. Main Technical Stages of Biomass Solid Densified Fuels

Biomass production contains the process of biomass from planting to harvesting. when planting, fertilizers and pesticides are needed. Considering that raw materials are carried by transport, vehicle fuels are necessary. Solid fuel forming is the most important stage of the whole life cycle, during which the loose and irregular raw material is processed to solid fuels with high density and heat value. The main energy input of this part is electricity. After forming, the products will be distributed to users. Similar to biomass transportation, vehicle fuels are also needed during distribution. The solid densified fuels are used for cooking or heating during the stage of end use.

3.2 Case Study

In this part, we select three typical cases of biomass solid densified fuels in China, Canada and Japan [11,12,13], trying to find out the influencing factors of the technical performance (These cases are called Chinese case, Canadian case and Japanese case respectively in 3.2).

Chinese case studied a production line of 20,000 tons of corn straw briquette fuels in Henan Province. As for economic indicators, this project can realize 36% internal rate of return. In the aspect of energy, the authors thought corn straws were residues, so there was no energy consumption during planting. Canadian

case discussed the environmental effect of biomass solid densified fuels and considered fertilizers and pesticides during crop planting. Besides, the authors thought that the carbon emission during combustion derived from the absorption by photosynthesis during growth. In Japanese case, abundant woody bioenergy resources were processed into woody pellets for heat and power in Gifu Prefecture, Japan. The products included not only solid densified fuels, but also electricity produced by woody waste and municipal solid waste. The electricity can be used during the process of solid fuel forming.

The technical performance of energy, environment and economy are shown in Table 1.

Table 1. Technical Performance Indicators of Biomass Solid Densified Fuels

Country	Year	Raw material	Product	Energy consumption (MJ/MJ)	Carbon emission (gCO_2, e/MJ)	Cost ($/t)	Profit ($/t)
China	2014	Corn straws	Biomass briquette fuels	0.0456	1	48.7	61.1
Canada	2011	Wheat straws	Biomass pellet fuels	0.1049	9.984		
Japan	2012	Woody biomass	Woody pellets				

The common raw materials of biomass solid densified fuels are woody waste, straws and other agricultural residues. The energy consumption and carbon emission are associated with research boundary, raw material type and fuel forming method. If the fertilizers and pesticides are not considered in the life cycle, the amount of energy consumption and carbon emission will decrease. For raw material type, generally, the heat value of woody biomass is higher than that of straws. The optimization of fuel forming method will also improve the technical performance of energy and environment. For economic performance, the cost of biomass solid densified fuels is relevant to production scale.

From the perspective of the whole life cycle, the process of solid fuel forming consumes the most energy. Fuel combustion contributes the most carbon emission. However, because of carbon absorption by photosynthesis, the carbon emission of biomass solid densified fuels is smaller than that of coals.

4 BIOMASS POWER

Biomass power technology refers to the electricity generation from direct combustion of biomass, or conversion of biomass into combustible gas [14].

4.1 Technical Stages

The main technical stages of biomass power are shown in Figure 2.

Figure 2. Main Technical Stages of Biomass Power

Raw material supply includes the process of biomass growth to material collection. The pretreatment procedure can be done either in the producing area or in the power plant. If mechanized operations are necessary, gasoline, diesel oil and other types of energy should be input. Then, the biomass raw materials are transported from the producing area to the power plant, which requires vehicle fuels. Power generation is the key point of biomass power technology. The bioenergy can be transferred to heat and electricity. Most of the electricity is supplied for end users, the other is used for the power plant itself.

4.2 Case Study

We select three cases of biomass power technology in China, Japan and Canada [15,16,17] (these cases are called Chinese case, Japanese case and Canadian case respectively in 4.3).

In Chinese case, the installed capacity of Salix direct-fired power generation system in Inner Mongolia is 24 MW. The cost of the electricity is higher than the price of local coal power (0.48 RMB/kWh). The installed capacity in Japanese case is 10 MW. The woody residues from power generation can be processed to solid densified fuels, establishing a comprehensive system with heat and power. Incentivized by feed-in

tariff programs, this project could obtain economic benefits. Canadian case discussed the application of woody residues. The case aimed at the capacity of 137 MW. The authors studied the effect of biomass processing place on carbon emission.

The information and technical performance of energy, environment and economy are shown in Table 2.

Table 2. Technical Performance Indicators of Biomass Power

Country	Year	Raw material	Generating efficiency	Energy consumption (MJ/kWh)	Carbon emission (gCO_2,e/kWh)	Cost (₡/kWh)	Profit (₡/kWh)
China	2015	Salix	18.7%	24.53	114	7.9	4.3 (with government subsidies)
Japan	2017	Woody biomass	25%				
Canada	2014	Woody residues			18.83 (producing area), 21.7 (power plant)		

Biomass power plants can use woody biomass, agricultural residues and energy crops as raw materials to generate electricity. The indicators of energy and environment are related to research boundary, raw material type, fuel pretreatment place and power generation mode. For research boundary, if we consider the energy input during biomass growth and power plant construction, the amount of energy consumption and carbon emission will increase without doubt. The heat value of raw material also influences the carbon emission. In terms of power generation mode, waste from electricity generation is worth recycling to supply heat. In general, the cost of biomass power is higher than that of coal-fired power, which needs government subsidies to support such projects.

5 BIOMASS PROJECTS

The main component of biogas is methane, followed by carbon dioxide and other components. Biogas fermentation requires proper carbon nitrogen ratio, the specific values of which range from 20:1 to 30:1 [18]. The products of biogas project include cooking fuels, vehicle fuels and electricity.

5.1 Technical Stages

The main stages of biogas project is shown in Figure 3. The whole life cycle can be divided into three parts, including raw material supply, biogas conversion and purification and product supply

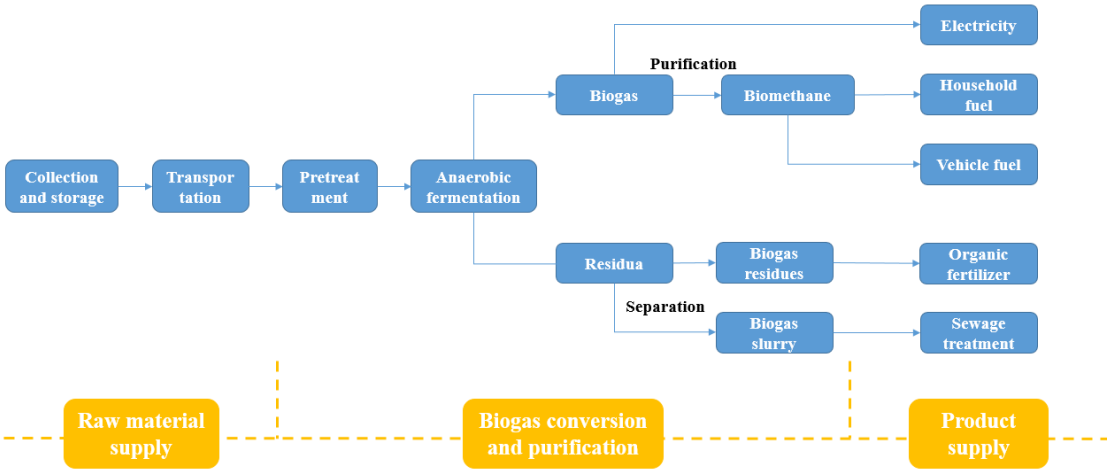

Figure 3. Main Technical Stages of Biogas Projects

The collection of some raw materials, such as crop straws, depends on seasons. As a result, it is necessary to store them after collection. The transportation process needs vehicle fuels as energy input. The proportion of methane can be increased and the proportion of carbon dioxide can be decreased after purification. The residua of fermentation can be separated to biogas residues and biogas slurry. Biogas can be used to generate

electricity or be applied to cogeneration. If biomethane meet the standards of fuels, it is accessible to gas network for residents, public service facilities and vehicle fuels. It is an effective way to use biogas residues for fertilizers and biogas slurry for recycle production.

5.2 Case Study

In this part, we select biogas projects in China and Germany to have a further discussion [19,20] (these cases are called Chinese case and German case respectively in 5.2).

In Chinese case, on account of high gas rate and convenience of transportation, the abundant corn straws become the main raw materials in Chifeng Biogas Project. Livestock manure are mainly used to initiate fermentation process. This project has totally 6000 m^3 anaerobic fermentation tanks, an organic fertilizer line and is expected to sell industrial carbon dioxide product during Phase Two. German case discussed the relationship between raw material types and environmental effect of biogas projects. Plan A of raw materials contained energy crops and chicken manure. Plan B used algae and chicken manure instead. The total fermentation volume is 4500 m^3. Biogas from this project is used for combined heat and power of 500 kW. The biogas residues and biogas slurry are available to give back to agricultural production.

The basic information and technical performance of energy and environment and are shown in Table 3.

Table 3. Technical Performance Indicators of Biomass Projects

Country	Year	Raw material	Product	Energy consumption (TJ)	Carbon emission (gCO_2,e/MJ)
China	2017	Corn straws and manure	Biomethane, organic fertilizer and industrial carbon dioxide	141.2	92.8
Germany	2017	Energy crops and chicken manure	Electricity, heat and fertilizer		28.9
		Algae and chicken manure			13.9

Biogas can be produced from agricultural and forestry residues, manure and sewage sludge. Generally, it needs mixture of different raw materials to obtain proper carbon nitrogen ratio. From the perspective of the whole life cycle, its energy consumption and carbon emission are relative to research boundary, raw material type and utilization model of products. Different types of raw materials have various biogas production rates and are collected and handled differently. For instance, in Germany case, energy crops need fertilizer and herbicide. For algae, fossil fuel input is necessary when using amphibian. From the perspective of product application, recycling the residua not only improves utilization rate of bioenergy resources, but also reduces energy consumption and carbon emission.

6 CONCLUSIONS

This paper reviews resource status, utilization status and technical performance of bioenergy in China. Based on typical cases of biomass solid densified fuels, biomass power and biogas projects in different countries, we analyze and discuss the main influencing factors of technical performance of energy, environment and economy. The conclusions are as follows:

(1) Specific cases have various raw materials, technology types and research boundaries. As a result, it is hard to form an accurate evaluation of technical performance.

(2) The results indicated that raw material type, fuel forming method and production scale are main factors for biomass solid densified fuels. Raw material type, fuel pretreatment place and power generation mode greatly affect the technical performance of biomass power. The main factors for biogas projects are raw material type and utilization model of products. Overall, the selection of raw material and comprehensive utilization of various kinds of bioenergy technologies greatly affect the technical performance.

According to the conclusions above, the following suggestions are given:

(1) It is necessary to strengthen the analysis and evaluation of newly-built bioenergy projects, timely provide first-hand data on technical performance of energy, environment and economy for relevant research, as well as the latest understanding of its influencing factors.

(2) It is of importance to explore the comprehensive utilization mode of bioenergy technologies in a specific region. That means, stakeholders in a specific region must select optimal bioenergy technology or technology combination according to raw material and market conditions, in order to achieve efficient utilization of regional bioenergy resources and large-scale development of bioenergy technologies.

ACKNOWLEDGEMENTS

This work was supported by the Chinese Academy of Engineering (Project No. 2016-ZD-14-2) and the State Key Laboratory of Power Systems in Tsinghua University (Project No. SKLD17Z02). The authors also gratefully acknowledge the financial support from the BP Company in the context of the Phase III Collaboration between BP and Tsinghua University, and from the Rio Tinto Group in the context of the Tsinghua-Rio Tinto Joint Research Center for Resources, Energy and Sustainable Development.

REFERENCES

[1] Z. B. Namsaraev, et al. Current status and potential of bioenergy in the Russian Federation, *Renewable and Sustainable Energy Reviews*, Vol. 81, pp. 625-634, 2018.
[2] Y. Jiang and Y. Cao, The comprehensive cost analysis of bioenergy from the perspective of carbon intensity reduction, *World Forestry Research*, Vol. 2, pp. 88-91, 2017.
[3] L. Lin and J. He, Is biomass power a good choice for governments in China, *Renewable and Sustainable Energy Reviews*, Vol. 73, pp. 1218-1230, 2017.
[4] P. Sun, et al. Prospects for modernization application of bioenergy in China, *Sino-Global Energy*, Vol. 6, pp. 21-28, 2014. (in Chinese)
[5] L. Peng, et al. Emissions inventory of atmospheric pollutants from open burning of crop residues in China based on a national questionnaire, *Research of Environmental Sciences*, Vol. 8, pp. 1109-1118, 2016. (in Chinese)
[6] D. Guo and C. Huang, Spatial and temporal distribution of crop straw resources in past 10 years in China and its use pattern, *Southwest China Journal of Agricultural Sciences*, Vol. 4, pp. 948-954, 2016. (in Chinese)
[7] Z. Yao, et al. Development status and experience of biomass pellet fuel in Sweden, *Renewable Energy Resources*, Vol. 6, pp. 145-150, 2010. (in Chinese)
[8] J. Huang, et al. Related questions research on biomass generation using agriculture and forest residue in China, *Journal of Shenyang Institute of Engineering (Natural Science)*, Vol. 1, pp. 7-14, 2008. (in Chinese)
[9] G. Ma and Y. Zhang, Discussions on current situation and problems of biomass energy development in China, *Management of Agricultural Science and Technology*, Vol. 1, pp. 20-22, 2013. (in Chinese)
[10] S. Song, et al. An economic and policy analysis of a district heating system using corn straw densified fuel: A case study in Nong'an County in Jilin Province, China, *Energies*, Vol. 10(1), pp. 8, 2017.
[11] J. Hu, et al. Economic, environmental and social assessment of briquette fuel from agricultural residues in China – A study on flat die briquetting using corn stalk, *Energy*, Vol. 64, pp. 557-566, 2014.
[12] A. Sultana and A. Kumar, Development of energy and emission parameters for densified form of lignocellulosic biomass, *Energy*, Vol. 36, pp. 2716-2732, 2011.
[13] T. Tabata and T. Okuda. Life cycle assessment of woody biomass energy utilization: Case study in Gifu Prefecture, Japan, *Energy*, Vol. 45, pp. 944-951, 2012.
[14] J. Wu, et al. Literature review on biomass power generation technology and economic feasibility, *Forest Engineering*, Vol. 4, pp. 102-106, 2012. (in Chinese)
[15] C. Wang, et al. Biomass direct-fired power generation system in China: An integrated energy, GHG emissions, and economic evaluation for Salix, *Energy Policy*, Vol. 84, pp. 155-165, 2015.
[16] Y. Kishita, et al. Scenario analysis for sustainable woody biomass energy business: The case study of a Japanese rural community, *Journal of Cleaner Production*, Vol. 142, pp. 1471-1485, 2017.
[17] A. Thakur, et al. Life-cycle energy and emission analysis of power generation from forest biomass, *Applied Energy*, Vol. 128, pp. 246-253, 2014.
[18] L. Deng, *Biogas projects*, Science Press, 2015.
[19] H. Liu, et al. Experience of producing natural gas from corn straw in China, *Resources, Conservation and Recycling*, in press, 2017.

[20] F. Ertem, et al. Environmental life cycle assessment of biogas production from marine macroalgal feedstock for the substitution of energy crops, *Journal of Cleaner Production*, Vol. 140, pp. 977-985, 2017.

TECHNO-ECONOMIC ANALYSIS OF BIO-HYDROGENATED DIESEL PRODUCTION FROM BIODIESEL IN THAILAND

A. Kantama[1], P. Hunpinyo[2], C. Prapainainar[3] and P. Narataruksa[4]

1. Department of Chemical Engineering, King Mongkut's University of Technology North Bangkok, Bangkok, Thailand; email: kukkik.che@gmail.com
2. Division of Chemical Process Engineering Technology (CPet), King Mongkut's University of Technology North Bangkok (Rayong Campus), Rayong, Research and Development Center for Chemical Unit Operation and Catalyst Design, Science and Technology Research Institute, King Mongkut's University of Technology North Bangkok, Bangkok, Thailand; email: piyapong.h@eat.kmutnb.ac.th
3. Department of Chemical Engineering, Research and Development Center for Chemical Unit Operation and Catalyst Design, Science and Technology Research Institute, King Mongkut's University of Technology North Bangkok, Bangkok, Thailand; email: chaiwat.r@eng.kmutnb.ac.th
4. Department of Chemical Engineering, Research and Development Center for Chemical Unit Operation and Catalyst Design, Science and Technology Research Institute, King Mongkut's University of Technology North Bangkok, Bangkok, Thailand; email: phavanee.n@eng.kmutnb.ac.th

ABSTRACT

Bio-hydrogenated diesel (BHD) production from biodiesel or fatty acid methyl esters was studied in Thailand. The feed rate of FAME to the BHD production process was 10 $m^3 \cdot h^{-1}$ according to biodiesel production rate from a palm oil refining plant in Thailand. Material and energy balance of BHD production was performed in Aspen Plus® to obtain minimum energy consumption using heat integration. Subsequently, economic evaluation was done to determine the attractiveness to investment. It was found that an investment in BHD production would be attractive to investment when the selling price of BHD was higher than 1,280 \$ m^{-3} with the net present value of 38.38 M \$.

Keywords: Techno-economic analysis; Fatty acid methyl ester; Bio-hydrogenated diesel; Hydroprocessing.

1 INTRODUCTION

The first generation of biofuels is biodiesel having already been commercially available. Biodiesel or fatty acid methyl esters (FAME) can be produced from vegetable oil or animal fat (bio-lipids) with alcohol via transesterification process to form ester compounds and glycerol [1]. FAME can be produced from many types of oils and the most common oils are rapeseed oil (rapeseed methyl ester, RME) in Europe, soybean oil (Soya methyl ester, SME) in the USA and palm oil in Asia [2-5]. Refined palm stearin (RPS) is an interesting feedstock for biodiesel production because it is a by-product from refine palm oil industry [1, 2].
Biodiesel production using transesterification is the most common process. It can operate under atmospheric pressure and low temperature and exhibit high yield with good quality biodiesel [2-4]. Density and oxidation stability are typically problematic properties for FAME for using in diesel engines because the presence of oxygenated compounds in FAME [5]. Therefore, blending ratio of FAME with conventional diesel has a limitation, such as up to 7% in Thailand [6]. To improve biodiesel properties, catalytic partial or full hydrogenation process of polyunsaturated methyl ester into monounsaturated compound can be introduced [8]. It has been reported that partial hydrogenation of vegetable oil [7-9] can improve oxidation stability and cetane number of fuel products but some properties of partial hydrogenated methyl ester does not meet diesel standard [10]. Due to a limitations of using biodiesel in engines, hydrodeoxygenation (HDO) process can be introduced to convert vegetable oils or methyl ester components to liquid alkane hydrocarbons and the products can be classified as 2nd generation biofuel as same as hydrogenated renewable diesel (HRD) [11]. HDO of methyl ester into alkane have been reported in literatures, such as, methyl heptanoate [12], ethyl stearate [13, 14] methyl stearate [15, 16], methyl laurate, and methyl hexanoate [17] or methyl palmitate [5]. At present, there are not sufficient researches studying the techno-economic assessment of bio-hydrogenated diesel (BHD) production from FAME via HDO process. Therefore, in this work, BHD production from FAME was studied by using chemical process simulation to perform material and energy balance. Economic evaluation for the investment of BHD production plant from FAME is preliminarily evaluated in a case study of Thailand. The attractiveness of project investment is reported as return on

investment, payback period, and net present value. The results can present economic potential of BHD production from biodiesel in Thailand.

2 METHODOLOGY

2.1 Process development

Bio-hydrogenated diesel (BHD) process production from FAME was simulated using Aspen Plus software. FAME was obtained from transesterification of refined palm stearin (RPS) in a capacity of 10 $m^3 \cdot hr^{-1}$. The composition of FAME, represented by methyl palmitate, was converted to BHD under the operating conditions of 495 K, 2 MPa using Ni/SAPO-11 catalysts in 360 minutes of reaction time [5]. This process was applied with heat exchanger network design and heat integration optimization by using pinch analysis. The reaction of hydrogenation, decarbonylation and decarboxylation [5] are in a semi-batch operation. From Figure 1, FAME and hydrogen gas are fed to the process and the reaction undergoes in hydroprocessing reactors. All products are cooled and sent to separation. Liquid product is fractionated in a distillation column into three groups: light gas, C5–C14 (Naphtha) and a mixture of C15–C18 mixed with unreacted FAME. Finally, the bottom products from distillation column are sent to upgrading cold flow properties by isomerization reaction [18].

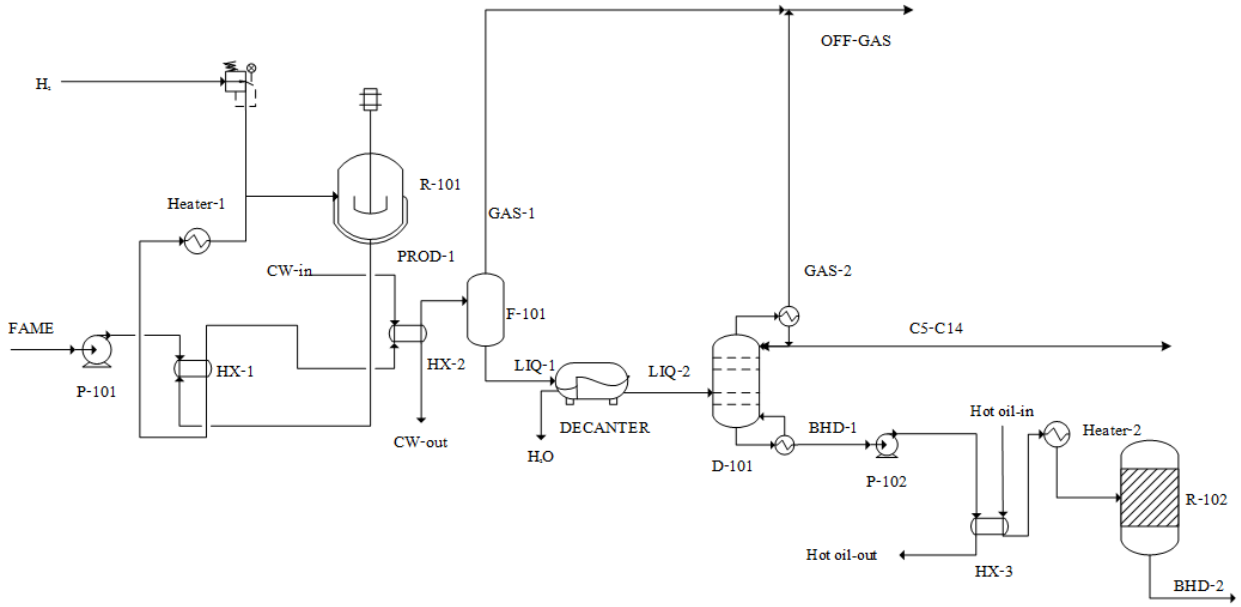

Figure 1 Process flow diagram of BHD production from FAME.

2.2 Economic analysis of BHD process

Cost estimation of process production was performed by using the study estimate and preliminary method to evaluate fixed capital investment (FCI), working capital (WC) and total capital investment (TCI), respectively. Mass and energy balance from the simulation model was used to determine equipment sizes and free on board (f.o.b.) purchased equipment costs [19]. Project annual profit can be indicated by rate of return on investment (ROI) and it can be calculated using equation 1.

$$\mathrm{ROI}(\%) = \left(\left(100 \times \mathrm{NP_A}\right) / \mathrm{N} \times \mathrm{TCI}\right) \qquad (1)$$

where NPA is total annual net profit and N is project life time.

Furthermore, payback period (PBP) and net present value (NPV) were used to analyse the profitability of a project investment with the minimum rate of return (MARR) of 10%. Key assumptions for economic analysis are shown in Table 1.

Table 1. Key assumptions for economic analysis

Parameters	Value
Project lifetime	15 y
Plant availability	345 d y^{-1}
Plant capacity	10 m^3 h^{-1} of FAME
MARR	10%
FAME price	710 \$ m^{-3}
Hydrogen price	4.3×10^{-1} \$ m^{-3}

3 RESULTS

3.1 Process simulation

The material balance for BHD production from FAME in a capacity of 10 m^3 hr^{-1} is shown in Table 2. After main products pass through separation section and upgrading section to improve fuel property, BHD yield from this process is 78.86% with 99.98% conversion. The property of BHD, which is produced from FAME, meets the standard properties of renewable diesel (10) with the heating value of 43.939 MJ kg^{-1} and density of 773 g dm^{-3}.

Table 2. Flow rate in BHD process

Parameters	FAME	H2	OFF-Gas	C5-C14	BHD-2
Mole Flow (kmol hr^{-1})	27.98	64.00	62.66	4.75	23.75
Mass Flow (kg hr^{-1})	7567	129	1491	921	5229
Volume Flow (m^3 hr^{-1})	10	1587	17065	1.36	13.32

3.2 Investment evaluation

The total f.o.b. cost of equipment of the BHD production is 28.663 M\$ leading to fixed capital investment (FCI), working capital (WC) and total capital investment (TCI) of 147.328 M\$, 25.510 M\$ and 172.838 M\$, respectively. The profitability of this process can be indicated by ROI, PBP, and NPV, which are shown in Table 3. The assumption of the project was that the plant was under construction in the first two years. When production starts, operating capacity are 50% and 80% of full capacity in the first year and second years of operation, respectively. Then, the following years, the plant was operated with 90% of full capacity. The selling prices used in this analysis were set based initially on the economic evaluation with the cost of FAME at 710 \$ m^{-3}. The considered prices are Thailand expected BHD price of 795 \$ m^{-3} (FAME from RPS price in Thailand + 85 \$ m^{-3}), 1,190 \$ m^{-3} (10%ROI), and 1,280 \$ m^{-3} (6 y of PBP).

Table 3. Profitability of BHD production

BHD price (\$ m^{-3})	ROI (%)	PBP (years)	NPV (M\$)
790	-8.00	-	-235.35
1,190	10.00	7.50	-12.48
1,280	14.10	6.00	38.38

In Table 3, it can be seen that the BHD selling price of 795 \$ m^{-3} and 1,190 \$ m^{-3} could not provide benefit to the project as it gives negative ROI and NPV. The selling price of 1,280 \$ m^{-3} gives 38.38 M\$ with 14.10% ROI.

4 CONCLUSIONS

Economic evaluation of BHD production plant from FAME is performed. The production uses FAME from RPS as feedstock with a capacity of 10 m^{-3} h^{-1}. The BHD yield was found to be about 78.86%. The techno-economic model was developed to estimate cost of BHD production plant. The total capital investment and operating cost for BHD production were 172.838 M$ and 97.584 M$, respectively. In the economic evaluation, the Thailand expected BHD selling price between 790 $ m^{-3} and 1,280 $ m^{-3}, it was found that the selling prices must be higher than 1,210 $ m^{-3} in order to meet 10% MARR. Therefore, there is potential in investment for BHD production. However, the appropriate selling price must be assigned.

ACKNOWLEDGEMENTS

The authors gratefully acknowledge the Thailand Research Fund (MSD57I0110) for financial support and Suksomboon Palm Oil Co., Ltd., Thailand, for providing technical information.

REFERENCES

[1] K.L. Theam, A. Islam, Y.M. Choo, Y.H. Taufiq-Yap, Biodiesel from low cost palm stearin using metal doped methoxide solid catalyst, *Industrial Crops and Products*, Vol. 76, pp. 281-289, 2015.

[2] T. Issariyakul, A.K. Dalai, Biodiesel from vegetable oils, *Renewable and Sustainable Energy Reviews*, Vol. 31, pp. 446-471, 2014.

[3] S. Lee, D. Posarac, N. Ellis, Process simulation and economic analysis of biodiesel production processes using fresh and waste vegetable oil and supercritical methanol, *Chemical Engineering Research and Design*, Vol. 89, pp. 2626-2642, 2011.

[4] E.M. Shahid, Y. Jamal, Production of biodiesel: A technical review, *Renewable and Sustainable Energy Reviews*, Vol. 15, pp. 4732-4745, 2011.

[5] H. Zuo, Q. Liu, T. Wang, L. Ma, Q. Zhang, Q. Zhang, Hydrodeoxygenation of Methyl Palmitate over Supported Ni Catalysts for Diesel-like Fuel Production, *Energy and Fuels*, Vol. 26, pp. 3747-3755, 2012.

[6] Committee on Energy Policy., in, http://www.eppo.go.th/nepc/kbg/kbg-172.html, 2013.

[7] A. Bouriazos, C. Vasiliou, A. Tsichla, G. Papadogianakis, Catalytic conversions in green aqueous media. Part 8: Partial and full hydrogenation of renewable methyl esters of vegetable oils, *Catalysis Today*, Vol. 247, pp. 20-32, 2015.

[8] A. Bouriazos, S. Sotiriou, C. Vangelis, G. Papadogianakis, Catalytic conversions in green aqueous media: Part 4. Selective hydrogenation of polyunsaturated methyl esters of vegetable oils for upgrading biodiesel, *Journal of Organometallic Chemistry*, Vol. 695, pp. 327-337, 2010.

[9] R. Fajar, Prawoto, B. Sugiarto, Predicting Fuel Properties of Partially Hydrogenated Jatropha Methyl Esters Used for Biodiesel Formulation to Meet the Fuel Specification of Automobile and Engine Manufacturers, *Kasetsart Journal (Natural Science)*, Vol. 46, pp. 629-637, 2012.

[10] S. Bezergianni, A. Dimitriadis, Comparison between different types of renewable diesel, *Renewable and Sustainable Energy Reviews*, Vol. 21, pp. 110-116, 2013.

[11] A. Kantama, P. Narataruksa, P. Hunpinyo, C. Prapainainar, Techno-economic assessment of a heat-integrated process for hydrogenated renewable diesel production from palm fatty acid distillate, *Biomass and Bioenergy*, Vol. 83, pp. 448-459, 2015.

[12] E.-M. Ryymin, M.L. Honkela, T.-R. Viljava, A.O.I. Krause, Competitive reactions and mechanisms in the simultaneous HDO of phenol and methyl heptanoate over sulphided NiMo/γ-Al2O3, *Applied Catalysis A: General*, Vol. 389, pp. 114-121, 2010.

[13] I. Kubičková, M. Snåre, K. Eränen, P. Mäki-Arvela, D.Y. Murzin, Hydrocarbons for diesel fuel via decarboxylation of vegetable oils, *Catalysis Today*, Vol. 106, pp. 197-200, 2005.

[14] M. Snåre, I. Kubičková, P. Mäki-Arvela, K. Eränen, J. Wärnå, D.Y. Murzin, Production of diesel fuel from renewable feeds: Kinetics of ethyl stearate decarboxylation, *Chemical Engineering Journal*, Vol. 134, pp. 29-34, 2007.

[15] P.T. Do, M. Chiappero, L.L. Lobban, D.E. Resasco, Catalytic Deoxygenation of Methyl-Octanoate and Methyl-Stearate on Pt/Al2O3, *Catalysis Letters*, Vol. 130, pp. 9-18, 2009.

[16] J. Chen, H. Shi, L. Li, K. Li, Deoxygenation of methyl laurate as a model compound to hydrocarbons on transition metal phosphide catalysts, *Applied Catalysis B: Environmental*, Vol. 144, pp. 870-884, 2014.

[17] N. Shi, Q.-y. Liu, T. Jiang, T.-j. Wang, L.-l. Ma, Q. Zhang, X.-h. Zhang, Hydrodeoxygenation of vegetable oils to liquid alkane fuels over Ni/HZSM-5 catalysts: Methyl hexadecanoate as the model compound, *Catalysis Communications*, Vol. 20, pp. 80-84, 2012.
[18] H.I. H. Ono, A. Koyama, Y. Iguchi, Production of BHD (Bio Hydrofined Diesel) with Improved Cold Flow Properties, in: *Proc. Int. Conf. On 19th Annual Saudi-Japan Symposium on Catalysts in Petroleum Refining and Petrochemicals 2009*, Dhahran, Saudi Arabia, pp. 14, 2009.
[19] W.D. Seider, J.D. Seader, D.R. Lewin, *Product and process design principles synthesis, analysis and evaluation*, Wiley, 2003.

TECHNO-ECONOMIC STUDY OF BIO-HYDROGENATED DIESEL PRODUCTION FROM JATROPHA OIL

J. Hard-arn[1], T. Konsila[2], S. Wongsakulphasatch[3], C. Prapainainar[4], K. Cheenkachorn[5], and P. Narataruksa[6]

1. Department of Chemical Engineering, King Mongkut's University of Technology North Bangkok, Bangkok, Thailand; email: snowflake.kiie@gmail.com
2. Department of Chemical Engineering, King Mongkut's University of Technology North Bangkok, Bangkok, Thailand; email: konsila.t@gmail.com
3. Department of Chemical Engineering, King Mongkut's University of Technology North Bangkok, Bangkok, Thailand; email: suwimol.w@eng.kmutnb.ac.th
4. Department of Chemical Engineering, Research and Development Center for Chemical Unit Operation and Catalyst Design, Science and Technology Research Institute, King Mongkut's University of Technology North Bangkok, Bangkok, Thailand; email: chaiwat.r@eng.kmutnb.ac.th
5. Department of Chemical Engineering, King Mongkut's University of Technology North Bangkok, Bangkok, Thailand; email: kraipsuwimolat.c@eng.kmutnb.ac.th
6. Department of Chemical Engineering, Research and Development Center for Chemical Unit Operation and Catalyst Design, Science and Technology Research Institute, King Mongkut's University of Technology North Bangkok, Bangkok, Thailand; email: phavanee.n@eng.kmutnb.ac.th

ABSTRACT

In this work, feasibility study of producing bio-hydrogenated diesel (BHD) from Jatropha oil in Thailand is focused. A block flow diagram for the process production is presented with the pre-treated Jatropha oil and hydrogen as the main feedstock. The production of BHD is carried out via hydroconversion using chemical process simulation software, Aspen Plus. The main process comprises of hydroprocessing that includes hydrodeoxygenation, decarbonylation and decarboxylation. Hydroprocessing is operated under temperature and pressure of 360ºC and 30 bar, respectively. With a base case of 5.0×10^3 kg h^{-1} of Jatropha feed capacity, the process produces 3.8×10^3 kg h^{-1} of BHD. The product BHD from the calculation has a density of 0.78 kg dm^{-3} and a heating value of 44 MJ·kg^{-1}, which are in the range of diesel standard. In the economic study, a minimum acceptable rate of return of 10% with 15 y of project life, the total capital investment cost is 7.10 M$. A selling price of bio-hydrogenated diesel was 1.10×10^3 $ m^{-3} gave the net present value at 145.72 M$. From this study, it is found that the production technology is viable for investment.

Keywords: Techno-economic assessment, Bio-hydrogenated diesel, Jatropha oil, Hydroprocessing

1 INTRODUCTION

Renewable and alternative energy sources are currently in focus for production of liquid fuels for transportation sector due to the limitation of fossil fuel sources and environmental concerns [1]. Biofuels from bioresources, especially oil from plants, has gained interests as an alternative energy resource because biofuels from plant oils are nitrogen- and sulphur-free fuel making it environmentally friendly [2]. Biodiesel or fatty acid methyl ester, FAME, the first generation of biofuel, derived from vegetable oil or animal fat has been produced commercially by transesterification reaction. Biodiesel, however, exhibits undesirable fuel properties derived from oxygenated compounds leading to limited blending ratio with liquid diesel from fossil fuel [3]. Bio-hydrogenated diesel (BHD) or green diesel, the second generation of diesel-based biofuel, has recently been in attention due to its good properties for blending with diesel fuel from petroleum [4]. Many types of vegetable oil have been researched in lab scale for BHD production with various type of catalysts to afford high BHD yield, high conversion and selectivity, at preferable operating conditions [5-8]. BHD can be produced from vegetable oil via hydroprocessing [9]. The products from hydroprocessing are mainly straight chain alkanes consisting a range of hydrocarbons with C15 to C20 and after isomerization, the liquid fuels have similar properties to fossil diesel [10-13]. Jatropha oil, a non-edible oil, is an oil derived from Jatropha curcus containing mainly Palmitic acid (16:0), 14.1 - 15.3, Oleic acid (18:1), 34.3-45.8, Linoleic acid (18:2), 29.0-44.2 and some other fatty acids [14-16]. Liu et al. (2012) reported experimental study of hydroprocessing of Jatropha oil using NiMoCe/Al2O3 catalyst. The main components in product oil are straight chain alkanes ranging from C15 to C18 with the maximum yield, selectivity, and conversion of

80%, 90%, and 89%, respectively under the operating condition of 370ºC, 3.5 MPa and 0.9 h^{-1} [1]. Yasir et al. (2016) used NiCe loaded on titania nanotubes catalysts (NiCe/TNT) in hydroconversion reaction of crude Jatropha oil under the reaction condition of reaction condition of 300ºC, 30 bar, and 1 h reaction time affording 85 % of triglyceride conversion obtaining hydrocarbon n-C15 to n-C18 [17]. In term of techno-economic study of BHD production, Miller and Kumar studied BHD production from canola and camelina oil [18], Cheah et al. investigated green diesel production from rubber seed oil using catalytic decarboxylation [19] and Kantama et al. reported study on BHD production from palm fatty acid distillate [20]. However, in term of techno-economic study on BHD production from Jatropha oil, there has not been any studies as far as the author's knowledge. Therefore, in this work a new process design and techno-economic assessment of producing BHD from Jatropha oil is focused to determine to potential of BHD production in industrial scale. The case study was based on potential Jatropha oil supply in Thailand with a feed rate of 5.0×10^3 kg h^{-1}. The process model was conducted to perform material and energy balance prior to cost estimation of the processing plant. Finally, economic potential of the production was evaluated.

2 METHODOLOGY

2.1 Process development and simulation model

A block flow diagram and a process flow diagram for a simulation model of BHD production from Jatropha oil in this work shown in Figure 1 and Figure 2 were developed based on process flow diagrams in the similar technology presented in publications [18-21]. Hydroprocessing of Jatropha oil is carried out in a reactor using NiMoCe/Al2O3 catalyst under the operating condition of 360 ºC, 30 bar and liquid hourly space velocity of 0.8 h^{-1} [1]. Under this operating condition, the reaction afforded 98.52% conversion [1]. Jatropha oil feed composition used in the model were palmitic acid 12.03%, linoleic acid 33.69%, oleic acid 45.41%, stearic acid 8.14%, and eicosenoic acid 0.16% [22]. Unsaturated fatty acids were converted to saturated fatty acid via hydrogenation. Consequently, oxygenated compounds in fatty acids components were undergone a set of reactions via three main reactions of hydrodeoxygenation, decarboxylation and decarbonylation following equation (1), (2), and (3) [7].

$$R-CH_2-COOH+3H_2 \rightarrow R-CH_2-CH_3+2H_2O \quad (1)$$

$$R-CH_2-COOH \rightarrow R-CH_2-CH_3+CO_2 \quad (2)$$

$$R-CH_2-COOH+H_2 \rightarrow R-CH_2-CH_3+CO+H_2O \quad (3)$$

Output stream from the reactor is fed to the first separating step to remove light gases and water in a flash drum and a decanter, respectively. Fuel products are then fractionated in distillation columns to obtain Bio-gasoline, Bio-jet, and BHD. The capacity of the BHD production plant in this study was assigned at 5.0×10^3 kg h^{-1} of Jatropha oil feed.

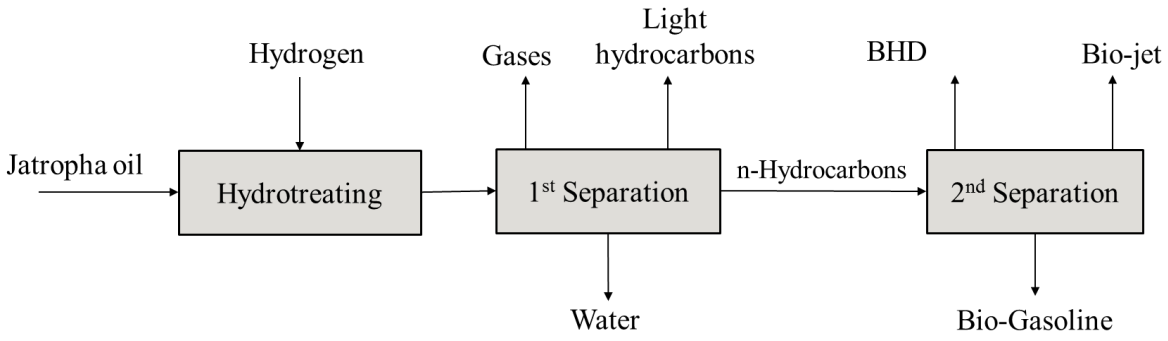

Figure 1 Block flow diagram of BHD production from Jatropha oil.

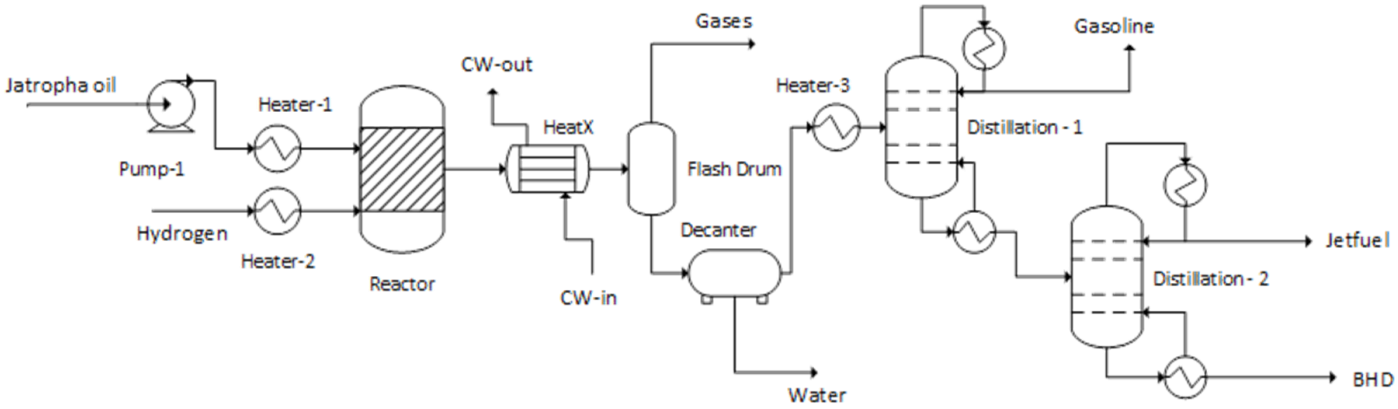

Figure 2 Process flow diagram of the simulation model of BHD production.

2.2 Economic analysis of BHD production from Jatropha oil

After affording mass and energy balance information from the simulation model, equipment sizes of major process equipment were determined and followed by calculation of free on board (f.o.b.) purchased equipment costs [2, 20, 23]. Subsequently, the percentage of delivered-equipment cost for calculating the total capital investment of bio-hydrogenated diesel was carried out and fixed capital investment (FCI), working capital (WC) and total capital investment (TCI), were afforded [23]. Operating cost of the BHD production plant was also calculated based on material and energy balance information [23]. Table 1 present major economic assumptions in this study.

Table 1. Key assumptions for economic analysis of BHD production from Jatropha oil

Parameters	Value
Project lifetime	15 y
Plant availability	345 d y^{-1}
Plant capacity	5.0×10^{3} kg h^{-1} of Jatropha oil feed
MARR	10%
Jatropha oil price	0.5 \$ kg^{-1}
Hydrogen price	4.80×10^{-1} \$ m^{-3}
BHD Price	1.10×10^{3} \$ m^{-3}

3 RESULTS AND DISCUSSION

3.1 Material and energy balance from the simulation

From the case study of BHD production from Jatropha oil with the feed rate of 5×10^{3} kg h^{-1}, reactor model in the simulation was set with adjusted reaction conversion to afford product distribution according to Lui et al. [22]. The root-mean-square-error from the simulation model and from the literature was 1.11×10^{-3} suggesting that the simulation model was reliable for the study. Material balance from the process showing key parameters from the simulation model is shown in Table 2. The overall performance of BHD production from the simulation model afforded 3.8×10^{3} kg h^{-1} of BHD product from 5×10^{3} kg h^{-1} of Jatropha feed. BHD product from the model afford a density of 0.78 kg dm^{-3} and a heating value of 44 MJ kg^{-1}, which are in the same range with diesel from petroleum [12].

3.2 Plant cost and economic study results

With the results from material balance, purchased equipment cost of major equipment in the process comprising of pumps, heaters, separators, heat exchangers, reactor and column was afforded with 1.19 M$. This led to a fixed capital investment cost and a total capital investment cost of 6.01 M$ and 7.10 M$, respectively. With the BHD selling price of 1.10×10^3 \$ m^{-3}, the project afforded a net present value of 145.72 M$ making investment in this project feasible.

Table 2. Material balance of BHD production from Jatropha oil

Stream	Mass flow rate, kg h^{-1}	Volumetric flow rate, m^3 h^{-1}
Jatropha oil	5×10^3	5.74
Hydrogen	201	191
Gases	790	1.65×10^3
Gasoline	240	0.27
Jet-fuel	178	0.31
BHD	3.8×10^3	4.87

4 CONCLUSIONS

Material and energy balance of BHD production plant from Jatropha oil was performed using chemical process simulation Aspen plus. The feasibility study on the BHD production was performed and it was found that, with the Jatropha oil feed rate of 5×10^3 kg h^{-1}, the BHD production rate was 3.8×10^3 kg h^{-1} giving the total capital investment cost of 7.10 M$. From the project life of 15 years, the selling price of BHD at 1.10×10^3 \$ m^{-3} gave the net present value of the project of 145.72 M$ showing that the preliminary study on the project was primarily attractive for investment.

REFERENCES

[1] J. Liu, K. Fan, W. Tian, C. Liu, L. Rong, Hydroprocessing of Jatropha oil over NiMoCe/Al2O3 catalyst, *International Journal of Hydrogen Energy*, Vol. 37, pp. 17731-17737, 2012.

[2] H. Li, B. Shen, J.C. Kabalu, M. Nchare, Enhancing the production of biofuels from cottonseed oil by fixed-fluidized bed catalytic cracking, *Renewable Energy*, Vol. 34, pp. 1033-1039, 2009.

[3] H. Zuo, Q. Liu, T. Wang, L. Ma, Q. Zhang, Q. Zhang, Hydrodeoxygenation of Methyl Palmitate over Supported Ni Catalysts for Diesel-like Fuel Production, *Energy & Fuels*, Vol. 26, pp. 3747-3755, 2012.

[4] S. Bezergianni, A. Dimitriadis, Comparison between different types of renewable diesel, *Renewable and Sustainable Energy Reviews*, Vol. 21, pp. 110-116, 2013.

[5] M. Mohammad, T. Kandaramath Hari, Z. Yaakob, Y. Chandra Sharma, K. Sopian, Overview on the production of paraffin based-biofuels via catalytic hydrodeoxygenation, *Renewable and Sustainable Energy Reviews*, Vol. 22, pp. 121-132, 2013.

[6] W. Kiatkittipong, S. Phimsen, K. Kiatkittipong, S. Wongsakulphasatch, N. Laosiripojana, S. Assabumrungrat, Diesel-like hydrocarbon production from hydroprocessing of relevant refining palm oil, *Fuel Processing Technology*, Vol. 116, pp. 16-26, 2013.

[7] A. Srifa, K. Faungnawakij, V. Itthibenchapong, N. Viriya-empikul, T. Charinpanitkul, S. Assabumrungrat, Production of bio-hydrogenated diesel by catalytic hydrotreating of palm oil over NiMoS2/γ-Al2O3 catalyst, *Bioresource Technology*, Vol. 158, pp. 81-90, 2014.

[8] F. Pinto, S. Martins, M. Gonçalves, P. Costa, I. Gulyurtlu, A. Alves, B. Mendes, Hydrogenation of rapeseed oil for production of liquid bio-chemicals, *Applied Energy*, Vol. 102, pp. 272-282, 2013.

[9] R. Sotelo-Boyás, Y. Liu, T. Minowa, Renewable Diesel Production from the Hydrotreating of Rapeseed Oil with Pt/Zeolite and NiMo/Al2O3 Catalysts, *Industrial & Engineering Chemistry Research*, Vol. 50, pp. 2791-2799, 2011.

[10] P. Priecel, D. Kubička, L. Čapek, Z. Bastl, P. Ryšánek, The role of Ni species in the deoxygenation of rapeseed oil over NiMo-alumina catalysts, *Applied Catalysis A: General*, Vol. 397, pp. 127-137, 2011.

[11] S. Gong, A. Shinozaki, M. Shi, E.W. Qian, Hydrotreating of Jatropha Oil over Alumina Based Catalysts, *Energy & Fuels*, Vol. 26, pp. 2394-2399, 2012.
[12] M. Patel, A. Kumar, Production of renewable diesel through the hydroprocessing of lignocellulosic biomass-derived bio-oil: A review, *Renewable and Sustainable Energy Reviews*, Vol. 58, pp. 1293-1307, 2016.
[13] Y. Liu, R. Sotelo-Boyás, K. Murata, T. Minowa, K. Sakanishi, Hydrotreatment of Jatropha Oil to Produce Green Diesel over Trifunctional Ni–Mo/SiO2–Al2O3 Catalyst, *Chemistry Letters*, Vol. 38, pp. 552-553, 2009.
[14] G.M. Gübitz, M. Mittelbach, M. Trabi, Exploitation of the tropical oil seed plant Jatropha curcas L, *Bioresource Technology*, Vol. 67, pp. 73-82, 1999.
[15] A. Datta, B.K. Mandal, Use of Jatropha Biodiesel as a Future Sustainable Fuel, *Energy Technology & Policy*, Vol. 1, pp. 8-14, 2014.
[16] A.S. Silitonga, A.E. Atabani, T.M.I. Mahlia, H.H. Masjuki, I.A. Badruddin, S. Mekhilef, A review on prospect of Jatropha curcas for biodiesel in Indonesia, *Renewable and Sustainable Energy Reviews*, Vol. 15, pp. 3733-3756, 2011.
[17] M. Yasir, M.T. Azizan, A. Ramli, M. Ameen, Hydroprocessing of Crude Jatropha Oil Using Hierarchical Structured TiO2 Nanocatalysts, *Procedia Engineering*, Vol. 148, pp. 275-281, 201).
[18] P. Miller, A. Kumar, Techno-economic assessment of hydrogenation-derived renewable diesel production from canola and camelina, *Sustainable Energy Technologies and Assessments*, Vol. 6, pp. 105-115, 2014.
[19] K.W. Cheah, S. Yusup, H.K. Gurdeep Singh, Y. Uemura, H.L. Lam, Process simulation and techno economic analysis of renewable diesel production via catalytic decarboxylation of rubber seed oil – A case study in Malaysia, *Journal of Environmental Management*, Vol. 203, pp. 950-961, 2017.
[20] A. Kantama, P. Narataruksa, P. Hunpinyo, C. Prapainainar, Techno-economic assessment of a heat-integrated process for hydrogenated renewable diesel production from palm fatty acid distillate, *Biomass and Bioenergy*, Vol. 83, pp. 448-459, 2015.
[21] J. Hancsók, T. Kasza, S. Kovács, P. Solymosi, A. Holló, Production of bioparaffins by the catalytic hydrogenation of natural triglycerides, *Journal of Cleaner Production*, Vol. 34, pp. 76-81, 2012.
[22] J. Liu, J. Lei, J. He, L. Deng, L. Wang, K. Fan, L. Rong, Hydroprocessing of Jatropha Oil for Production of Green Diesel over Non-sulfided Ni-PTA/Al2O3 Catalyst, *Scientific Reports*, Vol. 5, pp. 11327, 2015.
[23] W.D. Seider, J.D. Seader, D.R. Lewin, S. Widagdo, *Product and Process Design Principles: Synthesis, Analysis and Design*, John Wiley & Sons, 2008.

CATALYTIC UPGRADING OF BIO-TAR IN SUPERCRITICAL ETHANOL OVER Mg-Ni-Mo CATALYST SUPPORTED BY KOH-TREATED ACTIVATED CHARCOAL

Jin-Hyuk Lee[1,2] , In-Gu Lee[1*] , Kwan-Young Lee[2]

1. Biomass and Wastes to Energy Laboratory, Korea Institute of Energy Research, 152 Gajeong-ro, Yuseong-gu, Daejeon 305-343, Republic of Korea; email: samwe04@kier.re.kr (In-Gu Lee)
2. Department of Chemical and Biological Engineering, Korea University, Seoul 136-701, Republic of Korea; email: square8@kier.re.kr (Jin-Hyuk Lee), kylee@korea.ac.kr (Kwan-Young Lee)

ABSTRACT

Conversions of lignocellulosic biomass to fuels and/or valuable chemicals are effective methods to protect the earth from climate change caused by the overuse of petroleum. Fast pyrolysis is one of promising methods to produce both fuels and chemicals from lignocellulosic biomass. Biomass fast pyrolysis produces bio-tar which is a complex mixture of organic compounds including phenolics, acids and ketones. The presence of those oxygenated components is responsible for its high acidity, low heating value and high viscosity. In this work, catalytic hydrodeoxygenation of bio-tar in supercritical ethanol was carried out as an effort to produce hydrocarbon-based biofuel. Mg-Ni-Mo catalyst supported by KOH-treated activated charcoal (AC) was used to promote both the production of in-situ hydrogen from ethanol and hydrodeoxygenation of bio-tar. Reaction conditions include temperatures of 300-400^{o}C, an initial N_2 pressure of 10bar, and holding times of 0-120min. The catalyst was characterized by XRD, SEM, N_2-adsorption/desorption isotherms. Upgrading of bio-tar at 400^{o}C and 120min holding time produced liquid fuel with HHV of 36.2MJ/kg, TAN of 8.6mgKOH/g, and O/C ratio of 0.11. For comparison, bio-tar had HHV of 26.8MJ/kg, TAN of 40.3mgKOH/g, and O/C ratio of 0.38. Based on analysis results, possible reaction pathways for the bio-tar upgrading were proposed.

Keywords: Upgrading, Bio-tar, Mg-Ni-Mo catalyst, KOH-treated activated charcoal, Supercritical ethanol

1 INTRODUCTION

Renewable energy receives increasing attention to protect the earth from climate change caused by the overuse of fossil energy. Biomass is a unique renewable energy carrier to produce hydrocarbon fuels which can be used in the present energy production systems such as internal combustion engines. Since biomass is mostly present in a solid form, it should be first converted to liquid or gas forms for the production of hydrocarbon fuels. Fast pyrolysis is one of promising methods to produce liquid fuels from lignocellulosic biomass. Although biomass pyrolysis oil has much higher energy density than biomass itself, it still contains high amounts of oxygen. This oxygen determines deteriorate properties of the pyrolysis oil such as high acidity and low heating value [1]. Upgrading methods including hydrodeoxygenation (HDO) and catalytic cracking are under development to enhance fuel quality of the pyrolysis oil by removing the oxygen in the forms of water, carbon oxides, and organic oxygen components [1]. In particular, HDO is regarded as a promising method in a technical point of view for the production of hydrocarbon fuels from biomass pyrolysis oil. However the HDO method is not commercialized yet because of high process cost related to the supply of hydrogen, which is an expensive material. Consequently a cost-effective process should be developed for the production of hydrocarbon fuels from biomass pyrolysis oil without hydrogen supply from outsources. Recently significant efforts have been given for the deoxygenation of biomass pyrolysis oil in supercritical fluids. In this method, supercritical fluids are used not only to provide a nice reaction environment but also to produce hydrogen required for HDO reactions [2]. Most favorable species investigated for supercritical fluids include methanol, ethanol, and water. It is believed that heterogeneous catalysts are needed to promote the generation of hydrogen from supercritical fluids as well as catalyzing HDO reactions. In particular Ni-based catalysts present high activity in HDO of model compounds and pyrolysis oil [3]. Catalyst supports which have well-developed mesopores are also required due to the presence of high amounts of heavy molecules in the pyrolysis oil. Activated carbon is a good candidate as a catalyst support in the HDO reactions because of its high surface area, easy-to-design pore structure and low production cost [4]. Potassium hydroxide (KOH) treatment of activated carbon can increase the fraction of well-developed mesopores.

In this work, the effect of KOH treatment of activated charcoal (AC) as a support on the performance as a Mg-Ni-Mo catalyst support was investigated for HDO reactions of bio-tar (a heavy fraction of biomass pyrolysis oil) in supercritical ethanol. Reaction temperature and reaction time were optimized to reduce the oxygen content and acidity of bio-tar as an effort to produce hydrocarbon fuels from biomass.

2 EXPERIMENTAL

2.1 Materials

Bio-tar used in this study was obtained by fast pyrolysis of wood sawdust in a 2ton/d pilot plant. Ethanol (>99.9 %, anhydride grade) was purchased from OCI chemical and used as a supercritical fluid. AC was purchased from Sigma-Aldrich. Nickel(II) nitrate hexahydrate ($Ni(NO_3)_2 \cdot 6H_2O$), ammonium molybdate tetrahydrate ($(NH_4)_6Mo_7O_{24} \cdot 5H_2O$), and magnesium nitrate hexahydrate ($Mg(NO_3)_2 \cdot 6H_2O$) were purchased from Sigma-Aldrich and used as precursors for Ni, Mo, and Mg catalysts, respectively. A 30g of AC was mixed with 800mL of KOH solution (Samchun chemical), and stirred for 3h. The mass ratio of KOH : AC was 4 : 1. The mixture was dried in an oven at 200^{o}C overnight. The impregnated AC was activated in a tubular reactor at 800^{o}C for 1h under nitrogen flow at 15^{o}C/min. The sample was cooled down to room temperature under nitrogen to prevent oxidation followed by washing with 0.1M HCl solution (Samchun chemical), and stirring for 1h. The sample rinsed repeatedly with distilled water until the wash water had a pH value of 6-7. Finally, the sample was dried at 105^{o}C overnight, and stored in an airtight container.

2.2 Catalyst preparation and characterization

The Mg-Ni-Mo catalysts were prepared by an incipient wetness impregnation method with the catalyst precursors dissolved in distilled water and reduced in H_2 flow (400^{o}C, 5h) after drying (105^{o}C, 12h, air) and subsequent calcination in N_2 flow (500^{o}C, 3h). The catalysts includes 25wt% Ni, 10wt% Mo and 2wt% Mg based on the amount of the AC or KOH-treated AC. Characterization of the catalysts was carried out by X-ray diffraction (XRD), Scanning Electron Microscopy (SEM) and N_2-adsorption-desorption isotherms.

2.3 Catalytic upgrading procedure

The catalytic upgrading of bio-tar were conducted under supercritical ethanol conditions in a 100ml batch reactor without external hydrogen supply. For each run, 10.0g bio-tar, 40.0g ethanol were loaded in the reactor together with 2.0g catalyst. After setup, the reactor was purged with N_2 gas to remove air in the reactor and then pressurized with N_2 gas to 10 bar. The reactor was heated to desired temperatures under vigorous stirring conditions (500rpm). After reaction, the reactor was cooled down to room temperature and gas product was collected by a gas-tight bag for compositional analysis and then the remaining gas was vent. The reactor was disclosed to collect all the products and catalyst. The collected materials were filtered to separate the liquid product from solid materials including catalyst. Rinsing the filter was carried out several times with acetone to ensure a complete collection of all the liquid products. The separated solid materials were dried at 105^{o}C for 12 h and their amounts were measured to determine product yields. A vacuum evaporator was operated at 60^{o}C to remove ethanol (reaction medium) and washing solvent (acetone) from liquid products, and then remaining liquid product was weighed to calculate the product yield.

2.4 Product analysis

The quantative analyses of liquid and gas products were accomplished by GC-MS and GC-TCD-FID, respectively. In addition, total acid number (TAN), water content, higher heating value (HHV) and elemental composition of the liquid products were analyzed for fuel characterization.

3 RESULTS AND DISCUSSION

3.1 Characterization of support and catalyst

Table 1 summarizes the textural properties of the AC supports and the Mg-Ni-Mo catalysts on the ACs. It is demonstrated that KOH treatment enhanced the BET surface area and total pore volumes of the AC support. In particular mesopores volume increased from 0.36 to 0.51 cm^3g^{-1} after the KOH treatment. The Mg-Ni-Mo catalyst supported on AC treated by KOH (KOH-AC) showed a larger BET surface area than the Mg-Ni-Mo supported on AC without KOH treatment. However the KOH-AC had a smaller average pore diameter than the original one, indicating that the KOH treatment also created numerous micropores.

Table 1. Textural properties of the supports and catalysts.

Supports/Catalysts	S_{BET} (m^2g^{-1})	V_p (cm^3g^{-1})	$MesoV_p$ (cm^3g^{-1})	d_p (nm)
AC	687.9	0.56	0.36	3.51
KOH-AC	1310.1	0.97	0.51	2.96
Mg-Ni-Mo/AC	518.4	0.45	0.25	3.25
Mg-Ni-Mo/KOH-AC	786.3	0.54	0.30	2.73

Figure 1 shows the powder XRD patterns of the ACs and catalysts. The AC and KOH-AC exhibit a similar XRD pattern, indicating that the structure of the AC was not changed after KOH treatment. All the Mg-Ni-Mo catalysts demonstrated a diffraction peak located at 2 theta = 44.4º, 51.9º and 76.3º, corresponding to (111), (200) and (220) of the reduced form of nickel shown by JCPDS 04-0850. Interestingly, the nickel peak was significantly decreased when KOH-AC was used as a support. This result may be due to higher metal dispersion in the KOH-AC support which had larger surface area than the original AC support.

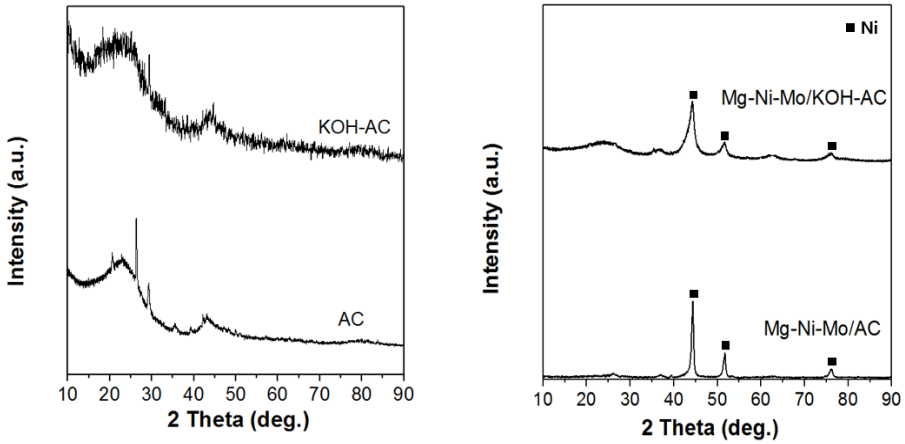

Figure 1. Powder XRD patterns of AC, KOH-AC, Mg-Ni-Mo/AC and Mg-Ni-Mo/KOH-AC.

The N_2-adsorption-desorption isotherms of the ACs and catalysts classified the Type 4 isotherm of IUPAC accompanied by hysteresis loop. It is clear that the supports and catalysts used in this study had the typical properties of mesopore structures [5] (figure is not shown here). Figure 2 illustrates that the AC and Mg-Ni-Mo/AC possess irregular surface morphology. However, the KOH-AC and Mg-Ni-Mo/KOH-AC have regular and sponge-like structures, which might be related to the higher BET surface area and total pore volumes.

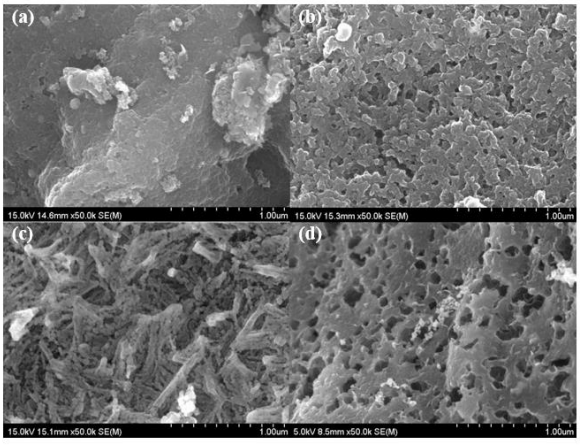

Figure 2. SEM images of catalysts (a) AC, (b) KOH-AC, (c) Mg-Ni-Mo/AC, and (d) Mg-Ni-Mo/KOH-AC.

3.2 Catalytic activity

The catalytic activity of the Mg-Ni-Mo/ACs catalysts for upgrading of bio-tar in supercritical ethanol was examined for 60min at 350ºC. Table 2 summarizes yields and properties of the bio-tar and liquid products. The liquid products had significantly lower water content than bio-tar reactant, probably due to the loss

during the vacuum evaporation process. The bio-tar experiments with Mg-Ni-Mo catalysts resulted in the production of liquid products with a little higher water content than the tests with ACs, indicating that water formation reactions such as ethanol dehydration and HDO reactions were activated over the catalysts. The TAN values of the liquid products were decreased by 34% compared to bio-tar feed. This means that the acidic components such as acetic acid present in bio-tar can be effectively converted to other compounds by chemical reactions such as esterification reaction [6]. According to elemental analysis, the oxygen content of the bio-tar significantly decreased from 30.5 wt% to 13.0 wt% over Mg-Ni-Mo/KOH-AC catalyst, leading to the increase in HHV. The product distribution in Table 2 demonstrates the fact that the catalytic upgrading process over the Ni-based catalyst increased the liquid products and reduced the solid products by suppressing char formation.

Table 2. Yield and Property of liquid product from supercritical ethanol treatment of bio-tar at 350°C and 60min reaction time.

Supports/Catalysts	Liquid (wt%)	Gas (wt%)	Solid (wt%)	H_2O content (wt%)	TAN (mgKOH g^{-1})	Elemental Analysis (wt%)				HHV (MJk g^{-1})
						C	H	O	N	
Bio-tar	-	-	-	14.8	40.3	62.5	6.9	30.5	0.1	26.80
Without catalyst	55.9	6.3	37.8	0.7	27.0	70.1	8.2	19.1	0.1	32.16
AC	75.7	7.6	16.7	0.5	26.2	70.2	8.3	19.3	2.2	32.44
KOH-AC	77.6	9.2	13.2	1.4	24.0	77.0	8.2	14.6	0.2	35.02
Mg-Ni-Mo/AC	82.3	9.6	8.1	2.6	21.5	77.8	8.6	13.2	0.4	35.88
Mg-Ni-Mo/KOH-AC	82.5	10.3	7.2	3.3	17.8	78.1	8.8	13.0	0.1	36.20

Figure 3 shows the composition of the liquid and gas products obtained under different catalytic conditions. The bio-tar consists of a number of oxygen-containing chemicals such as phenolics, ketones, aldehydes and acids. The acids in bio-tar significantly decreased accompanied by the increase in esters, indicating that esterification reaction of acids with ethanol occurred significantly during the supercritical ethanol treatment of bio-tar. Aldehydes were converted to other components such as phenolics or ketones via hydrogenation and deoxygenation [7]. In addition, Mg-Ni-Mo catalyst seems to promote the formation of hydrocarbons via deoxygenation reactions. Consequently the Mg-Ni-Mo is an efficient catalyst to upgrade the bio-tar through decarbonylation, decarboxylation and hydrogenation reactions. The gas products consisted of H_2, CO, CO_2, CH_4, C_2 and C_3 hydrocarbons. The KOH-AC and Mg-Ni-Mo/KOH-AC produced larger amounts of gaseous products with higher content of H_2 than the original AC and Mg-Ni-Mo/AC, respectively. The higher specific surface area, well-developed mesopores of KOH-AC and higher metal distribution of Mg-Ni-Mo/KOH-AC might promote the decomposition of ethanol to hydrogen and light gas species in supercritical conditions. The formation of CO and CO_2 indicates that the deoxygenation reactions of bio-tar also proceeded via decarbonylation and decarboxylation, respectively.

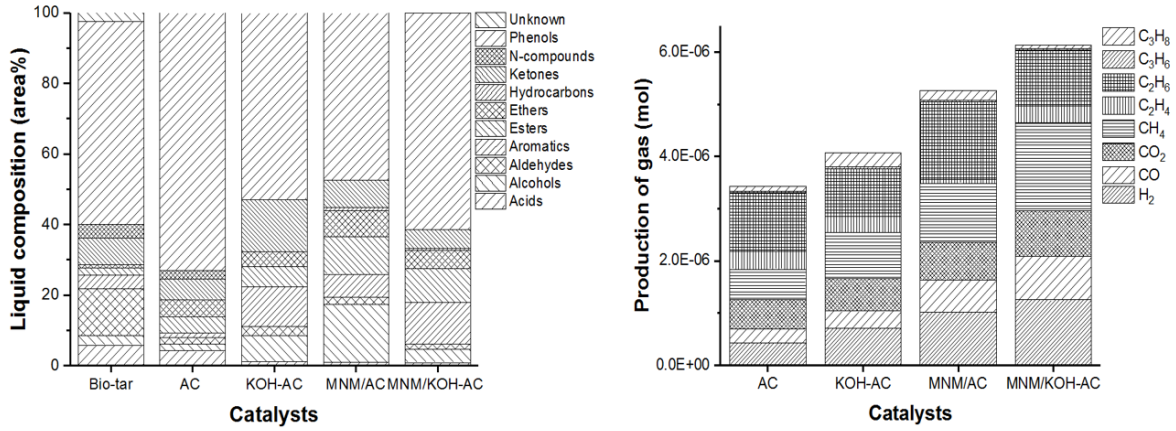

Figure 3. Composition of liquid and gas products from supercritical ethanol treatment of bio-tar at 350°C and 60min reaction time.

3.3 Effect of reaction parameter

Table 3 lists the properties of bio-tar and liquid products as a function of reaction temperature and time. The yields of liquid product decreased from 84.6 to 77.4 wt% while the yields of gas and solid products increased with the reaction temperature increasing from 300 to 400ºC. The water contents were gradually increased with increasing temperature, whereas the TAN values were decreased with increasing temperature. These results demonstrated that ethanol dehydration was favored along with esterification reaction at higher reaction temperatures. In addition, the higher temperatures promoted HDO reaction of bio-tar, resulted in the formation of liquid product with smaller content of oxygen. Table 3 also shows the effect of reaction time on liquid product yield and properties. The longer reaction time decreased liquid product yield but enhanced the fuel quality with a low TAN of 8.6 mgKOHg^{-1} and a lowest oxygen content of 11.7 wt% at 120 min. The longer reaction time might favor esterification and deoxygenation reactions. The higher amounts of solid product at longer reaction times indicate that the co-polymerization reaction between phenolics and aldehydes was activated by increasing holding time [7].

Table 3. Yield and property of liquid product from supercritical ethanol treatment of bio-tar over Mg-Ni-Mo/KOH-AC at various reaction temperature and time.

Reaction condition	Liquid (wt%)	Gas (wt%)	Solid (wt%)	H_2O content (wt%)	TAN (mgKOHg^{-1})	Elemental Analysis (wt%)				HHV (MJkg^{-1})
						C	H	O	N	
300ºC, 60min	84.6	7.8	7.6	1.2	19.1	78.7	7.7	13.5	0.1	35.03
350ºC, 60min	82.5	10.3	7.2	3.3	17.8	78.1	8.8	13.0	0.1	36.20
400ºC, 60min	77.4	12.5	10.1	4.2	13.2	79.5	8.5	11.8	0.2	36.50
400ºC, 0min	79.8	11.4	8.8	1.7	16.5	77.9	8.2	13.8	0.1	35.36
400ºC, 60min	77.4	12.5	10.1	4.2	13.2	79.5	8.5	11.8	0.2	36.50
400ºC, 120min	70.8	15.4	13.8	4.8	8.6	79.9	8.2	11.7	0.2	36.21

Figure 4 exhibits the composition of liquid and gas products obtained at different reaction temperatures. The acids and aldehydes were effectively converted to more stable compounds at higher temperatures. The higher temperature also promoted the formation of aromatics and hydrocarbons. It can be said that reaction temperature plays an important role in esterification and deoxygenation reactions. Meanwhile, the formation of H_2, CO and CO_2 gases gradually increased with increasing temperature due to the activation of both ethanol decomposition and deoxygenation reactions. In addition the high amount of C_2H_6 together with high amounts of water at 400ºC indicates that ethanol can react with hydrogen in supercritical ethanol at high temperature [7].

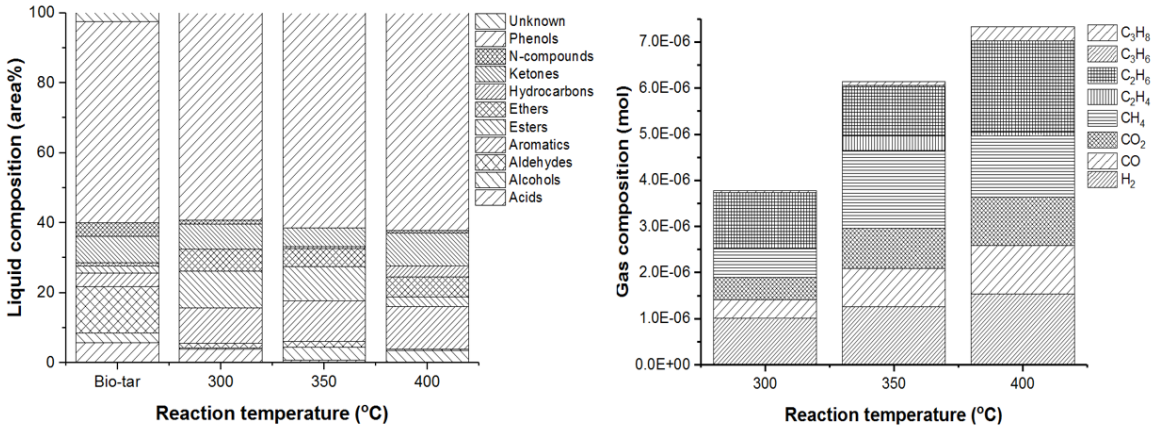

Figure 4. Composition of liquid and gas products from supercritical ethanol treatment of bio-tar over Mg-Ni-Mo/KOH-AC at various reaction temperature and time.

Figure 5 presents the composition of liquid and gas products as a function of reaction time. Acids and aldehydes were completely eliminated at 120min while aromatics and hydrocarbons were increased with longer reaction time. These results explained that longer reaction time favors esterification and HDO

reactions. In the case of gaseous product, the content of CO decreased while the content of CO_2 increased probably due to water gas shift (WGS) reaction promoted at longer reaction time [8].

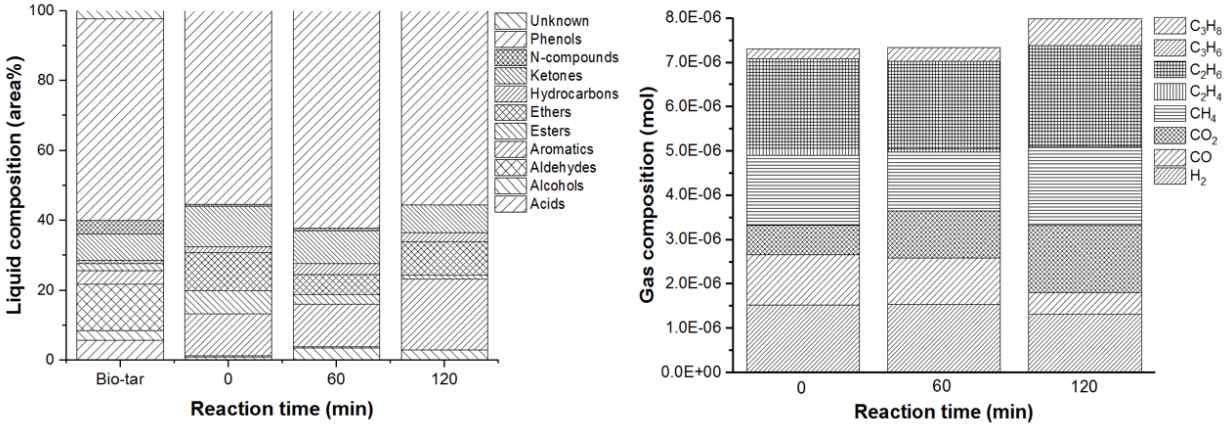

Figure 5. Composition of liquid and gas products as a function of reaction time.

4 CONCLUSION

Catalytic upgrading of bio-tar in supercritical ethanol over Mg-Ni-Mo catalyst supported by AC treated with and without KOH was carried out at 300-400°C and 0-120min reaction time. The AC treated with KOH showed a higher surface area of 1310.1 m^2/g and well-developed mesoporous structure than the original AC, leading to higher activity of Mg-Ni-Mo/KOH-AC for upgrading of bio-tar than Mg-Ni-Mo/AC. The highest quality of liquid fuel with HHV of 36.2MJ/kg and TAN of 8.6mgKOH/g was obtained over Mg-Ni-Mo/KOH-AC at 400°C and 120min reaction time. Acids and aldehydes present in bio-tar were effectively converted to deoxygenated compounds such as aromatics and hydrocarbons. This result suggested that the esterification and HDO reactions occurred simultaneously during catalytic upgrading of bio-tar in the system.

ACKNOWLEDGEMENTS

This work was funded by grants from the National Research Council of Science & Technology (NST) by the Korea government (MSIP) (No.CAP-16-05-KIMM), Republic of Korea.

REFERENCES

[1] Y. M. Isa, E. T. Ganda, Bio-oil as a potential source of petroleum range fuels, *Renewable and Sustainable Energy Reviews*, Vol. 81, pp. 69-75, 2018.

[2] H. Prajitno, R. Insyani, J. Park, C. Ryu, J. Kim, Non-catalytic upgrading of fast pyrolysis bio-oil in supercritical ethanol and combustion behavior of the upgraded oil, *Applied Energy*, Vol 172, pp. 12-22, 2016.

[3] C. Bioscagli, C. Yang, A. Welle, W. Wang, J.D. Grunwaldt, Effect of pyrolysis oil components on the activity and selectivity of nickel-based catalysts during hydrotreatment, *Applied Catalysis A*, Vol 544, pp. 161-172, 2017.

[4] J. L. Goldfarb, G. Dou, M. Salari, M. W. Grinstaff, Biomass-Based Fuels and Activated Carbon Electrode Materials: An Integrated Approach to Green Energy Systems, *ACS Sustainable Chem. Eng*, Vol 5, pp. 3046-3054, 2017.

[5] A. Ostiashtiani, B. Puertolas, E. Heracleous, K. Wilson, On the influence of Si:Al ratio and hierarchical porosity of FAU zeolites in solid acid catalysed esterification pretreatment of bio-oil, *Biomass Conv. Bioref.*, Vol 7, pp. 331-342, 2017.

[6] E. Saracoglu, B. B. Uzun, E. A. Varol, Upgrading of fast pyrolysis bio-oil over Fe modified ZSM-5 catalyst to enhance the formation of phenolic compounds, *International Journal of Hydrogen Energy*, Vol 42, pp. 21476-21486, 2017.

[7] A. D. Handoko, K. W. Chan, B. S. Yeo, $–CH_3$ Mediated Pathway for the Electroreduction of CO_2 to Ethane and Ethanol on Thick Oxide-Derived Copper Catalysts at Low Overpotentials, *ACS Energy Lett.*, Vol 2, pp. 2103-2109, 2017.

[8] C. Quan, S. Xu, C. Zhou, Steam reforming of bio-oil from coconut shell pyrolysis over Fe/olivine catalyst, *Energy Conversion and Management*, Vol 141, pp. 40-47, 2017.

DEVELOPMENT OF OIL PALM EMPTY FRUIT BUNCH FRACTIONATION FOR PRODUCTION OF VALUE-ADDED CHEMICALS FROM LIGNIN RESIDUE

Rangsalid Panyadee[1], Pattaraporn Posoknistakul[1], Woranart Jonglertjunya[1], Pataraporn Kim-Lohsoontorn[2], Navadol Laosiripojana[3], Chularat Sakdaronnarong[1,*]

[1]Department of Chemical Engineering, Faculty of Engineering, Mahidol University, Nakorn Pathom 73170, Thailand.

[2]Department of Chemical Engineering, Faculty of Engineering, Chulalongkorn University, Bangkok 10330, Thailand.

[3]The Joint Graduate School of Energy and Environment (JGSEE), King Mongkut's University of Technology Thonburi, Tungkru, Bangkok, 10140 Thailand.

**Corresponding author:* chularat.sak@mahidol.ac.th

ABSTRACT

Palm empty fruit bunches (EFB) are low-priced and abandoned residue from palm oil milling process. Owing to its low heating value, burning EFB as solid fuel is not promising and generates pollution e.g. NO_x and SO_x. Thus, palm oil manufacturers realize to use the innovation to improve the process efficiency and valorize this kind of solid waste from the process. As EFB is lignocellulosic biomass, in which the main components are cellulose, hemicellulose and lignin, to breakdown the structure of EFB, mechanical, physicochemical or thermochemical pretreatment is required. Cellulose and hemicellulose are polysaccharides that can be used by microorganisms to convert them to precious chemicals while lignin is predominantly found in black liquor after pretreatment. Lignin has been found potentially be value-added as phenolic compounds, which could be used for both fuels and chemicals for pharmaceutical industry. In this study, hot compressed water (HCW) technique was used (180- 210°C at 20 bar) for lignin fractionation into liquid phase while cellulose-rich material remained intact. Addition of alkaline during HCW substantially enhanced lignin yield from liquid phase. Subsequently, depolymerization of separated EFB lignin to monophenolic compounds was successfully done by using the Cu(II) and Fe(III) based catalysts in alkaline solution at high temperature (100-120°C). This work proposed the application of microwave irradiation for oxidative depolymerisation of EFB lignin. The optimal condition for depolymerization of lignin to phenolic compounds took place in 30 minutes at microwave power of 300 watts in NaOH solution with 4%w/w hydrogen peroxide when bimetallic $Cu(OH)_2$ and Fe_2O_3 catalysts were used. At this condition, 36.13 mgL^{-1} vanillin and 97.67 mgL^{-1} acetosyringone which are high price phenolic compounds were produced with high selectivity while syringol, acetovanillone and syringaldehyde were found in small amount.

Keywords: Palm empty fruit bunch, Microwave reaction, Depolymerization, Phenolic compound

1. INTRODUCTION

According to Thailand's demand on energy and refinery products from petroleum industry, more than 90 percent of crude oil has been imported from other countries. To have a balance of trade deficit and to create energy security for the whole nation, therefore the utilization of renewable energy from Thailand's alternative resources has been included into the research and development roadmap of the country. At present, palm oil manufacturers realize to use the innovation to improve the process efficiency and valorize both solid waste and wastewater from the process. Among all wastes, valorization of EFB which contains high amount of cellulose has been widely carried out on EFB conversion to high value chemicals or material such as ethanol and cellulose fibers. For process development and technology for EFB separation for value-added chemicals via sugar platform, crucial bottleneck steps are pretreatment and hydrolysis. As EFB is lignocellulosic biomass, in which the main components are cellulose, hemicellulose and lignin, to breakdown the structure of EFB, mechanical, physicochemical or thermochemical pretreatment is required. Cellulose and hemicellulose are polysaccharides that can be used by microorganisms to convert them to precious chemicals while lignin is predominantly found in black liquor after pretreatment. If the average capacity of the palm oil refinery plant is approximately 300 tons per day, approximately 200 tons per day of EFB containing 35-40% cellulose is generated from the process. To utilize cellulose for biorefinery purpose, valorization of lignin byproduct is recently of interest. Accordingly, this research aimed to study EFB

fractionation using HCW method. The base catalyst was used to reduce activation energy of the reaction resulting in lower temperature and pressure utilized. In basic solution, an increase of lignin solubility is also obtained [1]. Furthermore, the research also focused on valorization of lignin by converting it to phenolic compounds such as vanillin, syringaldehyde and phenol, etc. which could be used in pharmaceutical industry. The oxidative depolymerization of lignin by using transition metal ions at elevated temperature was found to produce 4-Hydroxybenzaldehyde, vanillin, syringol-type compounds and Guaiacol-type compounds in the products [2, 3] Consequently, the present work aimed to study the effect of Cu^{+}, Cu^{2+} and Fe^{3+} based catalysts which are cheap and high availability on EFB lignin depolymerization to monophenolic compounds in the presence of hydrogenperoxide under microwave irradiation.

2. EXPERIMENTAL

2.1 EFB fractionation by HCW technique

The fresh empty palm fruit bunch (EFB) from Chumporn Palm Oil Industry Public CO.,LTD was washed with water and sun dried for 12 h. After that, it was dried at 80ºC in an oven for 24 h to obtain 4.3% moisture content. Then, dry EFB was crushed to the particle size in a range of 50-200 mesh, which was separated by sieving machine. After milling to 50-200 mesh, EFB was added into a high pressure stainless steel autoclave reactor with jacketed electrical heating. Distilled water was added to the solid-liquid ratio of 1:5. Then, the reaction took place at 190, 200 and 210 ºC with alkaline catalyst (K_2CO_3 or NaOH) for 20 min at 20 bar. Solid and liquid phases were separated by filtration as shown in Fig. 1a.

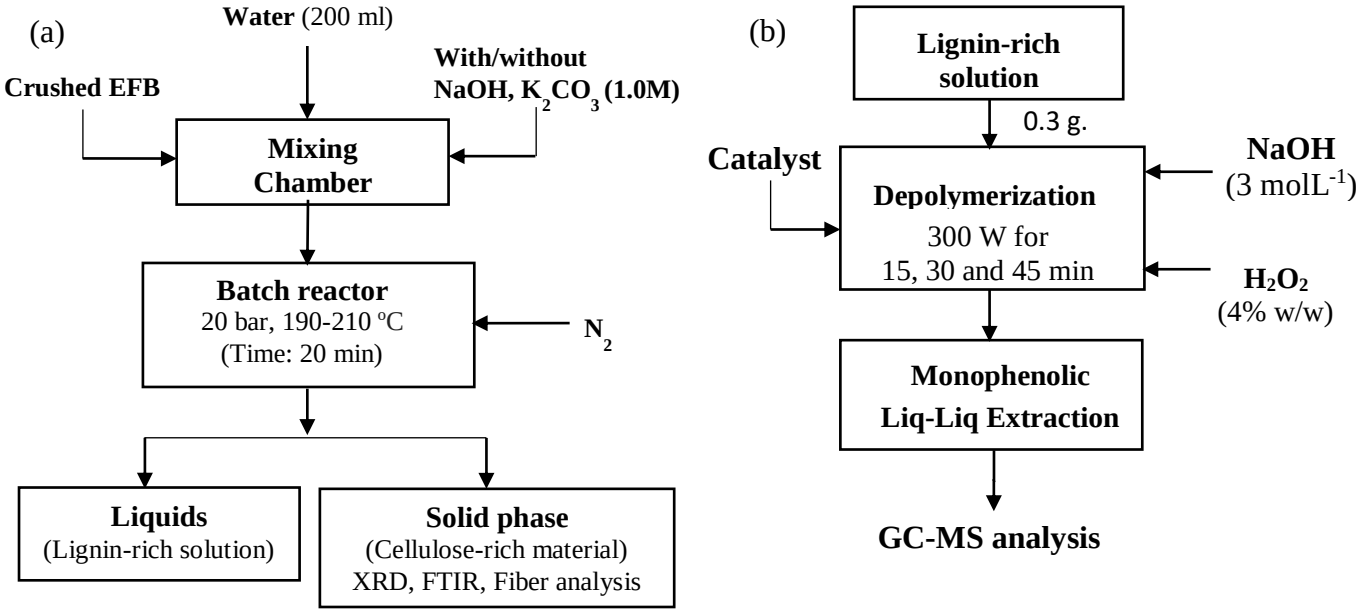

Fig.1 (a) Schematic diagram of experiments EFB pretreatment by HCW technique, and (b) EFB lignin depolymerization in a batch reactor.

2.2 EFB lignin separation process

After EFB was pre-treated, the liquid phase which was lignin-rich solution required to be separated by H_2SO_4 (72%w/w). H_2SO_4 was dropped into a known amount of black liquid until pH equal to 1. Lignin was precipitated and separated by centrifugation. After that, EFB lignin was washed by HCl (0.01M) until pH equal to 2. Then, it was washed with water again until neutral. Finally, the seperated lignin was dried at 50 ºC for 15 h [4].

2.3 Oxidative depolymerization of alkaline lignin with microwave (MW) irradiation

Firstly, an oxidative degradation of lignin was conducted by adding 0.3 g lignin into a microwave reactor containing 2 ml of H_2O_2 (4 wt%) and 14 g of 3 $molL^{-1}$ NaOH solution as shown in Fig.1b. The reaction was carried out under microwave irradiation at 300W for 30 min in the presence of catalysts such as 0.02g of CuO, Cu_2O, $Cu(OH)_2$ and 0.002g of Fe_2O_3. From the experimental design, a comparison of the conversion of alkaline lignin and the yields of monophenolic products in the presence of H_2O_2 concomitant with Cu^{+}, Cu^{2+} and Fe^{3+} was studied. After reaction, the products were extracted with ethyl acetate. After evaporation, monophenolic compounds in ethyl acetate were dissolved in methanol and subsequently analysed by Gas Chromatography-Mass Spectroscopy (GC-MS).

2.4 Characterization of pretreated EFB, separated lignin and monophenolic compounds

For EFB fractionation, conversion of EFB was calculated using Eq.(1). Pre-treated EFB was analysed to determine cellulose, hemicellulose and lignin content in lignocellulosic material according to Goering method [5]. Moreover, Fourier transform infrared (FTIR) spectroscopy in the wavenumber between 4000-400 cm^{-1} and X-ray diffraction (XRD) spectrometry were performed for pretreated EFB while Thermogravimetric analysis (TGA) was analysed for separated lignin. For lignin depolymerization, monophenolic compounds were identified by GC-MS (Agilent GC6890N and HP-5 MS capillary column with dimensions: 30 m, 0.25 mm, 0, 25 μm). 1 μL of monophenolic diluted in ethyl acetate was injected at 250 °C into the column using splitless mode. Helium was utilized as a carrier gas at a rate of 1 mL min^{-1}.

$$\text{Conversion (\%)} = (\text{Initial EFB} - \text{Solid residue})/\text{Initial EFB (g)} * 100 \quad (1)$$

3. RESULTS AND DISCUSSION

3.1 EFB fractionation using HCW technique

Alkaline catalysts significantly enhanced EFB conversion compared to the control without catalyst as shown in Fig. 2a. EFB solid yield reduced from 59.41% (without catalyst) to 47.40% when using K_2CO_3 as the catalyst at 210°C and to 46.57% when using NaOH as the catalyst at 200°C. Reduction of solid recovery caused by the degradation and release of hemicellulose and lignin into liquid phase. The results were in accordance with lignin and cellulose content in solid residue from fiber analysis as shown in Fig. 2b. It was found that HCW pretreatment in the presence of K_2CO_3 and NaOH considerably degraded lignin in raw EFB from 28.33% lignin to 2.32% for K_2CO_3 at 210°C and to 1.07% for NaOH at 210°C. FTIR spectroscopic analysis confirmed the enhancement of cellulose content and reduction of lignin content as shown in Fig. 3a. Various bands of cellulose absorption identified as O–H (3417 cm^{-1}), C–H (2924 cm^{-1}) were increased and C–O (1236 cm^{-1}) assigned as lignin was reduced because lignin was released into liquid phase [6]Furthermore, from the XRD patterns in Fig. 3b, it can be seen that the influence of catalyst K_2CO_3 > NaOH > No catalyst on the reduction of pretreatetd EFB crystallinity was found. These results suggested the superior effect of carbonate in EFB degradation compared to hydroxide.

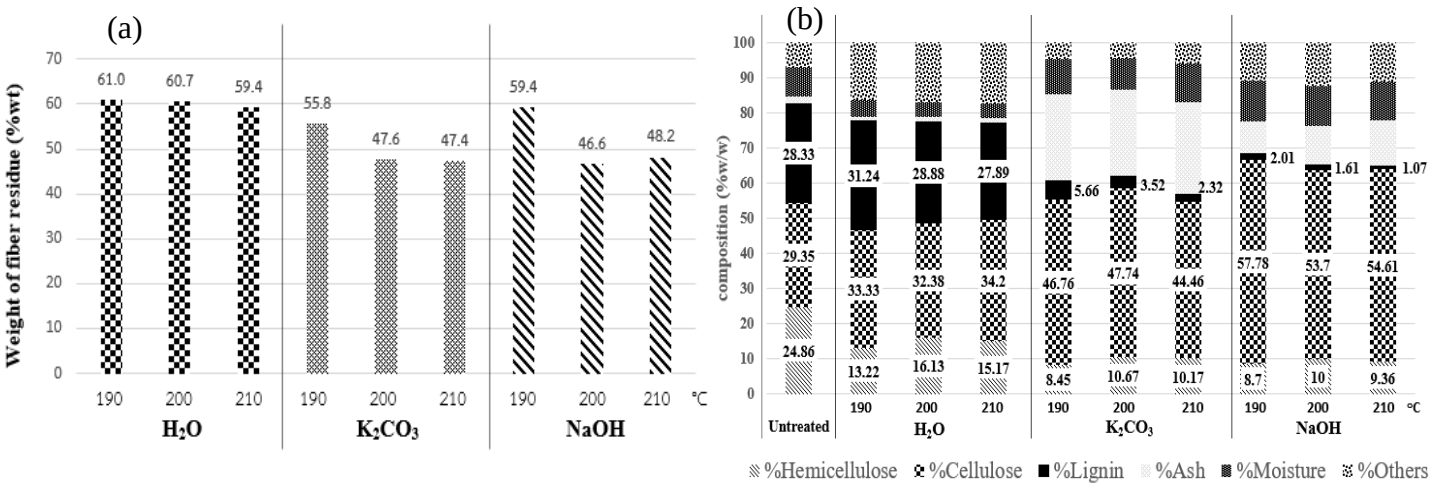

Fig. 2 (a) Solid recovery of pretreated EFB, and (b) Chemical composition in untreated and pretreated EFB.

3.2 EFB lignin characterization

After pretreatment, residual EFB was seperated by filtration and EFB lignin was precipitated from black liquor by acid condensation. FTIR spectroscopic analysis of precipitated lignin as shown in Fig. 4a indicated that lignin from EFB treated with K_2CO_3 and NaOH contained functional groups such as C–H (3360 cm^{-1}), CH_2 (2920-2850 cm^{-1}) and δ asymmetric C–H (1451 cm^{-1}) identified similarly as alkaline lignin. However, higher intensity of C–O vibration band near 1209 cm^{-1} attributed to syringyl and guaiacyl groups in separated EFB lignin were observed when compared with standard alkaline lignin [7].

For TGA results of EFB lignin (Fig. 4b), the results showed that K_2CO_3 and NaOH pre-treated lignin gave the lowest thermal degradation temperature at 250 ºC and 260 ºC, respectively while lignin derived from HCW without catalyst gave the highest thermal degradation temperature at 340 ºC.

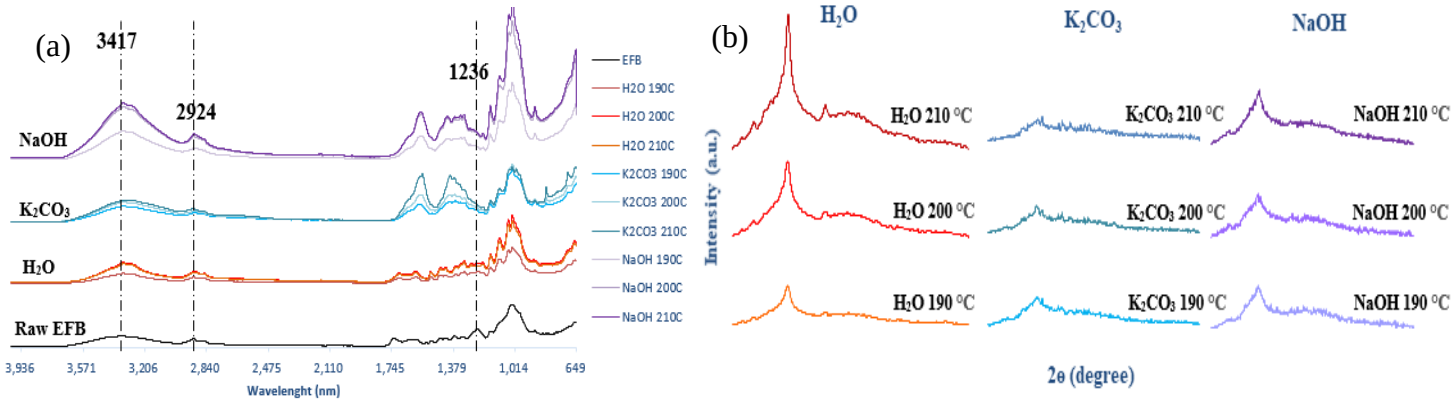

Fig. 3 (a) FTIR spectroscopic analysis of raw and pretreated EFB, and (b) XRD patterns of pretreated EFB.

This indicated that the EFB lignin from HCW pretreatment in the presence of alkaline either had smaller molecules or easier to break down than alkaline lignin and EFB lignin from pretreatment. Due to the abundance of β-O-4 interunit linkage in many types of lignin derived from alkaline catalyst, significant effort has been aimed at developing an efficient method to cleave the β-O-4 linkage in lignin and model compounds. The ether linkages in lignin are more changeable than C–C bonds. It was been reported that the cleavage of a significant portion of ether linkages occurs during biomass pretreatments and lignin separation processes [8]. Thus, β-O-4 ether linkages in EFB lignin were postulated to be easily cleaved and led to generate small lignin molecules during HCW in the presence of K_2CO_3 and NaOH. This findings were in good agreement with a previous work of Medina and colleagues [7].

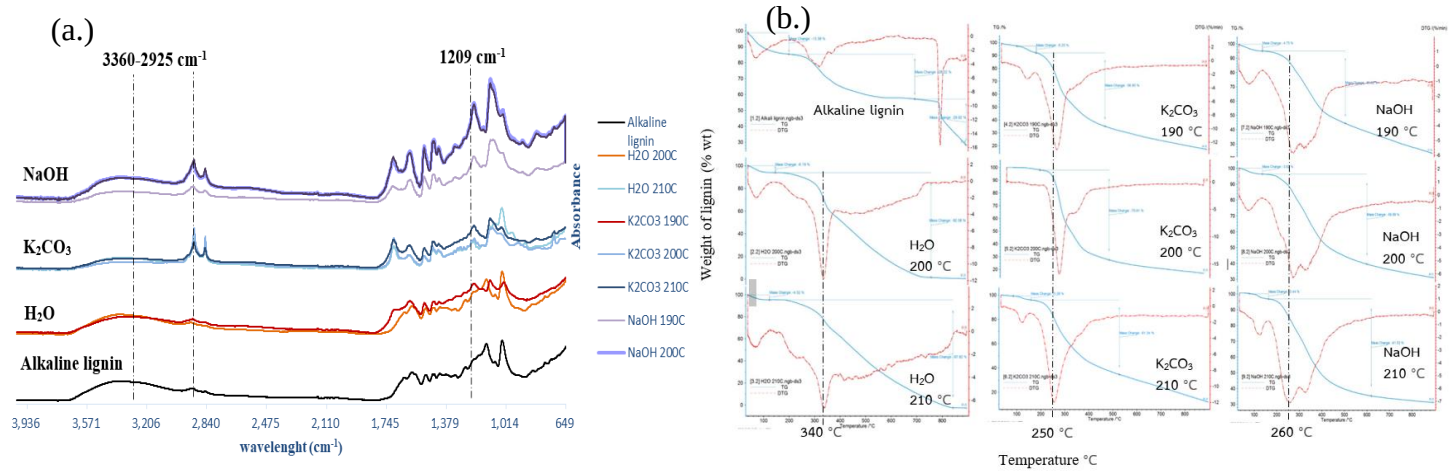

Fig. 4 (a) FTIR spectroscopic analysis of alkaline lignin and EFB lignin, and (b) TGA profiles of EFB lignin.

3.3 Phenolic compounds production from microwave EFB lignin depolymerization

The effect of catalysts on alkaline lignin conversion was studied. From Table 1, the results showed that the co-catalyst of Cu(II) and Fe(III) was able to increase the lignin conversion from 91.07% for CuO to 92.17% for CuO + Fe_2O_3 and from 89.03% for $Cu(OH)_2$ to 91.53% for $Cu(OH)_2$ + Fe_2O_3 catalyst. Thus, supplementing oxidation with transition metal ions such as Cu(II) and Fe(III), which is well known for treating lignin with oxidative reagents including peroxide, has been shown to enhance the oxygen reactivity and subsequently facilitate the cleavage of β-O-4 and pinacol type C–C linkages cleavage [9]. After the reaction, phenolic compounds such as vanillin, acetosyringone and p-Hydrobenzaldehyde were detected by GC-MS. It was found that vanillin and acetosyringone were the main products from EFB lignin degradation using $Cu(OH)_2$ + Fe_2O_3 catalyst at MW 300W for 30 min as shown in Fig. 5a. The concentrations of vanillin and acetosyringone were calculated based on standard peak area as shown in Table 2.

As demonstrated in Table 2, apart from the effect of different catalysts the influence of reaction time (15, 30 and 45 min) on vanillin and acetosyringone concentration was also investigated. For standard

alkaline lignin depolymerization, the highest concentration of vanillin was found in products at 342.50 mg/L from the reaction catalyzed with $Cu(OH)_2$ + Fe_2O_3 co-catalyst at MW 300 watts for 30 min. For the EFB lignin from K_2CO_3 and NaOH pretreatment, the highest concentration of vanillin were 32.5 mg/L and 25.21 mg/L, while acetosyringone concentration were 53.38 mg/L and 97.67 mg/L, respectively from the reaction catalyzed with $Cu(OH)_2$ + Fe_2O_3 co-catalyst at MW 300 watts for 30 min.

Table 1 The percentage of lignin conversion from microwave depolymerization (MW 300 watts, 30 min)

Lignin \ Catalyst	CuO	Fe_2O_3	$Cu(OH)_2$	CuO + Fe_2O_3	CuO + $Cu(OH)_2$	$Cu(OH)_2$ + Fe_2O_3	Cu_2O + Fe_2O_3	Without Catalyst
Alkaline lignin	91.07%	92.93%	89.03%	92.17%	91.56%	91.53%	90.53%	85.37%
EFB lignin (K_2CO_3)	n.d.	n.d.	n.d.	81.57%	85.93%	84.60%	81.71%	78.6%
EFB lignin (NaOH)	n.d.	n.d.	n.d.	80.17%	82.84%	84.11%	79.76%	77.12%

Table 2 The vanillin and acetosyringone concentration in lignin depolymerization product (MW 300 watts).

Type of Catalyst	Type of lignin	Vanillin(mg/L)			Acetosyringone (mg/L)		
		15 min	30 min	45 min	15 min	30 min	45 min
CuO + Fe_2O_3	Alk. lignin	n.d.	114.19	n.d.	n.d.	-	n.d.
	K_2CO_3 Lignin	-	-	-	117.14	23.91	80.39
	NaOH Lignin	-	-	12.32	131.28	50.14	58.87
CuO + $Cu(OH)_2$	Alk. lignin	n.d.	263.07	n.d.	n.d.	-	n.d.
	K_2CO_3 Lignin	-	-	-	64.7	24.61	117.63
	NaOH Lignin	-	8.15	17.07	113.2	61.35	115.99
$Cu(OH)_2$ + Fe_2O_3	Alk. lignin	n.d.	342.5	n.d.	n.d.	-	n.d.
	K_2CO_3 Lignin	-	32.5	-	68.09	53.38	84.94
	NaOH Lignin	-	25.21	24.32	145.47	97.67	121.77
Cu_2O + Fe_2O_3	Alk. lignin	n.d.	189.95	n.d.	n.d.	-	n.d.
	K_2CO_3 Lignin	-	27.88	-	67.89	61.56	76.07
	NaOH Lignin	10.63	29.42	32.51	141.09	82.53	91.78
No catalyst	Alk. lignin	n.d.	166.96	n.d.	n.d.	-	n.d.
	K_2CO_3 Lignin	-	-	-	-	-	10.04
	NaOH Lignin	-	-	-	63.64	-	54.88

** - = not detected
n.d. = not determined

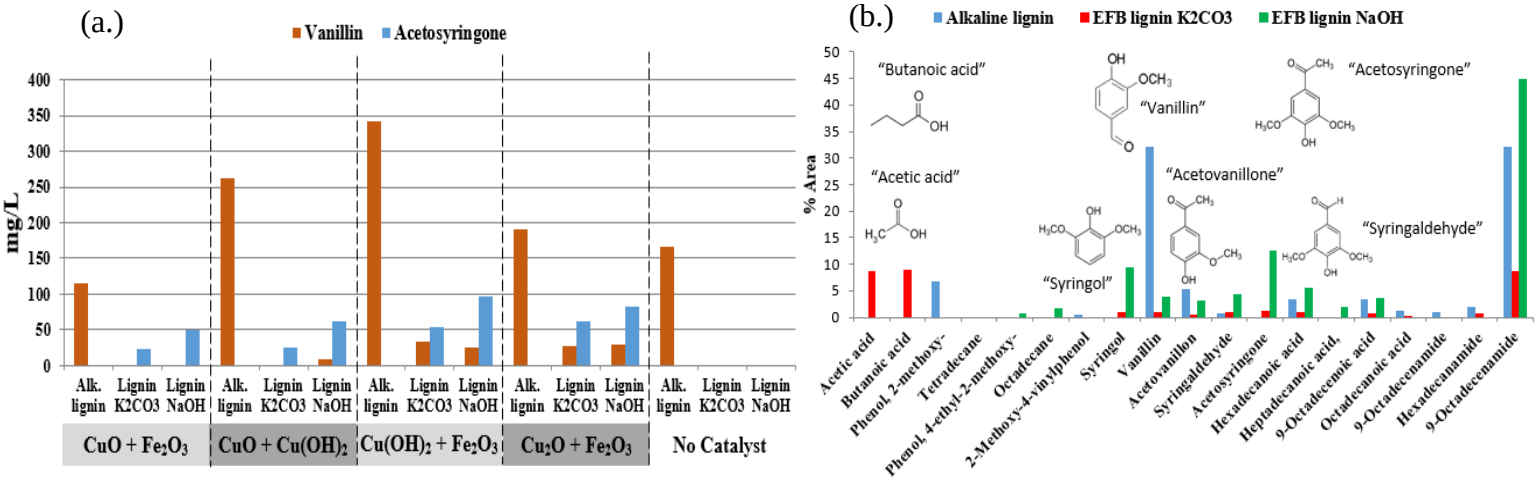

Fig. 5 The phenolic compounds from MW lignin depolymerization at 300 watts for 30min (a) concentration of vanillin and acetosyringone from each co-catalyst, and (b) percentage of phenolic compound concentration peak area from GC-MS analysis for lignin depolymerization with $Cu(OH)_2$ + Fe_2O_3 catalyst.

From Table 2, when the effect of reaction times on vanillin and acetosyringone concentration was investigated, the results showed that the concentration of vanillin was increased from 10.63 mg/L to 32.51

mg/L by increasing the time of MW depolymerization with NaOH pre-treated EFB lignin from 15 min to 45 min. In addition, the highest concentration of acetosyringone at 145.47 mg/L was found when the reaction time was 15 min for NaOH pre-treated EFB lignin. Moreover, syringol, acetovanillone and benzaldehyde were found in small amount. Since the depolymerizing lignin to aromatic and phenolic products is a sensible approach, there is an increasing number of recent research toward producing quinones and opening chain to hydrocarbon compounds from lignin [9]. Extensive oxidation of lignin can lead to aromatic ring oxidation to quinones and subsequent ring cleavage products. From the present study, the quinones and carboxylic acid were produced in a high amount from K_2CO_3 pre-treated EFB lignin. The main reason was because of the severe reaction on simplified structure of K_2CO_3 pre-treated EFB lignin compared with complex structure of standard alkaline lignin as demonstrated by the %area of lignin depolymerization products analysed by GC-MS (Fig. 5b).

4. CONCLUSION

For EFB fractionation, the most suitable HCW condition to achieve the highest cellulose content in residual EFB and highest lignin recovery was at 210 ºC /20 bars/20 min in the presence of NaOH catalyst. However, reactivity on alkaline catalyst on EFB crystallinity were K_2CO_3>NaOH>control (without catalyst).

For EFB lignin depolymerisation using microwave irradiation, bimetallic $Cu(OH)_2$ and Fe_2O_3 catalyst was the most effective catalyst among all catalysts tested and produced the highest amount of vanillin and acetosyringone products in the presence of H_2O_2 while syringol, acetovanillone and syringaldehyde were found in small amount. It was also found that oxidative degradation of EFB lignin with transition metal ions especially Cu(II) and Fe(III) gave a high degradation rate but moderate yield of monophenolic compounds was observed. Therefore, to improve the yield of monophenolic compounds, optimization of significant parameters on reaction severity i.e. concentration of H_2O_2, reaction time and microwave power is necessary.

ACKNOWLEDGEMENT

The authors were grateful for the research grant (MSD60I0016) and a kind support from Research and Researchers for Industries (RRi), The Thailand Research Fund (TRF) with a co-funding from Chumporn Palm Oil Industry Public Company Limited, Thailand. C.S. and N.L. would like to acknowledge the research grant from The Thailand Research Fund (RTA598006).

REFERENCES

[1] Imman S, Arnthong J, Burapatana V, Champreda V, Laosiripojana N. Effects of acid and alkali promoters on compressed liquid hot water pretreatment of rice straw. Bioresource Technology. 2014;171:29-36.

[2] Ouyang XP, Tan YD, Qiu XQ. Oxidative degradation of lignin for producing monophenolic compounds. Journal of Fuel Chemistry and Technology. 2014;42(6):677-82.

[3] Toledano A, Serrano L, Pineda A, Romero AA, Luque R, Labidi J. Microwave-assisted depolymerisation of organosolv lignin via mild hydrogen-free hydrogenolysis: Catalyst screening. Applied Catalysis B: Environmental. 2014;145:43-55.

[4] Jonglertjunya W, Juntong T, Pakkang N, Srimarut N, Sakdaronnarong C. Properties of lignin extracted from sugarcane bagasse and its efficacy in maintaining postharvest quality of limes during storage. LWT - Food Science and Technology. 2014;57(1):116-25.

[5] Goering HK, Soest PJV. Forage fiber analysis (Apparatus, reagent, procedures and some applications). 1970.

[6] Sun Ye, Cheng Jiayang. Hydrolysis of lignocellulosic materials for ethanol production: a review. Bioresource Technology. 2002;83(1):1-11.

[7] Coral Medina JD, Woiciechowski A, Zandona Filho A, Noseda MD, Kaur BS, Soccol CR. Lignin preparation from oil palm empty fruit bunches by sequential acid/alkaline treatment – A biorefinery approach. Bioresource Technology. 2015;194:172-8.

[8] Saha BC, Iten LB, Cotta MA, Wu YV. Dilute acid pretreatment, enzymatic saccharification and fermentation of wheat straw to ethanol. Process Biochemistry. 2005;40(12):3693-700.

[9] Ruoshui Ma, Mond Guo, Zhang X. Recent advances in oxidative valorization of lignin. Catalysis Today. 2018(302):50-60.

GENERALIZED PROTOCOL BY SYSTEMIC ANALYSIS FOR SIZING A SMALL SCALE GASIFIER ENGINE SYSTEM DEDICATED TO POWER GENERATION FROM BIOMASS

D. Fakra[1], D. Morau[1], K. Bayante[1], M.H. Radanielina[2] and T. Rakotondramiarana[2]

1. University of La Reunion, Physics and Mathematical Engineering Laboratory for Energy, Environment and Building (PIMENT) - 117 rue du Général Ailleret 97 430 Le Tampon, Reunion; email: fakra@univ-reunion.fr, dominique.morau@univ-reunion.fr, karim.bayante@hotmail.com
2. Institute for the Management of Energy (IME), University of Antananarivo, Po Box 566, Antananarivo 101, Madagascar; email: radanielin@yahoo.fr , rktmiarana@yahoo.fr

ABSTRACT

Production of syngas, or synthesis gas, from biomass wastes is an advantageous option for fuelling power generator. The most common components of a small-scale power generator system running with syngas are the boiler which gasifies the biomass, the cyclone which cools the output syngas and filters the solid particles, and the electricity generator. Although there are several sizing models for each of these three components, no model takes into account the coupling of these three subsystems. Moreover, no general procedure for characterizing the exact dimensions of these subsystems is available while the size of this kind of gasifier-power-generator system is a relevant parameter that significantly influences its performance. The aim of this work is to propose a generalized protocol by using systemic analysis approach for sizing a small-scale gasifier generally used for power production. This analysis is based on the block coupling of existing models. The EES software is used to aid for the numerical resolution. Comparison tests is conducted to assess the reliability degree of the protocol.

Keywords: Gasifier size, Biomass, Systemic analysis, Modelling, Electricity, Small-scale system

1 OBJECTIVE OF THE STUDY

A syngas production system can be dimensioned by the amount of electrical power or biomass flow. Several models exist to characterize each subsystem [1 - 5], but none takes into account the entire device. The main purpose of this paper is to considered the sizing the whole gasifier system. This sizing is investigated by coupling each element using energy balance and components size. In our study, we will see how to size the whole system by coupling models and using one of this information: knowledge of the electrical production or the existing quantity of biomass available. The aim of this study is to present combined sizing models of the boiler with cyclone and power motor to propose the size of the gasifier system in function of the power needed or the available quantity biomass (flow rate). Figure 1 gives a synoptic view of the gasifier and summarizes the objectives of this work.

Figure 1. Small-scale gasifier engine system

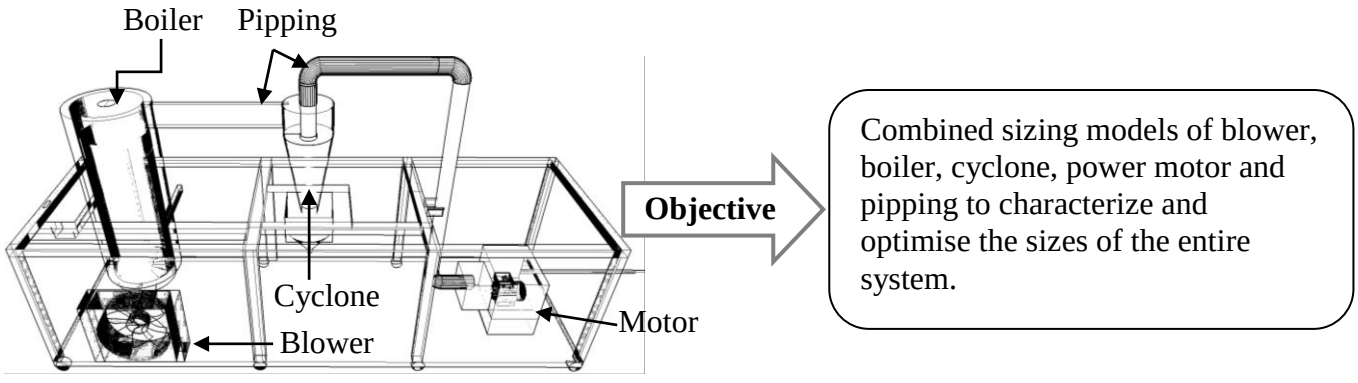

2 GENERALIZED PROTOCOL OF DIMENSIONING SMALL-SCALE GASIFIER (G.P.D.G)

The general idea of the G.P.D.G is established by systemic analysis; applicable only for fixed bed gasifier. Each subsystem is represented by a block model with an Input / Output (I/O) physical variables and parameters. All the blocks are interconnected via the I/O variables and physical parameters. These later allow each subsystem's models to simulate simultaneously their respectively sizes and propose an optimum volume of the whole system taking into account the piping sizes in the calculation. While sub-models of each subsystem changes according to the type of gasifier (downdraft, updraft or other technologies), the protocol for simulating dimensions remains the same. Once the system technology of gasifier being defined, the only information the protocol needs to predict the size of the system is either the biomass flow rate available (fuel) in $kg.h^{-1}$ or the amount of power consumption in kW. Table 1 to 4 define variables (I/O) and parameters corresponding to the Figure 2.

Figure 2. Synopsis of the P.G.D.G methods

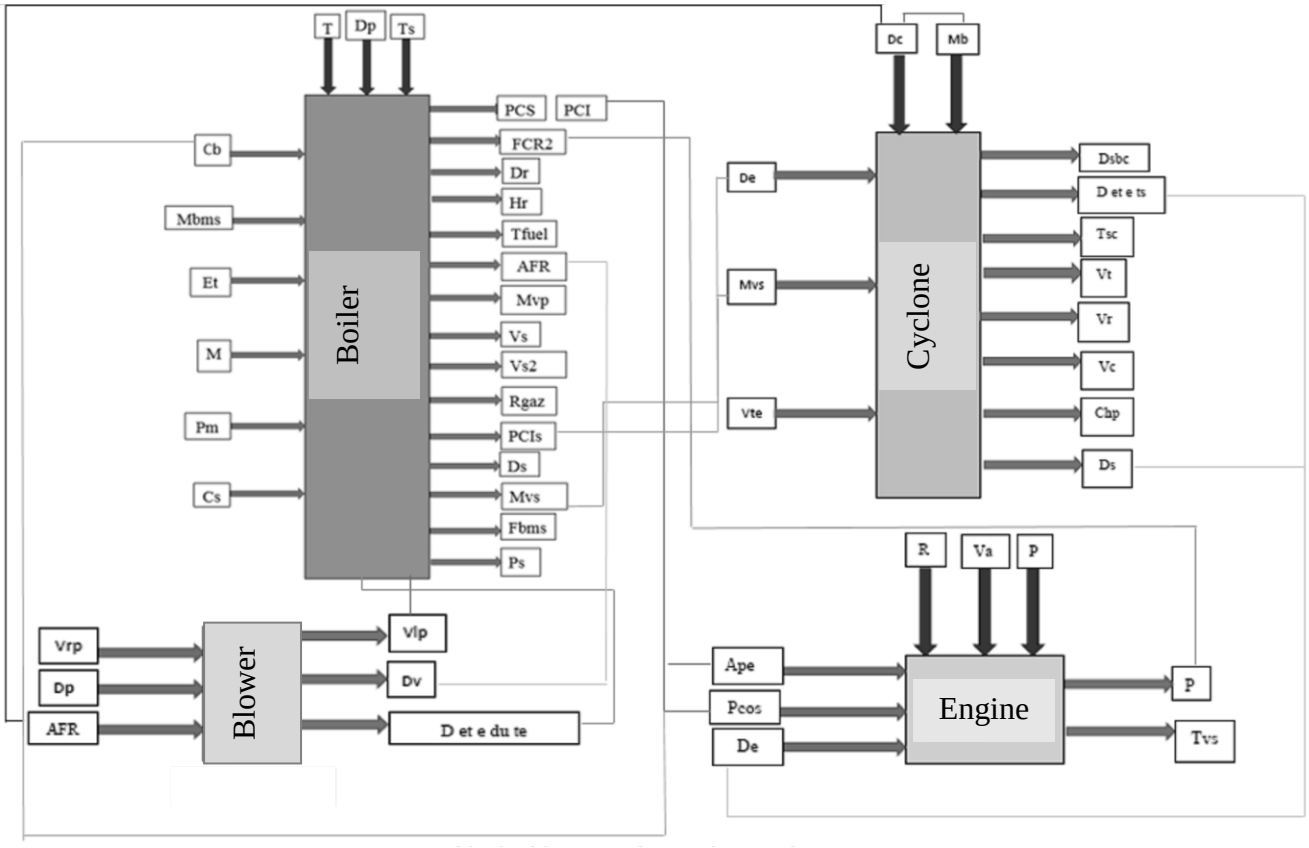

Table 1. Blower description (I/O and parameter) [6].

System	Input	Parameter	Output	Modeling reference
Blower	**Vrp** (**tr.m^{-2}**): Angular speed of the propeller	-	**Vip** (**m.s^{-1}**): Linear speed of the propeller	[6]
	AFR (**m^3.h**): Air flow necessary for the gasification	-	**Dv** (**m^3.h**): Blower flow	[6]
	Dp (**m**): Blade diameter	-	**D** (**m**) and **e** (**m**): Tubing diameter D and thickness e	[6]

Table 2. Engine description (I/O and parameter) [7].

System	Input	Parameter	Output	Modeling reference
Engine	**Ape** (**KWh.m^{-3}**): Air supply energy	**R** (-): Motor efficiency	**P** (**Kw**) : Power	[7]
	Pcos (**Nm^3 air/ Nm^3 gas**): Syngas comburivore power	**Va** (**m^3.min**): air volume in the motor	**Tvs** (**h**): necessary time to give the motor the syngas volume he need	[7]
	De (**m^3.h^{-1}**): Input fuel flow	**P** (**KVA**): Power	-	[7]

Table 3. Boiler description (I/O and parameter: further information can be found in [8 - 11]

System	Input	Parameter	Output	Modeling reference
Boilier	**Cb** (**-**): Biomass composition	**T** (**h**): Operating time of the gasifier	**PCI** (**Kj.Kg^{-1}**): Lower heating values biomass	[8]
	Mbms (**Kg.mol^{-1}**): Molecular mass of biomass	**Dp** (**m**): particular diameter integrated in the boilier	**PCS** (**Kj.Kg^{-1}**): Higher heating values biomass	[8]
	Et (%): Thermal efficiency of the electrical motor	**Ts** (**°C**): Syngas temperature	**FCR2** (**Kg.h^{-1}**): Fuel consumption rate	[8]
	M (**Kg.m^{-3}**): Fuel density	-	**Dr** (**m**): Reactor diameter	[8]
	Pm (**Kw**): Mecanical power of the electrical motor	-	**Hr** (**m**): Reactor height	[8]
	Cs (**-**): Syngas composition	-	**Tfuel** (**h**) : Fuel consumption time in the reactor	[8]
	-	-	**AFR** (**m^3.h^{-1}**): Air flow necesary for gasification	[8]
	-	-	**Mvp** (**Kg.m^{-3}**): Particles density	[8]
	-	-	**Vs** (**m.s^{-1}**): Superficial speed air in the reactor	[8]
	-	-	**PSG** (**m^3. Gas.s^{-1}.m^{-3}**): Superficial production gas in the reactor	[8]
	-	-	**Vs2** (**m.s^{-1}**): Superficial speed of syngas	[8]
	-	-	**Rgaz** (**-**): Gasifier efficiency	[8]
	-	-	**PCIs** (**Kcal.N^{-1}.m^{-3}**): Lower heating values syngas	[8]
	-	-	**Ds** (**m^3.h^{-1}**): Syngas flow	[8]
	-	-	**Mvs** (**Kg.m^{-3}**): Syngas density	[8]
	-	-	**Fbms Kg.h^{-1}**): biomass flow	[8]
	-	-	**Ps** (**Pa**): Syngas pressure	[8]

Table 4. Cyclone description (I/O and parameter): further information can be found in [12 - 16].

System	Input	Parameter	Output	Modeling reference
Cyclone	**De** (**m^3.h^{-1}**): Input flow	**Dc** (**m**): Cyclone diameter	**Dsbc** (**mm**): Section diameter between boilier and cyclone	[12]
	Mvs (**Kg.m^{-3}**): Syngas density	**Mb** (**-**): Barth values	**D and e** (**mm**): Tubing output diameter D and thickness e	[12]
	Vte (**m.s^{-1}**): Input speed flow tubing	-	**Tsc** (**°C**): Syngas temperature in the cyclone	[12]
	-	-	**Vt** (**m.s^{-1}**): Tangential velocity of the cyclone propeller	[12]
	-	-	**Vr** (**m.s^{-1}**): Radial velocity of the cyclone propeller	[12]
	-	-	**Vc** (**m^3**): Cyclone volume	[12]
	-	-	**Chp** (**Pa**): Pressure drop	[12]
	-	-	**Ds** (**m^3.h**): output gas flow	[12]

3 EXAMPLE OF APPLICATION: VERIFICATION TEST CASE IN THE G.E.K GASIFIER

G.E.K (i.e. Gasifier Experimenter's Kit) system is a small-scale gasifier system specifically dedicated to the experimental study. The system has a control panel with sensors used to measure different physical variables. Most compagnies [17] that work in biomass research fields use this system. The detailed description on how to operate the system as well as the dimensions are given on the website: http://wiki.gekgasifier.com. In this website, it's possible to download the CAD drawings for all the sheets

metals parts of the engine. Figure 3 illustrates the G.E.K gasifier system. The comparison between the P.G.D.G results and G.E.K gasifier engine given by the constructor is presented in Table 5. The results shows a significant difference in the height of the cyclone between the P.G.D.G method and the information given by the constructor. This difference is due to the specific configuration of the cyclone. To understand this difference, Figure 4 shows the configuration of G.E.K cyclone and how the P.G.D.G procedure takes into account the calculation of the subsystem. The height of the cyclone in the P.G.D.G. is (H) while the height in CAD drawing of the G.E.K engine is (H + x). However the value of (x) wasn't given by the constructor, so it's not possible to compare it.

Figure 3. G.E.K gasifier [17]

Table 5. Comparison between G.E.K system and the P.G.D.G procedure

Subsystem	**Variable name**	**Symbol**	**GEK system**	**P.G.D.G. method**
Boiler	Diameter Height Biomass flow rate	Dr Hr Fbms	0.15 m 0.508 m 6 kg/h	0.17 m 0.50 m 5.75 kg/h
Cyclone	Height Output diameter tubing	Mb D	0.508 m 0.020 m	0.32m 0.021 m
Tubing	Boiler/Cyclone diameter Cyclone/Engine diameter	- -	7.6 cm 4.2 cm	6.93 cm 4.1 cm
Engine	Power	P	5 kWh	5.21 kWh

Figure 4. G.E.K dimension of the cyclone (A) and the P.G.D.G calculation (B)

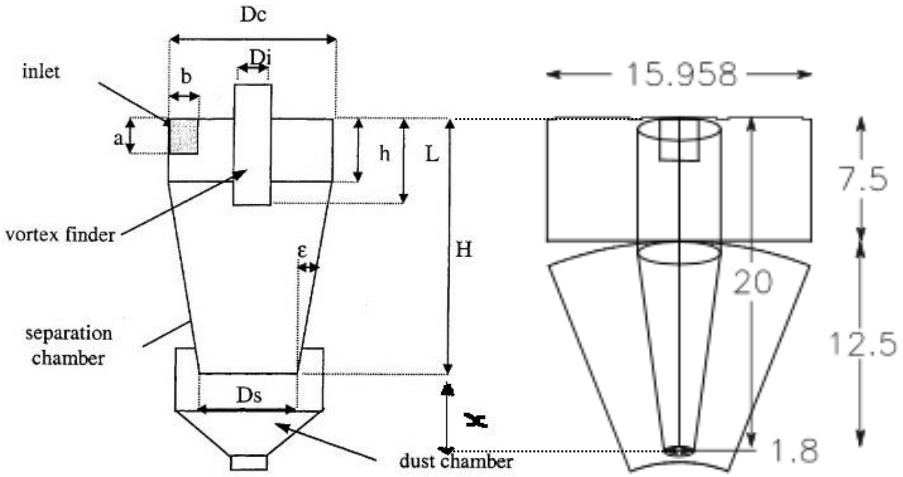

(B) (A)

4 CONCLUSION

The P.G.D.G procedure is based on a systemic analysis dedicated to calculate the sizes of the small-scale gasifier systems. This method has been tested in many systems to access its reliability. The P.G.D.G has 40 related equations with 45 variables (15 inputs and 30 outputs) and 8 parameters. EES software is applied to resolves the equations. Moreover, the P.G.D.G can be used in different configuration of small-scale gasifiers systems. Results of the tests prove that the P.G.D.G method is reliable. This method makes it easier to optimise the size as well as the electrical production of the system. Thereby, this study aids in finding a protocol to optimize the small-scale gasifier system using the P.G.D.G method.

REFERENCES

[1] P. J. Woolcock and R. C. Brown, 'A review of cleaning technologies for biomass-derived syngas', *Biomass Bioenergy*, vol. 52, pp. 54–84, May 2013.

[2] P. Basu, *Biomass gasification and pyrolysis: practical design and theory*. Burlington, MA: Academic Press, 2010.

[3] V. S. Sikarwar *et al.*, 'An overview of advances in biomass gasification', *Energy Environ. Sci.*, vol. 9, no. 10, pp. 2939–2977, 2016.

[4] J. A. Ruiz, M. C. Juárez, M. P. Morales, P. Muñoz, and M. A. Mendívil, 'Biomass gasification for electricity generation: Review of current technology barriers', *Renew. Sustain. Energy Rev.*, vol. 18, pp. 174–183, Feb. 2013.

[5] A. Molino, S. Chianese, and D. Musmarra, 'Biomass gasification technology: The state of the art overview', *J. Energy Chem.*, vol. 25, no. 1, pp. 10–25, Jan. 2016.

[6] F. Sun, Y. Yao, X. Li, J. Tian, G. Zhu, and Z. Chen, 'The flow and heat transfer characteristics of superheated steam in concentric dual-tubing wells', *Int. J. Heat Mass Transf.*, vol. 115, pp. 1099–1108, Dec. 2017.

[7] J. A. Ruiz, M. C. Juárez, M. P. Morales, P. Muñoz, and M. A. Mendívil, 'Biomass gasification for electricity generation: Review of current technology barriers', *Renew. Sustain. Energy Rev.*, vol. 18, pp. 174–183, Feb. 2013.

[8] A. T. Belonio, *Rotary flash paddy dryer : a technical handbook*, Technology Application and Promotion Institute : department of Science and Technology. Los Banos, Laguna: Philippine council for agriculture, forestry and natural resources research and development, 1993.

[9] E. Bocci, M. Sisinni, M. Moneti, L. Vecchione, A. Di Carlo, and M. Villarini, 'State of Art of Small Scale Biomass Gasification Power Systems: A Review of the Different Typologies', *Energy Procedia*, vol. 45, pp. 247–256, 2014.

[10] P. R. Bhoi, R. L. Huhnke, A. Kumar, S. Thapa, and N. Indrawan, 'Scale-up of a downdraft gasifier system for commercial scale mobile power generation', *Renew. Energy*, vol. 118, pp. 25–33, Apr. 2018.

[11] M. A. Chawdhury and K. Mahkamov, 'Development of a Small Downdraft Biomass Gasifier for Developing Countries', *J. Sci. Res.*, vol. 3, no. 1, Dec. 2010.
[12] S. Altmeyer *et al.*, 'Comparison of different models of cyclone prediction performance for various operating conditions using a general software', *Chem. Eng. Process. Process Intensif.*, vol. 43, no. 4, pp. 511–522, Apr. 2004.
[13] P. A. Funk, K. Elsayed, K. M. Yeater, G. A. Holt, and D. P. Whitelock, 'Could cyclone performance improve with reduced inlet velocity?', *Powder Technol.*, vol. 280, pp. 211–218, Aug. 2015.
[14] J. Chen *et al.*, 'How to optimize design and operation of dense medium cyclones in coal preparation', *Miner. Eng.*, vol. 62, pp. 55–65, Jul. 2014.
[15] C. Cortes and A. Gil, 'Modeling the gas and particle flow inside cyclone separators', *Prog. Energy Combust. Sci.*, vol. 33, no. 5, pp. 409–452, Oct. 2007.
[16] K. Elsayed and C. Lacor, 'The effect of cyclone inlet dimensions on the flow pattern and performance', *Appl. Math. Model.*, vol. 35, no. 4, pp. 1952–1968, Apr. 2011.
[17] 'http://wiki.gekgasifier.com'.

MECHANICAL PRE-TREATMENT OF MICROALGAE (CHLORELLA VULGARIS) THROUGH HIGH-PRESSURE HOMOGENIZER – A SOURCE FOR IMPROVED PROTEIN CONCENTRATION YIELD

Leonard E. N. Ekpeni[1], Khaled Benyounis[2], Joseph Stokes[3], A. G. Olabi[4]

1. School of Mechanical and Manufacturing Engineering, Dublin City University, Collins Avenue, Dublin 9, Ireland. email: Leonard.ekpeni3@mail.dcu.ie
2. School of Mechanical and Manufacturing Engineering, Dublin City University, Collins Avenue, Dublin 9, Ireland. email: Khaled.Benyounis@dcu.ie
3. School of Graduate Studies, Dublin City University, Collins Avenue, Dublin 9, Ireland. email: Joseph.t.Stokes@dcu.ie
4. School of Engineering, Institute of Energy and Engineering Technologies, University of the West of Scotland, Paisley Campus, Paisley, PA1 2BE, Scotland, UK. email: Abdul.Olabi@uws.ac.uk

ABSTRACT

The objective of this work was in consideration of the evaluation of high-pressure homogenizer (HPH) as a mechanical pretreatment of *Chlorella vulgaris* and to also consider the effect of this pretreatment on the conversion of microalgae *Chlorella vulgaris spp.* into protein by disrupting of the cell wall. Notably, not only the chemical composition determines *Chlorella vulgaris* disruption of the cell walls which has been highly considered but repetitively, has been one of the main issues for an efficient breakage of cell walls. Pre-treatments to open the cell wall structure have been widely studied in other lignocellulosic biomass, however there is not so much information regarding the effect of those pre-treatments on microalgae for example, in the likes of *Chlorella vulgaris*. Based on these facts, and for more efficiency influent from high pressure homogenizer (HPH) for an improved protein concentration yield after disruption. The HPH with serial identification GYB40-10S of a two-stage homogenizing valves pressure and maximum pressure of 100 MPa was employed in conducting the disruption process. The piece of equipment is adjustable to produce a superfine, homogeneous, stable liquid-liquid or solid-liquid under multiple actions of cavitation effect and high-speed impact.
In this research, the mechanical pretreatment of the use of HPH in the cell wall breakage of *chlorella vulgaris* has compared favorably well with the untreated sample of same species' protein concentration yielding 95.3% when considered under the same operating conditions.

Keywords: Operating conditions; Cavitation effect; GYB40-10S; HPH; Chlorella vulgaris; Microalgae

1. INTRODUCTION

The current energy trends and the need to forgo the use of fossil fuels which is now seen as unsuitable and unsustainable since the depletion of resources and greenhouse gases (GHGs) accumulation in the environment are seen to be on the rise. Shenk et al. [1] estimated this to have exceeded the dangerously high threshold of 450 ppm Co_2e. This trends globally made governments and environmentalists to think of biofuels as the most promising renewable alternatives needed in achieving the goals of reducing the overall dependence on fossil fuels as well lowering CO_2 emissions as this to a greater deal will support local agriculture and develop economies [2, 3]. Andres et al. [4] have explained that combustion of fossil fuels such as coal, oil and natural gas as the conventional method of producing transportation fuels, chemicals, and power, and has been established for many years. While Brennan and Owende [5] rated it accounting for 88% of the global primary energy consumption in the year 2008, Singh et al. [6] classified the current technological progress, potential reserves, and increase in exploitation leading to insecurity in energy and climate change because of increment of greenhouse gases (GHGs) emission

and due to our consumption rate of energy which is considered at a very high level. This therefore made Ben-Iwo et al. [7] to elucidate in their paper that combustion of fossil fuel is a significant global concern as it releases greenhouse gases (GHG) particularly carbon dioxide (CO_2) into the atmosphere. [8] reiterated Petroleum consumption for road transportation as currently the largest source of CO_2 emissions and Saboori et al. [9] confirmed it accounting for 23% of CO_2 emissions worldwide. Reducing emissions, means switching to low carbon alternatives in the likes of biomass fuel. This is because, biomass currently offers the only renewable source of energy that can substitute for petroleum fuels as well as reduce CO_2 emissions [10, 11]. Amongst these are microalgae, lignocellulosic materials and biomass substrates for energy production.

Based on the above, Chlorella vulgaris, a microalgae species of the strain identification; CCAP 211/11B will be considered in this research. Its pre-treatment through high-pressure homogenizer will be discussed and as a source for improved protein concentration yield, this is known to improve biogas production since protein yield influences its production as well [12-15].

2. CHLORELLA VULGARIS (MICRO-ALGAE)

Chlorella vulgaris suitability as a biomass substrate is beyond question because proteins and lipids content within their cell is high enough to yield biogas as compared to other biomass materials [5]. Their use has gone lately from human consumption to the production of energy [5]. They can grow autotrophically and heterotrophically with a wide range of tolerance to different temperatures, salinity, pH and nutrient availabilities. Chlorella vulgaris along with Chlorella Protothecoides are two widely available microalgae strains in the commercial applications for food and nutritional purposes. Heredia-Arroyo et al. [16] have indicated that they can show great potential as future industrial bioenergy producers due to their robustness, high growth rate, and high oil content. They can be cultured under the same conditions; autotrophic and heterotrophic. Accordingly, Heredia-Arroyo et al. [16] revealed in their results that Chlorella vulgaris could grow on autotrophic, mixotrophic and heterotrophic modes; and the mixotrophic cultivation especially could produce more cell biomass than the autotrophic or heterotrophic cultures, individually or combined [16]. This research work therefore analyze and consider these parameters; Pressure, Temperature, Number of cycles (Passes) and Dilution ratios in a bid to improved protein concentration yield after Chlorella vulgaris is fully homogenized and through optimization using the design of experiment (DoE).

3. CELL WALL BREAKDOWN PROCEDURES

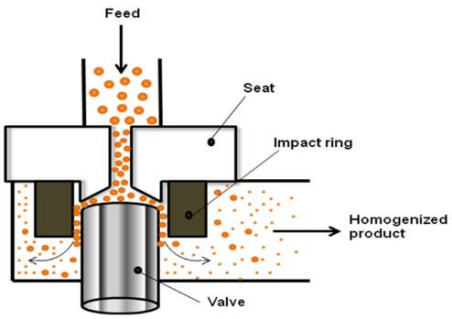

Figure 1: GYB40-10S 2 stage Homogenizing Valves **Figure 2:** HPH parts during cell disruption [21]

Previous works and researches on biomass substrates homogenization shows similarities with that of Chlorella vulgaris [17-20] in terms of the disruption processes and procedures required in the extraction and emulsification of protein from the substrates cell wall through constricting prepared soluble substrate via the exit point of high-pressure homogenizer. This is in fact the first step required in the cell wall breaking down process for the liberation of the inner content of protein concentration. This needed to match the protein release and contaminant profile of full-scale methods like homogenization

thereby enabling representative studies of subsequent downstream operations being performed. To achieve this, a pre-treatment phase is generally necessary in the breakdown of the cell wall for the liberation of protein within the biomass and which in this case is considered as the mechanical means of high-pressure homogenizer (Figure 1). For this research, the high-pressure homogenizer series GYB40-10S 2 stages Homogenizing Valves is employed as in (Figure1). The main structures and functionalities of the HPH will are as detailed in (Figure 2) showing the valve seat, impact ring and the valve head in operation.

4. MATERIALS AND METHODS

4.1 CHLORELLA VULGARIS SAMPLE AND STORAGE

Chlorella vulgaris general composition of microalgae – Chlorella vulgaris (% of dry matter) 51-58 protein, 12-17 carbohydrate and 14-22 lipids [22]. It showed Chlorella vulgaris to be higher in terms of the protein content when compared to others. This reflects the reason for one of its consideration as a biomass substrate amongst others in this research. A sample of the substrate is shown in Fig 3. This was supplied by a Culture Collection of Algae and Protozoa (CCAP) of the Scottish Marine Institute, United Kingdom. This determination of the strain was through the identification of CCAP 211/11B from the original author Beijerinck 1890, where freshwater in Delft, Holland was used [23]. The culture conditions as demanded by the CCAP required the temperature to be 15 °C ± 2 °C, and for faster growth, it should be grown at 20 – 25 °C in cool white fluorescent tubes about 10 cm from the culture, with an intensity of 30-40 μmol/m^2 s, and 12 hours light and 12 hours of darkness (for faster growth, use continuous light). Refer to Appendix A for further information on the strain data. On the other hand, microalgae species choices of Chlorella vulgaris is considered commercially important because of its green nature and own its potential to serve as a food and energy source because of their high photosynthetic efficiency. This in theory can reach 8% and can be grown with autotropic and heterotrophic modes [24]. Algal proteins are of high quality and comparable to conventional vegetable proteins and Rasoul-Amini et al. [25] therefore concluded that due to their high production costs and technical difficulties, its cultivation as protein is still under evaluation.

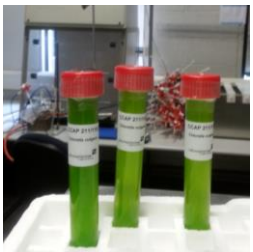

Figure 3: Chlorella vulgaris with strain number CCAP 211/11B [23]

4.2 EXPERIMENTAL PROCEDURE

The experimental procedure for microalgae was basically like the procedure described in [16-20], the difference was the measurement and quantification of the substrate against the phosphate buffer (solution C) pH 5.3. 10 ml of *Chlorella vulgaris* is mixed into 1000 ml of buffer solution C (phosphate buffer) at any time before pre-treating in the homogenization stage. The microalgae were not cultured and were pre-treated the same way as supplied (by the Institute; CCAP). After the pre-treatment using the HPH, the other steps taken were same for the Baker's yeast. For further reference on the strain supplied, refer to [19]

5. RESULTS AND DISCUSSION

Table 1: Design matrix with actual value

Exp. No.	Run Order	Factor 1 A:Pressure	Factor 2 B:No. of cycles	Factor 3 C: Temp	Factor 4 D:Ratio	Response 1 Protein Conc.
		MPa	-	(°C)	-	[mg/mL]
1	51	30	1	20	10:90	0.0914
2	25	90	1	20	10:90	0.2070
3	32	30	5	20	10:90	0.1559
4	3	90	5	20	10:90	0.2823
5	8	30	3	15	10:90	0.1532
6	7	90	3	15	10:90	0.2930
7	46	30	3	25	10:90	0.2823
8	30	90	3	25	10:90	0.2769
9	20	60	1	15	10:90	0.2150
10	9	60	5	15	10:90	0.2312
11	24	60	1	25	10:90	0.3602
12	40	60	5	25	10:90	0.3844
13	22	60	3	20	10:90	0.2688
14	13	60	3	20	10:90	0.2043
15	38	60	3	20	10:90	0.2258
16	42	60	3	20	10:90	0.2661
17	15	60	3	20	10:90	0.1909
18	4	30	1	20	20:80	0.1452
19	2	90	1	20	20:80	0.2194
20	43	30	5	20	20:80	0.2177
21	5	90	5	20	20:80	0.2930
22	50	30	3	15	20:80	0.2769
23	6	90	3	15	20:80	0.3172
24	29	30	3	25	20:80	0.3817
25	31	90	3	25	20:80	0.3306
26	18	60	1	15	20:80	0.2634
27	11	60	5	15	20:80	0.2312
28	47	60	1	25	20:80	0.3710
29	16	60	5	25	20:80	0.4113
30	17	60	3	20	20:80	0.2688
31	26	60	3	20	20:80	0.2903
32	12	60	3	20	20:80	0.2769
33	49	60	3	20	20:80	0.3038
34	37	60	3	20	20:80	0.2984
35	10	30	1	20	30:70	0.1694
36	33	90	1	20	30:70	0.2742
37	28	30	5	20	30:70	0.2581
38	27	90	5	20	30:70	0.4220
39	45	30	3	15	30:70	0.2823
40	48	90	3	15	30:70	0.3629
41	36	30	3	25	30:70	0.3011
42	41	90	3	25	30:70	0.4462
43	21	60	1	15	30:70	0.3091
44	39	60	5	15	30:70	0.2688
45	44	60	1	25	30:70	0.3790
46	23	60	5	25	30:70	0.4624
47	1	60	3	20	30:70	0.3091
48	19	60	3	20	30:70	0.3118
49	34	60	3	20	30:70	0.3172
50	35	60	3	20	30:70	0.3199
51	14	60	3	20	30:70	0.3065

Table 2: Process variables and experimental design level used

Variables	Code	Unit	Limits Coded/actual		
			-1	0	+1
Pressure	A	MPa	30	60	90
Number of Cycles	B	-	1	3	5
Temperature	C	°C	15	20	25
Ratio	D	-	10:90	20:80	30:70

Table 3: ANOVA for reduced quadratic model for Protein Concentration yield at (15-25°C)

Source	Sum of Squares	DF	Mean Square	F Value	Prob > F	
Model	0.2520	11	0.0229	18.7647	< 0.0001	Significant
A-Pressure	0.0425	1	0.0425	34.7949	< 0.0001	
B-No. of cycles	0.0157	1	0.0157	12.8673	0.0009	
C-Temperature	0.0583	1	0.0583	47.7505	< 0.0001	
D-Ratio	0.0590	2	0.0295	24.1627	< 0.0001	
AD	0.0082	2	0.0041	3.3643	0.0449	
BC	0.0035	1	0.0035	2.8493	0.0994	
A^2	0.0131	1	0.0131	10.7653	0.0022	
B^2	0.0037	1	0.0037	2.9998	0.0912	
C^2	0.0513	1	0.0513	41.9980	< 0.0001	
Residual	0.0476	39	0.0012			
Lack of Fit	0.0416	27	0.0015	3.0870	0.0220	Not Significant
Pure Error	0.0060	12	0.0005			
Cor Total	0.2996	50				
$R^2 = 0.8411$			Pred $R^2 = 0.7008$			
Adj $R^2 = 0.7963$			Adeq Precision = 20.503			

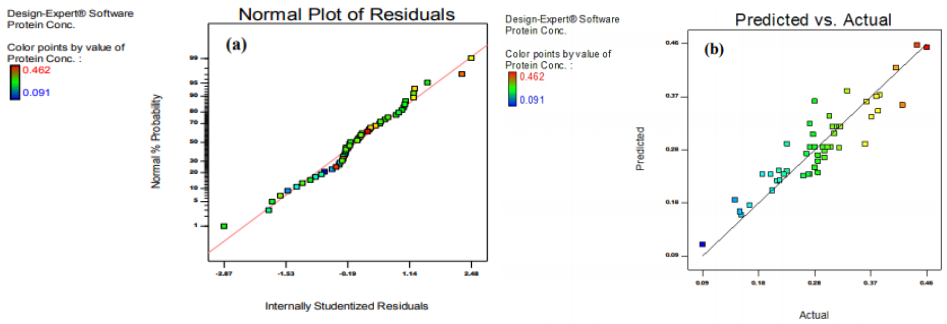

Figure 4: Scatter diagrams of normal plot of residuals (a) and of protein concentration yields (b)

The experiment was designed based on a three level Box Behnken design (BBD) which includes one full replication for this substrate. Trial samples of Chlorella vulgaris were performed by varying one of the process variables in determining the working range of each variable. With the maximum pressure of the high-pressure homogenizer considered as 100 MPa from the manufacturer, it was recommended never to go beyond 90 MPa as the operating working pressure. Also, with a pressure lower than 30 MPa considered as infinitesimal, and with whose application in the HPH, never showed appreciable effect. Hence the working pressure was set between 30 and 90 MPa. These were the criteria for choosing the working ranges. Temperature ranges were chosen as the homogenization process needed to be within ± 5 °C of room temperature since room temperature is around 20 °C [26]. The number of cycles used was chosen for an improved homogenization process. Table 2 shows homogenizer input variables along with the design levels used for this substrate and, the experiment was carried out according to the design matrix shown in Table 1 in a random order to avoid any systematic error using the HPH alongside with the measured response. 51 runs of experiments were carried out. Ratios as a

variable factor were used categorically and as identified by the design expert software. This was required to determine the effect of the dilution concentration of microalgae (Chlorella vulgaris) and the solution C on other parameters.

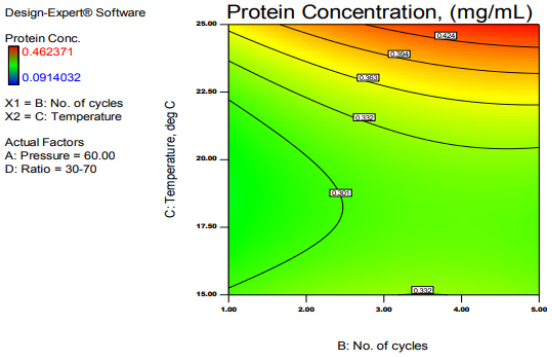

Figure 5: Contours plots showing effect of the number of cycles and temperature on the response – protein concentration yield (this shows zone with highest software-estimated protein concentration)

5.1 VALIDATION OF THE MODEL

From the ANOVA Table 3, the point prediction technique and an appropriate model indicated that, Adj R^2 minus Pred. R^2 was 0.096 that is < 0.2. The normality of plots and validation of data were also applicable here. This was necessary to determine good model discrimination based on the analysis of the ANOVA Table [27]. As R^2 equalled 0.8411 it implied that 84.1% of the variability in the data has been explained by the model. The F-Value model equalled 18.76, implying that the model was significant since it only led to 0.01% chance that the F-Value model occurred because of noise.

The Figures 4a and 4b showed linearity and therefore were normally distributed and that in Figure 5 explained temperature effect aiding the higher yield of protein concentration over number of cycles during homogenization. Parameters of cycles and temperature considered in the ratio of 30-70 homogenization of substrate played an important role in the yield of protein

6. CONCLUSION

- Implementing Design of Experiment (DoE) techniques to optimise the results found after HPH treatment.
- Identifying the most suitable variables as input parameters (Pressure, Temperature, Number of Cycle and Ratio) along with protein concentration (mg/mL) as output (Responses) via experimentation.
- Identifying the best parameters for optimum yields of intracellular protein release as an output.
- Establish the ratios of dilution (substrate against solution C) during experimental work which as a result, led to the categorical factors being determined as; 10:90, 20:80 and 30:70 and which was required to identify and optimize the highest yields from the results.

ACKNOWLEDGMENTS

The author gratefully thanks the organiser of the conference for the opportunity given to showcase the work.

REFERENCES

[1] Schenk, P.M., Thomas-Hall, S.R., Stephens, E., Marx, U.C., Mussgnug, J.H., Posten, C., Kruse, O., Hankamer, B., 2008. Second generation biofuels: high-efficiency microalgae for biodiesel production. Bioenergy Res. 1, 20–43

[2] Farrell, A. E., Plevin, R. J, Turner, B. T, Jones, A. D, O'Hare, M., & Kammen. D. M. (2006). Ethanol can contribute to energy and environmental goals. Science 311:506–508

[3] Goldemberg, J. (2007). Ethanol for a sustainable energy future. Science 315:808–810.

[4] Andres, R. J., Boden, T. A., Bréon, F. M., Ciais, P., Davis, S., Erickson, D., ... & Oda, T. (2012). A synthesis of carbon dioxide emissions from fossil-fuel combustion. *Biogeosciences*, *9*(5), 1845-1871.

[5] Brennan, L., Owende, P., 2010. Biofuels from microalgae-a review of technologies for production, processing, and extractions of biofuels and co-products. Renew. Sustain. Energy Rev. 14, 557–577

[6] Singh, A., Nigam, P. S., & Murphy, J. D. (2011). Renewable fuels from algae: an answer to debatable land-based fuels. *Bioresource technology*, *102*(1), 10-16.
[7] Ben-Iwo, J., Manovic, V., & Longhurst, P. (2016). Biomass resources and biofuels potential for the production of transportation fuels in Nigeria. *Renewable and Sust. Energy Reviews*, *63*, 172-192.
[8] Cannon JS, Sperling D, editors. (2009). Reducing climate impacts in the transportation sector. Dordrecht: Springer Netherlands.
[9] Saboori B, Sapri M, bin Baba M. (2014). Economic growth, energy consumption and CO2 emissions in OECD (Organization for Economic Co-operation and Development)'s transport sector: a fully modified bi-directional relationship approach. Energy 66, 150–61.
[10] Balat M, Balat H. (2009). Recent trends in global production and utilization of bioethanol fuel. Appl Energy 86, 2273–82.
[11] Melero, J.A, Iglesias J, Garcia A. (2012). Biomass as renewable feedstock in standard refinery units. Feasibility, opportunities and challenges. Energy Environ Sci 5, 73-93.
[12] Weiland, P. (2010). Biogas production: current state and perspectives. Applied microbiology and biotechnology, 85(4), 849-860.
[13] Amon, T., Amon, B., Kryvoruchko, V., Zollitsch, W., Mayer, K., & Gruber, L. (2007). Biogas production from maize and dairy cattle manure—influence of biomass composition on the methane yield. Agriculture, Ecosystems & Environment, 118(1), 173-182.
[14] Pöschl, M., Ward, S., & Owende, P. (2010). Evaluation of energy efficiency of various biogas production and utilization pathways. Applied Energy, 87(11), 3305-3321.
[15] Sialve, B., Bernet, N., & Bernard, O. (2009). Anaerobic digestion of Microalgae as a necessary step to make microalgal biodiesel sustainable. Biotechnology advances, 27(4), 409-416.
[16] Heredia-Arroyo, T., Wei, W., Ruan, R., & Hu, B. (2011). Mixotrophic cultivation of Chlorella vulgaris and its potential application for the oil accumulation from non-sugar materials. Biomass and Bioenergy, 35(5), 2245- 2253.
[17] Ekpeni, L. E. N., Nkem-Ekpeni, F. F., Benyounis, K. Y., Aboderheeba, A. K., Stokes, J., & Olabi, A. G. (2014). Yeast: a potential biomass substrate for the production of cleaner energy (Biogas). *Energy Procedia*, *61*, 1718-1731.
[18] Ekpeni, L. E. N., Benyounis, K. Y., Nkem-Ekpeni, F. F., Stokes, J., & Olabi, A. G. (2015). Underlying factors to consider in improving energy yield from biomass source through yeast use on high-pressure homogenizer (hph). *Energy*, *81*, 74-83.
[19] Ekpeni, L. E. N. (2015). *Investigation and disruption of baker's yeast/chlorella vulgaris in high-pressure homogenizer (HPH) to improve cost-effective protein yield* (Doctoral dissertation, Dublin City University).
[20] Ekpeni, L. E. N., Benyounis, K. Y., Stokes, J., & Olabi, A. G. (2016). Improving and optimizing protein concentration yield from homogenized baker's yeast at different ratios of buffer solution. *International Journal of Hydrogen Energy*, *41*(37), 16415-16427.
[21] High-pressure homogenization principle during operation. Available at http://nptel.ac.in/courses/102103045/module5/lec28/7.html (Accessed April 1st 2018)
22] Becker, W. (2004). 18 Microalgae in Human and Animal Nutrition. *Handbook of microalgal culture: biotechnology and applied phycology*, 312.
[23] Chlorella vulgaris. Culture collection of Algae Protozoa (CCAP), Scottish Marine Institute, Oban Argyll, PA37 1QA, Scotland, UK. <www.ccap.ac.uk >
[24] Heredia-Arroyo, T., Wei, W., & Hu, B. (2010). Oil accumulation via heterotrophic/mixotrophic Chlorella protothecoides. *Applied biochemistry and biotechnology*, *162*(7), 1978-1995.
[25] Rasoul-Amini, S., Ghasemi, Y., Morowvat, M. H., & Mohagheghzadeh, A. (2009). PCR amplification of 18S rRNA, single cell protein production and fatty acid evaluation of some naturally isolated Microalgae. *Food Chemistry*, *116*(1), 129-136.
[26] www.seai (Accessed April 19th 2018)
[27] Montgomery, D. C., & Myers, R. H. (1995). Response surface methodology: process and product optimization using designed experiments. Raymond H. Meyers and Douglas C. Montgomery. A Wiley-Interscience Publication.

REED, REED CANARY GRASS AND BIOMASS FROM WETLAND AS POTENTIAL RESOURCE ENHANCE LOCAL BIOECONOMY

I. Melts[1], M. Ivask[2], K. Takeuchi[1] and K. Heinsoo[3]

1. Integrated Research System for Sustainability Science, The University of Tokyo, Tokyo, Japan; e-mail: indrek.melts@gmail.com
2. Tartu College, Tallinn University of Technology, Tartu, Estonia; mari.ivask@ttu.ee
3. Institute of Agricultural and Environmental Sciences, Estonian University of Life Sciences, Tartu, Estonia; e-mail: katrin.heinsoo@emu.ee

ABSTRACT

In the current paper we analyse the variability and dynamics of chemical composition and energy potential of local bioresource. The information about biomass yield and crucial characteristics is required in order to analyse its feasibility and sustainability for different bio-based products. The study was carried out in different wetland types in Northern Europe. Area-specific yield, its chemical composition, calorific value and potential for different bioconversion methods was estimated. The results revealed that we can obtain more biomass from floodplain meadows or from reed in coastal meadows than from reed canary grass cultivations in extracted peatlands. The chemical composition and calorific value varied by species and by functional groups. Most of studied characteristics changed also during biomass growing period. The collected data were used for validating the empirical model between biomass chemical composition and its heating value. Theoretical potential for biomethane production and bioethanol synthesis were also under discussion.

Keywords: biomass, biobased products, natural vegetation, reed, reed canary grass, restoration, sustainable management, wetland

1 INTRODUCTION

Semi-natural communities (SNC) as a part of traditional landscape have been formed and shaped by extensive management over a long period of time and are characterised by high biodiversity [1]-[3]. These complex ecosystems have provided a variety of different functions and services [3]-[6], but during the last century the area of SNCs has decreased considerably due to land use changes (e.g. agricultural intensification, the draining of wetlands, abandonment etc.) [4] and [7]-[8]. During regional and local changes it is important to guarantee that SNCs are managed continuously with appropriate and the most effective methods for maintenance of biodiversity and traditional landscape [4] and [9]-[10]. One of the under-ecosystem services, source of bioenergy feedstock, is the herbaceous biomass obtained from different types of these agricultural landscape [11]-[14] etc. This herbaceous biomass from SNCs is available without land use change, almost without competition with the food production, but positive environmental impact and a large potential for increasing ecological improvements in the current global situation [14]. Biomass potential from diferent SNCs varies by local conditions and by types of semi-natural communites [11]-[15] and therefore a wide range of potential applications regarding different biobased products can be achieved. In current paper we give a short overview and analyse the variability and dynamics of chemical composition and energy potential of this local bioresource.

2 MATERIAL AND METHODS

The common reed biomass was sampled in July 2016. Biomass yield in flooded meadows and reed canary grass fields was measured in July 2011. The dry weight of biomass samples that were transported to lab was determined after drying in an oven for 48-72 h at 80 °C. The chemical composition of all samples was measured in the Laboratory of Plant Biochemistry of the Estonian University of Life Sciences. Calorific value (CV) was measured using bomb calorimeter e2K (Digital Data Systems (Pty) Ltd, South Africa) in the laboratory of the Tartu College of Tallinn University of Technology. The biochemical methane potential (BMP) experiment was carried out in the Laboratory of Bio- and Environmental Chemistry in the Estonian University of Life Sciences and described in full details earlier [13] and [15].

3 RESULTS AND DISCUSSION

3.1 Biomass productivity

Our results revealed that in Estonian conditions the area-specific biomass yield varied by vegetation type and more than 10% higher biomass yield can be obtained from natural vegetation types compared to reed canary grass fields (Figure 1). One of the reasons for higher biomass yield is the most suitable and efficient natural community evolutionally developed in specific area. The higher biomass has been also recorded in natural vegetation of tall sedges swamp (6.7 t ha^{-1}) [16] or sedges and tall forbs communities (both about 10.0 t ha^{-1}) in flooded wet meadows [17].

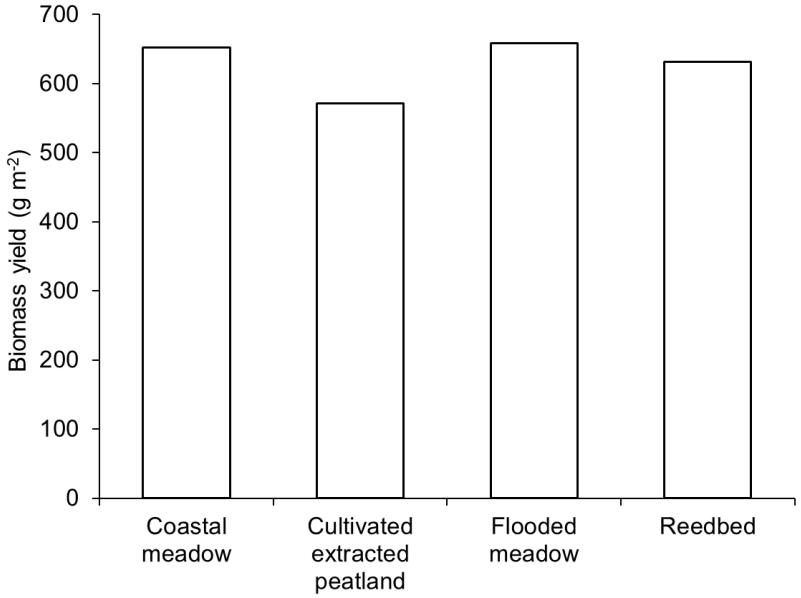

Figure 1. The average yield of herbaceous biomass from different type of wetland ([18]-[21], respectively).

3.2 Chemical composition of herbaceous biomass

The chemical composition and calorific value varied by species and by plant functional groups and by wetland types (Table 1 and 2) as reported earlier [16] and [22]. The large variability of herbaceous biomass chemical composition biomass is the most problematic issue regarding it conversion to bioenergy [23]-[24].

Table 1. Some organic and inert compounds (% DM) in biomass in July

Type/Characteristics	NDF[1]	Cellulose	Hemicellulose	Lignin	Protein	Ash	Source
Phalaris arundinaceae (extracted peatland)	n.a.[2]	n.a.[2]	n.a.[2]	n.a.[2]	9.0	5.1	[19]
Phragmites australis (reedbed)	n.a.[2]	28.8	39.4	4.1	n.a.[2]	n.a.[2]	OD[3]
Grasses Legumes Other forbs Sedges&rushes (flooded meadow)	68.2 51.4 54.5 70.9	n.a.[2]	n.a.[2]	6.2 10.0 12.7 5.6	6.4 14.1 10.0 9.1	7.9 5.2 6.4 5.5	[31]
Total biomass (flooded meadow)	59.7	n.a.[2]	22.8	n.a.[2]	9.4	6.1	[11]

[1] – neutral detergent fibre; [2] – not available; [3] – original data

For effective anaerobic digestion, usually a high ratio of easily biodegradable compounds in biomass is favoured [25]. Too high contents of protein or N in feedstock can form ammonium, thus inhibiting methane production [26]. Our results demonstrated that protein content in legumes from flooded meadows was higher than in other functional groups or species (Table 1). The high lignin concentration (critical level 100 g lignin

kg^{-1} [27]) is considered to be also unfavourable for effective anaerobic digestion or methane potential. In this study the critical level of lignin content was exceeded only by other forbs (Table 1). Therefore we agree that large proportion of other forbs in biomass can be crucial for biodigestibility [28]. On the other hand larger proportion of grasses as well reed and sedges&rushes from different wetland types with lower lignin content and higher cellulose and hemicellulose content (Table 1) can be more suitable for different high-valued bioproducts (e.g. [29]-[30]).

If thermochemical conversion or combustion is selected for energy conversion method, certain requirements for substrate quality become important. In general, herbaceous biomass has higher ash and lower carbon concentration than woody biomass [32]. Typically, a higher C concentration is considered to be in correlation with higher heating value [33]-[35], as each extra 1% of ash is assumed to decrease the heating value by 0.2 MJ kg^{-1} [36]. In this study it was not so clear that higher carbon content is related with higher calorific value (Table 2), but there could detect some negative correlation between high ash content and lower calorific value (see Table 1 and 2). If the combustion process is not regulated for burning herbaceous biomass, increased ash and alkali metal (especially K, P, S and Cl) contents can result in slagging, corrosion and fouling during thermochemical conversion [37]. The results of this study demostrated higher potassium content in reed, other forbs and in total biomass from coastal and flooded meaow (Table 2). The content of phosphorus is higher in reed compared to other different biomass types. High concentrations of chlorine,

Table 2. Chemical composition (% DM) and calorific value (CV, MJ kg^{-1}) in biomass in July

Type/Characteristics	C	N	P	K	Ca	Mg	Cl	S	CV	Source
Phalaris arundinaceae (extracted peatland)	46.3	1.4	n.a.[1]	n.a.[1]	n.a.[1]	n.a.[1]	0.4	0.2	16.7	[19]
Phragmites australis (reedbed)	n.a.[1]	2.8	0.3	1.5	0.5	0.1	n.a.[1]	n.a.[1]	18.1	OD[3]
Grasses	42.2	1.0	0.1	0.8	0.3	0.1	0.1	0.2	16.8	[31]
Legumes	45.2	2.3	0.1	0.9	1.3	0.3	0.03	0.2	18.2[2]	
Other forbs	44.3	1.6	0.2	1.4	1.0	0.5	0.05	0.2	16.7	
Sedges&rushes (flooded meadow)	43.8	1.5	0.1	1.3	0.6	0.1	0.1	0.2	17.5	
Total biomass (coastal meadow)	42.3	1.5	0.1	1.5	0.3	0.4	n.a.[1]	n.a.[1]	17.7[2]	[18]
Total biomass (flooded meadow)		1.5	0.2	1.5	0.8	0.2			18.4	[11]

[1] – not available; [2] – based on C content and formula of [35]; [3] – original data

nitrogen and sulphur in fuels can increase greenhouse gas emissions (limits for N and S to avoid emissions are assumed to be 6 g kg^{-1} DM and 2 g kg^{-1} DM, respectively and corrosion can be avoided lower than 1.0 g S kg^{-1} DM and 1 g Cl kg^{-1} DM) [38]. In general, grasses include less nitrogen than legumes and other forbs [39] and [40]. According to results of this study (Table 2), the average N concentration in legumes and in reed was higher than in other species, functional groups and in total biomass from other types of wetland. Among other non-metals studied, S concentration was found to be similar in all types of biomass and close to the limit for S below which SOx emissions is assumed to be negligible, but exceeded about twice the value which may cause corrosion. We found that reed canary grass and other monocotyledonous functional groups contained more Cl than legumes and other forbs (Table 2), which is in agreement with [16]. The critical value of Cl concentration for combustion, stated by [38] to avoid corrosion or HCl emissions, was surpassed only by reed canary grass in this study.

3.3 Bio-based products via energy conversion

According to BMP experiment the average cumulative methane yield of herbaceous biomass varied by functional groups (Figure 2). The first two weeks the higher methane yield was observed in legumes and it can be due to high content of easily degradable component. The highest feedstock-specific methane yield was observed for sedges&rushes followed by grasses, legumes, mix of total biomass and other forbs. Based on literature high ratio of sedges in herbaceous biomass is suggested to be less suitable as a feedstock for biogas production [41].

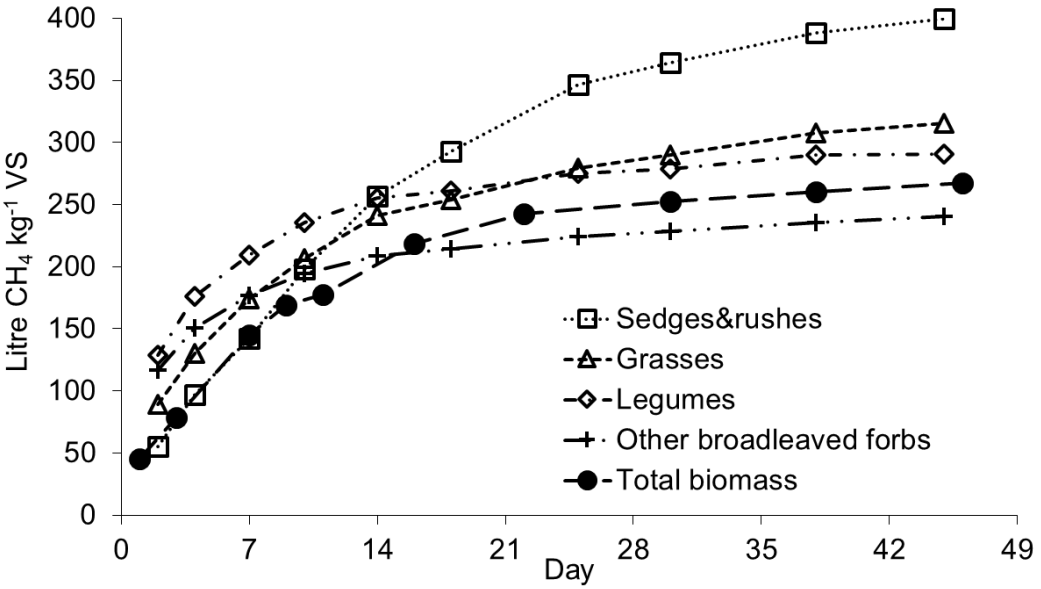

Figure 2. Methane production by different functional groups and total biomass from flooded meadows [13] and [15].

The energy output depend on different biomass to energy conversion routes [15], [42]. Although energy potential from flooded meadows was about 120 GJ ha^{-1}, about 100 GJ ha^{-1} can be possible to achive via combustion to produce heat only (efficiency 85% [42]). Via anaerobic digestion it was possible to obtain more than 50% of energy potential from herbaceous biomass in flooded meadows [15]. Area-specific ethanol energy yield [43] was approximately 23 GJ ha^{-1} and it is less than 20% of energy potential that can be obtained via energy potential of absolutely dry material.

4 CONCLUSIONS

Herbaceous biomass from semi-natural communities should be considered for bio-based products purposes to enhance local bioeconomy. Availability of improved technologies and comparison of different conversion and pretreatment options are essential to meet the needs of both resource efficiency usage for bio-based products and conservation of biodiversity and traditional landscapes in the future.

ACKNOWLEDGEMENTS

The authors thank Mai Olesk for the laboratory analyses and Epp Libe for fieldwork. Authors acknowledge support from the Japan Society for the Promotion of Science Postdoctoral Fellowship under the Grant-in-Aid program (No. JP16F16755) and grant PUT 1463 provided by the Estonian Research Council.

REFERENCES

[1] K. Takeuchi, R.D. Brown, I. Washitani, A. Tsunekawa and M. Yokohari, *Satoyama: The traditional rural landscape of Japan*, Springer, Tokyo, 2003.

[2] Ramsar Convention Secretariat, *The Ramsar Convention Manual: a guide to the Convention on Wetlands*, Ramsar Convention Secretariat, Gland, 2013.

[3] P. Veen, R. Jefferson, J. de Smidt and J. van der Straaten, *Grasslands in Europe of high nature value*, KNNV Publishing, Zeist, 2009.

[4] K. Kimmel, A. Kull, J.-O. Salm and Ü. Mander, The status, conservation and sustainable use of Estonian wetlands, *Wetlands Ecology and Management*, Vol. 18, pp. 375-395, 2010.

[5] B.E. Berglund, J. Kitagawa, P. Lagerås, K. Nakamura, N. Sasaki and Y. Yasuda, Traditional farming landscapes for sustainable living in Scandinavia and Japan: global revival through the Satoyama initiative. *Ambio: A Journal of the Human Environment*, Vol. 43, pp. 559-578, 2014.

[6] W.J. Mitsch, B. Bernal and M.E. Hernandez, Ecosystem services of wetlands, *International Journal of Biodiversity Science, Ecosystem Services & Management*, Vol. 11, pp. 1-4, 2015.

[7] M. Sammul, T. Kull, K. Lanno, M. Otsus, M. Mägi, and S. Kana, Habitat preferences and distribution characteristics are indicative of species long-term persistence in the Estonian flora, *Biodiversity and Conservation*, Vol. 17, 3531-3550, 2008.
[8] J. Paal, M. Ilomets, E. Fremstad, A. Moen, E. Burset, V. Kuusemets, L. Truus, and E. Leibak, *Estonian wetlands inventory 1997,* Eesti Loodusfoto, Tartu, 1998.
[9] M. Luoto, S. Rekolainen, J. Aakkula and J. Pykälä, Loss of plant species richness and habitat connectivity in grasslands associated with agricultural change in Finland, *Ambio: A Journal of the Human Environment*, Vol. 32, pp. 447-452, 2003.
[10] N. Kawano, K. Kawano and M. Ohsawa, Floristic diversity and the richness of locally endangered plant species of semi-natural grasslands under different management practices, southern Kyushu, Japan. *Plant Ecology and Diversity*, Vol. 2, pp. 277-288, 2009.
[11] K. Heinsoo, I. Melts, M. Sammul and B. Holm, The potential of Estonian semi-natural grasslands for bioenergy production, *Agriculture, Ecosystems and Environment*, Vol. 137, pp. 86-92, 2010.
[12] J. Corton, L. Bühle, M. Wachendorf, I.S. Donnison and M.D. Fraser, Bioenergy as a biodiversity management tool and the potential of a mixed species feedstock for bioenergy production in Wales, *Bioresource Technology*, Vol. 129, pp. 142-149, 2013.
[13] I. Melts, A., Normak, L. Nurk, and K. Heinsoo, Chemical characteristics of biomass from nature conservation management for methane production, *Bioresource Technology*, Vol. 167, pp. 226-231, 2014.
[14] K. Van Meerbeek, S. Ottoy, M. de Andrés García, B. Muys and M. Hermy, The bioenergy potential of Natura 2000 – a synergy between climate change mitigation and biodiversity protection, *Frontiers in Ecology and the Environment*, Vol. 14, pp. 473-478, 2016.
[15] I. Melts, K. Heinsoo, L. Nurk and L. Pärn, Comparison of two different bioenergy production options from late harvested biomass of Estonian semi-natural grasslands, *Energy*, Vol. 61, pp. 6-12, 2013.
[16] B. Tonn, U. Thumm and W. Claupein, Semi-natural grassland biomass for combustion: Influence of botanical composition, harvest date and site conditions on fuel composition, *Grass and Forage Science*, Vol. 65, pp. 383-397, 2010.
[17] L. Neuenkamp, J.-A. Metsoja, M. Zobel and N. Hölzel, Impact of management on biodiversity-biomass relations in Estonian flooded meadows, *Plant Ecology*, Vol. 214, pp. 845-856, 2013.
[18] M. Sammul, K. Kauer and T. Köster, Biomass accumulation during reed encroachment reduces effi ciency of restoration of Baltic coastal grasslands, *Applied Vegetation Science*, Vol. 15, pp. 219-230, 2012.
[19] K. Heinsoo, K. Hein, I. Melts, B. Holm and M. Ivask, Reed canary grass yield and fuel quality in Estonian farmers` fields, *Biomass and Bioenergy*, Vol. 35, pp. 617-625, 2011.
[20] I. Melts, *Biomass from semi-natural grasslands for bioenergy*, PhD Thesis, Estonian University of Life Sciences, 2014.
[21] Ü. Kask, L. Kask and S. Link, Combustion characteristics of reed and its suitability as a boiler fuel, *Mires and Peat*, Vol. 13, pp. 1-10, 2013
[22] J. Khalsa, T. Fricke, A. Weigelt and M. Wachendorf, Effects of species richness and functional groups on chemical constituents relevant for methane yields from anaerobic digestion: Results from a grassland diversity experiment, *Grass and Forage Science*, Vol. 69, pp. 49.63, 2014.
[23] A. Prochnow, M. Heiermann, M. Plöchl, T. Amon and P.J. Hobbs, Bioenergy from permanent grassland – A review: 2. Combustion. *Bioresource Technology*, Vol. 100, pp. 4945-4954, 2009a.
[24] A. Prochnow, M. Heiermann, M. Plöchl, B. Linke, C. Idler, T. Amon and P.J. Hobbs, Bioenergy from permanent grassland – A review: 1. Biogas, *Bioresource Technology*, Vol. 100, pp. 4931-4944, 2009b.
[25] E. Klimiuk, T. Pokój, W. Budzyński and B. Dubis, Theoretical and observed biogas production from plant biomass of different fibre contents, *Bioresource Technology*, Vol. 101, pp. 9527-9535, 2010.
[26] A. Pakarinen, M. Kymäläinen, F.L. Stoddard and L. Viikari, Conversion of carbohydrates in herbaceous crops during anaerobic digestion, *Journal of Agricultural and Food Chemistry*, Vol. 60, pp. 7934-7940, 2012.
[27] J.M. Triolo, L. Pedersen, H. Qu and S.G. Sommer, Biochemical methane potential and anaerobic biodegradability of nonherbaceous and herbaceous phytomass in biogas production, *Bioresource Technology*, Vol. 125, pp. 226-232, 2012.

[28] R.J. Garlock, B. Bals, P. Jasrotia, V. Balan and B.E. Dale, Influence of variable species composition on the saccharifi cation of AFEXTM pretreated biomass from unmanaged fields in comparison to corn stover, *Biomass and Bioenergy*, Vol. 37, pp. 49-59, 2012.
[29] S. Grass, Utilisation of Grass for Production of Fibres, Protein and Energy, *Biomass and Agriculture: Sustainability, Markets and Policies*, OECD, 2004.
[30] M.G. Mandl, Status of green biorefining in Europe, *Biofuels, Bioproducts & Biorefinery*, Vol. 4, pp. 268-274, 2010.
[31] I. Melts and K. Heinsoo, Seasonal dynamics of bioenergy characteristics in grassland functional groups. *Grass and Forage Science*, Vol. 70, pp. 571-581, 2015.
[32] M.J.F. Llorente and J.E.C. García, Concentration of elements in woody and herbaceous biomass as a function of the dry ashing temperature, *Fuel*, Vol. 85, pp. 1273-1279, 2006.
[33] D.A. Tillman, *Wood as an energy resource*. Academic Press, New York, 1978.
[34] A. Friedl, E. Padouvas, H. Rotter and K. Varmuza, Prediction of heating values of biomass fuel from elemental composition, *Analytica Chimica Acta*, Vol. 544, pp. 191-198, 2005.
[35] C. Sheng and J.L. Azevedo, Estimating the higher heating value of biomass fuels from basic analysis data, *Biomass and Bioenergy*, Vol. 28, pp. 499-507, 2005.
[36] K.A. Cassida, J.P. Muir, M.A. Hussey, J.C. Read, B.C. Venuto and W.R. Ocumpaugh, Biofuel component concentrations and yields of switchgrass in south central U.S. environments, *Crop Science*, Vol. 45, pp. 682-692, 2005.
[37] B.M. Jenkins, L.L. Baxter, T.R. Jr. Miles and T.R. Miles, Combustion properties of biomass, *Fuel Processing Technology*, Vol. 54, pp. 17-46, 1998.
[38] I. Obernberger, T. Brunner and G. Bärnthaler, Chemical properties of solid biofuels-signifi cance and impact, *Biomass and Bioenergy*, Vol. 30, pp. 973-982, 2006.
[39] A. García-Ciudad, A. Ruano-Ramos, B.R. Vázquez de Aldana and B. García-Criado, Interannual variations of nutrient concentrations in botanical fractions from extensively managed grasslands, *Animal Feed Science and Technology*, Vol. 66, pp. 257-269, 1997.
[40] J.B. Winkler and M. Herbst, Do plants of a semi-natural grassland community benefit from long-term CO2 enrichment?, *Basic and Applied Ecology*, Vol. 5, pp. 131-143, 2004.
[41] C. Herrmann, A. Prochnow, M. Heiermann and C. Idler, Biomass from landscape management of grassland used for biogas production: Effects of harvest date and silage additives on feedstock quality and methane yield. *Grass and Forage Science*, Vol. 69, pp. 549-566, 2014.
[42] European Environment Agency, EU bioenergy potential from a resource-efficiency perspective, *EEA Report*, Vol. 6, 2013.
[43] I. Melts, M. Tutt, A. Menind and K. Heinsoo, Potential of Bioenergy Source from Semi-Natural Grasslands, *Proc. 3rd Asian Conf. On Biomass Science*, Niigata, 2016.

CHARACTERIZATION OF BIODIESEL PRODUCED FROM COTTONSEED OIL USING DIFFERENT CATALYSTS

A.G. Alhassan[1] and A.B. Aliyu[2]

1. Department of Mechanical Engineering, Bayero University, Kano, Nigeria; email: aliyugaladi@yahoo.com
2. Department of Mechanical Engineering, Bayero University Kano, Nigeria; email: abaliyu.mec@buk.edu.ng

ABSTRACT

This paper presents a research carried out on the characterization of biodiesel produced from cottonseed oil using three different catalysts in order to determine the yield of biodiesel obtained using each of the catalysts and the reasons for the differences/variations in the properties of the biodiesel produced. The cottonseed oil biodiesel was produced via transesterification with methanol and catalyst. The reaction conditions employed were; methanol to oil molar ratio of 6:1, catalyst concentration of 1 wt. %, reaction temperature of 65^{o}C and 1hour reaction time. The catalysts used were; NaOH (as homogeneous catalyst), CaO (as heterogeneous catalyst), and Nano-CaO (as heterogeneous nano catalyst) with each of the catalysts used to produce single biodiesel sample. The Nano-CaO catalyst was prepared by calcination of ball-milled chicken eggshell waste and it was characterized using SEM and XRD. The crystalline size of the Nano-CaO catalyst was found to be about 30nm. The biodiesel samples produced were denoted according to the type of the catalyst used for its transesterification, i.e. B-NaOH, B-CaO and B-Nano-CaO, for NaOH, CaO, and Nano-CaO catalysts, respectively. The samples were characterized to determine their physico-chemical properties. The characterization results showed that Nano-CaO catalyst gave the highest biodiesel yield (99%) followed by CaO (96.5%) and NaOH (94%) after transesterification reaction of the esterified cottonseed oil with methanol. The results further showed that the properties of the B-CaO, and B-Nano-CaO biodiesel samples were similar (with negligible variation) and they differ from that of B-NaOH with reasonable margin. It was suggested that the differences were as a result of the purification steps undergone by B-NaOH biodiesel sample which was not done in the case of B-CaO, and B-Nano-CaO biodiesel samples.

Keywords: Biodiesel, Cottonseed oil, Transesterification, Homogeneous catalyst, Heterogeneous catalyst

1 INTRODUCTION

Biodiesel is a realistic alternative fuel, derived from vegetable oil or animal fat and can be used directly or blended with petroleum diesel at any percentage without engine modification [1]. It is economically feasible, renewable, and could provide a feasible solution to the twin crises of fossil fuel depletion and environmental degradation caused by the use of fossil fuels [2]. The biodiesel can be produced by either blending of crude oils, micro-emulsions, pyrolysis or transesterification. Transesterification is the most popular method of producing biodiesel. Transesterification is the chemical reaction that involves triglycerides and alcohol in the presence of a catalyst to form esters and glycerol [3].

Cottonseed oil is a vegetable oil extracted from the seeds of cotton plants of various species, mainly Gossypium hirsutum and Gossypium herbaceum, which are grown for cotton fibre, animal feed, and oil. While cultivation of the cotton crop is driven by demand for fibre to make cloth, the seeds of the cotton plant are also valuable. Oil extracted from the seeds is used for human consumption and the residual meal is fed to livestock. Lately, cottonseed oil demand in the food industry is diminishing because of the health problems linked to its consumption [4, 5]. For this reason, cotton seed oil has huge capability for biodiesel production. Transesterification of cottonseed oil has been carried out successfully using basic catalysts (both homogeneous and heterogeneous) by several research works. The results of the previous research works showed some great achievements with regards to the use of cottonseed oil such as obtaining high biodiesel yield and satisfactory biodiesel properties. However, the current trends on the biodiesel research include the optimization of production procedures and improvements of the fuel properties.

The various properties of cottonseed oil biodiesel which have been investigated by previous research works were cetane number, calorific value, flash point, viscosity, pour point among others. However, the value of these properties were observed to differ from one another (with respect to individual research results) which is contrary to the popular belief that the physical and chemical properties of biodiesel from the same

feedstock should be in close range irrespective of the production methods and conditions employed during the production. For instance, [6] found the kinematic viscosity (mm^2/s) at 40^oC to be 5.6mm^2/s using CaO and MgO as solid based catalysts for the transesterification of refined cottonseed oil, [7] obtained 5.2mm^2/s using NaOH as catalyst for the transesterification of cotton seed oil, and [8] obtained 2.04mm^2/s using NaOH as catalyst. Although, according to ASTM D 6751-02 standards, the kinematic viscosity at 40^oC should be within the range of 1.9-6.0mm^2/s, but wide margin of 2.04mm^2/s to 5.6mm^2/s shouldn't be ignored considering that viscosity is a key fuel property that influences the atomization of a fuel upon injection into the combustion chamber. Another example is the cetane number, [7] found the cetane number to be 51 using NaOH as catalyst for the transesterification of cotton seed oil; [9] successfully obtained the value of the cetane number of the cottonseed methyl ester to be 53 using sodium methoxide as catalyst, and [10] also found the cetane number to be 46 using two step catalytic processes in transesterification of the cottonseed oil.

However, these variations were not limited to viscosity and cetane number, but likewise all other important fuel properties such as density, calorific value etc. one of the suspected reasons for these variations in properties might be the type of catalyst used for the transesterification as observed. The suspicion was motivated by the results of the research conducted by [11] on biodiesel synthesis from cottonseed oil using homogeneous alkali catalyst and using heterogeneous multi walled carbon nanotubes. They found the viscosity of the biodiesel produced to be 2.975mm^2/s and 2.496mm^2/s; density of 0.898 g/cc and 0.963 g/cc using NaOH (homogeneous catalyst) and multi walled carbon nanotubes (heterogeneous catalyst) respectively. Although, the authors didn't specify the reason for the difference in the properties but, one may assume that it was because of the use of different catalyst for the biodiesel production. The current research is focused on the production and characterization of biodiesel from cottonseed using three different catalysts (NaOH, CaO, and Nano-CaO). The results of the research could help in determining which category of catalyst will give highest yield and it could also help in finding out more significant reasons for the variations in properties of the biodiesel from cottonseed oil.

2 MATERIALS AND METHODS

2.1 Materials

The materials used in this research are Cottonseed oil, chicken eggshell, methanol, sulphuric acid, sodium hydroxide, calcium oxide, characterization reagents, G Cussons P6310 bomb calorimeter set, Pensky Martens flash point tester, digital weight balance, Brookfield synchro-lectric viscometer, Porcelain cylindrical Jar ball mill, Nabertherm laboratory furnace (30^oC-3000^oC), hot plate with magnetic stirrer, Carl-Zeiss MA-10 series scanning electron microscope, PANanlytical Empyrean X-ray diffractometer, laboratory oven, thermometer, pipette, burette, tripod stand, measuring cylinder, beaker, round bottom conical flask, separating funnel, and reflux condenser.

2.2 Methods

Catalysts Preparation

Sodium hydroxide (NaOH), and bulk calcium oxide (CaO) catalysts were obtained as pure analytical grade reagents and therefore, they do not need further processing but the nano calcium oxide (Nano-CaO) was not available in analytical grade, and so was synthesized by high-energy ball milling followed by calcination method, in accordance with procedure reported by [12] and [13]. The chicken egg shells were collected and washed several times with a distilled water to remove impurities and then dried in a hot air oven at 120^oC for 5hours to completely remove moisture [12]. The dried egg shells were milled to fine powder of uniform sizes with the ball mill for 3 hours. The milled eggshells were then calcined in a furnace at 900^oC for 2 hours. The product obtained (Nano-CaO) was characterized using scanning electron microscope (SEM) and X-RAY Diffraction (XRD).

Biodiesel Production

Raw cottonseed oil has high free fatty acids (FFAs) value of about 5 wt. % [10]. However, when a raw material (oil or fats) contains a high percentage of free fatty acids (greater than 1wt. %), during transesterification, the alkali (basic) catalyst will react with the free fatty acids to form soap. Therefore, prior to the transesterification reaction, the acidic feedstock (containing high amount of FFAs) should be pre-

treated (esterification or alcoholysis) to inhibit the saponification reaction [10, 14]. Therefore, due to this factor, the biodiesel production was carried out in two stages.

The first stage utilised the Esterification process to reduce the FFA content of the raw cottonseed oil. It was done in this research to reduce the FFA level of the raw cottonseed oil. The esterification was carried out in a 1500ml two necks round bottom flask as a batch reactor placed on a hot magnetic stirrer and a magnetic bar inserted into the flask. A thermometer (to measure temperature) was also inserted into the flask and a reflux condenser (to condense the methanol back to the batch reactor) was attached to the flask. The reaction was carried out using crude cottonseed oil with methanol (using 12:1 methanol to oil molar ratio) and concentrated sulphuric acid (H_2SO_4) as the catalyst (1 wt. % of oil) at 40^oC. The acid value of the compound was determined at every 30 minutes until it dropped to 0.8 mg/g in 2 hours. The mixture was allowed to settle for eight hours in a separating funnel to remove some traces of glycerin, unreacted methanol and chemical water [14].

The second stage utilized transesterification process to obtain the final product (biodiesel). It was carried out using the same setup as the esterification. The reaction was carried out with methanol to oil molar ratio of 6:1, catalyst concentration of 1wt. %, reaction temperature of 65^oC and 1hour reaction time. These reaction conditions were regarded as the best conditions for the production of biodiesel by transesterification using basic catalyst [6]. The transesterification process was carried out in three separate batches using three different catalysts. The catalysts used were sodium hydroxide (NaOH) as homogeneous catalyst, calcium oxide (CaO) as heterogeneous catalyst and Nano Calcium oxide (Nano-CaO) as nano heterogeneous catalyst. After one hour of reaction, heating and stirring were stopped, and then the mixture was poured into a separating funnel and allowed to settle for 8 hours. After the settlement for 8 hours, the biodiesel was separated from the glycerol and the biodiesel samples were denoted according to the type of the catalyst used for its transesterification, i.e. B-NaOH, B-CaO and B-Nano-CaO, for NaOH, CaO, and Nano-CaO catalysts, respectively. B-NaOH being transesterified using a homogeneous catalyst (NaOH), was further purified by washing for several times with warm distilled water at 60^oC to remove impurities and traces of catalyst and then it was heated in an oven at 100^oC for 30minutes to remove traces of unreacted alcohol and water [10, 14].

3 RESULTS AND DISCUSSIONS

3.1 Results

Characterization of the Nano-CaO catalyst

The Nano-CaO catalyst was characterized using Carl-Zeiss MA-10 series Scanning electron microscope and PANanlytical Empyrean X-ray diffractometer. The Scanning Electron Microscope (SEM) image and X-Ray Diffraction (XRD) patterns a of the Nano-CaO catalyst are shown in the figures 1 and 2 respectively.

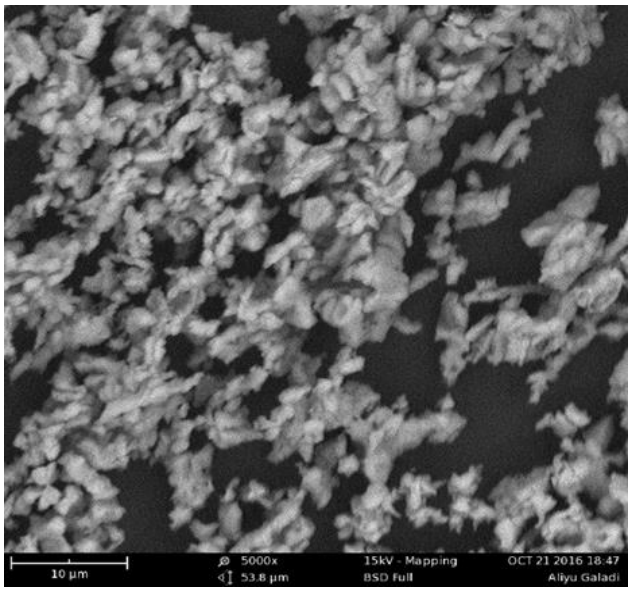

Figure 1: SEM image of Nano-CaO catalyst at 5000x magnification

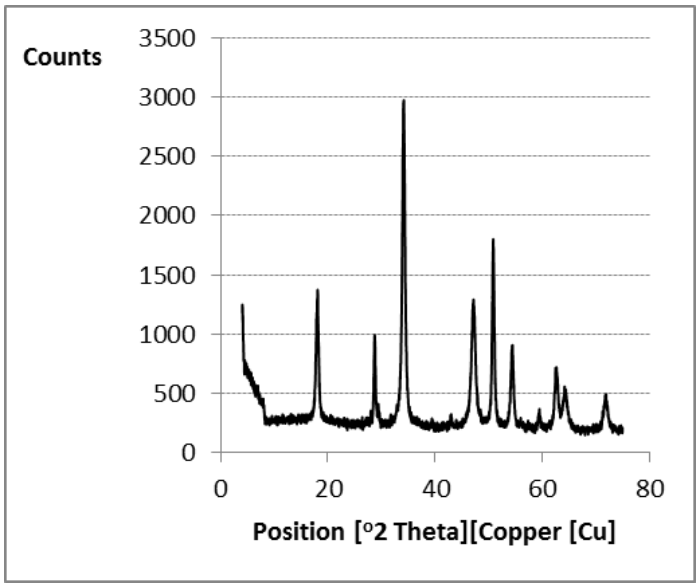

Figure 2: XRD Pattern of Nano-CaO Powder

Characterization of the biodiesel samples

The physico-chemical properties of the fuel samples are presented in Table 1 below:

Table 1: Physico-Chemical Properties of the Biodiesel Samples as Compared to Petro-Diesel and ASTM D6751 Biodiesel Standard

PROPERTY	**B-NaOH**	**B-CaO**	**B-Nano-CaO**	**Petro-diesel**	**ASTM D6751**
Percentage yield (%)	94	96.5	99	-	-
Density (g/ml)	0.8320	0.8655	0.8670	0.8250	0.83-0.88
Kin. Viscosity@ 40ºC (cSt)	3.00	3.65	3.65	2.25	1.9-6.0
Pour point (ºC)	-6	-8.5	-8.6	-20	-
Cloud point (ºC)	3	10	10	-	-
Flash point (ºC)	155	175	178	70	130minimum
Iodine Value (g/100g)	61.9272	72.0792	71.4440	38.0000	-
Saponification Value (mg/g)	193.96	200.98	202.38	-	-
Peroxide Value (mEq/g)	0.25	0.27	0.27	-	-
Cetane Number	60.5062	57.2391	57.1942	49.0000	47minimum
Calorific value (kJ/kg)	37412	37870	37907	42500	-

3.2 Discussion of results

Characteristics of Nano-CaO catalyst

From the SEM images presented in Figure 1, it can be seen that the calcined eggshells typically comprise of irregular shape of particles. The XRD analysis was performed at 2θ ranging from 4.0131º to 74.9931º with Cu radiation (λ=0.154056nm) and two-theta step of 0.026 at 18.87 s per step. From Figure 2, the XRD intense peaks at 2θ of 18.11, 34.12, 47.13, and 50.85 correspond to d-values of 4.90, 2.63, 1.93, and 1.80 respectively, of Calcium Hydroxide (Portlandite) (JCPDS-82-1690). This means that the calcined eggshell (CaO) has absorbed some moisture upon storage, and this was avoided during biodiesel production by further heating at 400ºC for 1hour prior to use [15]. The particle size of the calcined eggshells was determined from the XRD data using Sherrer's Equation and it was found to be approximately 30nm. The catalyst was denoted as Nano-CaO.

Characterization of biodiesel samples

The percentage of the biodiesel yield was determined by comparing the weight of layer of biodiesel with the weight of esterified cottonseed oil used. Nano-CaO catalyst gave the highest percentage yield (99%) followed by CaO (96.5%) and NaOH (94%) and this evidently showed that the Nano-CaO catalyst being relatively of smaller particle sizes (with large surface area), resulted in a rise in the number of catalytic active sites [16]. This large number of catalytic active sites gave more room for the reactants to interact and consequently resulted in higher yield of the desired product (Biodiesel).

From Table 1, the important fuel properties (such as density, kinematic viscosity, flash point, cetane number etc.) of all the biodiesel samples conform to the ASTM D6751 biodiesel standard and were comparable with the petro-diesel. Hence, the cottonseed oil biodiesel could perfectly serve as an alternative to the conventional diesel fuel.

From the characterization results presented in Table 1 however, it could be observed that the properties of the B-CaO and B-Nano-CaO biodiesel samples are similar (with negligible variation) and it differs from that of B-NaOH with reasonable margin. That was not a surprise because the B-CaO, and B-Nano-CaO bio-diesel samples were produced using the heterogeneous base-catalysed transesterification process which was carried out with the omission of the purification steps utilized by homogeneous base catalysed trans-esterification process (adopted for B-NaOH production). The purification steps which include washing the biodiesel with distilled water and drying, is believed to have further reduce the fatty acid content and moisture content of the biodiesel. This belief is supported by the fact that water is among the products of

transesterification (although in relatively little amount) as stated by [17], and it will be difficult to completely separate it from the products by the use of a separating funnel. Therefore, omission of the purification steps could lead to increase in water content of the biodiesel which in turns, increases the density as observed from the results. Furthermore, the omission could also be the reason for the increase in the iodine value (IV) and saponification value (SV) of the B-CaO, and B-Nano-CaO biodiesel samples which showed that they have more unsaturated fatty acids and higher molecular weight than the B-NaOH biodiesel sample. The relatively higher unsaturated fatty acids of the B-CaO, and B-Nano-CaO has resulted in their relatively lower cetane numbers and relatively higher viscosities, because low cetane number is associated with highly unsaturated fatty acids, so also viscosity increases with increase in length of the fatty acid chain [18, 19].

4 CONCLUSION

The biodiesel production was carried out by transesterification reaction of the esterified cottonseed oil with methanol using sodium hydroxide (NaOH) catalyst, calcium oxide (CaO) catalyst and nano calcium oxide (Nano-CaO) catalyst for B-NaOH, B-CaO and B-Nano-CaO biodiesel samples respectively. The reaction conditions employed were; Methanol to oil molar ratio of 6:1, catalyst concentration of 1 wt. %, reaction temperature of 65^{o}C and 1hour reaction time. Nano-CaO catalyst gave the highest percentage yield (99%) followed by CaO (96.5%) and NaOH (94%) after transesterification reaction of the esterified cottonseed oil with methanol. The yield obtained using Nano-CaO catalyst showed that the use of nano catalyst improves the transesterification efficiency of the cottonseed oil by obtaining biodiesel yield close to the theoretical value. The characterization results showed that B-CaO and B-Nano-CaO biodiesel samples possess similar properties (with negligible differences) while the properties of B-NaOH biodiesel sample differs with reasonable margin as it has the lowest kinematic viscosity, lowest density and highest cetane number compared to the other biodiesel samples. These differences were as a result of the purification steps utilized in the production B-NaOH which were omitted during the production of B-CaO and B-Nano-CaO biodiesel samples. These purification steps were believed to have further reduced the fatty acid content and moisture content of the B-NaOH biodiesel sample.

REFERENCES

[1] Ahmed and I. A. Rufai, Effect of Oxidative Stability of Jatropha Biodiesel on the Emission of Diesel Engine, *Proceedings of the 2ND National Engineering Conference, ACICON 2016*, held at the Faculty of Engineering, Bayero University, Kano, Nigeria, pp. 75-79, 2016.

[2] A. Refaat, Biodiesel Production using Solid Metal Oxide Catalysts, *International Journal of Environmental Science and Technology,* Vol. 8 No. 1, pp. 203-221, 2011.

[3] M. Fangrui and A. H. Milford, Biodiesel Production: A Review, *Journal of Bioresource Technology*, Vol. 70, pp. 1-15, 1999.

[4] M. I. Gurr, *Developments in Dairy Chemistry-2: Lipids*, Ed. P.F. Fox, Applied Science, London, pp. 365–417, 1983.

[5] M. Mustapha, M. K. Haruna, S. Awwal and A. Ibrahim, Optimization of Biodiesel Production from Crude Cotton Seed Oil Using Central Composite Design, *American Journal of Chemical and Biochemical Engineering*, Vol. 1 No. 1, pp. 8-14, 2016.

[6] N. Ude, E. J. Ahmed, M. I. Onyiah, O. E. Anisiji and E. N. Ude, Heterogeneous Catalyzed Transesterification of Refined Cottonseed Oil to Biodiesel, *Pacific Journal of Science and Technology*, Vol. 15 No. 2, pp. 71-77, 2014.

[7] K. VinuKumar, Production of Biodiesel used in Diesel Engines, *Innovare Journal of Engineering and Technology*, Vol. 1 No. 1, pp. 5-7, 2013.

[8] R. S. Anil, S. K. Shashank, M. M. Deepa, S. P. Rajath and V. R. Jagadish, Production and Characterization of Biodiesel from Cottonseed oil. *International Journal of Advances in Engineering, Science and Technology (IJAEST),* Vol. 2 No. 4, pp. 328-334, 2012.

[9] K. A. Siva, D. Maheswar, and K. R. Vijaya, Comparison of Diesel Engine Performance and Emissions from Neat and Transesterified Cotton Seed Oil. *Jordan Journal of Mechanical and Industrial Engineering,* Vol. 3 No. 3, pp. 190 – 197, 2009.

[10] J. S. Lebnebiso, F. Aberuagba, S. F. Ndagana and S. I. Okoye, Transesterification of Esterified Crude Cotton (Gossypium Hirsutum) Seed Oil. *International Journal of Scientific Research and Innovative Technology*, Vol. 2 No. 7, pp. 5-12, 2015.

[11] A. Shankar, P. R. Pentapati and R. K. Prasad, Biodiesel Synthesis from Cottonseed Oil using Homogeneous Alkali Catalyst and using Heterogeneous Multi Walled Carbon Nanotubes: Characterization and Blending Studies, *Egyptian Journal of Petroleum*, Vol. 26, pp. 125–133, 2016.

[12] M. B. Huda, R. Nuryanto, S. Suhandono, S. Fadhilah, S. Wiarsih and F. A. Prakoso, Synthesis and Characterization of Nano Calcium Oxide from Eggshell to be Catalyst of Biodiesel Waste Oil, *Proceedings of the 3rd Applied Science for Technology Innovation (ASTECHNOVA 2014,)* Held at International Energy Conference Yogyakarta, Indonesia, 2014.

[13] M. Elaheh and H. Asadollah, Preparation and Characterization of Nano-CaO Based on Eggshell Waste: Novel and green catalytic approach to highly efficient synthesis of pyrano[4,3-b]pyrans, *Chinese Journal of Catalysis*, Vol. 35 No.3, pp. 351–356, 2014.

[14] V. Gopal, V. Sridevi, A. J. Sarma and P. V. Rao, Processing and Characterization of Cotton Seed Methyl Ester, *Austin Chemical Engineering*, Vol. 2 No. 2, 2015.

[15] N. Tangboriboon, R. Kunanuruksapong and A. Sirivat, Preparation and properties of calcium oxide from eggshells via calcination, *Journal of Materials Science-Poland*, Vol. 30 No. 4, pp. 313-322.

[16] S.N. Naik, V. G. Vaibhav, K. R. Prasant, and K. D. Ajay, Production of First and Second Generation Biofuels (A Comprehensive Review), *Renewable and Sustainable Energy Reviews*, Vol. 14, pp. 578–597,2010

[17] U. A. Anya, N. C. Nwobia, and O. Ofoegbu, Optimized Reduction of Free Fatty Acid Content on Neem Seed Oil for Biodiesel Production, *Journal of Basic and Applied Chemistry*, Vol.2 No. 4, pp. 21-28, 2012.

[18] M. J. Ramos, C.M. Fernandez, A. Casas, L. Rodriguez and A. Perez, Influence of Fatty Acid Composition of Raw Materials on Biodiesel Properties, *Journal Bioresource Technology*, Vol. 100 No. 1, pp. 261-268, 2009.

[19] Demirbas (2002). Biodiesel from Vegetable Oils via Transesterification in Supercritical Methanol, *Energy Conversion and Management*, Vol. 43, pp. 2349-2356, 2002.

ARE BIOMASS BOILERS SOLUTION FOR LOW-CARBON TRANSITION IN HOUSEHOLDS?

G. Stegnar[1], M. Česen, J. Čizman, S. Merše and D. Staničić

1. Jožef Stefan Institute - Energy Efficiency Centre, Ljubljana, Slovenia; email: gasper.stegnar@ijs.si

ABSTRACT

Analyses estimate that more than 70% of residential buildings in Slovenia are energy inefficient and need a deep renovation, including energy systems. Renewable energy technologies, like biomass boilers, heat pumps and solar, offer an alternative to fossil fuels solutions and can extensively help to reduce CO2 emissions increasing the share of renewables at a national scale. Since forests in Slovenia cover almost 60% of the land area and due to economic reasons, wood biomass is the main energy source in households - almost 60% of households in rural and urban areas are using biomass for heating. Beside individual users there are 27 biomass district heating systems too. The question is what are the consequences of extensive use of biomass and fuel switch from light fuel oil to biomass in terms of air quality, GHG emissions and energy supply development.

The aim of the analysis is to identify: (1) energy saving potential by replacement of existing biomass boilers with new, efficient ones, and (2) CO2 abatement by replacing fuel oil boilers with biomass boilers in Slovenian households. The analysis is differentiating rural and urban areas. Technical and environmental potential is assessed taking into account spatial constrains. The results are used to support informed decision-making of long-term climate action planning.

Keywords: biomass, potential, savings, emissions

1 INTRODUCTION

Renewable energy sources (RES) are the focal point of state initiatives to move closer toward energy self-sufficiency in the European Union. The implication is that biomass resources come from diverse and heterogeneous sources. The technologies currently available allows the bioenergy products to replace any conventional energy, including solid, liquid, or gaseous fuels. Woody biomass can be used in combustion plants of all sizes: stoves and small boilers in single-family homes, central heating in small dwellings, and medium and large thermal power plants (Scarlat and Dallemand, 2011). In addition, biomass is the third largest primary energy resource in the world (Bilgen and Sarıkaya, 2015).

In Slovenia the issue of air pollution is largely linked to particles (PM10 and PM 2.5) and, in the summer, to ozone. Measurements of PM10 indicate an occasional exceedance of limit values across the whole of Slovenia, and especially in the urban areas, where long-lasting temperature inversions occur in winter. The Government of the Republic of Slovenia in 2013 for the purpose of reducing PM10 pollution on local level introduced Ordinances on air quality plans in the municipalities of Murska Sobota, Maribor, Celje, Kranj, Novo mesto, Ljubljana, Hrastnik, Zagorje and Trbovlje. In the scope of this plans the municipalities steer the local energy policy and list different measures to improve air quality. Subsidies for instalment of new biomass boilers provided by public fund in Slovenia are not available for households in above mentioned areas not to hamper air pollution reduction activities by municipalities. Currently only the Municipality of Ljubljana legally does not favour instalment of biomass boiler in households at new construction and renovation with the definition of the priority use of energy sources for heating (MOL, 2016) in the area of district heating.

Among energy sources consumed in households in 20156 wood fuels (which include firewood, wood waste, wood chips, pellets and briquettes) prevailed with a 42% share. Electricity consumption represented almost 254% and consumption of extra light heatingfuel oil almost 101% of total energy consumed in households. Households also consumed a considerable amount of natural gas (over 910%) and district heat (almost 7%) (SURS, 2018). In 2016, households consumed around 48,000 TJ of energy or 23% of total final energy consumption in Slovenia. Household energy consumption was around 3% higher than in the previous year. The sharpest increase was that of energy consumption for space heating (Figure 1, left).

In line with National Emission Ceiling Directive (EU) 2016/2284, Member states are obliged to reduce the health and environmental impacts and risks caused by air pollutants by 2030 (EC, 2016). The Directive imposes the requirement to reduce fine particulate matter emissions, which have been proven as the most harmful air pollutants. Slovenia has obliged to reduce fine particulate matter by 25 % by 2020 and by 60 % by 2030 compared with 2005. Regarding the greenhouse gas emissions, the goal of Slovenia is that by 2020 the emissions will not increase by more than 4% compared to 2005 (EC, 2009).

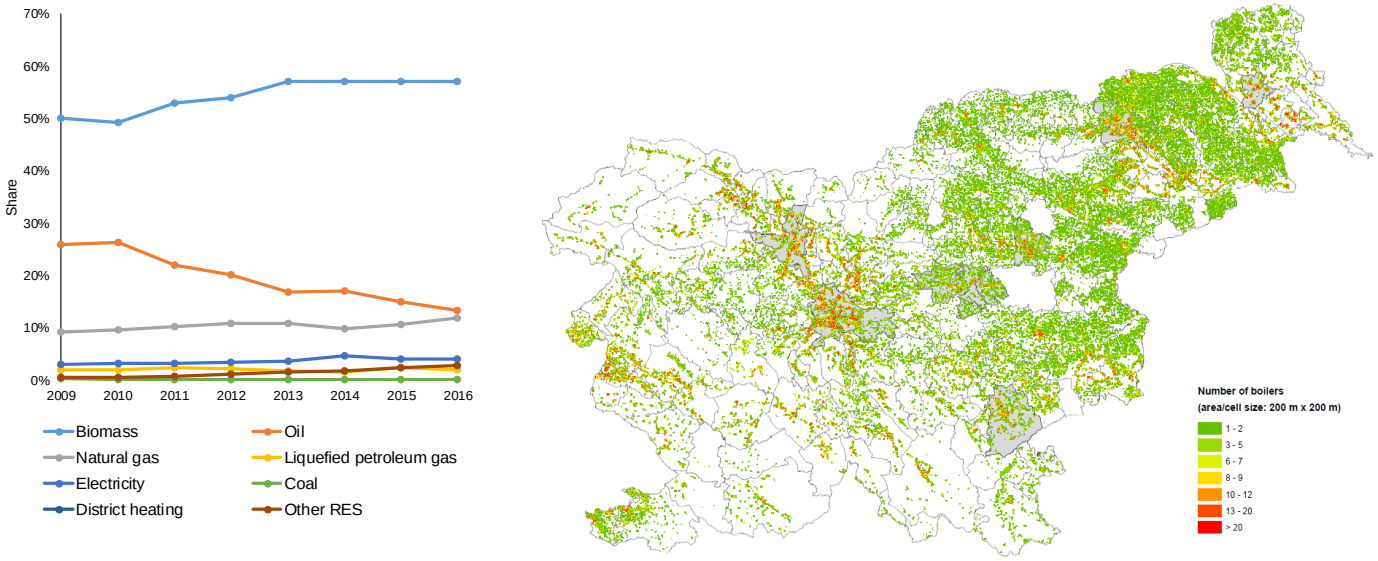

Figure 1 Final energy consumption for heating and energy source (SURS, 2018) – left and number of boilers, aggregated on area size 200x200 m in Slovenia - right

This paper explores the substitution of old inefficient biomass boilers with new, efficient ones, and the replacement of central light fuel oil (LFO) boilers with central biomass boilers to cover centrally all heating needs in single family buildings in Slovenia. A thorough energy, environmental, and economic analysis is conducted. The analysis focuses on energy, greenhouse has emissions and PM2,5 concentrations in air and aims to identify the additional savings potential.

2 MATERIALS AND METHODS

2.1 Data Sources

Several data sources were used in the bottom-up model of the building stock in order to ensure sufficiently accurate and comprehensive analysis of energy balance of the building stock. They possess energy performance related data from which the building can be classified according to building typology, such as age of construction and possible energy-related measures, e.g. façade renovation, boiler replacement. The main used data sources are:

- REN - Register of Real Estates (GURS, 2018);
- Eco Fund, Slovenian Environmental Public Fund (Eco Fund, 2018);
- Survey on energy consumption and fuels in households (SURS, 2014);
- SCP - Database of Small Combustion Plants (MOP, 2018).

Database REN is under management of Geodetic Administration of the Republic of Slovenia and has spatial, construction and energy-related data on buildings. Eco fund offers subsidies for energy renovation to households, SURS conducts surveys on energy consumption in buildings and Ministry for environment and spatial planning is administrating database on Small Combustion Boilers based on boiler inspections that are performed by chimney-sweepers.

2.2 Definition of Replacement Rates

The basic selection process works on an annual basis and is defined in a way, that for each year of the simulation period it is calculated the probability of the boiler replacement (expressed as share). The total share of building applying changes ($s_{mesaure}$) is calculated based on the age distribution of the boilers within the whole building stock using the Weibull distribution. Parameters for the distribution are determined on the basis of the data from Survey on energy and fuels consumption in households.

$$s_{measure} = \frac{\sum_{T=T_{min}}^{T_{max}} 1 - e^{-(T/\lambda)^k}}{\sum_{T=T_{min}}^{T_{max}} 1 - e^{-(T-1/\lambda)^k}} \quad (1)$$

λ ,k - are the scale and shape parameter of Weibull distribution
λ[yr] - characteristic lifetime at which a cumulative failure rate of 63,3 % occurs
T_{min}, T_{max} [yr] - are minimum and maximum age of the considered component

2.3 Characteristics of the building cluster

A building stock consisting of single-family dwellings was identified based on the typological characterizations defined by the European research project TABULA (Loga, 2016). Slovenian national typology consists of a classification scheme grouping buildings according to their size, age and further parameters and a set of exemplary buildings representing these building types. U-values of different age bands and energy expenditure factors of heat generators of these buildings were being compared. Based on the data structure the energy performance of the exemplary buildings was calculated in a standardised way to form simplified building stock model. Based on the identification of the building's energy-related characteristics from the existing data sources, to each single-family house in Slovenia an exemplary building and its energy performance was attributed.

2.4 Spatial Constraints

Air pollution

Households in the municipalities with increased PM10 and accepted Ordinances on air quality plans were identified. For each building, the age of boilers was calculated and energy source identified. In accordance with legal constraints, new biomass boilers should not be seen as an acceptable measure for the replacement of old boilers. Only Ljubljana legally does not favour biomass boiler instalment, but for the purpose of this research it is assumed that in the observed period all other 9 air pollution degraded municipalities will resort to similar approach. The model excludes buildings in these municipalities as a potential.

District Heating (DH) and Natural Gas (NG) Distribution Networks

Slovenia has over 90 distribution networks that supply heat to Slovenian households. By using Geographical Information System (GIS) the buildings connected to networks were identified. Buildings in the immediate proximity of the network represent the baseline. It is assumed that all these are connected to the grid, although this is not entirely correct. The use of exact data would be possible only by retrieving private data for each network, which is highly resource intensive.

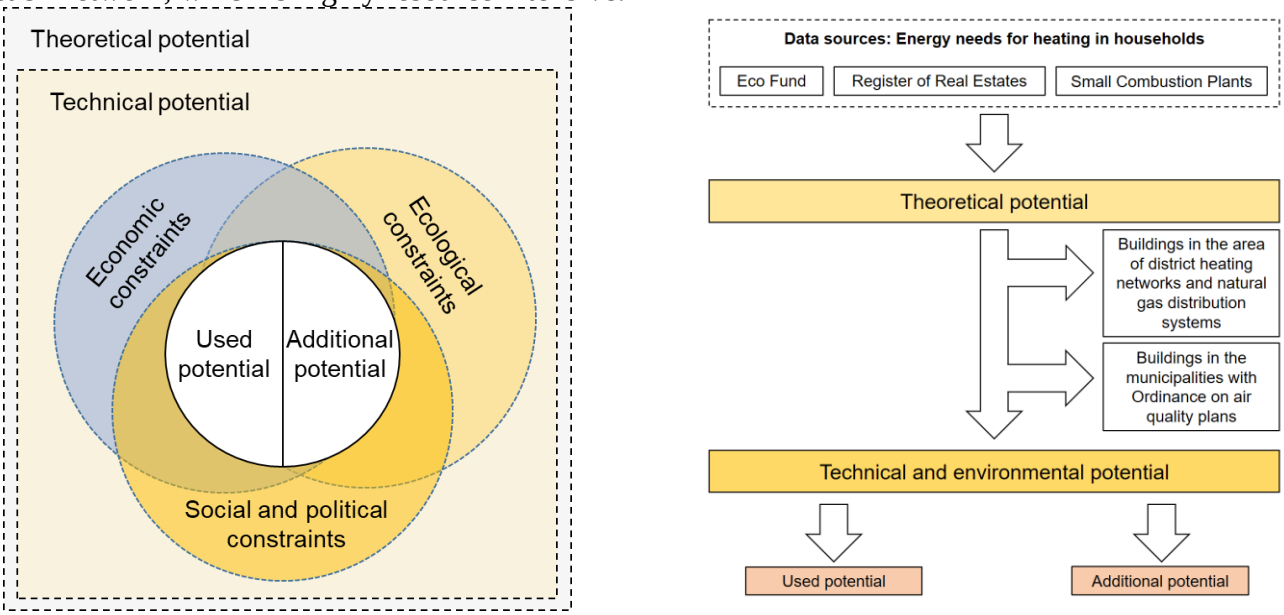

Figure 2 Illustration of the potential and constraints (left) and methodology for the identification of observed additional potential (right)

2.5 Identification of Potential

The savings potential assessment is based on the following analytical levels, following the approach of Steubing (Steubing et al., 2010):

- **Theoretical** potential (upper limit): Maximum annual biophysical availability of the biomass.
- **Technical and environmental potential**: The assessment of the potential was guided by the following criteria regarding the resources mobilization: technical viability, environmental impacts, as well as social and legal constraints.
- Already **used potential**: amount of biomass already used for energy production.
- **Additional potential**: difference between sustainable and already used potential.

The analysis in the scope of this paper focuses on the identification of additional potential, taking into account spatial and technical constraints on selected groups of buildings (Table 1). The main focus groups for biomass boiler replacement were (1) old biomass boilers and (2) old oil boilers. The observed period is 2015-2030.

Table 1 Observed group of buildings

Group	Buildings observed
1	All buildings, taking into account no constraints in the baseline year.
2	All buildings, taking into account the technical lifetime boiler period (30 years).
3	Buildings located outside municipalities with air quality plans.
4	Buildings located outside DH and NG distribution networks.
5	Buildings located outside DH and NG distribution networks and outside municipalities with quality plans.

3 RESULTS

The aim of the analysis was to identify energy saving potential by replacement of existing biomass and oil boilers with new, more efficient ones, and CO_2 abatement by replacing fuel oil boilers with biomass boilers in Slovenian households.

Based on the existing data (chapter 2.1), Weibull distribution curve (Figure 3, left) for boiler replacement was defined and used for modelling the boiler replacement rate for each year in the observed period 2015 – 2030. The analysis showed that in the period 2011-2017 Eco fund has granted subsidies to 1883 investments per year in average.

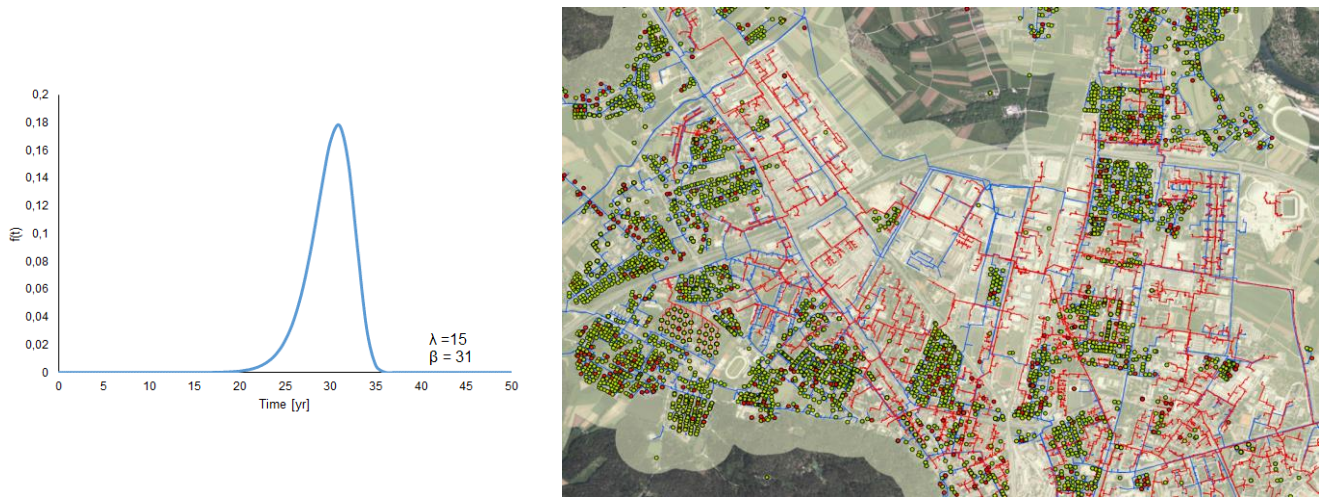

Figure 3 Probability density function of biomass boiler replacement (left) and observed boilers in part of Ljubljana, with highlighted 250 m buffer zone (right)

The modelled final energy consumption in households for space heating was 18 240 TJ (Table 2), while actual in the period 2009 – 2016 was on average 17 915 TJ (SURS, 2018). The biggest potential for additional savings was found in Group 1 (Table 1), which includes also the building that are very likely connected to the district heating or natural gas distribution network. This scenario is unrealistic, but it paints the image of possible saving outside municipalities with highly polluted air.

The analysis took into account spatial constraints and it was found out, that should DH and NG distribution network expand by 250 m (Figure 3, right), the potential in urban cities is minimal, since the replacement of old boilers would be dictated by local energy policy, either by Ordinances on air quality plans or priority use of energy sources for heating.

Group 5 presents the potential on rural areas and the model shows there is possible to achieve 12 % of energy savings by replacing old biomass boilers and 6 % by replacing old fuel boilers with new, more efficient biomass boilers.

Table 2 Results of energy modelling and spatial analysis

Original Energy Source	Savings	Unit	Baseline Energy Consumption	Group 1	Group 2	Group 3	Group 4	Group 5
Biomass	Energy	[TJ]	18 240	3 768	426	2.943	2 939	2 078
Fuel Oil	Energy	[TJ]	7 287	2 092	217	1 607	1 610	1 137
Biomass	PM2.5	[t]	1 696	350	40	274	273	193
Fuel Oil	PM2.5	[t]	678	195	20	149	150	106
Fuel Oil	CO_2	[kt]	536	154	16	118	119	84

From 2020 onwards the obligations of the Directive (EU) 2016/2284 applies and Slovenia has committed to reduce fine particulate matters for 60 % by 2030 and the analysis showed that saving on account of replacement of old biomass and fuel oil boilers can aggregate to 12.5 %. Furthermore, the replacement of oil fuel boilers with new, efficient ones lowers the carbon emissions reduction by 15 %.

4 CONCLUSIONS

The results indicate high relevance of biomass for the current and future position of the RES heating. For the further deployment of biomass heating, there are several aspects that should be considered. On one hand, the current market situation and policies support the further growth of biomass in the heat market. On the other hand, biomass potential for heating is already high in some European countries (e.g. Lithuania, Austria).

The presented paper focuses on the identification of the potential of boiler replacement only. Next steps of the research should include: (1) energy renovation of buildings on the level of thermal envelope, where energy need for heating is decreased and (2) presupposing the independence from irrelevant alternatives using multinomial logit model. Further on, the quality of data in existing data sources should be examined, due to possible inaccurate recordings. Further spatial planning analysis could identify plausible locations of biomass cogeneration plants instalment as well as DH with biomass, possibly for small towns.

Slovenia already has a high share of biomass boilers for heating, however, a large proportion of these are old. Old heating systems will be replaced by modern, more efficient heating systems. If biomass heating should grow in absolute terms, new systems have to overcompensate the replacement of old biomass boilers. Therefore, the growth within the biomass sector will be limited. The final energy consumption of biomass for heating might even decline, especially after 2020 with the introduction of nearly-zero energy buildings. These are defined as a highly energy buildings and require very low amount of energy, which should be

covered by a very significant extent by energy from RES. One of most important technologies that will achieve this is biomass boiler.

ACKNOWLEDGEMENTS

The work was carried out in the scope of LIFE ClimatePath2050 project coordinated by Jožef Stefan Institute – Energy Efficiency Centre (www.climatepath2050.com).

REFERENCES

Bilgen, S., Sarıkaya, İ., 2015. Exergy for environment, ecology and sustainable development. Renew. Sustain. Energy Rev. 51, 1115–1131. https://doi.org/10.1016/j.rser.2015.07.015

EC, 2016. European Commission. DIRECTIVE (EU) 2016/ 2284 OF THE EUROPEAN PARLIAMENT AND OF THE COUNCIL - of 14 December 2016 - on the reduction of national emissions of certain atmospheric pollutants, amending Directive 2003/ 35/ EC and repealing Directive 2001/ 81/ EC 2016, 31.

EC, 2009. European Commission. Decision No 406/2009/EC of the European Parliament and of the Council of 23 April 2009 on the effort of Member States to reduce their greenhouse gas emissions to meet the Community's greenhouse gas emission reduction commitments up to 2020 13.

Eco Fund, 2018. Annual Report on the Activities and Operations for Years 2009–2014, Ljubljana, Slovenia [WWW Document]. URL https://www.ekosklad.si/ (accessed 3.29.18).

GURS, 2018. . Geodetska Uprava Republike Slovenije, Geodetic Administration of the Republic of Slovenia. Register Nepremiˇcnin in Kataster Stavb. Register of Real Estates and Building Cadastre. [WWW Document]. URL http://prostor3.gov.si/javni/login.jsp?jezik=sl (accessed 3.29.18).

Loga, T., 2016. TABULA Building Typologies in 20 European countries − making energy-related features of residential building stocks comparable [WWW Document]. URL https://www.researchgate.net/publication/305077554_TABULA_Building_Typologies_in_20_European_countries_-_making_energy-related_features_of_residential_building_stocks_comparable (accessed 3.29.18).

MOL, 2016. Ordinance on the priority use of energy sources for heating in the area of the City of Ljubljana. Municipality of Ljubljana. [WWW Document]. URL https://www.uradni-list.si/glasilo-uradni-list-rs/vsebina/2016-01-1817/odlok-o-prioritetni-uporabi-energentov-za-ogrevanje-na-obmocju-mestne-obcine-ljubljana (accessed 3.29.18).

MOP, 2018. Database of Small Combustion Plants. Ministry for environment and spatial planning. [WWW Document]. URL http://www.mop.gov.si/ (accessed 3.29.18).

Scarlat, N., Dallemand, J.-F., 2011. Recent developments of biofuels/bioenergy sustainability certification: A global overview. Energy Policy 39, 1630–1646. https://doi.org/10.1016/j.enpol.2010.12.039

Steubing, B., Zah, R., Waeger, P., Ludwig, C., 2010. Bioenergy in Switzerland: Assessing the domestic sustainable biomass potential. Renew. Sustain. Energy Rev. 14, 2256–2265. https://doi.org/10.1016/j.rser.2010.03.036

SURS, 2018. Statistical Office of the Republic of Slovenia.

SURS, 2014. Survey on energy consumption and fuels in households. Statistical Office of the Republic of Slovenia. [WWW Document]. URL http://www.stat.si/StatWebArhiv/glavnanavigacija/oddajanje-podatkov/vpra%C5%A1alniki?id=5 (accessed 3.29.18).

GROWTH, BIOCHEMICAL AND METAL ACCUMULATION POTENTIAL OF BIOFUEL TREE SPECIES (*JATROPHA CURCAS* L AND *PONGAMIA PINNATA* L)

Rafia Abid[1, 2] Seema Mahmood[1] and Lena Q Ma[2]

1. Author's Affiliation, Institute of Pure and Applied Biology, Bahauddin Zakariya University, Multan-60800, Pk; email: profrafia@gmail.com, drseemapk@gmail.com
2. Author's Affiliation, Soil and Water Science Department, University of Florida, Gainesville, FL 32611, USA; email: lmqa@ufl.edu

ABSTRACT

The effluent from various industries is used for irrigation purposes in many agricultural countries to mitigate water scarcity and to save the cost of fertilizers. This poses considerable threats to the ecosystem when effluent containing several pollutants including heavy metals enters the environment and food chain. The present study aimed to assess the impact of effluent from a large fertilizer industry located in Multan, Pakistan on growth and development of *Jatropha curcas* L. and *Pongamia pinnata* L. popular biofuel tree species. An experiment was setup with Complete Randomized Design. One year old sapling were acclimatized and then wastewater was applied in a concentration of 20 and 40 ml L^{-1} while control plants were irrigated with tap water. The physico-chemical properties of the effluent revealed high values that is 179 mg L^{-1} and 257 mg L^{-1}, for biological oxygen demand (BOD) and chemical oxygen demand (COD), respectively. Similarly, exceeding values 1200 mg L^{-1} and, 274 mg L^{-1} were observed for total dissolved solid (TDS) and total suspended soil (TSS), respectively. Surprisingly, high concentrations of arsenic (15 µg L^{-1}) and Cd (0.78 mg L^{-1}) were also found. The levels applied caused a significant ($P \leq 0.05$) increase in plant growth and biomass. The plants showed greater collar diameter, number of leaves, and leaf area for both biofuel tree species at the elevated effluent treatment. The extent of membrane damage assessed via malondialdehyde (MDA) production was also greater in both roots and shoots. Photosynthetic pigments and carotenoids showed significant ($P \leq 0.05$) reduction in both species. Although the two species adopted different strategy for bioaccumulation of metals (As, Cd and Cr) in their roots and shoots through which the species have shown their growth potential in the presence of toxic pollutants contained in the effluent. The study signified the exploitation and efficient reuse of wastewater for plantation of the species with considerable survival potential for contaminated water.

Key words: biofuel tree species, photosynthetic pigments, lipid peroxidation and heavy metals.

INTRODUCTION

Water is most valuable resource on the planet earth. The changing pattern of rainfall and climate intensified water scarcity in many regions of the world. Like many other heavily populated countries of the world, Pakistan is also facing the challenge of water scarcity for crop production for exploding population of the country. Pakistan is declared as the most water scarced country of the world [1]. Thus, water shortage emerged as a limiting factor to endure water demand for agriculture and industrial sector. Water scarcity and high cost of fertilizer resulted in the use of industrial wastewater for agriculture and becomes a common practice for alleviating water shortage and the cost of chemical fertilizers. Despite this practise, the importance of chemical fertilizers cannot be eliminated in an agricultural country like Pakistan, about as 70% of the population is dependent on agricultural means of employment [2].

Pak Arab Fertilizer Industry, Multan (30°10'3.224"N, 71°29'31.762"E) is one of the major industry of the country. Industrial units produce important primary fertilizers such as nitrogen (N), phosphorus (P) and potassium (K) which are used for crop production. Besides production of fertilizers, the factory is a major contributor of various types of pollutants thereby discharging effluents with high biological oxygen demand (BOD), chemical oxygen demand (COD), total dissolved solid (TDS), total suspended solid (TSS) and heavy metals resulting in soil and water pollution [3].

Among heavy metals, Arsenic (As), Cadmium (Cd) and Chromium (Cr) are of serious concerns for soil and water pollution in Pakistan. In the Tehsil Mailsi, Punjab (29°48'1"N, 72°10'33"E), As concentration ranged from 12-488 (µgL^{-1}) in underground water thus drinking water contain more As than WHO permissible limit (10 µgL^{-1}) [4]. Similarly, in residential areas of Kasur, (31°06'6.02"N, 74°26'48.01"E), Cr concentration is about 9.80 mg L^{-1} which is far greater than permissible limit (0.05 mg L^{-1}) recommended by WHO [5]. Cr

(0.04 mg L^{-1}) in Charsadda (34° 8' 7.988" N, 71° 44' 34.0188" E) and Cd (0.003mg L^{-1}) in Risalpur (34°4' 4.4184"N and 71°9'34.0188"E) residential areas of the Province Khyber Pakhtunkhwa, have also been reported above safe limit [5]. Furthermore, metals remain persistent and are non-biodegradable causing phytotoxicity and hazardous health issues when enter in food chain [6]. Phytotoxicity results in chlorosis and necrosis thus stunted plant growth and development. Inhibitory functions involve cellular mechanism, photosynthesis, electron transport chain, metabolic activities and water uptake. Damage to biological membranes, biomolecules and oxidative stress are other common responses [7]. Malondialdehyde (MDA) is a lipid peroxidation or decomposition product and its amount directly correlate with the extent of membrane destruction. Nevertheless, both enzymatic and non-enzymatic antioxidantive system of plant become active and reduced oxidative stress generated by the production of free radicals [8].

During the past two decades, phytoremediation has been considered as a cost effective and environment friendly technique for removal of heavy metals from environment. The choice of plant species for remediation purpose is of prime significance as different species exhibit differential potential for metal tolerance. Some woody species are of great prospective for phytoremediation due to their high growth rate, deep root systems, high biomass and capacity to accumulate metals [8]. Although extensive work has been carried out to explore the potential of plants regarding As, Cd and Cr contamination but a little effort has been done so far to discover the responses of long lived biofuel tree species. Keeping in view the contamination of soils with As, Cd and Cr and significance of biofuel producing tree species in Pakistan we selected. *J. curcas* L. and *P. pinnata* L. as experimental material because of their high biomass production potential. Thus, the aim of present study is to assess the growth, biochemical responses of these valuable biofuel tree species and pattern of metal accumulation in their tissues when grown in soil irrigated with effluent from a fertilizer industry that contain substantial amount of As, Cd and Cr.

3. MATERIALS AND METHODS

3.1. Sample collection and Experiment Design

Effluent (35 litres) was collected from Pak-Arab Fertilizer Industry (Pvt) Ltd., Multan, Pakistan during peak working hours. The effluents is drained into main canal through water courses and drainage system without any treatment. Prior to growth experiment, the effluent was analysed for its physico-chemical properties following APHA [9]. During March 2016, one-year old saplings of *J. curcas* and *P. pinnata* from a local nursery were transplanted into each of 18 plastic pots (h x d 25 x 22 cm) filled with 6 kg of a sandy loam soil. The growth experiment with three replicates in a Complete Randomized Design was placed in a greenhouse with 28±^{o}C, 12 h day time, and 38% relative humidity. The species were grown under the treatments (20 and 40 ml L^{-1}), of effluent along with control (tap water). After acclimatization for 8 weeks, the pots were irrigated with 2 litres of effluent from June 2016 to April 2017 after every 3 months to field capacity. Water loss was compensated by gentle sprinkling of tap water as and when required. After 12 months plant were harvested and soil samples were collected from rhizospheric zone and were analysed by methods [10]. As, Cd and Cr concentration in soil and effluent was determined by method of Hseu [11] and APHA [9].Wet double acid digestion for soil and plants carried out with 3:1 HNO_3:$HClO_4$ (v/v) 100°C by using Microwave Digestion System (MDS 2000, Canada). Total As, Cd and Cr concentration in plant tissues were determined with Inductively Coupled Plasma-Optical Emission Spectroscopy (ICP-OES) Agilent 200 series, AA system California, USA.

3.2. Morphological, biochemical parameters and

Impact of effluent on plant growth, root and shoot lengths, dry root and shoot biomass, leaf area, number of leaves per plant and collar diameter were measured. A standard protocol was used for each parameter for consistent measurements. Further, to assess the impact of effluent on plants, biochemical parameters such as, chlorophyll a (Chl a), Chlorophyll b (Chl b), total chlorophyll (Chl t) and total carotenoids (Cx+c) were determined as described by Lichtenthaler [12].

3.3. Estimation of lipid peroxidation levels in plant tissue

Lipid peroxidation and membrane damage was determined in terms of MDA concentrations in roots and shoots of plants by following the method of de Oliveria et al [13].

3.3. Statistical analysis

Data presented as means of three replicates (±S.E) for each parameter were subjected to one way analysis of variance (One Way ANOVA) to elucidate significant effect of effluent on biofuel tree species independently.

Mean values were compared separately by using a post-hoc Turkey's HSD test. The level of significance for all tests were used P≤0.05 by using statistical software (SAS Version 13.1 Inc., Cary, NC, USA).

4. RESULTS AND DISCUSSION

4.1. Physico-chemical properties of effluent

Physico-chemical analysis of effluent revealed high Electrical Conductivity (EC), BOD, COD, TDS, TSS, As and Cd than permissible limit according to World Health Organization (WHO) for irrigation water (Table 1). The BOD, COD, TDS, TSS and heavy metals (As and Cd) were taken based on their exceeding amount to define widely used predictors or water quality parameters.The valid precedent for wastewater analysis also existed [9].

Table 1. Physico-chemical properties of effluent collected from Fertilizer Industry, Multan Pakistan.

Water parameters	Values	Permissible limit(WHO)	Heavy metals (mg L^{-1})	Values	Permissible Limit (WHO)
Color	Light yellowish	Colourless	Na	129	200
pH	7.6	6.5 to 8.5	Cl	14	250
Temperature (°C)	30	<30°C	N	176	2.5
EC (mS/cm)	1324	400	K	5.5	12
BOD (mg L^{-1})	179	80	P	0.97	0.05
COD (mg L^{-1})	257	10	As (µgL^{-1})	15	10 (µgL^{-1})
TDS (mg L^{-1})	1200	1000	Cd	0.78	0.003
DO (mg L^{-1})	2.6	4-7	Cr	0.04	0.05
TSS (mg L^{-1})	274	150	Hg	BDL	
Sulphate (mg L^{-1})	240	500	Pb	BDL	

4.2. Changes in physico-chemical properties of soil

The changes in soil properties after the application of effluent are given in (Table 2). Soil pH found to be alkaline and ranged from 8.4-9.4.This increase in soil pH is due to presence of various salts present in the effluent. An increase in soil organic matter content can also be attributed to increase in soil pH [3]. High nitrogen level in effluent (176 mg L^{-1}) can cause changes physical properties of soil. Soil organic matter is of particular interest for studies carried out for heavy metals sorption in soil as it affects the mobility of heavy metals by forming insoluble and soluble organic complex [14].

Table 2. Changes in soil properties and metal concentration (As, Cd and Cr) under varying levels of effluent from a fertilizer industry.

Soil Parameters	*J.curcas*			*P.pinnata*		
	T0	T1	T2	T0	T1	T2
pH	7.5 ± 0.09^{a}	8.9 ± 0.09^{b}	9.2 ± 0.07^{c}	7.0 ± 0.06^{a}	8.4 ± 0.06^{a}	9.4 ± 0.12^{b}
EC (mS/cm)	2.70 ± 0.04^{a}	3.13 ± 0.08^{b}	5.21 ± 0.07^{c}	1.73 ± 0.01^{a}	3.14 ± 0.03^{b}	4.90 ± 0.1^{c}
Total N (%)	0.29 ± 0.0^{a}	$9.7\pm0.02_{b}$	8.9 ± 0.01^{c}	0.94 ± 0.03^{a}	9.6 ± 0.02^{b}	10.1 ± 0.03^{b}
Available K(mg kg^{-1})	100 ± 4.04^{a}	260 ± 7.2^{b}	140 ± 6.00^{c}	120 ± 3.02^{a}	120 ± 5.57^{a}	$140\pm5.57.7^{b}$
Available P(mg kg^{-1})	0.26 ± 0.01^{a}	2.73 ± 0.09^{b}	0.14 ± 0.02^{c}	0.96 ± 0.02^{a}	0.16 ± 0.02^{b}	0.20 ± 0.02^{b}
As (mg kg^{-1})	1.20 ± 0.01^{a}	13.90 ± 0.01^{b}	13.80 ± 0.01^{b}	14.40 ± 0.01^{a}	13.80 ± 0.01^{b}	13.60 ± 0.01^{b}
Cd (mg kg^{-1})	0.66 ± 0.01^{a}	1.25 ± 0.01^{b}	0.85 ± 0.01^{ac}	0.94 ± 0.01^{a}	0.81 ± 0.01^{a}	1.03 ± 0.02^{b}
Cr (mg kg^{-1})	0.88 ± 0.01^{a}	0.92 ± 0.02^{b}	0.84 ± 0.01^{a}	0.63 ± 0.01^{a}	0.72 ± 0.02^{b}	0.79 ± 0.01^{b}

Control (T0), 20 ml L^{-1} (T1) and 40 ml L^{-1} (T2).Values are expressed as mean±S.E with n=3. Different letters at the top of each column depict significant variation between effluent levels at P≤0.05 using Turkey's HSD test.

A significant increase in soil EC 14-48% for *J.curcas* was noticed at 20 and 40 ml L^{-1} effluent, respectively. For *P.pinnata* 45-65% increase in soil EC was observed at respective levels of effluent. High values of soil EC is owing to high cations concentration including Na and NPK and it in turns also increase the soil NPK. Our results depicted that available phosphorus, potassium and total nitrogen (%) in soil increased when 20 and 40 ml L^{-1} effluent was applied.

4.3. Changes in morphological and biochemical parameters in *J.curcas* and *P.pinnata*

Figure 1 A&B showed that both biofuel tree species exhibited significant (P≤0.05) increase in root length, shoot length, collar diameter, root and shoot biomass, number of leaves and leaf area at 20 ml L^{-1}. Although,

J.curcas exhibited increase (18%) in shoot biomass while *P.pinnata* showed 58% increase in root biomass at 20 ml L^{-1} level than their respective control. Both species sustained growth at elevated level (40 ml L^{-1}) of effluent but *J. curcas* exhibited significant increase for dry biomass and collar diameter than control. At 40 ml L^{-1}, leaf area expanded by 24 and 25% in *J.curcas* and *P.pinnata*, respectively than control. *P.pinnata* had 11% more leaf area than *J.curcas.* Enhanced growth, biomass production and greater leaf area indicated the better performance of the species under effluent that contained many essential macro-and micronutrients included NPK. Nitrogen being important component of proteins, cellular material and production of chlorophyll including DNA, RNA and principal growth stimulating nutrient that has widely been reported for its beneficial impacts for health and vigor of the plant including leaf growth, leaf area and photosynthetic rate per unit leaf area [15]. Similarly phosphorus and potassium also influence positively because of the pivotal role of these elements on metabolic activities of the plants. The positive impact of NPK is also well documented for *J.curcas* and *P.pinnata* where fertilization induced greater production potential in terms of biomass in the species [3, 15]. Although, no significant reduction in chlorophyll b was found in *J.curcas* at more diluted level of the effluent but elevated concentration caused a profound reduction in chlorophyll a, chlorophyll b, total chlorophyll and total carotenoid in both species (Figure 2 C&D).This might be due to various salts and heavy metals present in the effluent as heavy metals substitute the Mg^{2+} in the chlorophyll molecules, decrease the activity of –SH group of enzymes forming heavy metals chlorophyll complexes thus decrease biosynthesis of chlorophyll and other pigments in plants. In addition, an early senescence with chlorophyll degradation owing to metal stress may be another reason for decline in photosynthetic pigments [16]. Nevertheless, the robust nature of these cytoplasmic organelles and modifications such as orientation of the chloroplast make them more efficient photosynthetically.

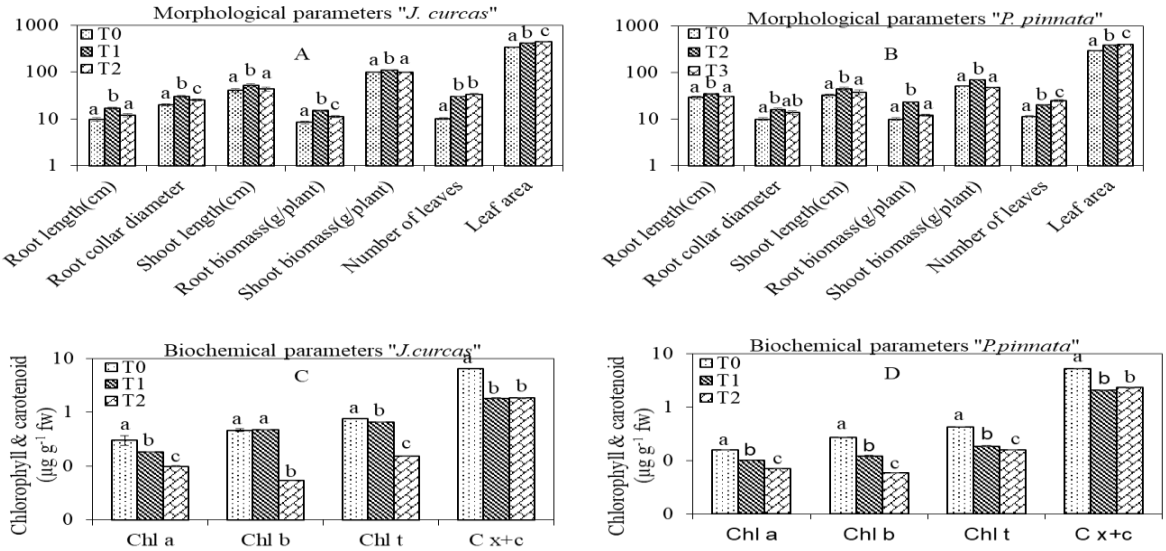

Figure 1. Morphological parameters (A& B), biochemical parameters (C&D) of *J.curcas* and *P.pinnata*, irrigated with effluent levels; control (T0), 20 ml L^{-1} (T1) and 40 ml L^{-1} (T2). Data presents mean± standard error. Different letters at the top of each column depict significant variation between effluent levels at $P \leq 0.05$ using Turkey's HSD test. Root collar diameter & leaf area were measured in (cm^2).

Table 3 depicted an increase in MDA by 73 and 60% in roots whereas 70 and 86% in shoots of *J.curcas* and *P.pinnata* correspondingly, at 40 ml L^{-1} level than control plants that signified oxidative stress [17].

4.4. Metal accumulation potential of *J.curcas* and *P.pinnata*

The concentration of As, Cd and Cr were determined in plant parts after effluent applications (Table 3) indicated ability of plants to translocate metals from root to shoot that is translocation factor (TF) (data not shown). A significantly higher ($P \leq 0.05$) As concentration in shoot than root in both species was observed consistently. These results are in agreement to Kumar et al [8] who reported more As concentration in shoot than root in *P.pinnata.* Arsenic is taken up in plant roots by phosphate transporter and translocated to xylem loading thus greater accumulation in shoots. *J. curcas* significantly accumulated more Cd and Cr in shoots than roots. Moreover, *P.pinnata* showed more Cd accumulation in shoots than roots at both effluent level. Our findings are parallel to Bernabé-Antonio et al [17] who reported more Pb and Cr in *J.curcas* shoot than

root. Although, *P.pinnata* exhibited differential response for Cr where roots accumulated more metal than shoots that can be ascribed to Cr immobilization in underground tissues as described by de Oliveria et al [13] *J.curcas* exhibited similar pattern of translocation for As, Cd and Cr from roots to shoots thereby suggesting phytoextration potential of the species. It is highly likely that the species acquired an active mechanism for the translocation of all three metals for their transport. Presumably, for As and Cr, sulphate, phosphate and iron served as common transporters [18]. However, Cd being non-essential element but owing to its greater bioavailability than As and Cr it uses Zn/Fe regulator-like protein (ZIP) [19] for its translocation. *P.pinnata* accumulated more As and Cd in shoots than Cr. This differential transport of metal ions to shoots may signify the variability of the state of the metal which profoundly influence either accumulation in roots or further translocation to shoots. These observations are in agreement to other workers [14, 18]. They clearly demonstrated it for Cr VI and Cr III, the former being with more mobilization than the later. Furthermore, various industrial effluents are well reported for the presence of Cr III [20]. *P.pinnata* appeared to be a metal tolerant species though phytostabilzation for Cr and metal extractor for As and Cd. Since the species are non-edible and potential biofuel trees and have shown differential metal accumulation strategy thus can be a choice for As, Cd and Cr contaminated soils or in situation where irrigation water contain these metals. Conclusively, both species have phytoremediation potential which is either acquired through phytostabilzation or phytoextraction thus as valuable future biofuel energy plants.

Table 3. Metal concentration and MDA contents in *J.curcas* and *P.pinnata* in plant tissue under varying levels of effluent from a fertilizer industry.

J.curcas

	As (mg kg^{-1} dw)		Cd (mg kg^{-1} dw)		Cr (mg kg^{-1} dw)		MDA content (µmol kg^{-1}fw)	
Treatment (ml L^{-1})	Root	Shoot	Root	Shoot	Root	Shoot	Root	Shoot
T0	3.00 ± 0.21^{a}	3.41 ± 0.04^{a}	1.0 ± 0.01^{a}	2.35 ± 0.02^{a}	1.16 ± 0.04^{a}	1.00 ± 0.01^{a}	1.04 ± 0.01^{a}	1.5 ± 0.12^{ab}
T1	4.92 ± 0.2^{b}	8.90 ± 0.02^{b}	3.03 ± 0.31^{b}	5.96 ± 0.00^{b}	1.32 ± 0.01^{b}	1.85 ± 0.03^{b}	1.40 ± 0.12^{b}	3.0 ± 0.18^{b}
T2	6.10 ± 0.06^{c}	8.48 ± 0.01^{c}	4.81 ± 0.04^{c}	7.07 ± 0.01^{c}	1.22 ± 0.01^{b}	1.69 ± 0.01^{c}	3.90 ± 0.03^{c}	5.01 ± 0.02^{b}

P.pinnata

	As (mg kg^{-1} dw)		Cd (mg kg^{-1} dw)		Cr (mg kg^{-1} dw)		MDA content (µmol kg^{-1}fw)	
Treatment (ml L^{-1})	Root	Shoot	Root	Shoot	Root	Shoot	Root	Shoot
T0	3.13 ± 0.19^{a}	3.22 ± 0.1^{a}	1.02 ± 0.04^{a}	1.89 ± 0.01^{a}	1.0 ± 0.021^{a}	0.87 ± 0.04^{a}	2.0 ± 0.34^{ab}	1.02 ± 0.02^{a}
T1	4.60 ± 0.24^{b}	8.60 ± 0.02^{b}	1.36 ± 0.02^{b}	2.30 ± 0.01^{b}	1.42 ± 0.01^{a}	1.27 ± 0.03^{b}	3.0 ± 0.34^{b}	5.02 ± 0.01^{b}
T2	4.20 ± 0.21^{b}	8.18 ± 0.03^{c}	2.47 ± 0.03^{c}	2.77 ± 0.09^{c}	2.2 ± 0.33^{b}	1.7 ± 0.02^{c}	5.0 ± 0.90^{b}	7.10 ± 0.06^{c}

CONCLUSION

The effluent from industrial source loaded with different substances was applied to these two specices.The species have respondent in a different manner to the effluent application. Although, some adverse effect of effluent was noticed on chlorophyll and carotenoid at higher doses but the positive impact of the effluent was observed for the growth parameters studied. Nevertheless, the innate tolerance for the heavy metals and its potential for growth make the two species a potential candidate for phytoremediation through phytoextraction and phytostsblizstaion. The biofuel species can be grown either on metal contaminated soil subject to fertilizers application or for future phytoremediation programme by employing abundant and derelict land using the effluent from such industries as a source of irrigation.

ACKNOWLEDGEMENTS

The data presented in this manuscript is a part of Ph.D. research of the first author. The research grant awarded by Higher Education Commission, Islamabad, Pakistan is gratefully acknowledged.

REFERENCES

[1] M. Abid, J. Schilling, J. Scheffran and F. Zulfiqar. Climate change vulnerability, adaptation and risk perceptions at farm level in Punjab, Pakistan, *Science of the Total Environment*, Vol. 47, pp.447-460, 2016.

[2] M. S. Arif, M. Riaz, S. M. Shahzad, T. Yasmeen, M. Ashraf, M. Siddique, M. S. Mubarik, L. Bragazza and A. Buttler, Fresh and composted industrial sludge restore soil functions in surface soil of degraded agricultural land, *Science of The Total Environment*, Vol.619, pp.17-27, 2018.

[3] S. Manzoor, S. Mirza, M. Zubair, W. Nouman, S. Hussain, S. Mehmood, A. Irshad, N. Sarwar, R. Abid and M. Iqbal, Estimating genetic potential of biofuel forest hardwoods to withstand metal toxicity in industrial effluent under dry tropical conditions, *Genetics and Molecular Research*,Vol.14, pp. 943-94, 2015.
[4] A. Rasool, T. Xiao, A. Farooqi, M. Shafeeque, Y. Liu, M. A. Kamran, I. A. Katsoyiannis and S. A. M.A. S. Eqani, Quality of tube well water intended for irrigation and human consumption with special emphasis on arsenic contamination at the area of Punjab, Pakistan. *Environmental Geochemistry and Health*, Vol.39, pp. 847-863, 2017.
[5] A. Azizullah, M. N. K. Khattak, P. Richter and D.-P. Häder, Water pollution in Pakistan and its impact on public health-a review, *Environment International*, Vol.37, pp.479-497, 2011.
[6] F.C. Chang, C.-H. Ko, M.-J. Tsai, Y.-N. Wang and C.-Y. Chung, Phytoremediation of heavy metal contaminated soil by *Jatropha curcas* L., *Ecotoxicology*, Vol. 23,pp. 1969-1978, 2014.
[7] M. Balestri, A. Ceccarini, L. M. C. Forino, I. Zelko, M. Martinka, A. Lux and M. R. Castiglione, Cadmium uptake, localization and stress-induced morphogenic response in the fern *Pteris vittata*, *Planta*, Vol. 239, pp.10-1064, 2014.
[8] D. Kumar, D. K. Tripathi, S. Liu, V. K. Singh, S. Sharma, N. K. Dubey, S. M. Prasad and D. K. Chauhan, *Pongamia pinnata* (L.) Pierre tree seedlings offer a model species for arsenic phytoremediation, *Plant Gene*, Vol.11, pp. 238-246, 2017.
[9] American Public Health Association. *Standard Methods for the Examination of Water & Wastewater*, 22nd Edition. Washington DC. APHA, 2012.
[10] United States Salinity Laboratory Staff. *Diagnosis and improvement of saline and alkali soils*, USDA Handbook 60, Washington, D.C.1954.
[11] Z.-Y. Hseu, Z.-S. Chen, C.-C. Tsai, C.-C. Tsui, S.-F. Cheng, C.-L. Liu and H.-T. Lin, Digestion methods for total heavy metals in sediments and soils, *Water, Air, and Soil Pollution*, Vol.141, pp. 189-205, 2002.
[12] H. K. Lichtenthaler. Chlorophylls and carotenoids: pigments of photosynthetic biomembranes, *Methods in enzymolo*gy, Vol.148, pp.30-382, 1987.
[13] L. M. de Oliveira, L. Q. Ma, J. A. Santos, L. R. Guilherme and J. T. Lessl. Effects of arsenate, chromate, and sulfate on arsenic and chromium uptake and translocation by arsenic hyperaccumulator *Pteris vittata* L, *Environmental pollution*, Vol.184, pp.187-192, 2014.
[14] M. Shahid, S. Shamshad, M. Rafiq, S. Khalid, I. Bibi, N. K. Niazi, C. Dumat and M. I. Rashid, Chromium speciation, bioavailability, uptake, toxicity and detoxification in soil-plant system: A review, *Chemosphere*, Vol.178, pp. 13-33, 2017.
[15] D. Kumar, D. K. Tripathi, S. Liu, V. K. Singh, S. Sharma, N. K. Dubey, S. M. Prasad and D. K. Chauhan. Irrigation Scheduling and Fertilization Improves Production Potential of Jatropha (*Jatropha curcas* L.): A Review, *International Journal of Current Microbiology and Applied Science*,Vol. 6, pp. 1703-1716, 2017.
[16] F. U. R. Shah, N. Ahmad, K. R. Masood, J. R. Peralta-Videa, D. M. Zahid and M. Zubair, Response of Eucalyptus camaldulensis to irrigation with the Hudiara drain effluent, *International journal of phytoremediation*, Vol.12, pp. 343-357, 2010.
[17] A. Bernabé-Antonio, L. Álvarez, L. Buendía-González, A. Maldonado-Magaña and F. Cruz-Sosa ,Accumulation and tolerance of Cr and Pb using a cell suspension culture system of *Jatropha curcas* L., *Plant Cell, Tissue and Organ Culture*, Vol. 120, pp.221-228, 2015.
[18] L. M. de Oliveira, J. Gress, J. De, B. Rathinasabapathi, G. Marchi, Y. Chen and L. Q. Ma, Sulfate and chromate increased each other's uptake and translocation in As-hyperaccumulator *Pteris vittata* L., *Chemosphere*,Vol. 147, pp.36-43, 2016.
[19] A. Zare, A. Khoshgoftarmanesh, M. Malakouti, H. Bahrami and R. Chaney, Root uptake and shoot accumulation of cadmium by lettuce at various Cd: Zn ratios in nutrient solution, *Ecotoxicology and environmental safety*, Vol, 148. pp.441-446, 2018.
[20] M. Afzal, G. Shabir, S. Iqbal, T. Mustafa, Q. M. Khan and Z. M. Khalid, Assessment of heavy metal contamination in soil and groundwater at leather industrial area of Kasur, Pakistan, *CLEAN–Soil, Air, Water*, Vol. 8, pp.1133-1139, 2014.

PREPARATION AND CHARACTERIZATION OF ANIMAL BONE POWDER IMPREGNATED FLY ASH CATALYST FOR TRANSESTERIFICATION

Vikranth Volli [*1,2], Mihir Kumar Purkait[2], and Chi-Min Shu[1]

1. Department of Safety, Health, and Environmental Engineering, National Yunlin University of Science and Technology (YunTech), Yunlin 64002, Taiwan, ROC.
2. Department of Chemical Engineering, Indian Institute of Technology Guwahati, India. 781039

ABSTRACT

In the present study, the utilization of class F fly ash, and calcined animal bone powder (CABP) as a raw material for the synthesis of heterogeneous solid base catalyst with varying ratios of CABP (10, 20, and 30 mass%), and their subsequent utilization in transesterification of mustard oil was presented. Physico–chemical characterization of CABP revealed a crystalline behavior signifying one of the components as hydroxyapatite (HAP); when calcined at 900 ºC transforms to β–tricalcium phosphate having a specific surface area of 100 m^2g^{-1}. The synthesized catalyst showed improved catalytic activity when compared to the parental species, and the optimal value to achieve the highest conversion of 90.4% would be at CABP loading of 10 mass%, 5.5:1 methanol/oil molar ratio, and 10 mass% catalyst concentration for 6 h. The experimental results exemplify that the impregnation of calcium enriched domestic waste in fly ash might yield a promising, and novel low cost heterogeneous catalyst for biodiesel production.

***Keywords*:** Fly ash, Animal bone powder, Heterogeneous base catalyst, Transesterification, Biodiesel.

1 INTRODUCTION

Heterogeneous catalyzed transesterification of triglycerides has become a promising approach in biodiesel production over the years because of their easier separation, and better recycling characteristics over conventional homogeneous catalyst which generates large quantities of wastewater during catalyst separation [1]. Considerable attention was focused on utilizing oxides of waste calcium from coral fragments [2], waste shells of egg [3], animal bone powder [4], mud crab, and cockle shells [5,6]. Obadiah et al. [7] reported the use of 20 mass% calcined waste animal bones as catalyst in biodiesel production from palm oil. Calcined bovine bone at 750 ºC with 8 mass% catalyst loading yielded 97% of methyl ester from soybean oil for a reaction time of 3 h at 65 ºC [8]. Waste egg shell derived CaO supported W-Mo mixed oxide catalyst was used for biodiesel production from waste cooking oil. The highest biodiesel yield of 96.2% was obtained with 15:1 methanol to oil molar ratio, 2 mass% catalyst loading, and 2 h reaction time [9].

The use of coal fly ash as a catalyst support, and efficient methodologies to exploit its mineralogy by chemical modification could result in the development of novel heterogeneous catalyst, and help subsiding pollution as well [10]. Jain et al. [11] reported the activity of a solid base catalyst synthesized using fly ash chemically activated with NaOH on condensation reaction of cyclohexanone, and benzaldehyde. For a reaction time of 8 h at 65 ºC, when fly ash based zeolites was used as catalyst in transesterification of sunflower oil, a methyl ester yield of 83.53% was obtained at methanol/oil ratio 6:1, catalyst – 3 mass% of oil [12]. A maximum conversion of 87.5% was achieved at 170 ºC when KNO_3 (5 mass%) loaded fly ash was used as catalyst for biodiesel production from sunflower oil. With increase in the methanol to oil molar ratio from 6:1 to 15:1, at 15 mass% catalyst concentration a significant increase in conversion from 52.2 to 86.1% was observed [13,14]. Oxides developed from waste egg, and mollusc shells when impregnated in fly ash resulted a biodiesel yields of 92–96% at 1 to 6 mass% catalyst concentration from soybean, and palm oil, respectively. [15,16].

From the above literature, it was clear that studies describing the use of modified fly ash as a support in developing heterogeneous catalyst from domestic waste were scant. Moreover, only a few studies were focused on synthesis of solid base catalyst by impregnation of waste animal bone powder in fly ash, and its application in biodiesel production from mustard oil. In light of the above, synthesis of a low cost, and highly effective heterogeneous solid base catalyst from fly ash, and a natural source of calcium (bone powder) was the main objective of the present research. Different catalysts were synthesized by varying calcined animal bone powder loading (10, 20, and 30 mass%) in fly ash, and its activity was studied for biodiesel production.

2. Experimental

2.1. Materials

Waste animal bone (sheep) was obtained from slaughter house near IIT Guwahati, India. Fly ash was obtained from M/s SARACA Laboratories Limited, Andhra Pradesh, India. Refined mustard oil (RMO), and methanol (commercial grade with 99.5% purity) was procured from local vendors in India.

2.2. Catalyst preparation

Fly ash used in the present study was milled, and dried overnight. The adherent tissue, and fat of animal bones was remove by boiling for 4 h using deionized water, and then calcined at 900 ^{o}C for 2 h. Conventional wet impregnation method was used to prepare fly ash–supported CABP catalyst. To prepare 20 mass% of CABP loaded catalyst, 6 g of CABP was added to 200 mL of water and this solution was then added to 24 g of pre–dried fly ash, and mixed vigorously under reflux for 4 h. The temperature was maintained at 70 ^{o}C with pH 12.1. The solution was aged for 24 h; filtered, dried, and calcined at 900 ^{o}C for 2 h.

2.3. Catalytic activity

The transesterification was performed at 65 ^{o}C in a 500 mL three–neck round bottom flask with methanol (alcohol/oil) molar ratio varying from 3:1 to 12:1. The product mixture was then centrifuged at 6000 rpm to separate ester phase from catalyst, and glycerol. A rotary evaporator was used to separate unreacted methanol and water content. The conversion of fatty acid methyl ester (% FAME) was estimated using the procedure described by Obadiah et al. [7]

Table 1. Elemental composition of CABP, C30, C20, and C10 fly ash based catalyst.

Characteristic	CABP (mass%)	Catalyst (mass%)		
		C30	C20	C10
O	47.15	16.2	22.3	28.3
Al	0.21	10.1	10.9	11.4
Si	0.39	42.4	41.4	42.3
Ca	29.79	21.3	17.2	11.5
Mg	0.48	1.5	1	0.9
Fe	NA	1.4	1.3	1.5
P	9.2	6.5	5.2	3.1
K	5.22	0.4	0.5	0.7
Na	NA	0.2	0.2	0.3

NA: Not applicable

2.4. Characterization

A SIMADZU Corp Fourier transform infrared spectroscopy (FTIR) was used to measure the FTIR spectra. The ultimate analysis was performed using elemental CHNS analyzer according to ASTM D5291-96. A LEO (LEO-1430 VP) scanning electron microscope equipped with a 6587 EDX scanning spectrometry detector was used to explore the surface morphology. A Perkin Elmer AAnalyst 200 Atomic adsorption spectroscopy (AAS) was used to determine the metal concentration. Bruker D Advance X-ray diffraction (XRD) system was used to detect the overall crystalline phases in the samples. X-ray fluorescence (XRF) analysis was performed using Philips PW 2404. ^{1}H-NMR spectra were obtained at 400 MHz in Varian DRX – 400 spectrometer using DMSO D6 as the solvent.

3. Results and discussion

3.1 Characterization of fly ash, and fly ash based catalyst

The bulk chemical composition of fly ash (mass%) was silica (56.6), alumina (23.2), ferrous oxide (5.8), and calcium oxide (7.9) along with minor quantities of MgO (1.5), K_2O (1.4), TiO_2 (1.3), SO_3 (0.5), P_2O_5 (0.3), Na_2O (0.2), SrO (0.06), and MnO (0.05) by mass% with loss on ignition (LOI) ≤ 1%. The presence of trace

elements was also observed with composition of chromium, nickel, arsenic, and zinc as 0.001, 0.002, 0.002, and 0.07 ppm, respectively. The presence of C, H, N, S, and O from ultimate analysis was 62.6, 1.24, 10.32, 2.72, and 23.05 mass%, respectively. Based on its chemical composition, fly ash used in the present study was of class 'F' [8]. The elemental composition of CABP, C10, C20, and C30 was shown in Table 1. A clear increase in the concentration of Ca, P, and Mg was observed when fly ash was loaded with 10, 20, and 30 mass% of CABP. Similar results were demonstrated reporting an increase in calcium content from 21.11 to 26.88 mass% when CaO-CeO_2 loading was increased from 20 to 40 mass% in synthesizing CaO–CeO_2/HAP catalyst [16].

The FTIR spectra of fly ash as shown in Figure 1(A) represents asymmetric stretching vibrations of Al, Si at 1053 cm^{-1}. Sharp peaks of weak aliphatic potassium bonds appeared at 1380–1400 cm^{-1} [17]. The characteristic peaks of hydroxyapatite, β–tricalcium phosphate, and calcium oxide were present in CABP with asymmetric P–O stretching vibrations at around 1047 to 1095 cm^{-1}. The Ca–O bending vibrations were observed at 500 – 580 cm^{-1}, and vibrations of O–P–O in calcium phosphate was observed at 632 cm^{-1} [18]. The synthesized catalyst had both the characteristic peaks of the parental species, and the appearance of band at 570 to 632 cm^{-1} with increase in CABP loading confirms the effective impregnation of CABP in fly ash.

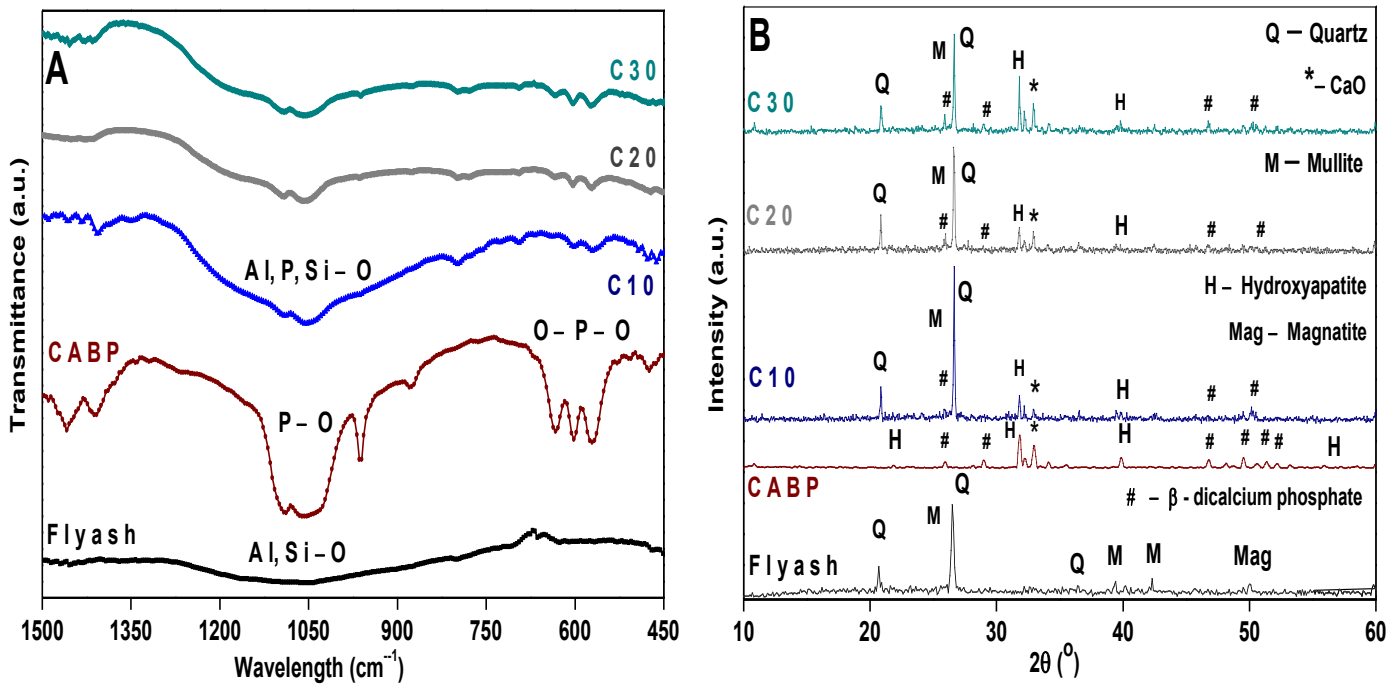

Figure 1. Spectra for (A) FTIR, and (B) XRD of fly ash, CABP, C10, C20, and C30 catalyst.

The powder XRD patterns, and mineral composition of fly ash, CABP, and fly ash based catalyst (C10, C20, and C30) are presented in Figure 1(B). Predominant phases of quartz (SiO_2) (JCPDS 33–1161) with major peak of *h, k, l* values at 20.86 (100), 26.65 (100), 36.54 (110), and 50.14 (112), degrees 2θ, and less intense peaks of mullite (JCPDS 15–776) at 39.4 (201) degrees 2θ, and magnetite were observed. The CABP rrepresents prominent 2h peaks at 21.8 (200), 31.8 (211), 32.2 (112), 32.9 (300), 40.4 (221), 51.3 (140), 52.1 (402), 60.5 (331) degrees of 2θ confirming the formation of hydroxyapatite (JCPDS 9–432), along with peaks of β–tri calcium phosphate (JCPDS 86-1585) at 25.8 (002), 28.9 (210), 46.8 (222), 48.1 (132), 48.7 (230), 49.5 (213), and 50.5 (321).The fly ash based catalysts (C10, C20, and C30) exhibited both the characteristic peaks of quartz, mullite, hydroxyapatite, and β–tri calcium phosphate as well. The presence of dicalcium silicate (Ca_2SiO_4), and CaO crystalline phase was also observed at 2θ = 31.4, and 32.2 (111), respectively.

The surface morphology of fly ash, CABP, and fly ash based catalysts was shown in Figure 2 (A–E). Fly ash (A) used in the present study were cenospheres, and CABP (B) were rod like crystalline particles. Heat treatment of fly ash based catalysts (C, D, and E) resulted in structure agglomeration due to the formation of metal oxide [19].

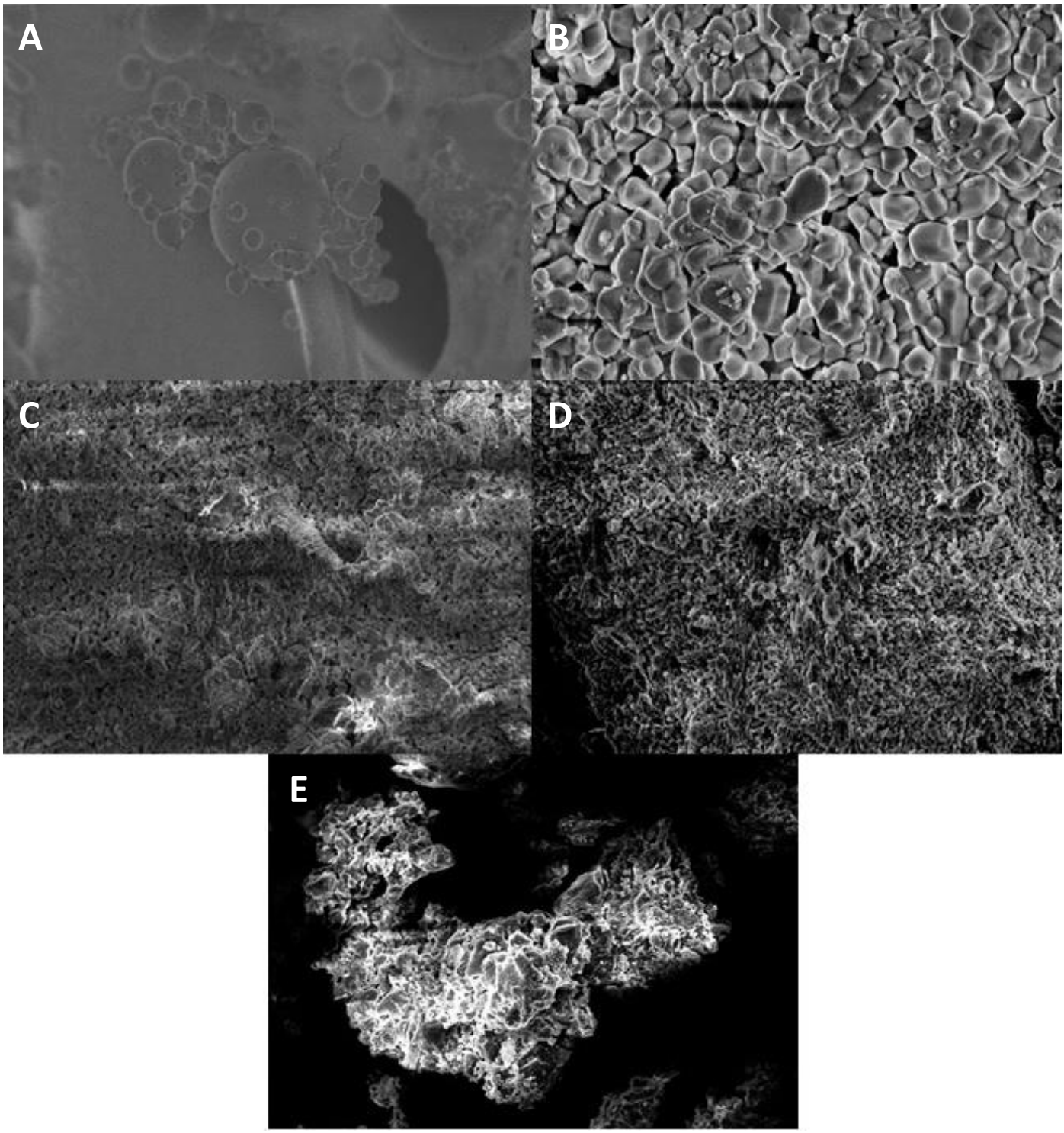

Figure 2. Surface morphology of (A) fly ash, (B) CABP, (C) C10, (D) C20, and (E) C30 catalyst.

3.2 Transesterification, and optimal process parameters

To estimate the reaction time, transesterification of mustard oil was performed in triplicate at 65 ^{o}C with methanol to oil molar ratio varying from 3:1 to 12:1 at 5 mass% catalyst concentration for 10 h. The maximum conversion achieved by using fly ash, and CABP was 7.3%, and 85.4%. The minimum time required for biodiesel production using C10, C20, and C30 catalyst was given in Figure 3(A). The catalyst C10, and C20 had almost same conversion and the biodiesel conversion increased gradually up to 6 h, and remained same thereafter.

Figure 3(B) shows the effect of methanol to oil molar ratio varying from 3:1 to 12:1 (3:1, 5.5:1, 7:1, 9:1, and 12:1) on biodiesel conversion for 6 h at 5 mass% catalyst concentration. The optimum methanol to

oil molar ratio was 5.5:1 and the order of conversion was C10 (86.4%), C20 (84.2%), and C30 (64.8%), respectively. With further increase in methanol: oil molar ratio, conversion decreased slightly

Transesterification was performed for 6 h at 65 ^{o}C to study the effect of catalyst concentration at an optimum methanol to oil molar ratio of 5.5: 1. From Figure 3(C), it was clear that with increase in catalyst concentration, conversion increased, and reached a maximum value at 10 mass% of oil. With further increase in catalyst concentration to 12, and 15 mass%, a slight decrease in conversion was observed. The order of conversion was 90.4% (C10), 87.2% (C20), and 79.7% (C30), respectively.

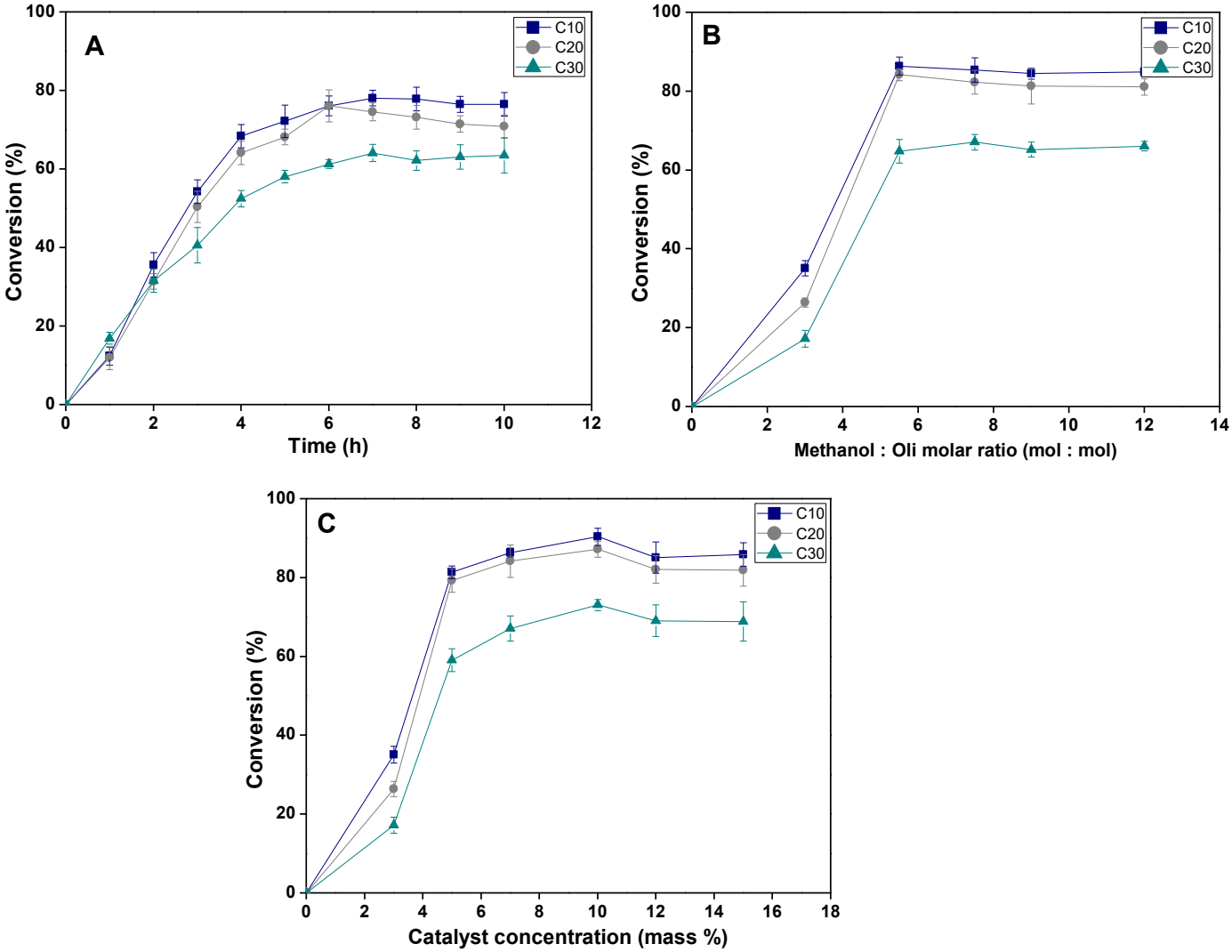

Figure 3. Effect of (A) time, (B) methanol: oil molar ratio, and (C) catalyst concentration on biodiesel conversion.

4. Conclusions

The synthesis, and characterization of fly ash supported calcined animal bone powder catalyst using conventional wet impregnation method was reported in this present research. Catalysts (C30, C20, and C10) with varying the concentrations of CABP was synthesized, and their activity was tested for biodiesel production from mustard oil. The optimal conditions were obtained at bone powder loading of 10 mass%, 5.5:1 methanol/oil molar ratio, and reaction time of 6 h would have biodiesel yield of 90.4%. Fly ash impregnated CABP catalyst proved to be a suitable candidate for transesterification.

Acknowledgement

This work is partially supported by a grant from the Fly Ash Unit, Department of Science and Technology (FAU-DST) New Delhi, India. Any opinions, findings and conclusions expressed in this paper are those of the authors and do not necessarily reflect the views of FAU-DST, New Delhi

References

[1] D.Y.C. Leung, X. Wu, and M.K.H. Leung, A review on biodiesel production using catalyzed transesterification, *Applied Energy*, Vol. 87, pp.1083–1095, 2010.

[2] W. Roschat, M. Kacha, B. Yoosuk, T. Sudyoadsuk, and V. Promarak, Biodiesel production based on heterogeneous process catalyzed by solid waste coral fragment, *Fuel*, Vol. 98, pp. 194–202, 2012.

[3] N. Viriya-empikul, P. Krasae, W. Nualpaeng, B. Yoosuk, and K. Faungnawakij, Biodiesel production over Ca-based solid catalysts derived from industrial wastes, *Fuel*, Vol. 92, pp. 239–244, 2012.

[4] S.M. Smith, C. Oopathum, V. Weeramongkhonlert, C.B. Smith, S. Chaveanghong, Pradudnet P. Ketwong, and S. Boonyuen, Transesterification of soybean oil using bovine bone waste as new catalyst. *Bioresource Technology*, Vol. 143, pp. 686–90, 2013.

[5] P.L. Boey, G.P. Maniam, and S.A. Hamid, Biodiesel production via transesterification of palm olein using waste mud crab (Scylla serrata) shell as a heterogeneous catalyst. *Bioresource Technology*, Vol. 100, pp. 6362–6368, 2009.

[6] S. Hu, Y. Wang, and H. Han, Utilization of waste freshwater mussel shell as an economic catalyst for biodiesel production, *Biomass Bioenergy*, Vol. 35, pp. 3627–3635, 2011.

[7] A. Obadiah, G.A. Swaroopa, S.V. Kumar, K.R. Jeganathan, and A. Ramasubbu, Biodiesel production from palm oil using calcined waste animal bone as catalyst, *Bioresource Technology*, Vol.116, pp. 512–516, 2012.

[8] S.M. Smith, C. Oopathum, V. Weeramongkhonlert, C.B. Smith, S. Chaveanghong, Pradudnet P. Ketwong, and S. Boonyuen, Transesterification of soybean oil using bovine bone waste as new catalyst. *Bioresource Technology*, Vol. 143, pp. 686–90, 2013.

[9] N. Mansir, S.H Teo, M.L Ibrahim, and T.Y. Hin, Synthesis and application of waste egg shell derived CaO supported W-Mo mixed oxide catalysts for FAME production from waste cooking oil: Effect of stoichiometry, *Energy Conversion and Management*, Vol. 151, pp. 216–226, 2017.

[10] R.S. Blissett, and N.A. Rowson, A review of the multi-component utilisation of coal fly ash, *Fuel*, Vol. 97, pp. 1–23, 2012.

[11] D. Jain, C. Khatri, and A. Rani, Synthesis and characterization of novel solid base catalyst from fly ash, *Fuel*, Vol. 90, pp. 2083–2088, 2011.

[12] O. Babajide, N. Musyoka, L. Petrik, and F. Ameer, Novel zeolite Na-X synthesized from fly ash as a heterogeneous catalyst in biodiesel production, *Catalysis Today*, Vol. 190, pp. 54–60, 2012.

[13] M.S. Kotwal, P.S. Niphadkar, S.S. Deshpande, V.V. Bokade, and P.N. Joshi, Transesterification of sunflower oil catalyzed by fly ash-based solid catalysts, *Fuel*, Vol. 88, pp. 1773–1778, 2009.

[14] O. Babajide, L. Petrik, N. Musyoka, B. Amigun, and F. Ameer, Use of coal fly ash as a catalyst in the production of biodiesel, *Petroleum and Coal*, Vol. 52, pp. 261–272, 2010.

[15] R. Chakraborty, S. Bepari, and A. Banerjee, Transesterification of soybean oil catalyzed by fly ash and egg shell derived solid catalysts, *Chemical Engineering Journal*, Vol. 165, pp. 798–805, 2010.

[16] B. Yan, Y. Zhang, G. Chen, R. Shan, W. Ma, and C. Liu, The utilization of hydroxyapatite-supported CaO-CeO2catalyst for biodiesel production, *Energy Conversion and Management*, Vol. 130, pp. 156–164, 2016.

[17] P.L. Boey, G.P. Maniam, S.A. Hamid, and D.M.H. Ali, Utilization of waste cockleshell (Anadaragranosa) in biodiesel production from palm olein: Optimization using response surface methodology, *Fuel*, Vol. 90, pp. 2353–2358, 2011.

[18] N. Zapata, M., Vargas, J.F., Reyes, and G. Belmar, Quality of biodiesel and press cake obtained from Euphorbia lathyris, Brassica napus and Ricinuscommunis. Industrial Crops *and* Products, Vol. 38, pp.1–5, 2012.

[19] H. Hadiyanto, S.P. Lestari, A Abdullah, W. Widayat, and H. Sutanto, The development of fly ash-supported CaO derived from mollusk shell of Anadara granosa and Paphia undulata as heterogeneous CaO catalyst in biodiesel synthesis, International *Journal of Renewable Energy* and *Environmental Engineering*, Vol. 7, pp. 297–305, 2016.

POTENTIAL AND CHALLENGES IN LIGNOCELLULOSIC BIOFUEL PRODUCTION TECHNOLOGY

M. Raud[1], T. Kikas[1], O. Sippula[2] N. Shurpali[2]

1. Estonian University of Life Sciences, Kreutzwaldi 1, 51014, Tartu, Estonia email: Merlin.raud@emu.ee
2. Department of Environmental and Biological Sciences, University of Eastern Finland, P.O. Box 1627, FI-70211 Kuopio, Finland

ABSTRACT

The EU renewable energy policy has been the driving force in biofuel research and development for wider use of biofuels since the Kyoto protocol. Owing to this, the utilization of biofuels and the scientific research to widen the scope of their commercialization are being increasingly promoted. We provide in this paper a short overview of different biofuels and their resources with a focus on the lignocellulosic biomass and biofuels derived from it. We also discuss and analyse here the technologies associated with the production of different biofuels. Many technologies that enable the production of different biofuels from lignocellulosic biomass are available. Bioethanol production using microbial fermentation, and production of synthetic fuels from syngas gained from pyrolysis of biomass are the most widely researched and promising technologies. Although the liquid biofuel production from lignocellulosic biomass promises a good bioethanol yield under laboratory scale, there are several challenges that exist and need to be tackled before the production process can be commercialized. In conclusion, we provide here an overview of the various possibilities and make recommendations for increasing biofuel production efficiency with a view to improving the overall yield and lowering the production costs.

Keywords: Lignocellulose, biofuel, biomass, bioethanol, thermochemical process

1 INTRODUCTION

Biomass and waste, as global energy sources, account for over 70% of all renewable energy production. Thus, their contribution to final energy consumption in 2015 was approximately on par with coal. Direct burning accounts for the largest end-use of biomass and waste [1]. However, various liquid biofuels can be produced from such feedstocks. The technologies for producing ethanol from sugar and starch-based feedstocks, and biodiesel from vegetable oils and other lipid feedstocks are well-established, and provide most of today's transport biofuels [2].

Since demand for biofuels has been increasing together with the demand for food, a lot of attention in recent years has been directed to the utilization of lignocellulosic biomass. Lignocellulosic materials are particularly attractive as feedstocks for biofuel production because of their relatively low cost, great abundance, and sustainable supply [3]. Traditional lignocellulosic feedstocks include mainly different energy crops and agricultural residues, which are widespread in all regions. Agricultural residues include a variety of agricultural wastes such as corn stover, cornstalks, rice and wheat straws as well as sugarcane bagasse. Additionally, dedicated energy crops are grown and harvested for energy use. In addition, forest residues, wood process wastes, and also industrial residues and urban greening waste can all be used as lignocellulosic feedstocks [4, 5]. The main advantage of the production of biofuels from such non-edible feedstocks is that it limits the direct food versus fuel competition associated with traditional biofuels.

Different liquid fuels can be made from lignocellulosic feedstock using either biochemical or thermochemical routes. However, in most cases, the processing technologies of these biofuels are currently immature and significant progress needs to be made in terms of perfecting the production process [6]. The most advanced out of these is lignocellulosic ethanol production, which has reached the early market development phase while the thermochemical technology is in demonstration stage and other biochemical routes are operational at the lab-scale yet [1]. The goal of this paper is to give an overview of current state-of-the-art in liquid biofuel production technologies from lignocellulosic biomass.

2 GOVERNMENT INITIATIVE

One of the earliest driving forces of European Union (EU) renewable energy policy was the adoption of Kyoto Protocol from 1998. The aim of the Kyoto Protocol was to reduce greenhouse gas emissions during 2008-2012

by 5%, compared to 1990. [7]. In order to achieve this target, the EU Member States set a goal to significantly increase the use of renewable energy sources in all fields including transportation [8] and a series of measures have been introduced to improve the development of energy from renewable sources.
Renewable Energy directive 2009/28/EC was approved in 2009, which sets targets for all EU countries to make renewable energy sources account for 20% of EU energy, 20% greenhouse gas (GHG) emission reduction and 20% of energy efficiency increase by 2020. A 10% target of energy in the transport sector from renewable resources was set to all member states [9]. Since the approval of these directives, the consumption of renewable sources has increased and in 2014, renewable energy sources accounted for a 12.5 % share of the EU-28's gross inland energy consumption. At the same time, the average share of energy from renewable sources in transport increased from 1.4 % in 2004 to 6.7 % in 2015 [10].
The directive (EU) 2015/1513 repeats the goal of 20% energy efficiency by 2020 set in previous directive. In addition, different types of new energy substrates such as waste, crops rich in starch, lignocellulosic material, processing residues etc. were identified and the transition from conventional first-generation biofuels to advanced second-generation biofuels was aimed. Therefore, a maximum limit – 7% of conventional first generation biofuels in transport sector by 2020 – was introduced [11].
Energy Roadmap 2050, which aims to decarbonize the EU economy by 2050, states that the renewables have the potential to provide approximately 30 % of total EU energy consumption by 2030 [12]. In order to gain these goals, a new greenhouse gas reduction target of 40% and a share of renewable energy in the EU of at least 27% by 2030 was agreed and set out [13]. With a proposal of new and revised Renewable Energy Directive published in 2016 a goal was set to make the EU a global leader in renewable energy and to ensure that the target of at least 27% renewables in the final energy consumption in the EU by 2030 is met. In addition, the 7% limit of conventional first generation biofuels in transport sector is to be reduced to 3.8% by 2030 [14].

3 FUELS FROM THERMOCHEMICAL PROCESS

For the production of liquid biofuels, two different approaches are mainly used - thermochemical or biochemical conversion [6, 15]. In case of thermochemical conversion, the biomass is heated either in the absence of oxygen (pyrolysis) or in the presence of oxygen (gasification) at high temperature, up to 800°. In gasification, the thermochemical process converts the biomass into synthesis gas (syngas) such as hydrogen, CO and CO_2 [15]. From syngas, a wide range of long carbon chain biofuels, such as synthetic diesel, aviation fuel, or ethanol, can be produced, based on the Fischer–Tropsch conversion [16].
Pyrolysis processes are distinguished between slow and fast pyrolysis. The slow pyrolysis is used mainly for the production of chemicals and biochar, while fast pyrolysis is more suitable for fuel oil production [17]. In fast pyrolysis, biomass is heated rapidly in the absence of oxygen to a temperature of around 500 °C. The thermal decomposition of the biomass produces vapors that are condensed, forming an organic liquid called fast pyrolysis bio-oil (FPBO). The production process is close to full maturity and commercial scale production is possible in Finland (Fortum) and Netherlands (Empyro) [18]. The FPBO can be used in heating and power plants and in diesel engine and gas turbine applications to replace fossil fuels [19, 20].
Fast pyrolysis liquid, bio-oil, is formed after cooling and condensing the vapors from this decomposition process. The liquid has a heating value about half that of the conventional fuel oil. The most prominent organic compounds in the FPBO include acetic acid, methanol, aldehydes and ketones, cyclopentenones, furans, alkyl-phenols, alkylmethoxyphenols, anhydrosugars, oligomeric sugars and water-insoluble lignin-derived compounds [18]. The high oxygen content leads to high viscosities and boiling points, and relatively poor chemical stability, which is one of the major challenges in storing the substance [17].

3.1 Challenges for commercialization

Although FPBO production has been successfully demonstrated in commercial utilization in boiler applications there are still challenges and development needs to improve its utilization in energy productions, including:

- Suspended char in the oil can cause e.g. erosion and burner equipment blockage, boiler deposits and high emissions [17]. Oil filtration can be used to solve these problems.
- Alkali metals present in the fuel can form deposits in the boiler and e.g. oil filtration, oil upgrading, as well as feedstock material control can be used as a solution.
- Low pH of the oil can cause corrosion in the fuel delivery system, which can be prevented by careful material selections [19].

- Polymers can affect sealing rings and gaskets. This needs to be taken into account when choosing the materials for these parts.
- High temperature sensitivity can cause liquid to decompose on hot surfaces. This can be solved using appropriate cooling facilities.

High viscosity can cause high pressure drops in pipelines. This can be solved with an addition of water/ethanol/methanol or other solvent.

- High fuel water content affects viscosity, heating value, density, stability, pH and homogeneity. Inhomogeneous fuel can also cause problems in the combustion processes. [17]

4 BIOETHANOL FROM BIOCHEMICAL PROCESS

In the biochemical route, the biomass polysaccharides are converted into sugars using chemical or enzymatic hydrolysis. Different sugars derived from lignocellulosic biomass can be further used for production of different alcohols, lipids and biogas using specific microbial fermentation processes [21]. One of the most common ways to produce biofuels from lignocellulose is to convert the biomass into sugars and ferment the sugars into alcohol fuel such as ethanol.

However, due to the tight binding of cellulose in lignin and hemicellulose cover, the cellulose is difficult to access for cellulases. Therefore, to make the conversion more efficient, biomass must be subjected to pretreatment to open its structure and allow easier release of fermentable monosaccharides [22]. The choice of a suitable method depends on the characteristics of the biomass. Based on the working principle and materials, the pretreatment methods can be divided into, biological, physical, and chemical methods and additional methods that combine characteristics of these.

Processing of pretreated biomass to ethanol consists of three major units of operations: hydrolysis of cellulose to sugars, fermentation of sugars to ethanol and product separation/purification. Cellulose hydrolysis, also known as saccharification, is the process in which the cellulose is converted into glucose [23, 24]. In addition to cellulose, hemicellulose can also be hydrolyzed into its components (mannan, xylan, glucan, galactan, and arabinan) [25]. For efficient conversion of cellulose into sugars, at least three categories of enzymes are necessary – endogluconases, exogluconases and β-glucosidases [26].

The hydrolyzed biomass containing different sugars can be fermented to ethanol by several microorganisms. However, while the hexoses (mainly glucose), can be fermented to ethanol by many naturally occurring organisms, the pentoses (xylose and arabinose) can be fermented to ethanol only by a few native strains at relatively low yields [24]. The most commonly used industrial fermentation microorganisms are yeast *S. cerevisiae* and bacterium *Z. mobilis* [23, 27]. The most promising organisms that have the ability to ferment both pentoses and hexoses are *P. stipitis*, *C. shehatae*, *P. tannophilus* and *K. marixianus* [25, 27].

Production of ethanol from biomass can be done using different approaches. The classic configuration is employing separate enzymatic hydrolysis, which is followed by fermentation (SHF) processes, where the hydrolysis of cellulose and the fermentation of glucose are carried out in separate units. In the simultaneous saccharification and fermentation (SSF), the hydrolysis and fermentation are performed in a single unit, which enables substantial reductions in equipment, investment, and operation costs [23, 25]. When SSF includes the co-fermentation of hexose and pentose sugars, it is called simultaneous saccharification and co-fermentation (SSCF). This can be achieved by application of mixed cultures or a single microorganism capable of assimilating both hexoses and pentoses with a high conversion efficiency and ethanol yield [27]. A step further is consolidated bioprocessing (CBP), where cellulase production, cellulose hydrolysis, and fermentation are carried out in a single step. In the CBP, the bioethanol is produced by a single microbial community and the entire process is centralized to one reactor. In addition to single strain processes, stable mixed cultures that can degrade lignocelluloses have been used [28].

4.1 Challenges for commercialization

Although the production of liquid biofuels from lignocellulosic biomass is promising with high biofuel yields under laboratory conditions, there are still several technical barriers hindering the large-scale and cost-effective production of cellulosic biofuels. Due to the large number of individual processes in the overall conversion of lignocellulosic biomass, considerable potential for process integration remains. Possibilities for this cost reduction include more effective pretreatment, reducing the cost of cellulase by improving enzyme efficiency, hydrolysis of both hemicelluloses and cellulose to sugars, use of both six-carbon and five-carbon sugars in fermentation, and process integration for reducing capital and energy costs [6, 29].

It is estimated that pretreatment step constitutes 40% of processing costs in bioethanol production process. Therefore, it is vital to select the optimal pretreatment technology, to gain the cost-effective bioethanol production process from lignocellulosic biomass [30]. In case of various chemical pretreatment methods, the key issue is the chemical recovery and economical usage of chemicals. Chemical free processes, such as steam explosion pretreatment, have more potential due to reduction of cost by elimination of chemicals. Currently, there is no ideal pretreatment method that can be adopted for all biomass types and therefore, a combination of different methods needs to be applied to find the suitable process for a given biomass type [31].

Enzymatic hydrolysis is one of the most challenging steps for the second generation biofuel commercialization and accounts for 25–30% of the operational costs [32]. Currently, the most common practices to enhance the enzyme efficiency and gain higher sugar yields from hydrolysis are the optimization of process conditions, application of different enzyme mixtures and additives to improve cellulase performance [33].

Additionally capital, operational and energy costs reduce integration of different processes in the hydrolysis and fermentation steps. The SSH and SSCF allow different operations in one processing unit and since the sugars formed from biomass are rapidly fermented into ethanol, the accumulation of inhibiting sugars can be avoided. Thus, higher ethanol yields with lower amounts of enzyme could be gained [34]. In the CBP method, all the processes are integrated into a single reactor and additionally the costs for enzyme production can be avoided. Thereby, compared to independent hydrolysis and fermentation steps, substantially lower production costs and enhanced efficiency of bioethanol production can be gained by integration of different production steps [35].

In order to improve the economic efficiency of lignocellulosic biofuel production, all biomass components and residual biomass should be utilized. Therefore, a highly effective bioethanol process is required for the complete hydrolysis of both cellulose and hemicellulose to sugars with minimum sugar losses and efficient fermentation of all sugars to ethanol [36]. The efficient degradation of hemicellulose to pentoses and hexoses requires the synergistic action of many enzymes including hemicellulases [37]. In addition, to fully utilize biomass, the hemicellulose hydrolysates must also be fermented and utilized [35]. However, when using *Saccharomyces cerevisiae* for ethanol fermentation, only hexoses will be fermented to ethanol, and the pentoses together with proteins and other carbon sources will remain unused in residual biomass [36]. Therefore, it is vital to research and develop genetically modified fermentative and cellulolytic microorganisms and co-culture systems to increase ethanol yield and productivity [15].

The overall revenues from the process could be increased with the production of co-products during the bioethanol production [6, 24] and the utilization of the residual material, residual lignin, unreacted cellulose and hemicellulose, enzymes, yeast, and other components, for production of biogas in anaerobic digestion process. Such integrated production technology could enable higher total energy yield than with just ethanol production from hexoses and pentoses [38].

A more advanced approach is through integrated biorefinery. This approach includes integration of biofuel production with other production facilities, which use biomass or process residues to make different co-products like biofuel, bio-chemicals, fertilizer, heat and energy etc. [39]. The economic benefit of this approach is gained when, in addition to biofuels, also high-value but low-volume co-products are produced. This way a broader variety of biomass feedstocks could be used in a more efficient way than current biofuel production units, and additionally, competition among different uses of biomass reduces [40].

5 CONCLUSIONS

Many technologies are available, which enable to produce liquid biofuels from lignocellulosic biomass. The most widely researched and perspective are bioethanol production using microbial fermentation, and production of synthetic fuels from syngas gained from pyrolysis of biomass. The production technologies of these different liquid biofuels are in is close to full maturity for the thermochemical biofuels and early commercial prototype phase for bioethanol production. Even though the liquid biofuel's production from lignocellulosic biomass shows high production yields, there are several challenges that exist before its commercialization.

ACKNOWLEDGEMENTS

We gratefully acknowledge the financial support of the European Regional Development Fund via the Mobilitas Pluss (project MOBERA2) of the Estonian Research Council, Doctoral School of Energy and Geotechnology III, supported by the European Union, European Regional

Development Fund (Estonian University of Life Sciences ASTRA project „Value-chain based bio-economy“) and the Academy of Finland through the INDO –NORDEN project (Holistic processes and practices for clean energy in strengthening bioeconomic strategies, 311970).

REFERENCES

[1] I. E. Agency, "Technology Roadmap Delivering Sustainable Bioenergy," 2017.
[2] P. S. Nigam and A. Singh, "Production of liquid biofuels from renewable resources," *Progress in Energy and Combustion Science,* vol. 37, pp. 52-68, 2011.
[3] V. B. Agbor, N. Cicek, R. Sparling, A. Berlin, and D. B. Levin, "Biomass pretreatment: Fundamentals toward application," *Biotechnology Advances,* vol. 29, pp. 675-685, 2011.
[4] M. Raud, R. Kesperi, T. Oja, J. Olt, and T. Kikas, "Utilization of urban waste in bioethanol production: Potential and technical solutions," *Agronomy Research,* vol. 12, pp. 397-406, 2014.
[5] M. Raud, M. Mitt, T. Oja, J. Olt, K. Orupõld, and T. Kikas, "The utilisation potential of urban greening waste: Tartu case study," *Urban Forestry & Urban Greening,* vol. 21, pp. 96-101, 1// 2017.
[6] R. E. H. Sims, W. Mabee, J. N. Saddler, and M. Taylor, "An overview of second generation biofuel technologies," *Bioresource Technology,* vol. 101, pp. 1570-1580, 2010.
[7] *Kyoto protocol to the United Nations framework convention on climate change* U. Nations, 1998.
[8] V. Katinas, V. Gaigalis, J. Savickas, and M. Marčiukaitis, "Analysis of sustainable liquid fuel production and usage in Lithuania in compliance with the National Energy Strategy and EU policy," *Renewable and Sustainable Energy Reviews,* vol. 82, pp. 271-280, 2018/02/01/ 2018.
[9] *Directive 2009/28/EC of the European Parliament and of the Council of 23 April 2009 on the promotion of the use of energy from renewable sources and amending and subsequently repealing Directives 2001/77/EC and 2003/30/EC,* 2009.
[10] Eurostat, "Key figures on Europe 2016 edition," 2017.
[11] *Directive (eu) 2015/1513 of the European Rarliament and of the Council of 9 september 2015 amending directive 98/70/ec relating to the quality of petrol and diesel fuels and amending directive 2009/28/ec on the promotion of the use of energy from renewable sources,* 2015.
[12] *Energy Roadmap 2050,* E. Commission, 2011.
[13] *COM(2014) 15 A policy framework for climate and energy in the period from 2020 to 2030* 2014.
[14] *2016/0382(cod) proposal for a directive of the European arliament and of the council on the promotion of the use of energy from renewable sources,* 2016.
[15] A. Limayem and S. C. Ricke, "Lignocellulosic biomass for bioethanol production: Current perspectives, potential issues and future prospects," *Progress in Energy and Combustion Science,* vol. 38, pp. 449-467, 2012/08/01/ 2012.
[16] F. M. Gírio, C. Fonseca, F. Carvalheiro, L. C. Duarte, S. Marques, and R. Bogel-Łukasik, "Hemicelluloses for fuel ethanol: A review," *Bioresource Technology,* vol. 101, pp. 4775-4800, 2010.
[17] A. V. Bridgwater, D. Meier, and D. Radlein, "An overview of fast pyrolysis of biomass," *Organic Geochemistry,* vol. 30, pp. 1479-1493, 1999/12/01/ 1999.
[18] A. Oasmaa, B. van de Beld, P. Saari, D. C. Elliott, and Y. Solantausta, "Norms, Standards, and Legislation for Fast Pyrolysis Bio-oils from Lignocellulosic Biomass," *Energy & Fuels,* vol. 29, pp. 2471-2484, 2015/04/16 2015.
[19] J. Lehto, A. Oasmaa, Y. Solantausta, M. Kytö, and D. Chiaramonti, "Review of fuel oil quality and combustion of fast pyrolysis bio-oils from lignocellulosic biomass," *Applied Energy,* vol. 116, pp. 178-190, 2014/03/01/ 2014.
[20] O. Sippula, Huttunen, K., Hokkinen, J., Kärki, S., Suhonen, H., Kajolinna, T., Kortelainen, M., Karhunen, T., Jalava, P., Uski, O., Yli-Pirilä, P., Hirvonen, M.-R., Jokiniemi, J. , "Emissions from a fast-pyrolysis bio-oil-operated district heating boiler: particulate emission physico-chemical and toxicological properties and comparison to emissions from wood and heavy fuel oil-fired boilers," *Fuel,* xxx.
[21] S. Ghosh, R. Chowdhury, and P. Bhattacharya, "Sustainability of cereal straws for the fermentative production of second generation biofuels: A review of the efficiency and economics of biochemical pretreatment processes," *Applied Energy,* vol. 198, pp. 284-298, 2017/07/15/ 2017.

[22] S. Haghighi Mood, A. Hossein Golfeshan, M. Tabatabaei, G. Salehi Jouzani, G. H. Najafi, M. Gholami, *et al.*, "Lignocellulosic biomass to bioethanol, a comprehensive review with a focus on pretreatment," *Renewable and Sustainable Energy Reviews,* vol. 27, pp. 77-93, 2013.
[23] Ó. J. Sánchez and C. A. Cardona, "Trends in biotechnological production of fuel ethanol from different feedstocks," *Bioresource Technology,* vol. 99, pp. 5270-5295, 2008/09/01/ 2008.
[24] N. Mosier, C. Wyman, B. Dale, R. Elander, Y. Y. Lee, M. Holtzapple, *et al.*, "Features of promising technologies for pretreatment of lignocellulosic biomass," *Bioresource Technology,* vol. 96, pp. 673-686, 2005.
[25] J. K. Saini, R. Saini, and L. Tewari, "Lignocellulosic agriculture wastes as biomass feedstocks for second-generation bioethanol production: concepts and recent developments," *3 Biotech,* vol. 5, pp. 337-353, 2015.
[26] J. Zhou, Y.-H. Wang, J. Chu, L.-Z. Luo, Y.-P. Zhuang, and S.-L. Zhang, "Optimization of cellulase mixture for efficient hydrolysis of steam-exploded corn stover by statistically designed experiments," *Bioresource Technology,* vol. 100, pp. 819-825, 1// 2009.
[27] M. Vohra, J. Manwar, R. Manmode, S. Padgilwar, and S. Patil, "Bioethanol production: Feedstock and current technologies," *Journal of Environmental Chemical Engineering,* vol. 2, pp. 573-584, 2014/03/01/ 2014.
[28] M. Rastogi and S. Shrivastava, "Recent advances in second generation bioethanol production: An insight to pretreatment, saccharification and fermentation processes," *Renewable and Sustainable Energy Reviews,* vol. 80, pp. 330-340, 2017/12/01/ 2017.
[29] A. Demirbas, "Competitive liquid biofuels from biomass," *Applied Energy,* vol. 88, pp. 17-28, 2011.
[30] A. W. Bhutto, K. Qureshi, K. Harijan, R. Abro, T. Abbas, A. A. Bazmi, *et al.*, "Insight into progress in pre-treatment of lignocellulosic biomass," *Energy,* vol. 122, pp. 724-745, 3/1/ 2017.
[31] F. Talebnia, D. Karakashev, and I. Angelidaki, "Production of bioethanol from wheat straw: An overview on pretreatment, hydrolysis and fermentation," *Bioresource Technology,* vol. 101, pp. 4744-4753, 7// 2010.
[32] J. Rocha-Martín, C. Martinez-Bernal, Y. Pérez-Cobas, F. M. Reyes-Sosa, and B. D. García, "Additives enhancing enzymatic hydrolysis of lignocellulosic biomass," *Bioresource Technology,* vol. 244, pp. 48-56, 2017/11/01/ 2017.
[33] E. M. Obeng, C. Budiman, and C. M. Ongkudon, "Identifying additives for cellulase enhancement—A systematic approach," *Biocatalysis and Agricultural Biotechnology,* vol. 11, pp. 67-74, 2017/07/01/ 2017.
[34] Y. Shen, Y. Zhang, T. Ma, X. Bao, F. Du, G. Zhuang, *et al.*, "Simultaneous saccharification and fermentation of acid-pretreated corncobs with a recombinant Saccharomyces cerevisiae expressing β-glucosidase," *Bioresource Technology,* vol. 99, pp. 5099-5103, 2008.
[35] S. Mohapatra, C. Mishra, S. S. Behera, and H. Thatoi, "Application of pretreatment, fermentation and molecular techniques for enhancing bioethanol production from grass biomass – A review," *Renewable and Sustainable Energy Reviews,* vol. 78, pp. 1007-1032, 2017/10/01/ 2017.
[36] B. Hahn-Hägerdal, M. Galbe, M. F. Gorwa-Grauslund, G. Lidén, and G. Zacchi, "Bio-ethanol – the fuel of tomorrow from the residues of today," *Trends in Biotechnology,* vol. 24, pp. 549-556, 2006/12/01/ 2006.
[37] K. A. Gray, L. Zhao, and M. Emptage, "Bioethanol," *Current Opinion in Chemical Biology,* vol. 10, pp. 141-146, 2006/04/01/ 2006.
[38] E. Kreuger, B. Sipos, G. Zacchi, S.-E. Svensson, and L. Björnsson, "Bioconversion of industrial hemp to ethanol and methane: The benefits of steam pretreatment and co-production," *Bioresource Technology,* vol. 102, pp. 3457-3465, 2011.
[39] F. Coppola, S. Bastianoni, and H. Østergård, "Sustainability of bioethanol production from wheat with recycled residues as evaluated by Emergy assessment," *Biomass and Bioenergy,* vol. 33, pp. 1626-1642, 2009/11/01/ 2009.
[40] I. E. Agency, "Technology Roadmap Biofuels for Transport," 2011.

WATER HYACINTH DERIVED MIXED-OXIDE HETEROGENEOUS CATALYST FOR BIODIESEL PRODUCTION

Minakshi Gohain and Dhanapati Deka
Department of Energy, Tezpur University, Napaam-784028, Assam, India.
E-mail: minakshiigohain@gmail.com; dhanapati@tezu.ernet.in

ABSTRACT

Homogeneous catalytic system for biodiesel synthesis is no longer justifiable by industries in the near future; mainly due to food verses fuel competition and ecological issues related to conventional homogeneous catalytic system. The present study is focused on the viability of environmentally benign heterogeneous catalyst synthesis from water hyacinth (WH) a renewable aquatic plant considered hazard for other useful aquatic crops. The synthesized catalyst were characterized by fourier transform infrared spectroscopy (FTIR), powder X-ray diffractograms (XRD), energy dispersive analysis of X-ray (EDAX), b*runauer–emmett–teller (*BET), scanning electron microscopy (SEM), transmission electron microscopy (TEM) and hammett indicator analysis. The catalyst demonstrated a superior catalytic performance achieving fatty acid methyl esters (FAME) conversion of 97.1% in 3 h. The catalyst could be reused efficiently with FAME conversion of more than 80 % after the third cycles. The present work reveals the possibility of developing heterogeneous catalyst from an aquatic weed for FAME synthesis, reducing the total production cost of biodiesel synthesis.

Keywords: Renewable, Heterogeneous, Mixed oxide, Biodiesel, Reused

1. INTRODUCTION

The global energy demand is increasing continuously due to rapid population growth, increased development of industries as well as transportation. Non-renewable fossil fuels generally supply this energy adding to environmental problem and crude petroleum fuel price increase, which has necessitated the need of alternatives that are renewable (1). Biodiesel is considered as a renewable alternative to fossil fuel as it is renewable, non toxic, biodegradable and as it possess properties similar to fossil fuels (2). Commercial production of biodiesel uses homogeneous catalyst like KOH, NaOH, HCl, H_2SO_4 etc. But these homogeneous catalyst are chemically synthesized, and is no longer sustainable as well as issues like separation, soap formation, reusability are associated along with (3, 4). Researchers are working on development of biobased heterogeneous catalysts that can be used to replace the commercial homogeneous catalysts used in biodiesel production which are renewable, recyclable and easily separable (5).

Naturally available wastes like hard animal tissues (2, 6) which contain calcium compounds like calcium carbonate and calcium phosphate that are can be easily converted to calcium oxide by calcination (7). The catalysts have sufficiently strong basicity (8) and are highly porous which helps in enhanced mass transfer that helps in higher FAME conversion (2). Heterogeneous catalysts from waste biomass like *Musa paradisiacal* peels (9), *Musa* 'Gross Michel' (10), *Musa balbisiana colla* (5), wood ash (11) has been developed that possessed high catalytic ability that resulted in high biodiesel conversion/yield. As they has been prepared from wastes hence it adds to the sustainability of fuels.

The aim of this work is to obtain heterogeneous catalyst production from water hyacinth (*Eichhornia crassipes*) for transesterification of *Scenedesmus obliquus* lipid into biodiesel. The WH is a renewable aquatic plant considered hazard for other useful aquatic crops which is available in plenty in Northeast India (12).

2. EXPERIMENTAL

2.1. Materials

Water hyacinth was collected from the ponds of Tezpur University campus, Assam. *Scenedesmus obliquus* lipid was procured from Gauhati University. All the chemicals used in the present work were of analytical grades purchased from Sigma Aldrich and were used without any purification.

2.2. Methods

2.2.1. Catalyst preparation

Water hyacinth was cleaned by washing with hot double distilled water, acetone and hexane to any unwanted material, cut into pieces and dried in oven at 100 °C for 3 h. The dried WH pieces were crushed to become fine particles using mortar pestle. The powdered WH was calcined in a muffle furnace at a temperature of 800 °C for 4 h. The synthesized WH catalyst was stored in close tight bottle till further use.

2.2.2. Catalyst characterization

The basicity of the WH catalyst was determined by using Hammet indicator test. The surface morphology of the WH catalyst was studied by SEM analysis (Jeol, JSM-6290 LV). The TEM and EDAX study were analyzed using TECNAI G2 20 S-TWIN (200 KV), USA. The XRD patterns were obtained using Rigaku miniflex diffractometer in 2Θ range 10-80° (CuKα radiation, λ = 1.5406 Å) at 2° scanning rate. The surface area, pore size and pore volume of the catalyst was measured using BET sorption isotherm method (NOVA 1000E, NOVA WIN, QUANTACHROME). The FTIR spectra were measured in a Nicolet FTIR spectrophotometer (Impact 410) on KBr pallets in 4000-500 cm^{-1} wavenumber range.

For reusability capacity of the catalyst, the reaction mixture was centrifuged (3500 rpm) and washed (hot methanol) to recover the catalyst and to remove any unwanted traces. The recovered catalyst was oven dried (120 °C, 3 h) and experiments were carried on using the required parameters [5].

2.2.3. FAME synthesis

The initial acid value of *Scenedesmus obliquus* lipid used for the study was 1.4 mg KOH/ g oil which can be easily employed for satisfactory transesterification using alkaline catalyst. Ten millilitres (10 ml) of *Scenedesmus obliquus* lipid was measured into a 100 ml one-neck glass reactor and placed on a magnetic stirrer hot plate and heated to 60 °C. Catalyst loading of 2 wt % was added to the lipid followed by addition of a known volume of methanol (6:1 methanol to oil molar ratio). Temperature was maintained at 60 °C throughout the reaction for 3 h. The mixture was transferred to a separating funnel and kept undisturbed overnight. The mixture got separated into three layers: the lower layer composed of catalyst, middle layer composed of glycerol and the upper layer composed of biodiesel. The upper layer was washed with hot double distilled water (40 °C) to remove any traces of unwanted substances. The washed biodiesel was dried using anhydrous sodium sulphate. The FAME conversion (%) was determined by using nuclear magnetic resonance (NMR) technique [13] using $CDCl_3$ as solvent (Eq. 1).

$$C_{MEster}(\%) = \frac{2 \times A}{3 \times B} \times 100 \quad (1)$$

A = integral of methoxy methyl ester peak at 3.6 ppm

B = integral of α-methylene peak at 2.3 ppm

2.2.4. Water hyacinth methyl ester (WHME) characterization

The properties of WHME were determined by American Society for Testing and Material (ASTM) methods and compared with ASTM D 6751 and European standards (EN 14214).

3. Results and discussion

3.1. Catalyst characterization

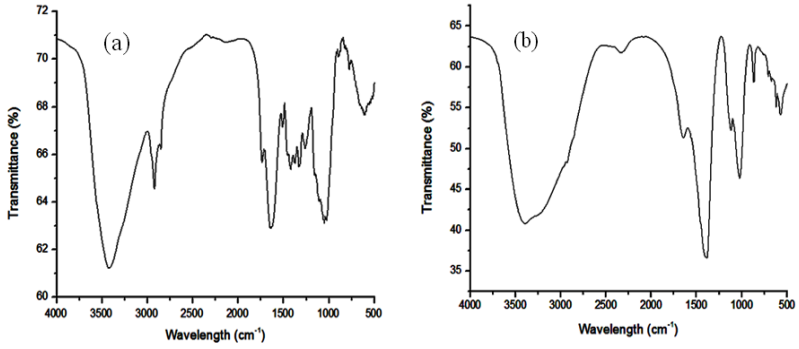

Fig. 1. The FTIR spectra of (a) WH and (b) CWH

The FTIR spectrum of WH and calcined water hyacinth (CWH) has been shown in fig. 3. The band at around 550 cm^{-1} and 1000 cm^{-1} in fig. 3, is attributed to Ca-O, K-O stretching and Si-O-Si bonds respectively (9, 10). The band at around 1385 cm^{-1} denotes K_2CO_3 presence which is prominent only in the CWH (11). The presence of calcium, potassium in form of oxides indicates the basic nature of the CWH.

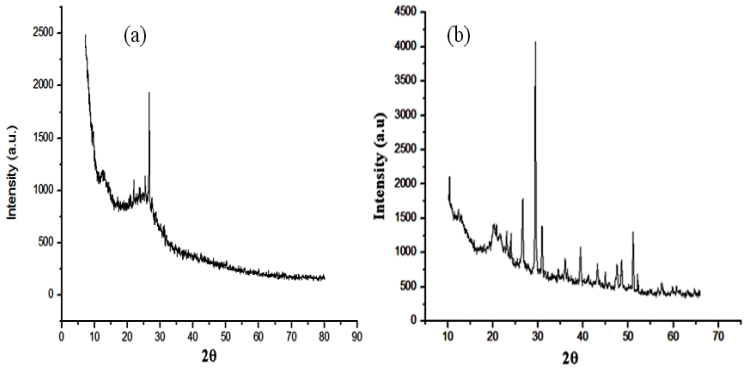

Fig. 2. The XRD patterns of (a) WH and (b) CWH

The fig. 2 shows the XRD patterns of WH and CWH. Strong peaks at 2θ = 25, 26, 31, 33, 41, 44, 46 (JCPDS reference code No 00-026-1327 and 00-16-820) are attributed to K_2O and K_2CO_3. The peaks seen at 2θ = 30, 39, 43, 47 (JCPDS reference code 01-085-0514) was due to presence of CaO [Fig. 4(b)]. Several small peaks were also seen that corresponds to KCl, K_2SO_4, K_2MgSiO_4 (JCPDS card no 004-0587, 002-0626, 021-0982, respectively). Increase in intensities of potassium compounds was seen that corresponds to strong basic sites (14).

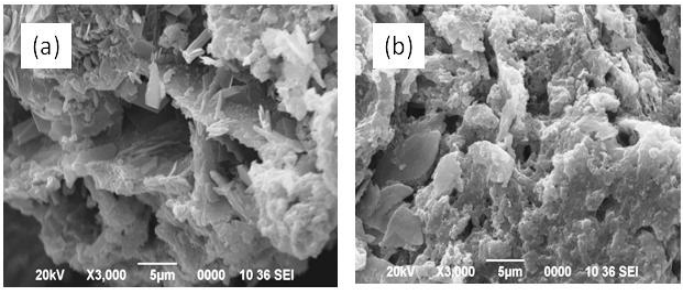

Fig. 3. The SEM image of (a) WH (b) CWH

The surface morphology of the WH and CWH has been shown in fig. 3. Both mesoporous and microporous structure is being evident in fig. 3, whereas more microporous and less mesoporous structure was seen after calcination [fig. 3(b)]. Porous structure indicates large surface area (15). The TEM image (Fig. 4) supported the SEM findings too.

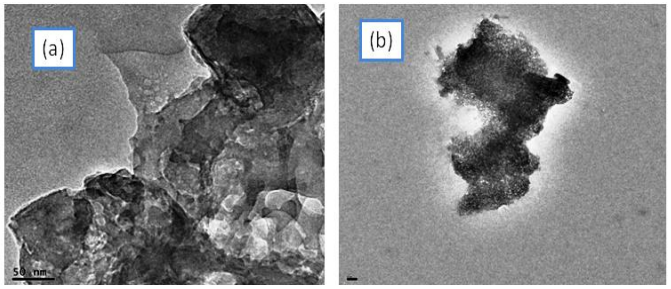

Fig. 4. The TEM image of (a) WH (b) CWH

The EDAX analysis strongly supported the findings of FTIR as well as XRD which revealed a high distribution of K, Ca, Na, Mg and Si oxides. The surface area of prepared catalyst (CWH) was found to be 48.662 m^2/g, with pore volume 0.358 cc/g and pore radius of 1.7074 nm respectively.
For testing the basicity Hammett indicator test was used [15] and obtained according to color variation. After analysis, the WH and CWH showed a basic strength of $9.8 < H_- < 12.2$ and of $9.8 < H_- < 15$ respectively.

3.2. Biodiesel characterization

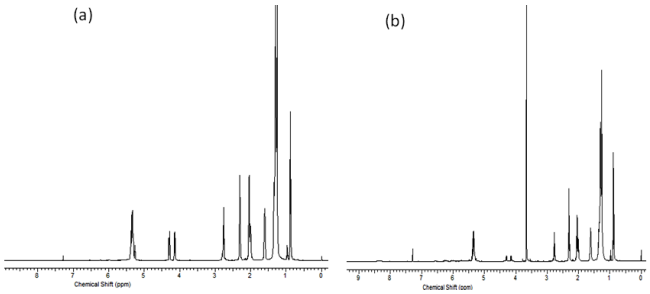

Fig. 5. ^{1}H NMR spectroscopy of (a) *Scenedesmus obliquus* lipid and (b) *Scenedesmus obliquus* biodiesel.

The presence of glyceridic protons in the range of 4.0-5.2 ppm in ^{1}H NMR is the characteristics of triglycerides present in *Scenedesmus obliquus* lipid [Fig. 5(a)] which is totally absent in the *Scenedesmus obliquus* biodiesel [Fig. 5(b)]. The methyl ester moiety protons at 3.66 ppm and α-carbonyl methylene groups at 2.30 ppm are due to methyl ester formation [Fig. 5(b)]. The shift at 5.3 ppm is due to the alkene proton which signifies that the main components of *Scenedesmus obliquus* is unsaturated fatty acid and for *Scenedesmus obliquus* biodiesel are methyl ester respectively (16). The FAME conversion of 97.1 % has been achieved by using 6:1 molar ratio of methanol to oil, catalyst loading of 2 wt % at 60 °C, for 3 h. The biodiesel was analyzed for physico-chemical properties (Table 1) and was found suitable for replacing the commercial diesel.

Table 1. Physico-chemical properties of produced *Scenedesmus obliquus* biodiesel (SOB)

Properties	SOB	ASTM D 6751	EN 14214
Acid value (mg KOH^{-1} g)	0.05	<0.80	0.5 max
Kinematic viscosity (cst) at 40°C	3.14	1.9-6.0	3.5-5.0
Density@ 15°C (gm cc^{-1})	0.85	0.86-0.90	0.85
Cloud point (°C)	-7	---	---
Pour point (°C)	-12	---	---
Flash point (°C)	145	93 min	120 min
Carbon residue (% wt)	0.014	0.050 max	0.3
Calorific value (MJ kg^{-1})	39.30	---	35 min
Cetane Number	53	47 min	51 min

3.3. Recycling potency of the catalyst

The catalyst reusability has been tested by using the same parameters i.e. 6:1 molar ratio of methanol to oil, catalyst loading of 2 wt % at 60 °C, for 3 h. The recovered catalyst was tested till fifth cycles (Fig. 6). High FAME conversion till 80 % was observed even after third cycles. Reduced conversion of biodiesel may be due to loss of catalyst amount due to washing or leaching of the catalyst as because leaching of K and Ca is more than other elements (17).

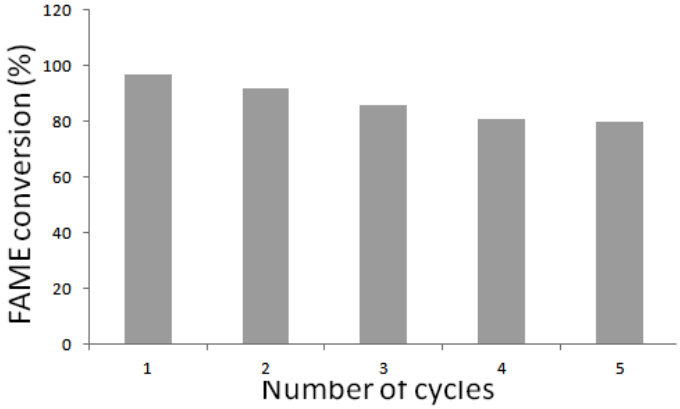

Fig. 6. Recycling potency of CWH catalyst

4. CONCLUSION

In this work a novel solid base catalyst was synthesized from water hyacinth to produce biodiesel from *Scenedesmus obliquus* lipid. The catalyst exhibited FAME conversion of 97.1 % using 2 wt % catalyst loading, methanol/oil molar ratio of 6:1 within 3 h. Reusability analysis showed that the catalyst exhibits good catalytic activity i.e. conversion of more than 80 % even after three repeated uses. The calcined water hyacinth was found to have efficient catalytic activity having the potency to replace other base catalysts that are chemically synthesized hence providing a new way to sustainability of fuels. The use of water hyacinth for catalyst development can lead to utilization of water hyacinth that is considered hazardous into valuable product.

FUNDING

The authors thank DBT, New Delhi, India for financial support (Grant No- DBT/IC-2/Indo-Brazil/2016-19/04).

REFERENCES

[1] S. A. Basha, K. R. Gopal and S. Jebaraj, A review on biodiesel production, combustion, emissions and performance, *Renewable and sustainable energy reviews*, Vol. 13, pp. 1628-1634, 2009.

[2] N. Nakatani, H. Takamori, K. Takeda and H. Sakugawa, Transesterification of soybean oil using combusted oyster shell waste as a catalyst, *Bioresource Technology*, Vol. 100, pp. 1510-1513, 2009.

[3] N. Viriya-Empikul, P. Krasae, W. Nualpaeng, B. Yoosuk and K. Faungnawakij, Biodiesel production over Ca-based solid catalysts derived from industrial wastes, *Fuel*, Vol. 92, pp. 239-244, 2012.

[4] A. Piker, B. Tabah, N. Perkas and A. Gedanken, A green and low-cost room temperature biodiesel production method from waste oil using egg shells as catalyst. *Fuel*, Vol. 182, pp. 34-41, 2016.

[5] M. Gohain, A. Devi and D. Deka, Musa balbisiana Colla peel as highly effective renewable heterogeneous base catalyst for biodiesel production, *Industrial Crops and Products*, Vol. 109, pp. 8-18 2017.

[6] A. Obadiah, G. A. Swaroopa, S. V. Kumar, K. R. Jeganathan and A. Ramasubbu, Biodiesel production from palm oil using calcined waste animal bone as catalyst, *Bioresource technology*, Vol. 116, pp. 512-516, 2012.

[7] S. Boonyuen, S. M. Smith, M. Malaithong, A. Prokaew, B. Cherdhirunkorn and A. Luengnaruemitchai, A. (2017). Biodiesel production by a renewable catalyst from calcined Turbo jourdani (Gastropoda: Turbinidae) shells, *Journal of Cleaner Production*, Vol. 177, pp. 925-929, 2018

[8] Y. Y. Wang, H. H. Wang, T. L. Chuang, B. H. Chen and D. J. Lee, Biodiesel produced from catalyzed transesterification of triglycerides using ion-exchanged zeolite Beta and MCM-22, *Energy Procedia*, Vol. 61, pp. 933-936, 2014.

[9] E. Betiku and S. O. Ajala, Modeling and optimization of Thevetia peruviana (yellow oleander) oil biodiesel synthesis via *Musa paradisiacal* (plantain) peels as heterogeneous base catalyst: a case of artificial neural network vs. response surface methodology, *Industrial Crops and Products*, Vol. 53, pp. 314-322, 2014.

[10] E. Betiku, A. M. Akintunde and T. V. Ojumu, Banana peels as a biobase catalyst for fatty acid methyl esters production using Napoleon's plume (*Bauhinia monandra*) seed oil: A process parameters optimization study, *Energy*, Vol. 103, pp. 797-806, 2016.

[11] M. Sharma, A. A. Khan, S. K. Puri and D. K. Tuli, Wood ash as a potential heterogeneous catalyst for biodiesel synthesis, *Biomass and bioenergy*, Vol. 41, pp. 94-106, 2012.

[12] A. Talukdar and D. C. Deka, Preparation and Characterization of a Heterogeneous Catalyst from Water Hyacinth (Eichhornia crassipes): Catalytic Application in the Synthesis of bis (indolyl) methanes and bis (pyrrolyl) methanes Under Solvent Free Condition, *Current Catalysis*, Vol. 5, pp. 51-65, 2016.

[13] G. Gelbard, O. Bres, R.M. Vargas, F. Vielfaure and U.F. Schuchardt, ^{1}H nuclear magnetic resonance determination of the yield of the transesterification of rapeseed oil with methanol, *Journal of American Oil Chemist Society*, Vol. 72, pp.1239-1241, 1995.

[14] P. Qiu, B. Yang, C. Yi, S. Qi, Characterization of KF/γ-Al2O3 Catalyst for the Synthesis of Diethyl Carbonate by Transesterification of Ethylene Carbonate, *Catalysis Letters*, Vol. 137, pp. 232-238, 2010.

[15] K. Tanabe, T. Yamaguchi, Basicity and acidity of solid surfaces, *Journal of the Research Institute for catalysis*, Hokkaido university, Vol. 11, pp. 179-184, 1964
[16] W. Roschat, M. Kacha, B. Yoosuk, T. Sudyoadsuk, and V. Promarak, Biodiesel production based on heterogeneous process catalyzed by solid waste coral fragment, *Fuel*, Vol. 98, pp.194-202, 2012.
[17] D.M. Alonso, R. Mariscal, R. Moreno-Tost, M.Z. Poves, M.L. Granados, Potassium leaching during triglyceride transesterification using K/γ-Al2O3 catalysts, Catal. Commun. 8 (2007) 2074-2080.

SUSTAINABLE DEWATERING OF MICROALGAE BY CENTRIFUGATION USING IMAGE 4-FOCUS AND MATLAB EDGE DETECTION

R.C. Anyanwu, F. Nisar, C. Rodriguez, A. Durrant, A.G. Olabi
Institute of Energy and Engineering Technologies, University of the West of Scotland, Paisley PA1 2BE United Kingdom
Ruth.Anyanwu@uws.ac.uk

ABSTRACT

In this study, we demonstrate the feasibility of centrifugation for the successful dewatering of microalgae species. Centrifuge experiments were conducted on *Scenedesmus quadricauda* and *Chlorella vulgaris* at different centrifugal speeds between 1000-4000 (rpm) and varying time between 5-30 (min). Dewatering efficiency and microalgae cell disruption were evaluated. Image-focus 4 and Matlab edge detection software were used to model the effect of centrifugation on microalgae cell walls and to determine the water removal ratio. Experimental results indicated that centrifugation technique is an effective approach for dewatering microalgae under specific conditions. *Scenedesmus quadricauda* showed a maximum dewatering efficiency of 82% and *Chlorella vulgaris* of 91%. Centrifugation under 4000 rpm at 10 minutes did not show any significant cell damage on the algae cell structure for both species. This study provides information on specific impact of centrifugation on *Scenedesmus quadricauda* and *Chlorella vulgaris* for the first time, which is, centrifugation technique under specific conditions (4000 rpm for 10 min) is a successful method for dewatering microalgae without damage to the cell wall. This study therefore provides sustainable option for microalgae dewatering technique in the energy industry.

Keywords: Microalgae, Centrifugation speed, Dewatering, Matlab edge detection.

Corresponding author: Ruth.Anyanwu@uws.ac.uk

1 INTRODUCTION

Microalgae are unicellular organisms with complex and robust cell walls. They have been appraised as biological solar panels as they have the capability to fix CO_2 efficiently from different sources, including atmosphere, industrial exhaust, and gases. They also have the ability to produce intracellular storage compounds mainly protein (50-60%), [1]carbohydrates (10-20%) [2], and lipids (20-30%) [3]. Microalgal lipids (20-40%) consist mainly of esterified glycerol saturated and unsaturated fatty acids with a chain length of primary C_{16} and C_{18} fatty acids, when processed are important in the production of products such as biodiesel [4], bioethanol, pyrolysis oil, bio-synthetic gas (syngas), refuse-derived fuel (RDF), biogas, biomethane [5], hydrogen technologies [6] and other advanced biofuels. Interestingly, end uses are in transport, electricity, heat [7] and contribute positively to the future of renewable energy [5], [8]. These contributes to a sustainable quality of life which is well reported as the basic driver for providing a clean, safe, reliable and secure energy supplies around the globe [6]. The combination of CO_2 fixation, biofuel production, wastewater treatment, as well as the production of high value end products such as human and animal and feed, pharmaceuticals

and cosmetics makes microalgae a very promising material for use in industrial processes [9], [10], [11]. Common microalgae harvesting and dewatering operations are accomplished through centrifugation [12] freeze drying [13], bioflocculation[14], flotation, flocculation, sedimentation [15], filtration [16], or combination of above methods. Currently there is no superior or universal method suited to all algae species for dewatering purposes. Major drawbacks are high capital cost, high energy consumption, risk of contamination, cell damage and time consumption, the suitability of each process depends on the properties of the microalgae specie, the required process design, the quality of the end product, and the related capital and production costs [17], [18].

Among these process, centrifugation is the most efficient method (over 95% algae biomass could be obtained) and is widely used for microalgae cells harvesting in lab-scale or pilot-scale microalgae cultivation systems. However, the cell damage by this technique impede its further application at a large scale [19], [20]. A careful review of the available literatures revealed that in spite of centrifugation study and the conclusion generally reported that this technique damage microalgae cell wall, none of these literatures assessed the level of damage on microalgal cell for centrifugation technique. Thus, in the present study, the effect of centrifugation on fresh water microalgae *Scenedesmus quadricauda* and *Chlorella vulgaris* is investigated to assess the level of cell damage and optimize the operational conditions for an increase dewatering efficiency.

2 MATERIALS AND METHODS

2.1 Microalgae strain and medium

Scenedesmus quadricauda and *Chlorella vulgaris* (UTEX 2714 and 1589) were obtained from University of Texas at Austin. The algae were cultivated in a closed photobiorector (PBR UTEX) (Fig 1) and sterilized BG 11 medium with the following composition $NaNO_3$Mm; K_2HPO_4 0.23Mm; $MgSO_4.7H_20$ 0.3Mm; $CaCl_2.H_20$ 0.24Mm$Na_2EDTA.2H_20$ 0.0027Mm; Na_2CO_3 0.19Mm.

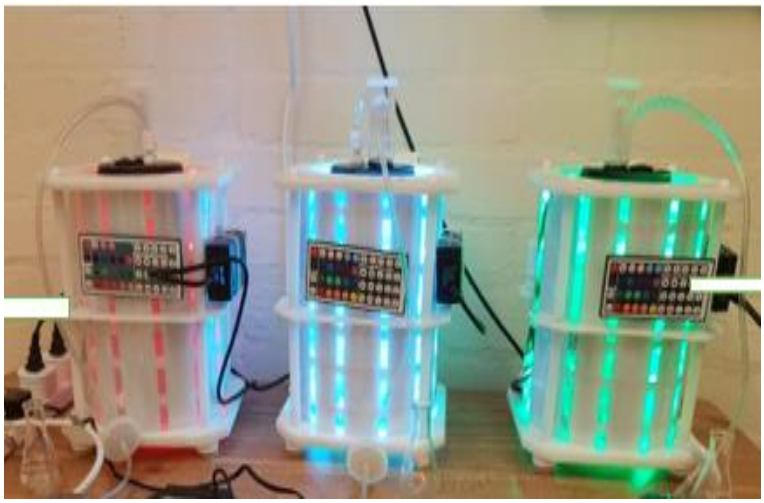

Fig 1. Closed PBR.

2.2 Centrifugation experimental design

Experiments were conducted at varying rotational speeds (RPM) and time (min) to investigate dewatering efficiency. Dewatering efficiency was calculated by Equation (1)

$$DE(\%) = \frac{\omega_1 - \omega_2}{\omega_1} x\ 100 \qquad (1)$$

where ω_1 is the moisture content of the sample before drying and ω_2 is the moisture content of the sample after drying. In centrifugation, it is important to differentiate between the speed of

centrifugation rotations per minute (RPM) and the relative centrifugal force (RCF or G) since these are often confused [21]. The centrifugation force is generated by a centrifuge can easily be calculated from the Equation 2

$$RCF = 11.18\ x\ R\ x\ \left(\frac{RPM}{1000}\right)^2 \quad (2)$$

Where R is the radius of the rotor in centimetres that is, the centrifugal force increases as the particle move down the centrifuge tube. As a rule the greater the centrifugal the shorter the separation time. However, centrifugation generates hydrostatic forces within the solution and so excessive centrifugal forces can disrupt some biological particles [21]. Medium size centrifuge (Centaur 2 MSE PA3985) was used in this study. The centrifuge consists of four 50ml swinging bucket rotor; the distance from the centre of rotation is 7.5 cm (Fig.2).

Fig 2 Centrifuge.

2.3 Image processing

Cell images were acquired using Novex B-range microscope (Holland) images were captured using Euromex microscope at 40x camera with ImageFocus 4 software. The force exerted on the microalgae sample in the centrifuge during experimentation was calculated using Equation 3. This is important as this gives better understanding of the mathematical process of the lab scale with anticipation that this will help scaling up from lab to pilot or commercial scale. Further, it is essential to determine the G-force this is represented by Equation 3.

$$G.force = \frac{rw^2}{g} \quad (3)$$

Where r is the radius from the centre of the rotor in (cm), w is the number of revolution, g is the relative centrifugal force (RCF). The experimental parameters, rotation per minute (rpm) and time varies between 1000-4000 while time varies between 5-30 minutes respectively. All experiments were run at least in duplicate. The total weight of dried algae sample was calculated.

2.4 MATLAB Edge Detection

MATLAB edge detection was performed to optimize the centrifugation process and to quantify the water removal ratio, to distinguish the significance within each centrifugation time and rpm and interactions between these parameters and to determine the significance within each factor based on the centrifugation results. MATLAB R2016b was used as the main software for the purpose of graphical method of analysis.

3.0 RESULTS AND DISCUSSION

3.1 Centrifugation effect on cell wall

Edges detection describes boundaries and is of fundamental importance when it comes to analysing data and images. Image Edge detection significantly reduces and filters out

unnecessary information, while preserving the vital structural properties in an image. Figure 3 shows the effect of varying centrifugation speed for *Scenedesmus quadricauda* and *Chlorella vulgaris*. The black and white images shown adjacent to each figure are after the edge detection, where the white part represents water and the black the cell wall. It was observed that centrifugation was effective in dewatering the algae culture. Further, the result shows that the cell walls are largely aligned within the sample surface area.

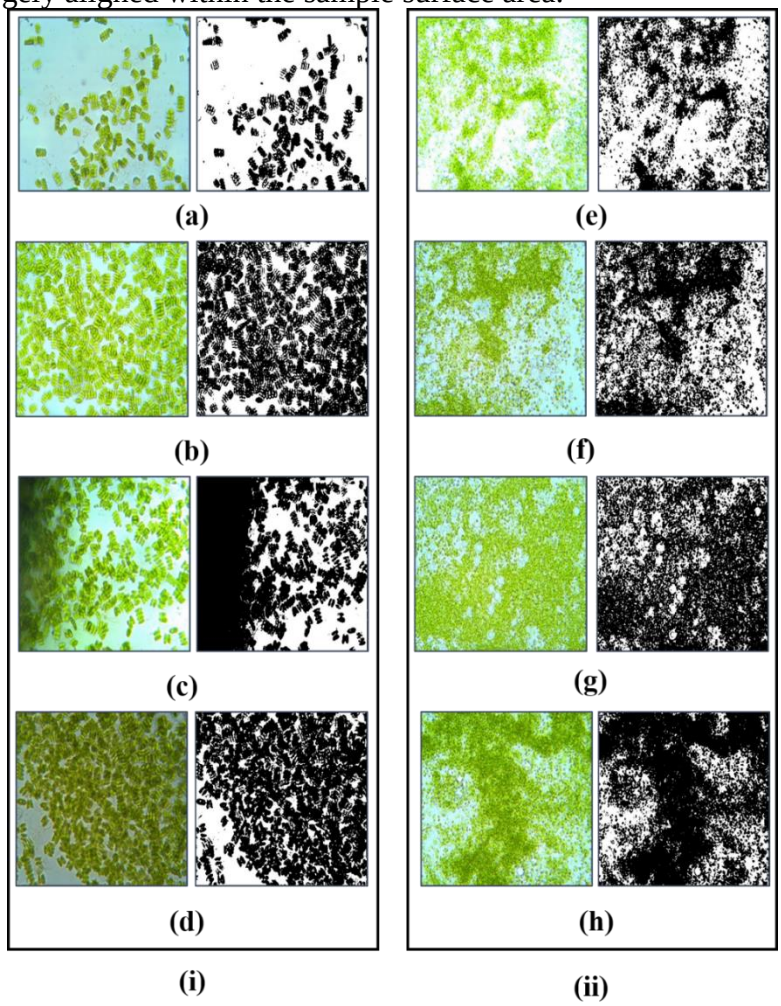

Figure 3. Image processing results for varying centrifugation speeds at constant time of 15 min (i) *Scenedesmus quadricauda* (a) 1000 RPM (b) 2000 RPM (c) 3000 RPM and (d) 4000 RPM, (ii) *Chlorella vulgaris* (e) 1000 RPM (f) 2000 RPM (g) 3000 RPM (h) 4000 RPM.

The Matlab data extracted from software illustrated in Fig 4 shows higher dewatering rate was obtained at higher RPM. Overall, water content decreases exponentially with increasing RPM. It was also observed that for centrifugal speed greater than 2500 RPM the water content removed remained constant. The biomass concentration increased greatly at 10min (Fig 5). Subsequently decreasing at increasing time, this is probably because the cell walls are affected significantly at increasing centrifugation time.

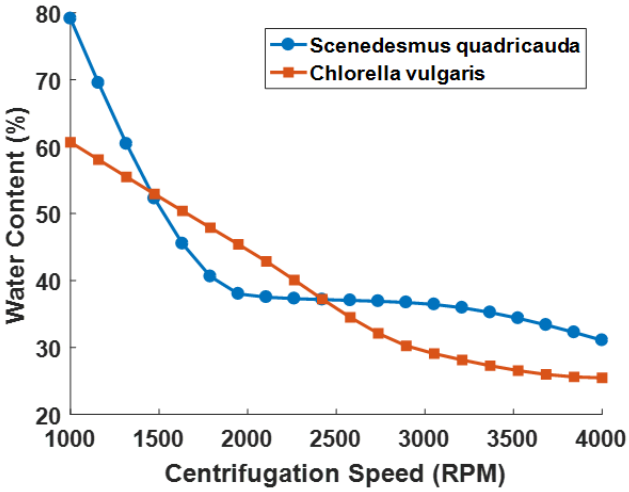

Figure 6. Data extraction of algae samples for varying centrifugation speeds between 1000 – 4000 RPM at constant time of 15 min using MATLAB Edge detection.

The experimental parameter time is observed to be more important, at 10 min as can be displayed (Fig 5), the biomass concentration of *Chlorella vulgaris* was found to be 17.6 g/L, similar pattern was reported by [22]. The minimum biomass concentration biomass concentration was at higher centrifugation time (30 min).

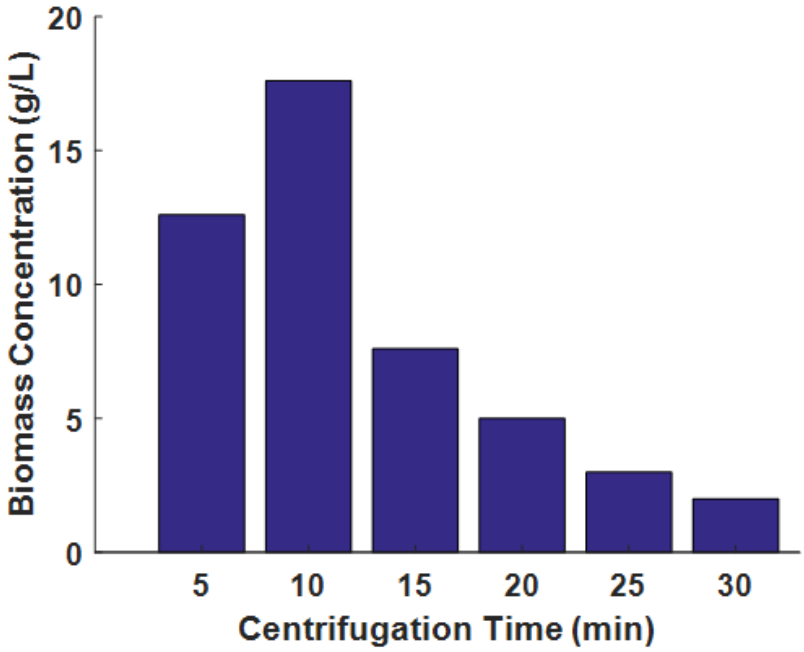

Figure 5. Biomass concentration v centrifugation time for *Chlorella vulgaris*

For centrifugation greater than 15 mins at 4000 RPM, the cell walls were damaged. Due to limitations with the edge detection method, the analysis was not performed on such samples. Figure 6 shows the images of control samples for centrifugation times greater than 15 mins where it can be seen that the cell walls are damaged. The cell walls for *Scenedesmus quadricauda* were greatly affected compared to *Chlorella vulgaris.*

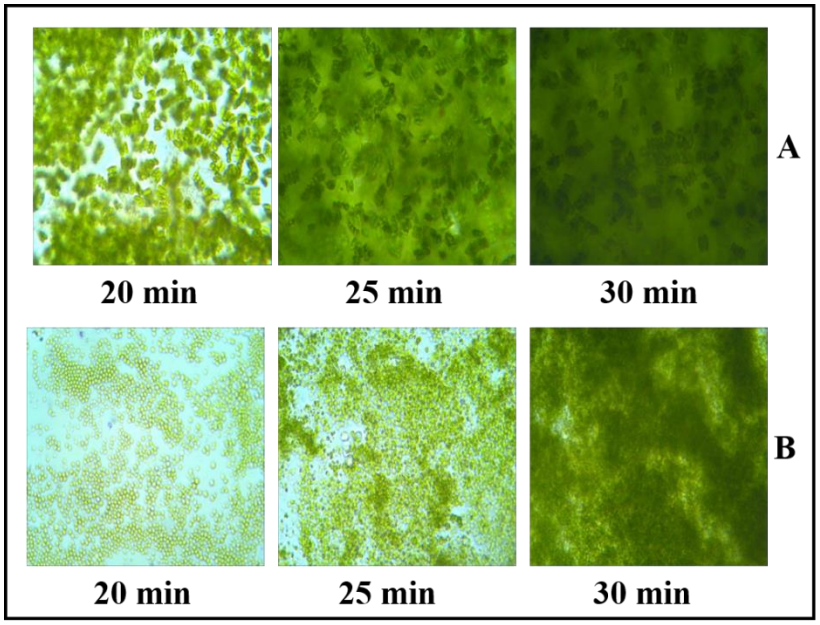

Figure 6 Cell wall damage at greater centrifugation times running at 4000 RPM for (A) *Scenedesmus quadricauda* (B) *Chlorella vulgaris.*

4 CONCLUSIONS

Centrifugation technique was assessed for efficient dewatering *Scenedesmus quadricauda* and *Chlorella vulgaris*. Using centrifugation is fast, in all treatments at 4000 RPM for 10 minutes comparing with the control cells, there was no damage on microalgae cell walls. Centrifugation time is what probably weakens the cell walls since prolong time exposes cell to extreme shear stress. Hence, centrifugation could be used at short duration as cells were more resistant to hydrodynamics force during centrifugation at 5 and 10 mins respectively. Current results suggest that centrifuges may be applied in microalgae pretreatment upon design and operation to minimize negative consequences on microalgae quality. From these findings consequently we conclude that

- Centrifugation can be applied for microalgae dewatering. This process enables algae dewatering efficiency (up to 82% *Scenedesmus quadricauda* and 91% *Chlorella vulgaris* this study).
- The specific performance can be scaled up to commercial scale. some authors have reported that the greater the centrifugal the shorter the separation time [21], an optimum RCF value of 167.7 was obtained for 4000 RPM in this study.
- For biodiesel and lipid extractions centrifugation is recommended as this will rupture the microalgae cell wall since this is related to time taken to pre-treat algal biomass using conventional pretreatment method. Overall this will save time also translates to low energy usage.
- On the basis of the observation from these extensive experiments, it is greatly possible to centrifuge microalgae in practice depending on time and rotation speed. It is expected that this work will be useful for the cultivation and dewatering application of microalgal in the industries.

REFERENCES

[1] C. Rodriguez, A. Alaswad, Z. El-Hassan, and A. G. Olabi, 'Improvement of methane production from P. canaliculata through mechanical pretreatment', *Renew. Energy*, vol. 119, pp. 73–78, 2018.

[2] C. Rodriguez, A. Alaswad, J. Mooney, T. Prescott, and A. G. Olabi, 'Pre-treatment techniques used for anaerobic digestion of algae', *Fuel Process. Technol.*, 2015.

[3] A. G. Alaswad, A Dassisti, M Prescott, T Olabi, 'Technologies and developments of third generation biofuel production', *Renew. Sustain. Energy Rev.*, vol. 51, pp. 1446–1460, 2015.

[4] C. Onumaegbu, A. Alaswad, C. Rodriguez, and A. Olabi, 'Optimization of Pre-Treatment Process Parameters to Generate Biodiesel from Microalga', *Energies*, vol. 11, no. 4, p. 806, Mar. 2018.

[5] A. G. Olabi, 'The 3rd international conference on sustainable energy and environmental protection SEEP 2009 – Guest Editor's Introduction', *Energy*, vol. 35, no. 12, pp. 4508–4509, Dec. 2010.

[6] T. Wilberforce, Z. El-Hassan, F. N. Khatib, A. Al Makky, A. Baroutaji, J. G. Carton, and A. G. Olabi, 'Developments of electric cars and fuel cell hydrogen electric cars', *Int. J. Hydrogen Energy*, no. September, 2017.

[7] Oecd, Iea, and Fao, 'Technology Roadmap : How2Guide for Bioenergy Roadmap - Development and Implementation', 2017.

[8] A. G. Olabi, 'Energy quadrilemma and the future of renewable energy', *Appl. Energy*, vol. 108, pp. 1–6, 2016.

[9] S. A. Razzak, S. A. M. Ali, M. M. Hossain, and H. deLasa, 'Biological CO2 fixation with production of microalgae in wastewater ? A review', *Renew. Sustain. Energy Rev.*, vol. 76, no. March, pp. 379–390, 2017.

[10] B. E. NAVEENA and S. PRAKASH, 'Biological Synthesis of Gold Nanoparticles Using Marine Algae Gracilaria COrticata and its Aplplication as a Potent Antimicrobial and Antioxidant Agent', *Asian J. Pharm. Clin. Res.*, vol. 6, no. 2, pp. 4–7, 2013.

[11] A. Mehrabadi, M. M. Farid, and R. Craggs, 'Potential of five different isolated colonial algal species for wastewater treatment and biomass energy production', *Algal Res.*, vol. 21, pp. 1–8, 2017.

[12] T. Ndikubwimana, X. Zeng, Y. Liu, J. S. Chang, and Y. Lu, 'Harvesting of microalgae Desmodesmus sp. F51 by bioflocculation with bacterial bioflocculant', *Algal Res.*, vol. 6, no. PB, pp. 186–193, 2014.

[13] M. Collotta, P. Champagne, W. Mabee, G. Tomasoni, G. B. Leite, L. Busi, and M. Alberti, 'Comparative LCA of Flocculation for the Harvesting of Microalgae for Biofuels Production', *Procedia CIRP*, vol. 61, pp. 756–760, 2017.

[14] S. Salim, *Harvesting microalgae by bio-flocculation and autoflocculation*. .

[15] K. Pirwitz, L. Rihko-Struckmann, and K. Sundmacher, 'Comparison of flocculation methods for harvesting Dunaliella', *Bioresour. Technol.*, vol. 196, pp. 145–152, 2015.

[16] C. Nurra, E. Clavero, J. Salvadó, and C. Torras, 'Vibrating membrane filtration as improved technology for microalgae dewatering', *Bioresour. Technol.*, vol. 157, pp. 247–253, 2014.

[17] A. Guldhe, R. Misra, P. Singh, I. Rawat, and F. Bux, 'An innovative electrochemical process to alleviate the challenges for harvesting of small size microalgae by using non-sacrificial carbon electrodes', *Algal Res.*, vol. 19, pp. 292–298, 2016.

[18] J. F. Reyes and C. Labra, ‘Biomass harvesting and concentration of microalgae scenedesmus sp. cultivated in a pilot phobioreactor’, *Biomass and Bioenergy*, vol. 87, pp. 78–83, 2016.
[19] A. R. Badireddy, S. Chellam, P. L. Gassman, M. H. Engelhard, A. S. Lea, and K. M. Rosso, ‘Role of extracellular polymeric substances in bioflocculation of activated sludge microorganisms under glucose-controlled conditions’, *Water Res.*, vol. 44, no. 15, pp. 4505–4516, 2010.
[20] X. Zhang, L. Wang, M. Sommerfeld, and Q. Hu, ‘Harvesting microalgal biomass using magnesium coagulation-dissolved air flotation’, *Biomass and Bioenergy*, vol. 93, pp. 43–49, 2016.
[21] D. Rickwood, ‘Centrifugation Techniques’, *Encycl. Life Sci.*, no. April 2001, 2001.
[22] N. K. Sahoo, S. K. Gupta, I. Rawat, F. A. Ansari, P. Singh, S. N. Naik, and F. Bux, ‘Sustainable dewatering and drying of self-flocculating microalgae and study of cake properties’, *J. Clean. Prod.*, vol. 159, pp. 248–256, Aug. 2017.

CO-PYROLYSIS OF WOODY BIOMASS WITH POLYSTYRENE TO IMPROVE BIO-CRUDE OIL QUALITY

Yeon Seok Choi[1,2], Quynh Nguyen Van[2], So Young Han[1], Seock Joon Kim[1,2], Sang Kyu Choi[1,2*]

1. Environmental and Energy Systems Research Division, Korea Institute of Machinery & Materials Daejeon, 34103, Republic of Korea; email: yschoi@kimm.re.kr, skchoi4091@kimm.re.kr
2. Department of Environment and Energy Mechanical Engineering, University of Science and Technology, Daejeon, 34113, Republic of Korea;

ABSTRACT

Biomass is considered one of the promising renewable energy sources which can reduce CO_2 emissions. Bio-crude oil can be produced by fast pyrolysis of biomass, and it has advantages in storage and transportation in comparison to the original biomass. But the bio-crude oil quality is lower than the petroleum fuels due to its larger oxygen content and smaller heating value. In this study, co-pyrolysis of woody biomass and polystyrene was performed to produce bio-crude oil in a bubbling fluidized bed reactor, and the bio-crude oil yield and characteristics are compared at various mixing ratios. The biomass feeding rate was 200 g/hr, and polystyrene was mixed with the biomass at the ratios of 5, 10, 15, and 20 wt%. The reactor temperature was set at 500 ˚C which was similar to the condition for maximum bio-crude oil yield of woody biomass. The bio-crude oil yields were 50.73, 51.45, 52.38, and 53.65 wt% for the mixing ratios of 5, 10, 15, and 20 wt%, respectively. The higher heating values of the bio-crude oil were 18.72, 19.61, 20.37 and 21,65 MJ/kg, which increased with the polystyrene mixing ratio. It was found that the bio-crude oil quality can be improved by mixing polystyrene.

Keywords: co-pyrolysis, wood, polystyrene, bio-crude oil quality

1 INTRODUCTION

Biomass is considered to be one of the sustainable energy sources suppressing the global climate change because the carbon emitted when plants are burned is equal to that absorbed during growing, which is called carbon neutral. There are several ways to utilize biomass as an energy source, such as direct combustion, gasification, liquefaction, and torrefaction. Among them the fast pyrolysis technology is a thermochemical process to convert solid biomass into a liquid fuel known as bio-crude oil or bio oil [1-4]. In about $500^{O}C$ with no oxygen inside fast pyrolysis reactor, biomass particles are quickly decomposed into three components; the volatiles, the non-condensable gases, and the char. When the volatiles are cooled by chiller quickly, they are condensed to liquid phase fuel, that is, bio-crude oil. Bio-crude oil has an advantage of cost reduction for storage and transportation in comparison to the original solid biomass, because it is a liquid material with high density. Bio-crude oil can be directly used as fuel for furnaces or boilers and indirectly used as feedstock for transportation fuel such as gasoline and diesel. But it has been pointed out that bio-crude oil has some unsatisfactory quality to be improved for its wide utilization, for instance, low calorific value, high oxygen fraction and high water contents. Co-pyrolysis of biomass and plastic waste in the fast pyrolysis reactor has been studied to produce the improved bio-crude oil during pyrolysis reaction [5-7]. Most plastics have high calorific value of about 35MJ/kg, because they are composed with carbon and hydrogen mainly and with negligible amount of oxygen. If biomass and plastic were co-pyrolysed under optimal operating conditions like temperature, mixing ratio, and feeding ratio, the bio-crude oil could be substantially improved to have high calorific value with low oxygen. In this study co-pyrolysis of woody biomass and polystyrene (PS) foam was performed to produce bio-crude oil in a bubbling fluidized bed reactor, and the bio-crude oil yield and characteristics are compared at various mixing ratios.

2 MATERIALS AND METHODS

2.1 Feedstock for fast pyrolysis

PS foam waste was used as plastic feedstock, while sawdust of Douglas fir as biomass feedstock in this study. PS foam is one of the most commonly used plastic in daily life as well as in industrial activity, for instance, as shock-absorbing packing materials and insulation materials, etc. With its consumption increased rapidly, large amount of PS foam wastes are also generated seriously and it becomes an urgent issue world-widely how to treat these wastes with economically and environmental friendly method. PS foam has much

higher volume than other plastic waste, which causes higher treating cost than others. Material recycling is known as successful treatment way, but this method can be used for only clean PS foam wastes. When PS foam waste is thrown away from many houses and factories, most of them are turned dirty due to careless and unconscious littering. New technology for treating PS foam waste is urgently required from many countries to reduce handling cost as well as to recover its potential values economically and eco-friendly. Sawdust of Douglas fir wood, meanwhile, was used for biomass feedstock in this study, because it is one of the most common trees used for furniture and construction materials all over the world.

PS foam waste was collected from general house and it was shredded to 2~4mm by the shredder in order to improve the mixing effect with Douglas fir sawdust. Figure 1 shows PS foam waste and shredded sample. The proximate and ultimate analysis of PS foam waste was carried out and the result was compared with Douglas fir sawdust. A proximate analysis was carried out using a TGA 701 LECO in accordance with ASTM D5142. A bomb calorimeter (LECO AC-350) was employed to measure the higher heating value (HHV) in accordance with ASTM D2015. The element analysis was performed by the Flash EA 1112 series. Bulk density of shredded PS foam waste was about 10~45Kg/m^3 and this is so low value that it was not mixed with Douglas fir sawdust uniformly in the feeding hoper. To solve this problem, the shredded PS foam waste was heated to reduce its particle size, which results in the bulk density increase up to 340kg/m^3. Table 1 shows the properties of sawdust and dried PS foam waste.

Figure 1.PS Foam Waste(left) and Shredded PS Foam(right)

Table 1. Proximate and Ultimate analysis data of sawdust and dried Polystyrene foam

	Moisture (wt%)	Volatile (wt%)	Ash (wt%)	Fixed Carbon (wt%)	Bulk density(kg/ m^3)
Sawdust	0.24	80.57	0.34	18.85	242
PS foam	0	99.94	0.06	0	340
	N (wt%)	C (wt%)	H (wt%)	O (wt%)	S (wt%)
Sawdust	0	50.75	6.28	42.97	0
PS foam	0.3	90.10	8.75	0.85	0

Apparent differences between sawdust and PS foam were found in those proximate and ultimate analysis data. The fixed carbon of sawdust was 18.85%, while PS has no fixed carbon. This means that PS foam doesn't produce pyrolysis char. The oxygen content of sawdust was 42.97%, while PS has only 0.85%. This data implies that PS bio-crude oil might have much higher heating value than that of sawdust.

Table 2 shows proximate and ultimate analysis data of sawdust and PS mixture with 4 different mixing ratio.

Table 2. Proximate and Ultimate analysis data of sawdust and dried Polystyrene Mixture

	Moisture (wt%)	Volatile (wt%)	Ash (wt%)	Fixed Carbon (wt%)	
BCO-PS 5(%)	30.08	58.87	1.4	9.65	
BCO-PS 10(%)	31.51	56.82	1.55	10.12	
BCO-PS 15(%)	27.58	60.11	1.81	10.5	
BCO-PS 20(%)	27.67	64.7	0.83	6.8	
	N (wt%)	C (wt%)	H (wt%)	O (wt%)	S (wt%)
BCO-PS 5(%)	0.73	45.46	7.5	46.31	0
BCO-PS 10(%)	0.77	46.58	7.57	45.08	0
BCO-PS 15(%)	0.99	50.05	7.67	41.29	0
BCO-PS 20(%)	1.19	51.47	7.66	39.68	0

2.2 Experimental method

Co-pyrolysis of two feedstock mixture was carried out in a bubbling fluidized bed reactor(BFBR) illustrated by a process schematic Figure 2 described in detail in previous studies [8-10]. The reactor chamber is cylindrical and SUS 316 with an inner diameter and height of 0.1 and 0.4 m respectively. Sand with average particle size of diameter 0.78 mm, bulk density of 1382 kg/m^3 and voidage fraction of 0.43 was used as the fluidizing material. The total sand weight used in the experiment was 1.45 kg which resulted in a sand bed height of 0.12 m. The flow rate of nitrogen gas was controlled at 25LPM with flow meter, and it was supplied to BFBR through the electric heater after being heated up to the reaction temperature. Superficial velocity of nitrogen gas in the reactor was 0.1 m/s on that condition to be utilized for sand fluidizing within the regime of bubbling fluidization. The vapour residence time was 1–2 seconds. Various mixing ratios of two feedstocks were fed into the reactor by a two stage screw feeder at a feeding rate of 200 g/hr. The condenser unit comprised of a graham condenser unit to collect the bio-crude oil was cooled by a chiller. An cylinder type electrostatic precipitator was used to trap fine oil mist from receding volatile gas, after the condenser phase.

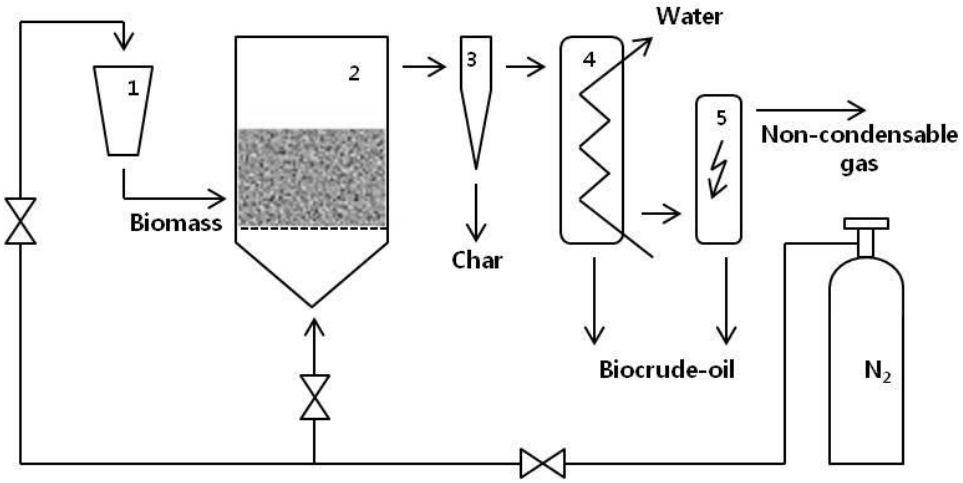

Figure 2. Schematic diagram of the fluidized bed reactor: (1) Biomass hopper (2) Fluidized bed reactor (3) Cyclone (4) Graham condenser (5) Electrostatic precipitator.

3 RESULTS AND DISCUSSION

3.1 Bio-crude oil yield

Figure 3 shows the yield change of bio-crude oil, char, and non-condensible gas according to PS mixing ratio variation. It was found that the bio-crude oil and char yields increased with PS mixing ratio, while the non-condensible gas yield decreased with increasing PS mixing ratio. Because the bio-crude oil yield increased monotonically with the PS mixing ratio, it is thought that larger mixing ratios needs to be tested to find out whether the maximum bio-crude oil yield is found.

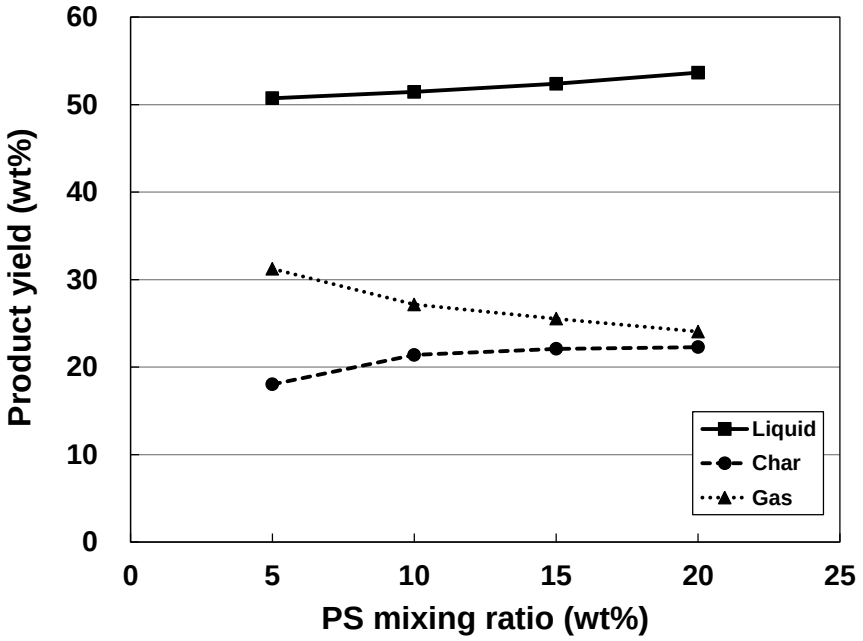

Figure 3. Product yields at various PS mixing ratios

3.2 Property analysis of bio-crude oil

Physicochemical properties analysis including water content and viscosity was conducted for the bio-crude oil produced from two feedstocks mixed with various ratios. The water content was measured by a Karl-Fisher titrator (870 KF Titrono plus) following ASTM D1744, and the viscosity was measured by a viscometer (Brookfield, Model DV-II+Pro). Table 3 shows the higher heating value (HHV) and water content of 4 different mixing ratio of sawdust and PS mixture. As PS mixing ratio increased, high heating value increased and water content decreased. These results indicate that PS mixing can improve the bio-crude oil quality.

Table 3. Physico-chemical properties of bio-crude oil produced from various sawdust/PS mixture

	High Heating Value (MJ/kg)	Water content (%)
BCO-PS 5	18.72	17.38
BCO-PS 10	19.61	17.07
BCO-PS 15	20.37	15.31
BCO-PS 20	21.65	13.81

4 CONCLUSIONS

Co-pyrolysis of woody biomass and waste polystyrene was performed in a bubbling fluidized reactor. The waste polystyrene foam was shredded and heated to decrease the particle size and to increase the bulk density. This pre-processing of waste polystyrene foam improved its feeding characteristics. The product

yields and the properties of bio-crude oil are compared at various polystyrene mixing ratios. It was found that the bio-crude oil yield and heating value increased with polystyrene mixing ratio, which implies that polystyrene mixing could be a useful option for the purpose of improve the quality of woody bio-crude oil. A more detailed analysis is needed for the bio-crude oil characteristics such as viscosity, solid residue, pH, etc. as a future work.

ACKNOWLEDGEMENTS

This work was supported by the "Technology development for biocrude-oil production by fast pyrolysis combined with stabilization procedure and green gasoline production" project of the Creative Convergence research Project (CAP) program under the auspices of the National Research Council of Science & Technology (NST). The authors gratefully acknowledge this support.

REFERENCES

[1] A. V. Bridgwater, D. Meier, D. Radlein, An overview of fast pyrolysis of biomass, *Organic Geochemistry*, Vol. 30, pp. 1479–1493, 1999.
[2] D. Mohan, C. U. Pittman, Jr., P. H. Steele, Pyrolysis of wood/biomass for bio-oil: A critical review, *Energy & Fuels*, Vol. 20, pp. 848–889, 2006.
[3] A. V. Bridgwater, Review of fast pyrolysis of biomass and product upgrading, *Biomass and Bioenergy*, Vol. 38, pp. 68–94, 2012.
[4] L. Qiang, L. Wen-Zhi, Z. Xi-Feng, Overview of fuel properties of biomass fast pyrolysis oils, *Energy Conversion and Management*, Vol. 50, pp. 1376–1383, 2009.
[5] P. Bhattacharya, Wood/plastic copyrolysis in an auger reactor: Chemical and physical analysis of the products, *Fuel*, Vol. 88, pp. 1251-1260, 2009.
[6] F. Abnisa, Co-pyrolysis of palm shell and polystyrene waste mixtures to synthesis liquid fuel, *Fuel*, Vo;. 108, pp. 311-318, 2013.
[7] M. Brebu, Co-pyrolysis of pine cone with synthetic polymers, *Fuel*, Vol.89, pp.1911-1918, 2010.
[8] J. P. Bok, H. S. Choi, Y. S. Choi, H. C. Park, S. J. Kim, Fast pyrolysis of coffee grounds: Characteristics of product yields and biocrude-oil quality. *Energy*, Vol. 47, pp. 17-24, 2012.
[9] Y. W. Jeong, S. K. Choi, Y. S. Choi, S. J. Kim, Production of biocrude-oil from swine manure by fast pyrolysis and analysis of its characteristics, *Renewable Energy*, Vol. 79, pp. 14-19, 2015.
[10] R. Soysa Y. S. Choi, S. J. Kim, S. K. Choi, Fast pyrolysis characteristics and kinetic study of Ceylon tea waste, *International Journal of Hydrogen Energy*, Vol. 41, pp. 16436-16443, 2016.

CHARACTERIZATION OF THE BIODIESEL PRODUCTION POTENTIAL OF SEWAGE SLUDGE

O.K. Choi and J.W. Lee†

Department of Environmental Engineering, Korea University, Sejong 30019, Korea; email: jaewoo@korea.ac.kr

ABSTRACT

This study characterizes the biodiesel production potential of sewage sludge obtained from various wastewater treatment plants. Biodiesel was recovered via *in situ* transesterification of dried primary sludge (PS) and waste activated sludge (WAS). The average transesterifiable product (TP) yield from the PS was 12.1 %, which was 1.7 times greater than that of the WAS due to the higher lipid contents in the PS. The TP yield was similar for the various PS samples; however, it differed among the WAS samples, depending on the process configuration and solid retention time (SRT). The average fatty acids methyl esters (FAMEs) content in the TP was 54.2 and 40.1 % for PS and WAS, respectively. Saturated FAMEs of C16 and C18 were the predominant FAME components regardless of the sludge samples. Difference of FAME compositions in the biodiesel among WAS samples was associated with microbial community structure which highly depended on SRT condition.

Keywords: Sewage sludge, Biodiesel production potential, *in situ* Transesterification, FAMEs, Lipid contents

1 INTRODUCTION

Sewage sludge production has been steadily increased to date, and is expected to continuously increase in the future. For example, that in the US has increased from 6.5 million dry ton in 2000, to 7.5 million dry ton in 2010, and was predicted to increase to 8.0 million dry ton by 2020 (Sanin et al., 2011). In addition to US, annual production of sewage sludge in the European Union (EU) and Korea recently reached 10.1 and 0.5 million dry ton, respectively (U.S. EPA, 2016; LeBlanc et al., 2009; MOE, 2014). The management of sewage sludge has become more stringent, and in many countries sewage sludge has moved towards energy and resources recovery.

Of the many technologies for energy recovery from sewage sludge, biodiesel recovery has recently received more attention. The use of sewage sludge as an alternative feedstock could be very attractive, since the cost for raw feedstock accounts for approximately 70 ~ 85% of the overall biodiesel production cost (Hass and Foglia, 2005). According to Kargbo (2010), sewage sludge could be suggested as a cost-effective alternative feedstock for biodiesel, compared to the existing feedstock. Various forms of lipids present in the sewage sludge, including fats, oil and fatty acids, could be a potential source of biodiesel. The lipids (or triglycerides) and phospholipids fatty acids (PLFAs) in sewage sludge could be transformed via esterification into biodiesel (fatty acid methyl esters, FAMEs), remaining glycerol or water byproduct, as follows:

$$\text{Triglyceride} + \text{Alcohol} \rightarrow \text{Fatty Acid Methyl Ester (FAME)} + \text{Glycerol} \quad (1)$$

$$\text{Fatty acids} + \text{Alcohol} \rightarrow \text{Fatty Acid Methyl Ester (FAME)} + \text{Water} \quad (2)$$

The possibility of biodiesel recovery from sewage sludge has been demonstrated in the positive results of many studies (Mondala et al., 2009; Revellame et al., 2011; Choi et al., 2014). Moreover, many engineering approaches have been undertaken to enhance the productivity, or to overcome the problems in the recovery of biodiesel from sewage sludge: a sequential extraction and esterification using various solvents to enhance the biodiesel yield (Dufreche et al., 2007); development of an in situ transesterification method to lower the water effect (Choi et al., 2014); and utilization of an enzymatic catalyst for sewage sludge with high free fatty acid content (Sangaletti-Gerhard et al., 2015). However, there has so far been little information made available on the characteristics of biodiesel linked to sewage sludge source, even though the properties of sewage sludge should be diverse, depending on the characteristics of the wastewater treatment plant (WWTP). The characteristics of biodiesel obtained from primary sludge (PS) and waste activated sludge (WAS) were noticeably different (Yi et al., 2016). It could be also different even in use of the same type of sludge, whether

PS or WAS, due to various factors. The properties of PS are most likely differentiated by the inclusion of industrial wastewater and the type of sewer system, whether combined or separated sewer. The properties of WAS may be more dependent on the process configuration and operating condition of the biological treatment process.

The goal of this study was to investigate the biodiesel potential (i.e. fatty acid methyl ester; FAME) in PS and WAS obtained from different WWTPs in Korea. Since the biodiesel potential in both quantity and quality could be substantially subject to the characteristics of the sludge, it is important to understand the major factors given to each WWTP that affect the biodiesel potential. The specific goals were 1) to estimate the lipid contents in sewage sludge obtained from various WWTPs, 2) to characterize the biodiesel potential by fractionating the recovered products obtained from in situ transesterification of the sewage sludge, and 3) to correlate the quantity and quality of FAME products with factors affecting the sludge characteristics, such as the sewer system, solid retention time (SRT), and microbial community structures, differently given to the WWTP candidates.

2 MATERIALS AND METHODS

2.1 Sewage sludge preparation

The PS and WAS were separately obtained from three different domestic WWTPs in Korea: 'J' in Seoul city, 'H' in Gangwon province, and 'D' in Daejeon city. Those plants were located apart by at least 100 km from each other. Except for 'D' WWTP, the PS and WAS samples were collected from the outlet pipe of the primary settler and the sludge return line in the biological process, respectively. Each sludge in 'D' WWTP was taken from the individual thickener, before mixing with each other. Two separate samples of PS and WAS were taken from each WWTP. The sludge samples were immediately transported to the laboratory in a refrigerated container, and then analyzed for moisture content (MC), total solids (TS), and volatile solids (VS), before drying in a furnace at 65°C for 90 hr (Willson et al., 2011). The dried sludge samples were stored in a desiccator, before conducting the experiments to estimate the lipid content and biodiesel potential. The WAS samples for microbial community analysis were centrifuged at 5,000 rpm, and the sludge pellets were preserved in a freezing refrigerator at -80°C. The moisture content of the dried sludge was kept at less than 5% for all samples. The TS and VS of the samples were determined as per Standard Methods (APHA, 2012).

Table 1. Summarized information about WWTP candidates where the sewage sludge samples were taken from

WWTP site	Influent Type	Biological Process	Solid Retention Time (d)
'J'	Domestic	MLE	15~20
'D'	Domestic	A2/O	4~10
'H'	Domestic	NPR	20~25

2.2 Analysis for lipid content

In order to identify the lipid content in the sewage sludge samples, the Bligh and Dyer extraction method, which is commonly used for biological sources, was used in this study (Iverson et al., 2001; Shin et al., 2014). 20 mL of a mixture of chloroform and methanol (2:1 volume ratio) was added to 1 g of the dried sludge. The chemical added sludge mixture was agitated for 15 ~ 20 min in an orbital shaker at 150 rpm under room temperature condition. The mixture was centrifuged at 2,000 rpm for 5 min. The liquid phase was washed with 4 mL of 0.9% NaCl solution, and then mixed by vortex, and centrifuged at 2,000 rpm for 2 min. The upper phase was discarded, and the lower chloroform phase containing lipids was separately collected. Chloroform was evaporated by a rotary evaporator (Bligh and Dyer, 1959).

2.3 In *situ* Transesterification

The in situ transesterification method used in this study was described in a previous study (Choi et al., 2014). 25 g of the dried sludge was added into a 500 mL reactor containing 250 mL of methanol solution and 100 mL of n-hexane. The methanol solution contained sulphuric acid at 5 % (v/v) as an acid catalyst. A condenser was connected to the top of the flask for recirculating the solvents. The reaction temperature and time were maintained at 55°C, 8 hr in a water bath. After the reaction ended, the mixture was cooled, and transferred into

a 500 mL separatory funnel. The mixture was separated by density into three phases: the top layer containing nonpolar miscible transesterifiable products (TP), such as fatty acid methyl esters (FAMEs) in n-hexane, the middle liquid layer containing byproducts of water soluble TP, and the bottom layer containing insoluble residual solids. The top layer (TP in solvent) was separately collected, and then treated by adding 100 mL of sodium chloride solution (2% water mass fraction) for salting-out of water miscible substances. After three times of the salting-out step, the remaining solvent was vaporized using a rotary evaporator at 50 °C under vacuum condition (R-124, Buchi, Switzerland), and the final TP samples were collected as crude biodiesel feedstock.

2.4 DNA extraction, PCR amplification and pyrosequencing analysis

In order to determine the relationship of the FAME yield and composition with the microbial community structure, microbial identification using pyrosequencing analysis was carried out for the WAS sample taken from the biological treatment process in each WWTP. After homogenizing the WAS sample, 1 g of pelleted samples was collected. Total DNA was extracted by using PowerSoil DNA kit (MoBio Laboratories, Inc., Carlsbad, USA), according to the manufacturer's instructions. PCR (PTC-200; Peltier Thermal Cyler, PharmaTech & GeneAmp, PCR System 9700) was conducted using 1 μL of extracted DNA under the following cycling condition: initial duration at 94°C for 5 min, 30 cycles at 94°C for 30 sec, 55°C for 45 sec, and final extension at 72°C for 90 sec. The products of PCR were used for pyrosequencing analysis. Pyrosequencing analysis was conducted by Roche/454 GC Junior system, following the manufacturer's instructions (Chun's Lab, Seoul, Korea). Raw sequence reads were sorted by unique barcodes. All linked sequences containing adaptor and linker were removed. Chimera sequences and low quality sequences, including low quality score (average < 25), or read lengths shorter than 300 base pair, were discarded. Thereafter, EzTaxon-e database (http://eztaxon-e.org) was used for the taxonomic assignment of each pyrosequencing read (Kim et al., 2012).

2.5 Analytical methods for biodiesel FAMEs

The extraction yield can be defined as the yield of the TP miscible in the nonpolar solvent of hexane through *in situ* transesterification:

$$\text{TP yield (\%)} = \frac{Mass\ of\ the\ TP\ in\ the\ solvent\ (g)}{Mass\ of\ dried\ solids\ in\ the\ sludge\ (g)} \times 100 \quad (1)$$

The total FAME in the nonpolar TP sample was determined by EN14103 method according to a procedure using internal calibration (nonadecanoic acid methyl ester). This method analysed using a gas chromatograph (GC) (Agilent 7890A, Agilent, USA) equipped with a mass selective detector (MSD, Agilent 5975C, Agilent, USA). Analytical conditions of GC/MS with carbowax capillary column (30 m x 0.32 mm x 0.25 μm) were as follows: both injector and detector temperatures were 250°C; the column temperature was programmed as the initial temperature of 60°C for 2 min; and then first increased to 200°C at 10°C /min, and subsequently to 240°C at 5°C /min, and then held for 7 min. The injection sample volume was 1 μL, and the split ratio was 1:50. Helium was used as a carrier gas, with a flow rate of 1 mL/min. The operating conditions for the mass spectrophotometer were electron multiplier of 1,200 V, and the interface an ion source temperature of 230°C. The FAMEs profiles and concentration were identified by comparison with a standard solution (37 comp. FAME mix, Supelco, USA) and NIST 2008 Libraries installed in GC/MS. The FAMEs content was defined as the percentage of FAMEs in the TP, and was determined as follows:

$$\text{FAME content (\%)} = \frac{(\sum A) - A_{EI}}{A_{EI}} \times \frac{C_{EI} \times V_{EI}}{m} \times 100 \quad (2)$$

where, ΣA is the total peak area, A_{EI} is the peak area that corresponds to nonadecanoic acid methyl ester, C_{EI} is the concentration of the nonadecanoic acid methyl ester solution (mg/mL), V_{EI} is the volume of nonadecanoic acid methyl ester (mL), and m is the injection mass of sample (mg).

3 RESULTS AND DISCUSSION

3.1 Lipid content and biodiesel production potential sewage sludge

Most of the information, except the SRT, was obtained from the official website. Information about the SRT could be obtained by contacting the facility operator of each WWTP. Contents of the solids (TS and VS) were similar between 'J' and 'H' sludge samples; however, 'D' sludge taken from the thickener had approximately two times higher solid content than the other two WWTP sludges. Nevertheless, the VS content (VS/TS) among all sludge samples were similar in the range from 76.5 to 87.1%, regardless of the WWTP.

The lipid content was in a relatively narrow range between 14.0 and 16.8 % for the PS from all WWTPs. That of the WAS was slightly lower than that of the PS; however, it was also in the narrow range between 10.9 and 11.7%. Nevertheless, the lipid content of the PS seemed to have a larger variation by country than that of the WAS: the average lipid content in the PS and WAS from domestic WWTPs was 7~35% and 5~12%, respectively (Metcalf and Eddy, 2003; Willson et al., 2010, Siddiquee et al., 2011; Olkiewicz et al., 2012). The reason for the large variation of the lipid contents of the PS among countries was little reported, but it was suspected that oil consumption and residue in the kitchen wastewater affect the lipid content in the incoming sewage. Based on the FAO report, European people consumed (164 g/d/cap) two times more fat than did Korean (86 g/d/cap) (FAO, 2010). Different from the PS, the regional difference between Korea and Europe for the lipid content of WAS did not look significant, which represents that the lipid content of the WAS was more dependent on the characteristics of the biological treatment process.

3.2 Biodiesel production potential of sewage sludge

The lipid in the sewage sludge could be distinguished into three fractions: FAMEs, non-FAME transesterifiable lipids, and non-transesterifiable lipids. The sum of the former two fractions was defined as the TP obtained from in situ transesterification. The fraction of TP, i.e. sum of FAMEs and non-FAME transesterifiable lipids, of the PS for three WWTPs varied in the range between 71 and 81%, representing that a relatively large portion of the lipids in the PS had the potential to be transesterified. The fraction for FAMEs of the PS was about half that of the TP, accounting for 36 ~ 41% of the total lipids content. Whereas, the TP yield of the WAS was lower than that of the PS, accounting for 52 ~ 67% of the total lipid content. The FAME fraction of the total lipid content in the WAS varied from 12 to 32%. This result indicates that the waste oil and lipids present in the PS were more readily extractable and convertible into FAME, than were microbial phospholipids in the WAS.

The conversion of microbial phospholipids into TP could be affected by various operating factors, typically such as the SRT condition of the biological treatment process of many operating factors, the content and composition of phospholipids in microbial cell membrane could typically be dependent on the SRT condition (Akarsubasi et al., 2009). Even though the lipid content of the WAS for the three WWTPs was similar each other in the range from 10.9 ~ 11.7%, the TP yield appeared to increase as the SRT increased. This means that the TP conversion efficiency was evidently dependent on the physiological state of microorganisms, i.e. microbial age, and might be less decomposable or more persistent to the chemical reaction of transesterification under shorter SRT condition, due to a stronger cellular membrane structure (Gossett and Belser, 1982).

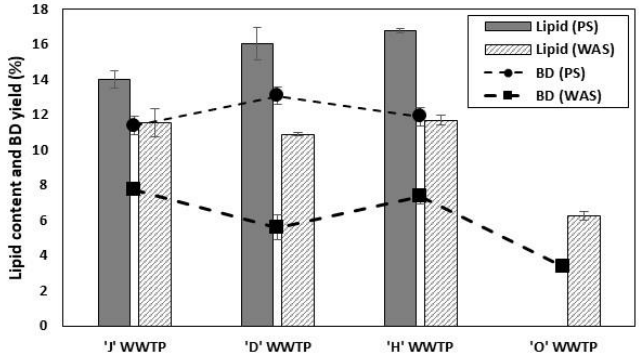

Figure 1. Comparisons of lipid contents and biodiesel production potential between PS and WAS

3.3 Evaluation of biodiesel quality as FAMEs composition

The PS had a markedly greater biodiesel potential in terms of the total FAME content than the WAS, as aforementioned. Among the whole FAME distributions, saturated FAMEs, such as C16 (21.49%) and C18 (9.43%), were predominantly found in both the PS and WAS samples; whereas, the proportions of the unsaturated FAMEs of C16:1 were predominantly higher in the WAS than the PS. The ratio between saturated and unsaturated FAMEs can influence the fuel quality of biodiesel. Higher contents of saturated and unsaturated FAMEs were associated with better burning properties, and better fluidity under cold temperature conditions, respectively (Knothe, 2005; Kenesey and Ecker, 2003). The optimal ratio between the saturated and unsaturated FAME has not yet been clarified; however, in the use of existing biodiesel feedstocks, such as palm oil or beef tallow, it was in the range between 0.1 and 2 (Ramos et al., 2009; Singh and Singh, 2010). The FAMEs from the WAS of 'J' and 'D' WWTPs were included in this range.

3.4 Effect of microbial community structure on FAMEs recovered from WAS

The total qualified reads of 13,367 were assigned to 53 formally described bacterial phyla in all of the WAS samples. The average microbial composition for all the WAS samples was in the order of *Proteobacteria* (48.81%), *Bacteroidetes* (26.11%), and *Nitrospirae* (6.59%). This composition was comparable with that of the other study, where *Proteobacteria* (57.30%) and *Bacteroidetes* (26.60%) were also dominant microbial groups (Mondala et al., 2011). The WAS samples from 'J' and 'D' WWTP exhibited a very similar microbial community distribution, whereas that of 'H' WWTP showed a noticeable difference in bacterial community structure, particularly in *Proteobacteria*, *Bacteroidetes* and *Nitrospirae*. Instead of a lower *Proteobacteria* content, the *Bacteroidetes* and *Nitrospirae* content in the WAS of 'H' WWTP was comparatively high, accounting for 30.97% and 11.59% of the total microbial group in phylum level, respectively (Fig. 4). The greater presence of *Bacteroidetes* and *Nitrospirae* was most likely associated with the type and condition of biological treatment process adopted in that plant. The NPR process being operated in 'H' WWTP is a biological nutrient removal process using suspended bio-media, which is commonly applied for supporting the slowly growing microorganisms such as *Bacteroidetes* and *Nitrospirae* under longer SRT condition (Pala-Ozkok et al., 2013). Although this study did not elucidate clear correlation of biodiesel productivity and quality with microbial community structure in WAS, the results obtained in this study did indicate that the quantity and quality of FAME as a biodiesel source could be dependent on the microbial communities.

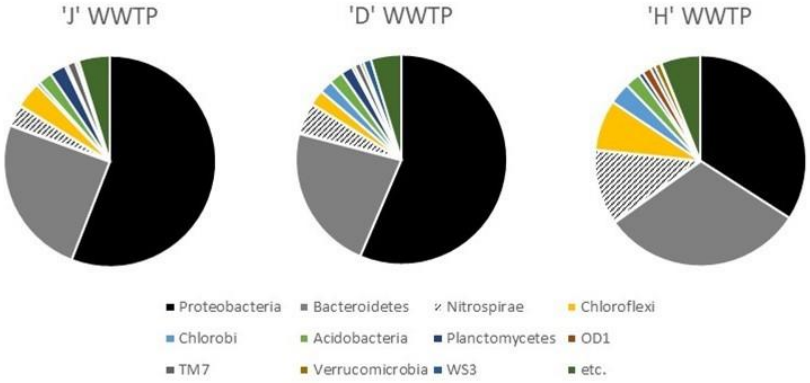

Figure 2. Comparisons of microbial community structures of WAS in each WWTP

4 CONCLUSION

In investigation of biodiesel potential from sewage sludge, both PS and WAS contained an extractable amount of lipids, which was efficiently transesterifiable into FAMEs. In terms of biodiesel productivity, PS was more feasible as a biodiesel feedstock than WAS, due to its high lipid contents. FAME production and composition from WAS was more dependent on the microbial community structure affected by SRT condition. Sewer system and SRT condition applied to WWTP should be considered in harnessing PS and WAS as a biodiesel feedstock, respectively.

ACKNOWLEDGEMENTS

This work was supported by the National Research Foundation of Korea (NRF) grant funded by the Korea government (MSIP) (NRF-2017R1A2B4012101) and Korea Ministry of Environment (MOE) as "Waste to Energy and Recycling Human Resource Development Project".

REFERENCES

[1] A. Mondala, K. Liang, H. Toghiani, R. Hernandez, T. French, Biodiesel production by in situ transesterification of municipal primary and secondary sludges. Bioresource Technology, Vol. 100, pp. 1203-1210, 2009.

[2] A. Mondala, R. Hernandez, T. French, L. McFarland, J.W. Santo Domingo, M. Meckes, H. Ryu, B. Iker, Enhanced lipid and biodiesel production from glucose-fed activated sludge: kinetics and microbial community analysis. AIChE. Journal, Vol .58, pp. 1279-1290, 2011.

[3] D.M. Kargbo, Biodiesel Production from Municipal Sewage Sludges. Energy and Fuels, Vol. 24, pp. 2791-2794, 2010.

[4] E.G. Bligh, W.J. Dyer, A rapid method of total lipid extraction and purification. Canadian Journal of Biochemistry and Physiology, Vol. 37, pp. 911-917, 1959.

[5] E. Metcalf, M. Eddy, Inc., Wastewater engineering, Treatment and reuse. New York, McGraw-Hill, 2003.

[6] E. Kenesey, A. Ecker, Oxygen connections to the improvement of the lubricity in fuels. Tribol. Schmierungstech, Vol 50, pp. 21-26, 2003.

[7] E. Revellame, R. Hernandez, W. French, W. Holmes, E. Alley, R. Callahan, Production of biodiesel from wet activated sludge, Journal of Chemical Technology and Biotechnology, Vol. 86, pp. 61-68, 2011.

[8] G. Knothe, Dependence of biodiesel fuel properties on the structure of fatty acid alkyl esters. Fuel Process Technology, Vol 86, pp. 1059-1070, 2005.

[9] H.Y. Shin, J.H. Ryu, S.Y. Bae, C. Crofcheck, M. Croker, Lipid extraction from Scenedesmus sp. Microalgae for biodiesel production using hot compressed hexane. Fuel, Vol. 130, pp. 66-69, 2014.

[10] I. Pala-Ozkok, A. Rehman, G. Kor-Bicakci, A. Ural, M.B. Schilhabel, E. Ubay-Cokgor, D. Jonas, D. Orhon, Effect of sludge age on population dynamics and acetate utilization kinetics under aerobic conditions. Bioresource Technology, Vol. 143, pp. 68-75, 2013.

[11] M.J. Haas, T.A. Foglia, Alternate feedstocks and technologies for biodiesel production. In The Biodiesel Handbook; Knothe, G.; Krahl, J.;Van Gerpen, J., Eds.; AOCS Press: Champaign, IL, pp. 42-61, 2005.

[12] M.J. Ramos, C.M. Fernandez, A. Casas, L. Rodriquez, A. Perez, Influence of fatty acid composition of raw materials on biodiesel properties. Bioresource. Technology, Vol. 100(1), pp. 261-268, 2009.

[13] M.N. Siddiquee, S. Rohani, Experimental analysis of lipid extraction and biodiesel production from wastewater sludge. Fuel Process Technology, Vol. 92, pp. 2241-2251, 2011.

[14] M. Olkiewicz, M.P. Caporgno, A. Fortuny, F. Stuber, A. Fabregat, J. Font, C. Bengoa, Direct liquid-liquid extraction of lipid from municipal sewage sludge for biodiesel production. Fuel Process Technology, Vol 128, pp. 331-338, 2014.

[15] O.K. Choi, J.S. Song, D.K. Cha, J.W. Lee, Biodiesel production from wet municipal sludge: Evaluation of in situ transesterification using xylene as a cosolvent. Bioresource Technology, Vol. 166, pp. 51-56, 2014.

[16] O.S. Kim, Y.J. Cho, K. Lee, S.H. Yoon, M. Kim, H. Na, S.C. Park, Y.S. Jeon, J.H. Lee, H. Yi, S. Won, J. Chun, Introducing Eztaxoneaz prokaryotic 16S rRNA gene sequence database with phylotypes that represent uncultured species. International Journal of Systematic and Evolutionary Microbiology, Vol. 62, pp. 716-721, 2012.

[17] R.M. Willson, Z. Wiesman, A. Brenner, Analyzing alternative bio-waste feedstocks for potential biodiesel production using time domain (TD)-NMR. Waste Management, Vol. 30, pp. 1881-1888, 2010.

[18] S.J. Iverson, S.L.C. Lang, M.H. Cooper, Comparison of the bligh and dyer and folch methods for total lipid determination in a broad range of marine tissue. Lipids, Vol. 36(11), pp. 1283-1287, 2001.

[19] S.P. Singh, D. Singh, Biodiesel production through the use of different sources and characterization of oils and their esters as the substitute of diesel: a review. Renewable and Sustainable. Energy Review, Vol. 14(1), pp. 200-216, 2010.

OPTIMIZATION AND MPC DESIGN FOR TWO STAGE ANAEROBIC DIGESTION FOR TEQUILA VINASSES TREATMENT

E. R. Piceno-Diaz[1], H.O. Mendez-Acosta[2], M. Gutierrez-Limon[1] and H. Puebla[1]

1. Departamento de Energia, Universidad Autonoma Metropolitana Azcapotzalco, Ciudad de México, MEXICO; email: enniopiceno@hotmail.com
2. CUCEI, Universidad de Guadalajara, Jalisco, MEXICO; email: hugo.mednez@cucei.udg.mx

ABSTRACT

In this work, a Nonlinear Model Predictive Control (NLMPC) strategy was applied to two-stage anaerobic digestion (AD) process, for the treatment of tequila vinasses. The AD process is divided into two bioreactors, being the first acidogenic and the second methanogenic, the main purpose of this configuration is to increase the activity of each bacterial community, and at the same time stability is improved. The proposed NLMPC uses the discretization of the AD model using OCFE (orthogonal collocation on finite elements). The nonlinear constrained optimization problem is solved using a simultaneous approach. The results show stable and good performance to reach the reference points and robustness to face perturbations in the inlet conditions.

Keywords: Biogas production, Two Stages Anaerobic Digester, Nonlinear Model Predictive Control.

1 INTRODUCTION

In the last decades, a great amount of physical, chemical and biological processes for wastewater treatment have been developed. Anaerobic digestion (AD) is one of the most attractive since it allows the degradation of organic matter with simultaneous production of biogas. Nevertheless, the sensibility of AD systems has been proved to be a challenge for maintaining high-efficiency processes because of the high nonlinearity nature, the limited availability of models for control purposes, uncertainties, not to mention that they are highly susceptible to inhibition, and their startup is very slow [7,12].

The two stages AD process has been presented by [13]. The main thesis of this work, consisted in that it is possible to provide optimal environments for each bacterial consortium so that their activity can be improved substantially and at the same time efficiency and stability are also improved. Since then, many researchers have investigated the convenience of separating the acidogenic from the methanogenic process [3,15,19].

Regarding control schemes applied to two stages AD processes, only a few works have been reported. The approaches found in literature encompasses from PID (proportional integral derivate), [18], multivariable nonlinear based on PDE (partial differential equations) model [2], non-linear passive control [5] to hybrid discrete-continuous control [10].

In recent years, model predictive control applied to chemical processes has been proved to be a good choice for complex nonlinear processes as several researchers [11,16,17] applied NLMPC algorithms for the case of continuous chemical reactors. Moreover, in what concerns to NLMPC algorithms applied to bioreactors and specifically for the case of anaerobic digesters, few works have been reported, and have been focused on the optimization of methane production and the productivity of product cells, usually using as manipulated variable the feed flow rate [4,16].

Based on the previous research of NLMPC applied to anaerobic digestion process, we propose in this paper an NLMPC approach for the continuous two-stage anaerobic digestion systems, based on a validated model for the control problem of regulation of COD.

2 MATERIALS AND METHODS

In this section, first, the case study and its mathematical model are described. Next, the NLMPC design is presented.

2.1 Two-stage AD of Tequila Vinasses.

The case study is reported by [14] and consists of two reactors. In the first reactor (Fig. 1) which is the acidogenic, only acidogenic bacteria is present, playing the role of degrading organic matter into carbon dioxide, methane and VFA's. In the second reactor which is methanogenic, both acidogenic and

methanogenic microorganisms are present. The former degrade VFA into acetic acid while the latter convert acetic acid into methane.

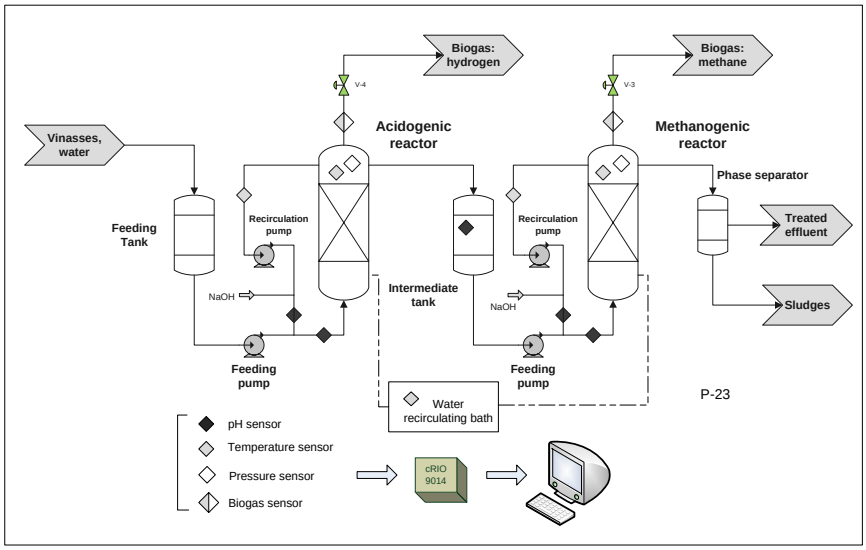

Figure 1. Flow diagram of the two-stage AD system applied for the treatment of tequila vinasses.

The two stages AD model [14] was developed for the isothermal treatment of tequila vinasses and is comprised of the following equations, from which the first three correspond to the acidogenic reactor, and the rest correspond to the methanogenic reactor.

$$\begin{bmatrix}\dot{x}_1(t)\\ \dot{x}_2(t)\\ \dot{x}_3(t)\\ \dot{x}_4(t)\\ \dot{x}_5(t)\\ \dot{x}_6(t)\\ \dot{x}_7(t)\end{bmatrix} = \begin{bmatrix}\mu_{1,1}(x_2)x_1\\ -\mu_{1,1}(x_2)x_1\\ \frac{k_2}{k_1}\mu_{1,1}(x_2)x_1\\ \mu_{1,2}(x_6)x_4\\ \mu_{2,2}(x_7)x_5\\ -\mu_{1,2}(x_6)x_4\\ \frac{k_5}{k_3}\mu_{1,2}(x_6)x_4 - \mu_{2,2}(x_7)x_5\end{bmatrix} + \begin{bmatrix}-\alpha_1 x_1 & 0\\ x_{2,ent}-x_2 & 0\\ x_{3,ent}-x_3 & 0\\ 0 & -\alpha_2 x_4\\ 0 & -\alpha_2 x_5\\ 0 & x_2 - x_6\\ 0 & x_3 - x_7\end{bmatrix}\begin{bmatrix}u_1\\ u_2\end{bmatrix} \quad (1)$$

With:

$$\mu_{1,1}(x_2) = \frac{\mu_{1,1\,max} x_2}{k_{s1,1}+x_2} \quad (2)$$

$$\mu_{1,2}(x_4) = \frac{\mu_{1,2\,max} x_4}{k_{s1,2}+x_4} \quad (3)$$

$$\mu_{2,2}(x_4) = \frac{\mu_{2,2\,max} x_7}{k_{s2,2}+x_7+\left(\frac{x_7}{k_{I2}}\right)^2} \quad (4)$$

Where x_1, x_4 represents the acidogenic biomass concentration (g/L) in the first and the second reactors respectively. The methanogenic biomass concentration (mmol/L) is represented by x_5, x_2, x_6, are the COD (g/L) while x_3, x_7, are the VFA concentrations in the acidogenic and methanogenic bioreactors respectively. $x_{2,ent}, x_{3,ent}$, are the process inputs of COD and VFA. The dilution rates at each bioreactor are represented by u_1, u_2, (d^{-1}). $\frac{k_2}{k_1}$, $\frac{k_5}{k_3}$, are relations between yield coefficients, (mmol VFA/g COD). α_1, α_2, represent the fraction of biomass that is not attached to the support and leaves the reactor. The maximum specific growth rate for each microbial community is represented by $\mu_{1,1,max}, \mu_{1,2,max}, \mu_{2,2,max}$, and $k_{s1,1}, k_{s1,2}, k_{s2,2}$ are the substrate affinity constants for each kind of kinetics, and also k_{I2} is the substrate inhibition constant associated with the methanogenic bacteria growth.

According to Fig. 1 the inlet flow to the acidogenic reactor (Q_{in}) must be the same of the outlet flow to the methanogenic reactor (Q_{out}), this is necessary to avoid reactor emptying, and biomass wash out. If β is the ratio between the volumes of both reactors (V_2/V_1) then the dilution rate of the acidogenic reactor (u_2) is related to the control input of the methanogenic reactor (u_1) by the following equations:

$$Q_{in} = Q_{out} = V_1 u_1 = V_2 u_2 \quad (5)$$

$$u_2 = \beta u_1 \quad (6)$$

This last relationship (6) has to be substituted in (1).

2.2 NLMPC.

The MPC may be described as a finite horizon open-loop optimal control problem that takes into account constraints. Based on measured or estimated states at the current time, it predicts future states and required control actions such that an objective function is minimized over a predefined horizon. Only the first of the predicted control actions is applied to the model, and new initial conditions for the next optimization sequence in the next sampling time are obtained, then the entire procedure is repeated.

The objective of NLMPC is to select a set of future control moves (over a control horizon, M), to minimize a function based on the desired output trajectory over a prediction horizon (N), this is done by solving the following optimization formulation:

$$\min_{u_t, u_{t+1}, \dots, u_{t+M-1}} \Phi(u) = \int_{t_i}^{t_i+T_N} e^2 dt = \sum_{i=1}^{N} \left[\left\| \hat{x}(t+i|t) - x_{t+i}^{ref} \right\|_Q^2 + \left\| u_{t+i} - u_{t+i}^{ref} \right\|_R^2 + \left\| \Delta u_{t+i} \right\|_S^2 \right] \quad (7)$$

Subject to:

$$\dot{x}(t) = f(t, x, u, p) \quad (8)$$

$$y = g(t, x, u, p) \quad (9)$$

$$x_{min} \leq \hat{x}(t+i|t) \leq x_{max} \quad (10)$$

$$u_{min} \leq u_{t+i} \leq u_{max} \quad (11)$$

$$\Delta u_{min} \leq \Delta u_{t+i} \leq \Delta u_{max} \quad (12)$$

Where x(t+i|t) is the predicted state, x_{t+i}^{ref} is the reference of the state, u_{t+i}^{ref} is the reference of the input, N is the prediction horizon over which future states are determined, and the objective function is minimized and M is the control horizon over which control actions are optimized, and Q, R, and S are weighting matrices. To be feasible, it is necessary that, and after the control horizon M, the control actions are kept constant. For convenience the objective function can also be formulated for the output variables directly:

$$\min_{u_t, u_{t+1}, \dots, u_{t+M-1}} \Phi(u) = \sum_{i=1}^{N} \left[\left\| g(\hat{x}(t+i|t)) - y_{t+i}^{ref} \right\|_Q^2 + \left\| u_{t+i} - u_{t+i}^{ref} \right\|_R^2 + \left\| \Delta u_{t+i} \right\|_S^2 \right] \quad (13)$$

To apply the NLMPC method, we have to discretize the set of ODE's given by (8). One method that has become convenient is the OCFE (orthogonal collocation on finite elements) method [8,9]. Thus in this work, we have used OCFE with three internal collocation points using Legendre polynomials. The discretized ODE's structure according to the number of finite elements has the following form,

$$\check{A}\check{X} = \Delta t' \check{F}(\check{X}, \check{U}) \quad (14)$$

where $\check{A}$ is a matrix formed by A and A_0 submatrices, and depends on the number of internal points of collocation. Matrix A contains the first-derivative weights at the collocation points, $\check{X}$ is the vector of discretized space states, $\check{F}$ is the function vector corresponding to each ODE and evaluated for each point of discretization and $\Delta t'$ is the variable change that accounts for sampling intervals other than 1. For more details about the OCFE method, the reader can consult [6,8,9]. So, to solve the optimization problem represented by (13), (8)-(12), it is necessary to replace (8) for (14).

3 RESULTS AND DISCUSSION

In this section, the control methodology described above is applied to the two-stage AD treating tequila vinasses. First, steady-state optimization results are presented. Next, we consider the effect of the prediction horizon and the effect of the sampling time concerning the length of the finite element in the NLMPC formulation. Finally, the NLMPC controller is tested against typical disturbances and setpoint changes.

3.1 Steady-state optimization results.

A static nonlinear constrained optimization of the two stages AD process was carried out using Matlab v.7 and its *fmincon* solver. The initial conditions were set as: [x_1, x_2, x_3, x_4, x_5, x_6, x_7] = [94.79, 27, 50, 23.2, 100, 10, 30].

The optimization problem solved was the minimization of COD at the methanogenic reactor outlet. The COD lower limit considered at the process outlet, was 0.75 g/l. The following results were obtained: $[x_1, x_2, x_3, x_4, x_5, x_6, x_7, u_1, u_2] = [154.52, 6.91, 120.31, 16.21, 312.70, 0.75, 7.02, 0.464, 0.232]$.

3.2 Programming of the NLMPC.

In the application of the NLMPC algorithm to our study case, the output variable is x_6 that is the COD at the outlet of the system of bioreactors and the manipulated variables is u_2, which is the dilution rate of the methanogenic reactor, so this is a SISO regulation problem. Simulation of the NLMPC algorithm was programmed in Matlab v.7 using simultaneous solving approach [1], and the *fmincon* function was used together with the choice of the *interior point method* instead of *SQP*. In all the simulations carried out, the initial conditions given for the steady-state optimization problem were used. In each simulation done, the results of the static optimization (16) were considered as starting points, this is before the controller was activated. Also, the constant values of the limits for (11) were $u_{min} = 0.05\ d^{-1}, u_{max} = 0.585\ d^{-1}$, obtained by simulating the model and selecting the maximum dilution rates before the appearance of biomass wash out.

3.3 Prediction horizon and sampling time effects.

First, we have considered the effect of the prediction horizon and the effect of the sampling time concerning the length of the finite element. The first two graphs in Fig 2. shows the effect of prediction horizons of 1, 8 and 15, using a sampling time (st) equal to 1 day. It is evident that after N=8 there is no change both in the input and the output. Moreover, the set point of 2.0 g/L of COD is reached relatively fast.

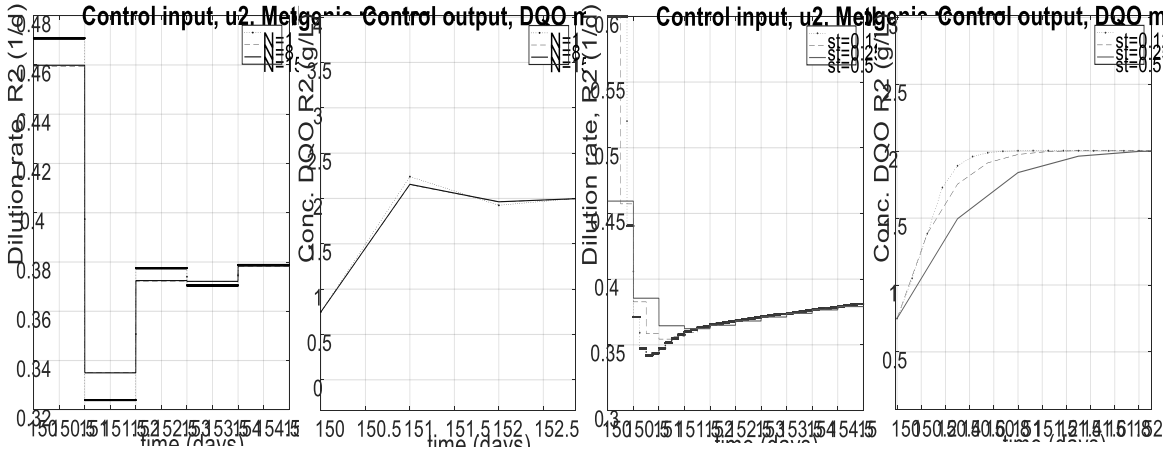

Figure 2. Effect of Horizon length and the sampling time in the input and control output

In the study of the effect of the sampling time (Fig. 2, right side graphs), we picked a prediction horizon of 8, and the sampling times (st) of 0.125 d, 0.25 d, and 0.50 d. The finite element length in each case was 0.25, 0.50 and 1.0 d. Regarding the NLMPC tuning, when the sampling time was chosen very small, the controller tends to saturate at different prediction horizons. On the other hand, the results were not entirely different when various prediction horizons were tested. Therefore, the effect of the sampling time was more important than the effect of the prediction horizon, so good results were obtained using prediction horizon of 8 and sampling time of 0.5 d, because using a lower sampling time tends to saturate the input.

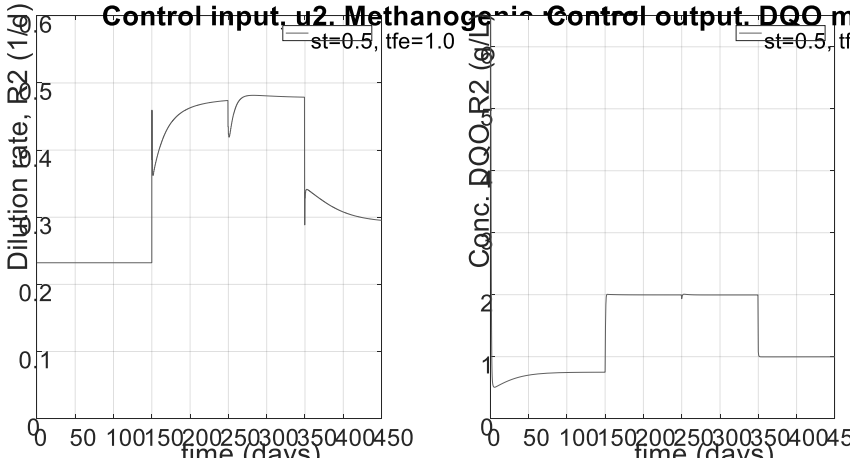

Figure 3. Control performance of the NLMPC.

3.4 Control performance.

The NLMPC scheme was also tested in a simulation run of 450 days (Fig. 3 & Fig. 4) and in the first 150 days no control was applied, then after 150 days, the NLMPC is activated with an initial reference of COD of 2.0 d/L. Until 250 days of operation, suddenly a perturbation took place, consisting in a 20% increase in $x_{2,ent}$ and 20% decrease of $x_{3,ent}$. Afterward, when 300 days have passed a step change in the output's reference was required as it was changed from 2.0 to 1.0 g/L of COD. As seen in all figures the successful regulation of COD at the outlet of the methanogenic reactor is achieved and the most critical state when it comes to stability, the VFA concentration at the inlet of the methanogenic reactor behaves stably without overshoots. Also, no saturation of the controller occurs which is good to avoid the biomass wash out.

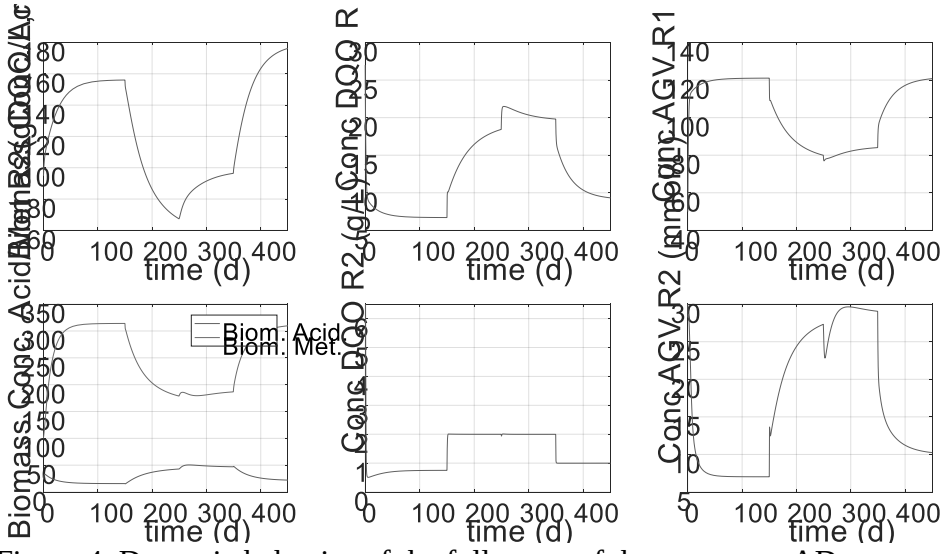

Figure 4. Dynamic behavior of the full states of the two-stage AD system.

4 CONCLUSIONS

A nonlinear model predictive controller was applied to a two-stage AD process in the presence of both disturbances in the organic load and user step changes. Results have shown a good performance to reach a desired stable state and robustness features against perturbations. Therefore NLMPC is a promising and useful tool to be applied to complex biological processes. Future research is required for the following issues: (i) Although good results were obtained, an assumption in this paper, is that the whole set of state variables is assumed to be known at any instant of time, this is a challenging situation to achieve because of the expensive instrumentation and other issues. So, the need for applying observers to obtain estimates of certain states arises. (ii) It is worth to explore the possibility of designing an MPC controller in which the measured state would be the VFA concentration to ensure at the same time that the COD is regulated because of the difficulty in determining the COD.

ACKNOWLEDGEMENTS

Ennio Piceno-Diaz acknowledge the financial support of CONACyT from a grant for master degree studies, and partial support of the UAM for supporting the participation in the SEEP 2018 conference.

REFERENCES

[1] P.S. Agachi, M.V. Cristea, A.A. Csavdari and B. Szilagyi, *Advanced Process Engineering Control*, Walter de Gruyter, 2017.

[2] E. Aguilar-Garnica, E., D. Dochain, V. Alcaraz-Gonzalez, A.K. Dramé and V. Gonzalez-Alvarez, COD and VFA's control in a two-phase anaerobic digestion process, IFAC Proc., Vol. 10, pp. 67-72, 2007.

[3] J. Arreola-Vargas, A. Flores-Larios, V. González-Álvarez, R.I. Corona-González and H.O. Méndez-Acosta, Single and two-stage anaerobic digestion for hydrogen and methane production from acid and enzymatic hydrolysates of Agave tequilana bagasse. *International Journal of Hydrogen Energy*, Vol. 41, pp. 897-904, 2016.

[4] S. Attar and F.A. Haugen, Simulation of a model-based predictive control system to optimize the methane production of a biogas reactor, *Proc. IEEE 11th Asian Control Conference*, 2017, pp. 1590-1595.

[5] V. Alcaraz-Gonzalez, D. Dochain and V. Gonzalez-Alvarez, Passive control of a Two-stages Anaerobic Digestion Process. In *XVI Congreso Latinoamericano de Control Automático*, 2014.

[6] B.A. Finlayson, *Nonlinear Analysis in Chemical Engineering*, McGraw-Hill Chemical Engineering Series, 1980.

[7] M. Henze, M. Van Loosdrecht, G. Ekama and D. Brdjanovic, *Biological Wastewater Treatment, Principles. Modelling and Design*, Cambridge University Press, 2008.

[8] B. Huang, Y. Qi and A.M. Murshed, *Dynamic modeling and predictive control in solid oxide fuel cells: first principle and data-based approaches*, John Wiley & Sons, 2013.

[9] B. Kouvaritakis and M. Cannon, Non-linear Predictive Control: theory and practice, The Institution of Electrical Engineers, 2001.

[10] H.O. Méndez-Acosta, A. Campos-Rodríguez, V. González-Álvarez, J.P. García-Sandoval, R. Snell-Castro, R. and E. Latrille, A hybrid cascade control scheme for the VFA and COD regulation in two-stage anaerobic digestion processes, *Bioresource Technology*, Vol. 218, pp. 1195-1202, 2016.

[11] A.A. Patwardhan, J.B. Rawlings and T.F. Edgar, Nonlinear model predictive control. *Chemical Engineering Communications*, Vol. 87, pp. 123-141, 1990.

[12] P.E. Poh, D. Gouwanda, Y. Mohan, A.A. Gopalai and H.M. Tan, Optimization of wastewater anaerobic digestion using mechanistic and meta-heuristic methods: current limitations and future opportunities, *Water Conservation Science and Engineering*, Vol. 1, pp. 1-20, 2016.

[13] F.G. Pohland and S. Ghosh, Developments in anaerobic stabilization of organic wastes: the two-phase concept, *Environmental Letters*, Vol. 1, pp. 255-266, 1971.

[14] C. Robles-Rodríguez, V. Alcaraz-González, J.P. García-Sandoval, V. González-Álvarez and H.O. Méndez-Acosta, Modelling and parameter estimation of a two-stage anaerobic digestion system for the treatment of tequila vinasses. In *Proc. Anaerobic Digestion Congress AD13*, Spain, 2013.

[15] A. Schievano, A. Tenca, S. Lonati, E. Manzini and F. Adani, Can two-stage instead of one-stage anaerobic digestion really increase energy recovery from biomass? *Applied Energy*, Vol. 124, pp. 335-342, 2014.

[16] R. Silva and W. Kwong, Nonlinear model predictive control of chemical processes, *Brazilian Journal of Chemical Engineering*, Vol 16, pp. 83-99, 1999.

[17] P.B. Sistu, B.W. Bequette, Nonlinear predictive control of uncertain processes: Application to a CSTR. *AIChE Journal*, Vol. 37, pp. 1711-1723, 1991.

[18] J. Von Sachs, U. Meyer, P. Rys and H. Feitkenhauer, New approach to control the methanogenic reactor of a two-phase anaerobic digestion system, *Water Research*, Vol. 37, pp. 973-982, 2003.

[19] E. Yazar, K. Cirik, S. Ozdemir, D. Akman, Y. Cuci and O. Cinar, Optimization of two-stage and single-stage anaerobic reactors treating cheese whey, *Journal of Engineering Sciences*, Vol. 19, pp. 25-36, 2016.

REMOVAL OF COPPER IONS FROM AQUEOUS SOLUTION USING LOW TEMPERATURE BIOCHAR DERIVED FROM THE PYROLYSIS OF MUNICIPAL SOLID WASTE USING HEAT PIPE BASED REACTOR

John Hoslett [a], Darem Ahmad [a], Hussam Jouhara [a]
[a]*College of Engineering, Design and Physical Sciences, Brunel University London, Uxbridge, Middlesex UB8 3PH, UK*

ABSTRACT

Sustainable methods to produce filter materials are needed to remove a variety of pollutants found in water including organic compounds, transition metals, and other harmful inorganic and biological contaminants. This study focuses on the removal of Cu(II) from solution by raw biochar derived from mixed municipal discarded material (MMDM). Preliminary findings indicate a Cu(II) adsorption capacity of at least 13mg/g. However, the perceived presence of organic compounds that interfere with the UV-Vis spectra of later experiments cast uncertainty on this result. The overall finding is that, whilst further experiments and analyses are required to quantitatively, prove the capability of the raw biochar derived from MMDM to remove Cu(II), and potentially organics from solutions.

Keywords: Adsorption, Biochar, Pyrolysis, Spectrophotometry

1. INTRODUCTION

Activated carbon (AC) has been used since ancient times in the world of medicine and water remediation, with seafarers using barrels with activated carbon in to store water on long voyages since 400BC [1]. Hippocrates at around the same period suggested water should be filtered through wood char to reduce bad tastes and odours and reduce the risk of contracting diseases such as anthrax [2]. In more recent times activated carbon has come to prominence as a filtration media due to stricter environmental regulations regarding drinking water and effluent water [2]. Activated carbon is commonly produced using pyrolysis temperatures >500 ^{o}C, and/or chemical activation using chemicals including Na_2CO_3, $CaCl_2$, $ZnCl_2$, and NaOH.

Typical temperatures of pyrolysis in general exceed 500 ^{o}C and an activation step involving either chemical, steam or high temperature activation is often employed to enhance the properties of a pyrolyzed substance. Some studies that report "Low temperature pyrolysis" involve temperatures around 500^{o}C [3–5], whilst other studies concerning low temperature pyrolysis consider temperatures of sub 350 ^{o}C [5,6]. Some studies show that for production of activated carbon towards the use as an adsorbent in water report higher pyrolysis temperatures >600 ^{o}C, and may also involve activation temperatures of 800 – 1000 ^{o}C [7].

Due to the polluting and finite nature of fossil materials, there is increasing emphasis on producing AC from sources that are more readily regenerated such as plant and discarded organic matter. Adsorption studies commonly isolate and pyrolyze a precursor material and study its ability to remove specific aqueous pollutants [8–11]. There is a lack of information available on AC for water filtration produced from mixtures of precursor materials. Studies that do consider municipal discarded material often pyrolyze at around 500^{o}C and use high temperature, steam, chemical or microwave activation [12]. Despite the lack of information regarding mixtures of municipal discarded material, there is a wealth of recent study regarding municipal, industrial and agricultural sewage sludge as a precursor [13–15] with these also commonly employing the same activation procedures listed already.

Heavy metals will be removed in greater amounts by an AC with a more highly negative surface charge due to electrostatic attraction between positive aqueous heavy metal ions and the surface [16]. However heavy metals such as copper may be effectively removed at pH values as low as 2.2 [16]. Additionally, at higher pH, insoluble complexes of transition metals such as $[Fe(H_2O)_3(OH)_3]$, $[Cu(H_2O)_4(OH)_2]$ form, so sorption by

biochar may not be a significant removal mechanism at pH values above 7. Studies have found that there is little increase in metal removal by chemisorption after pH 5 [17,18]. Additionally, Abdelhadi et al. [17] found that biochar had a high affinity towards heavy metal removal due to the presence of hydroxy, phenolic, carboxylic and methoxy functional groups even after pyrolysis at 350^{o}C. This indicates that some aqueous heavy metals may not need pyrolyzed material to be activated for effective removal. Other studies report favourable removal of transition metal ions with low temperature biochar.

1.1 Mixed municipal discarded material

Mixed municipal discarded material (MMDM) consists of all materials discarded by a household, this includes plastics, organic material, paper, metals, and other materials such as glass. Additionally the fractions of different materials present in MMDM varies between nations, and regions [19], with information provided by the world bank group [20] showing that more affluent nations tend to discard higher proportions of plastics and papers and lesser amounts of organic materials than less affluent nations. This shows the potential for pyrolysis to be used to produce biochar and activated carbon from MMDM, where potential biochar precursors make up >70% of MMDM in all the income levels presented in.

However, studies on mixed municipal discarded material (MMDM) are required to assess the capability of it to be pyrolyzed and used as an aqueous filtration media. Any use of MMDM would need to be more efficient and have a lesser environmental footprint than those procedures currently used by an entity. This study used low temperature (≈300 ^{o}C), biochar produced from MMDM as adsorbents and will assess their capability to remove the transition metal ion Cu^{2+} from solution in batch and filtration experiments.

2. EXPERIMENTAL SET-UP

Biochar was obtained from the Home Energy Resource Unit (HERU), this contained a mixture of plastic, meat, paper and other food waste such as bread. These were produced by pyrolysis temperatures of around 300 ^{o}C. The biochar was then crushed by pestle and mortar so that all material passed through a 3mm sieve, and none of the material used for the experiment passed through a 250 μm sieve.

0.00506 mol/l solution of Cu^{2+} ions was prepared by dissolving 0.633g $CuSO_4.5H_2O$ in 500ml distilled water. Once this solution had been prepared a 10ml sample was taken and 2ml of concentrated ammonia was added to produce the deep blue tetraamine copper sulphate complex. Once this first sample had been taken, 2g of the biochar was dosed into the solution and stirred magnetically. Every 80 minutes the magnetic stirrer was turned off to allow the biochar to settle, then a 10ml sample of the fluid was taken with 2ml concentrated ammonia being added as before. The sampling procedure was repeated every 80 minutes for during the first 6 hours and 2 final samples were taken after 24 hours and 24h +80mins.

3. ANALYTICAL TECHNIQUES USED FOR ANALYSIS

3.1 UV-Vis Spectroscopy

Different concentrations of the selected heavy metals will be made up to determine their elimination constants in UV-Vis spectroscopy, as well as the specific wavelengths they eliminate. Aqueous Co(II) has a characteristic transmission (λ_{max}) of around 550-560nm [21], Cu(II) has a λ_{max} of 455nm, and absorbance values of 880nm for $[Cu(H_2O)_6]^{2+}$, 380 and 880 nm for $CuCl_2$ dissolved in water [22,23]. Depending on the hydrolysis product Fe(III) has several absorbance values over the range 280-460nm, this could make the determination of Fe(III) concentration using UV-Vis potentially problematic [24], however, a reduction in concentration of Fe(III) is still anticipated for observation. Additionally, the Fe(III) could be made more easily identifiable through ligand exchange with thiocyanate ions.

It is assumed that the contaminants will follow Beers law seen in **Error! Reference source not found.** and **Error! Reference source not found.**. This assumes that absorbance is directly proportional to the concentration of the water contaminant. Different concentrations of each target ion will be made up and analysed using UV-Vis spectroscopy and plots of concentration against absorbance at selected absorbance

wavelengths will be produced. This will ascertain whether the assumption can be made. This assumption makes possible the determination of the concentrations seen in filtered water of different transition metal ions.

$$Log\left(\frac{I_0}{I}\right) = A \quad (1)$$

$$A = \varepsilon bc \qquad (2)$$

A = Absorbance, I_0 = initial light intensity at a given wavelength, I = measured light intensity at a given wavelength, ε = molar absorptivity, b = path length, c = concentration

Copper (II) sulphate

A previous study found that Cu(II) dissolved in distilled water had absorbance peaks between 205-230nm [25] as well as the absorbance peaks at 380 and 880nm identified in other literature [22,23]. However, at lower concentration lesser absorbance is observed. Therefore, an ammonia solution will be added to produce a deeper blue colour for easier concentration determination in UV-Vis spectroscopy [26]. The equations for which can be seen in **Error! Reference source not found.** and **Error! Reference source not found.**.

$$[Cu(H_2O)_6]^{2+} + 2NH_3 \rightarrow [Cu(H_2O)_4\,(OH)_2] + 2NH_4{}^{+} \qquad (3) \quad [27]$$

$$[Cu(H_2O)_6]^{2+} + 4NH_3 \rightarrow [Cu(NH_3)_4\,(H_2O)_2]^{2+} + 4H_2O \qquad (4) \quad [27]$$

Tetraamine copper sulphate

Table 1 - spectrophotpometry constants for teraamine copper

Copper (II) concentration	**260nm**		**610nm**	
	Molar absorptivity ($l{\cdot}cm^{-1}{\cdot}mol^{-1}$)	R^2	Molar absorptivity ($l{\cdot}cm^{-1}{\cdot}mol^{-1}$)	R^2
>0.004mol/l	51.23 (intercept=1.55)	0.81	47.21	0.99
<0.004mol/l	410.47	0.97	54.32	0.90

Table 1 shows molar absorptivity constants for $[Cu(NH_3)_4(H_2O)_2]^{2+}$ dissolved in water. At Cu(II) concentrations >0.004 mol/L the wavelength of 610nm was used to determine the concentration of copper in solution. This provides a better fit than the 260nm plot for the same concentrations. Conversely below 0.004 mol/L, the wavelength of 260nm was used to determine concentration as this returns a better fit than 610nm, but more importantly this wavelength is more sensitive to concentration below 0.004 mol/L.

4. RESULTS AND DISCUSSION

The preliminary experimental results using 40g/L biochar having an initial Cu^{2+} concentration of 1270mg/L, shown in **Figure 1**, indicate a favourable reduction of Cu^{2+} concentration by raw biochar produced from municipal waste. These, however, did not seem to fit any adsorption kinetic model well. Therefore, the follow up experiment was conducted using 4g/L biochar and 322mg/L initial Cu^{2+}. This was carried out to show, if any, an equilibrium concentration where the preliminary results didn't. However, as seen in **Figure 2** an increase in absorbance at 610nm and 260nm was observed, there are also significant increases at other wavelengths particularly around 310nm.

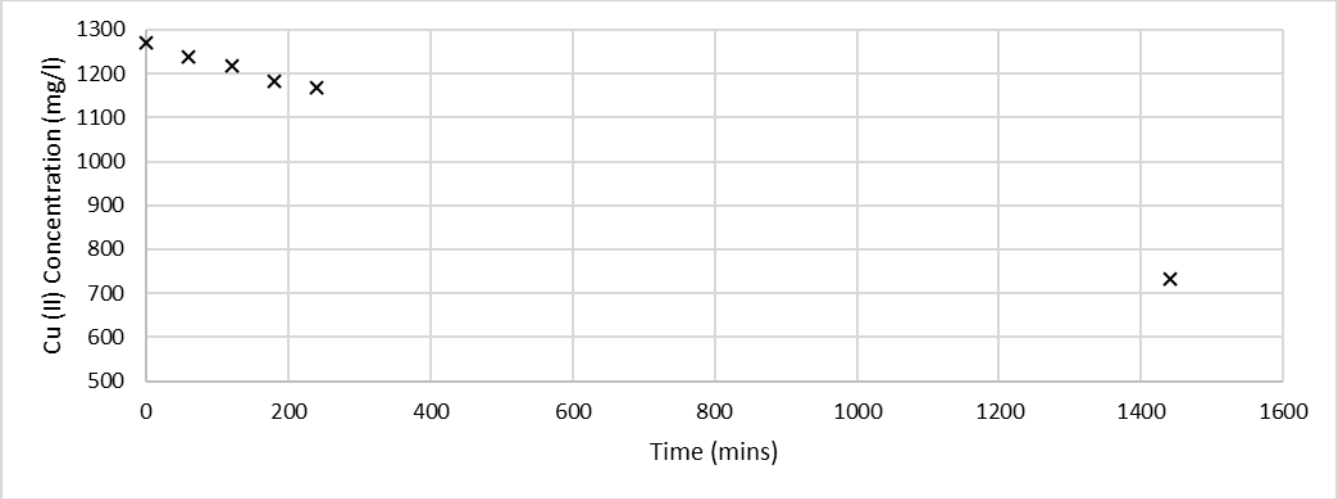

Figure 1 - The apparent reduction in concentration of Cu(II) by 40g/L biochar

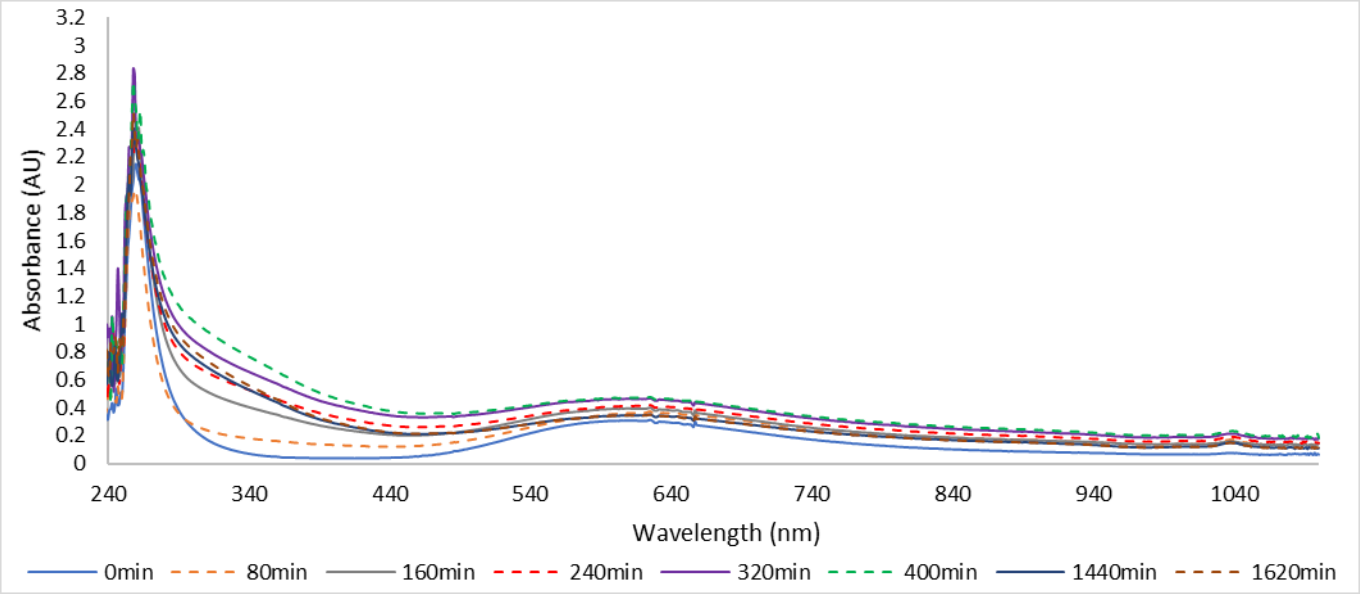

Figure 2 - UV-VIS spectra for samples taken after different times (0-400min magnetically stirred) for 4g/L biochar

Additionally, SEM-EDAX analysis showed little-no presence of copper in the biochar. Therefore, it is unlikely the biochar was leaching copper. It is however possible that the biochar was leaching organic compounds that provided a “background” in each sample. What can be seen is that with increased magnetic stirring time (0-400 mins), the “background” increases. The organics could potentially be remaining bio-oils and gases initially trapped in pores but released when a biochar particle breaks due to stirring [28]. Alternatively, it could be the case that the background is provided by soluble organic compounds that are originally bound to the surface of the biochar by weak intermolecular forces, being dissociated with agitation [29]. When left overnight, not being stirred (1440-1620 mins) there is a reduction in “background” this suggests that with increased stirring time, more organic compounds are released from virgin char. However, when agitation ceases, some of these compounds are re-adsorbed by the char.

This is an interesting development and highlights the need to investigate these organic compounds further to determine whether they are safe for human consumption. The aim of this project is to produce biochar that can be used to filter a wide range of pollutants from water that would otherwise remain in developing nations. The preliminary experiment proves the ability of raw biochar produced from municipal waste to remove copper and potentially other transition metals from water. However, the potential presence of organic compounds in the samples for 4g/L dosage of char casts uncertainty on the quantitative results for copper sorption. Further

analysis is therefore needed to determine the copper removal capability of the biochar, potentially using ICP-MS. Analysis is also needed to determine what soluble organics are present in raw municipal biochar to assess the risk they pose to human health. Further analysis is needed and will be conducted using ICP-MS for water samples, and SEM-EDAX for biochar, as well as stirring biochar in just distilled water. The SUVA technique employed by Constantino et al., [30] is also a method that will be used to assess aromaticity of organic compounds leached by biochar . The latter will provide the UV-Vis spectra produced by soluble organic compounds; these could then be subtracted from UV-Vis spectra for biochar in copper solution.

5. CONCLUSION

Raw biochar derived from mixed municipal waste can remove copper from solution, however, the quantitative results of this are yet to be identified. This will be completed using ICP-MS, SEM-EDAX as well as further UV-Vis spectrophotometry.

The results of the study indicate that it is indeed possible to produce filter material from mixed municipal discarded material, and that this material has an affinity to remove both transition metals and organics from solution. This will be investigated further with the intention of providing a method of production for effective granular filtration media in developing nations.

REFERENCES

[1] Carbon J. THE HISTORY OF ACTIVATED CARBON n.d. https://www.jurassiccarbon.com/blogs/news/12186281-the-history-of-activated-carbon (accessed January 29, 2018).

[2] González-García P. Activated carbon from lignocellulosics precursors: A review of the synthesis methods, characterization techniques and applications. Renew Sustain Energy Rev 2018;82:1393–414. doi:https://doi.org/10.1016/j.rser.2017.04.117.

[3] Xia W, Niu C, Ren C. Enhancement in floatability of sub-bituminous coal by low-temperature pyrolysis and its potential application in coal cleaning. J Clean Prod 2017;168:1032–8. doi:https://doi.org/10.1016/j.jclepro.2017.09.119.

[4] Meng F, Gupta S, Yu J, Jiang Y, Koshy P, Sorrell C, et al. Effects of kaolinite addition on the thermoplastic behaviour of coking coal during low temperature pyrolysis. Fuel Process Technol 2017;167:502–10. doi:https://doi.org/10.1016/j.fuproc.2017.08.005.

[5] Liu J, Chen L, Wang Y, Fu Y, Guo Y, Zhang Y. Studies of low-temperature pyrolysis characteristics of the binder cold-briquetted lignite-II: Three-phase pyrolytic products. J Energy Inst 2017;90:776–86. doi:https://doi.org/10.1016/j.joei.2016.06.006.

[6] Chang G, Miao P, Yan X, Wang G, Guo Q. Phenol preparation from catalytic pyrolysis of palm kernel shell at low temperatures. Bioresour Technol 2017. doi:https://doi.org/10.1016/j.biortech.2017.12.084.

[7] Menya E, Olupot PW, Storz H, Lubwama M, Kiros Y. Production and performance of activated carbon from rice husks for removal of natural organic matter from water: A review. Chem Eng Res Des 2018;129:271–96. doi:https://doi.org/10.1016/j.cherd.2017.11.008.

[8] Rashidi NA, Yusup S. Potential of palm kernel shell as activated carbon precursors through single stage activation technique for carbon dioxide adsorption. J Clean Prod 2017;168:474–86. doi:https://doi.org/10.1016/j.jclepro.2017.09.045.

[9] El Maguana Y, Elhadiri N, Bouchdoug M, Benchanaa M. Study of the influence of some factors on the preparation of activated carbon from walnut cake using the fractional factorial design. J Environ Chem Eng 2018;6:1093–9. doi:https://doi.org/10.1016/j.jece.2018.01.023.

[10] Enniya I, Rghioui L, Jourani A. Adsorption of hexavalent chromium in aqueous solution on activated carbon prepared from apple peels. Sustain Chem Pharm 2018;7:9–16. doi:https://doi.org/10.1016/j.scp.2017.11.003.

[11] Marques SCR, Mestre AS, Machuqueiro M, Gotvajn AŽ, Marinšek M, Carvalho AP. Apple tree branches derived activated carbons for the removal of β-blocker atenolol. Chem Eng J 2018. doi:https://doi.org/10.1016/j.cej.2018.01.076.

[12] Kumar V, Ganesapillai M. Preparation of Activated Carbon from Municipal Organic Solid Wastes.

Mater Today Proc 2017;4:10648–52. doi:https://doi.org/10.1016/j.matpr.2017.06.436.
[13] Al-Malack MH, Dauda M. Competitive adsorption of cadmium and phenol on activated carbon produced from municipal sludge. J Environ Chem Eng 2017;5:2718–29. doi:https://doi.org/10.1016/j.jece.2017.05.027.
[14] Li J, Xing X, Li J, Shi M, Lin A, Xu C, et al. Preparation of thiol-functionalized activated carbon from sewage sludge with coal blending for heavy metal removal from contaminated water. Environ Pollut 2018;234:677–83. doi:https://doi.org/10.1016/j.envpol.2017.11.102.
[15] Kaçan E, Kütahyalı C. Adsorption of strontium from aqueous solution using activated carbon produced from textile sewage sludges. J Anal Appl Pyrolysis 2012;97:149–57. doi:https://doi.org/10.1016/j.jaap.2012.06.006.
[16] Da'na E, Awad A. Regeneration of spent activated carbon obtained from home filtration system and applying it for heavy metals adsorption. J Environ Chem Eng 2017;5:3091–9. doi:https://doi.org/10.1016/j.jece.2017.06.022.
[17] Abdelhadi SO, Dosoretz CG, Rytwo G, Gerchman Y, Azaizeh H. Production of biochar from olive mill solid waste for heavy metal removal. Bioresour Technol 2017;244:759–67. doi:https://doi.org/10.1016/j.biortech.2017.08.013.
[18] Zhou Y, Gao B, Zimmerman AR, Fang J, Sun Y, Cao X. Sorption of heavy metals on chitosan-modified biochars and its biological effects. Chem Eng J 2013;231:512–8. doi:https://doi.org/10.1016/j.cej.2013.07.036.
[19] Jouhara H, Czajczyńska D, Ghazal H, Krzyżyńska R, Anguilano L, Reynolds AJ, et al. Municipal waste management systems for domestic use. Energy 2017;139:485–506. doi:10.1016/j.energy.2017.07.162.
[20] Group WB. Waste Composition 2012;2017. http://siteresources.worldbank.org/INTURBANDEVELOPMENT/Resources/336387-1334852610766/Chap5.pdf.
[21] Irvine) (University of California. VISIBLE SPECTROSCOPY 2014:1–7.
[22] Mannard ME. Magnesium and Copper (II) Chloride: A Curious Redox Reaction. Indiana University of Pennsylvania, 2013.
[23] RSC (Royal Society of Chemistry). Investigating Transition Metal Complexes 2009.
[24] Yeh M, Hahn RL. Spectroscopic Investigation of Ferrous, Ferric, and Manganese Ions in Aqueous Solution. 2001.
[25] Tan, C. H. (School of Physics USM, Moo, Y. C. (School of Physics USM, Matjafri, M. Z. (School of Physics USM, Lim, H. S. (School of Physics USM. UV Spectroscopy Determination of Aqueous Lead and Copper Ions in Water. SPIE Photonics Eur., Brussels: 2014, p. 1–6. doi:https://doi.org/10.1117/12.2052349.
[26] Wen T, Qu F, Li NB, Luo HQ. A facile, sensitive, and rapid spectrophotometric method for copper(II) ion detection in aqueous media using polyethyleneimine. Arab J Chem 2017;10:S1680–5. doi:https://doi.org/10.1016/j.arabjc.2013.06.013.
[27] Silava ND. (University of the P. DETERMINATION OF COPPER (II) CONCENTRATION BY COLORIMETRIC METHOD. Quezon City: 2010.
[28] Wang B, Zhang W, Li H, Fu H, Qu X, Zhu D. Micropore clogging by leachable pyrogenic organic carbon: A new perspective on sorption irreversibility and kinetics of hydrophobic organic contaminants to black carbon. Environ Pollut 2017;220:1349–58. doi:https://doi.org/10.1016/j.envpol.2016.10.100.
[29] Heitkötter J, Marschner B. Interactive effects of biochar ageing in soils related to feedstock, pyrolysis temperature, and historic charcoal production. Geoderma 2015;245–246:56–64. doi:https://doi.org/10.1016/j.geoderma.2015.01.012.
[30] Constantino C, Gardner M, Comber SDW, Scrimshaw MD, Ellor B. The impact of tertiary wastewater treatment on copper and zinc complexation. Environ Technol 2015;36:2863–71. doi:10.1080/09593330.2015.1050072.

INFLUENCES OF MELTING TEMPERATURE, MELTING ATMOSPHERE AND CARBON CONTENT IN THE BIO-CHAR ON THE MELTING CHARACTERS OF THE BIO-CHAR FORMED FROM OXYGEN-ENRICHED GASIFICATION OF REFUSED-DERIVED FUEL

Changqi Liu, Yaji Huang*, Lingqin Liu, Yongxing Wang, Lu Dong, Ligang Xu
Key Laboratory of Energy Thermal Conversion and Control of Ministry of Education, School of Energy and Environment, Southeast University, Nanjing 210096, China;
E-mail: heyyj@seu.edu.cn (Y. Huang)

ABSTRACT

Combination of oxygen-enriched gasification and high-temperature melting system to deal with waste is an effective technology to improve syngas quality and reuse the bottom ash and slag as road construction materials. The melting characteristics of the bio-char formed from oxygen-enriched gasification of refused-derived fuel in a fluidized bed were investigated in a high-temperature melting drop tube furnace with variations of melting temperature, melting atmosphere and carbon content in the bio-char. The results showed that the bio-char completely melted and flowed above 1250 ˚C in the reducing atmosphere and the homogeneous slag with few holes inside was produced. The densification of the slag improved with temperature increasing. The melting speed and melting degree in different atmospheres and at the same temperature ranked as follow: reducing atmosphere > inert atmosphere > oxidizing atmosphere. With lower carbon content in the bio-char, the slag began to completely melt at a lower temperature and the melting speed increased. The designed temperature of the high-temperature furnace should be higher than the flowing temperature of the ash formed from the combustible feedstock. The results can provide useful information to build a large-scale gasification system, combining oxygen-enriched gasification and high-temperature melting system, to deal with waste.

Keywords: Oxygen-enriched gasification; High-temperature melting system; Melting characters; Morphology

1 INTRODUCTION

Gasification is a promising technology to deal with waste and biomass, which can convert the feedstock to a mixture of combustible gases such as CO, H_2 and CH_4. The producer gas can achieve further use such as producing heat, electricity and chemical substances [1-3]. Air usually was regarded as gasification agent during gasification. However, dilution of nitrogen in the air can reduce the low heating value (LHV) of the syngas produced through gasification. Therefore, using oxygen as gasification agent can solve this issue and improve LHV of the syngas, however, the pure oxygen production required a high cost. In summary, using oxygen-enriched air as gasification agent not only save capital cost but also prompt the quality of syngas produced during gasification [4-5].

It is a serious issue hindering the gasification technology development that high tar content in the syngas leads to blocking problems of downstream equipment during gasification [6-8]. Many effective strategies were developed to reduce tar content in the syngas [8-11]. Our research group used two stages measures to deal with tar. Using high-alumina bauxite replacing silica sand as bed material could crack tar in the fluidized bed in the primary measure, the secondary measure was using high-temperature furnace as the high-temperature melting system to decompose the tar in the syngas. Using high-temperature melting system not only can reduce tar content in the syngas, but also can reuse bottom ash and slag as construction material though removing carbon, some heavy metal and other harmful organic matters in the bottom ash [12-13]. Therefore, uniting oxygen-enriched gasification and these two stages measure to reduce tar in the syngas is an effective way to produce clean syngas for further use.

The gasification performances using high-alumina bauxite as bed material and oxygen-enriched air as gasification agent were investigated in a lab-scale and a pilot-scale fluidized bed, respectively [4, 14]. The operating performance of the high-temperature melting system was not fully understood. Therefore, in this study, the influences of melting temperature, melting atmosphere and carbon content in the bio-char on the melting characteristics of the bio-char formed from oxygen-enriched gasification of refused-derived fuel. The

results can provide useful information for scaling up the combination of oxygen-enriched gasification and high-temperature melting system to deal with waste.

2 METHOD AND MATERIAL

2.1 Characteristics of bio-char

The bio-char was formed from oxygen-enriched gasification of refused derived fuel (RDF) in a polite-scale fluidized bed, which was described in reference [14].The properties of RDF is shown in Table 1 and the operating condition, in which the bio-char was produced, is presented in Table 2. The characteristic of bio-char can be seen in Table 3. It is observed from Figure 1 that the sizes of bio-char are not uniform and a lot of holes with different sizes located in the bio-char. The results show that the volatile of the RDF releases during oxygen-enriched gasification in the fluidized bed, which leads to form the holes in the bio-char. The carbon structure in the feedstock is complete and it indicates fewer carbons take part in reactions in this gasification condition.

Table 1. Properties of RDF

	Ultimate analysis (wt. %, ar)				Elemental analysis (wt. %, ad)					Low heating value (MJ/kg)
	M_{ar}	V_{ar}	FC_{ar}	A_{ar}	C_{ar}	H_{ar}	N_{ar}	O_{ar}	S_{ar}	
RDF	8.52	64.23	17.05	10.20	37.00	7.73	0.63	35.56	0.21	14.76

Table 2. The operating condition of the bio-char producing

Air flow rate (Nm^3/h)	Oxygen flow rate (Nm^3/h)	Oxygen concentration (%)	Feeding flow rate (kg/h)	Equivalence ratio	Bed temperature (℃)	fluidization velocity (m/s)
11.4	3.6	38.76	53.27	0.133	705	1.134

Table 3. Characteristics of bio-char

	Ash (wt. %)	Volatile (wt. %)	FC (wt. %)	Low heating value (MJ/kg)
Bio-char	69.46	11.92	18.41	9.37

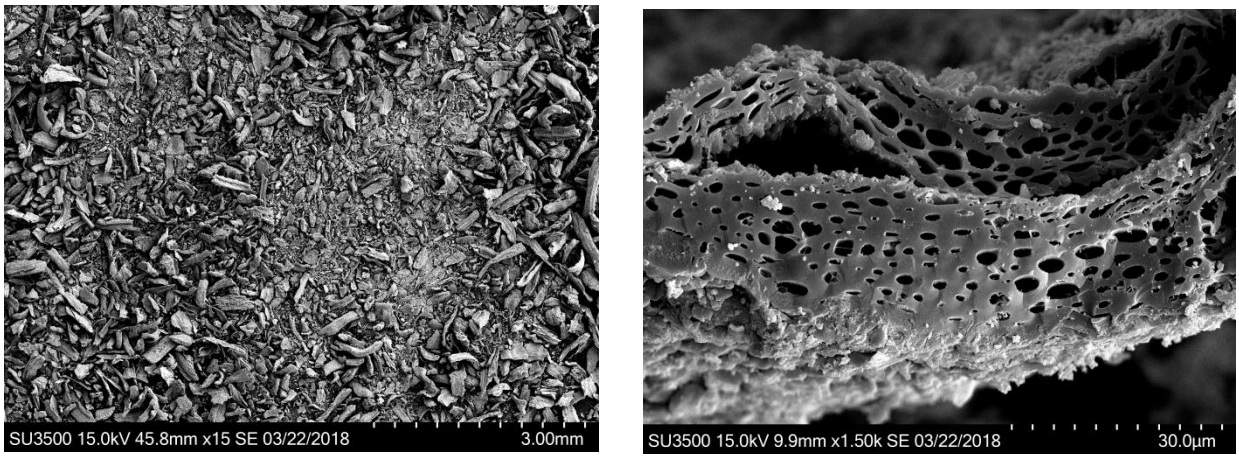

(a) Overall view of bio-char **(b) Partial enlargement of bio-char**

Figure 1. SEM of bio-char

2.2 Experimental installation

In order to investigate the melting characteristics of the bio-char in the high temperature, the experimental installation was designed and shown in Figure 1. This installation includes the gas supplying system, high-temperature melting furnace and temperature controlling system. CO, N_2 and CO_2 with the volume ratio 6:10:4 supplied by three different gas cylinders, respectively, are used for simulating the reducing atmosphere in the flue gas. The air is supplied by the air compressor to form the oxidizing atmosphere. Only high pure N_2 is sent to the high-temperature melting furnace to generate the inert atmosphere. The high-temperature melting furnace is made of alundum tube with 50mm internal diameter and 800mm height. Silicon-molybdenum rod heater is equipped around outside of the tube to reach the designed temperature.

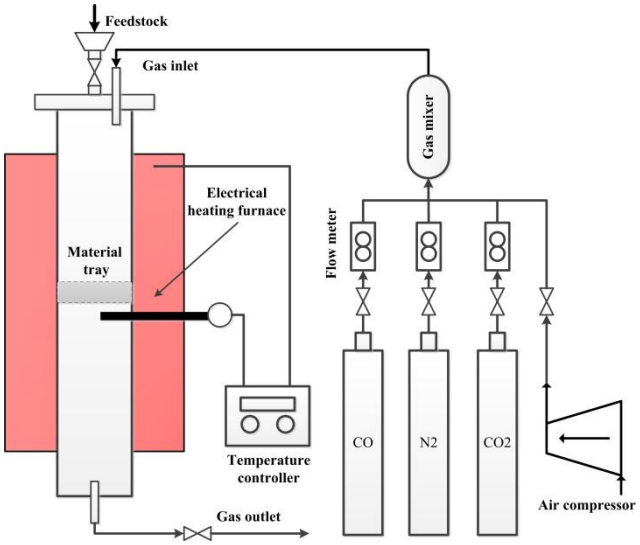

Figure .2 Schematic diagram of the experimental installation

2.3 Experimental procedure

The temperature in the furnace reached the designed temperature, and then the related gases were sent into the furnace to form the specific atmosphere (reducing atmosphere, inert atmosphere and oxidizing atmosphere). 2 g bio-char was fed into the furnace form the top of the furnace. The bio-char stayed in the furnace about 60 min. Then the furnace stopped heating and the residue of the bio-char was cooled to room temperature and was sampled for SEM analysis.

3 RESULTS AND DISCUSSION

3.1 Effect of temperature

It can be observed from Figure 3 that the higher temperature can improve the melting degree of the bio-char in the high-temperature furnace. Compared with the four figures on the left of each row in Figure 3, the average sizes of residues form bio-char increased with the temperature rising from 1150℃ to 1300℃. While compared with the other four figures on the right of each row in Figure3, the surface of the residues from bio-char became smooth at 1300 ℃from rough at 1150℃, and the holes and pits in the surface of the residues gradually disappeared with the temperature increasing. It also can be found that the residues can be fully melted and flowed to the holes and pits and make the residues flatter when the temperature was at or above 1250 ℃. However, compared with residues at 1250℃ and that at 1300℃, there was almost no holes and pits in the surface of the residues at 1300℃, while there still were a few holes in the surface of the residues at 1250℃. Therefore, 1300℃ is the best temperature for this bio-char melting.

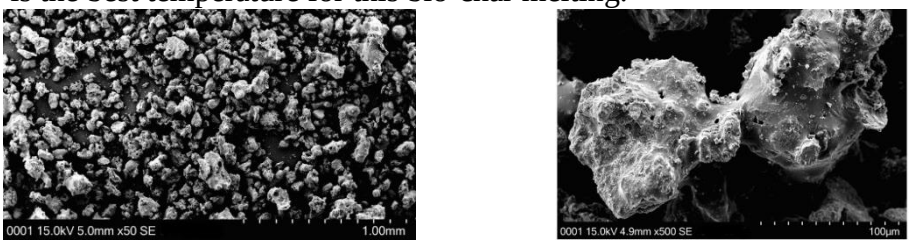

(a) 1150℃

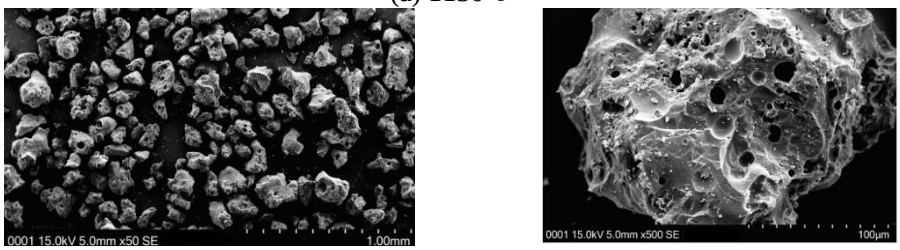

(b) 1200℃

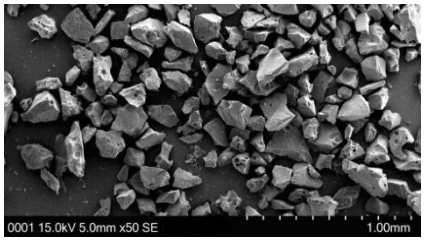

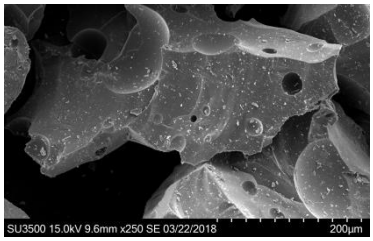

(c) 1250℃

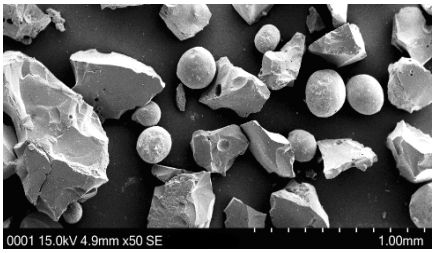

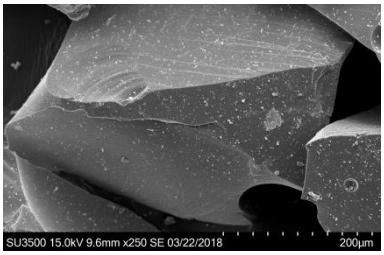

(d) 1300℃

Figure 3. Morphology of residues of bio-char in reducing atmosphere at the different temperature

3.2 Effect of melting atmosphere

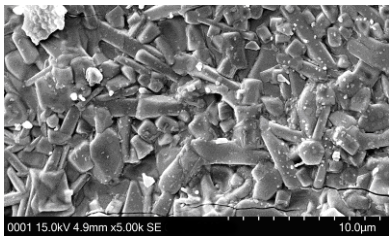

(a) Reducing atmosphere, 1150℃

(b) inert atmosphere, 1150℃

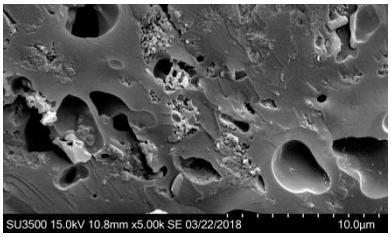

(c) oxidizing atmosphere, 1150℃

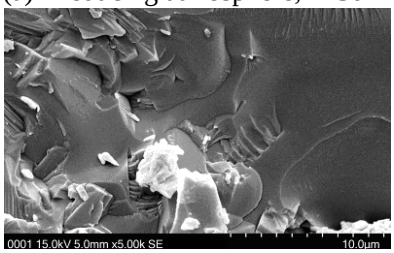

(d) Reducing atmosphere, 1200℃

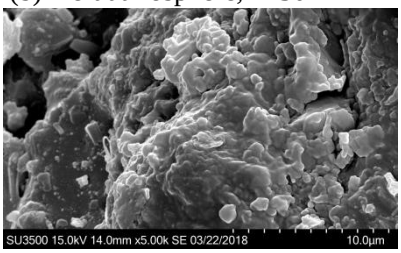

(e) inert atmosphere, 1200℃

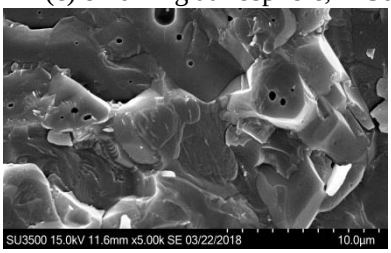

(f) oxidizing atmosphere, 1200℃

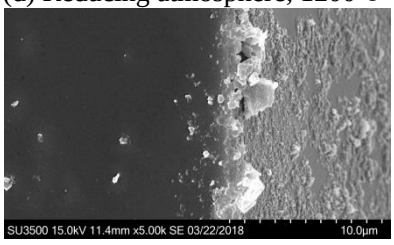

(g) Reducing atmosphere, 1250℃

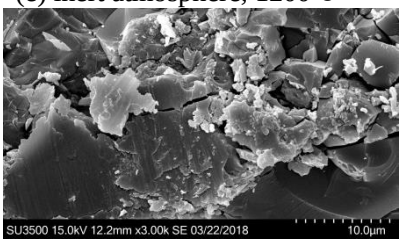

(h) inert atmosphere, 1250℃

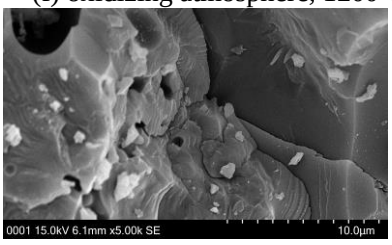

(i) oxidizing atmosphere, 1250℃

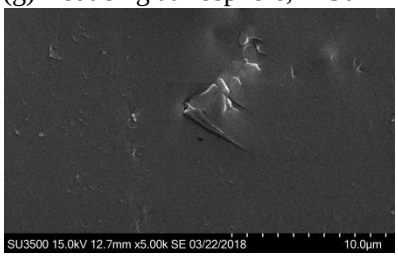

(j) Reducing atmosphere, 1300℃

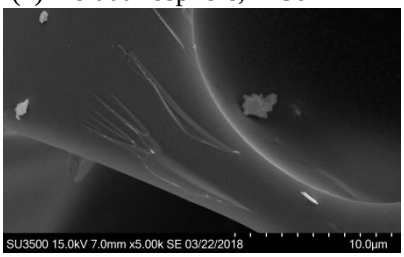

(k) inert atmosphere, 1300℃

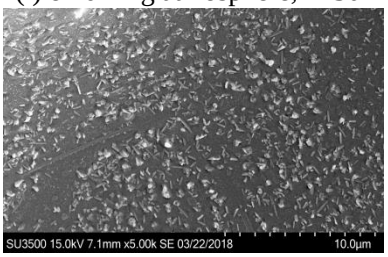

(l) oxidizing atmosphere, 1300℃

Figure 4. Morphology of residues of bio-char in different conditions

It can be found the same conclusion as above section from comparing with four figures in each column in Figure 4 that the melting temperature prompts the melting degree no matter in which atmosphere (reducing, inert or oxidizing atmosphere). Compared with three figures in each row at the same temperature in Figure 4, there were some holes and pits in the surface of residues formed in the oxidizing atmosphere, only some

protrusions appeared and no holes appeared in the surface of the residues formed in the inert atmosphere. While the surface of the residues formed in the reducing atmosphere was the flattest and smoothest. Therefore, in comparison to other two atmospheres, the melting speed was fastest and the melting degree was highest in the reducing atmosphere at the same temperature. The same results were obtained by Huffman at el. [15] when the coal ash melting behaviours were investigated. This is due to CaO and FeO as fluxing medium produced in the reducing atmosphere to further form the low-temperature eutectics such as fayalite, hercynite, hedenbergite etc. [16]. It was worthy to note that the residues formed in reducing atmosphere was complete liquefied and flowing at 1300℃ while that in other two atmospheres were insufficient flowing until the temperature reached 1300℃.

3.3 Effect of carbon content in the bio-char

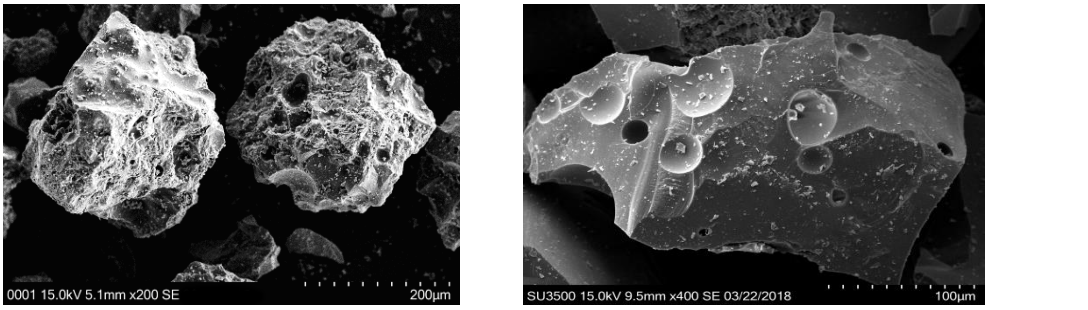

(a) 1150 ℃ (b) 1200℃

Figure 5. Morphology of residues of the ash in the reducing atmosphere

The ash used for SEM analysis in this section was obtained in the muffle furnace at 700 ℃ for 3h, and it can be regarded as a kind of bio-char with lower carbon content in comparison to the real bio-char obtained during oxygen-enriched gasification. Figure 5 showed the morphology of the residues of the ash in reducing atmosphere at 1150℃and 1200℃. It can be seen from Figure 5 (a) that there still were some holes and pits on the surface of the residues indicating insufficient melting at 1150℃in reducing atmosphere, this morphology is similar as that at 1200℃in Figure 3 (b). However, the residues almost complete melted and flow to the holes at 1200℃, which is similar as that at 1250℃in Figure 3 (c). This meant that the temperature for bio-char complete melting increased and the melting speed slowed down with the carbon content in the bio-char increasing. Therefore, the designed temperature of the high-temperature furnace should be higher than the flowing temperature of the ash formed from the combustible feedstock.

4. Conclusion

The melting characterizations of bio-char formed from oxygen-enriched gasification of RDF were investigated in a high-temperature furnace. The melting degree and speed gradually improved with temperature varying from 1150 ℃ to 1300℃in the reducing atmosphere. Compared with other two atmospheres (inert and oxidizing atmospheres), the reducing atmosphere was in favor to bio-char melting due to the fluxing medium such as CaO and FeO generated in the reducing atmosphere to further form the low-temperature eutectics. Complete melting of bio-char with higher carbon content need a higher temperature, therefore, the operating temperature of the high-temperature furnace should be controlled over the flowing temperature of the ash formed from the combustible feedstock to ensure the bio-char complete melting.

ACKNOWLEDGEMENTS

This work was supported by National Key Technology Research and Development Program of the Ministry of Science and Technology of China (2015BAD21B06), National Key Basic Research Program of China (2013CB228106) and Jiangsu Province Science and Technology Support Project (BE2013705) on this work.

REFERENCES

[1] T P Thomsen, Z Sárossy, B Gøbel, et al. Low temperature circulating fluidized bed gasification and co-gasification of municipal sewage sludge. Part 1: Process performance and gas product characterization, *Waste Management*, Vol. 66, pp. 123-133, 2017.

[2] S Werle. Impact of feedstock properties and operating conditions on sewage sludge gasification in a fixed bed gasifier. *Waste Management & Research*, Vol. 32(10), pp. 954-960, 2014.

[3] W K Jin, H M Choi, H K Bo, et al. Gasification and tar removal characteristics of rice husk in a bubbling fluidized bed reactor, *Fuel*, Vol. 181, pp. 942-950, 2016.
[4] M M Niu, Y J Huang, B S Jin, et al. Enriched‐Air Gasification of Refuse‐Derived Fuel in a Fluidized Bed: Effect of Gasifying Conditions and Bed Materials. *Chemical Engineering & Technology*, Vol. 37(10), pp. 1787-1796, 2015.
[5] Q R Fu, Y J Huang, M M Niu, et al. Experimental and predicted approaches for biomass gasification with enriched air-steam in a fluidised bed. *Waste Management & Research*, Vol. 32(10), pp. 988-996, 2014.
[6] D D Feng, Y J Zhao, Y Zhang, et al. Synergies and progressive effects of H_2O/CO_2 and nascent tar on biochar structure and reactivity during gasification. *Fuel Processing Technology*, Vol. 168, pp.1-10, 2017.
[7] H M Yu, Z Zhang, Z Li, et al. Characteristics of tar formation during cellulose, hemicellulose and lignin gasification. *Fuel*, Vol. 118(1), pp. 250-256, 2014.
[8] N Berguerand, T B Vilches. Alkali-Feldspar as a Catalyst for Biomass Gasification in a 2-MW Indirect Gasifier. *Energy & Fuels*, Vol. 31, pp. 1583−1592, 2017.
[9] S Unyaphan, T Tarnpradab, F Takahashi, et al. Improvement of tar removal performance of oil scrubber by producing syngas microbubbles. *Applied Energy*, Vol. 205, pp. 802-812, 2017.
[10] T Ahmed, S N Xiu, L J Wang, et al. Investigation of Ni/Fe/Mg zeolite-supported catalysts in steam reforming of tar using simulated-toluene as model compound. *Fuel*, Vol. 211, pp. 566-571, 2018.
[11] H Y Yuan, S B Wu, X L Yin, et al. Adjustment of biomass product gas to raise H 2 /CO ratio and remove tar over sodium titanate catalysts. *Renewable Energy*, Vol. 115, pp. 288-298, 2018.
[12] N Tanigaki, K Manako, M Osada. Co-gasification of municipal solid waste and material recovery in a large-scale gasification and melting system. *Waste Management*, Vol. 32(4), pp.667-75, 2012.
[13] S I Sakai, M Hiraoka. Municipal solid waste incinerator residue recycling by thermal processes. *Waste Management*, Vol. 20(2), pp. 249-258, 2000.
[14] C Q Liu; Y J Huang; L Q Liu, et al. Influences of equivalence ratio, oxygen concentration in the gasification agent and fluidization velocity on the characteristics of syngas, tar and bio-char during oxygen-enriched gasification of biomass in a pilot-scale fluidized bed. Submitted to *International Journal of Hydrogen Energy*.
[15] G P Huffman, F E Huggins, G R Dunmyre. Investigation of the high-temperature behaviour of coal ash in reducing and oxidizing atmospheres[J]. *Fuel*, Vol. 60(7), pp. 585-597, 1981.
[16] M M Niu, Q Dong, Y J Huang, et al. Characterization of ash melting behaviour at high temperatures under conditions simulating combustible solid waste gasification[J]. *Waste Management & Research*, 2018 (https://doi.org/10.1177/034242X18763064).

BIOALCOHOLS UPGRADING TO HYDROCARBON FUELS OVER MFI/AL_2O_3 SUPPORTED CATALYSTS

P.A. Zharova[1], A.V. Chistyakov[1], M.V. Tsodikov[1], S.A. Nikolaev[2]

1. Topchiev Institute of Petrochemical Synthesis RAS, Russia; email: zharova@ips.ac.ru
2. Moscow State University, Russia; email: serge2000@rambler.ru

ABSTRACT

Here we used Pd-Zn, Au-Cu, Au-Ni, Au-Pd bimetallic catalysts supported on MFI/γ-Al_2O_3. Si/Al ratio was 30, alumina was used as a binder for zeolite, its content was 30 wt.%. Ethanol, acetone, 1-butanol, ABE-mixture and fusel oil were used as a feed as well as its mixtures with water containing 5-50 vol.% of water. Found that at 330°C, VHSV 0.6-2.4 h^{-1}, 5 atm Ar Au-Pd and Pd-Zn catalysts possess the longest stability about 25-40 hours being on stream with pure oxygenates. Water addition to oxygenates allows to increase catalyst stability up to 100 hours without any recovery procedure. Also water addition positively effects on C_{3+} hydrocarbons yield reaches up to 80-98 wt.% calculated on loaded carbon.

Keywords: zeolite, bioalcohols, heterogeneous catalysis, biofuels

1 INTRODUCTION

With increased demands for energy, stricter environmental regulations, and continued depletion of fossil feedstock, alternative and renewable energy resources have attracted increased interest in recent research. [1]. Due to its renewable nature with low CO_2 emission [2], biomass has been recognized as one of the most viable resources to produce biofuels, such as ethanol, which can be readily integrated into the infrastructure of the current end user (i.e., engine). Recent advantages in catalytic conversion of biooxygenates to fuels and chemicals showed increasing availability and decreasing cost of the bioindustry [3]. The expansion of biomass derived products industry allow to suggest such biooxygenates as ethanol, acetone, butanol and fusel oil as the prospective raw for the production of transportation fuels and chemicals. Ethanol conversion to hydrocarbons employing zeolites as catalysts dates back to 1970s [4]. Since then, a large number of reports have appeared in literature on ethanol conversion to hydrocarbons [5-13]. The reaction temperature for ethanol transformation is generally about 350 °C and the pressure ranges from ambient to several atmospheres [5-14]. But still the problems of catalytic stability and effect of water content in raw ethanol are not completely solved.

The effect of water and the possibility of water-ethanol mixtures conversion to aromatic was studied in several papers. Oudejans et al. reported that with a water content of about 30% and a VHSV of ethanol 0.07 h^{-1}, water has no effect on the yield of the aromatic fraction (45%) [15]. Moreover 30 vol.% of water provide higher catalytic stability of MFI-based catalysts. Complex study of water content effect on catalytic stability of MFI-based catalysts presented by Agyayo et al. Shown that under 500°C even 5 vol.% of water leads to slow dealuminization of zeolite but under 400 °C stable work of catalyst was observed with water content up to 75 vol.%. Similar result was obtained by Shulz [16]. Also Shulz noted that 40 vol.% of ethanol and 60 vol.% of water mixture conversion make catalyst works stable during approximately 30-40 h. After 50 hours on stream in products only ethylene was observed.

First time ever the possibility of conversion of liquid alcohols and ethers with a fluid mass of ZSM-5 type catalyst into aliphatic and aromatic hydrocarbons was reported in 1974 Patent number: 4138440. But recently in an attempt to conduct an effective conversion of bioethanol into gasoline rich in aromatics and iso-paraffins, a ZSM-5 type zeolite with special features such as nano crystalline size and acidity has been synthesized [17]. The reported catalyst exhibits highest gasoline yield of about 73.8 wt % with aromatics and iso-paraffins as major components. The product measures Octane Number (RON) of about 95, which is desirable for the gasoline specifications. Moreover, considerable amounts of the Liquefied Petroleum Gas (LPG) (15 wt %) and light olefins (14 wt %) are also formed as by-products that add value to the process. The nano crystalline ZSM-5 catalyst exhibits the stability in activity in terms of bioethanol conversion and aromatics yields for the reaction time period of 40 h. So the problem of catalytic stability in ethanol to gasoline process is still on the front burner.

Should be noticed that pure MFI zeolite is not suitable for industry use due to its mechanical properties. Zeolite with binder is more applicable that permits to form granulated catalyst. But retaining the chemical properties of such a catalytic system is a serious task.
This work aims to development of catalysts based on MFI type zeolites modified with Pd and Zn or Pd and Au that possess high catalytic activity and stability in ethanol to gasoline process.

2 EXPERIMENTAL

The catalyst used in this study was a pilot sample of the Pd–Zn/MFI/Al_2O_3 catalyst (Angarsk plant ofcatalysts and organic synthesis) with an active component content of 0.5 wt.% Pd and 1 wt.% Zn and an Al/Si ratio of 30 [18] and original Au-containing systems.
The metal content of the catalysts was determined by atomic absorption on a Thermo iCE 3000 AA spectrometer.
Analytical grade ethanol (96%) was used without further purification. As fusel oil a model mixture of alcohols was used containing 20% n-propanol, 5% iso-propanol, 20% iso-butanol, 5% n-butanol, 50% isoamyl alcohol.Catalyst testing was performed in a PID Eng & Tech microcatalytic fixed-bed flow reactor unit, equipped with relevant instrumentation and control devices, under pressure 5 atm of Ar, temperature 330°C, and volume hourly space velocity 1.2 h^{-1}.
Qualitative and quantitative analyses of the C_1–C_5 hydrocarbon gases were performed by gas-liquid chromatography (GLC) with a Kristall-4000M chromatograph (detector: FID, carrier gas: He, column: HP-PLOT/Al_2O_3, 50 m × 0.32 mm). GLC analyses of CO, CO_2 and H_2 were performed with a Kristall-4000 chromatograph (detector: TCD, carrier gas: Ar, column: SKT, 1.5 m × 4 mm). The qualitative composition of the liquid products were identified by gas chromatography coupled to a mass spectrometry (GC-MS) using a MSD 6973 - and an Autowt.-150 spectrometer - (EI = 70 eV, catalyst volume = 1 µl, columns: HP-5MS, 50 m × 0.32 mm and CPSil-5, 25 m × 0.15 mm). The quantitative content of the organic compounds was determined by GLC using a Varian 3600 chromatograph (detector: FID, carrier gas: He, column: Chromtec SE-30, 25 m × 0.25 mm). The ethanol content in the aqueous phase was determined by GC-MS using the absolute calibration method on the ratio of alcohol to water integral signals. Calibration of the GC was carried out with commercial standards using method [19].

3 RESULTS AND DISCUSSION

The conversion of ethanol over different catalysts based on MFI/Al_2O_3 support has been studied at 330 °C, ethanol volume hourly space velocity (VHSV) 1.2 h^{-1} and argon pressure 5 atm. The results are given in Table 1.

Table 1. Ethanol conversion products obtained over different catalysts.

	Products yield, wt.%			
catalyst	C_1	C_2	aliphatics C_3-C_7	aromatics C_6-C_{11}
MFI/Al_2O_3	0.0	10.1	51.8	38.1
Au/ MFI/Al_2O_3	0.0	16.7	53.6	29.7
Pd MFI/Al_2O_3	0.1	10.8	51.4	37.7
Au-Pd MFI/Al_2O_3	0.0	8.4	61.9	29.7
Au-Cu MFI/Al_2O_3	0.1	4.9	67.6	27.5
Au-Ni MFI/Al_2O_3	0.4	4.0	58.2	37.5
Pd-Zn MFI/Al_2O_3	0.8	6.2	53.1	39.9

The uncoated support has high activity, the total yield of the target fraction of aliphatic hydrocarbons C_3-C_7 and aromatic C_6-C_{11} reaches 90% in its presence. Support modification with gold or palladium results in a slight decrease of the aim fraction yield, probably due to a decrease of the free surface and a change in the acidity of the catalyst. Similar results were observed over uncoated MFI zeolite [20]. The yield of the aim fraction of hydrocarbons over bimetallic catalysts reaches 92-96%. The highest yield of aliphatic hydrocarbons C_3-C_7 was achieved over Au-Pd and Au-Cu catalysts and is 62 and 67%, respectively. The highest yield of aromatics was achieved over Au-Ni and Pd-Zn catalysts. From the data presented in Table 1, it can be concluded that the support MFI/Al_2O_3 shows a high activity in the conversion of ethanol into a fraction of aliphatic C_3-C_7 and aromatic hydrocarbons C_6-C_{11}. Modification of the support with various

metals allows to control of the selectivity in the direction of obtaining either aliphatic hydrocarbons or aromatic hydrocarbons. The methane yield over the tested catalysts did not exceed 1%. It should be noted that the achieved yield of hydrocarbons of the gasoline fraction exceed those obtained in [17].

In industrial alcohol plants, fusel oil and ethyl alcohol are recovered from the fermented liquors and separated by distillation. To avoid the costly treatments of water removal (azeotropic distillation, separation by molecular sieves and pervaporation) required for the production of ethanol we tested our catalyst in fusel oil conversion into hydrocarbons.

A typical fusel oil contains 60–70 percent of amyl alcohol, smaller amounts of n-propyl and isobutyl alcohols, and traces of other components. The problem of usage of fusel oil is catalyst cocking activation due to high molecular alcohols. The results of the catalytic tests are presented in Table 2. Fusel oils are converted into a fraction of hydrocarbons identical to that obtained by ethanol conversion with yields reaching 97-99%. In the products of the fusel oils conversion, the methane yield does not exceed 1%, and the ethylene yield does not exceed 2%, which indicates a low cracking intensity at 330°C. The maximum yield of aliphatic hydrocarbons C_3-C_7, as in the case of ethanol conversion, is observed over Au-Pd and Au-Cu catalysts. The maximum yield of arenes was 57 and 59% was obtained over Au-Ni and Au-Pd catalysts, respectively.

Table 2. Fusel oil conversion products obtained over different catalysts under T=330 °C, VHSV=1.2 h-1, P=5 atm Ar.

	Products yield, wt.%			
catalyst	C_1	C_2	aliphatics C_3-C_7	aromatics C_6-C_{11}
MFI	0.37	0.62	41.69	57.32
Au	0.10	2.50	51.00	46.40
Pd	0.10	0.56	43.03	54.31
Au-Pd	0.10	1.3	52.2	46.4
Au-Cu	0.11	1.43	53.68	44.78
Au-Ni	0.62	1.10	41.02	57.3
Pd-Zn	0.90	1.90	38.00	59.2

With the aid of ABE process using Clostridium acetobutylicum, which was developed by Chaim Weizmann (the first Israel President) in 1916, the acetone and butanol outputs were increased to 3000 and 6000 tons per year as soon as in 1918. The production plants of this type quickly spread all over the world. In connection with increasing oil prices, exhaustibility of oil reserves, and the search for renewable sources of energy and chemicals, the ABE process was revived, and many production units, especially in China, were revamped or constructed again [21, 22]. In order to expand the resource base for the process of obtaining gasoline components from renewable raw materials, ABE products were converted over the studied catalysts. The results of the experiments are presented in Table 3. The total yield of the aim fraction over the catalysts studied was 93-97%. Methane yield did not exceed 1%. Compared with the conversion of ethanol, the conversion of ABE products results in a higher yield of aromatic compounds and a lower yield of aliphatic products. Thus, the results presented in Table 3 indicate the possibility of using a mixture of alcohols as a feedstock for the production of gasoline components over the study catalysts.

Table 3 ABE fermentation mixture conversion products obtained over different catalysts under T=330 °C, VHSV=1.2 h^{-1}, P=5 atm Ar.

	Products yield, wt.%			
catalyst	C_1	C_2	C_3-C_7	C_6-C_{11}
MFI	0.1	3.1	44.5	52.3
Au	0.10	4.10	48.10	47.7
Pd	0.20	6.30	42.20	51.3
Au-Pd	0.34	3.97	34.29	61.4
Au-Cu	0.46	5.45	41.29	52.8
Au-Ni	0.50	2.90	47.10	49.5
Pd-Zn	0.50	4.30	44.30	50.9

For further studies, Au-Pd/MFI/Al_2O_3 and Pd-Zn /MFI/Al_2O_3 catalysts were selected for lifetime tests. The results of the experiments carried out (Tables 1-3) show that over the Pd-Zn system, the largest number of arenes are formed in the reaction products, and over the Au-Pd system, the highest amount of aliphatic hydrocarbons is formed. In addition, the activity of the Au-Pd/ MFI/Al_2O_3 catalyst is comparable to that of the Pd-Zn/MFI/Al_2O_3.

The results of stability tests of the catalysts during the conversion of ethanol and a mixture of ethanol with 30 vol.% of water are shown in Figures 1-4.

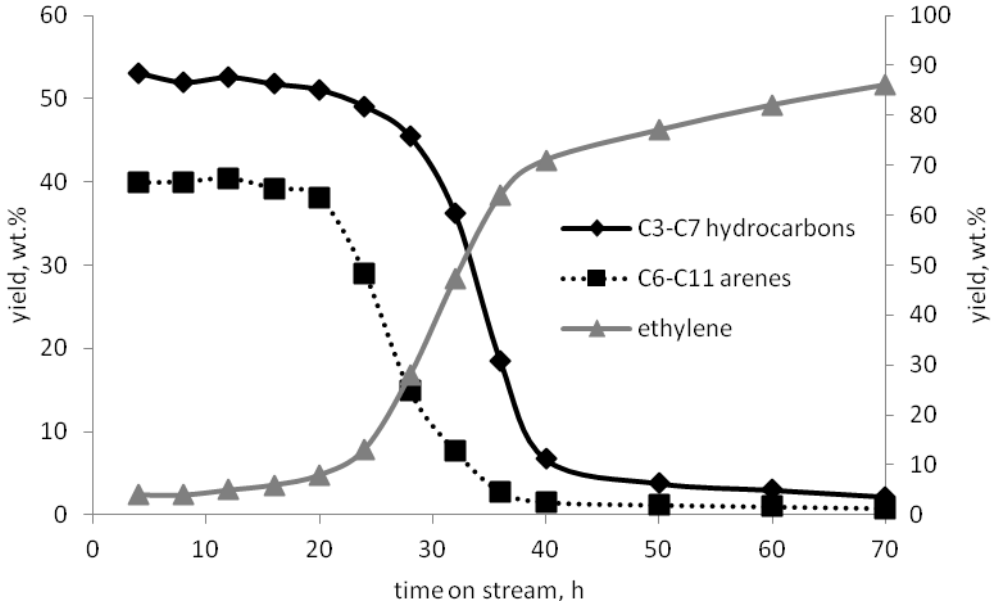

Figure 1. Evolution with time on stream of the ethanol conversion products yield, obtained over Pd-Zn/MFI/Al_2O_3

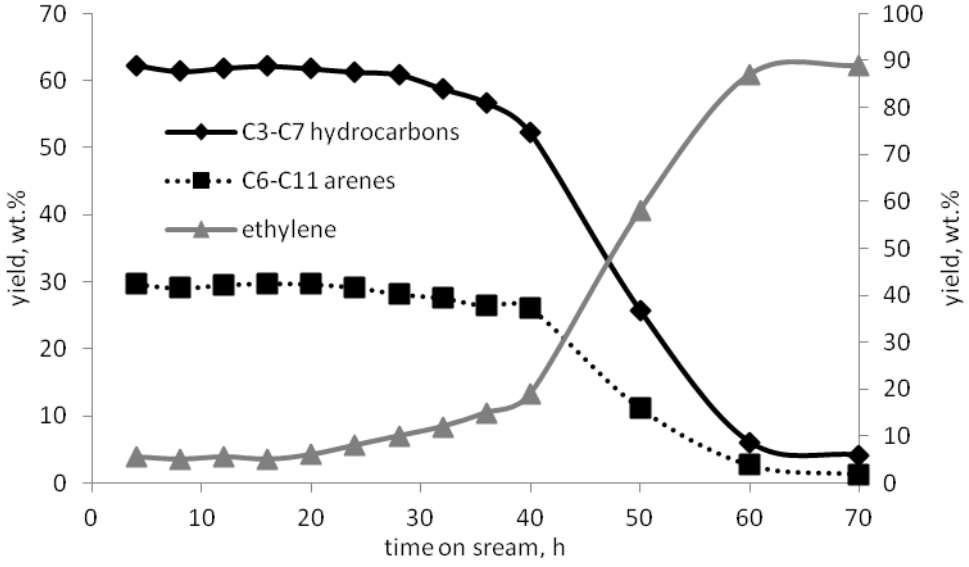

Figure 2. Evolution with time on stream of the ethanol conversion products yield, obtained over Au-Pd/MFI/Al_2O_3

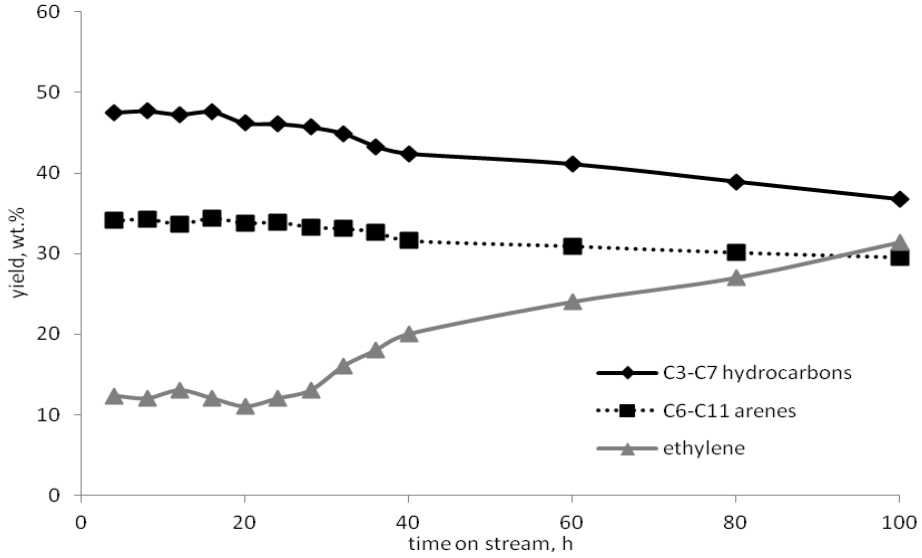

Figure 3. Evolution with time on stream of the ethanol water mixture conversion products yield, obtained over Pd-Zn/MFI/Al_2O_3.

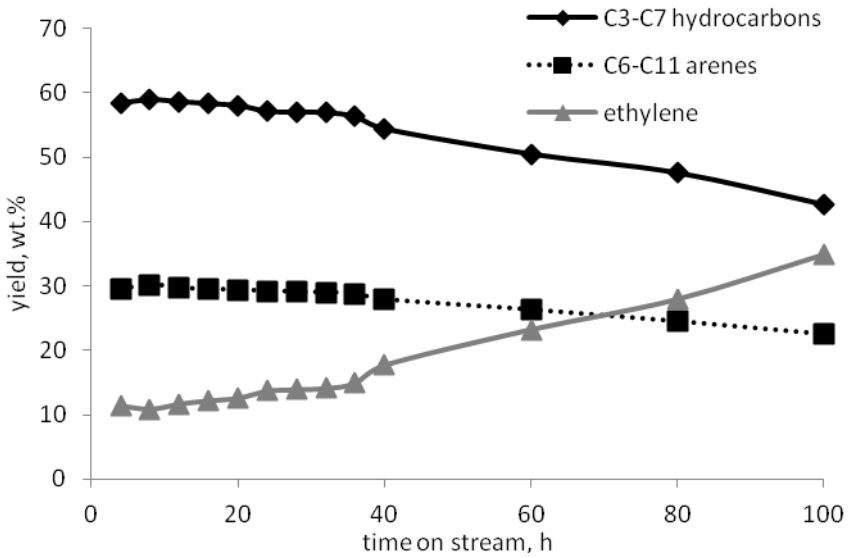

Figure 4. Evolution with time on stream of the ethanol water mixture conversion products yield, obtained over Au-Pd/MFI/Al_2O_3.

Figure 1 shows that the activity of Pd-Zn catalyst reduce dramatically after 20 hours on stream. After 40 hours on stream ethylene dominates in the reaction products, its yield is approximately 90 %, the total yield of aliphatic and aromatic hydrocarbons C_3-C_{11} does not exceed 7%. It is known that the addition of gold to catalysts based on zeolite-type MFI reduce the coke formation [23]. This fact has been confirmed in our work. In the case of Au-Pd catalyst, the stable operation time is 40 hours. During the first 40 hours on stream over this catalyst, the yield of the aim fraction decrease by no more than 10% and a symbate increase in the yield of ethylene (Figure 2). After 40 hours on stream, yield of the aim hydrocarbon fraction reduce dramatically and yield of ethylene increase to 90%.

Conversion of ethanol containing 30 vol.% of water allows to enhance the catalysts life up to 100 h (Figures 3-4). It should be noted that during the life test, a decrease of the yield of the aim hydrocarbon fraction and an increase of the yield of ethylene are observed, however, in 100 hours the productivity is reduced by less than 20%. Thus, the use of water-ethanol mixtures can be considered an effective approach to increasing the life of the catalyst.

ACKNOWLEDGEMENTS

This work was done as part of TIPS RAS State Plan.

REFERENCES

[1] G. W. Huber, S. Iborra, A. Corma, Synthesis of transportation fuels from biomass: chemistry, catalysts, and engineering, *Chemical reviews*, Vol. 106, pp. 4044-4098, 2006.

[2] A.E. Farrell, R.J. Plevin, B.T. Turner, A.D. Jones, M. O'Hare, D.M. Kammen, Ethanol can contribute to energy and environmental goals, *Science*, Vol. 311, pp. 506−508, 2006.

[3] J. Sun, Y. Wang, Recent advances in catalytic conversion of ethanol to chemicals, *ACS Catalysis*, Vol. 4, pp. 1078-1090, 2014.

[4] E.G. Derouane, J.B. Nagy, P. Dejaifve, J.H. van Hooff, B.P. Spekman, J.C. Védrine, C. Naccache, Elucidation of the mechanism of conversion of methanol and ethanol to hydrocarbons on a new type of synthetic zeolite, *J. Catal*., Vol. 53, pp. 40–55, 1978.

[5] G.A. Aldridge, X.E. Verykios, R. Mutharasan, Recovery of ethanol from fermentation broths by catalytic conversion to gasoline, Energy analysis, *Ind. Eng. Chem. Process Des. Dev.*, Vol. 23, pp. 733–738, 1984.

[6] V. Calsavara, M. L. Baesso, N. R. C. Fernandes-Machado, Transformation of ethanol into hydrocarbons on ZSM-5 zeolites modified with ion in different ways, *Fuel*, Vol. 87, pp. 1628–1636, 2008.

[7] Q. Zhu, J. N. Kondo, S. Inagaki, T. Tatsumi, Catalytic activities of alcohol transformations over 8-ring zeolites, *Top. Catal.*, Vol. 52, pp. 1272–1280, 2009.

[8] Y.I. Makarfi, M.S. Yakimova, A.S. Lermontov, V.I. Erofeev, L.M. Koval, V.F. Tretiyakov, Conversion of bioethanol over zeolites, *Chem. Eng. J*., Vol. 154, pp. 396–400, 2009.

[9] K.K. Ramaswamy, H. Zhang, J.M. Sun, Y. Wang, Conversion of ethanol to hydrocarbons on hierarchical HZSM-5 zeolites, *Catal. Today*, Vol. 238, pp. 103–110, 2014.

[10] K.K. Ramaswamy, Y. Wang, Ethanol conversion to hydrocarbons on HZSM-5: Effect of reaction conditions and Si/Al ratio on the product distribution, *Catal. Today*, Vol. 237, pp. 89–99, 2014.

[11] F.F. Madeira, K.B. Tayeb, L. Pinard, H. Vezin, S. Maury, N. Cadran, Ethanol transformation into hydrocarbons on ZSM-5 zeolites: Influence of Si/Al ratio on catalytic performances and deactivation rate. Study of the radical species role, *Applied Catalysis A: General*, Vol. 443, pp. 171-180, 2012.

[12] A.T. Aguayo, A.G. Gayubo, A. Atutxa, B. Valle, J. Bilbao, Regeneration of a HZSM-5 zeolite catalyst deactivated in the transformation of aqueous ethanol into hydrocarbons. *Catal. Today*, Vol. 107–108, pp. 410–416, 2005.

[13] A.K. Talukdar, K.G. Bhattacharyya, S. Sivasanker, HZSM-5 catalysed conversion of aqueous ethanol to hydrocarbons, *Applied Catalysis A: General*, Vol. 148, pp. 357-371, 1997.

[14] B. Yilmaz, U. Müller, Catalytic applications of zeolites in chemical industry, *Topics in Catalysis*, Vol. 52, pp. 888-895, 2009.

[15] J.C. Oudejans, P. F. Van Den Oosterkamp, H. Van Bekkum, Conversion of ethanol over zeolite H-ZSM-5 in the presence of water, *Applied Catalysis*, Vol.3, pp. 109-115, 1982.

[16] J. Schulz, F. Bandermann, Conversion of ethanol over zeolite H-ZSM-5, *Chemical engineering & technology*, Vol. 17, pp. 179-186, 1994.

[17] Patent US 2014/0081063 Mar. 20, 2014.

[18] RU Patent No. 2248341, 2003.

[19] T. Riittonen, E. Toukoniitty, D K. Madnani, A.R. Leino, K. Kordas, M. Szabo, J.P. Mikkola, One-pot liquid-phase catalytic conversion of ethanol to 1-butanol over aluminium oxide—the effect of the active metal on the selectivity, *Catalysts*, Vol. 2, pp. 68-84, 2012.

[20] A.G. Gayubo, A. Alonso, B. Valle, A.T. Aguayo, M. Olazar, J. Bilbao, Hydrothermal stability of HZSM-5 catalysts modified with Ni for the transformation of bioethanol into hydrocarbons, *Fuel*, Vol. 89, pp. 3365-3372, 2010.

[21] Y. Ni, Z. Sun, Recent progress on industrial fermentative production of acetone-butanol-ethanol by Clostridium acetobutylicum in China, *Appl Microbiol Biotechnol*, Vol. 83, pp. 415–23, 2009.

[22] E. Green, Fermentative production of butanol – the industrial perspective, *Curr Opin Biotech*, Vol. 22, pp. 337–43, 2011.

[23] M. Inaba, K. Murata, M. Saito, I. Takahara, Ethanol conversion to aromatic hydrocarbons over several zeolite catalysts, *Reaction Kinetics and Catalysis Letters*, Vol. 88, pp. 135-141, 2006.

SORPTION ENHANCED REFORMING: TRANSPORT CHARACTERISTICS OF CO_2 AND CHAR

J. Fuchs[1], J.C. Schmid[1], S. Müller[1], and H. Hofbauer[1]

1. Institute of Chemical, Environmental and Bioscience Engineering (ICEBE), TU Wien, AT; email: josef.fuchs@tuwien.ac.at

ABSTRACT

A dual fluidized bed reactor system allows the thermochemical conversion of biomass or wastes into a valuable nitrogen-free product gas by steam gasification. Since the system consists of two reactors (gasification reactor and combustion reactor), a circulating bed material as heat carrier is necessary to thermally connect the reactors and provide the heat for the overall endothermic steam gasification. By using limestone as bed material, in-situ removal of CO_2 out of the product gas is possible. This so-called sorption enhanced reforming operation leads product gas with an H_2 contents up to 75 vol.-%$_{db}$. Research activities in the last years mainly focused on temperature dependency of the process. Recent results showed other main influencing factors besides temperature dependency (e.g cycle rate). Therefore, scope of this work is to investigate the solids inventory to increase the understanding of the mechanisms of CO_2 sorption and desorption, and the carbon transport characteristics in general. A model for the characteristics of CO_2 transport via bed material and char transport over temperature is presented in this work.

Keywords: biomass, process modeling, 100 kW pilot plant, carbon sequestration

1 INTRODUCTION

The increasing standard of living and the fact that developed or industrialized nations consume more energy per capita than developing countries combined with future challenges of climate change and the exorbitant carbon dioxide (CO_2) emissions from fossil fuels lead to a high demand of CO_2-neutral technologies in future. Biomass as renewable source releases the same amount of CO_2 as it aggregates during its growth. Therefore, dual fluidized bed (DFB) steam gasification of biomass is a reliable technology for the reduction of greenhouse gas emissions and for gaining a valuable product gas for the production of heat, electric power and syngas. Further, hydrogen (H_2) is considered as a viable alternative fuel and "energy carrier" of the future. The so-called sorption enhanced reforming process combines the advantages of both, biomass gasification and H_2 production. Via this process a H_2-rich product gas from biomass can be produced by the usage of limestone as bed material. Usually, the product gas from DFB steam gasification is nearly N_2-free and consists of hydrogen (H_2), carbon monoxide (CO), methane (CH_4), and carbon dioxide (CO_2). A steam-blown gasification reactor and an air-blown combustion reactor are the main parts. The combustion reactor provides the necessary heat for the overall endothermic steam gasification via combustion of residual char from gasification. Usually silica sand or olivine is used for conventional gasification applications as bed material, but due to the usage of limestone as bed material and suitable temperature levels in both reactors (**Figure 1**) the production of a product gas with up to 75 vol.-%$_{db}$ H_2 is possible.

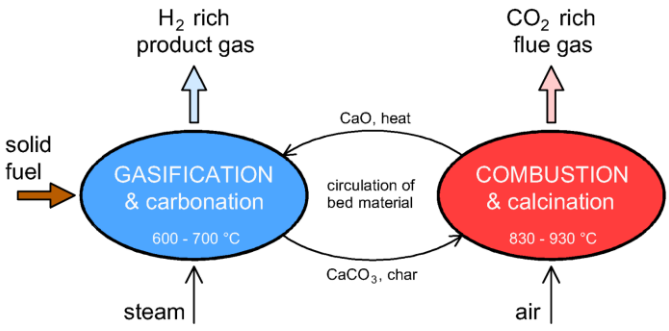

Figure 1. Principle of Gasification with CO_2 Capture (SER)

2 MATERIALS AND METHODS

2.1 Sorption Enhanced Reforming

The main function of the circulating bed material is the heat transport from the combustion reactor to the gasification reactor and its function as a transport medium of the residual char from the gasification reactor to the combustion reactor. Furthermore, the bed material can also act as a catalyst and therefore contributes to tar reduction in the product gas. Another possible function of the bed material is the capture of gaseous components from the product gas (**Figure 1**): In the sorption enhanced reforming (SER) process limestone ($CaCO_3$) is used as bed material. In-situ CO_2 capture in the gasification reactor according to **Equation (1)** and its release in the combustion reactor is possible (reverse of **Equation (1)**) by operating both reactors in a suitable temperature range. The temperature ranges for gasification and combustion reactor during SER depend on the equilibrium partial pressure of CO_2 in **Equation (1)**. Typical temperatures in the gasification reactor are between 600 and 700 °C, whereas in the combustion reactor the bed material is heated up above 830 °C. A stimulation of the water-gas shift reaction is obtained by the decreased CO_2 content (**Equation (2)**). Therefore, a product gas composition with a H_2 content up to 75 vol.-%$_{db}$ and CO_2 contents of 5 vol.-%$_{db}$ can be reached. Müller et al. [1] showed that the SER process produces a hydrogen-based reducing agent for the use in e.g. steel producing industry.

$$CaO + CO_2 \rightarrow CaCO_3 \qquad \Delta H_R^{650} = -170\ kJ/mol \tag{1}$$

$$CO + H_2O \leftrightarrow CO_2 + H_2 \quad \Delta H_R^{650} = -36\ kJ/mol \tag{2}$$

For many synthesis processes (e.g. Fischer-Tropsch, methanation) a certain H_2 to CO ratio is necessary. Typically, the product gas composition of the SER process is highly dependent on gasification temperature and bed material cycle rate. Via SER an in-situ adjustment of the H_2 to CO ratio between 2 and 9 is possible, which is clearly superior over conventional gasification with olivine as bed material, where only a H_2 to CO ratio up to 2 can be adjusted. **Figure 2** shows the main product gas composition and the H_2 to CO ratio of SER (limestone) and the conventional gasification with olivine as bed material over temperature.

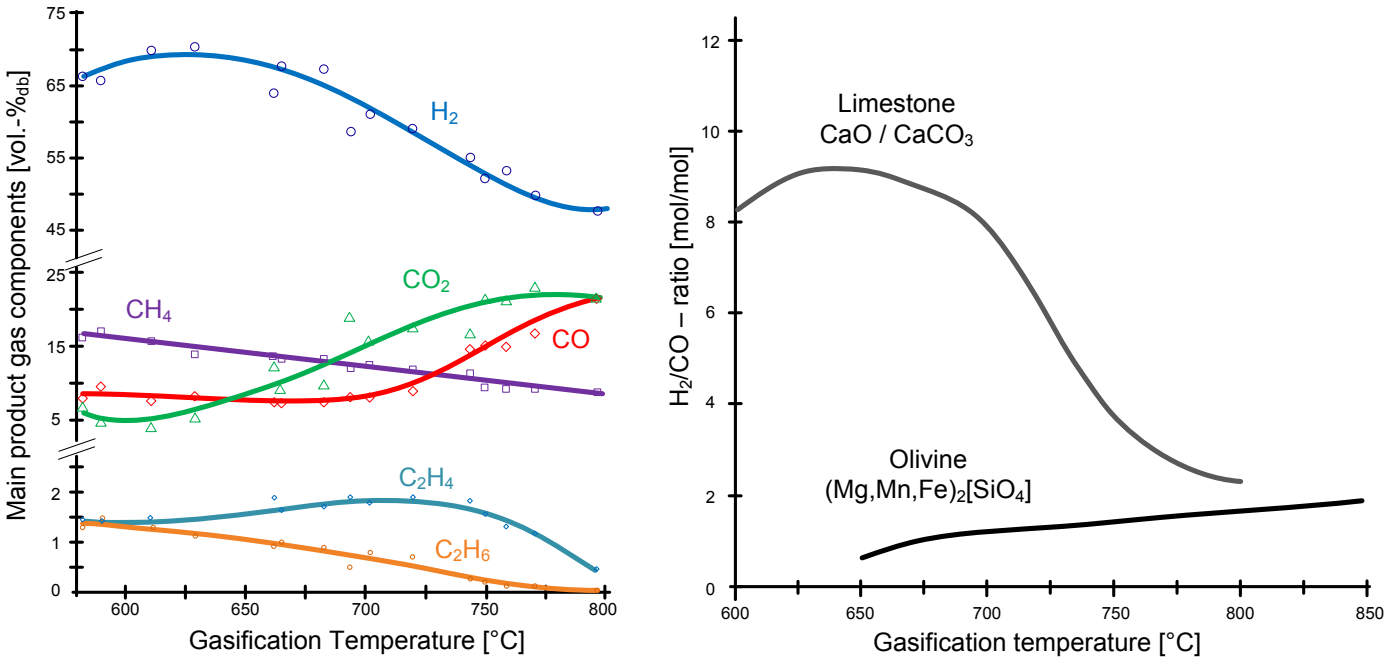

Figure 2. Main product gas composition (left) and H_2 to CO ratio of the SER process (right) over temperature

2.2 Advanced 100 kW_{th} DFB Test Plant

TU Wien has designed a novel dual fluidized bed test plant for the gasification of various fuels. A sketch and a picture of the plant are shown in **Figure 3**.

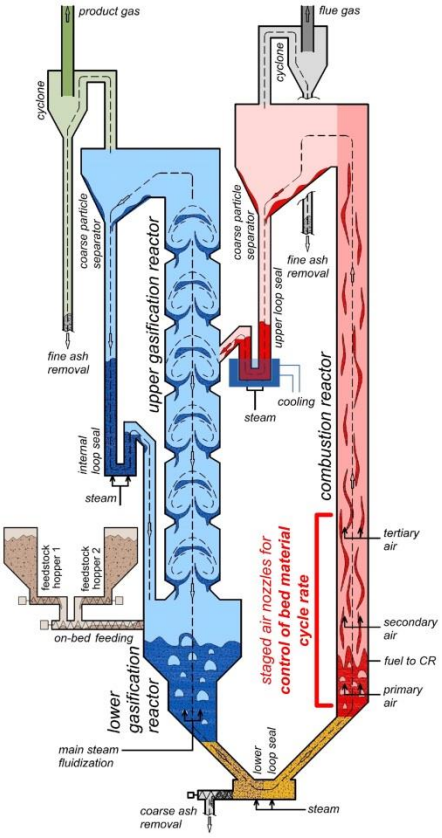

Figure 3. Advanced 100 kW_{th} Test Plant at TU Wien

The advanced reactor design enhances the gas-solid contact by a column with turbulent fluidized zones (upper gasification reactor), which is placed subsequent to the lower bubbling bed of the gasification reactor. The geometrical modifications in this upper part lead to an improved bed material hold-up [2] and enlarge the range of applicable fuels because of higher tar and char conversion rates compared to other DFB systems. Further, gravity separators with gentle separation characteristics instead of cyclones support the use of soft bed materials such as limestone. The new separation system prohibits high velocities of gas and particles and minimizes attrition effects. Additionally, a bed material cooling in the upper loop seal enables the defined setting of temperature differences between the gasification and combustion reactor for SER. Different plant designs and results can be found in [3]–[5]. For the presented investigations in this work data of all of the mentioned sources were used and averaged to gain highly representative results for detailed investigation of the process.

3 RESULTS AND DISCUSSION

The experimental results of different plants with significant plant size (mainly 100 kW fuel input and more) were investigated and summarized (**Figure 4**). Based on these results a model was invented to calculate the full carbon balance of the process over a temperature range of 600 to 850 °C (including char and CO_2 bound in $CaCO_3$, which leaves the gasification reactor). To calculate the full mass balance, information about the introduced fuel is necessary. Since the fuel for all test runs, which were used as a basis for this work, was soft wood, the model is strictly seen only valid for the fuel soft wood. However, **Table 1** shows the fuel composition of different types of fuel and therefore shows that biogenic fuels usually have a similar fuel composition regarding the carbon (C), hydrogen (H) and oxygen (O) content. Also the amount of volatiles is in a narrow range for biogenic fuels (volatiles typically indicate if the amount of residual char from gasification is similar). Therefore, it can be assumed that the applied model is valid for a broad range of biogenic fuels and not only for soft wood. **Table 1** also shows that the results cannot be used for other fuel types like lignite or heating oil: The ratio between the elements C, H, and O and also the volatiles are too different. $C_1H_{1.5}O_{0.7}$ was used as a general formula representing biomass for modeling of the process.

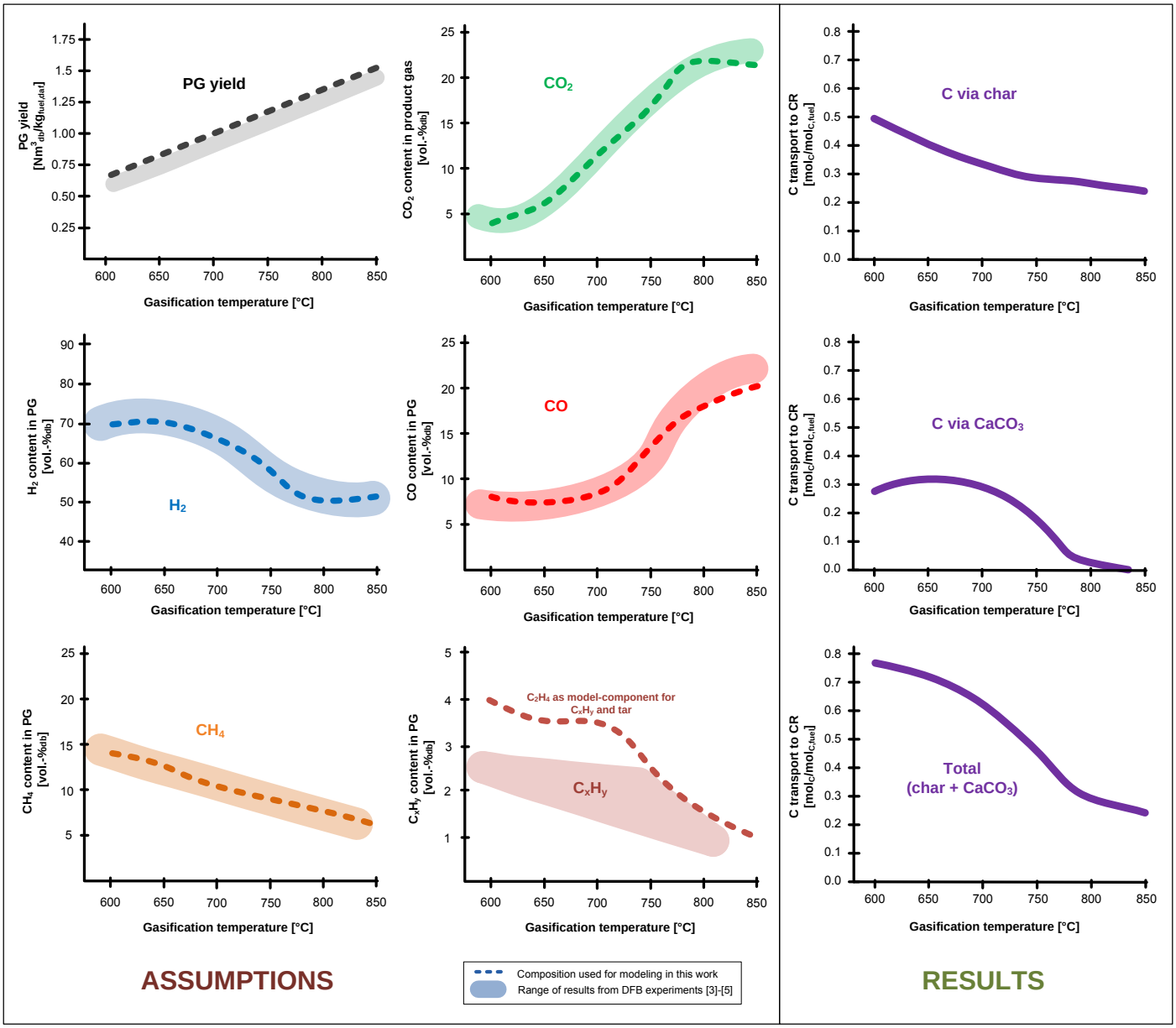

Figure 4. Range of main product gas composition from different sources [3]–[5] and assumptions used for modeling plus results of modeling (C transport to combustion reactor)

Table 1. Typical fuel compositions of different fuel types and composition used for modeling

		soft wood	rice husks	hazelnut shells	exh. olive pomace	lignite	heating oil (ultra light)
Volatiles	wt.-%$_{daf}$	86	81	76	80	54	
Carbon (C)	wt.-%$_{daf}$	50.8	51.2	52.8	52.4	68.4	~86.5
Hydrogen (H)	wt.-%$_{daf}$	5.9	6.1	5.6	6.2	3.9	~13.5
Oxygen (O)	wt.-%$_{daf}$	43.1	42	41.2	40.1	26.3	
Nitrogen (N)	wt.-%$_{daf}$	0.2	0.55	0.4	1.1	0.88	
Sulfur (S)	wt.-%$_{daf}$	0.005	0.07	0.027	0.11	0.4	
Chlorine (Cl)	wt.-%$_{daf}$	0.005	0.11	0.028	0.15	0.052	
$C_1H_xO_y$		$C_1H_{1.39}O_{0.64}$	$C_1H_{1.43}O_{0.62}$	$C_1H_{1.28}O_{0.59}$	$C_1H_{1.42}O_{0.57}$	$C_1H_{0.68}O_{0.29}$	$C_1H_{1.87}$
$C_1H_xO_y$ model		$C_1H_{1.5}O_{0.7}$				model not valid	

By comparing the range of the experimental results with the values used for modeling in this work (**Figure 4**), it can be seen that a significantly higher amount of ethene (C_2H_4) was used for the model than found in experimental investigations (sum of C_2H_4, C_2H_6 and C_3H_8 is displayed as C_xH_y in **Figure 4**): In the model C_2H_4 is used as a model component for all higher hydrocarbons including tar.
The model is based on the assumption that all the components introduced into the gasification reactor (fuel $\dot{N}_{i,fuel,in}$ and steam $\dot{N}_{i,H2O,in}$) must either leave the reactor as (i) product gas $\dot{N}_{i,PG,out}$, (ii) steam $\dot{N}_{i,H2O,out}$ or remain as solid residuals and are subsequently transported to the combustion reactor (**Equation 3**): the two possible ways are (iii) char $\dot{N}_{i,char,out}$ and (iv) CO_2 in the bed material (as $CaCO_3$) $\dot{N}_{i,CO2inCaCO3,out}$.

$$\dot{N}_{i,fuel,in} + \dot{N}_{i,H2O,in} = \dot{N}_{i,PG,out} + \dot{N}_{i,H2O,out} + \dot{N}_{i,char,out} + \dot{N}_{i,CO2inCaCO3,out} \qquad i = C,H,O \tag{3}$$

$$\dot{N}_{C,PG,out} = Y_{PG} * \dot{m}_{fuel}/V_m * (y_{CO,PG} + y_{CO2,PG} + y_{CH4,PG} + 2 * y_{C2H4,PG}) \tag{4}$$

$$\dot{N}_{H,PG,out} = Y_{PG} * \dot{m}_{fuel}/V_m * (2 * y_{H2,PG} + 4 * y_{CH4,PG} + 4 * y_{C2H4,PG}) \tag{5}$$

$$\dot{N}_{O,PG,out} = Y_{PG} * \dot{m}_{fuel}/V_m * (y_{CO,PG} + 2 * y_{CO2,PG}) \tag{6}$$

$$\dot{N}_{H,H2O,out} = \dot{N}_{H,fuel,in} + \dot{N}_{H,H2O,in} - \dot{N}_{H,PG,out};\ \dot{N}_{O,H2O,out} = \dot{N}_{H,H2O,out}/2 \tag{7}$$

$$\dot{N}_{O,CO2inCaCO3,out} = \dot{N}_{O,fuel,in} + \dot{N}_{O,H2O,in} - \dot{N}_{O,PG,out} - \dot{N}_{O,H2O,out}; \tag{8}$$

$$\dot{N}_{C,CO2inCaCO3,out} = \dot{N}_{O,CO2inCaCO3,out}/2$$

$$\dot{N}_{C,char,out} = \dot{N}_{C,fuel,in} - \dot{N}_{C,PG,out} - \dot{N}_{C,CO2inCaCO3,out} \tag{9}$$

Equation 4 – 6 show the equations for every component (C, H, O) in the product gas according to stoichiometric considerations. The molar flow of H and O in the gaseous water from gasification ($\dot{N}_{i,H2O,out}$) can be calculated by the assumption that all the H, which is not in the dry product gas must be in the gaseous water (**Equation 7**). This is only valid if the char is modeled as pure C and therefore does not contain any H or O. Further, **Equation 8** demonstrates the calculation of the molar flow of O via bed material (CO_2 transport in $CaCO_3$): All the remaining O, which is not leaving the system via product gas or gaseous water, contributes to the molar flow of O in the bed material. Finally, the molar flow of C in the char can be calculated by subtracting the C flow in the product gas and the C flow in the bed material (**Equation 9**). As already mentioned, in **Equation 7 – 9** the char composition is modeled as pure C. In fact, char also contains H and O. A model for pyrolysis of biomass and the composition of the remaining char over temperature has been proposed by Neves et al. [6]. For this work it is assumed that the model for pyrolysis is approximately valid for biomass steam gasification as well. This fact has already been verified in a previous work [7] and the used equations are presented in **Equation 10 – 12**.

$$y_{total,char} = \frac{0.93 - 0.92 * \exp(-0.42 * 10^{-2} * T)}{12} + \frac{0.07 - 0.85 * \exp(-0.48 * 10^{-2} * T)}{16} + \frac{-0.41 * 10^{-2} + 0.10 * \exp(-0.24 * 10^{-2} * T)}{1} \tag{10}$$

$$y_{C,char} = (0.93 - 0.92 * \exp(-0.42 * 10^{-2} * T))/12/y_{total,char} \tag{11}$$

$$y_{O,char} = (0.07 - 0.85 * \exp(-0.48 * 10^{-2} * T))/16/y_{total,char} \tag{12}$$

$$y_{H,char} = (-0.41 * 10^{-2} + 0.10 * \exp(-0.24 * 10^{-2} * T))/1/y_{total,char} \tag{13}$$

The integration of **Equation 10 – 12** into the model (**Equation 3 - 9**) leads to the modification of **Equation 7 – 9** to **Equation 7.1 – 9.1**. The set of equations is now nonlinear and is solved by iteration.

$$\dot{N}_{H,H2O,out} = \dot{N}_{H,fuel,in} + \dot{N}_{H,H2O,in} - \dot{N}_{H,PG,in} - \dot{N}_{C,char,out}/y_{C,char} * y_{H,char} \tag{7.1}$$

$$\dot{N}_{O,CO2inCaCO3,out} = \dot{N}_{O,fuel,in} + \dot{N}_{O,H2O,in} - \dot{N}_{O,PG,out} - \dot{N}_{O,H2O,out} - \dot{N}_{C,char,out}/y_{C,char} * y_{O,char} \tag{8.1}$$

$$\dot{N}_{C,char,out} = \dot{N}_{C,fuel,in} - \dot{N}_{C,PG,out} - \dot{N}_{C,CO2inCaCO3,out} \tag{9.1}$$

The solution of the set of equations **Equation 3 – 9** and **Equation 7.1 – 9.1** is shown in **Figure 4**: At 600 °C nearly 50% of the C in the fuel is transported to the combustion reactor via char. Further, about 30% are sorbed by the bed material as CO_2 and therefore are also transported to the combustion reactor. At 800 °C only 30% of the C remains in the char, and practically no C is removed via the bed material as $CaCO_3$. This makes sense, since from a thermodynamic point of view the SER process can take place up to 760 °C [8]. The model applied in this work shows CO_2 transport via bed material also for higher temperatures than 760 °C. This is dedicated to the fact, that the temperature distribution in the gasification reactor is not uniform in most cases. It is most likely that for an indicated gasification temperature of e.g. 800 °C colder spots exist, where CO_2 sorption may be possible. Last but not least, it can be noticed that between 70 and 80% of the total C from the fuel can be transported to the combustion reactor at low temperatures.

ABBREVIATIONS

$\dot{N}_{i,y,in/out}$	Molar flow of component 'i' (C, H or O) in 'y' (fuel, PG, etc.) as 'in' (input) or 'out' (output) of the modeled system [mol/s]
$\dot{m}_{fuel}$	Biomass mass flow [kg/s]
V_m	Molar volume at 1 atm and 0 °C (0.0224 m^3/mol)
Y_{PG}	Product gas yield [$m^3_{STP,db}/kg_{fuel,daf}$]
$y_{j,y}$	Molar fraction 'j' (CO, H_2, etc) in 'y' (fuel, PG, etc.)
CR	Combustion reactor
daf	Dry and ash free
GR	Gasification reactor
mass.-%	Percent by mass
PG	Product gas
SER	Sorption enhanced reforming

REFERENCES

[1] S. Müller, S. Koppatz, M. Fuchs, T. Pröll, and H. Hofbauer, "Hydrogen Production Based on Conventional Dual Fluid Gasification versus Sorption Enhanced Reforming," in *International Conference on Polygeneration Strategies (ICPS13)*, 2013.

[2] J. Schmid, T. Pröll, H. Kitzler, C. Pfeifer, and H. Hofbauer, "Cold flow model investigations of the countercurrent flow of a dual circulating fluidized bed gasifier," *Biomass Convers. Biorefinery*, vol. 2, no. 3, pp. 229–244, 2012.

[3] N. Poboß, "Experimentelle Untersuchung der sorptionsunterstützten Reformierung," Universität Stuttgart, PhD Thesis, 2016.

[4] G. Soukup, "Der AER – Prozess , Weiterentwicklung in einer Technikumsanlage und Demonstration an einer Großanlage," TU Wien, PhD Thesis, 2009.

[5] N. Armbrust, D. Schweitzer, A. Gredinger, M. Beirow, T. B. N. Poboss, C. Hawthorne, H. Dieter, and G. Scheffknecht, "Gasification of Biomass with In-Situ CO_2 Capture and Separation in a 200 kW th Pilot Plant Fluidized bed gasification infrastructure," in *Gasification Technologies 2014*, 2014.

[6] D. Neves, H. Thunman, A. Matos, L. Tarelho, and A. Gómez-Barea, "Characterization and prediction of biomass pyrolysis products," *Prog. Energy Combust. Sci.*, vol. 37, no. 5, pp. 611–630, 2011.

[7] J. Brellochs, "Experimentelle Untersuchung und Prozess-Simulation der AER-Biomassevergasung zur Erzeugung eines regenerativen Erdgassubstitutes," *Dissertation*, 2014. [Online]. Available: https://cuvillier.de/de/shop/publications/6859-experimentelle-untersuchung-und-prozess-simulation-der-aer-biomassevergasung-zur-erzeugung-eines-regenerativen-erdgassubstitutes. [Accessed: 07-Mar-2016].

[8] S. Müller, J. Fuchs, J. C. Schmid, F. Benedikt, and H. Hofbauer, "Experimental development of sorption enhanced reforming by the use of an advanced gasification test plant," *Int. J. Hydrogen Energy*, vol. 42, no. 50, pp. 29694–29707, 2017.

INCREASING THE BIOH2 PRODUCTION IN A CSTR VIA DARK FERMENTATION USING STEADY-STATE OPTIMIZATION AND ROBUST CONTROLLERS

M. Rodriguez-Jara[1], E. Piceno-Diaz[1], H. Flores-Mejia[1] and H. Puebla[1]

1. Departamento de Energia, Universidad Autonoma Metropolitana Azcapotzalco, Ciudad de México, MEXICO; email: mariana_rj13@hotmail.com

ABSTRACT

In the last few years, biohydrogen (bioH2) has been explored as an alternative fuel for internal-combustion motors and electric vehicle fuel-cells. Dark fermentation is the most important bioH2 production method, which consists of a complicated process where anaerobic organism produces carboxylic acids, hydrogen gas, carbon dioxide and organic solvents from carbohydrate-containing organic wastes. A significant drawback of bioH2 production is associated with its low production. Continuous operation is preferable to increase the long-term production. The conventional operation of continuous biotechnological processes is subject to important changes in the substrate organic load, microbial activity, and environmental conditions. Furthermore, there is a need to optimize process conditions to improve its long-term productivity. Controlling a biotechnological process may be considerably complicated due to inherent difficulties such as nonlinear kinetics and model uncertainties. In this work, three optimization problems are formulated for the bioH2 production in a CSTR via dark fermentation. Furthermore, to guarantee the process operation in the optimal conditions two practical robust control approaches are proposed. The results show that it is possible to improve the conventional operation and production of bioH2 in a continuous reactor.

Keywords: Biohydrogen, biological CSTR, Optimization, Robust Control.

1 INTRODUCTION

The growth and development of society depend on a reliable and sustainable supply of energy. Thus, research into energy sources is of utmost relevance. For more than a century, fossil fuels have been extensively used to satisfy the needs of humans [1, 2]. However, concerns about the impact of the use of fossil fuels in global warming and acid rain have impulse the research on alternative fuels [1, 2]. Hydrogen, which is a clean energy carrier, is one of the most promising next-generation fuels [2]. Hydrogen production research is focused on reducing capital equipment, operations, and maintenance costs as well as improving the efficiency of hydrogen production technologies [2-5].

Biological processes show strong potentialities for sustainable hydrogen production. Indeed, hydrogen can be produced by micro-organisms using renewable raw materials such as organic wastes. The most important bioH2 production method is the dark fermentation [3, 4]. It is a complex process where an anaerobic organism (such as Enterobacter, Clostridium, and Bacillus) produces carboxylic acids, hydrogen gas, carbon dioxide and organic solvents from carbohydrate-containing organic wastes. Dark fermentation has been carried in both batch and continuous operation modes [3-5]. However, the continuous operation is preferable due to its higher long-term production and better quality control [6, 7].

The conventional operation of biological reactors is subject to important internal and external disturbances. For instance, changes in the substrate organic load, microbial activity, and environmental conditions. Thus, the production of bioH2 process through dark fermentation could be improved via the introduction of control schemes that guarantee the process operation in a given optimal condition [7,8].

In this work, we have designed two simple robust controllers for regulation of bioH2 production in a CSTR reactor. First, we have formulated and solved a steady-state optimization problem. Then, to maintain the operation at the optimal point, a robust control problem that considers model uncertainties and external perturbations is formulated. Two control designs are proposed based on a low-order model obtained with a step-response methodology [9-12]. A mathematical model that considers four species, glucose, biomass, hydrogen in both, liquid and gaseous phases, is used for optimization and control design purposes [13]. The results show that it is possible to improve the conventional operation and production of bioH2 in a continuous reactor using the proposed robust controllers.

2 MATERIALS AND METHODS

In this section, first, the case study and its mathematical model are described. Next, three steady-state optimization problems are formulated. Finally, the control design is presented based on two robust control approaches.

2.1 Dark Fermentation of Biohydrogen in a CSTR

Dark Fermentation

Biohydrogen production via dark fermentation is a very complex process and influenced by many factors, including the substrate, reactor type, and the hydraulic retention time [3-5]. In particular, a variety of fermentative pathways exist in dark fermentation. In the case of glucose as the substrate, it is converted to pyruvate by hydrogen-producing bacteria, with a production of the NADH. Pyruvate is then converted to acetyl-coenzyme A (acetyl-CoA), carbon dioxide, and hydrogen by the action of pyruvate-ferredoxin oxidoreductase and hydrogenase enzymes [3-5].

Mathematical Model of DF in a CSTR

A simple model of four species is considered for the production of biohydrogen in a CSTR [7,13]. The assumptions to derive the model are: (i) Homogeneous conditions. (ii) Reactions in the reactor are described using only two pseudo-stoichiometric reactions occurring in parallel according to Aceves-Lara et al. [7] (iii) Hydrogen in liquid-phase is in equilibrium with the hydrogen in gas-phase.

$$\begin{aligned}
\frac{dG}{dt} &= \frac{Q}{V}(G_{in}-G)-\frac{\mu_{\max 1}G}{k_{s1}+G}X-\frac{\mu_{\max 2}G}{k_{s2}+G}X\\
\frac{dX}{dt} &= -\frac{Q}{V}X+0.0829\frac{\mu_{\max 1}G}{k_{s1}+G}X+0.1068\frac{\mu_{\max 2}G}{k_{s2}+G}X\\
\frac{dH_2}{dt} &= -\frac{Q}{V}H_2+0.0351\frac{\mu_{\max 1}G}{k_{s1}+G}X-k_L(H_2-M_{H2}K_{H2}p_{H2,Gas})\\
\frac{dH_{2,G}}{dt} &= -\frac{Q_G}{V_G}H_{2,G}+\frac{V}{V_G}k_L(H_2-M_{H2}K_{H2}p_{H2,Gas})
\end{aligned} \qquad (1)$$

where G, X, and H_2 represent the concentrations (g/L) of glucose, biomass and hydrogen in the liquid phase, and $H_{2,G}$ is the hydrogen concentration (g/L) in the gas phase.

Conventional Operation

The nominal operation is obtained using the following parameter values [13]: Q = 3 L/d, G_{in} = 20 g/L, μ_{max1} = 37.3197, k_{s1} = 0.2896, μ_{max2} = 27.2416, k_{s2} = 9.2596, V = 0.9 L, V_G = 0.35 L, k_L = 3065 d^{-1}, M_{H2} = 2.016 g/mol, K_{H2} = 7.38x10^{-4} mol/L·bar, R = 8.314x10^{-2} bar·L/mol·K, T = 308 K, and,

$$p_{H2,Gas}=\frac{H_{2,G}RT}{M_{H2}}$$

The corresponding steady-state is: [G, X, H_2, $H_{2,G}$, qH_2]*= [0.343 g/L, 1.833 g/L, 1.885x10^{-3} g/L, 7.789x10^{-2} g/L, 14.97 L/d].

2.2 Steady-State Optimization

In this section, we formulate three steady-state optimization problems for the optimization of biohydrogen in a CSTR.

Maximization of the substrate consumption

The conventional optimization problem in biological reactors using organic wastes is the maximization of the substrate consumption. The objective function is defined as follows,

$$\min J=\left(1-\frac{G_{in}-G}{G_{in}}\right)^2 \qquad (2)$$

where G_{in} is the glucose input.

Maximization of the BioH2

A second optimization problem is aimed at the maximization of BioH2 in the liquid phase. The objective function is defined as follows,

$$\min J = -H \tag{3}$$

where H is the bioH2 in liquid-phase.

Maximization of the biohydrogen production

The last optimization problem is formulated as the maximization of the gas-flow of biohydrogen, which is written as follows,

$$\max J = \frac{RT_{amb}}{P_{atm} - p_{vap,H2}} \frac{V}{M_{H2}} k_L (H_2 - M_{H2} K_{H2} p_{H2,Gas}) \tag{4}$$

with P_{atm} = 1.013 bar, P_{atm} = 0.0557 bar, and T_{amb} = 298 K.

All optimization problems are completed with three type of constraints: (i) the steady-state model equations, (ii) process variables constraints, and (iii) maximum and minimum constraints on the control variable, $Q_{min} <= Q <= Q_{max}$. Where Q_{min} and Q_{max} stand to guarantee minimum processing of organic loading rate and avoid the washout condition, respectively. Moreover, we have also imposed a minimum input substrate degradation of 95 %, i.e., $G <= G_{in}*0.1$.

2.3 Robust Control Designs

In this section, we first define the control problem. Next, a simple input-output model is obtained based on the step-response method. Finally, proposed robust controllers are described.

Control Problem

The control problem can be stated as the regulation of the bioH2 gas-flow rate to an optimal reference provided by the steady-state optimization problem, via the manipulation of the input flow rate. The following assumptions for the control design are considered:

A1 The control input $u = Q$, is subjected to a saturation nonlinearity, i.e., $u_{min} <= u <= u_{max}$.

A2 The bioH2 gas-flow rate is available without a measurement delay.

A3 The input-output model representation is affected by unmodeled nonlinearities and external disturbances.

Input-Output Model

For control design purposes a simple model retaining the dominant input-output dynamics is highly desirable. In this work, the robust control design is based on an input-output response model determined from the reaction curve process [14]. The step response method is applied to the relationship between the input volumetric flow, Q and the bioH2 gas-flow, qH_2. Numerical simulations (not shown) illustrates that the step response is smooth, almost monotonous, and convergent, such that it is reasonable to model the input-output response with a simple stable first-order model.

The first order transfer function model is given by,

$$G_P(s) = \frac{Y(s)}{U(s)} = \frac{k_p}{\tau_0 s + 1} \tag{5}$$

where k_p is the steady-state process gain, and τ_0 is the process time constant. Using the step-response results the following parameters are obtained: k_p = 4.9, and τ_0 = 0.013.

Modeling Error Compensation Approach

The control approach is based on MEC ideas that lead to controllers with a simple linear structure, good closed-loop performance, and robustness properties [9, 10]. The control design consists of the following steps:

1. Lump the uncertain model terms, including terms containing uncertain parameters, in a single new state.
2. Estimate the uncertain term via a reduced order observer.
3. Design a feedback action to assign a desired closed-loop behavior.

Using the ideas proposed by Alvarez-Ramirez et al. [9], the resulting controller is given as follows,

$$u(t) = \frac{\tau_0}{k_p}\left(\left(\frac{1}{\tau_0} - \frac{1}{\tau_c}\right)e(t) + \frac{de(t)}{dt} - \frac{1}{\tau_e}\left(\omega(t) + e(t)\right)\right)$$
$$\frac{d\omega(t)}{dt} = \frac{1}{\tau_0}e(t) - \frac{k_p}{\tau_0}u(t) - \frac{1}{\tau_e}\left(\omega(t) + e(t)\right) \quad (6)$$

where the controller parameters are τ_c and τ_e, which can be interpreted as a closed-loop time constant, and the estimation time constant. Following the tuning rules by Alvarez-Ramirez et al. [9], they are set as follows: $\tau_0 > \tau_c > \tau_e$.

Sliding Mode Control Design

Sliding mode control techniques have long been recognized as a powerful robust control method for compensating model nonlinearity and uncertainty. The control design consists of two control actions, which are derived as follows [11]:

1. Introduce a specific sliding surface s(t), along which the controlled variable can slide to its desired final value. A continuous control action is derived which meet the conditions s(t) = 0 and ds(t)/dt = 0.
2. Introduce a control action based on the sign function, which forces the controlled state to the sliding surface when s(t) ≠ 0 (reaching phase).

Using the ideas proposed Abu-Rmileh et al. [12], the resulting controller is,

$$u(t) = \frac{1}{k_p}\left(\tau_0\lambda e(t) + \tau_0\frac{de(t)}{dt}\right) + k_D sign(s(t))$$
$$s(t) = e(t) + \lambda\int e(\tau)d\tau \quad (7)$$

where k_D and λ are controller parameters.

3 RESULTS AND DISSCUSION

In this section, the control methodology described above is applied for the bioH2 production in a CSTR via some numerical experiments. The control action is activated at t = 2 *d*. To show the controllers robustness properties disturbances in the glucose input are considered at t = 3 *d* and t = 5 *d*. Moreover, a set point change to 20 L/d at t = 4 *d* is applied.

3.1 Optimization of the biohydrogen production.

Proposed optimization problems in the above section are nonlinear and constrained, which can be solved via nonlinear programming methods. In this case, we have used the interior point algorithm using Matlab v.7. Optimal results are [*G*, *X*, H_2, $H_{2,G}$, qH_2, *Q*]:

- Problem 1: [0.03 g/L, 1.868 g/L, 1.546x10^{-3} g/L, 7.789x10^{-2} g/L, 2.26x10^{-6} L/d, 0.53 L/d].
- Problem 2: [0.856 g/L, 1.783 g/L, 2.038x10^{-3} g/L, 7.789x10^{-2} g/L, 20.06 L/d, 4.09 L/d].
- Problem 3: [1 g/L, 1.7693 g/L, 2.055x10^{-3} g/L, 7.789x10^{-2} g/L, 21.65 L/d, 4.23 L/d].

Thus, it can be noted that the optimization problems 2 and 3 leads to a significant increase of bioH2 with a 90 % of degradation of the input substrate.

3.2 Robust control of the biohydrogen production.

Based on the optimal results, we have set as the control objective the regulation of the bioH2 gas-flow rate at 21.5 L/d, via the manipulation of the input flow rate.

Robust control based on the MEC approach

The results are shown in Figure 1. It is noted that the controller can successfully regulate the output even in the presence of disturbances in the glucose input. Moreover, the change of set point is achieved with an acceptable control effort. From Figure 1, it can be observed that to regulate the bioH2 gas-flow to its optimal basal value, the input flow rate is stabilized at the optimal condition. However, when the disturbances and setpoint change are applied, the input flow rate adjust its value to maintain the desired closed-loop behavior.

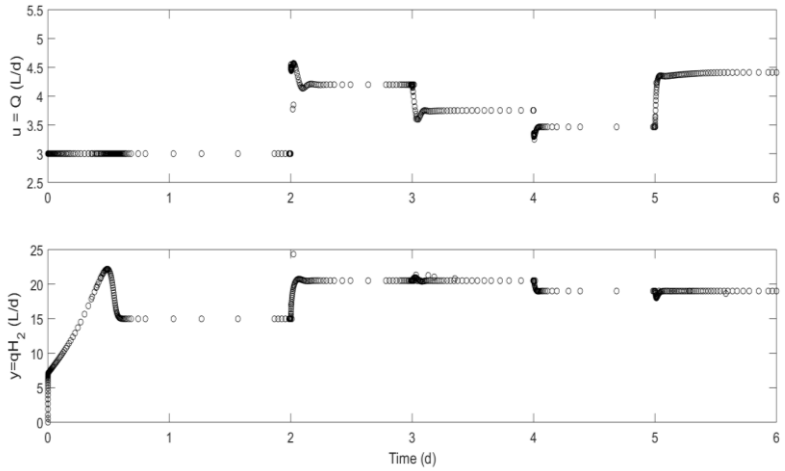

Figure 1. Control performance of the MEC robust controller.

Robust control based on SMC

The results are shown in Figure 2. It is observed that the proposed SMC is able also to regulate the bioH2 gas-flow to the desired reference. In this case, the control effort shows a significant effort under the effect of disturbances. Furthermore, the SMC selection of the tuning parameters was more involved, since the proposed simple tuning rules by Abu-Rmileh et al. [12] lead to a poor control performance.

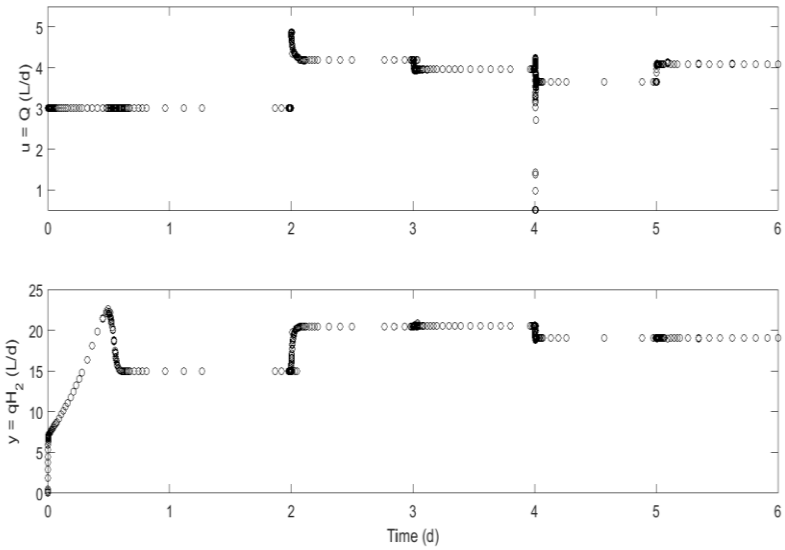

Figure 2. Control performance of the SMC robust controller.

4 CONCLUSIONS

In this work, based on a simple step input-output model, two simple and robust controllers are proposed for the regulation of the biohydrogen gas-flow in a CSTR. First, we formulate and solve three steady-state optimization approaches aimed to increase the biohydrogen production. Optimization results shown that is possible to increase the biohydrogen production via the adjustment of the input volumetric flow rate. Next, we design and applied via numerical simulations two robust controllers aimed to control the biohydrogen gas-flow to the optimal conditions and reject external disturbances in the substrate input. Numerical simulations on a nonlinear model of four states show that the resulting control performance with the proposed robust controllers design is very satisfactory.

ACKNOWLEDGEMENTS

Mariana Rodriguez-Jara and Ennio Piceno-Diaz acknowledge the financial support of CONACyT from a grant for master degree studies, and partial support of the UAM for supporting the participation in the SEEP 2018 conference.

REFERENCES

[1] A. Demirbas, Present and future transportation fuels, *Energy Sources: Part A*, Vol. 30, pp. 1473-1483, 2008.

[2] J.D. Holladay, J. Hu, D.L. King and Y. Wang, An overview of hydrogen production technologies, *Catalysis Today*, Vol. 139, pp. 244-260, 2009.

[3] Y. Kalinci, A. Hepbasli and I. Dincer, Biomass-based hydrogen production: a review and analysis, *International Journal of Hydrogen Energy*, Vol. 34, pp. 8799-8817, 2009.

[4] J.R. Bastidas-Oyanedel, F. Bonk, M.H. Thomsen and J.E. Schmidt, Dark fermentation biorefinery in the present and future (bio) chemical industry, *Reviews in Environmental Science and Bio/Technology*, Vol. 14, pp. 473-498, 2015.

[5] M.M. Arimi, J. Knodel, A. Kiprop, S.S. Namango, Y. Zhang, S.U. Geisen, Strategies for improvement of biohydrogen production from organic-rich wastewater: a review. *Biomass and Bioenergy*, Vol. 75, pp. 101-118, 2015.

[6] J.S. Chang, K.S. Lee and P.J. Lin, Biohydrogen production with fixed-bed bioreactors. *International Journal of Hydrogen Energy*, Vol. 27, pp. 1167-1174, 2002.

[7] C.A. Aceves-Lara, E. Latrille and J.P. Steyer, Optimal control of hydrogen production in a continuous anaerobic fermentation bioreactor. *International Journal of Hydrogen Energy*, Vol. 35, pp. 10710-10718, 2010.

[8] K. Nath and D. Das, Modeling and optimization of fermentative hydrogen production. *Bioresource Technology*, Vol. 102, pp. 8569-8581, 2011.

[9] J. Alvarez-Ramirez, A. Morales and I. Cervantes, Robust proportional-integral control. *Industrial & Engineering Chemistry Research*, Vol .37, pp. 4740-4747, 1998.

[10] H. Puebla, E. Hernandez-Martinez, R. Hernandez-Suarez, J. Ramirez-Muñoz and J. Alvarez-Ramirez, J., A simple feedback control approach for output modulation of spatiotemporal patterns in a class of tubular reactors, *Industrial & Engineering Chemistry Research*, Vol. 52, pp. 17517-17528, 2013.

[11] Y. Shtessel, C. Edwards, L. Fridman and A. Levant, *Sliding mode control and observation*, Birkhäuser, 2014.

[12] A. Abu-Rmileh, W. Garcia-Gabin and D. Zambrano, Internal model sliding mode control approach for glucose regulation in type 1 diabetes, *Biomedical Signal Processing and Control*, Vol. 5, pp. 94-102, 2010.

[13] I.T. Zúñiga, A. Vargas, E. Latrille and G. Buitrón, Robust observation strategy to estimate the substrate concentration in the influent of a fermentative bioreactor for hydrogen production. *Chemical Engineering Science*, Vol. 129, pp. 126-134, 2015.

[14] B.A. Ogunnaike and W.H. Ray, *Process Dynamics, Modelling, and Control*, Oxford University Press, 1994.

CHEMOMETRIC STUDY OF THE METABOLITES FORMED IN DARK FERMENTATION OF CHEESE WHEY FOR THE BIOHYDROGEN PRODUCTION BY THE PSYCHROPHILIC G088 STRAIN

S. Cisneros-de la Cueva[1], C. L. Alvarez-Guzmán[1], V. E. Balderas-Hernández[1], A. Smoliński[2] J. T. Ornelas-Salas[3], and A. De Leon-Rodriguez[1]

1. División de Biología Molecular, Instituto Potosino de Investigación Científica y Tecnológica A. C., Camino a la Presa San José 2055, Lomas 4ª Sección, C.P. 78216 San Luis Potosí, S.L.P., México; email: aleonr@ipicyt.edu.mx
2. Department of Energy Saving and Air Protection, Central Mining Institute, PI. Gwarków 1, 40-166 Katowice, Poland.
3. Universidad Autónoma de Guadalajara, Facultad de Ciencias, Av. Patria 1201, Lomas del Valle 3ª Sección, Zapopan, Jalisco. C.P. 45129, México.

ABSTRACT

In this study, the response surface method with a central composite experimental design was applied to evaluate the effect of temperature, pH and cheese whey powder concentration on biohydrogen production by the psychrophilic G088 strain ([EU636029], which is closely related to *Polaromonas rhizosphaerae* [EF127651]). Biohydrogen production was performed in 120 mL serological bottles with a production medium containing 2.75 g L^{-1} tryptone, 0.25 g L^{-1} yeast extract and cheese whey powder concentration in the range of 4.7-55.2 g L^{-1}, pH 3.4-10.1 and temperature of 4.7-55.2 °C. Maximum biohydrogen yield of 87.3 mL H_2 g^{-1} lactose was reached under pH 6.8, temperature 30 °C and cheese whey powder concentration of 30 g L^{-1}. Moreover, the chemometric analysis was applied for the comparison and visualization of the effect of the operating conditions on the production of the metabolites produced during the fermentations. Maximum production of metabolites of industrial importance, such as 2,3-butanediol (5.7 g L^{-1}) and ethanol (6.3 g L^{-1}) were achieved at 30 °C and pH of 6.8, and at 15 °C and pH of 8.8, respectively. This bioprocess may constitute an alternative in the production of bioenergy mainly by formation of products, which could be commercially interesting.

Keywords: Biohydrogen, Response surface methodology, Chemometric analysis

1 INTRODUCTION

The growing energy demand has caused serious environmental problems; this has created the necessity of replacing fossil fuels with energy sources [1-2]. Hydrogen is now considered as a promising, clean and environmental friendly energy carrier and a potential alternative to conventional fossil fuels [3-6]. It has a high-energy yield of 122 kJ g^{-1}, which is almost three times higher than hydrocarbon fuels [7]. Although hydrogen has illustrated its capability to be used for clean energy purposes, it is produced mostly by fossil fuel processing technologies; which are expensive and highly polluting due to the operating conditions [8].

In biological methods hydrogen is produced by metabolic transformation of a carbon source by a variety of microorganisms under conditions of anaerobic dark fermentation [9]. Among the important environmental parameters to be controlled in dark fermentation focused on biohydrogen production are: temperature, pH and substrate concentration [10]. The previous work by Alvarez-Guzmán et al. [3] proved that the maximum biohydrogen yield by the psychrophilic G088 strain using glucose as substrate was reached at the optimum temperature of 26.3 °C, showing an advantage of energy demand reduction since no external energy need to be used to maintain the optimum temperature of the process.

The agro-industrial residues are composed of simple carbohydrates, which make them promising substrates for biohydrogen production. The cheese whey (CW) powder is the by-product from cheese production. It represents 85-90% of the total volume of processed milk and contains approximately 70% of lactose on a dry basis. It is estimated that 10^8 Mg $year^{-1}$ of CW is produced worldwide. It causes a potential environmental risk due to the high organic load together with an inadequate disposal [7,11,12]. The use of agro-industrial residues has gained interest from an economic and environmental point of view since its use is advantageous due to the land disposal residues reduction and valorisation as raw materials for the production of marketable products by renewable and environmentally friendly processes such as dark fermentation.

Metabolism of hydrogen producing bacteria can be affected by changes in the temperature, pH and substrate concentration resulting in a change of the distribution of the metabolic by-products, like solvents and volatile fatty acids (VFAs) produced during the fermentation [13]. Therefore, the objective of the present study was to apply a chemometric analysis of the experimental data concerning the metabolites produced during the formation of biohydrogen in a dark fermentation of the CW powder by the G088 strain, depending on the process conditions applied. The aim of the study was to find and group various fermentation conditions for the different metabolites of industrial interest.

2 MATERIALS AND METHODS

2.1 Strain and culture media conditions

The strain used in the study was G088 [EU636029] was isolated from the Collins glacier at Fildes Peninsula, King George Island, Antarctica [14], and the closest relative of this strain according to NCBI is *Polaromonas rhizosphaerae* [EF127651]. The strain was cultured in agar plates with growth medium YPL containing 0.25 g L^{-1} of yeast extract (Difco), 2.75 g L^{-1} of Bacto-tryptone (Difco), and 20 g L^{-1} of lactose (Sigma). The plates were incubated at 25 °C for 5 days [15].

2.2 Experimental design

A central composite design 2^3 was applied to find the optimal conditions for the biohydrogen production, using the following factors: pH, temperature and CW powder concentration (Table 1).

Table 1. Experimental design of the process conditions for biohydrogen production

Test	X_1-Temperature (°C)	X_2-pH (-)	X_3- CW powder concentration (g L^{-1})
1	30	6.8	4.77
2	15	4.8	15
3	45	4.8	15
4	15	8.8	15
5	45	8.8	15
6	30	3.44	30
7	4.77	6.8	30
8	30	6.8	30
9	30	6.8	30
10	55.23	6.8	30
11	30	10.16	30
12	15	4.8	45
13	45	4.8	45
14	15	8.8	45
15	45	8.8	45
16	30	6.8	55.23

The empirical second order polynomial model was applied (see equation 1) to determine the optimal experimental conditions:

$$Y = \beta_0 + \sum_{i=1}^{k} \beta_i X_i + \sum_{i=1}^{k} \beta_{ii} X_i^2 + \sum_{i=1}^{k-1} \sum_{j=2}^{k} \beta_{ij} X_i X_j \quad (1)$$

Where Y is the predicted biohydrogen yield, βo is the model intercept, βi is the linear coefficient, βii is the quadratic coefficient, β_{ij} is the interaction coefficient, whereas X_i X_j are independent variables [16]. The statistical analysis was performed with software Design Expert version 7.0.

2.3 Batch fermentation

The experiments were performed 120 mL serological bottles. Each bottle contained 110 mL of medium of different concentration of CW powder determined according to the experimental design and summarized in

Table 1 (Land O'Lakes, Arden Hills Minnesota). Medium consisted of 0.25 g L^{-1} of yeast extract (Difco) and 2.75 g L^{-1} of Bacto-tryptone (Difco) supplemented with 1 mL L^{-1} of trace elements solution: 0.015g L^{-1} of $FeCl_3 \cdot 4H_2O$, 0.00036g L^{-1} of $Na_2MoO_4 \cdot 2H_2O$, 0.00024g L^{-1} of $NiCl_2 \cdot 6H_2O$, 0.0007g L^{-1} of $CoCl_2 \cdot 6H_2O$, 0.0002g L^{-1} of $CuCl_2 \cdot 2H_2O$, 0.0002 g L^{-1} of Na_2SeO_3 and 0.01g L^{-1} of $MgSO_4$. It was inoculated with strain at initial optic density of 0.5 to absorbance at 600 nm. The pH was adjusted in each reactor according to the experimental design (Table 1) [15].

2.4 Determination of concentrations of carbohydrates, metabolites and biohydrogen

Lactose, formic acid, lactic acid, and acetic acid were determined with a high-performance liquid chromatograph Infinity LC 1220 (Agilent Technologies) using a refraction index detector (Agilent Technologies) and a column Rezex ROA (Phenomenex, Torrance) at 60 °C, and 0.0025 M H_2SO_4 as a mobile phase at 0.5 mL min^{-1}. The concentrations of ethanol, acetoin and propionic acid were determined with the use of a gas chromatograph 6890N (Agilent Technologies) with a capillary column HP-Innowax (30 m x 0.25 mm i.d. x 0.25µm film thickness). The analyses were performed with a split ratio of 5:1 and the following temperature program: 25 °C for 10 min, 175 °C for 1 min, heating with a heating rate of 5 °C min^{-1} to 280 °C and maintaining this temperature for a final time of 10 min [15]. The concentrations of hydrogen was determined with a use of a gas chromatograph 6890N (Agilent Technologies), equipped with a thermal conductivity detector and using Agilent J&W HP-PLOT Molesieve (30 m x 0.32 mm i.d. x 12 µm film thickness) [12].

2.5 Data organization and methods of data exploration

The studied experimental data set was organized into matrix **X** (16 x 6), which rows represent 16 objects (tests of biohydrogen production under various conditions), whereas the columns correspond to the studied parameters (metabolites produced in CW powder fermentation), listed in Table 2.

Table 2. Matrix X (16X6) of the metabolites and the biohydrogen yield by the psychrophilic strain G088 under different experimental conditions

Objects	**Parameters**						
Test	**Lactic acid (g L^{-1})**	**Succinic acid (g L^{-1})**	**Formic acid (g L^{-1})**	**Acetic acid (g L^{-1})**	**2, 3-butanediol (g L^{-1})**	**Ethanol (g L^{-1})**	**H_2 Yield (mL H_2 g^{-1} lactose)**
1	0.034	0.098	0.144	0.421	0.509	0.824	53.79
2	0.033	0.162	0.255	0.665	0.051	5.021	5.23
3	0.068	0.394	0.532	0.447	0.082	0.625	0.00
4	0.033	0.321	0.376	0.773	0.931	6.036	50.41
5	0.097	0.296	0.052	0.507	0.901	0.191	0.00
6	0.059	0.000	0.000	0.000	0.000	0.715	0.00
7	0.056	0.193	0.000	0.037	0.000	0.511	0.00
8	0.095	0.601	0.000	0.773	5.422	1.717	86.10
9	0.098	0.713	0.000	0.665	5.732	1.610	87.39
10	0.058	0.000	0.000	0.000	0.000	0.000	0.00
11	0.031	0.000	0.000	0.000	0.000	0.000	0.00
12	0.033	0.280	0.407	0.510	0.058	5.326	0.87
13	0.053	0.053	0.038	0.614	0.082	0.355	0.00
14	0.050	0.492	0.501	0.200	0.964	6.347	4.72
15	0.051	0.043	0.065	0.451	0.112	0.782	3.66
16	0.082	0.698	0.366	0.608	5.379	1.429	56.59

The hierarchical clustering analysis (HCA) is one of the most often applied methods in data exploration. This method [17-20] allows investigating the similarities between studied objects in the parameter space, and between the parameters in the object space. The results of HCA are presented in the form of dendrograms

differing in terms of the applied similarity measure between objects, as well as the way the similar objects are connected.

3 RESULTS AND DISCUSSION

3.1 Yield of biohydrogen produced under different operational conditions

The effect of different experimental variables on the biohydrogen production yield was simultaneously investigated employing a central composite experimental design. Three variables (temperature, pH and CW concentration) were taken into consideration. The following second order polynomial equation (eq. 2) was found to give the biohydrogen yield:

$$Y = -504.76791 + 8.66885X_1 + 121.44280X_2 + 3.32497X_3 - 0.18903e^{-3}X_1X_2 + 0.029834e^{-4}X_1X_3 - 0.15696e^{-3}X_3X_2 - 0.14266e^{-3}X_1^2 - 8.02458X_2^2 - 0.055936e^{-4}X_3^2 \quad (2)$$

Where Y is biohydrogen yield and X_1, X_2 and X_3 are the coded values of temperature, initial pH and initial CW powder concentration, respectively. The biohydrogen production yield corresponding to the different operational conditions are shown in Table 2. As it can be seen, the maximum biohydrogen yield of 87.39 mL H_2 g^{-1} lactose was achieved at 30 °C, slightly acidic pH of 6.8 and 30 g L^{-1} of lactose. A change in temperature, pH and CW concentration below or above the optimum values led to a decrease in the yield of biohydrogen production.

3.2 Chemometric analysis

The dendrograms constructed with the application of the Ward's linkage method are presented in Fig. 1. The Euclidean distance was employed as the similarity measure.

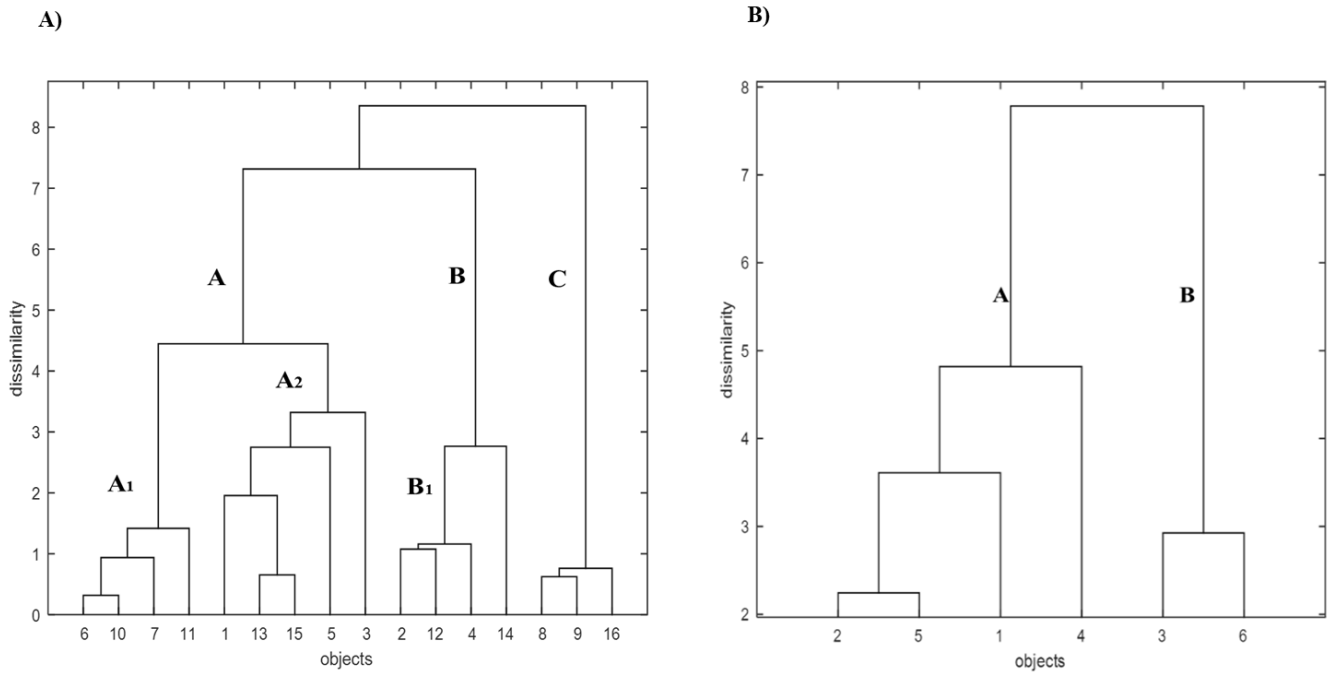

Figure 1. Dendrograms of (A) studied objects (experiments of biohydrogen production under various conditions) and (B) parameters (metabolites produced during CW powder dark fermentation) in the objects space based on the Ward's linkage method and using the Euclidean distance as the similarity measure.

The dendrogram presented in Fig. 1A revealed tree clusters: A, B and C of biohydrogen production yield experiments under various operating conditions.

-Cluster A composed of the objects nos. 1, 3, 5, 6, 7, 10, 11, 13 and 15

-Cluster B composed of the objects nos. 2, 4, 12 and 14

-Cluster C composed of the objects nos. 8, 9 and 16.

Within the main clusters the following sub-clustering structures may be distinguished: two sub-clusters within cluster A (A1 and A2) and one sub-cluster within cluster B (B1):

-Sub-cluster A1 composed of the objects nos. 6, 7, 10 and 11
-Sub-cluster A2 composed of the objects nos. 1, 3, 5, 13 and 15
-Sub-cluster B1 composed of the objects nos. 2, 4 and 12.
Particularly, the objects in cluster A differ from the remaining ones, mainly in terms of low concentration of 2,3-butanediol and ethanol (parameters nos. 5 and 6). The uniqueness of cluster B was related to high concentrations of formic acid, acetic acid and ethanol (parameters nos. 3, 4 and 6). On the other hand, cluster C was characterized by the highest concentrations of succinic acid and 2,3-butanediol (parameters nos. 2 and 5) among all the studied objects.
The dendrogram constructed for the metabolites produced during the fermentation tests under various operating conditions (see Fig. 1B) revealed two main classes:
-Class A containing parameters nos. 1, 2, 4 and 5 (corresponding to lactic acid, succinic acid, acetic acid and 2,3-butaneidol, respectively).
-Class B containing parameters nos. 3 and 6 (corresponding to formic acid and ethanol, respectively).

4 CONCLUSIONS

The concentration of different metabolites produced in dark fermentation of CW powder by G088 strain depends on several variables including temperature, initial pH and initial CW powder concentration. At a low temperature of 15 °C and pH of 8.8 the maximum concentration of ethanol is attained, whereas the higher concentration of 2,3-butanediol is achieved at 30 °C and pH of 6.8. The biohydrogen yield is also affected by the operational conditions since its higher value is reached at 30 °C, pH 6.8 and 30 g L^{-1} CW powder. These results indicate that G088 strain may be considered for the production of valuable metabolites of industrial interest using a low-cost substrate such as CW powder.

ACKNOWLEDGEMENTS

The authors thank to CONACyT-Pro Nal 247498 and CONACYT Ciencias Básicas 281700

REFERENCES

[1] T. da Silva Veras, T.S. Mozer, D. da Costa Rubim Messeder dos Santos, A. da Silva César. Hydrogen: Trends, production and characterization of the main processes worldwide. *International Journal of Hydrogen Energy*, Vol. 42, pp. 2018-2033, 2017.
[2] D.H. Lee, D.J. Lee, A. Veziroglu. Econometric models for biohydrogen development. *Bioresource Technology*, Vol. 102, pp. 8475-8483, 2011.
[3] C.L. Alvarez-Guzmán, E. Oceguera-Contreras, J.T. Ornelas-Salas, V.E. Balderas-Hernández, A. De León-Rodríguez. Biohydrogen production by the psychrophilic G088 strain using single carbohydrates as substrate. *International Journal of Hydrogen Energy*, Vol. 41, pp. 8092-8100, 2015.
[4] A. Smoliński, M. Stempin, N. Howaniec. Determination of rare earth elements in combustion ashes from sselected Polish coal mines by wavelength dispersive X-ray fluorescence spectrometry. *Spectrochimica Acta Part B: Atomic Spectroscopy*, Vol. 116, pp. 63-74, 2016.
[5] A. Smoliński, N. Howaniec, K.A. Stańczyk. A comparative experimental study of biomass, lignite and hard coal steam gasification. *Renewable Energy*, Vol. 36, pp. 1836-1842, 2011.
[6] A. Smoliński, N. Howaniec. Chemometric Modelling of Experimental Data on Co-gasification of Bituminous Coal and Biomass to Hydrogen-Rich Gas. *Waste and Biomass Valorization*, Vol. 8 pp. 1577-1586, 2017.
[7] L.M. Rosales-Colunga, E. Razo-Flores, L.G. Ordoñez-Acevedo, F. Alatriste-Mondragón, A. De León-Rodríguez. Hydrogen production by *Escherichia coli* Δ*hycA* Δ*lacI* using cheese whey as substrate. *International Journal of Hydrogen Energy*, Vol. 35, pp. 491-499, 2009.
[8] J.D. Holladay, J. Hu, D.L. King, Y. Wang. An overview of hydrogen production technologies. *Catalysis Today*, Vol. 139, pp. 244-260, 2009.
[9] S.V. Mohan, K. Chandrasekhar, P. Chiranjeevi, P.S. Babu. *Biohydrogen Production from Wastewater*, Elsevier, 2013.

[10] J.A. Puhakka, D. Karadag, M.E. Nissilä. Comparison of mesophilic and thermophilic anaerobic hydrogen production by hot spring enrichment culture. *International Journal of Hydrogen Energy*, Vol. 37, pp. 16453-16459, 2012.
[11] G. Davila-Vazquez, C.B. Cota-Navarro, L.M. Rosales-Colunga, A. De León-Rodríguez, E. Razo-Flores. Continuos biohydrogen production using cheese whey: Improving the hydrogen production rate. *International Journal Hydrogen Energy*, Vol. 34, pp. 4296-4304, 2009.
[12] J. Carrillo-Reyes, L.B. Celis, F. Alatriste-Mondragón, E. Razo-Flores. Different start-up strategies to enhance biohydrogen production from cheese whey in UASB reactors. *International Journal of Hydrogen Energy*, Vol. 37, pp. 5591-5601, 2012.
[13] S. Zhang, T.H. Lee, Y. Lee, S.J. Hwang. Effect of VFAs Concentration on Bio-hydrogen Production with Clostridium Bifermentans 3AT-ma. *Energy Procedia*, Vol. 14, pp. 518-523, 2012.
[14] S.A. García-Echauri, M. Gidekel, A. Gutiérrez-Moraga, L. Santos, A. De León-Rodríguez. Isolation and phylogenetic classification of culturable psychrophilic prokaryotes from the Collins glacier in the Antarctica. *Folia microbiologica (Praha)*, Vol. 56, pp. 209-214, 2011.
[15] Z.D. Alvarado-Cuevas, A.M. López-Hidalgo, L.G. Ordoñez, E. Oceguera-Contreras, J.T. Ornelas-Salas, A. De León-Rodríguez. Biohydrogen production using psychrophilic bacteria isolated from Antarctica. *International Journal of Hydrogen Energy*, Vol. 40, pp. 7586-7592, 2015.
[16] D.C. Montgomery. *Design and Analysis of Experiments 6th Edition with Design Expert Software*. John Wiley & Sons. 2004.
[17] L. Kaufman, P. Rousseeuw. *Finding Groups in Data: An Introduction To Cluster Analysis.* John Wiley & Sons. 1990.
[18] C.H. Romesburg. *Cluster Analysis for Researches. 1 ed.* Lulu Press. 1984.
[19] A. Smoliński. Gas chromatography as a tool for determining coal chars reactivity in the process of steam gasification. *Acta Chromatographica*, Vol. 20, pp. 349-365, 2008.
[20] A. Smoliński. Analysis of the impact of physicochemical parameters characterizing coal mine waste on the initialization of self-ignition process with application of cluster analysis. *Journal of Sustainable Mining*, Vol. 13, pp. 36-40, 2014.

EFFECT OF MICROELEMENTS (ZINC AND COPPER) SUPPLEMENTATION ON THE ANAEROBIC CO-DIGESTION OF FOOD WASTE AND DOMESTIC WASTEWATER

P.C. Chan, R.A. de Toledo, H.I. Iu, H. Shim*

Department of Civil and Environmental Engineering, Faculty of Science and Technology, University of Macau, Taipa, Macau SAR, China; *E-mail: hjshim@umac.mo

ABSTRACT

The effects of microelements (zinc and copper) supplementation (provided as $ZnSO_4$ and $ZnCl_2$ at 50, 70, and 100 mg/L Zn^{2+} and as $CuSO_4$ and $CuCl_2$ at 10, 30, and 50 mg/L Cu^{2+}) on biogas (methane) production were evaluated while co-digesting a mixture of food waste(water) and domestic wastewater. Regardless of zinc and copper supplementations, both microelements increased the cumulative methane yield compared to the control without supplementation ($p<0.05$) and were considered providing the synthesis of enzymes required for both acetoclastic and hydrogenotrophic methane production. The supplementation of zinc and copper stimulated the conversion of organic matter to methane at concentrations 50-100 mg/L and 10 mg/L, respectively. The improvements on the cumulative methane yield obtained could be associated with not only the intermittent feed strategy but also the micronutrient supplementation. Microelements may improve the long chain fatty acids (LCFAs) removal by two different mechanisms, biological and physical (precipitation). The exact role of each mechanism warrants further studies, but both definitely contribute to alleviate the toxic effects of LCFAs. The upflow anaerobic sludge blanket reactor used operated under the stable and steady condition during 260 days.

Keywords: Anaerobic digestion, food waste, methane yield, microelement supplementation

1 INTRODUCTION

Approximately food worth of $32 billion is discharged annually in China and the food waste comprises 70% of all wastes nationwide [1]. In two Special Administrative Regions of China, Hong Kong and Macau, even though with different statistics, the food waste disposal and management is still a huge problem. In Hong Kong, food waste has been landfilled with other municipal solid waste (MSW). In 2015, 10,159 tonnes/day of MSW were landfilled and the food waste consisted of 33% MSW (3,382 tonnes) [2]. In Macau, food waste has been incinerated due to the limited territory (area, 30 km^2). In 2016, 503,867 tonnes of MSW were incinerated (38.5% of food waste) [3].

Anaerobic digestion (AD) is a promising technology among all the options available for the food waste valorization due to the simultaneous waste management, renewable energy generation (biogas), and nutrients recovery (digestate) [4]. Although AD is a mature technology on converting organic matter to methane gas and has been widely applied to treat different kinds of substrates (including sewage sludge, high-strength wastewater, and animal manure), still there exist many challenges to be addressed during the AD of food waste, including technical, economical, and social issues [5]. The mono-digestion of food waste generally results in the digester instability/failure even at low organic loading rates (ORL; 2-3 g COD/L/d) as a result of short and long chain fatty acids (SCFAs and LCFAs) accumulation and ammonia generation at the early stage of the digestion process [6]. In comparison, the co-digestion of food waste with different substrates is feasible and has provided a more stable environment for the microbial community involved, enhanced the balance of nutrients, and adjusted the C/N ratio. Our research group has recently evaluated the viability to co-digest a mixture of food waste and domestic wastewater together with the intermittent feed mode (48 h feed/48 h feedless) and concluded the feeding strategy was responsible for the effective lipid degradation. The inhibition/failure observed in the continuous mode could be successfully recovered under the intermittent feed and the reactor could be stably operated at OLRs higher than 2 g COD/L/d [7].

The microelement supplementation is another strategy commonly used to maximize the conversion of organic matter to methane gas in the AD of different kinds of substrates [8]. The supplementation of micronutrients is a prerequisite for the microbial growth and also plays an important role in the synthesis of

essential coenzymes or cofactors in methanogenic pathways. It has also been well established that Co, Ni, Cu, Fe, Zn, Mo, Se, and W are important in the methanogenic system for the enzymatic activity [8]. However, food waste is generally poor in essential micronutrients vital for a stable reactor performance [9], which would further justify the supplementation of Zn^{2+} and Cu^{2+}carried out in this study. The effects of both microelements supplementation on the AD have not been that conclusive, using substrates other than food waste due to the complex mechanisms happening during its AD, such as microbial adaptation, precipitation, and adsorption [10]. The concentration ranges chosen for both microelements (50, 70, and 100 mg/L Zn^{2+} and 10, 30, and 50 mg/L Cu^{2+}) were based on their concentrations commonly found in food waste (7.8-75 mg/L Zn^{2+} and 7-30 mg/L Cu^{2+}) [9, 11]. The objective of this study was to maximize the conversion of organics to methane gas while supplementing microelements (Zn^{2+} and Cu^{2+} separately) into the influent and to further find out their stimulatory/inhibitory effects on the SCFAs and LCFAs accumulation.

2 MATERIALS AND METHODS

2.1 Influent

The influent used was a mixture of food waste and domestic wastewater (at 0.183, v/v). Food waste was collected from university canteen and domestic wastewater was obtained from local wastewater treatment plant. The food waste pre-treatment was carried out following Chan et al. [7]. The food wastewater was characterized in terms of chemical oxygen demand (COD: 42,700 mg/L), total nitrogen (TN: 450 mg/L), total phosphorus (TP: 76 mg/L), C/N ratio (29.4), and pH, 6.9.

2.2 UASB reactor operation and micronutrient supplementation

The activated digested sludge (10 L) from local wastewater treatment plant was used as seed for the upflow anaerobic sludge blanket (UASB) reactor. The reactor (working volume, 38 L) was first operated under mesophilic conditions (35±1°C) at a hydraulic retention time (HRT) of 10 days for the sludge maturation and granulation, fed with the synthetic wastewater (similar to domestic wastewater at COD:TN:TP, 50:4:1). After 40 days, a stable biogas production was obtained and the influent was switched to food wastewater (mixture of food waste and domestic wastewater). The reactor was operated under the intermittent mode (48 h feed/48 h feedless) at the organic loading rate (OLR) of 3.8 g COD/L/day [7]. Alkalinity (as $CaCO_3$, 3.5 g/L) was added daily to control the pH. After one HRT cycle (control), the microelement supplementation was carried out as follows: Zn^{2+} (as $ZnSO_4$ and $ZnCl_2$) was supplemented at different concentrations (50, 70 and 100 mg/L) in the following cycles of 10-day HRT each. Then, Cu^{2+} (as $CuSO_4$ and $CuCl_2$,) was added at 10, 30, and 50 mg/L, following the same procedure as for the Zn^{2+} addition. The parameters monitored (during both feed and feedless periods) daily were COD removal, biogas production, methane content, and intermediates (SCFAs, LCFAs, and ammonia-nitrogen) accumulation in the effluent.

2.3 Analytical measurements

HACH methods were used to measure COD, TP, TN and ammonia-nitrogen (Hatch, Loveland, CO, U.S.A.). The biogas composition and the concentrations of LCFAs and SCFAs were analysed by gas chromatography (GC) equipped with thermal conductivity detector (TCD) and flame ionization detector (FID), respectively (Agilent, U.S.A.). The LCFAs analysed were palmitate, oleate, and linolate, while the SCFAs analysed were acetate, butyrate, valerate, and propionate. The details about analysing methane content, LCFAs, and SCFAs can be found elsewhere [7]. The analysis of variance (ANOVA) at 95% confidence was used to evaluate the statistical significances of results after the microelements supplementation.

3 RESULTS AND DISCUSSION

In the first 20 days of reactor operation, no microelement was supplemented, and this condition was set as control. During this period, even though the reactor was operated relatively stable, showing an acceptable COD removal efficiencies (76.0±1.2%), the cumulative methane yield was low (0.17 L CH_4/g $COD_{removed}$), suggesting most COD present in the feed were not directly converted to methane gas but probably to other intermediates such as SCFAs and LCFAs instead. Acetate (303±99.4 mg/L) and propionate (220±129 mg/L) were the main SCFAs accumulated, but the pH remained stable (7.7±0.1) during this period. The accumulation of acetate implies the methanogenic population was not that much effective on the methane generation. According to Ünal et al. [12], microelements are essential components of enzymes or cofactors

of the metabolic pathways associated with methanogens, and the deficit on the methane production observed in the control could be associated with the lack of necessary micronutrients in the feed substrate. Food waste is generally poor in micronutrients, which further necessitate the microelement supplementation to maximize the conversion of organics to methane gas. Therefore, the low methanization observed in the control could be associated with the imbalance/lack of micronutrients. Figure 1 shows the cumulative methane yield obtained when the reactor was operated without microelement supplementation (control) and with different concentrations of zinc (as $ZnSO_4$ and $ZnCl_2$) and copper (as $CuSO_4$ and $CuCl_2$).

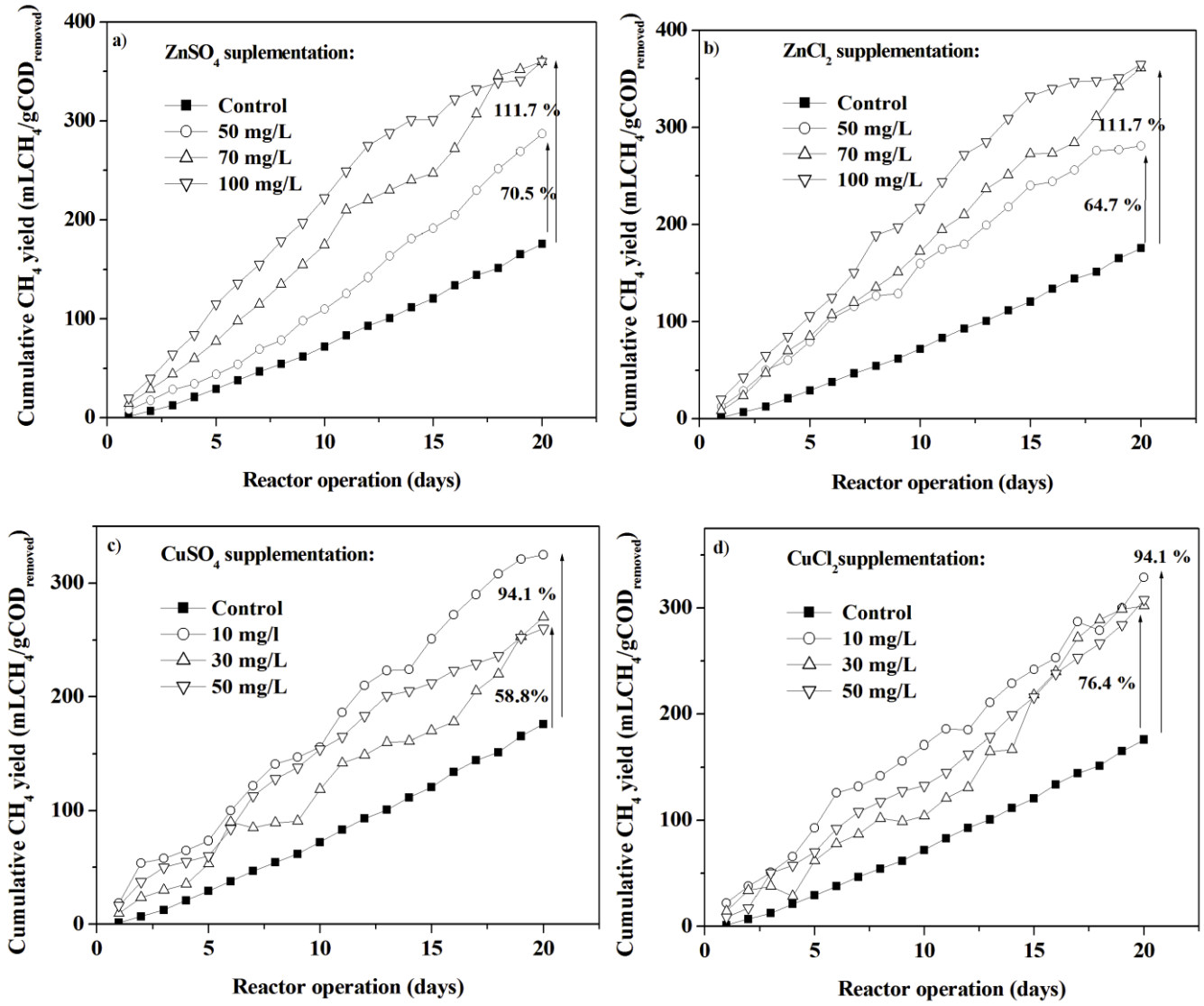

Figure 1. Cumulative methane yields for the control and for different zinc and copper supplementations.

Regardless of zinc and copper supplementations, both microelements increased the cumulative methane yield compared to the control ($p<0.05$), suggesting both played important roles in the methanogenic activity. However, there were no significant differences in the cumulative methane yield among the cycles with different zinc ($p=0.24$) and copper ($p=0.44$) supplementations. Among the zinc and copper concentrations used, the highest increase of cumulative methane yield, 111.7% and 94.1%, was obtained when 70-100 mg/L Zn^{2+} and 10 mg/L Cu^{2+} were added, respectively. The higher Cu^{+2} concentrations (30-50 mg/L) started to inhibit the process to some extent. The COD removal and methane content increased by 14.8-22.6% and 6.5%, respectively, in the presence of microelements (Tables 1 and 2). The supplementation of increasing concentrations of both microelements generally followed a similar trend (Tables 1 and 2) regardless of the counter ions used (SO_4^{2-} and Cl^-), further confirming the stimulation on methane production was attributable

to Zn^{2+} and Cu^{2+} ions. The stimulatory/inhibitory thresholds for copper and zinc ions are still not conclusive compared to previous literature, and the differences observed are commonly associated with the degree of sludge granulation, the nature of substrate used, the degree of microbial community adaptation, and the total microelement concentration added, readily available to microorganisms [13, 14].

Table 1. COD removal, CH_4 content and yield, total SCFAs and LCFAs, and ammonia-nitrogen after zinc supplementation

Parameter	Control	$ZnSO_4$ (50 mg/L)	$ZnCl_2$ (50 mg/L)	$ZnSO_4$ (70 mg/L)	$ZnCl_2$ (70 mg/L)	$ZnSO_4$ (100 mg/L)	$ZnCl_2$ (100 mg/L)
COD removal %	76.0±1.2	75.7±3.7	81.3±1.4	76.4±4.7	78.8±2.8	82.1±3.7	88.2±2.2
CH_4 content %	61.0	63.0	64.0	63.8	63.5	64.5	65.0
CH_4 yield[a]	0.17	0.29	0.28	0.36	0.36	0.36	0.37
Total SCFAs[b]	572±253	513±135	545±120	302±104	206±80	316±110	307±94
Acetate[b]	303.0±99.4	242.4±11.4	151.9±55.8	160.5±56.5	294.2±125	85.5±53.1	138.1±37.2
Total LCFAs[b]	377.7±60.3	14.6±1.4	15.9±0.5	22.9±5.1	21.1±3.1	24.8±8.8	26.9±8.2
NH_3-N[b]	835±101.2	818±50.6	858±36.6	738±44	795±81.9	659±66.9	564±57.8

[a] L CH_4/g $COD_{removed}$
[b] In mg/L

Table 2. COD removal, CH_4 content and yield, total SCFAs and LCFAs, and ammonia-nitrogen after copper supplementation

Parameter	Control	$CuSO_4$ (10 mg/L)	$CuCl_2$ (10 mg/L)	$CuSO_4$ (30 mg/L)	$CuCl_2$ (30 mg/L)	$CuSO_4$ (50 mg/L)	$CuCl_2$ (50 mg/L)
COD removal %	76.0±1.2	94.2±2.9	91.9±2.3	92.4±2.3	89.4±2.1	91.1±1.9	91.3±2.9
CH_4 content %	61.0	63.3	63.7	63.7	64.4	61.5	61.7
CH_4 yield[a]	0.17	0.33	0.33	0.27	0.30	0.26	0.31
Total SCFAs[b]	572.0±253.0	181.6±59.5	219.6±66.1	154.3±49.1	187.7±79.2	195.3±34.3	184.7±56.8
Acetate[b]	303.0±99.4	90.0±20.4	98.2±33.3	75.9±22.9	86.6±32.0	88.0±25.4	76.0±10.5
Total LCFAs[b]	377.7±60.3	13.6±4.0	14.3±5.2	18.8±5.1	14.7±0.8	19.7±2.4	16.3±2.0
NH_3-N[b]	835.0±101.2	687.9±82	665.5±115.3	430.0±26.6	460.0±21.9	480.7±52.7	539.5±28.9

[a] L CH_4/g $COD_{removed}$
[b] mg/L

The intermittent feeding was another strategy used in this study to stabilize the AD, due to the high content of lipids (~32%, w/w) in the Chinese food [15]. There was an increase of 40% on the methane production when the intermittent mode was applied instead of operating the reactor continuously [7], and this increase further suggested the intermittent mode was more effective on converting the COD from the influent to methane gas. The obtained result was also in agreement with Nadais et al. [16] where the methane production rate was 25% higher when the UASB reactor was operated under the intermittent mode to treat synthetic dairy wastewater. The cumulative methane yield might be further enhanced by extending the feedless (mainly for stabilization) period or by increasing the OLR. For the current study, it was considered the improvements on the cumulative methane yield could be associated with the intermittent feeding strategy used and especially the microelements supplementation might have played a role in increasing the methanization. The relative decrease of SCFAs accumulation after the microelements supplementation (Tables 1 and 2) with the concomitant increase of cumulative methane yield (Figure 1) could also confirm the addition of zinc and copper contributed to the enzyme synthesis crucial for the methane production, as also reported by Banks et al. [17]. Regardless of the zinc and/or copper supplementation, the total accumulation of SCFAs was significantly different from the control ($p<0.05$) as well as when different concentrations of microelements were supplemented ($p<0.05$).

The addition of microelements was also considered efficient for the LCFAs removal (Tables 1 and 2). The total LCFAs concentrations in the effluent were significantly different ($p<0.05$), regardless of the influent feed supplemented with different zinc and/or copper concentrations. Palmitate, oleate, and linoleate were the main LCFAs present in the control effluent, while after the microelement supplementation, palmitate was the only one accumulated, which was already expected as a result of the slow kinetics of β-oxidation for the saturated LCFAs. Microelements may improve the LCFAs removal by two different mechanisms, biological and physical precipitation. For the first possibility, the microelement supplementation could stimulate the bioremoval of LCFAs. The effects (stimulatory/inhibitory) of zinc and copper on the LCFAs biodegradation are scarce but other microelements (tungsten and selenium) were already confirmed stimulatory to the LCFAs degradation [18]. The second possible mechanism is the precipitation of LCFAs by divalent cations, which is known to mitigate the LCFAs adsorption on the sludge surface and prevent the reactor failure. The specific role/importance of each mechanism on the LCFAs removal should be evaluated in details, but they definitely contribute to minimize the toxic effects of LCFAs adsorption on sludge surface to a great extent, and the UASB reactor could operate under the stable and steady condition during 260 days in the current study.

Another parameter monitored during the anaerobic co-digestion of food waste and domestic wastewater was the ammonia-nitrogen generation. The inhibitory concentrations of ammonia-nitrogen in the AD vary greatly under mesophilic conditions (1,200-5,500 mg/L) and the differences were mainly attributed to the microbial community adaptation. The ammonia-nitrogen concentration was significantly different from the control ($p<0.05$) and during the microelements (zinc and copper) supplementation, and varied from 835.0±101.2 to 430.0±26.6 mg/L. The decrease of ammonia-nitrogen concentration during the microelement supplementation could be associated with the nitrogen fixation for biomass production as proposed/suggested previously [17].

4 CONCLUSION

The supplementation of zinc and copper stimulated the conversion of organic matter to methane, at 50-100 mg/L and 10 mg/L, respectively. The improvements on the cumulative methane yield could be associated not only with the intermittent feeding strategy but also with the microelements supplementation. The simultaneous supplementation of zinc and copper, together with other microelements, would be further studied to find out the existence of synergistic/antagonistic effects of microelement addition to improve the methane production as well as the reactor performance.

ACKNOWLEDGEMENTS

This work was supported by grants from the University of Macau Multi-Year Research Grant (MYRG2017-00181-FST) and the Macau Science and Technology Development Fund (FDCT115/2016/A3 and FDCT044/2017/AFJ).

REFERENCES

[1] World Watch Institute. Food waste and recycling in China: A growing trend? <http://www.worldwatch.org/food-waste-and-recycling-china-growing-trend-1>> Accessed on 05 March 2018.

[2] The Government of Hong Kong Environmental Protection Department. Monitoring of solid waste in Hong Kong <https://www.wastereduction.gov.hk/sites/default/files/msw2015.pdf> Accessed on 10 March 2018.

[3] Macao Environmental Protection Bureau. Report of the state of the environment of Macao 2016. <http://www.dspa.gov.mo/StateReportHTML/2016/pdf/en/2016en.pdf> Accessed on 12 March 2018.

[4] G. Capson-Tojo, D. Ruiz, M. Rouez, M. Crest, J.P. Steyer, N. Bernet, J.P. Delgenès. R. Escudié, Accumulation of propionic acid during consecutive batch anaerobic digestion of commercial food waste, *Bioresource Technlogy,* Vol. 245, pp. 724-733, 2017.

[5] F. Xu, Y. Li, X. Ge, L. Yang, Y. Li, Anaerobic digestion of food waste – Challenges and opportunities, *Bioresource Technology,* Vol. 247, pp. 1047-1058, 2018.

[6] S.L.H. Chiu and I.M.C. Lo, Reviewing the anaerobic digestion and co-digestion process of food waste from the perspectives on biogas production performance and environmental impacts, *Environmental Science and Pollution Research*, Vol. 23, pp. 24435-24450, 2016.
[7] P.C. Chan, R.A. de Toledo, H. Shim, Anaerobic co-digestion of food waste and domestic wastewater – Effect of intermittent feeding on short and long chain fatty acids accumulation, *Renewable Energy*, in press.
[8] X.M. Feng, A. Karlsson, B.H. Svensson, S. Bertilsson, Impact of trace element addition on biogas production from food industrial waste-linking process to microbial communities, *FEMS Microbiology Ecology*, Vol. 74, pp. 226-240, 2010.
[9] L. Zhang and D. Jahng, Long-term anaerobic digestion of food waste stabilized by trace elements, *Waste Management*, Vol. 32, pp. 1509-1515, 2012.
[10] J. Guo, A. Ostermann, J. Siemens, R. Dong, J. Clemens, Short term effects of copper, sulfadiazine and difloxacin on the anaerobic digestion of pig manure at low organic loading rates, *Waste Management*, Vol. 32, pp. 131-136, 2012.
[11] R. Zhang, H.M. El-Mashad, K. Hartman, F. Wang, G. Liu, C. Choate, P. Gamble, Characterization of food waste as feedstock for anaerobic digestion, *Bioresource Technology*, Vol. 98, pp. 929-935. 2007.
[12] B. Ünal, V.R. Perry, M. Sheth, V. Gomez-Alvarez, K.J. Chin, K. Nüsslein, Trace elements affect methanogenic activity and diversity in enrichments from subsurface coal bed produced water, *Frontiers in Microbiology*, Vol. 3, pp. 1-14, 2012.
[13] H. Hao, Y. Tian, H. Zhang, Y. Chai, Copper stressed anaerobic fermentation: biogas properties, process stability, biodegradation, and enzyme responses, *Biodegradation*, Vol. 28, pp. 369-381, 2017.
[14] R. Zhang, X. Wang, J. Gu, Y. Zhang, Influence of zinc on biogas production and antibiotic resistance gene profiles during anaerobic digestion of swine manure, *Bioresource Technology*, Vol. 244, pp. 63-70, 2017.
[15] Y. Meng, S. Li, H. Yuan, D. Zhou, Y. Liu, B. Zhu, A. Chufo, M. Jaffar, X. Li, Evaluating biomethane production from anaerobic mono- and co-digestion of food waste and floatable oil (FO) skimmed from food waste, *Bioresource Technology*, Vol. 185, pp. 7-13, 2015.
[16] H. Nadais, M. Barbosa, I. Capela, L. Arroja, C.G. Ramos, A. Grilo, S.A. Sousa, J.H. Leitão, Enhancing wastewater degradation and biogas production by intermittent operation of UASB reactors, *Energy*, Vol. 36, pp. 2164-2168, 2011.
[17] C. Banks, Y. Zhang, Y. Jiang, S. Heaven, Trace element requirements for stable food waste digestion at elevated ammonia concentrations, *Bioresource Technology*, Vol. 104, pp. 127-135, 2012.
[18] A. Karlsoon, A. Bjorn, S.S. Yekta, B.H. Svensoon, Improvement of the biogas production process. Biogas Research Center (BRC) Report. http://liu.diva-portal.org/smash/get/diva2:776575/FULLTEXT01.pdf (2014) Accessed 15 March 2018.

PORE STRUCTURE CHARACTERISTICS OF SLUDGE RESIDUES AFTER THE PROLYSIS PROCESS

Kuo-Hsiung Lin[1], Zhi-Wei Chou[1], Hung-Lung Chiang[2]

[1]Department of Environmental Engineering and Science, Fooyin University, Kaohsiung, Taiwan; email: xx407@fy.edu.tw

[2]Departmentof Health Risk Management, China Medical University, Taichung, Taiwan; email: hlchiang@mail.cmu.edu.tw

ABSTRACT

Waste disposal could be an important issue in the industrialization countries, especially for the urban area. Public concerns the waste treatment associated with the release of contaminants into the environment and ecological systems that could be the serious risks to affect the human health and the environment. Therefore, the developments of the reuse procedures are the important work for the waste well disposal. Sludge is an inevitable product of biological wastewater treatment procedures and its high carbon and energy content leads to be a biomass. The sludge disposal is a challenging environmental issue and high treating costs that is a high portion fees associated with wastewater treatment plants. Sludge was mixed with KOH activation reagent, and then the pyrolysis process was conducted to remove the water, volatile constituents and develop the pore structure of pyrolysis residues. In this work, high temperature enhances the gas products and reduces the yield of residues. The increment of the total pore volume could result from the increase in mesopores. The high fraction of mesopore formation contributed the pore structure after pyrolysis of KOH immersed sludge.

Keyword: Waste disposal, Sludge, Potassium hydroxide (KOH), Wastewater treatment plants

1 INTRODUCTION

Biosludge is a product of wastewater treatment facility and it is a high organic content. The waste sludge disposal can account for over half of the operating costs of wastewater treatment plants (WWTPs)[1]. Due to its rapidly increasing amount and potential risks for the environment and human health, the sludge issue has raised significant for public concerns. The reduce, recycle, and reuse are the important concepts for sludge disposal [2]. Owing to the high volatile matter and carbon content of sludge, it can be converted into useful products after suitable procedures. Therefore, sewage sludge is recognized as having high potential energy recovery for sustainable development [3]. The pyrolysis technique for sludge disposal could achieve many advantages including inhibiting the heavy metal vaporization due to the decrease of pyrolysis temperature, reducing the leaching of heavy metals from the pyrolysis carbonaceous residue[4], and offering relatively low pollution control cost compared to combustion technique [5,6]. High moisture content of sludge, therefore the microwave system was used to combine the dewatering and pyrolysis to improve the energy efficiency of pyrolysis.

In this work, microwave pyrolysis technology was employed to treat sludge from a petrochemical wastewater treatment plant. The raw sludge and KOH immersed sludge were conducted to determine their mass fraction distribution and pore characteristics for the further application.

2 EXPERIMENTAL

2.1. Materials

Sludge samples were obtained from the wastewater treatment plant of a petrochemical industry. In addition, the sludge contains microorganisms obtained from an activated sludge process of the wastewater treatment plant. The raw sludge cakes contained 85wt.% water and had a volatile solids concentration of 63wt.% (ash of 38 wt.%) within the total solids content of 15±0.3 wt.%. Sludge was stored at 4^{o}C before pyrolysis.

Sludge (moisture content 85%) was immersed and mixed with KOH at the mass ratio of 1:0.25 (sludge: KOH, by weigh). The mixture put into the oven at 80°C for 4hrs. Then the KOH impregnated sludge was pyrolyzed at 400, 500 and 600°C for 30 min.

2.2. Sludge Pyrolysis

Sludge drying and pyrolysis processes were conducted in a multimode-microwave oven. Wet sludge was placed into a quartz container (A tube reactor was 25 cm length, 5.5 cm inner diameter, and 9 cm outer diameter), which was put inside the heating oven of microwave. 200 mL/min of N_2 gas was flowed through the reaction bed at a rate of to maintain an inert atmosphere. A rubber-silicon-ring and stainless steel cap were selected to seal the quartz reactor. A thermocouple (0-1000 °C) was installed in the reactor and connected to a temperature controller. Sludge sample was heated to the desired temperatures from 400 to 600°C, and then held for 30 min. The vapour produced during the experiment was immediately cooled by an ice-water bath condenser. The condensable part of the vapour was collected by a liquid collector. Microwave pyrolysis was conducted on three samples in duplicate for different temperatures.

2.3 Pore Characteristics of Residues

After pyrolysis, the sludge residues were determined their physical characteristics including specific surface area, pore volume distribution and pore diameter, were measured via N_2(gas) adsorption (in liquid N_2 condition at 77K) in an ASAP 2010 micropore analyzer. The BET method [7] and BJH method [8] were selected to determine the surface area and pore volume distribution, respectively. Silica-alumina, alumina and molecular sieve were purchased from Micrometrics and these materials were used in the quality assurance and quality control procedures for the determination of pore characteristics of sludge residues.

3.0 RESULTS AND DISCUSSION

3.1 Sludge Pyrolysis and Mass Distribution

Dewatering biosludge cakes (moisture content: 85 wt.%) obtained from the wastewater treatment plant of the petrochemical industry. With microwave heating, the wet sludge was heated to 135°C and held for 3 min for the dehydration. Then, the wet sludge was continuously heated to the desired temperature and held for 30 min. Results indicate the pyrolyzed products were 15-21 wt.% in gas phase, 16-20 wt.% in liquid oil phase, and 60-69 wt.% in solid residue under a dried sludge basis at pyrolytic temperatures from 400-600°C (shown in Fig.1a).

The KOH impregnated wet sludge was heated to the set temperature and held for 30 min. The pyrolyzed products the gas phase fraction was 13-29 wt%, liquid oil phase fraction was14-17 wt%, and solid residue fraction was 54-73wt.%, at pyrolytic temperatures from 400-600°C (shown in Fig. 1b). The mass fraction of three phases could be changed significantly due to the addition of KOH. In this work, high temperature reduces the yield of residues and enhances the gas products. The liquid oil reaches a higher yield at about 500-600°C, after which, due to its volatility at high temperatures, increasing the temperature reduces the liquid oil production (data not shown). However, the KOH impregnated sludge has higher yield of gas than that of raw sludge after pyrolysis at 600°C.

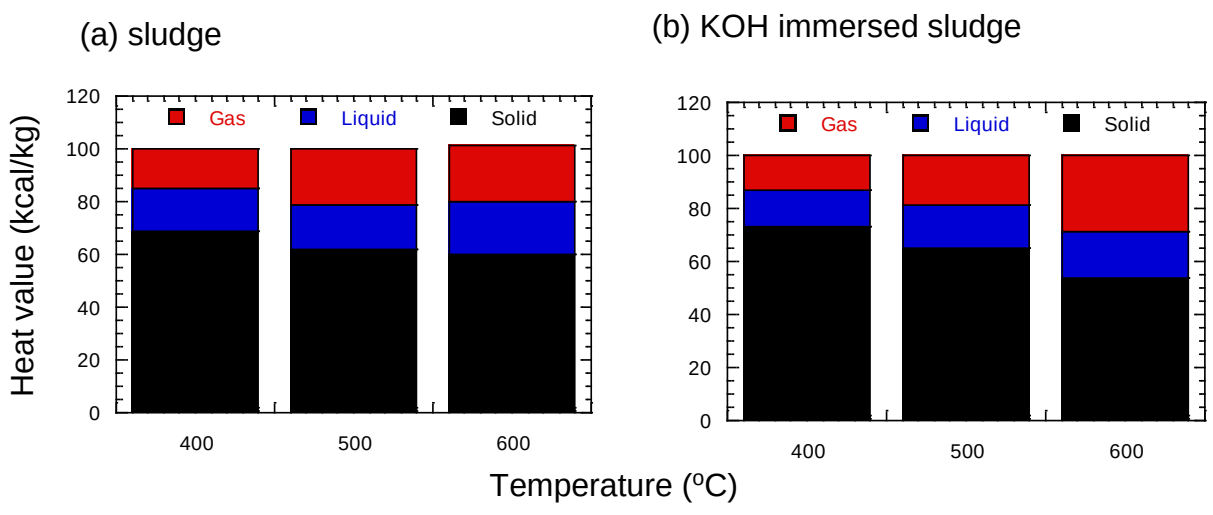

Figure 1 Mass fraction distribution of (a) sludge-raw materials and (b) KOH immersed sludge

3.2 Pore Characteristics of Materials

Table 1 shows the pore characteristics of specific surface area, micropore surface area, total pore volume and micropore volume of pyrolysis residues. Results indicated that the pyrolysis residues of raw sludge have few micropores, with low contribution in total pore volume. When the pyrolytic temperature was higher than 400^{o}C, the total pore volume increased in temperatures up to 600^{o}C, although the micropore volume decreased (see Table 1). This suggests that the increment of the total pore volume resulted from the increase in mesopores. As a result, the specific surface area of pyrolysis residues increased with an increase in temperature, with the BET surface areas close to 25 m^2/g at 600^{o}C. When compared to pyrolysis of raw sludge, the KOH immersed sludge has the higher total pore volume and lower micropore volume at 400-600^{o}C. It suggests that the pyrolysis of KOH immersed sludge occurs more significantly increase in mesopores resulted in the increment of the total pore volume.

Table 1 Pore characteristics of sludge raw materials and KOH immersed sludge

Pore characteristics		BET surface area (m^2/g)	Total pore volume (cm^3/g)	Micropore volume (cm^3/g)	Pore diameter (Å)
Raw material-sludge	400℃	8.43	0.0536	0.00167	254.14
	500℃	16.12	0.0975	0.00102	241.82
	600℃	25.10	0.1089	0.00056	173.50
KOH immersed Sludge	400℃	11.22	0.0768	0.000101	273.83
	500℃	12.89	0.0820	0.000136	254.46
	600℃	22.30	0.1226	0.000204	219.16

4.0 CONCLUSIONS

High temperature reduces the yield of residues and enhances the gas products. The liquid oil reached a higher yield at about 500-600^{o}C, after which increasing the temperature reduced the yield of liquid oil because of its volatility at high temperature. The increment of the total pore volume could result from the increase in mesopores. The high fraction of mesopore formation contributed the pore structure after pyrolysis of KOH immersed sludge. The KOH impregnation could change the pore development, but the high impregnated dose could be necessary to enhance the development of pore structure.

REFERENCE

J.L. Campos, L. Otero, A. Franco, A. Mosquera-Corral, E. Roca, Ozonation strategies to reduce sludge production of a seafood industry WWTP. Bioresource Technology, Vol.100,pp.1069-1073, 2009.

[2] Romero P., M.D. Coello, J.M. Quiroga, C.A. Aragon, Overview of sewage sludge minimisation: techniques based on cell lysis-cryptic growth. Desalination and Water Treatment, Vol.51, pp. 5918-5933, 2013.

[3] A. Bridgwater, Renewable fuels and chemicals by thermal processing of biomass. *Chemical Engineering Journal*, Vol.91, pp. 87-102,2003.

[4] I.H. Hwang, Y. Ouchi, T. Matsuto, Characteristics of leachate from pyrolysis residue of sewage sludge. *Chemosphere*, Vol.68,pp.1913-1919,2007.

[5] D. Fytili, A. Zabaniotou, Utilization of sewage sludge in EU application of old and new methods—a review. *Renewable & Sustainable Energy Reviews*, Vol.12, pp.116-140, 2008.

[6] Y. Kim, W. A. Parker, Technical and economic evaluation of the pyrolysis of sewage sludge for the production of bio-oil. *Bioresource Technology*, Vol.99, pp. 1409-1416, 2008.

[7] S. Brubauer, H. P. Emmett, E. Teller, Adsorption of gas in multimolecular layers. *Journal of the American Chemical Society*, Vol. 60, pp. 309–319, 1938.

[8] E.P. Barrett, L.G. Jovner, P.P. Halenda, The determination of pore volume and area distribution in porous substances .I. computations of nitrogen isotherms. *Journal of the American Chemical Society*, Vol. 73, pp.373-380, 1951.

TRANSESTERIFICATION OF WASTE COOKING OIL USING PYROLYSIS RESIDUE SUPPORTED EGGSHELL CATALYST

Anjani R.K. Gollakota[1*], Vikranth Volli[1], and Chi-Min Shu[1]

1. Department of Safety, Health, and Environmental Engineering, National Yunlin University of Science and Technology, Douliu, Taiwan, 64002, ROC. Email: gollakota.iitg@gmail.com

ABSTRACT

The present study focusses on synthesis and characterization of eggshell supported pyrolysis residue (char) as a heterogeneous base catalyst for transesterification of waste cooking oil. The influence of structural, compositional, and morphological properties on catalytic activity to optimize reaction time, methanol: Oil molar ratio (6:1, 9:1, 12:1, 15:1, and 18:1) and catalyst concentration (10, 20, and 30 mass %) in biodiesel production were evaluated. The particle size distribution of pyrolysis residue, calcined eggshell, and the synthesized catalyst was in the range of 0.06–14 µm. The decomposition of eggshell revealed a two-stage mass loss from 300–900 ^{o}C indicating the removal of moisture content and the formation of CaO from $CaCO_3$. Biodiesel with higher conversion rate over 95% was observed at 65^{o}C using 10 mass% catalyst concentration with methanol to oil molar ratio of 12:1 in 3 h.

Keywords: Eggshell, Pyrolysis residue, Heterogeneous base catalyst, Transesterification

1 INTRODUCTION

Development of methods and technologies to proficiently utilize biomass (agricultural wastes), a renewable, economic, and biodegradable source of energy has become the primary intent of the scientific community. Pyrolysis, a flexible and alluring technology that can provide viable solutions to ecological impediments effecting global, climatological, biological, and environmental changes [1]. Numerous research articles were published reporting the efficient techniques in employing the products of biomass pyrolysis (bio-oils, bio-chars and gases) as an alternative to fossil fuels, and petroleum products after chemical treatment and modification [2–6]. Bio-char (pyrolysis residue) a carbon rich substrate has far reaching applications in the fields of pollutant adsorption, carbon sequestration, syngas production, soil amendment, and heterogeneous catalysis [7].

Biodiesel is a widely accepted, sustainable, and renewable source of energy and the economic way to produce it is by catalytic (homogeneous, and heterogeneous) transesterification of tri-glycerides [8]. The most common feed stock for biodiesel production are vegetable oils, resulting in increased production costs and capital investment [9]. The use of waste cooking oils (WCO), a non-edible, cheap and readily available source of tri-glycerides could be a feasible alternative and can help subsiding pollution as well [10]. The major drawback of using WCO was its higher free fatty acid (FFA < 3%), water content, and the presence of other solid impurities resulting in saponification, and hydrolysis during transesterification reducing biodiesel conversion. Several techniques were proposed to overcome this problem and to improve the biodiesel yields, such as: Esterification with acids and ion exchange resins [11], use of heterogeneous bi-functional catalysts and layered double hydroxides [12,13], and metal doped zeolites [14].

Foo et al. [15] prepared microwave induced KOH activation of granular activated carbon produced from oil palm biodiesel solid residue for adsorption of methylene blue dye. Farid et al. [6] utilized KOH impregnated char produced from oil palm empty fruit brunch as adsorbent for purification of waste cooking oil biodiesel. The use of KOH modified carbon catalyst derived from waste date pits for transesterification by Abu-Jrai et al. [16]. The optimized yield obtained was 91.6% at 65 ^{o}C, with 6 mass% KOH loading on carbon and with 9:1 methanol to oil ratio within 1 h. Malins et al. [17] synthesized 4-sulfophenyl activated carbon based solid acid catalyst for biodiesel production from rapeseed oil. Thushari et al. [18] prepared sulfonated coconut meal residue carbon catalyst for biodiesel production from waste palm oil. The highest biodiesel yield of 92.7% was obtained at 5 mass% catalyst concentration with 12:1 methanol to oil molar ratio for 8 h. Transesterification of jatropha and karanja oils were performed using waste egg shell derived Zn, Fe, Mn, and Al mixed metal oxides [19]. Waste egg shell derived CaO supported W-Mo mixed

oxide catalyst was used for biodiesel production from waste cooking oil [20]. The highest biodiesel conversion of 96.2% was obtained with 15:1 methanol to oil molar ratio, 2 mass% catalyst loading and 2 h reaction time. Transesterification of palm oil was performed through biomimetic silicification of eggshell and Na_2SiO_3 as raw materials [21]. The optimum conditions to achieve biodiesel yield of 87.7% was: methanol-to-oil molar ratio, 15:1, catalyst loading 9 mass%; and reaction time, 8 h. Teo et al. [22] developed $Ca(OCH_3)_2$ carbon catalyst from cockle shells and bulk char coal. The optimal conditions to achieve maximum biodiesel yield of 98.6% were methanol/oil molar ratio of 12:1 and 3 mass% of catalyst at 60 °C for 1 h reaction time.

In the current study, calcined eggshell supported pyrolysis residue catalyst with different CaO loading were synthesized and their activity was estimated in transesterification of waste cooking oils. The synthesized catalyst was characterized (i.e., morphology, physico-chemical and phase identification) via FESEM, FTIR, and XRD analysis. Effects of the catalyst loading, molar ratio of methanol to oil, and reaction time on the catalyst activity were investigated to optimize transesterification conditions.

2 EXPERIMENTAL

2.1. Materials

Chicken eggshell and waste cooking oil (WCO) was collected from restaurants near YunTech, Douliu, Taiwan. Whatman (1001–150 Grade I) was used to filter solid particulate from the collected WCO. The Sesame de-oiled cake pyrolysis residue (SCPR) was obtained using our previously reported method [23]. Anhydrous methanol for synthesis (Merck, < 99.8%) and $CDCl_3$ for nuclear magnetic resonance analysis (NMR) (Merck, < 99.97%) were acquired and used as received.

2.2. Catalyst preparation

Conventional wet impregnation method was used for the synthesis of eggshell supported pyrolysis residue catalyst. The collected eggshells were washed with distilled water, oven dried overnight at 105 ^oC for constant mass. The dried eggshell was crushed, sieved into a uniform size (< 2 mm) and then calcined at 900 ^oC for 2 h. The obtained pyrolysis residue was milled and sieved to a particle size of 250 µm and was used as carbon support for catalyst preparation without any further modification. In typical preparation, 0.5 g of calcined eggshell (CES) was suspended in 50 ml distilled water, stirred vigorously (600 rpm) for 20 min, followed by the addition of 4.5 g of pyrolysis residue. Subsequently, the mixture was ultrasonically dispersed for 10 min to ensure total homogeneity, refluxed overnight at 65 ^oC. The resultant grey suspended slurry was filtered, dried and then calcined at 700 ^oC in a furnace for 2 h. The obtained solid powder was denoted as AEC – 10 and stored in desiccators for further use.

2.3. Catalytic activity

Biodiesel from waste cooking oil was produced in a 500 mL three-neck borosil flask with reflux condenser. An oil bath was used to maintain isothermal conditions. Fixed quantities of catalyst and methanol was suspended for 5 minutes at 65 ^oC and then the desired quantity of WCO was added and stirred at 500 rpm for a period of time. The operating conditions were methanol: Oil molar ratio (6:1, 9:1, 12:1, 15:1, and 18:1), catalyst concentration (3, 5, 7, 10, 12 and 15 mass%) for 7 h. At the end of the reaction, the mixture was cooled to room temperature, centrifuged at 6000 rpm for 10 min to separate catalyst and the unreacted methanol was removed using rotary evaporator. The conversion of biodiesel was estimated using the procedure described elsewhere [24].

2.4. Characterization

Existence of various characteristic functional groups were evaluated in the range of 400 – 4000 cm^{-1} using Perkin Elmer (Spectrum 100) Fourier transform infrared spectroscopy (FTIR). The surface morphology was examined using Sigma/Zeiss FESEM. The overall crystalline phases of samples were determined by Bruker D Advance X-ray diffraction (XRD) system using a Ni-filtered Cu K_α radiation (λ=1.5406 Å) between 10 and 65° of 2θ. ^{1}H-NMR analyses were acquired at 25 ^oC on a Varian DRX-600 using DMSO D6 as the solvent and trimethyl siloxysilane (TMS) as the internal standard.

Table 1. Elemental Composition and Surface Properties of SCPR, CES, AEC 10, AEC 20, and AEC 30

Characteristic	SCPR	CES	AEC 10	AEC 20	AEC 30
C	70.6	--	29.43	22.73	19.47
O	19.13	23.85	45.23	43.35	36.17
P	3.22	4.35	6.33	7.33	7.58
Ca	0.71	71.8	11.25	19.02	28.59
Na	1.23	--	1.61	0.99	1.44
Mg	1.63	--	4.01	3.46	3.34
K	3.48	--	2.14	3.12	3.41

3 RESULTS AND DISCUSSION

3.1. Characterization of catalyst

Three different heterogeneous base catalysts were prepared (AEC 10, AEC 20, and AEC 30) and the influence of CES chemical impregnation on texture, morphology, and composition was analysed to assess the effective incorporation of CaO. The major chemical composition of SCPR was carbon 70.6% with phosphorous 3.22% and potassium 3.48% as its minor components. Calcined eggshell contained 71.8% calcium (Ca) and 4.35% of phosphorous (P) which is analogous with eggshell calcined at 900 ^{o}C reported to exhibit 63.8% of calcium [25]. Table 1 represents the elemental composition of SCPR, CES, AEC 10, AEC 20, and AEC 30. From the table, it can be observed that, with increase in CSE loading a clear increase in calcium content of AEC10 (11.25%) < AEC 20 (19.02%) < AEC 30 (28.59%) was observed in the synthesized catalyst.

FTIR spectra of SCPR represent peaks of Ca–O bending (500–580 cm^{-1}), C–H bending (680 cm^{-1}), and O–C–O asymmetric stretching (1075 cm^{-1}) of unidentate carbonate, respectively [26,27]. Stretching –OH (1150–1270 cm^{-1}) vibration of phenolic aromatic ring, and H–O–H bending (1645 cm^{-1}) of water was also observed [6]. In CES, the peaks at 960 and 1043 cm^{-1} correspond to symmetric and asymmetric stretching vibrations of P–O [28]. Broad bands at 875, 1423, and 1786 cm^{-1} indicated asymmetric C=O stretching vibrations of carbonate species. A sharp peak at 3642 cm^{-1} signifies asymmetric hydroxyl–OH stretching vibrations [6]. Presence of a band below 500 cm^{-1} attributes to pure CaO vibrations. The surface functional groups of SCPR, CES, AEC 10, AEC 20, and AEC 30 was presented in Figure 2(A). The synthesized catalyst had both the absorption bands of parent species with a shift of higher energy absorption.

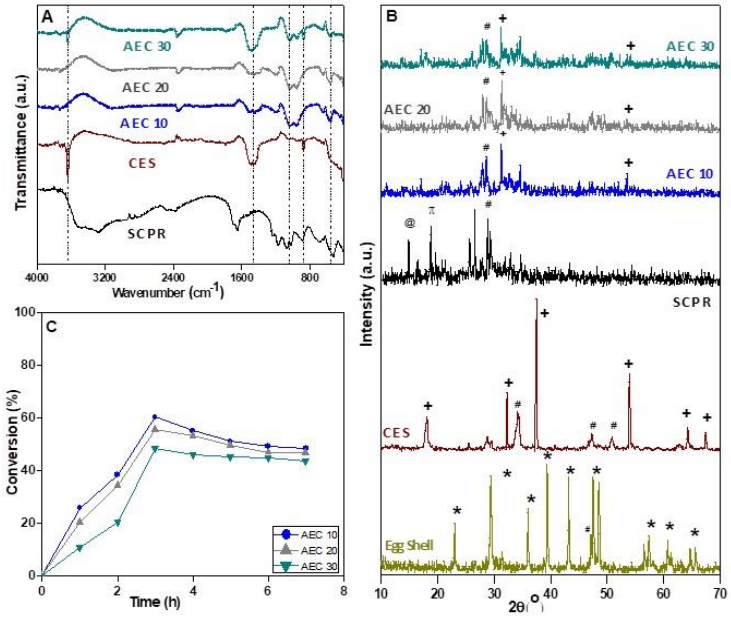

Figure 1. Spectra of (A) FTIR, (B) XRD, and the effect of reaction time on conversion of calcined egg shell, AEC 10, AEC 20, and AEC 30.

bands at 560, 1040, and 1490 cm^{-1}. The disappearance of bands between 3100–3550, 1645 and 1150–1270cm^{-1} indicating the removal of organic material and associated water molecules, respectively in the prepared catalyst. This could be due to the reduced mass of carbonate species upon calcination at higher temperatures [19].

The XRD diffractogram of eggshell, CES, SCPR, AEC 10, AEC 20, and AEC 30 was shown in Figure 2(C). Raw eggshell exhibited the peaks associated with calcite (JCPDS 47–1743) with major peak at 2θ: 29.4º (104) of *h, k, l* along with 23.17º (012), 36.00º (110), 39.4º (113), 43.1º (202), 47.5º (016), 48.5º (018), and 56.61º (122). XRD profiles of CES illustrate well-defined peaks of CaO (JCPDS 82–1690) at 2θ angle of 18.1º (001), 32.2º (111), 37.4º (200), 54.0º (220), 64.3º (311), and 67.5º (222). The disappearance of calcite phase (2θ = 29.4º) was observed in XRD pattern of the calcined eggshell, implying that the $CaCO_3$ phase was completely transformed to CaO phase but with a mixture of $Ca(OH)_2$ (JCPDS 087–0674) phase at 2θ: 28.8º (100), 47.3º (102), and 50.8º (110) [29]. SCPR exhibited a sharp peak at 14.8º (101) representing the presence of cellulose. The intensities at 2θ: 26.6º (002), 28.8º (100), and 29.4º (104) were associated with graphite fraction, calcium oxide, and calcium hydroxide. Peaks between 35º–40º were due to the existence of amorphous aromatic carbon [30].

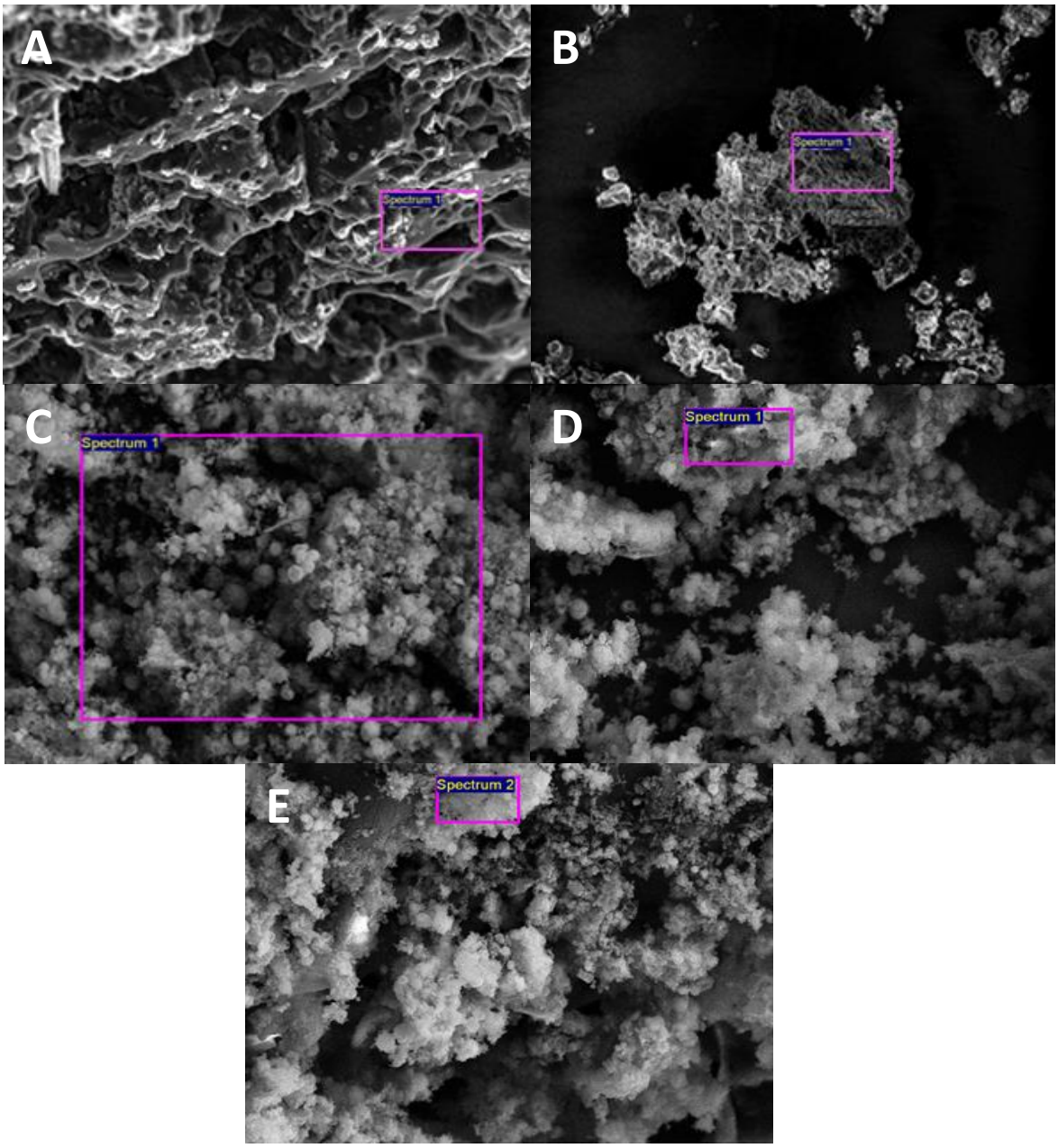

Figure 2. Surface morphology of (A) SCPR, (B) CES, (C) AEC 10, (D) AEC 20, and (E) AEC 30

The surface morphology of SCPR, CES, AEC 10, AEC 20, and AEC 30 was shown in Figure 3(A – E). The SCPR (A) represents dense, irregular and heterogeneous surface containing some grains in varied pore sizes and shapes. CES calcined at 900 ^{o}C was found to be irregular in shape and were bonded together as aggregates which can be considered to be less or even nonporous [31]. The synthesized catalysts depicted agglomerated particles peculiar to irregular spherical CaO structure. From the figure, it was clear that increase in CES loading resulted in the aggregation of calcium particles on the external surface of the prepared catalyst [22].

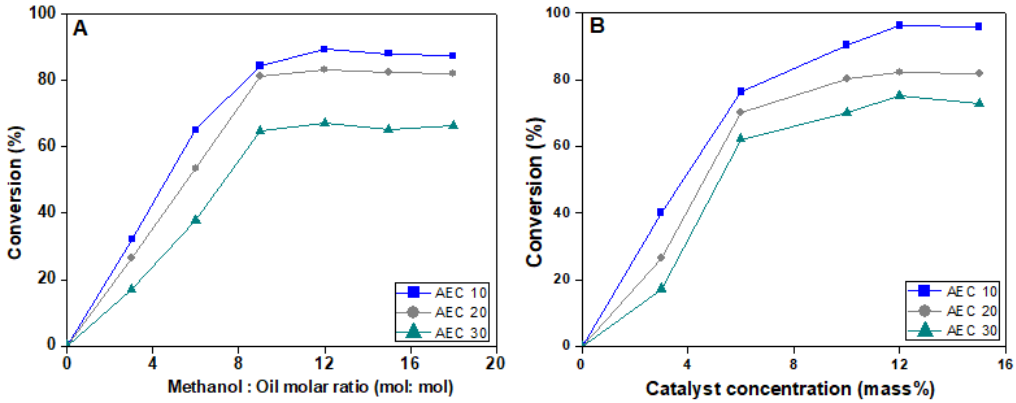

Figure 3. Plots showing the effect of (A) methanol: oil molar ratio, and (B) catalyst concentration on AEC 10, AEC 20 and AEC 30.

3.2. Catalytic activity, and biodiesel quality assessment

The catalytic activity of CES, AEC 10, AEC 20, and AEC 30 was evaluated in biodiesel production from WCO at 65 ^{o}C with methanol to oil molar ratio of 9:1 at 6 mass% catalyst concentration for 7 h to estimate the optimum reaction time and the conversion was monitored for every 1 h. When catalysts AEC 10, AEC 20, and AEC 30 were used for biodiesel production, conversion increased gradually up to 3 h, reached a maximum value and remained unchanged thereafter and the order of conversion was 50.4%, 45.6%, and 38.6%, respectively as shown in Figure 4 (A).

Transesterification was performed at 6 mass% catalyst concentration with a varying methanol to oil molar ratio from 6:1 to 18:1 for 3 h and the result is shown in Figure 4 (B). The order of conversion at optimum methanol to oil molar ratio of 12:1 was AEC 10 (89.4%), AEC 20 (83.3%), and AEC 30 (67.1%), respectively.

At the optimum conditions of 12:1 methanol to oil molar ratio, and 3 h of reaction time with reaction temperature of 65 ^{o}C, transesterification was performed to estimate the minimum catalyst concentration to achieve maximum conversion. With increase in catalyst concentration (3, 6, 10, 12, and 15), conversion increased and reached a maximum value (96.3%) at 10 mass% of oil when AEC 10 catalyst was used for transesterification as shown in Figure 4(C). The order of conversion was AEC 10 (96.3%), AEC 30 (82.3%), and AEC 20 (75.1%), respectively

From the above, it is clear that performance of catalyst AEC 10 was better when compared to CES, AEC 20, and AEC 30 in the transesterification of WCO. A maximum biodiesel conversion of 96.9% and the optimum conditions of transesterification were: 12:1 methanol to oil molar ratio, 10 mass% catalyst concentration, reaction time of 3 h at temperature of 65 ^{o}C.

4 CONCLUSION

The present study successfully demonstrated the synthesis of pyrolysis residue supported calcined eggshell catalyst in biodiesel production from waste cooking oil. Three different catalysts (AEC 10, AEC 20, and AEC 30) were synthesized varying CES loading up to 30 mass%. The surface area and total pore volume of AEC 10 was found to be higher when compared to other catalysts. The catalysts AEC 10, AEC 20, and AEC 30 had mean diameters of 1.2, 1.8, and 5.4 µm, respectively. Activity of AEC 10 catalyst was better when compared to AEC 20 and AEC 30 in transesterification of WCO to produce a maximum biodiesel conversion of 96.9% and the optimum conditions of transesterification were 12:1 methanol to oil molar ratio, 10 mass% catalyst concentration, reaction time of 3 h at temperature of 65 ^{o}C.

REFERENCES

[1] R.E. Guedes, A.S. Luna, and A. R. Torres, Operating parameters for bio-oil production in biomass pyrolysis: A review, *Journal of Analytical and Applied Pyrolysis*, vol. 129, pp. 134–149, 2018.

[2] L. Wei, S. Liang, N.M. Guho, A.J. Hanson et al., Production and characterization of bio-oil and biochar from the pyrolysis of residual bacterial biomass from a polyhydroxyalkanoate production process, *Journal of Analytical and Applied Pyrolysis*, Vol. 115, pp. 268–278, 2015.

[3] P. Roy and G. Dias, "Prospects for pyrolysis technologies in the bioenergy sector: A review, *Renewable and Sustainable Energy Reviews*, Vol. 77, pp. 59–69, 2017.

[4] F. Ronsse, S. van Hecke, D. Dickinson, and W. Prins, Production and characterization of slow pyrolysis biochar: Influence of feedstock type and pyrolysis conditions, GCB Bioenergy, Vol. 5, pp. 104–115, 2013.

[5] B.V. Babu, Biomass pyrolysis: a state-of- the-art review, *Biofuels, Bioproduction, Biorefining*, Vol. 6, pp. 246–256, 2012.

[6] M. A. Ahmad Farid, M.A. Hassan, Y. H. Taufiq-Yap, Y. Shirai, M. Y. Hasan, and M. R. Zakaria, Waterless purification using oil palm biomass-derived bioadsorbent improved the quality of biodiesel from waste cooking oil, *Journal of Cleaner Production*, Vol. 165, pp. 262–272, 2017.

[7] M. Jeguirim, L. Limousy, Biomass Chars: Elaboration, Characterization and Applications, *Energies*, Vol. 10, p. 2040, 2017.

[8] M. Hajjari, M. Tabatabaei, M. Aghbashlo, and H. Ghanavati, A review on the prospects of sustainable biodiesel production: A global scenario with an emphasis on waste-oil biodiesel utilization, *Renewable and Sustainable Energy Reviews*, Vol. 72, pp. 445–464, 2017.

[9] N. Mansir, Y.H. Taufiq-Yap, U. Rashid, and I. M. Lokman, Investigation of heterogeneous solid acid catalyst performance on low-grade feedstock for biodiesel production: A review, *Energy Conversion Management*, Vol. 141, pp. 171–182, 2017.

[10] A. N. Phan, T.M. Phan, Biodiesel production from waste cooking oils, *Fuel*, Vol. 87, pp. 3490–3496, 2008.

[11] Z. Yaakob, M. Mohammad, M. Alherbawi, Z. Alam, K. Sopian, Overview of the production of biodiesel from Waste cooking oil, *Renewable and Sustainable Energy Reviews*, Vol. 18, pp. 184–193, 2013.

[12] N. Kondamudi, S.K. Mohapatra, M. Misra, Quintinite as a bifunctional heterogeneous catalyst for biodiesel synthesis, *Applied Catalysis A Gen*, Vol. 393, pp. 36–43, 2011.

[13] L. Gao, G. Teng, G. Xiao, R. Wei, Biodiesel from palm oil via loading KF/Ca-Al hydrotalcite catalyst, *Biomass and Bioenergy*, Vol. 34, pp. 1283–1288, 2010.

[14] H. Wu, J. Zhang, Q. Wei, J. Zheng, J. Zhang, Transesterification of soybean oil to biodiesel using zeolite supported CaO as strong base catalysts, *Fuel Processing Technology*, Vol. 109, pp. 13–18, 2013.

[15] K.Y. Foo, B.H. Hameed, Utilization of oil palm biodiesel solid residue as renewable sources for preparation of granular activated carbon by microwave induced KOH activation, *Bioresource Technology*, Vol. 130, pp. 696–702, 2013.

[16] A. M. Abu-Jrai, F. Jamil, A.H. Muhtaseb, M. Baawain et al., Valorization of waste Date pits biomass for biodiesel production in presence of green carbon catalyst, *Energy Conversation Management*, Vol. 135, pp. 236–243, 2017.

[17] K. Malins, V. Kampars, J. Brinks, I. Neibolte, R. Murnieks, Synthesis of activated carbon based heterogenous acid catalyst for biodiesel preparation, *Applied Catalysis B Environonment*, Vol. 176–177, pp. 553–558, 2015.

[18] I. Thushari, S. Babel, Sustainable utilization of waste palm oil and sulfonated carbon catalyst derived from coconut meal residue for biodiesel production, *Bioresource Technology*, Vol. 248, pp. 199–203, 2018.

[19] G. Joshi, D.S. Rawat, B.Y. Lamba, et al., Transesterification of Jatropha and Karanja oils by using waste eggshell derived calcium based mixed metal oxides, *Energy Conversion Management*, Vol. 96, pp. 258–267, 2015.

[20] N. Mansir, S. Hwa Teo, M. Lokman Ibrahim, T. Y. Yun Hin, Synthesis and application of waste egg shell derived CaO supported W-Mo mixed oxide catalysts for FAME production from waste cooking oil: Effect of stoichiometry, *Energy Conversion Management*, Vol. 151, pp. 216–226, 2017.

[21] G. Chen, R. Shan, S. Li, J. Shi, A biomimetic silicification approach to synthesize CaO-SiO_2 catalyst for the transesterification of palm oil into biodiesel, *Fuel*, Vol. 153, pp. 48–55, 2015.

[22] S. H. Teo, A. Islam, H.N. Chi et al., Methoxy-functionalized mesostructured stable carbon catalysts for effective biodiesel production from non-edible feedstock, *Chemical Engineering Journal*, Vol. 334, pp. 1851–1868, 2018.

[23] V. Volli and R. K. Singh, "Production of bio-oil from de-oiled cakes by thermal pyrolysis," *Fuel*, Vol. 96, 2012.

[24] A. Obadiah, G. A. Swaroopa, S. V. Kumar, K. R. Jeganathan, and A. Ramasubbu, Biodiesel production from Palm oil using calcined waste animal bone as catalyst, *Bioresource Technology*, Vol. 116, pp. 512–516, 2012.

[25] P. R. Pandit and M. H. Fulekar, Egg shell waste as heterogeneous nanocatalyst for biodiesel production: Optimized by response surface methodology, *Journal of Environmental Management,* Vol. 198, pp. 319–329, 2017.

[26] R. Ljupkovic, R. Micic, M. Tomic, N. Radulovic, A. Bojic, A. Zarubica, Significance of the structural properties of CaO catalyst in the production of biodiesel: An effect on the reduction of greenhouse gases emission, *Hemijska Industrija,* Vol. 68, pp. 399–412, 2014.

[27] Z. Al-Qodah, R. Shawabkah, Production and characterization of granular activated carbon from activated sludge, *Brazilian Journal of Chemical Engineering*, Vol. 26, pp. 127–136, 2009.

[28] N. Tangboriboon, R. Kunanuruksapong, A. Srivat, Meso-porosity and phase transformation of bird eggshells via pyrolysis, *Journal of Ceramic Processing Research*, Vol. 13, pp. 413–419, 2012.

[29] R. Mohadi, K. Anggraini, F. Riyanti, A. Lesbani, Preparation Calcium Oxide (CaO) from Chicken Eggshells, *Sriwijaya Journal of Environment*, Vol. 1, pp. 32–35, 2016.

[30] H. Hwang, O. Sahin, J. W. Choi, Manufacturing a super-active carbon using fast pyrolysis char from biomass and correlation study on structural features and phenol adsorption, *RSC Advances*, Vol. 7, pp. 42192–42202, 2017.

[31] A. Piker, B. Tabah, N. Perkas, A. Gedanken, A green and low-cost room temperature biodiesel production method from waste oil using egg shells as catalyst, *Fuel*, Vol. 182, pp. 34–41, 2016.

ANAEROBIC CO-DIGESTION OF LEATHER FLESHING WASTE AND FOOD WASTE LEACHATE

J. Lee[1], D. Jang[2], K.J. Min[3] and K.Y. Park[4]

1. Department of Civil and Environmental Engineering, Konkuk University, Seoul, Republic of Korea; email: leejk84@konkuk.ac.kr
2. Department of Civil and Environmental Engineering, Konkuk University, Seoul, Republic of Korea; email: dorung2@naver.com
3. AinchemTech Co. Ltd., Gyeonggi, Republic of Korea; email: kyungjinm@hanmail.net
4. Department of Civil and Environmental Engineering, Konkuk University, Seoul, Republic of Korea; email: kypark@konkuk.ac.kr

ABSTRACT

The huge amount of both solid and liquid wastes generated from leather processing industries. Currently, the leather fleshing waste is widely treated through conventional disposal methods (i.e., landfill and incineration). However, the conventional disposal methods may be inappropriate consideration as they fail to find a solution for solid waste disposal problems in an environmental friendly manner. Leather fleshing waste mainly consist of moisture and solid fraction. Since the solid fraction of leather fleshing waste being composed mostly of lipids and proteins, the leather fleshing waste may be an attractive substrate for methane production during anaerobic digestion. Even though the leather fleshing waste has potential as a suitable substrate for methane production, several problems, high pH and C/N ratio values for stable anaerobic digestion and the existence of inhibitory substances for microbial activities, have to be settled. In this study, the effects of anaerobic co-digestion for leather fleshing solid waste and food waste leachate were investigated. The cumulative biogas production of co-digesting was higher than that of single digesting and the highest biogas production was observed at C/N ratio of 20. This result indicated that co-digesting leather fleshing waste and food waste leachate can promote biogas production, and the adjusting C/N ratio helps converting biomass to biogas as a result of substrate biodegradation.

Keywords: Anaerobic digestion, Co-digestion, Food waste leachate, Leather fleshing waste

1 INTRODUCTION

The huge amount of both solid and liquid wastes generated from leather processing industries. Currently, the leather fleshing waste (LFW) is widely treated through conventional disposal methods such as landfill and incineration. However, the conventional disposal methods may be inappropriate consideration as they fail to find a solution for solid waste disposal problems in an environmental friendly manner (Zupančič and Jemec, 2010). Thus, a suitable LFW disposal method needs be considered in terms of its biomass reduction and energy recovery from unused biomass.

Anaerobic digestion can be an alternative disposal for LFW based on biological process in which microorganisms degrade organic matter and convert it into useful gas (i.e., methane) as the end product. LFW mainly consist of moisture and solid fraction, and the solid fraction being composed mostly of lipids and proteins. The characteristics of composition make LFW as an attractive substrate for methane production during anaerobic digestion. Since anaerobic digestion is related to microbial activities, the process is sensitive to physiology, nutrient needs, growth kinetics, and environmental conditions (Pohland and Ghosh, 1971). The LFW has potential as a suitable substrate for methane production, however, several problems (i.e., high pH, inappropriate C/N ratio values for stable anaerobic digestion, and the existence of inhibitory substances for bacterial activities) have to be settled. Although, an optimum C/N ratio of substrate for the stable anaerobic digestion process is still debatable in the literatures, 20-30 is widely accepted (Yen and Brune, 2007). A high C/N ratio could lead to rapid consumption of nitrogen and low biogas production (Kayhanian, 1999), whereas accumulation of potential inhibitors such as total ammonia-N (TAN) and volatile fatty acid (VFA) could be caused by low C/N ratio (Li et al., 2011). The C/N ratio in typical LFW is known as around 35, which is high for the digestion. The drawbacks of LFW as an anaerobic digestion feedstock may cause unstable process, resulting in inhibition to anaerobic microbial activities and causing possible process upset or failure. Single digestion of LFW without co-substrate may not feasible, thus, a proper co-substrate should be selected and be complemented.

Optimising the substrate C/N ratio and implementing reactor pH control is a feasible approach to alleviate harmful effects of inappropriate condition for anaerobic digestion. Co-digestion of different substrates can promote the anaerobic digestion performance due to enhanced carbon to nitrogen balance (Mshandete et al., 2004; Parawira et al., 2004). According to previous study (Mata-Alvarez et al., 2000), co-digestion of more than two substrates in the same digester will generate synergetic effects and the addition of nutrients can support microbial activities. Shanmugam and Horan (2009) and Thangamani et al (2010) reported that LFW digestion efficiencies including biogas yield were increased through co-digestion with municipal solid waste and primary sludge, respectively. Food waste leachate (FWL) has widely applied as a desirable substrate to co-digest with various organic matters because of its high biodegradability. In this study, we assumed that high C/N ratio of LFW may hinder single digestion performance and FWL which has relatively low value of C/N ratio is an appropriate co-substrate for LFW treatment through anaerobic digestion.

The main objective of this research was to investigate the biogas production potential of co-digesting LFW and FWL as compared to single digesting LFW and FWL, respectively. Biochemical methane potential (BMP) tests were conducted as a tool for evaluating improved effect of anaerobic co-digestion. The performance of anaerobic co-digestion was determined in terms of biogas yield from test conditions.

2 MATERIALS AND METHODS

2.1 Leather fleshing waste and food waste leachate

In this study, LFW was collected (following liming process, before tanning leather manufacturing process) from T tanner's association at G province, Korea. The LFW used as substrate was ground to less than 5 mm diameter and homogenized using a commercial blender. FWL was collected form a food waste recycling center in G province, Korea. A total of three visits, each on a different day of the week, were made to the recycling center to make the feedstock more representative of the actual FWL generated. Drying and grinding were used as pretreatment method for FWL. Pretreated FWL was mixed to apply homogeneity and was used as immediate as to avoid spoil. The limed LFW and FWL were characterized by analysis with the Standard methods (ASTM, 2006a, 2006b, and 2007).

The characterization of substrates (i.e., LFW and FWL) are summarized in Table 1.

Table 1. Characterization of LFW and FWL used in this study

Characterization		LFW	FWL	Unit
Proximate analysis	Moisture content	64.73	88.57	% (wet, w/w)
	Total solid	35.27	11.43	
	Volatile solid	21.45	8.76	% (dry, w/w)
Ultimate analysis	C	49.9	49.8	% (dry, w/w)
	H	7.9	6.8	
	N	1.5	3.7	
	S	0.0	0.2	
	O (diff.)	16.1	37.1	
	C/N	34.1	13.5	-

2.2 Biochemical methane potential test

The BMP test was conducted as a tool for evaluating the anaerobic digestion process. The BMP test can be used as an index of the anaerobic biodegradation potential as it is the experimental value of the maximum quantity of methane produced per gram of VS (Esposito G. et al., 2012). BMP tests conducted in this study modified the method as described by Owen et al. using 250 mL bottles at 35°C and 150 rpm for 36 days. Gas production and gas composition were analyzed to assess the efficiency of the anaerobic digestion on the BMP test by Gas Chromatography (GC, Younglin ACME 6100, Korea).

3 RESULTS AND DISCUSSION

Figure 1 shows the cumulative biogas curves of specimens with different C/N ratios.

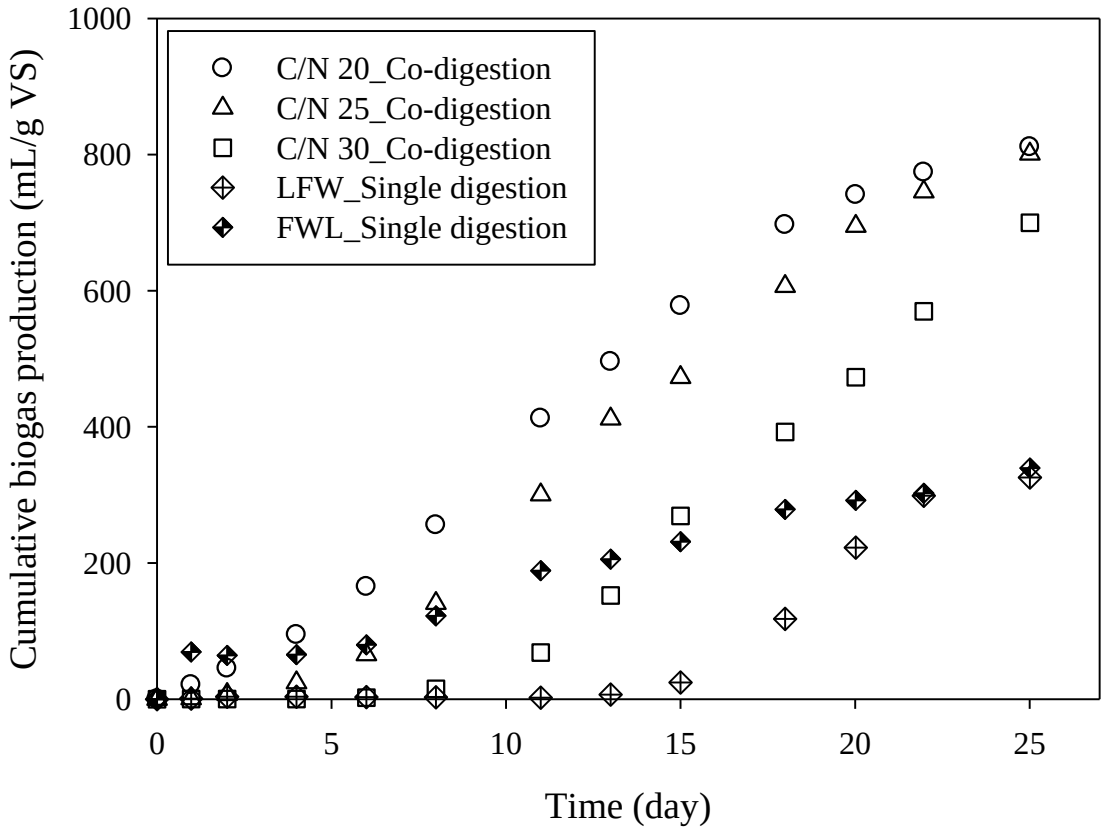

Figure 1. Cumulative biogas production from BMP test

According to Figure 1, cumulative biogas productions of co-digesting condition were higher than that of single digesting. This difference between co-digesting and single digesting was probably due to synergy effects of co-substrate in anaerobic digestion system. Among the co-digesting conditions with different C/N ratios, cumulative biogas become higher according to decrease of C/N ratio. The lower C/N ratio indicated that contains more FWL than LFW. In comparison with single digesting conditions, the biogas production kinetic of early digestion stage (until 20 days) for FWL was faster than LFW. This observation is in accordance with aforementioned easily biodegradable characteristic of FWL. Thus, higher concentration of FWL in co-substrate promoted biogas production yield.

4 CONCLUSIONS

This study aimed to investigate the effects of co-digesting LFW and FWL onto biogas production potential. Since biogas from substrates are under production, it is early to conclude that co-digesting LFW and FWL has benefit comparing with single digesting in terms of biogas production. However, it is certain that adjusting C/N ratio can promote biodegradation of substrate. From this study, the co-digesting LFW and FWL may considered to increase the biogas production.

ACKNOWLEDGEMENTS

This work is financially supported by the Korea Ministry of Environment as Waste to Energy-Recycling Human Resource Development Project.

REFERENCES

[1] A. Mshandete, A. Kivaisi, M. Rubindamayugi and B. Mattiasson, Anaerobic batch co-digestion of sisal pulp and fish wastes, *Bioresource Technology*, Vol. 95, pp. 19-24, 2004.

[2] A. Thangamani, Suseela Rajakumar and R. A. Ramanujam, Anaerobic co-digestion of hazardous tannery solid waste and primary sludge: biodegradation kinetics and metabolite analysis, *Clean Technologies and Environmental Policy*, Vol. 12, pp. 517-524, 2010.
[3] F. G. Pohland and S. Ghosh, Developments in anaerobic stabilization of organic wastes – the two-phase concept, *Environmental Letters*, Vol. 1, pp. 255-266, 1971.
[4] G. D. Zupančič, and A. Jemec, Anaerobic digestion of tannery waste: semi-continuous and anaerobic sequencing batch reactor processes. *Bioresource technology*, Vol. 101, pp. 26-33, 2010.
[5] G. Esposito, L. Frunzz, F. Liotta, A. Panico and F. Pirozzi, Bio-Methane Potential Tests to measure the biogas production from the digestion and co-digestion of complex organic substrates, *The Open Environmental Engineering Journal*, Vol. 5, pp. 1-8, 2012.
[6] H. W. Yen and D. E. Brune, Anaerobic co-digestion of algal sludge and waste paper to produce methane, *Bioresource technology*, Vol. 98, pp. 130-134, 2007.
[7] J. Mata-Alvarez, S. Macé and P. Llabrés, Anaerobic digestion of organic solid wastes: an overview of research achievements and perspectives, *Bioresource Technology*, Vol. 74, pp. 3-16, 2000.
[8] M. Kayhanian, Ammonia inhibition in high-solids biogasification: an overview and practical solutions, *Environmental Technology*, Vol. 20, pp. 355-365, 1999.
[9] P. Shanmugam and N. J. Horan, Optimising the biogas production from leather fleshing waste by co-digestion with MSW, *Bioresource Technology*, Vol. 100, pp. 4117-4120, 2009.
[10] W. Parawira, M. Murto, R. Zvauya and B. Mattiasson, Anaerobic batch digestion of solid potato waste alone and in combination with sugar beet leaves, *Renewable Energy*, Vol. 29, pp. 1811-1823, 2004.
[11] Y. Li, S. Y. Park and J. Zhu, Solid-state anaerobic digestion for methane production from organic waste, *Renewable and Sustainable Energy Reviews*, Vol. 15, pp. 821-826, 2011.

A REVIEW ON AVAILABLE TECHNOLOGIES FOR BIOFUEL-FED CHP INTEGRATION IN THE CERAMIC FIRING PROCESS

Eleonora Bongiovanni[1], Nicola Raule[1], Diego Bartolomè[1], Giulia Broglia[1], Enrico Callegati[1], Michele Frascaroli[1], Marco Baracchi[1], Gabriele Frignani[2], Simone Mazzali[2]

1. CRIT Srl, Vignola (MO), Italy; email: info@crit-research.it
2. SACMI Forni Spa, Casalgrande (RE); email: sacmi_forni@sacmi.it

ABSTRACT

This paper is about the state of the art analysis performed within the H2020 funded DREAM project for the defining the application parameters of the CHP unit to the ceramic kiln. The purpose of this CHP unit is double. On one side, a CHP unit may provide enough electrical power to the kiln to grant its functions even in case of a prolongated blackout on the grid. This feature is particularly relevant for those countries where the power network lacks the necessary stability and frequent black out happen. The second goal that can be reached by applying a CHP unit to a ceramic kiln is to increase the overall system efficiency thanks to cogeneration. In fact, the process of ceramic preparation is eager of heat and in this particular case we plan to use it in the drying process that precedes the effective cooking of the tile. Due to better efficiency, cogeneration will not only reduce costs of energy production, but also decrease process emissions. Cogeneration can be done with different technologies, which are reported in the paper. In this study, we explain why we found that gas turbine is the more suitable technology for the ceramic industrial process.

Keywords: Ceramic Process, Cogeneration, Renewal Energy, Biofuels

1 INTRODUCTION

The DREAM project runs from October 2016 to September 2019, and is funded by the European Union's Horizon 2020 research and innovation program under grant agreement N° 723641. It is coordinated by Sacmi Forni world-leading producer of thermal machines for ceramics industry. DREAM aims to design, develop and demonstrate a radically improved architecture for ceramic industrial furnaces, characterised by optimised energy consumption, reduced emissions, and lower operating costs compared to currently available technological solutions. This will be obtained by substantially enhancing specific furnace parts (control system, refractories, emissions abatement system) and by adding new modules and sub-systems (CHP unit, heat pipes) to the current furnace architecture. With specific regards to CHP integration in firing stage, DREAM will design a solution for integrating a biofuel fed Combined Heat and Power (CHP) unit within the ceramic product firing process. Such unit will increase the overall firing efficiency by feeding the electric kiln appliances, while at the same time generating thermal high-temperature power that will be recovered to reduce the use of gas-powered burners. CHP integration within the firing process will enable end-users to reduce the electric and natural gas power need by 20% and 2% respectively compared to the current industry practice, with an initial investment payback time lower than 2,5 years.

2 CHP UNIT TECHNOLOGIES

Combined heat and power (CHP)) stands for the cluster of technologies which generates electric power and useful thermal energy from a single fuel source. Power production is placed near the area there the heat is needed, so that the heat released from power production can be used directly. Industrial processes, particularly in factories with continuous processing and high heat requirements, are perfect target for CHP applications. The direct benefits of combined heat and power for facility operators are:

- Reduced energy related costs;
- Potential power autonomy from the public grid;
- Reduction of emissions.

A summary of CHP technologies is listed in Table 1 together with main advantages and disadvantages.

Table 1: Summary of CHP technology advantages and disadvantages

CHP system	Advantages	Disadvantages	Available sizes
Reciprocating engine	• High power efficiency • Fast start-up • Relatively low investment cost • Can be overhauled on site with internal operators • Operates at low pressure gas	• High maintenance costs • Limited lower temperature cogeneration applications • Must be cooled even if recovered heat is not used • High level of low frequency noise	1kW to 10 MW
Steam turbine	• High overall efficiency – steam to power. • Can be mated to boilers firing a variety of gaseous, liquid or solid fuels. • Ability to meet more than one site heat grade requirement. • Long working life and high reliability. • Power to heat ratio can be varied.	• Slow start up. • Very low power to heat ratio. • Requires a boiler or other steam source.	50 kW to several hundred MWs
Gas turbine	• High reliability. • Low emissions. • High grade heat available. • No cooling required.	• Require high pressure gas or in-house gas compressor. • Poor efficiency at low loading. • Output falls as ambient temperature rises.	500 kW to 300 MW
Fuel cell	• Small number of moving parts. • Compact size and light weight. Low emissions. • No cooling required.	• High costs. • Relatively low mechanical efficiency. • Limited to lower temperature cogeneration applications.	30 kW to 250 kW with multiple unit packages up to 1,000 kW

A general comparison of all the technologies was published in 2015 by the US EPA [1].

3 CERAMIC KILN

The roller kilns are used to fire ceramic products (tiles, sanitary ware, crockery etc). This kiln in particular is used to fire tiles. It is called “single-layer roller kiln” because the product is placed directly in one channel on a roller conveyor. The product is fed through the channel inside the kiln along the rollers and is fired along the way. The heat required to fire is generated by the combustion process of the gas in the burners distributed along the tunnel. This is a list of the inputs to the kiln:

- Raw products to be fired (tiles);
- Fuel (gas) + combustion agent (air);
- Cold air to cool the fired product.

The following are delivered from the kiln:

- Fired product;
- Combustion fumes;
- Cooling air (heated as it goes through the kiln).

Figure 1 - Inputs and outputs scheme of the kiln

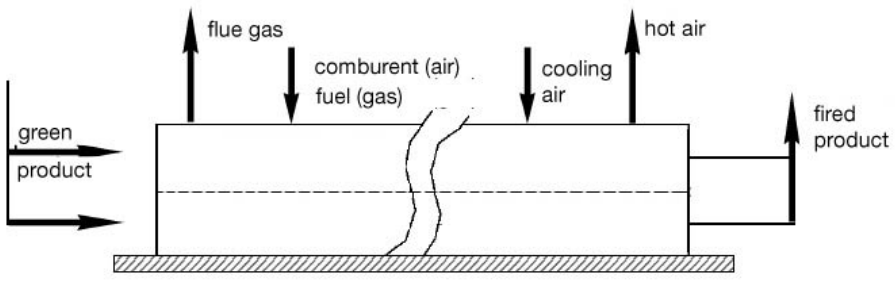

The entire Kiln is subdivided in to six different zones: (i) Forekiln; (ii) Pre-Kiln; (iii) Firing; (iv) Rapid Cooling; (v) Indirect Cooling (Slow); (vi) Final Cooling.

Figure 2 – Ceramic kiln zones

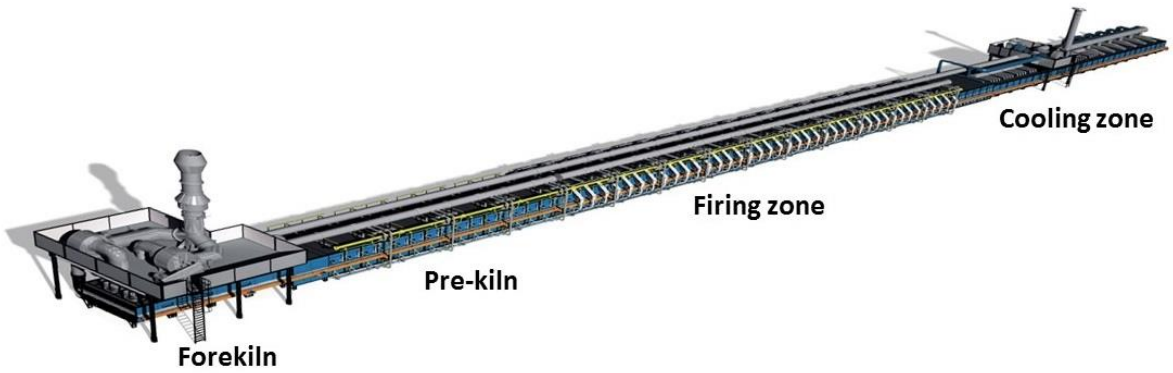

The process is totally automated and is governed and controlled from a control panel and an electrical system. The system includes instruments, indicators, controls and actuators, on both the kiln and on the control panel. The fundamental variables to be simultaneously monitored are the following:

- the speed at which the product goes through the kiln and therefore how long it stays in the kiln (cycle);
- the heat in the kiln, considering two important aspects (firing curve):
    - quantity of heat in relation to the volume and therefore the temperature inside the kiln;
    - heat distribution with respect to the product (over and under each roller conveyor).

By modulating and combining these variables appropriately along the different kiln sections, the right firing curve is obtained for each product.

4 BIOFUEL: STATE OF THE ART IN EUROPE

4.1 Biogas

Biogas is characterized based on its chemical composition and the physical characteristics which result from it [3]. It is primarily a mixture of methane (CH4) and inert carbonic gas (CO2). However, the name "biogas" gathers a large variety of gases depending from specific treatment processes, starting from various organic waste - industries, animal or domestic origin waste etc.

Biogas is mainly produced through Anaerobic Digestion, by processing organic waste in dedicated digesters. Biogas, however, can be also obtained by trapping landfill gas, which has a high methane content, by means of a piping system. Although this technique is carried out in order to reduce greenhouse gas emissions due to waste disposal, the trend is to reduce landfill disposal of Municipal Solid Waste (MSW) and therefore, the landfill biogas production. The leading country regarding landfill biogas production is the United Kingdom, according to a EurObservER study [2]. Italy, France and Spain rank in the top positions although they provide a much lower landfill biogas production.

Biogas production, together with biomethane upgrading, shows a clear upward trend in the last years in Europe. It is particularly Germany the country that leads biogas production. Biogas may be burned for thermal applications, but it can also be used for electricity and Combined Heat and Power (CHP) applications. Furthermore, it can be processed in order to obtain upgraded biogas, that may be used to power vehicles or introduced into the natural gas grid.

4.2 Biomethane

Biogas may be directly used as a thermal resource for heating and thermal processes or may be used for electric power and CHP generation. However, its high content in methane (CH4) makes biogas a candidate to be fitted in Natural Gas networks. In order to do so, further processing is required providing the network requirements are complied.

Biogas upgrading is not an innovative technique since it has been applied since the 1980s. Nevertheless, the biogas upgrading technology only took off in the last decade, with lots of biogas upgrading plants being built in Germany since 2006. The biogas upgrading market currently lacks a clear standardization, which is already being developed by the CEN Technical Committee 408.

Germany started biomethane injection in 2006 [5] and through its experience we can now say that this is a sustainable way of handling biogas even if it doesn't lack problems. In fact even if the biomethane is supposed to have by requirement a composition very similar to natural gas, it not quite identical and this may lead to a 2-5% calorific power difference between the two. This difference may influence the final user of gas from the grid, especially if he is located near to a biomethane injection point to the grid. In fact biomethane production could be rather discontinuous and this would produce an alternate flux rich in natural gas/biomethane. This will significantly affect the final heat produced by the burner of the final user and if it might not be such a problem for newer systems which are automatically regulated by thermostats, it does create problems with older machines.

4.3 Biofuel assessment

The new CHP system has to be paired to pair with the ceramic kiln in order to make it both independent from the local power grid and more efficient/sustainable. For this reason, it was decided that the new CHP would have to be compatible with a biofuel feed.

It should be made clear that this idea comes from the intent to push the research ahead of the current real capability of the ceramic industry. In fact, right now the ceramic industry in Europe produces heat only through the use of natural gas. The use of a different fuel is not currently a feasible option from the economic sustainability point of view. In fact, any kind of biogas would be needed to be transported by truck to the ceramic plant taking its cost to very high level and also requiring additional fossil fuel for transportation, de facto spoiling the whole point of using a biofuel.

Yet, designing and testing a system that would allow for a use of biofuel, when available, is still an interesting achievement that could have some application soon in countries outside Europe, where there might be availability of biogas near the ceramic plant premises.

Starting from this point, it was attempted to find a CHP system that would support both natural gas and biogas. We found that gas turbines allow a dual input feeding of natural gas and biomethane, which is to all effect a kind of biogas.

This approach is also very flexible because, according to all manufacturers, gas turbine does not require any major modification when switching from one kind of fuel to the other. On the contrary it is only a matter of a 1-minute setup of the CHP software configuration.

In order to be able to perform the test with biomethane a gas truck with biomethane will be send to the ceramic plant and plugged to the new CHP. The truck will hold enough biomethane to feed the turbine for at least 2 to 3 days, which will be enough to test the system.

On the contrary, a gas turbine CHP designed to work with natural gas will not work with biogas (not upgraded) unless severe modifications are applied. In principle, it would be possible to purchase a CHP unit that would work only with biogas, but then it would not be suitable for natural gas and it would have no use for the European ceramic factories until a new distribution network is created for this gas. Furthermore, considering the huge infrastructure investment that such a project would require, it is very likely that this kind of distribution will never be realized. In fact, it is a generally agreed that the non-upgraded biogas will be either upgraded to biomethane, or burned on the same site of production to obtain electric power to inject in the power grid. Any cost of transportation would make the biogas production not sustainable or even a loss (both from an environmental and economical point of view).

5 CHP UNIT ASSESSMENT

An evaluation of which CHP technology would be more suitable for the ceramic kiln application was carried on considering the specifications of the three type of CHP described before. We have already discussed the

fact that steam turbines represent a technology suitable for larger plants and it is currently leaving the floor to newer gas turbines or reciprocating engines. We need to define which of these two is better considering: electrical capacity, emissions, energy efficiency and overall costs. It should be kept in mind that whatever technology is chosen, it will need to support natural gas feeding, because this is the primary fuel that nowadays is available in the ceramic industry. The DREAM project has the goal of defining a solution that will natively support also a biofuel feeding. In this case, the process will be ready to switch to a biofuel use as soon as it will be available.

5.1 Reciprocating Engines CHP

We interviewed several reciprocating engine based CHP producers and they all reported similar operational parameters. This is also related to the fact that, besides the whole CHP assembly, engines producers are only a few in the world. Most of the commercial CHP are operated by MANN, Perkins, Caterpillar or Iveco engines. For each company, we chose the model with the capacity closer to 200kW of electrical power produced, which is the size required by the ceramic kiln. As far as maintenance is concern, all the engines would require a fast service about every 1500 working hours and a full service around 6-800 working hours, where a fast service would include oil and filter change, and a full service will additionally require a complete engine overhaul.

Furthermore, a reciprocating engine CHP global efficiency is generally in the 80-85% range, where only 35-38% comes from the electrical power production, and the remaining is due to the heat production. Reciprocating engines produce heat in two ways: one at low temperatures (60°-90°) comes from the cooling system of the engine, and the second at high temperatures (~500°) comes from the exhaust gases.

For the application to the ceramic industry the heat at lower temperature is useless, because it has no application in any step of the production process. Other applications of this heat are equally useless because typically the ceramic industry has plenty of low temperature heat to discard or to use for space climatization. The high temperature heat could be used either in the preheating section of the kiln or, adequately mixed with warm air in the dryer, but this represent only about 50% of the heat produced by the engine.

5.2 Gas microturbine CHP

Reciprocating engines are much more diffuse for cogeneration than gas turbines. This is mainly due to the fact that up to a few years ago gas turbines were only suitable for high quantity of electric power production, with a minimum set to a few megaWatt of power. In the last few years microturbines with an electrical peak production of a few hundred kW or less have become available. Lately their price has also become more and more competitive up to the point that is quite comparable to the cost of a reciprocating engine based CHP.

While collecting the specifications of all the microturbine CHP we also realized that some key aspects make them a better choice for the ceramic industry application. First of all, turbines have a lower maintenance costs and consequently downtime. This is very important not only because of the reduced costs, but mainly because typically a ceramic kiln is operative 24/7 and any downtime represents a damage for the factory. A second fundamental point is represented by the efficiency of the turbine compared to that of the engine. As it was said before about ¼ of the total efficiency of the engine is produced as low temperature heat. Unfortunately, a ceramic plant would have no use for this kind of energy and therefore it would be wasted. On the contrary, a gas turbine produces most of the thermal energy from the exhaust which are expulsed at about 280%. This temperature is perfecto to have them injected in the dryer. Last but not least an important note should be done about emissions. In fact all turbine producer reported similar values of emissions: CO is less than 32mg/Nmc, NOX is lower than 14 and VOCs are almost negligible. This puts the turbine at about 1 fold lower emissions than reciprocating engines.

There are other characteristics that in principle make a turbine a better choice, but they are minor aspects and they don’t affect much the industrial application of a CHP. For instance, turbines are much less noisy than reciprocating engines peaking 80dB at 1 mt, whether engines have about the same level of noise at 10 mt, but this inconvenient can be overcome by adding insulation to the container of the engine for indoor installation. Another aspect is related to vibrations, which are much higher in an engine due to the presence

of alternate movements, but also this aspect does not affect too much a possible application in the ceramic industry.

We have pointed out several aspects that give an advantage to gas turbines against reciprocating engines in small CHP units. In fact, the main reason that made reciprocating engines so much more diffuse than microturbines is the cost. This reason is now not applicable anymore because the cost of turbines has decreased to a level similar to the cost of engines.

Table 2 - Technology comparison chart

	Reciprocating engine	Gas turbine
Heat efficiency	~ 25% (low T) + 25% (High T)	~ 50% (High T)
Fuel compatibility	Natural gas + biomethane	Natural gas + biomethane
Start-up time	**~ 5min.**	~30
Level of emissions	Higher	**Lower**
Maintenance	More expensive	**Less expensive**
Sensitivity to temperature and humidity	**Low**	High
Vibration and acoustics	High	**Low**
Space requirements	6x2.5x.2.5mt	**0,9x1,8x28mt**
Cost	~ 1500Eu/Kw	~ 1500Eu/Kw

It is clear from this table that a gas turbine would be preferable for the ceramic kiln application, considering also that some aspects, such as the start-up time has no influence in the choice because the CHP unit would be always working in a ceramic plant.

6 CONCLUSIONS

This paper summarizes the rationale that is guiding the choice of the best technological solution for integrating biofuel-fed CHP into the ceramic firing process. It describes how the various options of cogeneration were deeply evaluated and why it was decided to select gas turbine cogeneration.

Much attention was paid to the selection of the fuel. The ceramic industry is based on natural gas and it has not the capability of producing any kind of biogas. On the other side one of the objectives of the project is to introduce a technology that is capable to accept also some kind of biofuel. We found that in principle it should be possible to feed gas turbines both with natural gas or biomethane with minimal adjustments. Right now, biomethane is not directly available in any ceramic plant, but in the future, it will probably be distributed through the natural gas network. Therefore, we will test the capability of the turbine to work with biomethane by bringing it to the demonstrator with a truck. A full truck of biomethane will carry enough fuel to run the cogenerator for 2 or 3 days and that will be enough to verify that everything is working fine. During the test data will be collected to verify the energy consumption of the kiln with and without the cogeneration.

Given the requirements of the ceramic kiln it was decided that the Ansaldo AE-T100 is the more suitable product for the DREAM demonstrator. This turbine has a capacity of 100kW of electrical power production and in the case of commercialization could be coupled to obtain a useful redundancy in the cogeneration.

7 REFERENCES

[1] K. Darrow, R. Tidball, J. Wang, and A. Hampson, “Catalog of CHP Technologies,” 2015.
[2] EBA, “EBA Biomethane & Biogas Report 2015,” 2015.
[3] M. Herout, J. Malaták, L. Kucera, and T. Dlabaja, “Biogas composition depending on the type of plant biomass used,” Res. Agric. Eng., vol. 57, no. 4, pp. 137–143, 2011.
[4] D. Thrän et al., Biomethane - status and factors affecting market development and trade, IEA Bioene., no. September 2014. 2014.
[4] B. Linke, “Country Report Denmark biogas plant inventory,” IEA Bioenergy Task 37, no. October, 2014.
[5] European Biogas Association (EBA), “Biogas 2013 report,” no. December, pp. 1–25, 2013.

The Future of Renewable Energy, Barriers and Solution

O. Emmanuel , Tabbi Wilberforce, A. Alanzi, O. Ijaodola, F.N. Khatib, Zaki El – Hassan, A.G. Olabi
Institute of Engineering and Energy Technologies, University of the West of Scotland, UK

ABSTRACT

This investigation exposes the future of renewable energy by considering new renewable energy generation technologies which is usualy a modification of the existing renewable energy like the solar geothermal, wind biofuels and biodisels). The ocean or marine energy was clearly discussed as well as concentrated solar photovolataics and enhanced geothermal systems. Each of these new technology is currently at the developing stages and have a long way to go into becoming commercialized but the major obstacles impeding the advancement of each technology was also reviewed and discussed. Some possible solutions were equally proposed. The work concluded that a good balance between existing renewable energy sources and the emerging ones will create a good competition with the other energy generation mediums and this will help reduce the high dependency on fossil fuel which have a negative impact on the environmental.

Keywords: Renewable Energy, Fossil Fuel, Geo thermal systems, Marine Energy,

1 INTRODUCTION

One of the parameters that determine the quality of life and the economy is energy. This has led to it being considered as the major issue being discussed worldwide. According to statistics, nearly two billion people around the world do not have constant supply or even any access to power at all [1]. There has been a sudden surge up on the demand of energy due to the high dependence on technology, high standard of living especially in most developed countries. To mitigate the high demand of energy, the consumption of fossil fuel is increasing tremendously across the entire globe. This in effect leads to the depletion of the ozone layer, sudden changes in climatic conditions, environmental pollution leading to health problems with all living species in the world. The prices of petroleum commodities keep increasing since the oil crisis in 1973 and the gulf war [2]. It is anticipated that the amount of energy absorbed as solar radiations must be same as the amount of energy leaving back into the atmosphere with longer wavelengths and infra-red in order to maintain a thermodynamic balance of the atmosphere at a constant temperature [3]. In instances where the ozone layer is destroyed, these greenhouse gases absorb and reemit infrared radiations while keeping the lower atmosphere and earth's surface warm [4]. The share of CO_2 emissions from fossil fuel keep increasing. The high rise of CO_2 leads to an increase in the average CO_2 level in the atmosphere. The CO_2 in the atmosphere was 280ppm during the pre-industrial era and 390ppm presently showing a significant increase of 110ppm in recent times [5]. For good development process, the quality of energy being generated is very important. For a sustainable environment, it is imperative that clean consistent and very secure form of power is being considered [6,7,8]. Fossil fuel supplies nearly 85% of the world energy demand [9] but accounts for 56.6% of GHG emissions [10]. Renewable energy technology is today being encouraged as a way to counter the effect of the ozone layer depletion. There are three categories of energy sources. These are: nuclear resources, fossil fuel and renewable energy sources [11]. Renewable energy is the future of the world's energy generation medium. It is possible to generate an enormous amount of energy through renewable means, that is, solar energy, wind energy, geothermal energy, marine energy, biomass energy and biofuels [12]. Renewable energy sources produce nearly zero emissions [13]. They are very affordable and environmentally sustainable way to harvest the renewable energy in a decentralized manner to meet rural and small – scale energy needs [14, 15]. In the 21st century, there are several renewable energy being developed around the world. According to statistics, about 23.7% of the total world energy demand is being supplied by renewable energy but in 1998, it was estimated that renewable energy accounted for only 2% of the world energy demand including seven exajoules of modern biomass and two exajoules of all other renewable sources [16]. Countries like Germany and other European countries are actively relying on renewable energy as their main source of power generation. Geothermal energy, wind, solar, biomass, biofuel and hydropower are all being considered today around the world as main source of energy generation contributing significantly to the world. There has been some latest form of energy generation as the common ones as shown Fig. 1.

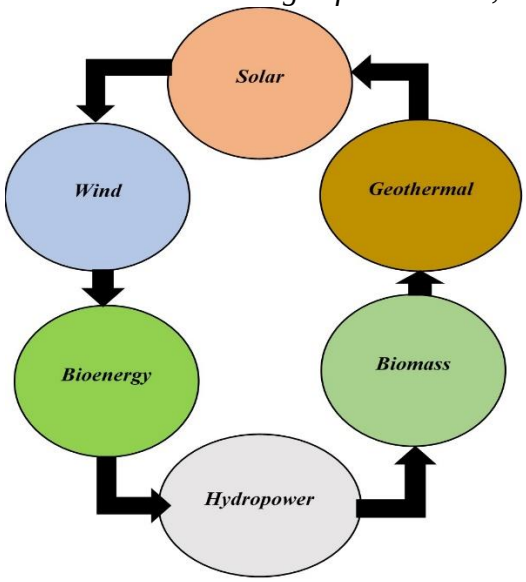

Fig 1. Common renewable energy generation medium

These new form of energy generation are equally environmentally friendly. They are considered as emerging renewable technologies i.e marine energy, concentrated solar photovoltaic (CSP), enhanced geothermal energy (GE) Cellulosic ethanol and artificial photosynthesis (AP) as shown in Fig. 2. This paper reports the recent development of renewable energy as well as the emerging ones. The investigation further explores some opportunities, setbacks, possible solutions and policies to improve the current status of the renewable energy industry.

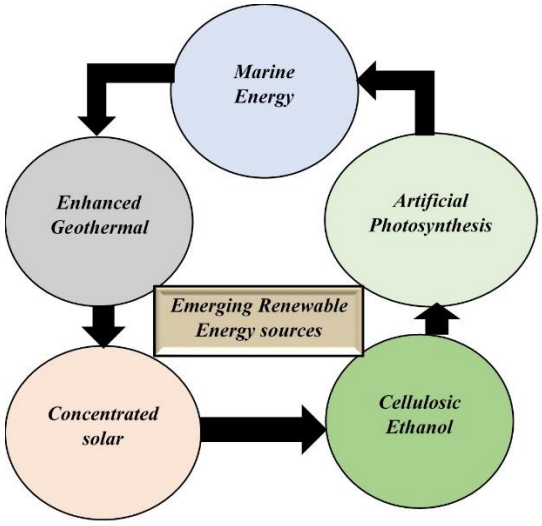

Fig. 2: Emerging renewable energy generation medium

2.0 Present Day – Renewable Energy

The theoretical and sustainable potential of renewable energy is higher than any form of energy generation medium. The absolute size of the global technical renewable energy potential is unlikely to retard the progress of renewable energy development [17]. Renewable energy in 2008 accounted for 12.9% of the total 492EJ of primary energy supplied then. Biomass has always been a major contributor to renewable energy accounting for 10.2% often used in most developing countries for cooking and heating purposes. On the other hand, hydropower accounted for 2.3% and the other types of renewable energy accounted for only 0.4%. An investigation conducted by Renewable Energy Sources and Climate Change Mitigation captured that 19% of electricity supplied in 2008 was from renewable energy sources. 2% of the global road transport fuel supply was from biofuel whiles biomass, solar and geothermal together contributed to 27% of global

demand of heat [17]. It must be noted that the primary objective of all; these renewable sources are to meet the defined social, economic and environmental aspects of human lives as shown in Fig. 3.

Aspect	Bearable	Equitable	Viable	Sustainable
Social	○	○		○
Economical		○	○	○
Environmental	○		○	○

Fig. 3 Social, economic and environmental aspects of human lives

Today due to technological advancement, other energy generating mediums are springing up like the shore wind, solar, concentrated solar, geothermal, marine energy and bio energy. In 2012, 19% of the estimated final energy consumption was provided by renewable energy but there was a sharp increase to 23.7% in 2014 [16]. Fig. 4 shows the world energy sources. In 2015, there was a high increase in global capacity of renewable energy [16]. Hydropower generated 16.6% of the total 22,7% while wind, bio power and solar power shares was 3.7%, 2.0% and 1.2% respectively. Other renewable energy sources like concentrated solar photovoltaic, marine, geothermal and others contribute to only 0.4% from Fig. 4.

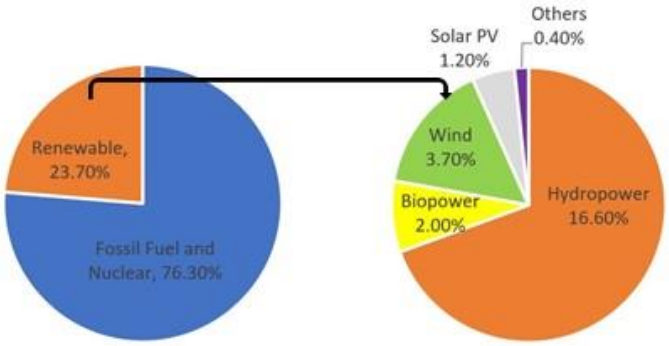

Fig. 4: Renewable Energy Share of Global Energy [16]

The global status report (GSR) reported that the highest growth in sustainable energy occurred in the power sector with the global capacity exceeding 1560GW (including small hydropower). The last decade also experienced an increase for investment on renewable energy resources. Fig. 5 shows the investment made in the last 12 years by developed and developing countries. Global investors around the world invested $40 billion in renewable energy in 2004. In 2011, this amount increased further to $27 billion but saw a sharp decline after 2011.

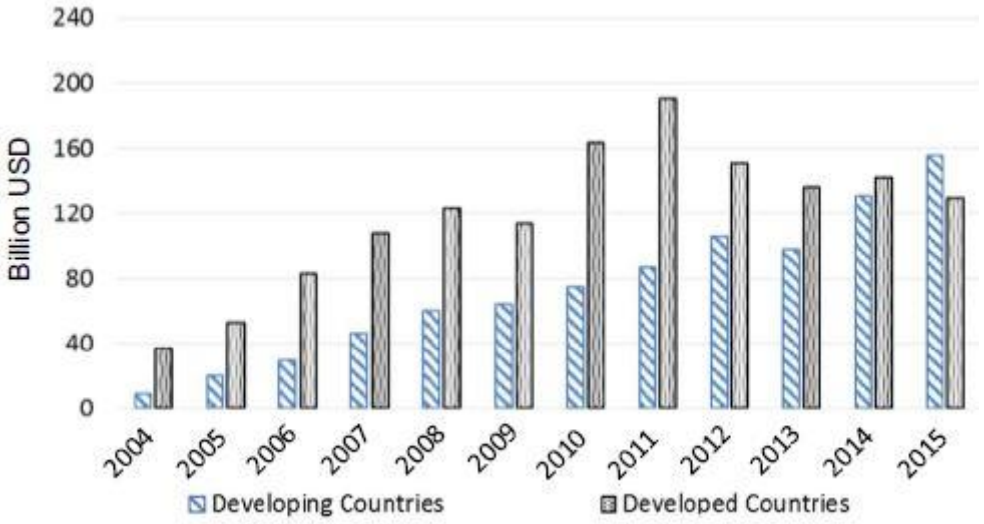

Fig. 5: Investment made on renewable energy by developing and developed countries [18].

This was due to the drastic reduction in technology costs especially for solar PV, which saw a record of new installations despite a reduction in dollar investment [18]. The world has seen a paradigm shift in renewable energy between 2004 and 2017. The sudden rise of renewable energy in the last decade clearly shows the future prospects of this viable energy generation medium hence are currently competing with the traditional power generation medium. The contribution of renewable energy in the field of energy supply varies by country and region because of different geographic distribution of manufacturing, usage and export. From the report of the GSR – 2016, China, the United States, Brazil, Canada and Germany were the top countries for non – hydrogen capacity and were followed by Spain, Italy and India. Jamaica, Morroco, Uruguay, Honduras and Mauritania invested huge amount of money into renewable power and fuels relative to the annual GDP. The renewable energy investments (GTREI) report made in the Frankfurt school under the UN climate and sustainable energy finance group was published in 2016. The renewable energy generation capacity and capacity change as a percentage of global power is shown in Fig. 6. Over the last eight years there has been a zigzag behavior from the graph but also a linear increase in the share of renewable energy to global power is observed.

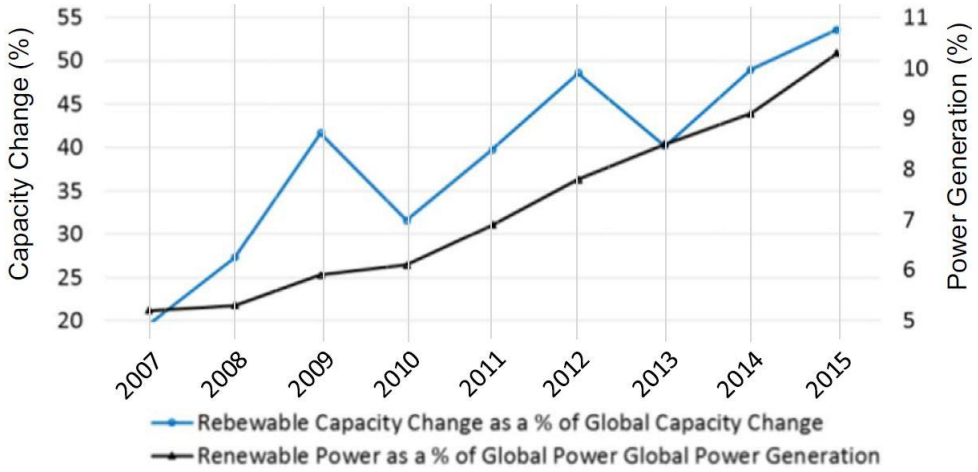

Fig. 6: Renewable Energy Generation capacity as a share of Global power [18].

Again, the graph clearly shows a high increment in the year 2015. The performance of renewable energy in terms of investment has seen high rise in the last decade as well. The seed money(capital cost) for the establishment of wind turbines and Solar photovoltaics has reduced in the last few decades as well. In the year 2015, nearly 103GW of renewable energy capacity was established. Large hydropower that was established during this period was not factored into the 103GW power capacity reordered. Wind and solar were the dominant source of renewable energy in 2014 with their supply capacity reaching 49GW and 46GW respectively but in the year 2013, only 32GW of energy was generated from wind whiles solar supplied 40GW to meet the worlds energy demand [18]. The IEA in 2014 published the price of electricity

produced by renewable energy sources taking some journals and publications into consideration [19]. A comparison between the United States of America generation prices and the residential end – use in 2014 was clearly presented. Hydropower was observed to very competitive when compared with the other types of renewable energy generation mediums. The main setback published using hydropower was the availability of suitable place(Land) where the plant will be installed. Other renewable energy that have equally reached grid parity were equally presented in the report. Geothermal and wind – on – shore that can be installed by individuals (end users) mainly for residential purposes were presented in the report as having reached parity. Renewable energy sources continue to be recognized in the research community as the future of energy generation compared to the total primary energy supply (TPES) as shown in Fig. 7.

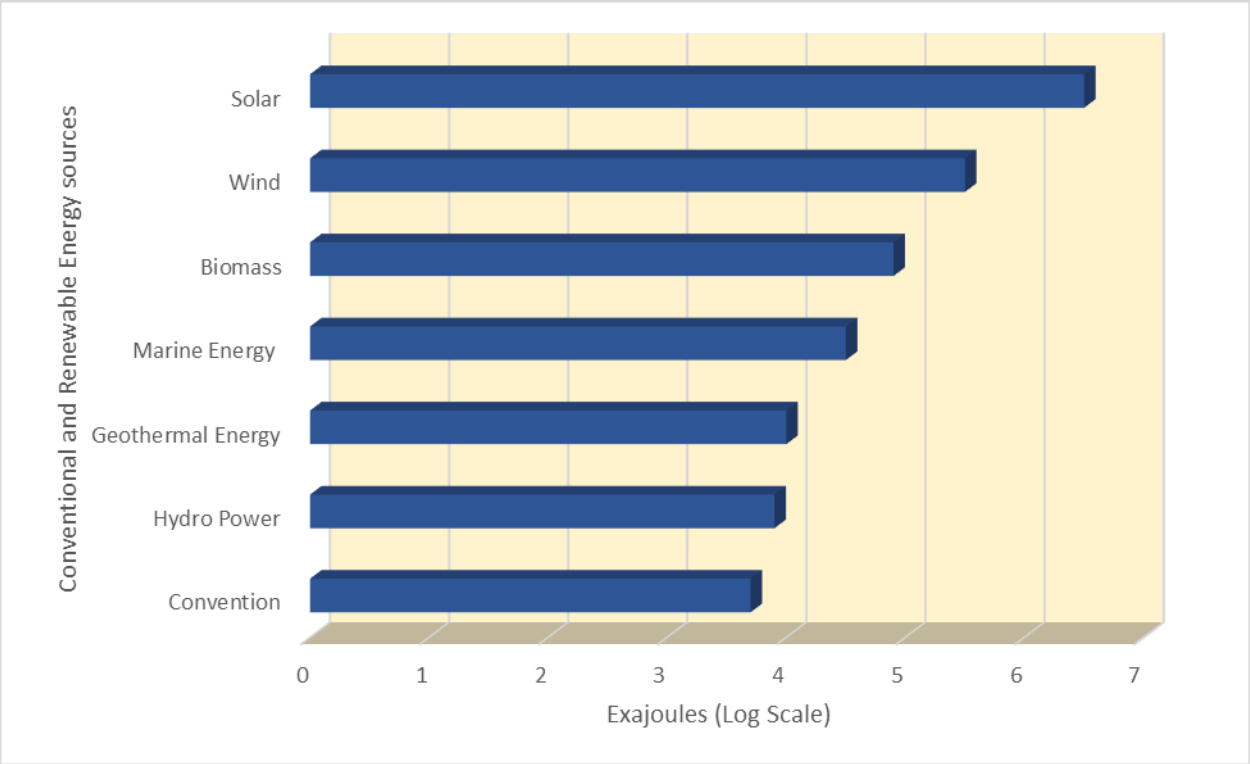

Fig.7: Different renewable energy sources potential compared with convential total primary energy supply [66]

3.0 Ocean Energy

Current research in renewable energy is geared towards the exploitation of ocean energy. The earth is being covered by oceans and these oceans cover nearly three – quarters of the earth surface. Intensified research and investigations are being conducted daily to determine how this viable energy generation medium can be harnessed at its full potential [30]. Specific strategies being adapted today to explore this type of energy are wave power, tidal power, tidal current, salinity gradients and temperature gradients. The consistency and predictability of ocean energy makes them more suitable for energy generation compared to the other type of renewable energy [31]. The energy that can be generated from marine energy sources can supply the entire world with its energy demand. The sad truth today is ocean energy supply just a small portion of the world's energy demand. Many research has been also conducted to ascertain the best sites suitable for ocean energy generation, the efficiency of the existing ocean energy technologies, the power being generated and the impact of these technology to the environment. Governments around the world continue to introduce good policies in order to expand the ocean energy generation mediums [32 – 39]. In 2015, the executive committee of the ocean energy systems(OES) published the statistical over view of marine energy specifically in chapter 7 of the report. Table 2 and 3 shows the installed and consented marine projects capacity for some countries around the world. The start of the agreement for implementing OES was done by 3 countries in the year 2011. The countries by December 2015 increased to 23 and most of the countries that came to join the agreement were mostly from developing and some developed countries in ocean energy [40]. Offshore wind is the commonly known renewable energy sources mainly classified under main stream

but other types of technology as explained earlier is also equally being developed. These are the tidal, wave, tidal currents, salinity gradient and ocean thermal energy conversion (OTEC) [41 – 43].

Table 2: Installed ocean energy for some countries in the world

Country projects	Installed capacity (kW)				
	Wave power	Tidal Power	Salinity gradient	OTEC	Tidal currents
Belgium					
Canada	9	20000			
China	450	4100			170
Denmark					
France		240000			2500
Italy					
Netherlands			50		1300
Norway	200				
Portugal	400				
Singapore	16	5			
South Korea	500	254000		220	1000
Spain	296				
Sweden	200	8			
USA					
UK	960				2100
All countries	3031	518113	50	220	7070

Table 3: consented ocean energy projects for some countries around the world

4.0 Conclusion

The report showed some renewable energy technologies which are currently emerging like the marine energy, concentrated solar power and the enhanced geothermal energy. The work clearly shows that renewable energy by 2014 contributed to 22% of the worlds energy demand. The IEA has made projections that carbon emission into the atmosphere is likely to rise by 2050 if the situation is not carefully checked. This review also reported the best method of reducing carbon dioxide emissions into the atmosphere by selecting the right technology for a specific location. The report also vividly explained the current nature of these novel technology mostly under development. Some of the obstacles reducing the commercialization of the technology was also presented and discussed and some possible solutions suggested as well. All the novel renewable energy technology discussed in this report are capable of meeting the worlds energy demand if they are properly harnessed.

5.0 References

1. Tabbi Wilberforce, A. Alaswad, A. Palumbo, A. G. Olabi. Advances in stationary and portable fuel cell applications. International Journal of Hydrogen Energy 41(37) March 2016.
2. Tabbi Wilberforce, Ahmed Al Makky, A. Baroutaji, Rubal Sambi, A.G. Olabi. Computational Fluid Dynamic Simulation and modelling (CFX) of Flow Plate in PEM fuel cell using Aluminum Open Pore Cellular Foam Material. Power and Energy Conference (TPEC), IEEE, Texas. 2017. DOI: 10.1109/TPEC.2017.7868285.
3. Tabbi Wilberforce, Ahmed Al Makky, A. Baroutaji, Rubal Sambi, A.G. Olabi Optimization of bipolar plate through computational fluid dynamics simulation and modelling using nickle open pore cellular foam material. International conference on reneable energies and power quality (ICREPQ'17), ISSN 2171-038X, No 15 April 2017.
4. Tabbi Wilberforce, A. Alaswad, J. Mooney,A.G.Olabi.Hydrogen Production for Solar Energy Storage. A Proposed Design Investigation.Proceedings of the 8th International Conference on sustainable Energy and Environmental Protection. ISBN: 978-1-903978-52-8.

5. Tabbi Wilberforce, F. N. khatib, O. Emmanuel, O. Ijeaodola, A. Abdulrahman, Ahmed al Makky A. Baroutaji, A.G. Olabi. Experimental study of operational parameters on the performance of pemfcs in dead end mode. Proceedings of SEEP2017, 27-30 June 2017, Bled Slovenia.
6. Tabbi Wilberforce, F. N. Khatib, Ahmed Al Makky, A. Baroutaji, A.G. Olabi Characterisation Of Proton Exchange Membrane Fuel Cell Through Design Of Experiment (DOE). Proceedings of SEEP2017, 27-30 June 2017, Bled, Slovenia.
7. Tabbi Wilberforce, Zaki, El-Hassan, F.N. Khatib, A. Al Makyy, A. Baroutaji, J. G. Carton and A. G. Olabi. Developments of electric cars and fuel cell hydrogen electric cars. DOI: 10.1016/j.ijhydene.2017.07.054
8. T. Wilberforce, Z. El-Hassan, F.N. Khatib, A. Al Makyy, A. Baroutaji, J. G. Carton and A. G. Olabi, Modelling and Simulation of Proton Exchange Membrane Fuel cell with Serpentine bipolar plate using MATLAB, International journal of hydrogen, 2017. DOI: 10.1016/j.ijhydene.2017.06.091.
9. Baroutaji, A., Carton, J, G., Stoke, J., Olabi, A, G., 2014. Design and Development of Proton Exchange Membrane Fuel cell using the Open Pore Cellular Foam as flow plate material. Journal of Energy Challenges and Mechanics. Volume 1 (2014) issue 3.
10. Moomaw W, Yamba F, Kamimoto M, Maurice L, Nyboer J, Urama K, Weir T. Introduction. In: Edenhofer O, Pichs-Madruga R, Sokona Y, Seyboth K, Matschoss P, Kadner S, Zwickel T, Eickemeier P, Hansen G, Schlomer S, von Stechow C, editors. IPCC Special Report on Renewable Energy Sources and Climate Change Mitigation. Cambridge, United Kingdom and New York, NY, USA.: Cambridge University Press; 2011.
11. FS-UNEP Collaboration Center, Frankfurt School. Global trends in renewable energy investments; 2016.
12. EIA Annual Report 2014. US Energy information Administration (EIA); 2014
13. Dincer I. Renewable energy and sustainable development: a crucial review. Renew Sustain Energy Rev 2000;4(2):157–75.
14. Sharma A, Chen CR, Lan NV. Solar-energy drying systems: a review. Renew Sustain Energy Rev 2008;13(6–7):1185–210.
15. Okoro OI, Madueme TC. Solar energy: a necessary investment in a developing economy. Int J Sustain Energy 2006;25(1):23–31.
16. Kumar A, Kandpal TC. Potential and cost of CO2 emissions mitigation by using solar photovoltaic pumps in India. Int J Sustain Energy 2007;26(3):159–66.
17. Kralova I, Sjoblom J. Biofuels-renewable energy sources: a review. J Dispers Sci Technol 2010;31(3):409–25.
18. lorenteI L, lvarez JL A´, Blanco D. Performance model for parabolic trough solar thermal power with thermal storage: comparison to operating plant data. Sol Energy 2011;85:2443–60.
19. Gaudiosi G. Offshore wind energy prospects. Renew Energy 1999;16(1–4):828–34.
20. Barbier E. Geothermal energy technology and current status: an overview. Renew Sustain Energy Rev 2002;6:3–65.
21. Ragauskas AJ, Williams CK, Davison BH, Britovsek G, Cairney J, Eckert CA, et al. The path forward for biofuels and biomaterials. Science 2006;311(5760):484–9.
22. Wydrzynski TJ, Satoh K. (editors). Photosystem II: The Light-Driven Water: PlastoquinoneOxidoreductase, Advances in Photosynthesis and Respiration; 2006; 87. p. 331–5.
23. International Energy Agency. Renewables in global energy supply. An IEA facts sheet OCED; 2007.
24. J. Crus Ed. Ocean Wave Energy: Current Status and Future Perspectives. Springer: Berlin; 2008.
25. Vining JG, Muetze A. Economic factors and incentives for ocean wave energy conversion. IEEE Trans Ind Appl 2009;45(2):547–54.
    Takahashi P, Trenka A. Ocean thermal energy conversion. New York: Wiley; 1996.
26. Pelc Robin, Fujita Rod M. Renewable energy from the ocean. Mar Policy 2002;26:471–9.
27. Gareth P, Harrison , Robin Wallace A. Climate sensitivity of marine energy. Renew Energy 2005;30:1801–17.
28. Shields a Mark A, Woolf DK. The ecological implications of altering the hydrodynamics of the marine environment Ocean & coastal management. Mar Renew Energy 2011;54:2–9.
29. Boehlert Gorge W, Gi l l An drew B. Environmental and ecological effects of ocean renewable energy development. Oceanography 2010;23(2):68–81.

30. Wright Glen. Marine governance in an industrialized ocean: a case study of the emerging marine renewable energy industry. Mar Policy 2015;52:77–84.
31. Kerr Sandy, Colton John, Johnson Kate, Wright Glen. Rights and ownership in sea country: implications of marine renewable energy for indigenous and local communities. Mar Policy 2015;52:108–15.
32. Quirapas Ann Joy Robles, Lin Htet. Ocean renewable energy in Southeast Asia: a review. Renew Sustain Energy Rev 2015;41:799–817.
    Lewis A, Estefen S, Huckerby J, Musial W, Pontes T, Torres-Martinez J. Ocean energy. IPCC Spec Rep Renew Sources Clim Change Mitig 2011, [chapter 6].
33. OES, Annual report on implementing agreement on ocean energy systems; 2014
34. Barstow S, Mollison D, & Cruz J (2007) The Wave Energy Resource. In J. Cruz, ed. Ocean Wave Energy: Current Status and Future Perspectives. pp. 93–132.
35. Mørk G et al (2010), Assessing the global wave energy potential. In Proceedings of OMAE2010 (ASME), 29th International Conference on Ocean, Offshore Mechanics and Arctic Engineering. Shanghai, China.
36. Pelc R, & Fujita RM (2002), Renewable energy from the ocean. Marine Policy, 26, pp.471–479
37. Thorpe T (1999) A Brief Review of Wave Energy
38. Cornett AM (2008) A Global Wave Energy Resource Assessment. Proceedings of ISOPE 8(March), p.9
39. Lewis A, Estefen S, Huckerby J, Musial W, Pontes T, Torres-Martinez J. Ocean energy. IPCC Spec Rep Renew Sources Clim Change Mitig 2011, [chapter 6].
40. OES, Annual report on implementing agreement on ocean energy systems; 2014.
41. Clement Alain, Cullen Pat Mc. Wave energy in Europe: current status and perspectives. Renew Sustain Energy Rev 2002;6:405–31.
42. Titah-Benbouzid Hosna, Benbouzid Mohamed. IEEE Electronics and Application Conference and Exposition (PEAC), France:338–342; 2014.
43. Falcao FAO. Wave energy utilization: a review of the technologies. Renew Sustain Energy Rev 2010;14(3):899–918.

A REVIEW OF THE CONCEPTS OF SMART GRID, ENERGY INTERNET AND SMART ENERGY SYSTEMS

Yunlong Zhao, Pei Liu, Linwei Ma*, Chinhao Chong, Zheng Li, Weidou Ni

State Key Laboratory of Power Systems, Department of Energy and Power Engineering, Tsinghua-BP Clean Energy Centre, Tsinghua-Rio Tinto Joint Research Center for Resources, Energy and Sustainable Development, Tsinghua University, Beijing 100084, China;email: malinwei@tsinghua.edu.cn

ABSTRACT

The innovation of energy system integration is an essential part in addressing energy challenges and deploying renewable energy, and several new concepts emerged in recent years in this regards, including "smart grid", "energy internet" and "smart energy systems" (or smart energy). However, as the construction of energy systems following these concepts is still in an early stage and the academic discussion on them is still going on, there are confusing, even conflicting, understandings of these concepts in global and Chinese society. This paper attempts to review the origin and historical development of these concepts, compare their different definitions in published literatures, analyze their concepts by system functions and elements, and conclude their general definitions. The results indicate that these concepts are mutually inherited and developed, evolving from smart grid, energy internet to smart energy systems. Based on the requirements of system functions of "smart grid" on security, flexible, economic and green, "energy internet" further emphasizes the integration of energy network and information network and the new requirement of equity and sharing. The smart energy systems further puts forward the new requirement of "synergy", which emphasizes cross-sectoral integration, overall optimization and the adoption of flexible energy storage methods.

Key words: systems analysis; smart grid; energy internet; smart energy systems

0 INTRODUCTION

Global sustainable development in the 21st century faces severe energy challenges such as energy poverty, energy security, environmental pollution and climate change [1]. While countries actively respond to these challenges, the situation remains grim. In particular, the ecological environment continues to deteriorate [2]. Therefore, it is necessary to accelerate the transition of the global energy systems and technological innovation. However, the large-scale introduction of new energy resources, technologies and systems still face their own problems and doubts, and they continue to bring challenges to the energy system integration (ESI), especially the construction and operation of energy infrastructure.

The rapid development of information and communication technologies (ICT) provide new opportunities for the ESI. Therefore, in recent years, several new ESI concepts have emerged, including "smart grid", "energy internet", "smart energy" and "smart

* Corresponding author.

E-mail address: malinwei@tsinghua.edu.cn (L.-w. Ma).

energy systems", and have become the hot spots of ESI research and development. For example, several national polices in China, vigorously promoting the revolution of energy production and consumption[3][4], have been enacted to promote the development of energy internet (originally called “internet plus and smart energy”)[5][6] and actively building smart energy systems.[7]

However, while the relevant policy measures and pilot demonstrations have been promoted following these policies, the public understanding of those concepts is still inconsistent and even controversial. Moreover, as related research and discussion going on, the boundaries between these concepts become unclear and are often confused with each other. Although unclear concepts will not necessarily affect the independent research and early demonstrations, it will make it difficult to determine the goals, directions and priorities of governments and enterprises at the level of strategic decisions, thus affecting the effectiveness of related resource inputs

Therefore, this paper attempts to review the origin, development and systems connotation of these concepts to provide a preliminary reference for a clear understanding and effective application of these concepts.

1. METHODOLOGY

Referring to the origin of those concepts (see Section 2), "smart grid" and “energy internet” first appeared in literatures in 2001 and 2004 respectively. Afterwards, "smart energy" and "smart energy systems" originated in 2009. Given their scopes, "smart grid" only focuses on power grid while "energy internet" contains not only power grids but heating networks, fuel grids, and transportation networks. “Smart energy" and "smart energy systems" (these two concepts are difficult to be distinguished strictly) nearly cover the entire energy systems. Therefore, these concepts have a progressive relationship by their orders of spatial and temporal evolution, as shown in Figure 1, which decides the sequences of the review, starting from "smart grid", "energy internet" to "smart energy" and "smart energy systems."

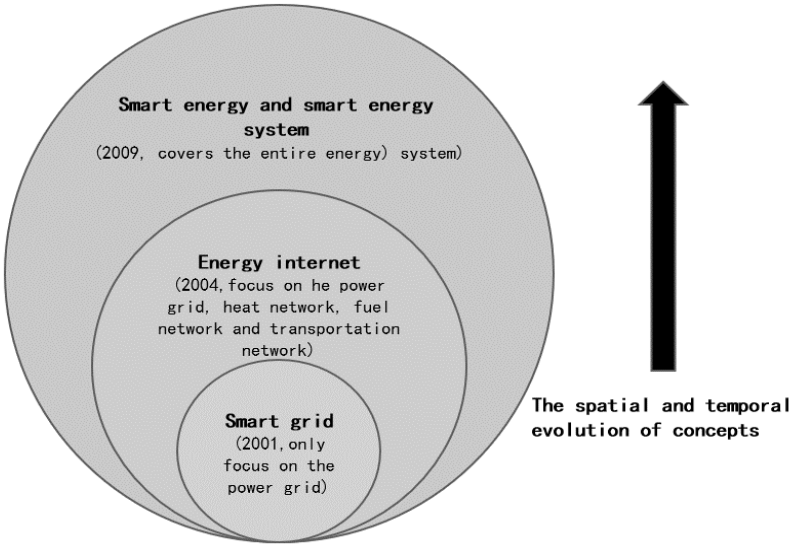

Fig.1. Conceptual Evolution of "Smart Grid," "Energy Internet," "Smart Energy," and "Smart energy systemss."

In the review, the origin of each concept mentioned above is first introduced. Then, the development of these concepts are discussed by comparing various definitions in later literature. Afterwards, based on the general system theory proposed by Bertalanffy in 1969 [8], their systems connotation is defined by analyzing the system functions and elements beneath. Finally, their general definitions are summarized. Referring to this theory, the systems connotation of a concept is defined as: 1) system function: the role of the system in the external environment; 2) system elements: the system consists of two or more elements which are interconnected and mutual influencing.

2 RESULTS AND DISCUSSIONS

2.1 The concept of smart grid

The origin: It went back to the concept of "IntelliGrid" (Intelligent Grid) proposed by the Electric Power Research Institute (EPRI) in 2001[9]. Later in 2003, the U.S. government officially started the construction of smart grid.

The development: After that, many scholars discussed the definition of the smart grid, which is close to each other and mainly emphasizing the integration of power grid and ICT. The principal opinions are:1) Using ICTs to fully accommodate distributed power sources and effectively uses the consumers' information[11]; 2) Exchanges information intelligently in all aspects of the power grid system [12]. Other literature [9][13]~[18] also give similar ideas.

The systems connotation: The system functions can be summarized as follows referring to literatures [9][10][14][16][19][20]:1) Security, such as strong, safe and self-healing; 2) Flexibility, such as compatibility (compatible with different power types and storage modes.) and interaction(two-way exchange of energy and information between grid and users);3) Economy, such as low cost, high quality and high efficiency;4) Green, such as environmental protection and low carbon. The system elements can also be summarized [9][12]~[17][20][21], as shown in Figure 2. The smart grid system consists of two kinds of elements, one kind is part of the power system, including generation, transmission, distribution and use of each link, and the other is an integral part of intelligent dispatching system, including transmission, distribution, scheduling and management.

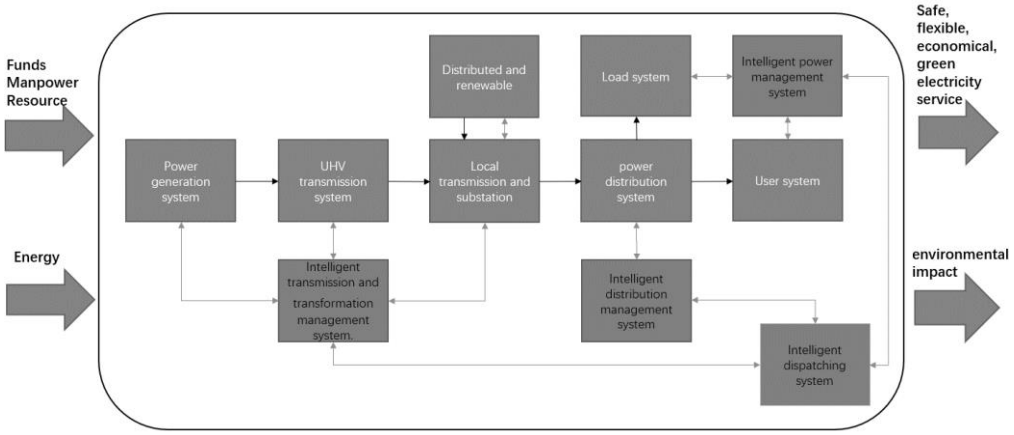

Fig.2. Schematic diagram of system elements of smart grid

Final definition: It is concluded as "by using advanced ICT, smart grid is a modern

power grid system with safe, flexible, economical and green power services and an intelligent dispatching system, which comprehensively schedules the physical links of power generation, transmission, distribution, electricity consumption and the various business links of power supply and electricity sales".

2.2 The concept of energy Internet

The origin: it went back to the literature entitled Building the Energy Internet in 2004, which proposed the concept of energy internet[21]. Its concept was more focused on grid security issues through intelligence, distribution and energy storage. In 2011, Rifkin put forward that the energy Internet is one of the core of the third industrial revolution and is also the infrastructure support for the large-scale use of renewable energy, which gave the concept a wider focus[22].

The development: while scholars have differences in the range of energy systems, they all agree that[27]~[38]:1) Energy Internet is the interaction and integration of the information internet and the energy network;.2) ICT is the basis and the power grid is the core[28];3) The role of multi-energy synergies is valued[29].And several pilot projects on energy internet carried out("E-Energy" in Germany [21], [23], "FREEDM" [24] ~ [26] in the US and "Digital Power Grid" in Japan [27])

The systems connotation: The system functions can be summarized as follows referring to literatures[22][23][28]~[39]:1) It inherits the functions of smart grid(severity, flexible, economy and green)while possessing the new system function requirements of peer-to-peer openness (sharing);2) Each participant in the energy network can act as both a consumer and a producer;3)Related equipment can be plug-and-play. In conclusion, energy internet is a network for energy transmission and information management as well as a sharing communication platform for energy and information. Energy internet includes two major subsystems, energy network and information network. And the relationship between different elements can be summarized as shown in Figure 3

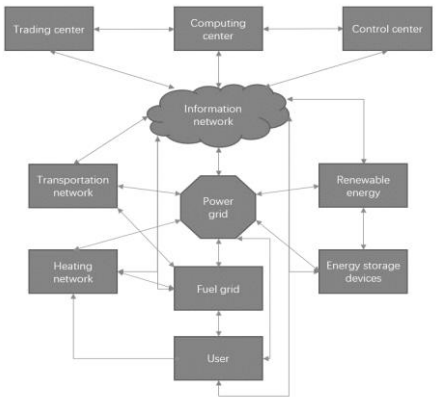

Fig.3. Schematic diagram of system elements of energy Internet

Final definition: it is concluded as "by using renewable energy technologies, ICT and advanced energy storage technologies, energy internet, which takes the power grid as a hub and couples the power grid with the oil and gas network, the heat network and the electrified transportation network, is a secure, flexible, economical, green, sharing

energy service network with efficient use of multiple energy sources and multiple subjects to participate".

2.3 The concept of smart energy and smart energy systems

The origin: it went back to the concept of "smarter planet" proposed by IBM's expert team in 2009[41]. They proposed that the utilization of ICT, big data analysis and cloud computing could help to form a wise "internet of things", which can change people's lifestyle and make the whole earth to reach a state of "full of wisdom".

The development: according to a review published by Henrik Lund in 2017 [45], a total of 72 literatures mentioning smart energy or smart energy systems in titles, summaries, keywords or references are contained by the Scopus database, and they can be divided into two groups. In group 1, smart energy systems are similar to the concept of smart grid[42].In group 2,the concept is used in systems integration across sectors and industries, which is closer to the concept of the Internet of things[43]~[45].

The systems connotation: The system functions can be summarized as follows referring to literatures[41]~[45]:1)It continues the idea that integrating information networks and energy networks and the functions of security, flexibility, economy, green and sharing, and covers a wider range(industry, transportation and construction) than energy internet;2)It places special emphasis on the coordination of multi-energy infrastructure as well as the role of energy storage;3) It no longer focuses on highlighting the centrality of any single sector, energy variety and technology but rather highlights the importance of their synergies. Smart energy systems use smart power grid, smart fuel network, and smart heating network as the infrastructure for sustainable energy systems. Through them, every energy-related department connects to each other and works together to achieve synergistic effects of multiple energy to achieve local and overall optimality. As is shown in figure 4.

Final definition: it is concluded as"smart energy systems, which regards smart grid, smart heating network and smart fuel network as the three pillars, is a safe, flexible, economical, green, sharing and synergistic sustainable energy system that integrates multiple functions such as power generation, industry, construction and transportation in order to achieve synergic effect through flexible energy storage".

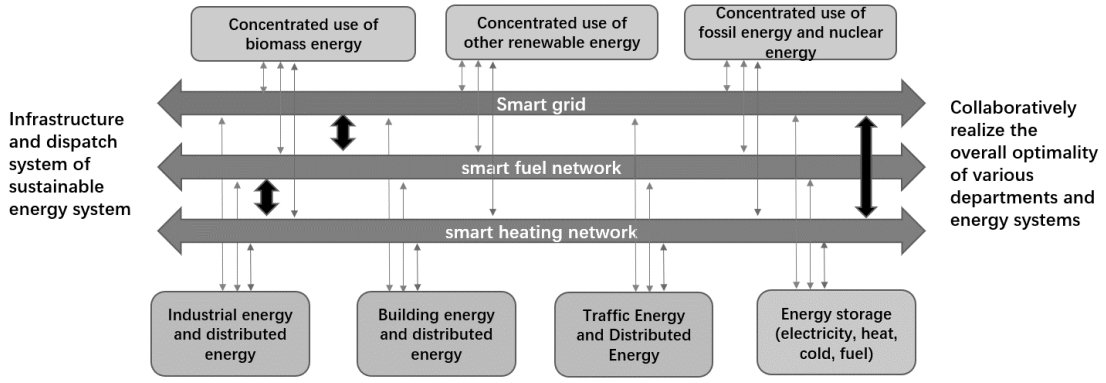

Fig.4. Schematic diagram of system elements of smart energy systems.

2.4 Discussions

The development process of these concepts reflects the continuous development

and improvement of the concept and understanding of the sustainable energy systems and their ESI methods. A safe, flexible, economical, and green smart grid is the foundation of the latter two concepts. Energy Internet further covers oil and gas networks, heat networks, and transportation networks, and sets new requirement of sharing among various parts of energy systems. Smart energy system further extends to the entire energy systems including industry, transportation and construction, and puts forward new "collaboration" requirement of cross-sectoral integration and overall system optimization. Therefore, judging from the sustainable development of energy resources at national and regional levels, smart energy systems are the ultimate goal. Smart grid and energy Internet are basic ways and preconditions to realize it.

3 CONCLUSIONS AND RECOMMENDATIONS

This paper analyzes the origin, development and the system functions and elements of the concepts of “smart grid”, “energy internet” and “smart energy and smart energy systems”, and then concludes their general definitions. Based on it, we can further put forward following thoughts and recommendations on how to construct smart energy systems for sustainable development in China and other regions.

1) The establishment of smart energy systems requires taking into account objective conditions of the country and the region, such as resource endowments, energy demand, economic level, social development and infrastructure, etc. An early demonstration of pilot projects is urgently required to specify suitable system integration methods in special areas.

2) The construction of smart energy systems must further introduce humanities and social elements, and gradually increase their intelligent level. At the beginning, the system relies on massive human interference and expert wisdom. Then intelligent information and network systems can replace most human interventions. Finally, the entire system can form a completely “smart” operation from observation, reflection, adjustment and adaptation.

3) The construction of smart energy systems requires a thorough transformation of design ideas and methods. It is necessary to break the boundaries among various departments to establish a lumped design idea of cross-sector and overall system optimization. This transformation involves not only the development of engineering thoughts, but also the breakthrough in aspects of social and cultural systems.

ACKNOWLEDGEMENTS

This work was supported by the State Key Laboratory of Power Systems in Tsinghua University (Project No. SKLD17Z02). The authors also gratefully acknowledge the financial support from the Rio Tinto Group in the context of the Tsinghua-Rio Tinto Joint Research Center for Resources, Energy and Sustainable Development.

REFERENCES

[1] Jefferson M. A global energy assessment [J]. Wiley Interdisciplinary Reviews: Energy and Environment, 2016, 5(1): 7-15. http://onlinelibrary.wiley.com/doi/10.1002/wene.179/full.

[2] Dancer I. and Acar C. Smart energy systems for a sustainable future. Applied Energy, Vol. 194, pp. 225-235,

2017.
[3] Xinhua, Report of Hu Jintao at the Eighteenth National Congress of the Communist Party of China, Xinhua,2012. http://www.xj.xinhuanet.com/2012-11/19/c_113722546.htm.
[4] Xinhua, Xi Jinping: Promoting the Revolution in Energy Production and Consumption, Xinhua, 2014. Available from, http://news.xinhuanet.com/mrdx/2014-06/14/c_133406376.htm.
[5] The State Council of the People's Republic of China, Guiding opinions of the State Council on promoting "Internet plus" action. July 2015. Available from, http://www.gov.cn/gongbao/content/2015/content_2897187.htm.
[6] The National Development and Reform Commission, Energy Bureau, Ministry of industry and information of the People's Republic of China, Guiding opinions on promoting the development of smart energy and “Internet plus”. February 2016. Available from, http://www.nea.gov.cn/2016-02/29/c_135141026.htm
[7] The National Development and Reform Commission of the People's Republic of China. March 2016. Available from, http://www.ndrc.gov.cn/zcfb/zcfbghwb/201603/P020160318573830195512.pdf.
[8] Bertalanffy LV. General System Theory: Foundations, Development, Application [M]. New York: George Braziller Inc., 1969.
[9] Gu LP, An overview of the development of smart grid in foreign countries, Electric Power Information Technology, Vol. 8, pp. 29-32, 2010.
[10] Wang YZ, The Brief History of the Development of the Smart Grid Technology[D], Taiyuan, Shanxi: Shanxi University, 2012.
[11] Zhao ST, Zhao ZG, Analysis of the structure and development trend of smart grid, Scientific and Technological Innovation, Vol. 27, pp. 13-14, 2016.
[12] China Measurement and control network, Analysis of three layers of smart grid based on the Internet of things sensor, Cards World, Vol. 12, pp. 58-57, 2015.
[13] Lei JY, Smart Grid Analysis, Internet of Things Technologies, Vol. 10, pp. 50-51, 2014.
[14] Wang L, Discussion on the development process and Prospect of smart grid, Journal of Beijing Electric Power College (NATURAL SCIENCE EDITION), Vol. , pp. 13, 2011.
[15] Zhao YB, Discussion on the characteristics and development prospect of smart grid and the current situation, application and practice of the construction of Yunnan power network intelligent network, Silicon Valley, Vol. 23, pp. 14, 2010.
[16] Liu QQ, Construction of American Intelligence Network, Shanxi Energy and Conservation, Vol. 1, pp. 74-75, 2010.
[17] Zhou S, Analyze the new form of smart grid construction grid operation, Technology Innovation and Application, Vol. 28, pp. 160, 2013.
[18] Delucchi M A, Yang C, Burke A F, et al. An assessment of electric vehicles: technology, infrastructure requirements, greenhouse-gas emissions, petroleum use, material use, lifetime cost, consumer acceptance and policy initiatives. Philosophical Transactions, Vol. 2006, pp.372 , 2013.
[19] Zhou H, The influence of foreign smart grid research on the construction of smart grid in China, High-Technology & Industrialization, Vol. 5(10), pp.53-54, 2009.
[20] Yang DC, Li Y, C.Rehtanz, Liu ZH, Luo LF, Study on the Structure and the Development Planning of Smart Grid in China, Power System Technology, Vol. 32(20), pp.13-20, 2009.
[21] Energy Internet Research Group, Energy Internet Development Research, Tsinghua University Press,2017.
[22] Rifkin J. The third industrial revolution : how lateral power is transforming energy, the economy, and the world, 2011.
[23] Tian SM, Luan WP, Zhang DX, Liang CH, Sun YJ, Technical Forms and Key Technologies on Energy Internet, Proceedings of the CSEE, Vol. 35(14), pp.3482-3494, 2015.
[24] Huang A. FREEDM system - a vision for the future grid, Power and Energy Society General Meeting. IEEE,

San Diego, California, 2010.
[25] Huang A Q. Renewable energy system research and education at the NSF FREEDM systems center, Power & Energy Society General Meeting, Calgary, Alberta, 2009.
[26] Huang AQ, Crow ML, Heydt GT, Zheng JP,Dale SJ. The Future Renewable Electric Energy Delivery and Management (FREEDM) System: The Energy Internet, Proceedings of the IEEE, Vol. 99(1), pp.133-148, 2010.
[27] Abe R, Taoka H, Mcquilkin D. Digital Grid: Communicative Electrical Grids of the Future, IEEE Transactions on Smart Grid, Vol. 2(2), pp.399-410, 2011.
[28] Zeng M, et al, Development Model, Mechanism and Key Technology of Energy Internet Based on Complex Adaptive System Theory, Power System Technology, Vol. 40(11), pp.3383-3390, 2016.
[29] Zeng M, et al, The Preliminary Research for Key Operation Mode and Technologies of Electrical Power System With Renewable Energy Sources Under Energy Internet, Power System Technology, Vol. 36(3), pp.681-691, 2016.
[30] Sun HB, Guo QL, Pan ZG, Energy Internet: concept, architecture and frontier outlook, Automation of Electric Power Systems, Vol. 19, pp.1-8, 2015.
[31] Yan TS, Cheng HZ, Zeng PL, Ma ZL, Zhang LB, System Architecture and Key Technologies of Energy Internet, Power System Technology, Vol. 40(1), pp.105-113, 2016.
[32] Zeng M, et al, “Generation-Grid-Load-Storage” Coordinative Optimal Operation Mode of Energy Internet and Key Technologies, Power System Technology, Vol. 40(1), pp.114-124, 2016.
[33] Cha YB, Zhang T, Tan SR, Huang Z, Wang WG, Understanding and Thinking of the Energy Internet, National Defense Science & Technology, Vol. 33(5), pp.1-6, 2012.
[34] Yao JG, Gao ZY, Yang SC, Understanding and Prospects of Energy Internet, Automation of Electric Power Systems, Vol. 23, pp.9-14, 2015.
[35] Zeng M, et al, Key Problems and Prospects of Integrated Demand Response in Energy Internet, Power System Technology, Vol. 40(11), pp.3391-3398, 2016.
[36] Cao JW, Meng K, Wang JY, Yang MB, Chen Z, An energy internet and energy routers, Scientia Sinica(Informationis), Vol. 44(16), pp.714-727, 2014.
[37] Wang Z, Wang HY, Understanding and thinking about the energy Internet, Electric power industry informatization conference, Beijing, 2015.
[38] Dong CY, Zhao JH, Wen FS, Xue YS, From smart grid to energy Internet: basic concepts and research frameworks, Automation of Electric Power Systems, Vol. 38(15), pp.1-11, 2014.
[39] Ma Z, Zhou XX, Shang YW, Sheng WX, Exploring the Concept, Key Technologies and Development Model of Energy Internet, Power System Technology, Vol. 39(11), pp.3014-3022, 2015.
[40] Shen Z, Zhou JH, Yuan XD, Yang W, Development and Suggestion of the Energy-Internet, Jiangsu Electrical Engineering, Vol. 33(1), pp.81-84, 2014.
[41] Wang Y, Zhang BB, Smart Energy, Tsinghua University Press, 2012.
[42] Crossley P, Beviz A, Smart energy systems: Transitioning renewables onto the grid, Renewable Energy Focus, Vol. 11(5), pp.54,58-56,59, 2010.
[43] Lund H, et al, From electricity smart grids to smart energy systems – A market operation based approach and understanding, Energy, Vol. 42(1), pp.96-102, 2012.
[44] Lund H, et al, Renewable energy systems - A smart energy systems approach to the choice and modelling of 100 % renewable solutions, Chemical Engineering Transactions, Vol. 39(4), pp.1-6, 2014.
[45] Lund H, et al, Smart Energy and Smart Energy Systems, Energy, Vol. 137, pp.556-565, 2017.

AC SYSTEM PERFORMANCE IMPROVEMENT BY USING WELL WATER

R. Murr[1], M. Ramadan[1,2], H. Elhage[1] and M. Khaled[1,3]

1. School of Mechanical Engineering, Lebanese International University (LIU), Beirut, Lebanon; email:
2. Associate member at FCLAB, CNRS, Univ. Bourgogne Franche-Comté, Belfort cedex, France.
3. Univ Paris Diderot, Sorbonne Paris Cité, Paris Interdisciplinary Energy Research Institute (PIERI), Paris, France

ABSTRACT

With the tremendous social and economic evolution that the world has seen the last three decades, Heating ventilating and air conditioning (HVAC) systems have change from being a means of comfort to an essential device in almost each home especially in zones with extreme weather condition such as regions near deserts. With this in mind, it should be noted that from energy consuming point of view, HVAC systems are among the most expensive appliances. That said and to be in line with the international trend that imposes the reduction of fuel consumption, it is of high interest to find new technologies that allows to reduce energy consumption. In this frame, the present paper suggests a new energy concept that permits to decrease energy consumption by increasing the performance of HVAC system by using well water as a cold source to precool the supply air. A thermal modeling is developed based on the energy balance and an in-house code is developed to perform the simulation. It has been shown that the suggested technology enhances the coefficient of performance of the system up to 200%.

Keywords: HVAC, AC, energy storage, well water, pre-cooling

1 INTRODUCTION

Decreasing the fuel consumption is currently considered as a primary objective at the public and private sectors. That said many strategies have been adopted by governments to reach this object. In this frame, huge number of research works is focusing on constructing systems that involve renewable resources. Solar energy [1-2] as well as wind energy are the most investigated systems in addition to other systems such as geothermal energy [3]. On the other hand, heat recovery is another domain that is showing a tremendous progress. It consists in reusing waste heat as a new source of heat to supply other systems. It covers many applications such as recovering heat of exhaust gas [4-6] or heat of drain water [7-8]. Other approaches are mainly investigating energy storage system such as fuel cell [9]. Having said that, Heating ventilating and air conditioning (HVAC) has been highly affected by the energy revolution that is occurring in all domains since HVAC systems are among the most energy consuming systems. That is why many works have been dedicated to enhance the efficiency of HVAC system either by optimizing its operational mode or by recovering heat and using it to increase its performance [10]. The present paper is a combination between energy storage and HVAC system. It discusses the concept of using the cold water of well to enhance the performance of the HVAC systems.

2 REFRIGERATION CYCLE

Cooling of spaces is generally ensured using air conditioning (AC) systems that currently operate using refrigeration cycle. These cycles have four main components: an electric compressor, a condenser, an expansion valve and an evaporator. Figure 1 shows a schematic of an AC system. The main problem that faces the users of AC systems is the high consumption of electric energy and then the high electric bill of the house and the air pollution especially when non-renewable sources are used to produce the electricity.

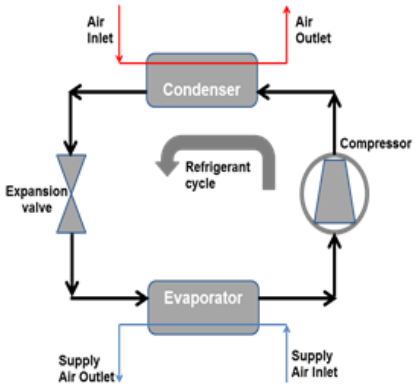

Figure 1. Schematic of AC system

3 PRINCIPLE OF WELL WATER SYSTEM

Well water is water extracted from underground aquifers by digging or drilling in the ground. This water has usually a temperature higher than the one of the ambient air in winter which may be below 10°C in cold regions and lower in summer which may be above 30°C in hot regions. Besides, wells are frequent in Lebanon. Using well water to pre-cool or cool the air supplied to a conditioned space will lead to a decrease in the electric consumption of the AC systems during hot seasons. The principle of well water cooling system (WWCS) is described in figure 2. The well water can cool or pre-cool a supply air by the usage of a heat exchanger. In the frame of this paper, well water is considered as heat sink and the main goal is to improve the performance of an air-to-air AC system.

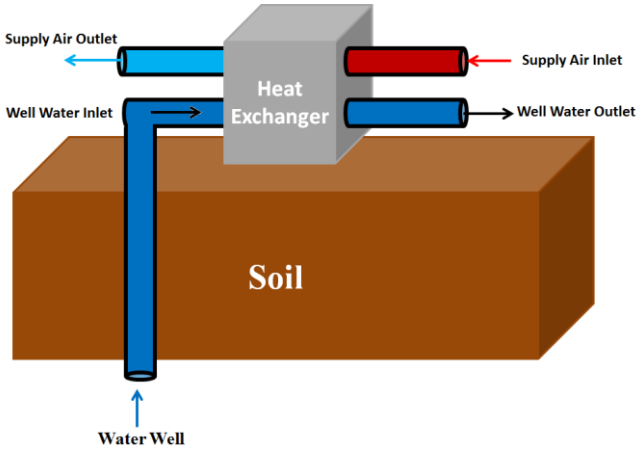

Figure 2. Schematic of pre-cooling principle inside a heat exchanger

4 SUGGESTED WWCS: E-WWCS

A configuration that may improve the performance of the AC system is suggested: the evaporator well water cooling system (E-WWCS).

4.1 Principle of the E-WWCS

In this system, well water is used to pre-cool the supply air by using a water-to-air heat exchanger (HEX) where the supply air releases its heat to the well water. In order to reach the required temperature in the space, this supply air passes then through the evaporator of the air-to-air AC system as shown in figure 3.

4.2 Modeling of the E-WWCS

In order to study the performance of this system and compare it to the basic air-to-air AC system, each component is modeled and the thermal model is based on the calculation of the overall coefficient of performance (COP) of the system. The principle of conservation of mass and the first law of thermodynamics are applied on each component and on the entire system.

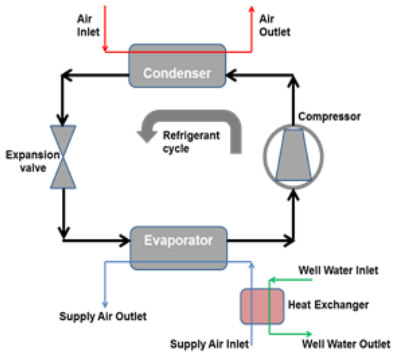

Figure 3. Schematic of the E-WWCS.

The rate of heat gain by the air passing through the condenser is given by the following equation.

$$\dot{Q}_{Cond} = \dot{m}_{a,Cond} \cdot C_{pa} \cdot (T_{a,C,o} - T_{a,C,i}) = \dot{m}_{ref} \cdot (h_2 - h_3) \quad (1)$$

Where $\dot{m}_{a,Cond}$ is the mass flow rate of the air passing through the condenser, C_{pa} is the specific heat of air, $T_{a,c,o}$ is the temperature of the air leaving the condenser, $T_{a,c,i}$ is the temperature of the air entering the condenser, $\dot{m}_{ref}$ is the mass flow rate of the refrigerant, h_2 and h_3 are the specific enthalpies of the refrigerant entering and leaving the condenser.

The rate of heat released by the air passing through the evaporator and absorbed by the refrigerant is given by the following equation.

$$\dot{Q}_{Evap} = \dot{m}_{a,Evap} \cdot C_{pa} \cdot (T_{a,E,i} - T_{a,E,o}) = \dot{m}_{ref} \cdot (h_1 - h_4) \quad (2)$$

Where $\dot{m}_{a,Evap}$ is the mass flow rate of the air passing through the evaporator, C_{pa} is the specific heat of air, $T_{a,E,o}$ and $T_{a,E,i}$ are the temperatures of the air leaving and entering the evaporator respectively, and h_1 and h_4 are the specific enthalpies of the refrigerant leaving and entering the evaporator respectively.

The power of the compressor is given by the following equation.

$$\dot{W}_{Comp} = \dot{m}_{ref} \cdot (h_2 - h_1) \quad (3)$$

The isentropic efficiency of the compressor is given by the following equation.

$$\eta_{is} = \frac{(h_{2,is} - h_1)}{(h_2 - h_1)} \quad (4)$$

Where $h_{2,is}$ is the specific enthalpy of the refrigerant leaving the compressor isentropically.

The coefficient of performance COP of any AC cycle is the ratio of the evaporator capacity to the power of the compressor; it is given by the following equation:

$$COP = \frac{\dot{Q}_{Evap}}{\dot{W}_{Comp}} \quad (5)$$

By applying the first law of thermodynamics on the entire AC system, the following equation is obtained:

$$\dot{Q}_{Cond} = \dot{Q}_{Evap} + \dot{W}_{Comp} \quad (6)$$

The heat exchanger (HEX) heat rate is calculated using the following equation:

$$\dot{Q}_{HEX} = \dot{m}_{a,Evap} \cdot C_{pa} \cdot (T_{a,HEX,i} - T_{a,HEX,o}) = \dot{m}_{WW} \cdot C_{p,WW} \cdot (T_{WW,o} - T_{WW,i}) \quad (7)$$

Where $T_{a,HEX,o}$ and $T_{a,HEX,i}$ are the temperatures of the air leaving and entering the (HEX)and $T_{WW,i}$ and $T_{WW,o}$ are the temperatures of the well water entering and leaving the (HEX). In this case, $T_{a,HEX,o}$ is equal to $T_{a,E,i}$.

(HEX) has a maximum heat rate which is given by the following equation:

$$\dot{Q}_{HEX,MAX} = (\dot{m} \cdot C_p)_{\min} \cdot (T_{a,HEX,i} - T_{a,HEX,o}) \quad (8)$$

Where $(\dot{m}.C_p)_{min}$ is the minimum value between ($\dot{m}_{a,Evap} \cdot C_{pa}$) and ($\dot{m}_{WW} \cdot C_{p,WW}$)

The effectiveness of the (HEX) is given by the equation (9).

$$\varepsilon = \frac{\dot{Q}_{HEX}}{\dot{Q}_{HEX,MAX}} \quad (9)$$

The overall coefficient of performance $COP_{Overall}$ of the (E-WWCS) is given by the following equation:

$$COP_{Overall} = \frac{\dot{Q}_{Evap} + \dot{Q}_{HEX}}{\dot{W}_{Comp}} \quad (10)$$

5 COMPUTATIONAL CODE

The thermal model of the suggested system developed in the previous section is integrated in an in-house code to calculate the overall coefficient of performance in order to compare it to the one of the basic air-to-air AC system. Figure 4 shows a schematic of the code developed. In this figure, the input parameters are presented to the left and the outputs to the right.

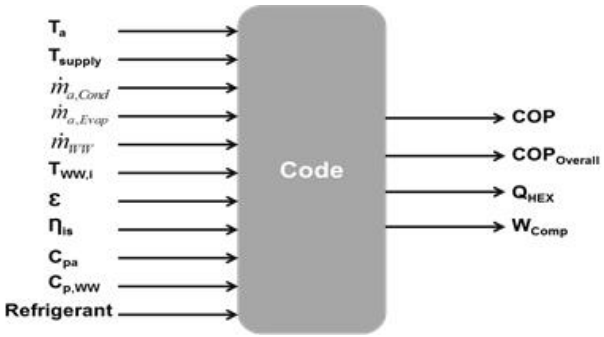

Figure 4. Schematic of the developed code.

6 EXPERIMENTAL STUDY

In order to study the cooling system by using the well water, some measurements have been done on the well water temperature and the ambient temperature over a period of 12 hours in August in Bekaa region in Lebanon. 2 k-type thermocouples with accuracy of 2% have been used. The schematic of the prototype is shown in figure 5 and the results are shown in figure 6.

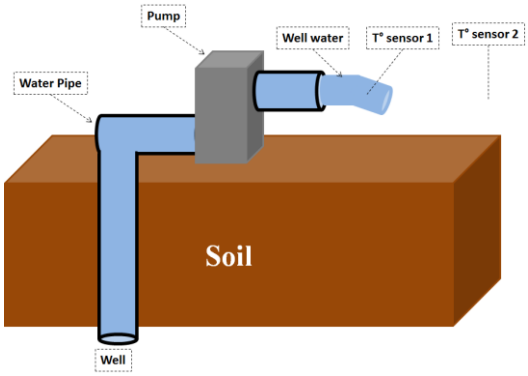

Figure 5. Prototype schematic

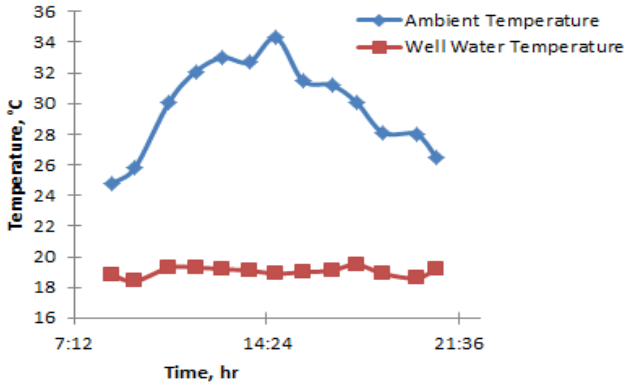

Figure 6. Well water and ambient temperature in function of time

Figure 6 shows that the well water temperature was almost constant around 19°C while the ambient temperature increased from 25°C to 35°C.

7 RESULTS AND DISCUSSION

The computational code described in part 5 is used to calculate the gain on COP and the reduction of the compressor power of the E-WWCS (figure 3) in comparison with the basic air-to-air AC cycle based on the values of temperatures retrieved in part 6. The impact of four different well water mass flow rates (0.01 kg/s, 0.02 kg/s and 0.04 kg/s) is simulated. In this case, the ambient air temperature is 32°C, the supply air temperature and mass flow rate are 16°C, and 0.12 kg/s respectively, the condenser air mass flow rate is 0.6 kg/s, the temperature of the well water is 19°C, the isentropic efficiency of the compressor is 75%, the effectiveness of the heat exchanger is 0.8 and the refrigerant is R-22. The results of the COP gain and compressor power reduction are shown in figure 7.

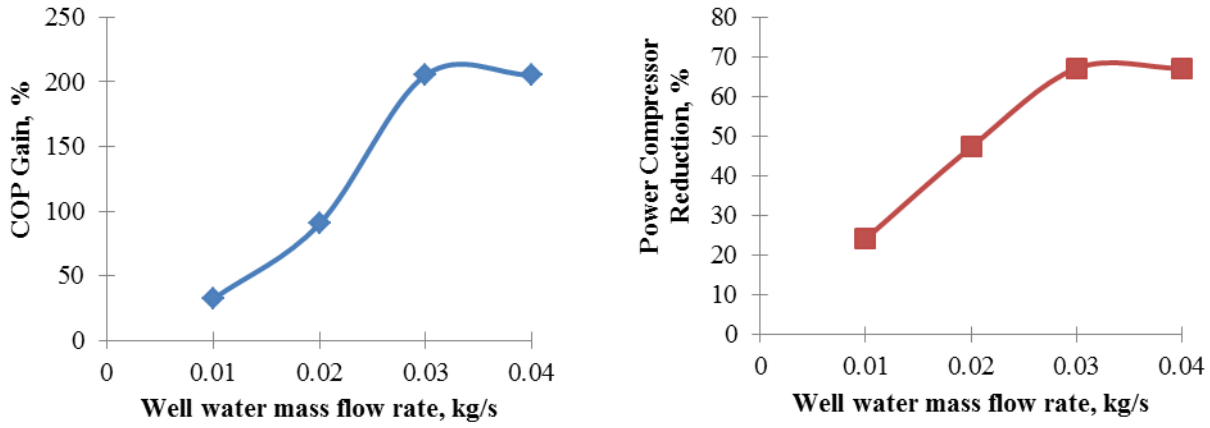

Fig. 7. Results for (a) COP gain and (b) compressor power reduction as function of the well water mass flow rate

Figure 7 shows that the COP gain and the compressor power reduction increase with the well water mass flow rate. For example, the COP gain is 32% and the compressor power reduction is 24.1% for a well water mass flow rate of 0.01 kg/s. They increase to 205.2% and 67.1% respectively for a well water mass flow rate of 0.03 kg/s.
Also, figure 7 shows that for a well water mass flow rate above 0.03 kg/s (0.04 kg/s); the gain of COP and compressor power reduction remain the same and equal to those of 0.03 kg/s. This is due to the effectiveness of the heat exchanger which is considered constant and equal to 0.8.

8 CONCLUSION

A new geothermal technique is proposed to enhance the performance of heat pump. It consists in using the well water to pre-cool the air of air conditioner, which allows to decrease the energy consumption of Air Conditioning systems by reducing the load needed to cool the air. A code is developed to simulate the energy balance and calculate the percentage of enhancement in the coefficient of performance. Results show that the coefficient of performance increases with the well water mass flow rate. For instance, the COP gain is 32% and the compressor power reduction is 24.1% for a well water mass flow rate of 0.01 kg/s. They become 205.2% and 67.1% respectively for a well water mass flow rate of 0.03 kg/s.

REFERENCES

[1] A. El Mays, R. Ammar, M. Hawa, M. Abou Akroush, F. Hachem, M. Khaled, M. Ramadan. Improving Photovoltaic Panel Using Finned Plate of Aluminum. *Energy Procedia*, Volume 119, 2017, Pages 812-817.
[2] F. Hachem, B. Abdulhay, M. Ramadan, H. El Hage, M. Gad El Rab, M. Khaled, Improving the performance of photovoltaic cells using pure and combined phase change materials – Experiments and transient energy balance. *Renewable Energy*, Volume 107, July 2017, Pages 567-575.
[3] A. Herez, M. Khaled, R. Murr, A. Haddad, H. Elhage, M. Ramadan, Using Geothermal Energy for cooling - Parametric study. *Energy Procedia*, Volume 119, 2017, Pages 783-791.
[4] H. Jaber, M. Ramadan, T. lemenand, M. Khaled. Domestic thermoelectric cogeneration system optimization analysis, energy consumption and CO_2 emissions reduction, *Applied Thermal Engineering*, Volume 130, 2018, Pages 279–295.
[5] M. Khaled, M. Ramadan, Study of the thermal behavior of multi concentric tube tank in heat recovery from chimney – Analysis and optimization, *Heat Transfer Engineering Journal*, Volume 8, Pages 1-11, 2017.
[6] M. Khaled, M. Ramadan, Heating fresh air by hot exhaust air of HVAC systems, *Case Studies in Thermal Engineering*, Volume 8, September 2016, Pages 398-402.
[7] M. Ramadan, T. Lemenand, M. Khaled, Recovering heat from hot drain water—Experimental evaluation, parametric analysis and new calculation procedure, *Energy and Buildings*, Volume 128, 15 September 2016, Pages 575-58.
[8] Mohamad Ramadan, Rabih Murr, Mahmoud Khaled, Abdul Ghani Olabi, Mixed numerical - Experimental approach to enhance the heat pump performance by drain water heat recovery, *Energy*, Volume 149, 2018, Pages 1010-1021, ISSN 0360-5442.
[9] M. Ramadan, M. Khaled, H.S. Ramadan, M. Becherif, Modeling and sizing of combined fuel cell-thermal solar system for energy generation, *International Journal of Hydrogen Energy*, Volume 41, Issue 44, 26 November 2016, Pages 19929–19935.
[10] M. Ramadan, S. Ali, H. Bazzi, M. Khaled. New hybrid system combining TEG, condenser hot air and exhaust airflow of all-air HVAC systems, *Case Studies in Thermal Engineering*, Volume 10, September 2017, Pages 154-160.

"G-C_3N4 PROMOTED DBD PLASMA ASSISTED DRY REFORMING OF METHANE

Debjyoti Rey, Devadutta Nepak, Subrahmanyam Challapalli*

Department of Chemistry, Indian Institute of Technology Hyderabad, Telangana 502 285, India; email: csubbu@iith.ac.in

ABSTRACT

The CO_2 reforming of Methane to synthesis gas was performed by non-thermal DBD plasma assisted g-C_3N_4 & g-C_3N_4 coupled with TiO_2, ZnO and TiO_2+ ZnO catalysts. The superior activity in conversion of CH_4 and CO_2 was shown by 5 wt.% TiO_2+g-C_3N_4 and 5 wt.% ZnO+g-C_3N_4 respectively. The catalytic activity of 5 wt.% MO + g-C_3N_4 in conversion of both reactants are high and performed next to their mono metal oxide counter parts. This optimum performance by 5 wt.% MO + g-C_3N_4 in activation of C─H and C─O bonds of CH_4 and CO_2 via DBD plasma assisted catalysis was achieved due to the synergistic effect relented by the electronic and acid-base properties. It deduces that the redox potential of g-C_3N_4 can be tuned by coupling with suitable metal oxides and hence a significant improvement in activation and reaction of CO_2 and CH_4 can be achieved. The g-C_3N_4 and 5 wt.% TiO_2 + g-C_3N_4 catalysts were shown poor selectivity towards H_2 and CO formation. Whereas, no pack and 5 wt.% ZnO+g-C_3N_4 obtained high H2 and CO selectivity. The selectivity towards H_2 and CO were found optimal over 5 wt.% MO + g-C_3N_4 and not declined with increase in SIE. The combination of TiO_2+ ZnO coupled with g-C_3N_4 exhibited significant effect on carbon balance. The generation of various active species was evidenced by emission spectroscopic study.

Keywords: DBD plasma, carbon nitride, reforming, methane, carbon dioxide.

1 INTRODUCTION

Time to act now on the adverse effects of climate change caused by greenhouse gases (CH_4 & CO_2), rapid exhaustion of fossil fuel, increase in global energy demands, discovery of worldwide shale gas reserves has lead much more attention towards dry reforming of methane (DRM) to control and utilize GHGs. In addition, the importance of product syngas (CO and H_2) as a primary feedstock for the gas to liquid fuel additive production processes, such as Fischer―Tropsch synthesis and methanol synthesis have been realized. Various technologies to valorise GHGs studied such as Steam reforming of methane (SRM), partial oxidation of methane (POM) and autothermal reforming (ARM) for syngas have their own drawbacks. Furthermore, the traditional thermo-catalytic DRM has been extensively investigated, however they suffer with unfavourable thermodynamic limitation ($\Delta G > 0$ at $T > 700$ °C), water gas shift reaction and rapid deactivation of catalysts due to coke formation [1,2]. Hence, nonthermal plasma technology (NTP) appears to be an alternative and interesting technology as initiation of chemical processes can takes place at room temperature by plasma generated high energy electrons (1-10 eV) and ability to produce UV-Vis light which can activate photocatalysts [3-5]. Among the NTP technique, Dielectric Barrier Discharge (DBD) plasma has been successfully applied in many applications such as ozone production [6], VOC removal [7,8], surface treatment [9,10] and reforming reactions [2]. Direct CO_2 dissociation (CO_2 splitting) was also investigated either with pure CO_2 or diluted by Ar or He [5,11].

However, alone DBD dry reforming of methane is disadvantageous due to the production of undesired hydrocarbons (C_2-C_4), lower syngas ratio, low selectivity of products, lower energy density and polymeric carbon deposition [12,13]. Therefore, the combination of a heterogeneous catalyst with plasma has been an emerging area of research in order to achieve high conversions and selectivity to the target product [14,15]. Heterogeneous catalysts such as Ni/γ-Al2O3 [16-18], Ni/Al2O3–CeO2 [19], Ni–Co/Al2O3 [20], BaTiO3 [21], M/□-Al2O3 (M = Ni, Co, Cu and Mn) [22] and La2O3/Al2O3 [23,24] assisted with plasma have been extensively studied for the reforming of methane. Where, this combination leads to synergistic effect transforms the mode of DBD micro discharge to combination of surface discharge and micro discharge [18, 25]. However, the deactivation of catalyst present in plasma zone is inevitable due to the formation of coke and sintering of active metals in metal-based catalysts. Therefore, in the search of novel, noble metal-free and stable catalyst for improved catalytic performance in discharge zone, Graphitic carbon nitride (g-C_3N_4) coupled with TiO_2 a photo-active catalyst was reported by Lu et al., [26]. Further improvements can be

attained by considering the acid-base nature and properties of metal oxide and taking into account the band gap tenability.

In the current work, the performance of g-C_3N_4 coupled with TiO_2, ZnO and TiO_2 + ZnO materials in DBD plasma assisted CO_2 reforming of CH_4 to syngas, the nature of catalysts on C─H and C─O bonds activation was investigated and reported for the first time.

2 EXPERIMENTAL

2.1. Experimental set-up:

A quartz tube reactor with outer and inner diameters of 23 and 20 mm respectively was placed horizontally. An 8 mm stainless steel rod was arranged at centre of the quartz tube acts as an inner electrode and a stainless steel wire mess of 12 cm length was wrapped around the outer walls of quartz tube act as outer electrode (Fig. 1). With that, the effective discharge volume was 29 mL with discharge gap of 6 mm was attained. The total gas flow rate was fixed to 30 mL/min accordingly the residence time was 58 s. A 400 nF capacitor was kept as a bridge in between outer electrode and ground electrode. The applied voltage was varied from 16 kV to 24 kV with constant frequency 50 Hz. The applied voltage was recorded by a high voltage probe (Agilent 34136AHV probe) connected to the inner electrode. A digital oscilloscope (Tektronix TDS2014B) was used to record the charge-voltage signals to plot Lissajous figure and to calculate the discharge power. A constant feed ratio (CH_4:CO_2 = 1:1) was sent through the reactor and the output reaction mixture was analysed by an online gas chromatography (Agilent 490 micro GC equipped with two TCD).

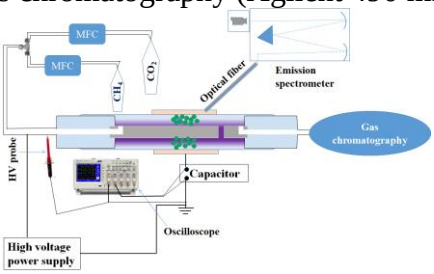

Fig. 1. Experimental set up

The conversion of reactants, selectivity of products, yield of products, specific input energy (SIE) and H_2/CO mole ratio have been calculated through the following equations.

$$CH_4\ conversion\ (\%) = \left(1 - \frac{[CH_4]_{out}\ mmol/min}{[CH_4]_{in}\ mmol/min}\right) \times 100 \quad (1)$$

$$CO_2\ conversion\ (\%) = \left(1 - \frac{[CO_2]_{out}\ mmol/min}{[CO_2]_{in}\ mmol/min}\right) \times 100 \quad (2)$$

$$H_2\ selectivity\ (\%) = \frac{H_2\ produced\ (mmol/min)}{2 \times ([CH_4]_{in} - [CH_4]_{out})(mmol/\text{min})} \times 100 \quad (3)$$

$$CO\ selectivity\ (\%) = \frac{CO\ produced\ (mmol/min) \times 100}{\{([CH_4]_{in} - [CH_4]_{out}) + ([CO_2]_{in} - [CO_2]_{out})\}(mmol/min)} \quad (4)$$

$$H_2\ yield\ (\%) = \frac{H_2\ produced\ (mmol/min)}{2 \times [CH_4]_{in}\ (mmol/min)} \times 100 \quad (5)$$

$$CO\ yield\ (\%) = \frac{CO\ produced\ (mmol/min)}{([CH_4]_{in} + [CO_2]_{in})(mmol/min)} \times 100 \quad (6)$$

$$SIE\ (J/mL) = \frac{Power\ (W)}{Total\ gas\ flow\ rate\ (mL/min)} \times 60 \quad (7)$$

$$\frac{H_2}{CO} = \frac{H_2\ produced\ (mmol/min)}{CO\ produced\ (mmol/min)} \quad (8)$$

$$B_{carbon}(\%) = \frac{([CH_4]_{out} + [CO_2]_{out} + [CO]_{out})(mmol/min)}{([CH_4]_{in} + [CO_2]_{in})(mmol/min)} \times 100 \quad (9)$$

2.2. Catalyst preparation:

Melamine powder was taken in a semi closed aluminium crucible and heated at 500^0C (4^0C/min) in tubular furnace under N_2 flow for 4 hours. Then the yellow colour powder collected after naturally cooling under N_2 flow was graphitic carbon nitride (g-C_3N_4). Then commercially available TiO_2 and ZnO were coupled

individually with g-C_3N_4 at a weight ratio of 5:95, by simple physical mixing for 30 min using a mortar piston. In addition, mixed oxide (TiO_2 + ZnO; 1:1 wt.%) coupled g-C_3N_4 at a weight ratio of 5:95 obtained was designated as MO + C_3N_4. All the powder materials were pelletized (6 mm diameter) before loading in reactor.

2.3. Characterization techniques:

The structural elucidation of the prepared catalysts was carried out using an X-ray diffractometer (X'Pert PRO PANalytical, Netherlands) with Cu Kα radiation (λ = 0.15418 nm) at a scan rate of 0.01670 s−1 from 2θ of 10^0 to 90^0. Diffuse reflectance UV-Vis spectra were acquired in the range of 200 to 800 nm using a UV-Vis spectrometer (Shimadzu, UV-2450) with $BaSO_4$ as reference standard. An emission spectrometer (Princeton Instrument Action SpectraPro®SP-2300) equipped with three gratings was used to record active species formed inside the reactor.

3 RESULTS AND DISCUSSION

3.1. Catalyst characterization

The XRD patterns of prepared catalysts shown in Fig. 2 have indicated a characteristic X-ray diffraction peak at 2θ=27.4° corresponds to (002) plane of the graphitic carbon nitride (JCPDS no.087-1526) having interplanar graphitic stacking of aromatic system [26]. The peak around 13° corresponds to the interlayer periodicity within a layer of the carbon nitride sheet. For 5% TiO_2 + g-C_3N_4 catalyst, a peak observed at 25.20 corresponds to the diffraction of (101) to anatase phase of TiO_2. In addition, other diffraction peaks at 37.9^0, 48.2^0 and 55.3^0 correspond to (103), (004) and (105) respectively were observed signify the body centred tetragonal structure of TiO_2 deposited on the surface of g-C_3N_4 [26,27]. Further, the diffraction peaks for 5% ZnO + g-C_3N_4 material were found at 2θ values of 31.8^0, 34.4^0, 36.3^0,47.5^0, 56.6^0, 62.9^0, and 67.9^0 correspond to the (100), (002), (101), (102), (110), and (112) crystalline planes, respectively confirms the hexagonal wurtzite structure of ZnO [28].

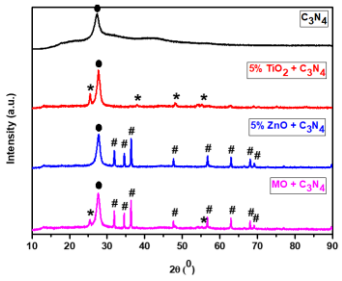

Fig. 2. XRD patterns of fresh catalysts (g-C3N4, * TiO2, # ZnO)

The electronic properties of the studied catalytic materials were obtained by optical absorption from DR UV-Vis spectral analysis (Fig. 3). Absorption in the visible region with a steep band at 450-500 nm resulted due to the band gap transition from nitrogen 2p to carbon 2p orbitals (wide band gap of 2.6 eV). As TiO_2 and ZnO are UV light active materials, their absorption edge appeared under 400 nm. The band gap for TiO_2 and ZnO coupled g-C_3N_4 materials become narrower can have advantage of exhibiting superior catalytic performance.

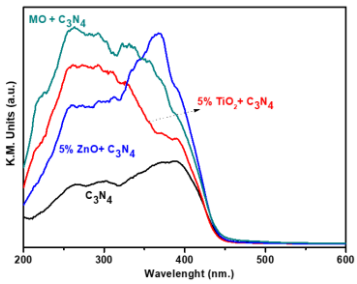

Fig. 3. DRS UV-Vis absorption for prepared catalysts.

3.2. Effect of catalyst on the conversion of reactants

Fig. 4 showed the conversion of reactants with respect to SIE change. The conversion of reactants increased with the gradual increase of SIE as the electron density increased. G-C_3N_4 showed the more conversion compared the without packing condition. The methane conversion was boosted up with the introduction of 5% TiO_2 on g-C_3N_4 whereas highest CO_2 conversion was observed over 5% ZnO + g-C_3N_4 catalyst. The reason may be the acidic site is more for TiO_2 based catalyst whereas ZnO coupled g-C_3N_4 offered more

basic site which is responsible for CO_2 adsorption and activation. It was clearly observed that 5 wt.% TiO_2 + g-C_3N_4 catalyst showed lower CO_2 conversion compared to bare g-C_3N_4. On other hand, 5 wt.% ZnO + g-C_3N_4 gave lower CH_4 conversion compared to bare g-C_3N_4. This indicates that TiO_2 is responsible for CH_4 cracking whereas CO_2 cracking was happening by ZnO loaded catalyst. So that, mixture of TiO_2 and ZnO coupled with g-C_3N_4 was prepared and employed as a catalyst for CO_2 reforming of methane. The MO coupled with g-C_3N_4 showed optimum results in the conversion of both reactants (35.5% for CH_4 and 13% for CO_2) and the satisfactory results came out due to the synergistic effects (electronic & acid-base properties) of mixed metal oxides coupled with g-C_3N_4.

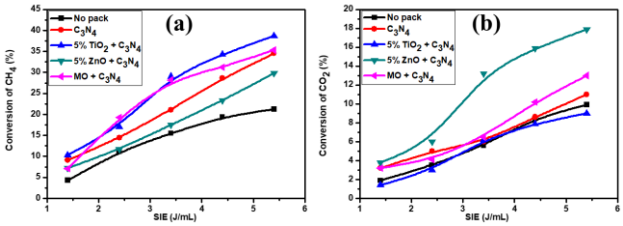

Fig. 4. Effect of catalysts on (a) conversion of CH_4 and (b) conversion of CO_2 with the variation of SIE.

3.3. Effect of catalyst on the selectivity of products

The selectivity of products with the variation of SIE has been shown in fig. 5. The selectivity of products was almost constant with the increase of SIE. The highest H_2 selectivity was observed with 5% ZnO + g-C_3N_4 whereas the best CO selectivity was observed with no packing condition. This infers that the carbon formation was low for no packed condition. Whereas, the presence of catalyst adsorbs more carbon onto its surface and they were unable to convert as CO in plasma region.

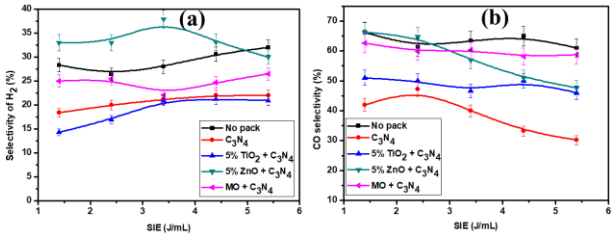

Fig. 5. Effect of catalyst on (a) selectivity of H_2 and (b) selectivity of CO with the variation of SIE.

3.4. Effect of catalyst on the yield of products

Fig. 6 showed the yield of products at highest SIE. According to this experiment, H_2 yield showed ascending order with the incorporation of different catalyst. But CO yield decreased with C_3N_4 packed condition compared to without packing may be due to the carbon formation on catalyst surface depress the CO production which is not possible in without pack condition. The CO yield was boosted up with the addition of TiO_2, ZnO with g-C_3N_4. The highest CO yield (14%) was observed with the inclusion of mixed oxide on g-C_3N_4 and maximum H_2 yield of 9.3%.

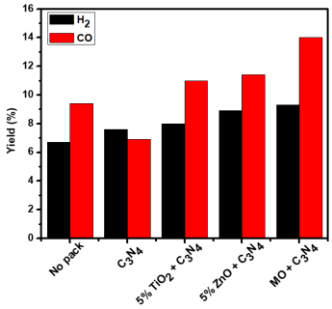

Fig. 6. Effect of catalyst on (a) yield of H_2 and CO at highest SIE 5.4 J/mL.

3.5. Effect of catalyst on syngas ration and carbon balance

The syngas (H_2/CO) ratio with the variation of SIE for different catalyst has been presented in Fig. 7(a). The syngas ratio increased with the increase of SIE for all catalyst due to the excessive production of H_2 as reported earlier [29]. The maximum H_2/CO ratio (1.1) was observed with bare g-C_3N_4 packed condition at SIE 5.4 J/mL. G-C_3N_4 packed system obtained high H_2/CO ratio compared to that of other catalyst packing system which signify that the carbon formation was more in g-C_3N_4 packed DBD reactor. This result was further supported by the evidence of lowest carbon balance (84.1%) [Fig. 7(b)]. The interesting observation was that more carbon balance was revealed by no pack DBD system in comparison with catalyst packed

DBD conditions. This can be explained by the adsorption nature of the catalyst which perhaps playing the important role to adsorb carbon particles on their surface. Where, in the case of no-catalyst/no pack DBD condition has no source (catalyst surface) to bind carbon and if carbon formed can immediately be oxidized to CO in oxygen rich circumstance.

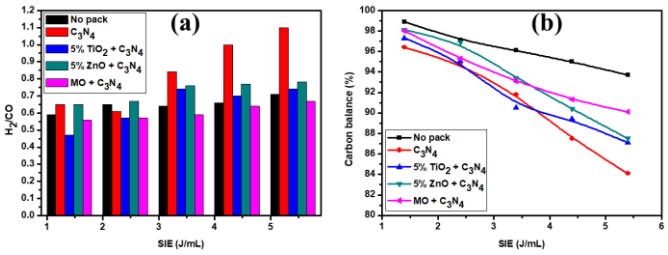

Fig. 7. Effect of catalyst on (a) syngas ratio; (b) carbon balance of dry reforming reaction.

3.6. Effect of catalyst on energy efficiency of DRM

The energy efficiency in terms of feed gas (CH_4 or CO_2) conversion has been interpreted as

$$E_{CH_4}(mmol/kJ) = \frac{([CH_4]_{in} - [CH_4]_{out})\ (mmol/\min) \times 1000}{Discharge\ power\ (W) \times 60} \quad (10)$$

$$E_{CO_2}(mmol/kJ) = \frac{([CO_2]_{in} - [CO_2]_{out})\ (mmol/\min) \times 1000}{Discharge\ power\ (W) \times 60} \quad (11)$$

The total energy efficiency of DBD dry reforming reaction with respect to conversion of both reactants (CH_4 and CO_2) has been calculated as [30]

$$E\ (mmol/kJ) = \frac{\{([CH_4]_{in} - [CH_4]_{out}) + ([CO_2]_{in} - [CO_2]_{out})\}(mmol/min) \times 1000}{Discharge\ power\ (W) \times 60} \quad (12)$$

Fig. 8 represented the energy efficiency of the conversion of reactants at highest SIE (5.4 J/mL) in separate and combined way with the variation of catalyst. The highest energy efficiency in terms of CH_4 conversion (1.5987 mmol/kJ) was observed by TiO_2 integrated catalyst whereas ZnO integrated catalyst showed the highest energy efficiency with respect to CO_2 conversion (0.7419 mmol/kJ). It is already reported that the energy efficiency does not improve always with the combination of catalysts [22]. The maximum energy efficiency of 1.973 mmol/kJ was achieved by 5 wt.% ZnO+ g-C_3N_4 packed DBD reactor.

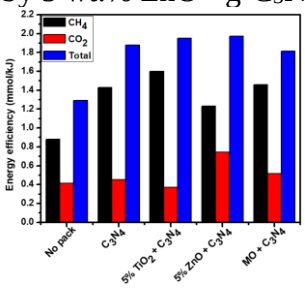

Fig. 8. Effect of catalyst on energy efficiency of the DRM (same reaction condition).

ACKNOWLEDGEMENTS

The author sincerely thanks to the MNRE, Delhi for financial support.

REFERENCES

[1] V. Pawar, Study of Short-Term Catalyst Deactivation Due to Carbon Deposition during Biogas Dry Reforming on Supported Ni Catalyst, *Energy & Fuels*, 29, 8047−8052, 2015.

[2] D. Ray, Ni-Mn/γ-Al_2O_3 assisted plasma dry reforming of methane, *Catalysis Today*, http://dx.doi.org/10.1016/j.cattod.2017.07.003, 2017.

[3] T. Nozaki, Non-thermal Plasma catalysis of methane: Principles, Energy efficiency, and applications, *Catalysis Today*, 211, 29–38, 2013.

[4] X. Tu, Plasma-catalytic Dry reforming of methane in an atmospheric dielectric barrier discharge: Understanding The synergistic effect at low temperature, *Applied Catalysis B: Environmental*, 125, 439–448, 2012.

[5] D. Ray, CO_2 decomposition in a packed DBD plasma reactor: influence of packing materials, *RSC Advances*, 6, 39492, 2016.

[6] B Eliasson, Ozone synthesis from oxygen in dielectric barrier discharges, *Journal of Physics D: Applied Physics* 20, 1421-1437, 1987.
[7] Ch. Subrahmanyam, Catalytic abatement of volatile organic compounds assisted by non-thermal plasma Part 1. A novel dielectric barrier discharge reactor containing catalytic electrode, *Applied Catalysis B: Environmental*, 65, 150–156, 2006.
[8] Ch. Subrahmanyam, Catalytic abatement of volatile organic compounds assisted by non-thermal plasma Part II. Optimized catalytic electrode and operating conditions, *Applied Catalysis B: Environmental*, 65, 157–162, 2006.
[9] S. Kameshima, Pulsed Dry methane reforming in plasma-enhanced catalytic reaction, *Catalysis Today*, 256, 67–75, 2015.
[10] A. Mizuno, Generation of non-thermal plasma combined with catalysts and their application in environmental technology, *Catalysis Today*, 211, 2–8, 2013.
[11] D. Ray, DBD Plasma Assisted CO_2 Decomposition: Influence of Diluent Gases, *Catalysts*, 7, 244, 2017.
[12] V. Goujard, Use of a non-thermal plasma for the production of synthesis gas from biogas, *Applied Catalysis A: General*, 353, 228–235, 2009.
[13] D. Ray, Glass Beads Packed DBD-Plasma Assisted Dry Reforming of Methane, *Topics in Catalysis*, 60(12-14), 869-878, 2017.
[14] W. C. Chung, Review of catalysis and plasma performance on dry reforming of CH_4 and possible synergistic effects, *Renewable and Sustainable Energy Reviews*, 62, 13–31, 2016.
[15] Istadi, Co-generation of synthesis gas and C 2 C hydrocarbons from methane and carbon dioxide in a hybrid catalytic-plasma reactor: A review, *Fuel*, 85, 577–592, 2006.
[16] F. Zhu, Plasma-catalytic reforming of CO_2 -rich biogas over Ni/γ-Al_2O_3 catalysts in a rotating gliding arc reactor, *Fuel*, 199, 430–437, 2017.
[17] D.H. Mei, CO_2 reforming with methane for syngas production using a dielectric barrier discharge plasma coupled with Ni/γ-Al_2O_3 catalysts: Process optimization through response surface methodology, *Journal of CO_2 Utilization*, 21, 314–326, 2017.
[18] Sk. Mahammadunnisa, Catalytic Nonthermal Plasma Reactor for Dry Reforming of Methane, *Energy & Fuels*, 27, 4441–4447, 2013.
[19] N. Rahemi, CO_2 Reforming of CH_4 Over CeO_2-Doped Ni/Al_2O_3 Nanocatalyst Treated by Non-Thermal Plasma, *Journal of Nanoscience and Nanotechnology*, 13, 4896–4908, 2013.
[20] N. Rahemi, Plasma Assisted Synthesis and Physicochemical Characterizations of Ni–Co/Al_2O_3 Nanocatalyst Used in Dry Reforming of Methane, *Plasma Chemistry Plasma Process*, 33, 663–680, 2013.
[21] D. Mei, Plasma-assisted conversion of CO_2 in a dielectric barrier discharge reactor: understanding the effect of packing materials, *Plasma Sources Sciences & Technology*, 24, 015011 (10pp), 2015.
[22] Y. Zeng, Plasma-catalytic dry reforming of methane over γ-Al_2O_3 supported metal catalysts, *Catalysis Today*, 256, 80–87, 2015.
[23] M.H. Pham, Activation of methane and carbon dioxide in a dielectric-barrier discharge-plasma reactor to produce hydrocarbons—Influence of La_2O_3/γ-Al_2O_3 catalyst, *Catalysis Today*, 171, 67–71, 2011.
[24] K.W. Siew, Syngas production from glycerol-dry(CO_2) reforming over La-promoted Ni/Al_2O_3 catalyst, *Renewable Energy*, 74 ,441-447, 2015.
[25] J.L. Liu, Renewable and high-concentration syngas production from oxidative reforming of simulated biogas with low energy cost in a plasma shade, *Chemical Engineering Journal*, 234, 240–246, 2013.
[26] N. Lu, Non-Thermal Plasma-Assisted Catalytic Dry Reforming of Methane and Carbon Dioxide Over G-C3N4 -Based Catalyst, *Topics in Catalysis*, 60(12-14), 855-868, 2017.
[27] P. Subramanyam, Bismuth sulfide nanocrystals and gold nanorods increase the photovoltaic response of a TiO_2/CdS based cell, *Solar Energy Materials & Solar Cells*, 159, 296–306, 2017.
[28] K. V. A. Kumar, Phenol and Cr(VI) degradation with Mn ion doped ZnO under visible light photocatalysis, *RSC Advances*, 7, 43030, 2017.
[29] X.Tu, Dry reforming of methane over a Ni/Al_2O_3 catalyst in a coaxial dielectric barrier discharge reactor, *Journal of Physics D: Applied Physics*, 44, 274007 (10pp), 2011.
[30] X. Tu, Plasma dry reforming of methane in an atmospheric pressure AC gliding arc discharge: Co-generation of syngas and carbon nanomaterials, *International Journal of Hydrogen Energy*, 39, 9658-9669, 2014.

DESIGN AND ANALYSIS OF AN ACTIVE DAYLIGHT HARVESTING SYSTEM FOR BUILDING

Xiujie Li[1], Zhuojun Yin[1], Peng Jin[1]*

1. Green Lighting System Lab, School of Environment and Energy, Peking University, E-321A, University Town，Shenzhen, P.R. China, 518055; E-mail: jinpeng@pkusz.edu.cn

ABSTRACT

A daylight harvesting system is to guide and distribute sunlight into the building where natural lighting is limited. The daylight harvesting system can effectively reduce the electrical load, and more increase visual comfort and offer numerous health benefits. In this paper, we will systematically analysis a new daylight harvesting system (DHTS) with active tracking and light concentration, where the solar tracker, concentrator mirrors and light pipe are seamlessly integrated. Through a novel four-mirror tracking system, a near collimated solar ray with x100 sun will pass through the light pipe deep into the building from sunrise to sunset. With x100 sun concentration, a 0.1m diameter light pipe will transmit an average of 10,000 lumen natural light with over 8 hours lighting time through solar tracking. Using natural light will not only reduce power consumption on lighting, but also reduce the heating, ventilation and air conditioning (HVAC) load. The low cost petal reflector's manufacturing error of and related effects on light guiding are also studied by ray tracing.

Keywords: Daylight harvesting, Non-imaging optics, Solar tracking, Petal concentrator, Energy efficiency

1 INTRODUCTION

The world economic development still largely depends on fossil fuels such as coal, petroleum and natural gas. Traditional buildings consume 40% of the total fossil fuel energy in developed countries which is significant contributors of greenhouse gases [1]. Whilst the lighting consumes up to 40% electricity in commercial and residential buildings [2].

Daylight harvesting will produce less heat for the same amount of light compared with that of artificial lighting, such as incandescent, fluorescent and solid-state lighting [3]. Zain-Ahmed et al. [4] mentioned that daylight harvesting alone can achieve minimum energy savings of 10%. Besides, daylighting has the advantages of full spectrum natural lighting and related health benefits. Galasiu, A.D. and J.A. Veitch [5] concluded that daylighting also gives better visual environment inside the building. In fact, daylighting has gradually become the major part of the green architecture design. There are many types of daylight using. Lim, Y.W [6] evidenced that light shelf with partial window blinds tilted at 45° increased daylight distribution uniformity. Vu, N.H. [7] presented a hybrid daylighting and LED system, the incident sunlight falling on a Fresnel lens area is focused onto optical fiber bundles for indoor illumination. Shao, L. [8] presented a tubular daylighting device with the polymer light rods, the maximum measured output is around 360 lm per rod. Of these systems, the light transmission distance and flux into the building envelope is limited, which is due to the low solar energy utilization, low illuminance, short lighting time, large energy loss and other issues.

In this study, we demonstrated a design of daylight harvesting system using solar tracker, concentrator mirrors and light pipe. To lower the weight and tooling cost, the solar concentrator is constructed by petal reflectors using 3D printing of carbon fiber reinforced PLA. The new DHTS system should ensure a fixed direction output to reduce the loss of energy due to the reflection, the installation positions of mirrors are at the junction between the optical path and the rotating axis, as shown in Figure 1. The light pipe passes the collimated beams collected by solar concentrator deep into the building achieving higher efficiency and uniformity.

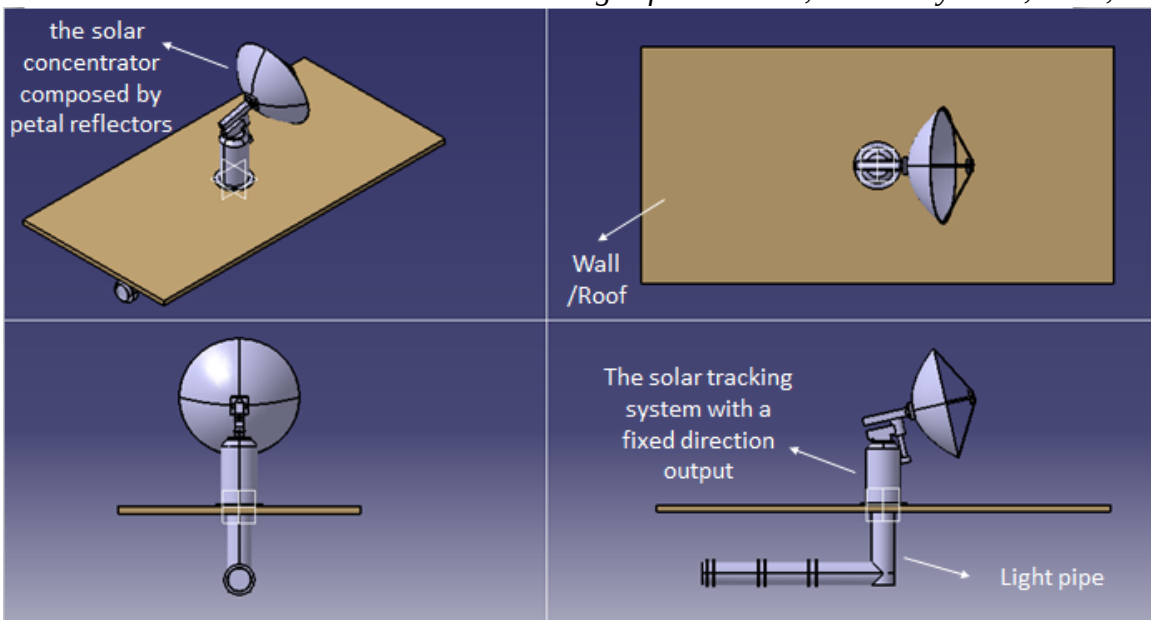

Figure 1 the DHTS system structure diagram

We will describe the three major components of DHTS system in more detail: Solar tracking system, solar concentration and light pipe system, describing the functions of these components in the system.

2 SOLAR CONCENTRATION SYSTEM

There are two basic requirements for its performance in any daylighting system. The first is to collect enough sunlight, preferably from sunrise to sunset, the second requisite is to ensure that the collected sunlight can be distributed into the building. The design of solar concentration system should be low-cost and delivering near collimated solar ray into the light pipe system. The collimation will reduce the numbers of reflection, thus reducing the light loss and improve efficiency of the overall system.

To collimating the solar ray in a solar concentration system, we choose a design of solar concentration system based on low cost petal reflector for the primary mirror and small parabolic mirror as the second collimating mirror which shares a same focal point as that of primary mirror, as shown in the figure 2. The maximal concentration ratio of the system is the square of the focal length ratio η.

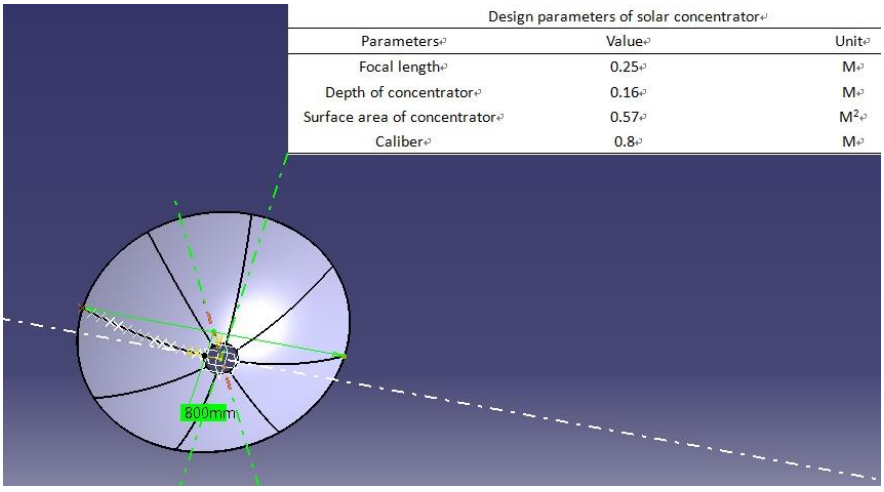

Design parameters of solar concentrator

Parameters	Value	Unit
Focal length	0.25	M
Depth of concentrator	0.16	M
Surface area of concentrator	0.57	M^2
Caliber	0.8	M

Figure 2 the primary mirror is composed of 8 petal reflectors

Table 1 comparison of various daylight harvesting systems

	Window blinds	Tubular Daylighting	Optical Fiber Lighting	Active tracking with concentrator
Solar Tracking	No	No	Yes	Yes
Daily Effective time	4 h	6 h	8 h	8 h
Installation site	Window	Roof top	Roof top /window	Roof top /window
Max. flux density	200~800 lm/m^2	2000 lm/m^2	$1x10^6$ lm/m^2	$2x10^4$ lm/m^2
Cross section area	1- 10 m^2	0.1 ~0.5 m^2	1 mm^2	0.1 ~0.5 m^2
transmission distance	~3 m	~10 m	~10 m	~ 50 m
Light Collimation	No	No	Yes	Yes
Initial Cost	Low	Medium	High	High
Installation	Easy to retrofit	Need drill hole	More flexible	Smaller hole

Table 1 compares the characteristics of various daylight system in cost and transmitted light flux, etc. The transmitted light flux, in lumen, is the combined result of flux density and cross section area of light pipe. The existing optical fiber lighting system can have tracking and up to 600 suns concentration ratio, however, due to diameter of the optical fiber is limited to 1mm, the total transmitted light flux is much smaller than that of tubular daylighting system. The tubular system in market don't have solar tracking and concentration, therefore, limited working hour to less than 6 hours. In the window blinds system, the light is scattered and can not be guided deep into the building. In our new DHTS with solar tracking, the effective time is almost from sunrise to sunset, and with 10 suns concentration ratio, the light flux density is x10 that of regular tubular system. More importantly, when the light is collimated, the number of light reflection can be reduced and the transmission distance can be increased by up to 5 folds.

The weight of the dual -mirror concentrator will not only increase the cost of the tracking but also cause the deflection on mirror itself. Therefore, the material selection and optical properties of mirrors are critical. We chose to use light weight fiber grass material to build the primary mirror, and covered it with highly reflective film. The error between the actual mirror surface and a perfect parabolic surface profile can be classified into slope error and specularity error [11], whilst the film's specularity error is 0.5mrad and reflectivity is $95\pm0.5\%$ [12]. The divergence in actual surface normal vector will have an impact on the daylighting system. We analysis the relationship between focused beams and slope error. The relationship between slope error and the concentration ratio is shown in figure 3.

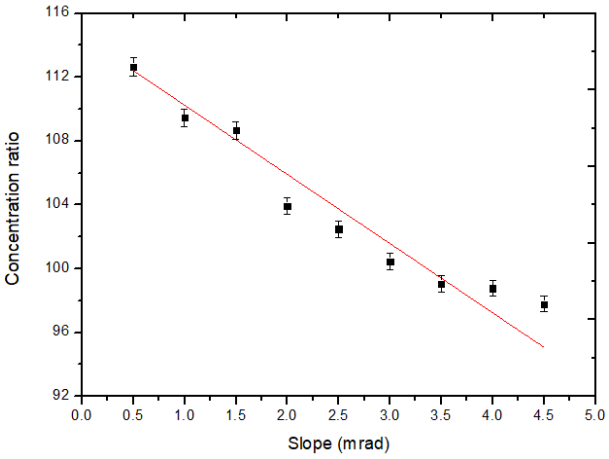

Figure 3 the relationship between slope error and the concentration ratio

3 THE TRACKING AND LIGHT PIPE SYSTEM

Compared with the optical fiber bundle, the light pipe offer larger cross section are, but cannot be flexed freely during solar tracking. To meet the requirements tracking the sun and make sure the incoming ray is always normal to the light pipe opening, a five-mirror solar tracking system with a fixed direction output is proposed, as shown in the figure 4. The two flat mirrors, M3 and M4, are at the junction between the optical path and the rotating axis, and the tilt angle of two flat mirrors should be at 45°. M3 rotates with two tracking axes (RA axis and Polar axis), M4 rotates with RA axis, and the M 5 is motionless in order to obtain a fixed direction output.

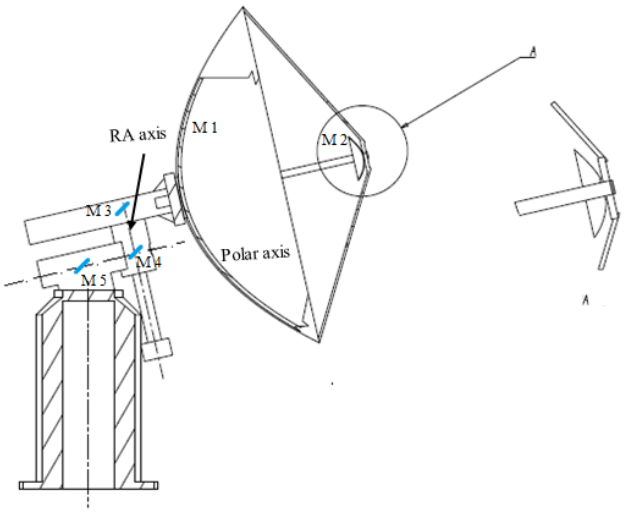

Figure 4 the solar tracking system with a fixed direction output. M1 and M2 are the parabolic mirror pair which shares the same focal point; M 3, M 4, M 5 are the flat mirrors.

The light pipe system is designed to drive most of flux collected by solar concentration system to the interior of the building achieving higher efficiency and uniformity. For this purpose, a complete simulation is proposed，all components of the DHTS system and the divergence angle of the solar light are considered. We also analyse the relationship between the spot diameter in reflectors, the total light path and the conduction efficiency.

The concentrated sun rays have multiple reflections inside the light pipe, therefore the inner light pipe materials should have high reflectivity. We will use ALANOD 4200AG，whose reflectivity reaches 98%. The length and the diameter of light pipe are set at 5m and 0.1m respectively. The complete simulation on the DHTS system with consideration of solar divergence angle of 0.0093 rad and diverging effect on light

spot size after travelling through all five mirrors and the light pipe. In the simulation, the diameter of M1 is 800 mm, diameter of M2 is 80 mm, the concentration ratio is 100, the equivalent spot diameter of flat mirror M3 is 88.8mm to flat mirror M5 is 105mm during the transmission, the total traveling distance from M2 to M5 is 540mm. If keep the light pipe diameter at 100 mm, this leading to ~ 8.6% of light falling outside the opening of light pipe.

We used the measured solar radiation level in our Peking university campus to do the simulation. As shown in figure 5, the highest solar radiation was about 914W/m^2 during noon time, while the lowest solar radiation at work hour was about 102W/m^2 at16:30 pm, the solar duration is about 10 hours in March.

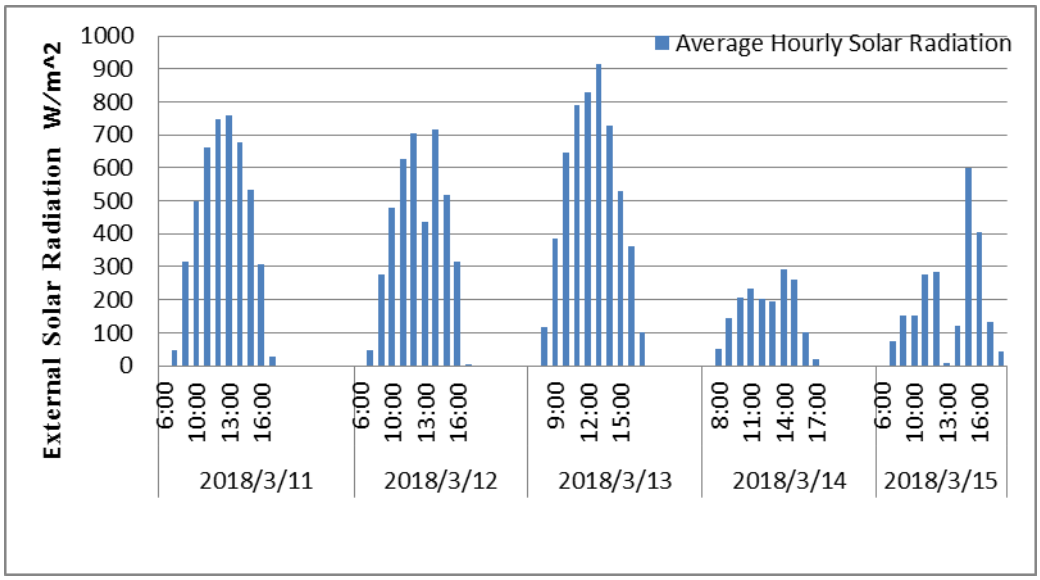

Figure 5 External solar radiations in vertical direction measured facing the sun during 11-15 March 2018 at Peking University (Lat.: 22.59255, Lon.: 113.97843)

The illuminance map is obtained through the complete simulation by using DHTS system and the solar radiation value at Shenzhen in March 11th. The room dimensions are 5m and 3m in length and height respectively. According to the simulation with DIAlux, the average illumination of the work plane is about 100lux with 41.6% light is extracted, when external solar radiation is 800 W/m^2. The illumination distribution is shown in figure 6.

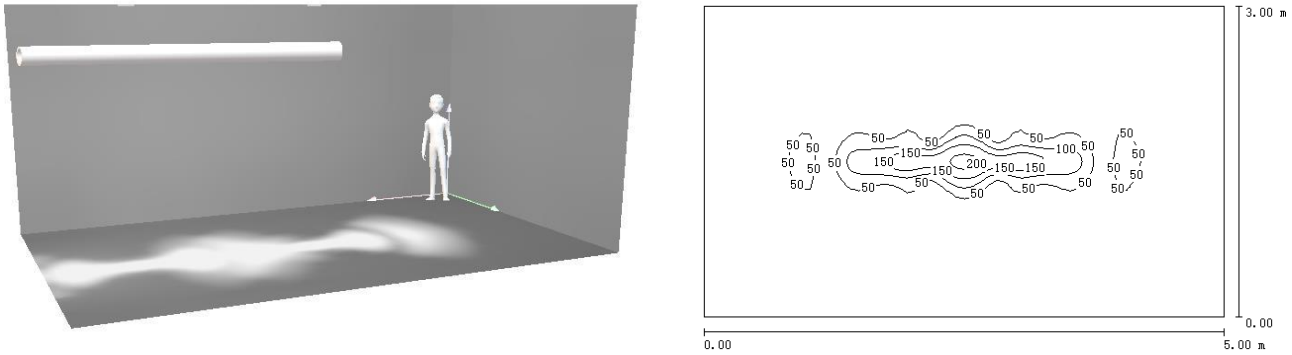

Figure 6 the illumination distribution of light pipe with solar radiation at 800W/m2 in a room.

4 CONCLUSION

A new daylight harvesting system (DHTS) with active tracking and light concentration, was successfully designed to effectively tracking, collimating and distributing sun light far into the building, reducing lighting power consumption and reducing HVAC load. More importantly, those natural sun light is can be well controlled uniformity and offer numerous health benefit. In addition, the low cost and weight pedal reflector

mirror design is analysed against slope error and concentration ratio. The field test and simulate result on DHTS are also presented to show illumination level inside the room.

ACKNOWLEDGEMENTS

This research is financially supported by Shenzhen Basic Research Fund - JCYJ20150529095551499 & JSGG 20170824094716462.

REFERENCES:

[1]. EIA (US Energy Information Administration) Office of Energy Markets and End Use. Annual Energy Review 2007..
[2]. EIA (US Energy Information Administration). Independent statistics and analysis: how much energy is consumed in U.S. residential and commercial buildings; 2017.
[3]. Robbins, C.L., Daylighting : design and analysis. 1986.
[4]. Zain-Ahmed, A., et al., Daylighting as a passive solar design strategy in tropical buildings: a case study of Malaysia. Energy Conversion & Management, 2002. 43(13): p. 1725-1736.
[5]. Galasiu, A.D. and J.A. Veitch, Occupant preferences and satisfaction with the luminous environment and control systems in daylit offices: a literature review. Energy & Buildings, 2006. 38(7): p. 728-742.
[6]. Lim, Y.W., M.Z. Kandar and M.H. Ahmad, Building façade design for daylighting quality in typical government office building. Building & Environment, 2012. 57: p. 194-204.
[7]. Vu, N.H. and S. Shin, Optical Fiber Daylighting System Combined with LED Lighting and CPV based on Stepped Thickness Waveguide for Indoor Lighting. Journal of the Optical Society of Korea, 2016. 20(4): p. 488-499.
[8]. Shao, L. and J.M. Callow, Daylighting performance of optical rods. Solar Energy, 2003. 75(6): p. 439-445.
[9]. Qian, S., G. Sostero and P.Z. Takacs, Precision calibration and systematic error reduction in the long trace profiler. Optical Engineering, 2000. 39(1): p. 304-310.
[10]. Riverosrosas, D., et al., Assessment of a polymeric reflective coating for high concentration point focus applications. Journal of Renewable & Sustainable Energy, 2012. 4(6): p. 674-683.

INVESTIGATION ON THE COUPLING OF FUEL CELL WITH SOLAR CHIMNEY AND WIND TURBINE SYSTEMS

M. Ramadan[1,2], A. Haddad[1], M. Khaled[1,3], H. Ramadan[4,5] and M. Becherif [5]

1. School of Engineering, Lebanese International University LIU, PO Box 146404 Beirut, Lebanon.
2. Associate member at FCLAB, CNRS, Univ. Bourgogne Franche-Comte, Belfort cedex, France.
3. Univ. Paris Diderot, Sorbonne Paris Cité, Interdisciplinary Energy Research Institute (PIERI), Paris, France.
4. Zagazig University, Faculty of Engineering, Electrical Power and Machines Dept., 44519, Zagazig, Egypt.
5. FEMTO-ST UMR CNRS 6174, FCLab FR CNRS 3539, UTBM, 90010 Belfort cedex, France.

ABSTRACT

With the tremendous increase of energy demand, establishing new energy strategies become unescapable not only to cover the required load but also to reduce the negative effect of energy generation. With this in mind, the two major aspects of any energy strategy are the energy source and the energy storage. That said, if the objective is to reduce the pollution's foot print of energy generation then a green-green system should be adopted. In other terms the source should be green as well as the storage system. A typical solution is to couple renewable source to fuel cell. In this frame, the present paper aims at investigating the coupling of two renewable energy systems that are wind turbine and solar chimney to Fuel cell. A case study on the region of Rayak in the west of Lebanon is performed. Results show that in the first half of the year wind turbine-fuel cell coupling provides higher power supply whereas from June till November, solar chimney-fuel cell coupling is better.

Keywords: Solar Chimney, Wind Turbine, Fuel Cell, Hybrid System, Hydrogen Energy.

1 INTRODUCTION

Renewable energy is considered the most efficient solution to reduce the negative impact of the technological development especially on the environmental level. Indeed, renewable energy systems covers wide range of natural sources of energies such as wind energy, solar energy, and geothermal energy. Having said that the main disadvantage of renewable energy sources is that they are intermittent and as a matter of fact they induce an oscillation in power supply if they are adopted alone without energy storage system. From her is born the idea of using storage systems that allow to provide a continuous power supply even when the conditions of the renewable source do not allow the required energy demand. Super capacitor, batteries, compressed air storage are among the possible energy storage solutions. However, from an environmental point of view, fuel cell is still the star of the solutions indeed it has the lower pollution foot print. That said, a green-green energy system could be constructed by coupling a renewable source to fuel cell in order to obtain a pollution free system including both the source and the storage systems. With this in mind, many works have been devoted to investigate different form of green-green energy systems. For instance, hybrid system combining photovoltaic cell and fuel cell is investigated in [1-3]. Ramadan et al [4], suggest a system combining fuel cell and solar thermal system and. The solar system is utilized to supply an electrolyser that supplies the fuel cell by hydrogen. The study, evaluates the power supply in terms of the efficiency of the solar system on a daily basis. Other studies are devoted to study the coupling between photovoltaic cell, wind turbine and fuel cell [5-9]. In the frame of this paper a hybrid system coupling solar chimney, wind turbine and fuel cell is investigated. The remaining part of this paper is composed of five sections. Section two presents the modelling of solar chimney. In section three the sizing if the wind farm is presented. Section four is devoted to present the modelling of the electrolyser. Modelling of fuel cell is discussed in section 6, then section 7 is dedicated to present the results.

2 WIND FARM SIZING AND MODELING

The wind farm (WF) is composed of a number of wind turbines (WT) arranged in an optimum way so that to produce maximum power. The WT is sized according to the maximum operational wind speed in the studied location (Rayak-Bekaa, Lebanon). Based on wind speed data, the maximum speed in Rayak-Bekaa is around $9\ m/s$. Accordingly, a WT having the characteristics presented in Table 1 is considered.

Table 1. Characteristics of the selected WT.

Rated power	100 kW
Rotor Diameter	25 m
Cut in speed	2.7 m/s
Rated speed	10 m/s
Cut out speed	25 m/s

The profile of the power curve versus wind speed for the selected WT is shown in Figure 1.

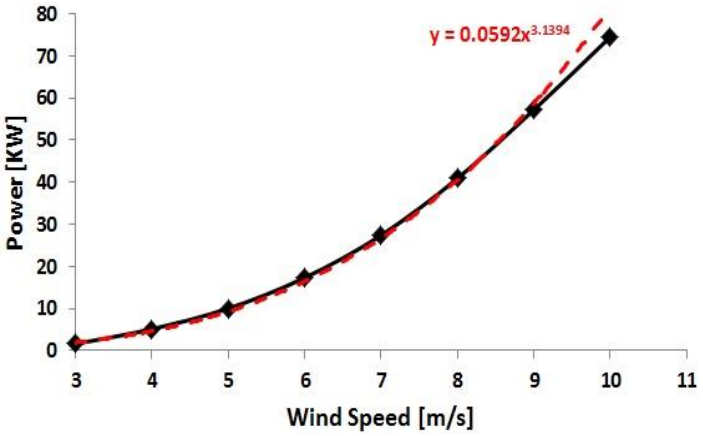

Figure 1. WT power profile versus wind speed.

Results show that for a velocity up to $9\ m/s$ the profile can be approximated, with minor error, to a power curve having the following model:

$$P_{WT} = 0.0592 \times S^{3.1394} \qquad (1)$$

Where, P_{WT} is the WT output power in kW and S is the wind speed in m/s. The model presented in equation 1 is utilized to calculate of the wind turbine power variation over the entire year. The wind farm size is determined according to the WT rotor's diameter and the available land area. Spacing between wind turbines is a critical factor that should be taken into consideration in sizing wind farms. In fact, a minimum spacing is needed to allow for wind recovery or else the wind power will be lost. In general, optimum spacing is estimated to be 3 to 5 times rotor diameter between towers and 5 to 9 times between rows as shown in Figure 2. These spacing considerations are the main factor that contributes in sizing the wind farm (number of wind turbines in each row and column) based on the available land area.

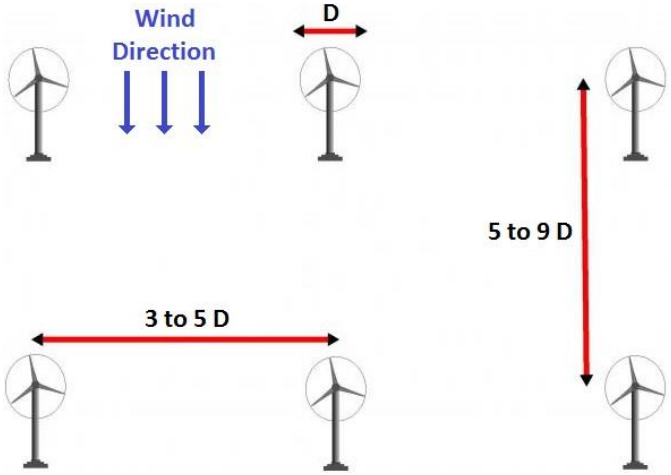

Figure 2. Optimum spacing between wind turbines.

In this work a land of $10{,}000\ m^2$ area is considered. Since the rotor's diameter is $25\ m$, the spacing between towers in a row is set to be $125\ m$ (5 D). Therefore, the maximum number of wind turbines than can fit the

available land area is 8 if we consider a $10\ m \times 1000\ m$ rectangular area. Hence, the WF will be composed of 8 wind turbines placed in one row facing the wind direction. Hence, the total wind farm power is:

$$P_{WF} = 8 \times 0.0592 \times S^{3.1394} \qquad (2)$$

3 MODELING OF SOLAR CHIMNEY SYSTEM

Solar chimney is a technique that allows to produce electricity by converting thermal energy absorbed from solar rays into kinetic energy. The principle consists in using a large solar collector to increase the amount of received power and thus the amount of received energy. On the other hand, air is used as working fluid where the absorbed energy permits to increase air temperature and as a matter of fact its density is reduced. The collector is linked to a chimney that is open at its end to the atmosphere. A pressure difference is thus produced between the lower part of the chimney that is to say the exit of the collector and the upper part forcing the heated air to flow through the chimney. The air stream is thus utilized to drive a turbine generating power. Figure 3 presents a schematic of the operational mode of solar chimney. The power obtained from solar chimney [10] is calculated in terms of the solar irradiation G, the height of the chimney H, the area of the collector A_C, the efficiency of the turbine E_T, the efficiency of the collector E_C, the specific heat of the air, C_p the air temperature T_o, and the constant g:

$$P = \frac{2}{3} E_T Ec \frac{g}{T_o C_p} H A_C G \qquad (3)$$

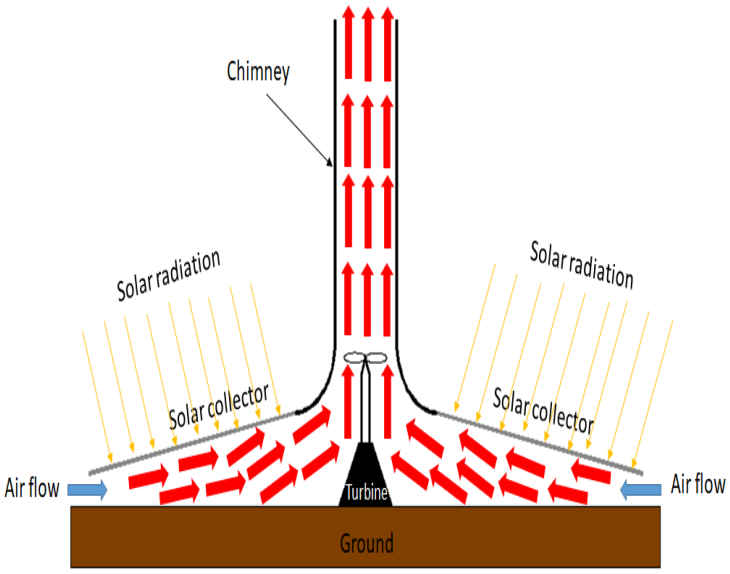

Figure 3. Schematic of the operational mode of solar chimney.

4 ELECTROLYZER MODELING

To meet the load demand at night and during periods of low insulation, energy storage is essential. Conventional battery bank concept used in small scale projects do not apply in case of large power generation. Indeed, controlling the state of charge of a big battery bank to protect it against overcharge/overdischarge is a challenging problem. Furthermore, batteries' lifetime is limited and harmfully affected with temperature increase. Moreover, they are not environmentally friendly. On the other hand, thermal storage for the solar chimney power cannot provide long period storage. For all these reasons we propose to use hydrogen production as a storage medium using an electrolyzer. The hydrogen and oxygen production rates $\dot{m}_{H_2}$ and $\dot{m}_{O_2}$ are:

$$\dot{m}_{H_2} = 2\dot{m}_{O_2} = \frac{n_{cells} \times i_E \times \eta_F}{2\,F} \times 3600 \times \frac{M_{H_2}}{\rho_{H_2}} \qquad (4)$$

Where

n_{cells} : Number of electrolyzer's cells.

F : Faraday's constant.

M_{H_2} : Molar mass of hydrogen.

ρ_{H_2} : Density of hydrogen.

η_F : Faraday's efficiency.
i_E : Electrolyzer's current.

5 FUEL CELL MODELING

Hydrogen and oxygen produced by the electrolyzer are used to feed the Fuel Cell system for power generation in absence of solar radiations or wind. The fuel cell's output current is function of hydrogen consumption rate as shown in the following equation:

$$i_{FC} = \frac{2F \times \dot{m}_{H_2}}{3600} \times \frac{\rho_{H_2}}{M_{H_2}} \quad (5)$$

The output voltage per cell is:

$$V_{cell} = E_{nernst} - V_{act} - V_{ohm} - V_{conc} \quad (6)$$

Where
E_{nernst} : Open circuit voltage.
V_{act} : Activation voltage loss given by:
V_{ohm} : Ohmic voltage loss given by:
V_{conc} : Concentration voltage loss given by:

The fuel cell's output power is:

$$P_{FC} = V_{FC} \times i_{FC} = N_{cells} \times V_{cell} \times i_{FC} \quad (7)$$

N_{cells} : Number of cells.

6 SIMULATION RESULTS

Figure 4 presents the yearly AC power variation for both coupled systems FC-WT and FC-SC based on the direct normal insulation and average wind speed data for the studied location.

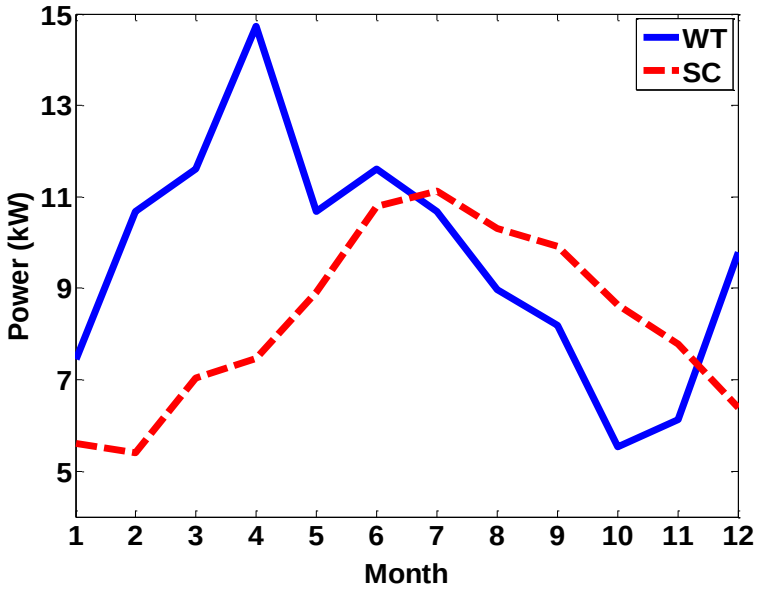

Figure 4. Yearly FC-WT and FC-SC output AC powers for 10,000 m^2.

Results show that there is no absolute advantage of one technology on the other. In fact, from mid-November to mid-June the WT power is greater than the one of SC. This latter exceeds the WT from mid-June to mid-November. Hence, the choice between the two technologies depends on the selection criterion. If the criterion is the total energy, the two systems are nearly equivalent with a negligible advantage for the WT. If the criterion is a minimum threshold power around 5 kW, the two systems are equivalent. If the criterion is to have maximum power during winter and spring periods, the advantage is for the WT. Finally, SC is recommended in summer and fall periods.

7 CONCLUSION

The paper presents, a study on the coupling of solar chimney and wind turbine to fuel cell as a *green-green* energy system. On one hand the modelling of the electrolyser and the fuel cell is developed. On the other hand, the wind turbine and the solar chimney are also modelled. The objective is to find the optimal configuration of coupling with respect to the geographic and environmental conditions. A case study on the region of Rayak in the west of Lebanon is considered. Two different coupling strategies are examined. The first one is wind turbine-fuel cell whereas the second one is solar chimney-fuel cell. Simulation aims at highlighting the potential of each configuration of coupling. It has been shown that wind turbine-fuel cell coupling is better in the first 6 months of the year whereas solar chimney-fuel cell coupling provides high power supply from June to November.

REFERENCES

[1] Samia Bensmail, Djamila Rekioua, Halim Azzi, Study of hybrid photovoltaic/fuel cell system for stand-alone applications, International Journal of Hydrogen Energy, Volume 40, Issue 39, 19 October 2015, Pages 13820-13826, ISSN 0360-3199.

[2] Ekin Özgirgin, Yılser Devrim, Ayhan Albostan, Modeling and simulation of a hybrid photovoltaic (PV) module-electrolyzer-PEM fuel cell system for micro-cogeneration applications, International Journal of Hydrogen Energy, Volume 40, Issue 44, 26 November 2015, Pages 15336-15342, ISSN0360-3199, https://doi.org/10.1016/j.ijhydene.2015.06.122.

[3] I. Tegani, A. Aboubou, M.Y. Ayad, R. Saadi, M. Becherif, M. Bahri, M. Benaouadj, O. Kraa, Experimental validation of differential flatness-based control applied to stand alone using photovoltaic/fuel cell/battery hybrid power sources, International Journal of Hydrogen Energy, Volume 42, Issue 2, 12 January 2017, Pages 1510-1517, ISSN 0360-3199, https://doi.org/10.1016/j.ijhydene.2016.06.081.

[4] M. Ramadan, M. Khaled, H.S. Ramadan, M. Becherif, Modeling and sizing of combined fuel cell-thermal solar system for energy generation, International Journal of Hydrogen Energy, Volume 41, Issue 44, 26 November 2016, Pages 19929-19935, ISSN 0360-3199, https://doi.org/10.1016/j.ijhydene.2016.08.222.

[5] Mehmed Eroglu, Erkan Dursun, Suat Sevencan, Junseok Song, Suha Yazici, Osman Kilic, A mobile renewable house using PV/wind/fuel cell hybrid power system, International Journal of Hydrogen Energy, Volume 36, Issue 13, July 2011, Pages 7985-7992.

[6] Nabil A. Ahmed, A.K. Al-Othman, M.R. AlRashidi, Development of an efficient utility interactive combined wind/photovoltaic/fuel cell power system with MPPT and DC bus voltage regulation. Electric Power Systems Research, Volume 81, Issue 5, May 2011, Pages 1096-1106.

[7] Nabil A. Ahmed, Masafumi Miyatake, A.K. Al-Othman, Power fluctuations suppression of stand-alone hybrid generation combining solar photovoltaic/wind turbine and fuel cell systems. Energy Conversion and Management, Volume 49, Issue 10, October 2008, Pages 2711-2719.

[8] D.B. Nelson, M.H. Nehrir, C. Wang, Unit sizing and cost analysis of stand-alone hybrid wind/PV/fuel cell power generation systems. Renewable Energy, Volume 31, Issue 10, August 2006, Pages 1641-1656.

[9] Thanaa F. El-Shatter, Mona N. Eskander, Mohsen T. El-Hagry, Energy flow and management of a hybrid wind/PV/fuel cell generation system. Energy Conversion and Management, Volume 47, Issues 9–10, June 2006, Pages 1264-1280.

[10] Belkhir Negrou, Noureddine Settou, Nasreddine Chennouf, Boubekeur Dokkar, Valuation and development of the solar hydrogen production, International Journal of Hydrogen Energy, Volume 36, Issue 6, 2011, Pages 4110-4116.

PERFORMANCE OF A CONSTANT SPEED SELF-EXCITED INDUCTION GENERATOR CONNECTED TO GRID

I.Z. Mohammedi[1], I. Bouray[1] and S. Mekhtoub[1]

1. Electrical Engineering Department, Ecole Nationale Polytechnique, Algiers, Algeria ; imene_zoulikha.mohammedi@g.enp.edu.dz

ABSTRACT

In this paper, the performance of a self-excited induction generator (SEIG) driven at constant speed in both stand-alone and grid-connected modes is studied. For priming purpose, a bank of capacitors with convenient value is used to provide with the required magnetizing energy. First, an equivalent R. H. Park-based diphase system is used for modelling. As the magnetic saturation represents a necessary condition for the self-excitation to occur, saturation and cross-coupling effects are both took into account in the nonlinear magnetics model. Both the generator parameters identification and the nonlinear magnetics model come to be validated through simulation and experiment. Then, the same SEIG is connected to a three-phase 220/380V, 50 Hz grid. Transient current peaks at the instant of connection show a strong dependency upon the phase shifting angle between the grid phase voltage and its associated stator voltage terminal.

Keywords: Stand-Alone, Grid-Connected, Capacitance Bank, Saturation Model, Cross Effect, Phase Shift

1 INTRODUCTION

In light of the current economic and ecological issues, the need to explore green energy alternatives has become an insistent request. Many countries around the world have recognized that challenge and have sought to improve the exploitation mechanisms and to expand their use on the largest scale.

Despite theirs old conception and remarkable reactive power consumption, squirrel cage induction generators (IGs) are still prised for their robustness, low cost and the lightweight of their rotating armature [1]. These features have allowed the SEIGs to emerge as a suitable candidate for generating electric energy from free and clean energy sources (wind [2] [3] [4] and hydro [5, 6] power plants).

For rural electrification [1] [7], or for growing energy demand problem solving [8], the SEIGs are able to operate in standalone [9] or grid-connected modes.

Maximum energy extraction and voltage regulation of SEIGs are the main objectives of study that have paid attention of many researchers. Indeed, automatic voltage regulation diagram by switching capacitor was developed in [10]. Real-time digital simulation results obtained during contingencies are presented and analysed in [8]. New fuzzy logic-based control strategy of standalone SEIG was proposed to enhance its dynamic performance [9].

By varying the amount of injected reactive power, the starting up time of SEIG was minimized and the problem of voltage regulation has been alleviated [11]. Whereas reactive power regulators have been used in [12] to minimize the maximum transient voltages and currents.

Since it is very important to make sure not to damage the fed loads and to minimize the SEIG heat losses, transient current peaks have to be limited. This work has pointed the influence of the connection-to-grid instant on the transient current amplitudes at no load. In other terms: the influence on transients of phase-shifting between the SEIG voltage outputs and the grid voltages on which the SEIG is connected, is analysed. First, the system including the SEIG and the capacitance bank is modelled by means of the d-q Park transformation. In this diphase model, saturation effect cannot be neglected, as the operating point is reached only when the SEIG magnetic and the external capacitor characteristics are crossed. Hence, the magnetizing inductance cannot be considered constant during the self-excitation process. The least squares regression method was used to approximate the experimental magnetizing curve of the machine by choosing the most convenient polynomial degree that yields an acceptable accuracy. Experiments have been carried out on a 4-kW 1500-r/min squirrel rotor IG. Wind turbine has been substituted by a DC motor to rotate the SEIG. In order to have 50 Hz (grid frequency), this last was driven at the synchronous speed. Once the SEIG started up, the device is connected to a three-phase distribution electric grid 220/380V. Simulation results show a good agreement with measurements.

The paper is organised as follows: first, the SEIG saturation modelling have been introduced in section 2. This latter has been validated by simulation and experiment in section 3.Next, Phase-shifting influence on transient current peaks when the system is connected to the electric grid, has been analysed at no load. The last section sums up the found results.

2 SEIG MODELLING

As often as not, the remaining magnetic flux in the moved SEIG squirrel rotor leads to a low electromotive force (EMF), then, given sufficient speed and for convenient capacitance values [13], the magnetizing current through the capacitance bank enables the EMF to be generated and increased up to a useful value that allows the self-excitation of the IG [14].

When the machine is saturated, cross-coupling effect: a magnetic coupling between windings of **d** and **q** axes of the diphase equivalent effect, cannot be neglected [15].

The magnetic saturation is taken into account via the variable magnetizing inductance L_m given in Equation (4) and the cross-coupling inductance L_{dq}in Equation (7).

Since the rotor is moved at the synchronous speed, the SEIG is represented in an R.H Park stator-linked reference frame in order to decrease the number of unknown variables.

The electrical equations that accounts for magnetic saturation are given by [14]:

$$\begin{bmatrix} V_{sd} \\ V_{sq} \\ 0 \\ 0 \end{bmatrix} = \begin{bmatrix} R_s & 0 & 0 & 0 \\ 0 & R_s & 0 & 0 \\ -R_r & \omega_r L_r & R_r & -\omega_r(L_m + L_r) \\ -\omega_r L_r & -R_r & \omega_r(L_m + L_r) & R_r \end{bmatrix} \begin{bmatrix} i_{sd} \\ i_{sq} \\ i_{md} \\ i_{mq} \end{bmatrix} + \begin{bmatrix} l_s & 0 & L_{md} & L_{dq} \\ 0 & l_s & L_{dq} & L_{mq} \\ -l_r & 0 & l_r + L_{md} & L_{dq} \\ 0 & -l_r & L_{dq} & l_r + L_{mq} \end{bmatrix} \begin{bmatrix} \frac{di_{sd}}{dt} \\ \frac{di_{sq}}{dt} \\ \frac{di_{md}}{dt} \\ \frac{di_{mq}}{dt} \end{bmatrix} \quad (1)$$

WhereR_s,R_r, l_s and l_r are the stator and rotor phase resistances and leakage inductances respectively, L_m is the magnetizing inductance and ω_r the rotor pulsation.

BesidesV_{sd}, i_{sd}, V_{sq} and i_{sq} are the d-q stator voltages and currents respectively, i_{md} and i_{mq} are the magnetizing currents, along the d and q axis, defined by:

$$\begin{cases} i_{md} = i_{sd} + i_{rd} \\ i_{mq} = i_{sq} + i_{rq} \end{cases} \quad (2)$$

Where i_{rd} and i_{rq} are the d-q rotor currents.

Thus, the saturation effect is taken into account by the expression of the magnetizing inductance L_m with respect to the magnetizing current i_m defined as:

$$i_m = \sqrt{{i^2}_{md} + {i^2}_{mq}} \quad (3)$$

L_m in function of i_m is expressed in Equation (4) , the experimentally collected corresponding values are mathematically approximated by the use of 12th polynomial function.

$$\begin{cases} L_m = f(|i_m|) = \sum_{j=0}^{n} a_j |i_m|^j \\ {L'}_m = \frac{dL_m}{d|i_m|} = \frac{df(|i_m|)}{d|i_m|} = \sum_{j=0}^{n} j a_j |i_m|^{j-1} \end{cases} \quad (4)$$

To simplify the writing of the equations, we put:

$$L_{md} = L_m + {L'}_m \frac{{i_{md}}^2}{|i_m|} \quad (5)$$

$$L_{mq} = L_m + {L'}_m \frac{{i_{mq}}^2}{|i_m|} \quad (6)$$

$$L_{dq} = {L'}_m \frac{i_{md} i_{mq}}{|i_m|} \quad (7)$$

Such as L_{dq} represents the cross-coupling inductance.

Where $C_e$denotes the excitation capacitance, Equation (8) describes the phase voltages across each C_e coupled in parallel to stator terminals.

$$\frac{d}{dt}\begin{bmatrix} V_{sa} \\ V_{sb} \\ V_{sc} \end{bmatrix} = \begin{bmatrix} \frac{1}{C_e} & 0 & 0 \\ 0 & \frac{1}{C_e} & 0 \\ 0 & 0 & \frac{1}{C_e} \end{bmatrix} \begin{bmatrix} i_{sa} \\ i_{sb} \\ i_{sc} \end{bmatrix} \quad (8)$$

3 STANDALONE MODE

Experimental bench and parameter identification of the self-excited induction-generator in the standalone mode is first presented. Then comparison between simulation and experiment results at no load is built up.

3.1 Experimental Bench and Parameter Identification

The test bench is made up of a squirrel induction machine (IM) mechanically coupled to a DC motor (see Figure 1). The stator windings of the IM are, in their turn, connected to a three-phase capacitance bank of 99 µF for each. Except for R_s, l_s and l'_r determination tests, the rotating armature of the SEIG is driven at a constant speed of synchronism for all the remaining tests. Based on the per-phase equivalent circuit of the IM, the main features of the considered generator are summarized in Table 1. Stator currents and voltages *.dat files have been acquisitioned using SGS2020, Figures 3-5.

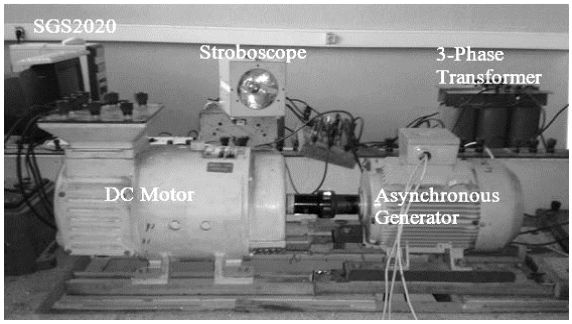

Figure 1. Experimental Bench

Table 1. The SEIG Parameters

Characteristic	Value	Parameter	Value
P_N	4 kW	Rs	0.84 Ω
U_N	220/380 V	Rr	2.25 Ω
Ω_N	1435 rpm	ls	7.20 mH
P	2	l'r	7.20 mH
f	50 Hz	M	70.14mH

As the developed saturated nonlinear model requires the magnetizing inductance function with respect to the magnetizing current. In Figure 2, both the measured and approximated magnetic characteristics of the IM are illustrated.

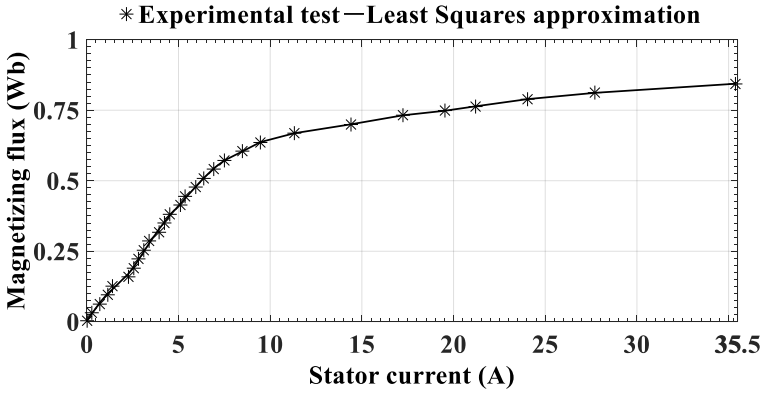

Figure 2. Magnetic characteristic of the SEIG

The self-priming phenomenon of the SEIG corresponds to the passage from the unstable equilibrium state (beginning of the phenomenon) to a stable equilibrium state (final operating point). This last, is reached by the intersection between the SEIG magnetic characteristic (Figure 2) with the capacitor external characteristic whose equation is: $V = \frac{1}{C\omega} I$

Since the SEIG under study generates the nominal synchronous frequency, the capacitor value is chosen close to the resonance with the stator self-inductance: $L_s = l_s + M$.

3.2 Experimental and simulation results comparison

Along this work, simulation calculations were performed using the MATLAB platform.

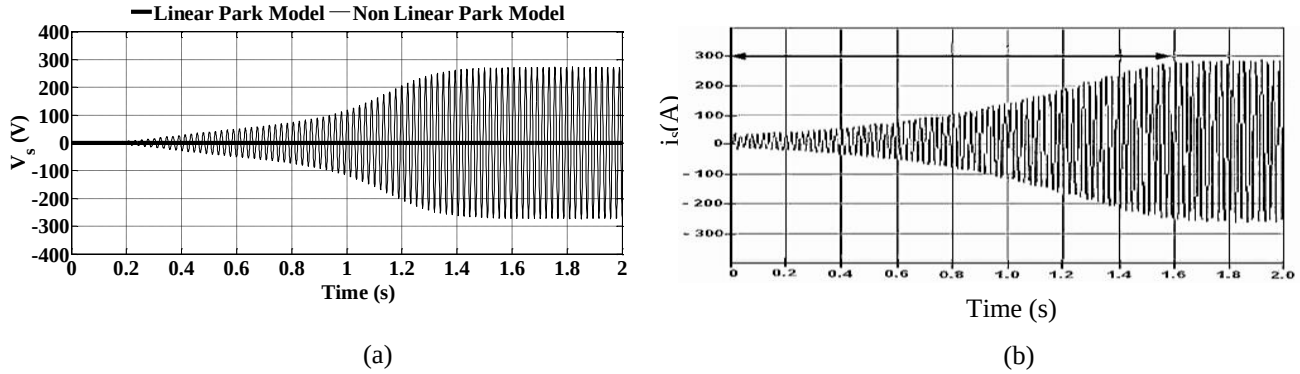

(a) (b)

Figure 3. Computed (a) and measured (b) stator voltage of the SEIG during the self-excitation process at 1500 rpm

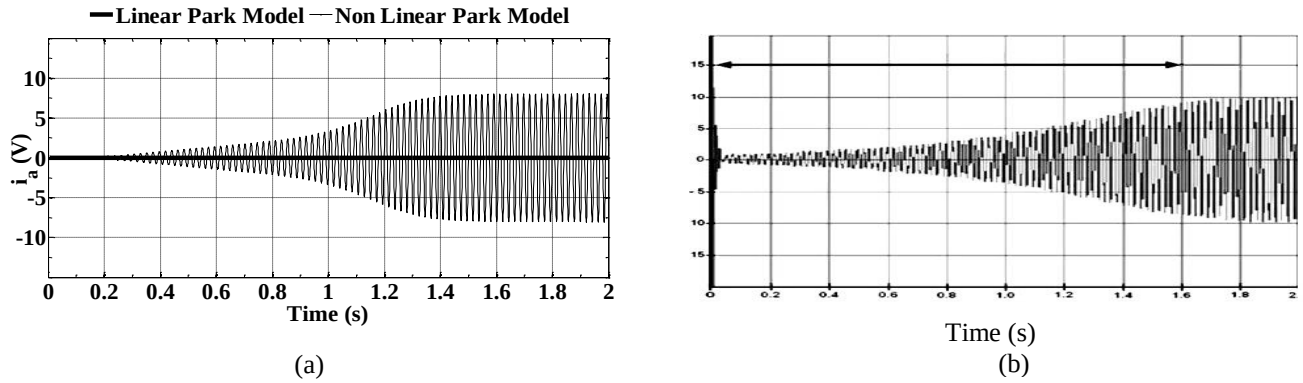

(a) (b)

Figure 4. Computed (a) and measured (b) stator current of the SEIG during the self-excitation process at 1500 rpm

Figure 3-a and 4-a depict stator phase voltage and current simulation respectively when the "linear "and the "nonlinear" Park model is used.

Based on the classical linear Park model [16], current and voltage simulation results in Figure 3-a and 4-a respectively, show the non-convenience of this model for describing the SEIG self-excitation. Indeed, according to these figures, the IG is unable to start up. Whereas, the "nonlinear" model has given good agreement with experiment. Hence, the necessity of the saturation accounting in self-excitation phenomenon. Simulation results of the SEIG at no load in Figure 3-b and Fig4-b gave: a starting-up time equal to 1.5s, phase voltage and current amplitudes of about 280V and 10A respectively. While Measurements yield 1.6s, 272V and 8A. We can notice in Figure 4-b that the stator voltage at t=0 is different of zero, this is due to the EMF generated by the remaining magnetic flux from eventual previous utilizations of the SEIG.

4 PHASE SHIFT INFLUENCE IN GRID-CONNECTION MODE

With the same capacitance bank, the SEIG is connected to a 220/380 V, 50 Hz three-phase grid. Experimental results on Figure 5 and 6 show an important difference in the transient SEIG current peak values while connected to the grid. Hence, we conclude that transient stator currents behaviour highly depends on the instant of connection, in other terms, on the phase shifting angle θ between the grid phase voltage and its associated stator voltage terminal. It should be specified that measured stator phase have been acquisitioned at random phase angle θ. That explains the disparity of transient current amplitudes in Figure 5-a and 5-b.

However, no influence of phase shifting between the formers is noticed on the stator voltage transients. Indeed, the SEIG stator voltage instantly reaches the grid voltage as it is shown in Figure (7) with a voltage amplitude equal to $\sqrt{2} * 220V \cong 311V$. In fact, the grid imposes its voltage amplitudes upon the induction generator

terminals. Figure (7) depicts the simulated stator voltage at no load when connected to the grid, this waveform remains the same whatever the value of θ is.

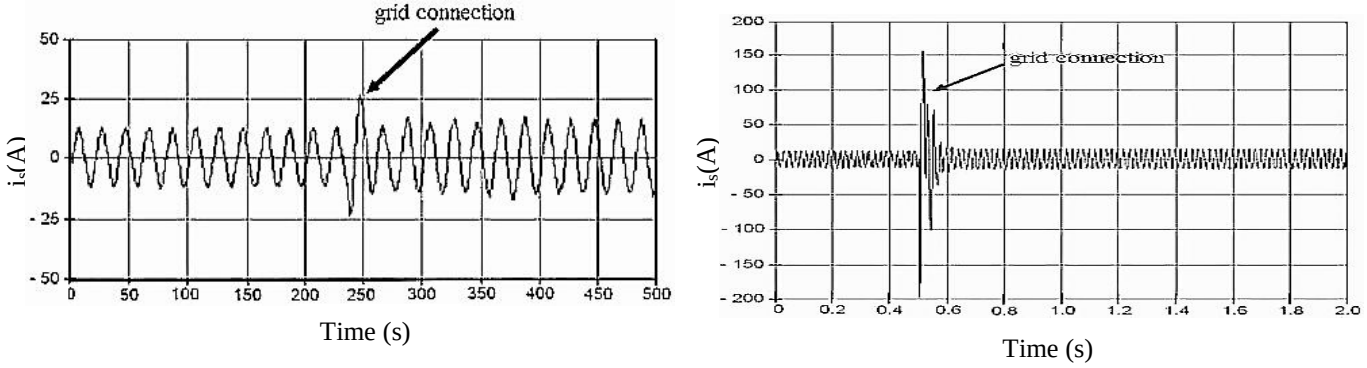

Figure 5. Measured stator phase current of the SEIG before and after grid connection process at different θ

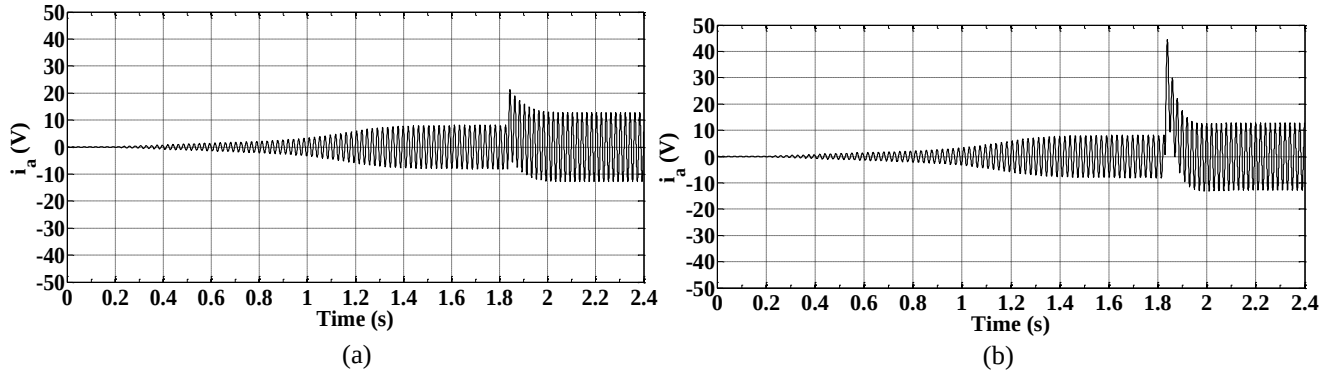

Figure 6. Computed stator voltage of the SEIG before and after grid connection process at 1500 rpm (a) $\theta = 0$ (b) $\theta = \frac{\pi}{2}$

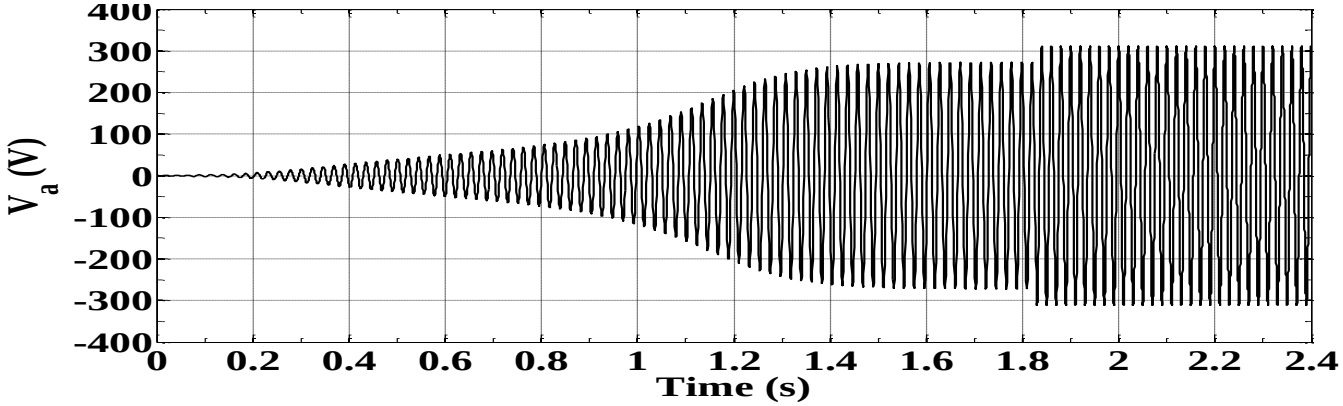

Figure 7. Computed stator voltage of the SEIG before and after grid connection process at 1500 rpm

Table 2. The Calculated Current Pic Variation according to θ

θ (rd)	0	$\frac{\pi}{4}$	$\frac{\pi}{2}$	$\frac{3\pi}{4}$	π	$\frac{5\pi}{4}$	$\frac{3\pi}{2}$	$\frac{7\pi}{4}$
Ipeak (A)	21.12	35.76	44.36	43.82	34.59	**46.08**	44.07	32.00

5 CONCLUSION

The self-excited induction generator seems to be a very interesting low cost alternative for generating electricity in isolated areas.

In order to debit voltages at industrial frequency (50 Hz), the IG rotor shaft has been driven at a constant speed that equals the synchronous rotating speed. Practically, a speed regulator should be used for this purpose.

Satisfactory accordance between simulation and experiment results is gained in standalone mode, which validates the nonlinear model for self-excitation description.
The transient current peaks strongly depend upon the phase displacement between the SEIG stator voltage terminals and theirs corresponding grid voltage phases at the grid connection instant. According to simulation results, connection-to-grid instant is optimal when both stator voltage and grid phase to which is connected are in phase.

REFERENCES

[1]H. K. Ahmed and M. Abouzeid, "Utilization of wind energy in Egypt at remote areas," Renewable Energy, vol. 23, pp. 595-604, 2001/07/01/ 2001.
[2]A. Honrubia-Escribano, F. Jiménez-Buendía, E. Gómez-Lázaro, and J. Fortmann, "Field Validation of a Standard Type 3 Wind Turbine Model for Power System Stability, According to the Requirements Imposed by IEC 61400-27-1," IEEE Transactions on Energy Conversion, vol. 33, pp. 137-145, 2018.
[3]V. Z. Silva, Â. J. J. Rezek, and R. D. L. Corrêa, "Transients analysis of synchronous and induction generators in parallel operation mode in an isolated electric system," in 2017 Brazilian Power Electronics Conference (COBEP), 2017, pp. 1-6.
[4]A. Mesbahi, M. Khafallah, A. Saad, and A. Nouaiti, "Emulator design for a small wind turbine driving a self excited induction generator," in 2017 International Conference on Electrical and Information Technologies (ICEIT), 2017, pp. 1-6.
[5]E. G. Marra and J. A. Pomilio, "Self-excited induction generator controlled by a VS-PWM bi-directional converter for rural applications," in Applied Power Electronics Conference and Exposition, 1998. APEC '98. Conference Proceedings 1998., Thirteenth Annual, 1998, pp. 116-122 vol.1.
[6]F. R. Gentile, V. H. Kurtz, L. G. Scherer, and R. F. d. Camargo, "A zero axis robust model reference adaptive controller applied to voltage regulation in standalone self-excited induction generator under unbalanced loads," in 2017 Brazilian Power Electronics Conference (COBEP), 2017, pp. 1-6.
[7]Z. Alnasir and M. Kazerani, "A small-scale standalone wind energy conversion system featuring SCIG, CSI and a novel storage integration scheme," Renewable Energy, vol. 89, pp. 360-370, 2016/04/01/ 2016.
[8]M. Ouhrouche, "Transient analysis of a grid connected wind driven induction generator using a real-time simulation platform," Renewable Energy, vol. 34, pp. 801-806, 2009/03/01/ 2009.
[9]S. A. Deraz and F. E. Abdel Kader, "A new control strategy for a stand-alone self-excited induction generator driven by a variable speed wind turbine," Renewable Energy, vol. 51, pp. 263-273, 2013/03/01/ 2013.
[10]K. Charafeddine, K. Sangov, and S. Tsyruk, "Automatic voltage regulation and stability analysis of three-phase self-excited induction generator for wind energy," in 2017 2nd International Conference on the Applications of Information Technology in Developing Renewable Energy Processes & Systems (IT-DREPS), 2017, pp. 1-6.
[11]M. Taoufik, B. Abdelhamid, and S. Lassad, "Stand-alone self-excited induction generator driven by a wind turbine," Alexandria Engineering Journal, 2017/02/01/ 2017.
[12]L. I. Mazurenko, O. V. Dzhura, and S. P. Shevchuk, "Transients in a transistor-switched capacitor regulator of a stand-alone induction generator supplying a single-phase load," in 2017 International Conference on Modern Electrical and Energy Systems (MEES), 2017, pp. 244-247.
[13]D. Samajpati, S. N. Mahato, and H. S. Chatterjee, "Selection of excitation capacitance for three phase self-excited induction generator using graph theory and differential evolution," in 2016 11th International Conference on Industrial and Information Systems (ICIIS), 2016, pp. 166-171.
[14]K. Idjdarene, D. Rekioua, T. Rekioua, and A. Tounzi, "Performance of an Isolated Induction Generator Under Unbalanced Loads," IEEE Transactions on Energy Conversion, vol. 25, pp. 303-311, 2010.
[15]H. Hofmann, S. R. Sanders, and C. Sullivan, "Stator-flux-based vector control of induction machines in magnetic saturation," in Industry Applications Conference, 1995. Thirtieth IAS Annual Meeting, IAS '95., Conference Record of the 1995 IEEE, 1995, pp. 152-158 vol.1.
[16]P. Barret, Régimes transitoires des machines tournantes électriques, Eyrolles ed., 1982.

INFLUENCE OF EQUIPMENT SIZE AND INSTALLATION HEIGHT ON ELECTRICAL ENERGY PRODUCTION IN ARCHIMEDES SCREW BASED ULTRA-LOW HEAD SHP

H. Lavrič, A. Rihar, and R. Fišer

University of Ljubljana, Faculty of Electrical Engineering, Tržaška cesta 25, 1000 Ljubljana, Slovenia, e-mail addresses: henrik.lavric@fe.uni-lj.si, andraz.rihar@fe.uni-lj.si, rastko.fiser@fe.uni-lj.si

ABSTRACT

Simulations of electrical energy production are based on archived hydrological data for a water stream with ultra-low head of 1.4 m in the area with rich precipitation. Equipment models are constructed out of the manufacturer's data taking into account conditions for safe operation of Archimedes screw water engine. Four simulation variants are performed with SHP equipment, designed for 1.4 m head and 1.5 m head. In the first iteration, equipment is positioned to obtain nominal levels and in second iteration displaced 5 cm and 10 cm higher. Simulation results show that moderate displacement from optimal installation height only slightly affects the production. When larger unit is placed on proper installation height, practically the same production can be obtained as with optimally designed bespoke equipment. Employing the equipment of the same nominal parameters on sites with somewhat different nominal heads avoids bespoke installations and can significantly decrease the costs of development and maintenance, and subsequently increase the economic viability of the SHP projects on sites with ultra-low heads.

Keywords: renewable energy, Archimedes screw, water mill, revitalization, hydrology

1 INTRODUCTION

In order to mitigate with the human activity provoked climate changes, rapid transition to RES (Renewable Energy Sources) and environment friendly technologies is mandatory. In the sphere of RES-E (-Electricity), besides the use of established hydropower and intensive development in wind power and photovoltaics, the quest for currently less favourable ways of renewable energy generation is still opened. Therefore, we are searching for ways to utilize energy of water streams with ultra-low heads on locations of abandoned mills, sawmills, and smithies. Such locations are socially acceptable due to existing buildings and already equipped with weirs. This segment became technically and economically interesting after 2000, when Archimedes screw (AS) as a turbine was introduced [1]. It ensures relatively high water-to-wire efficiency (> 70 %), despite very low heads [2], [3]. The shortcoming is in high cost of equipment, because units with large flow capabilities are needed for certain nominal power. SHPs based on AS are for now bespoke installations and this uniqueness impedes the possible ways for production cost optimization. If AS of certain size was produced in smaller series, taking into account latest discoveries for obtaining the highest efficiency [4], [5], the production costs would be lowered. However, on the other hand the question arises, whether the demand for larger number of the certain size can exist.

The idea for possible application of units of the same size on sites with moderately different heads was brought forth some time after the finish of an EU co-founded project "With revitalization of mills towards green energy" in 2012. This project ran under the leadership of three southern Slovenian communities and owners of 14 locations with mostly abandoned and some even ruined mills and sawmills, located on the border river Kolpa and its left bank tributaries had participated in it. The aim of the project was to obtain an inventory of the mills as cultural heritage, to generate a conceptual solution for SHP, acceptable from different points of view, and to prepare documents on professional and legal basis for later use when obtaining the construction permits. The quest for the appropriate technology in this project revealed that AS is preferred, since it is the most fish friendly water engine technology and SHP construction is relatively unpretentious, ensuring less adverse impacts on fauna, flora, and landscape. The available heads on these 14 locations measure from 1 m to 1.6 m and a lot of them have heads within 1.4 m to 1.6 m. One owner with valid construction permit had already been refused to be given subsidies twice, because he was not able to offer competitive price of electrical energy (EE), mostly due to high price of the bespoke equipment of the planned SHP. Speculation now exists that if cooperative of more owners with similar head is formed and all of them opt for the equipment of the same size they can negotiate for better price.

In this paper, simulations of EE production are presented for a particular site, for which the 1.4 m head and

appropriate installation height of SHP was determined by the experts. The flow that could be utilized for the SHP operation at nominal conditions equals 5 m^3/s. Besides simulations performed for optimally dimensioned and positioned 1.4 m SHP equipment, also simulations for larger 1.5 m equipment and different installation heights are presented. In the first iteration the 1.5 m equipment is positioned on installation height, where nominal head 1.5 m can actually be obtained and in the next iteration its installation height is displaced 10 cm higher. This results in symmetrical position regarding the optimal installation height of 1.4 m equipment. Finally, simulation with 1.4 m is performed, displaced 5 cm higher from optimal height.

2 HYDROLOGICAL SITUATION

The Kolpa river is a very dynamical watercourse with extremely low water in dry periods, and very large discharges during the spring and autumn rain periods, causing floods. During floods the water levels can rise up to 4 m above normal levels and the electromechanical equipment must be capable of withstanding flooding for several days. The control cabinet can be installed at higher level inside the mill. Average values for daily discharges (river flow Q_r), on which the EE production simulation is based, are for the analysed site location in Krasinec obtained from the archived average daily discharges of the closest downstream measuring station Metlika by using a multiplication factor of 0.8 [6]. The era of last 35 recorded years, namely from 1982 to 2016 was used, as 35 years is a long enough period to compensate for extreme years. River flow distribution with numbers of days inside the individual flow segment of 2.5 m^3/s is provided in Fig. 1. On the right side graph, flow duration and head duration curves for the given 35 years are shown. The 100-year flood flow values can reach up to 800 m^3/s.

The optimal parameters for SHP nominal values on particular location were defined by the experts on the basis of the river flow distribution and the acquired measurements. In this way the nominal upper and lower water levels, the installation height, as well as nominal head were determined. Nominal head amounts to 1.4 m and occurs at Q_r 14.5 m^3/s. Dependences of upper and lower water levels and available head versus the river flow were determined by on-site measurements and observations. Long time period was needed to obtain systematic conditions with almost constant or slowly changing river flow for each measurement, since determination of Q_r was performed by reading data from automatic measuring station on the remote location. Discrete points in Fig. 2 are the measured upper Δh_{up} and lower Δh_{low} water level differences from nominal levels and resulting available head H_{avail}. There are separate graphs for 1.4 m and 1.5 m head obtained by nominal levels at Q_r 14.5 m^3/s and 8 m^3/s, respectively.

The lines in Fig. 2 are gained by fitting the discrete points with 2nd order polynomial functions. These functions are for 1.4 m optimal installation, presented by (1), (2), and (3):

$$\Delta h_{up} = -0.00372 \cdot Q_r^{\,2} + 0.749547 \cdot Q_r - 9.473964, \quad (1)$$

$$\Delta h_{low} = -0.008927 \cdot Q_r^{\,2} + 2.081199 \cdot Q_r - 28.89733, \quad (2)$$

$$H_{avail} = 0.005419 \cdot Q_r^{\,2} - 1.35358 \cdot Q_r + 159.861749. \quad (3)$$

Seasonal limitations of water use due to the biotic diversity preservation are defined for river flows below 20 m^3/s for five months (from February to June). During this time of the year, fish spawn and plants experience lush growth. On basis of this limitation, no flow is available for the SHP, whenever river flow is 7 m^3/s or less. The relationship between SHP flow limitation Q_{LIM} and Q_r is presented by

$$Q_{LIM} = -0.000131 \cdot Q_r^{\,4} + 0.00961 \cdot Q_r^{\,3} - 0.261 \cdot Q_r^{\,2} + 3.35 \cdot Q_r - 13.6. \quad (4)$$

In practice, sluice gate on the intake needs to be appropriately controlled to ensure sufficient limitations. For the remaining period of time a biological minimum of 2 m^3/s is supposed to flow over the weir crown. In the

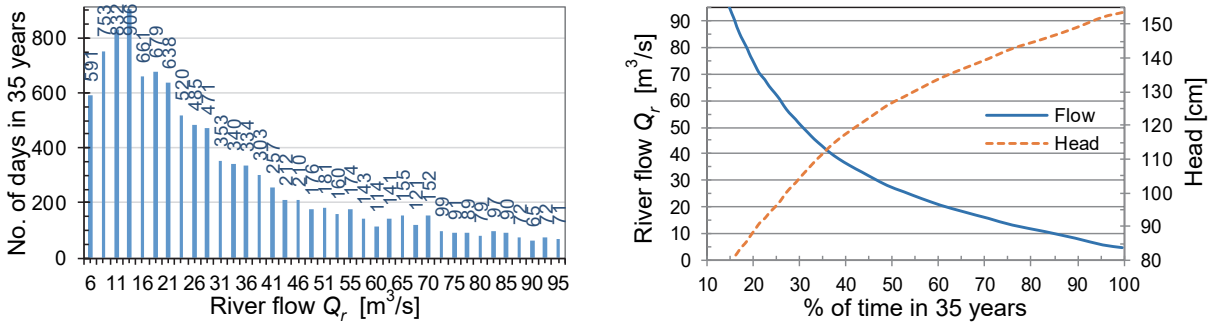

Fig. 1. River flow distribution and head duration curves of the analysed site for 35 years

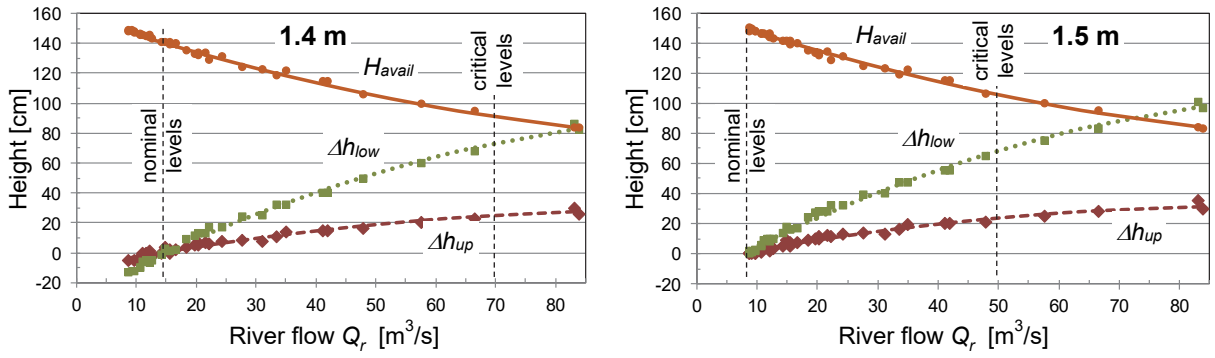

Fig. 2. Water level differences from nominal levels and resulting head for 1.4 m and 1.5 m variant

presented simulations the flow will never be this low, due to the equipment technical limitations.

3 MODELING THE CHARACTERISTICS OF EQUIPMENT

High utilizable flow requires the use of two AS and SHP is designed for two identical parallel lines. Each line consists of AS, speed multiplier, and an induction generator. This is the so-called constant or fixed speed (CS) installation, since no static power converter is implemented in neither line to obtain variable speed (VS) installation.

Characteristics for one line of SHP are given in the manufacturer's specifications. Nominal output power for one line of 1.4 m and 1.5 m equipment are 23.9 kW and 24.85 kW, respectively. Dependencies of net head, AS water flow, efficiency, and output power are all specified versus intake height. This is the difference between the upper water level and chute point (UW-CP). In order to obtain usable models, characteristics are translated into dependencies, related to the in-situ hydrological conditions. Relation between the intake water height difference and the actual upper water levels, regarding the nominal upper level (Fig. 2) is thus incorporated into AS water flow relation (5). This is polynomial function of AS water flow Q_{AS}, which depends on the upper water level Δh_{up}, whereas the latter is the function of instantaneous river flow Q_r (1).

$$Q_{AS} = 0.26951 \cdot (1.34 + \Delta h_{up}/100)^2 + 1.52529 \cdot (1.34 + \Delta h_{up}/100) - 0.06505. \quad (5)$$

Eq. (5) is made for 1.4 m equipment. Whenever in practice water flow limitations need to be obeyed the water flow through the AS can be controlled by sluice gates at the intake.

Dependence of output electrical power of one line P_{CS} versus AS flow is shown in Fig. 3. Solid line with markers is extracted from manufacturer's data, which are provided only up to nominal AS flow of 2.5 m^3/s. This nominal AS flow is obtained at nominal upper water level ($\Delta h_{up} = 0$). At higher river flows, when water levels exceed the nominal levels, more water enters the AS and theoretically the line can generate more power. Dashed lines of P_{CS} in Fig. 3 are obtained by fitting and extrapolating the manufacturer data by using 4th order polynomial function. Eq. (6) is valid for 1.4 m equipment:

$$P_{CS} = -1.2235 \cdot Q_{CS}^{\ 4} + 5.9168 \cdot Q_{CS}^{\ 3} - 5.6977 \cdot Q_{CS}^{\ 2} + 6.3346 \cdot Q_{CS} - 1.0884. \quad (6)$$

In eq. (6), Q_{CS} represents the instantaneous working water flow of AS. When there is no flow limitation, Q_{CS} is simply Q_{AS} (5) otherwise Q_{CS} needs to be determined considering the current limiting condition. However, obtaining higher output power than nominal in practice is hardly ever possible due to real hydrological conditions. At ultra-low head, the river water flow rising causes noticeable change in water levels. In the studied situation the lower water level rises more rapidly than the upper level (Fig. 2). After the nominal lower water level is surpassed ($\Delta h_{low} > 0$), the AS rotation becomes hindered, which results in lower efficiency. This effect was already studied by Lyons [7], showing that output electrical power approaches to zero, when effective head is approaching half of the nominal head. The reported dependence is implemented in the presented model. A functional relationship was thus created between the output electrical power, calculated for the given AS flow at nominal lower water level and the actual output electrical power at instantaneous water level. Using the polynomial representations of water levels (1), (2) and the available head (3) in relation to the river flow (Fig. 2), the output power ratio k was determined. The output power ratio k is for 1.4 m equipment in optimal installation height represented by

$$k = P_{1L}/P_{CS} = 1.56 \cdot 10^{-6} \cdot Q_r^{\ 3} - 2.7095 \cdot 10^{-4} \cdot Q_r^{\ 2} + 2.73293 \cdot 10^{-3} \cdot Q_r + 1.00499491; \ \Delta h_{low} > 0,$$
$$k = 1; \quad \Delta h_{low} \le 0. \quad (7)$$

Output electrical power of one line at the actual water level is denoted by P_{1L}, while P_{CS} is the calculated

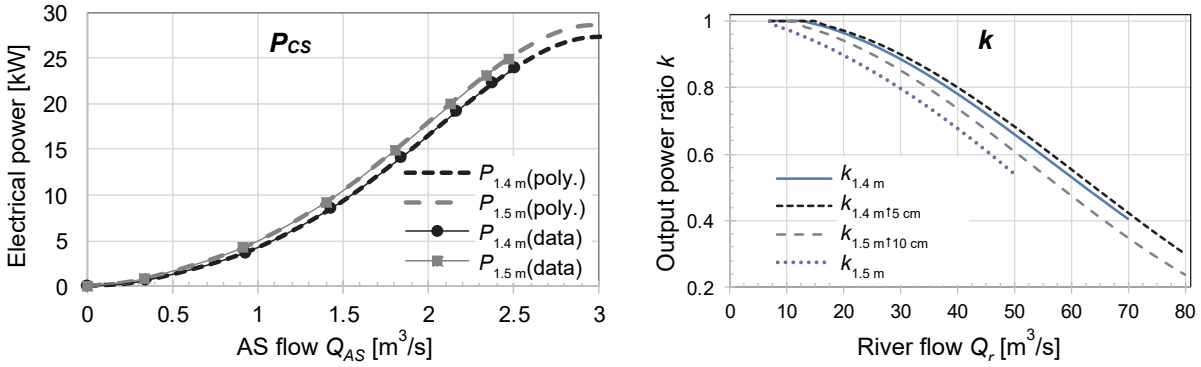

Fig. 3. Output electrical power of one line P_{CS} for 1.4 m and 1.5 m equipment (manufacturer's data and polynomial approximation) and output power ratio k for all four variants

power before attenuation (6) calculated at nominal lower water level. The output power ratio k in Fig. 3 is shown for all simulation variants. Besides 1.4 m and 1.5 m equipment at installation heights with nominal levels, k for displaced variants is also presented.

4 SIMULATION MODEL OF SHP

The aim at designing the architecture of the simulation model was to maximize the output power for the available flow, considering the limitation due to biotic diversity preservation and requirements for safe AS operation. The AS can be put into operation when minimal water flow of 1.5 m^3/s is provided and it must be stopped when the AS water flow Q_{AS} exceeds the design flow for more than 20 %. The latter condition is for different installation heights obtained at different critical river flows Q_{crit}. For 1.4 m equipment at optimal installation height Q_{crit} is 70 m^3/s. Each curve of k shown in Fig. 3 ends at Q_{crit} for the particular variant.

Since the SHP consists of two identical lines, the nominal output power P_n is twice as large as the nominal output power of one line. Regarding the availability or water flow limitations it is possible to operate with only one line or both lines in parallel, assuming that sluice gate control will ensure conformity to the limitations. Input data of the simulation model are average daily river flows Q_r (Fig. 4). In the first branch, conditions for the SHP operation are tested. If Q_r exceeds Q_{crit} the output electrical power P_{el} for the current date is zero.

In the second branch, the date is tested. From February to June, SHP flow limitation is needed for river flow below 20 m^3/s, thus further branches are provided according to the calculated Q_{LIM} value (4). When Q_{LIM} exceeds 1.5 m^3/s, the first line can be put into operation safely. Up to Q_{LIM} equal to Q_{LIM1} (2.4 m^3/s; values in parentheses are for 1.4 m equipment at optimal installation height), the working flow Q_{CS} equals Q_{LIM} and output power of one line P_{CS} is calculated (6). Since only one line is in operation, P_{CS} is assigned P_{el} for the current date. If Q_{LIM} for the current date is between Q_{LIM1} and Q_{LIM2} (3.45 m^3/s), the SHP will still operate with only one line. However, Q_{CS} for the working line in this case is not equal to Q_{LIM}, but is equal to the free intake flow Q_{AS} (5), which can enter the AS based on Δh_{up} (1). In such way, the obtained P_{el} is higher as if at Q_{LIM} above 3 m^3/s available flow would be divided into two lines. For Q_{LIM} above Q_{LIM2}, both lines are in operation and they get equal share of the available water flow. When determining P_{el} we need to apply k (7), since at higher river flows lower water level exceeds the nominal level. When Q_r exceeds 20 m^3/s, both lines are filled with Q_{AS}, because limitation does not apply.

From July to February, no flow limitation is needed and only one line is in operation for Q_r starting from Q_{min} (4.6 m^3/s) up to Q_{r1} (5.3 m^3/s). In this case free intake flow Q_{AS} is assigned to Q_{CS}. Two lines are in operation, when Q_r is between Q_{r1} and Q_{r2} (6.7 m^3/s), whereas each receives half of the flow residuum, because ecological minimum for the weir is 2 m^3/s. When Q_r is higher than Q_{r2}, each line is filled with Q_{AS} and P_{CS} is attenuated using the output power ratio k.

Output electrical power obtained at the end of each branch $P_{el}(date)$ is multiplied by 24 hours to obtain EE of the current date and summed within a particular year to obtain W_{year}. Then average annual energy $W_{AV,y}$ for the 35 years era is obtained:

$$W_{year} = \sum_{date=1.1.year}^{31.12.year} P_{el}(date) \cdot 24\ h, \qquad W_{AV,y} = \left(\sum_{year=1982}^{2016} W_{year} \right) / 35 \text{ years.} \tag{8}$$

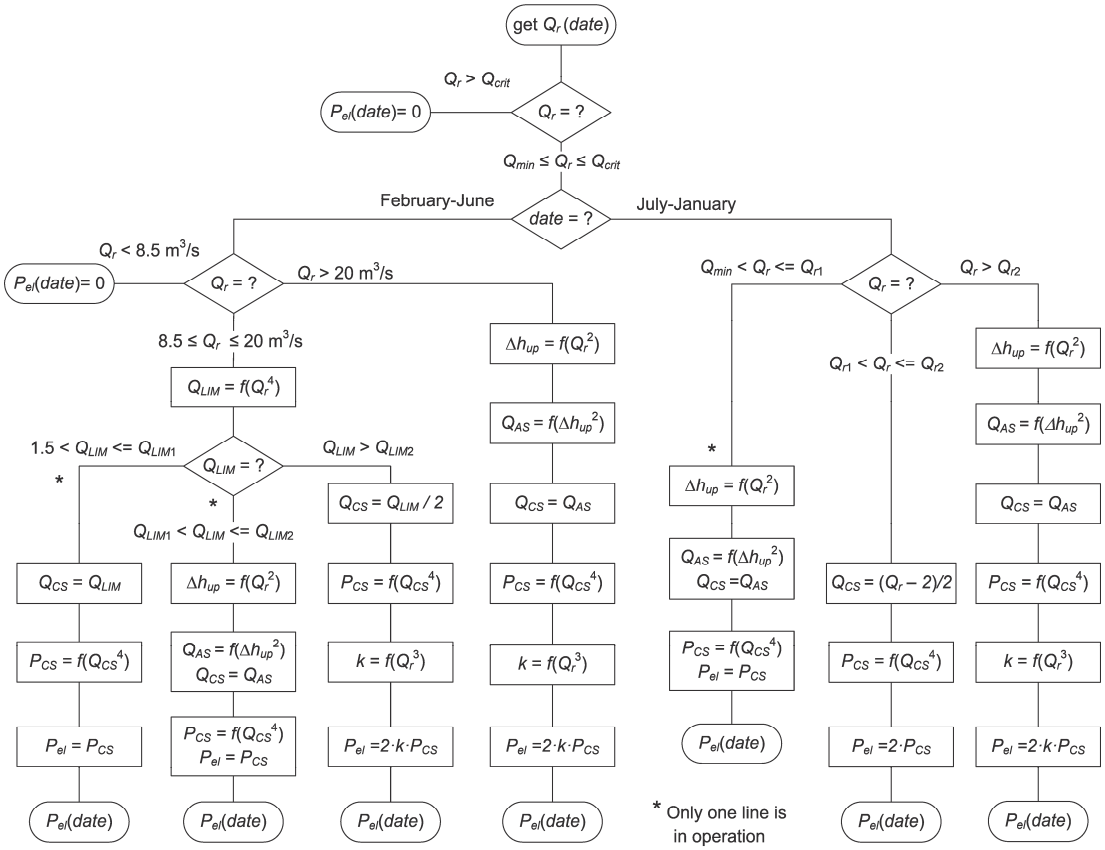

Fig. 4. Scheme of the simulation model for SHP with CS operation

5 SIMULATION RESULTS

Simulation results provide information on possible quantity of EE, which can be produced by SHP on water stream of ultra-low head taking into account real hydrological conditions, equipment technical restrictions and limitation of water flow utilization due to nature conservation.

In Fig. 5 graphs of P_{el}, Q_r, Q_{crit}, and SHP utilized flow Q_{SHP} are shown for three years. Graphs on the left are for 1.4 m and on the right for 1.5 m equipment at installation heights with nominal levels. Year 2016 is the last year in the hydrological archive and has W_{year} close to the average value of all 35 years (Table 1). Year 2011 has the highest value of W_{year}, although it was the droughtiest year, as can be seen from the average and median values of Q_r. In contrast, 2014 was the wettest year with the highest values of average and median Q_r, but it yields the smallest W_{year}. This is true for all four simulated variants, 1.4 m, 1.5 m, 1.4 m displaced 5 cm higher (1.4 m↑5 cm) and 1.5 m displaced 10 cm higher (1.5 m↑10 cm). Graphs for the latter two variants are not shown, since the results are close to 1.4 m variant. However, 1.5 m variant in the droughtiest year produces 1 % more EE and in the wettest year 17 % less EE than 1.4 m variant. The main reason is in the height of the outlet of 1.5 m equipment, which is positioned 15 cm lower regarding the outlet of 1.4 m equipment. Low water levels in drought years lead to longer time of 1.5 m equipment operation at optimal conditions. On the other hand in water rich years the flooding of the lower end is more intensive and also because of lower Q_{crit} the 1.5 m equipment has longer and more frequent standstill intervals.

Table 1. EE production, median and average river flow in characteristic years and total energy production in 35 years for all four simulated variants

	Q_r,median m^3/s	Q_r,average m^3/s	EE 1.4 m MWh	EE 1.4 m↑5 cm MWh	EE 1.5 m MWh	EE 1.5 m↑10 cm MWh
2016 (latest)	29.00	65.10	283.46	276.21	265.52	280.44
2011 (dry)	17.97	28.78	340.81	328.00	344.08	338.64
2014 (wet)	49.63	84.94	221.61	224.44	185.41	221.72
35 years aver.	28.97	54.25	275.93	272.95	258.39	276.45
W_{Total} (35 years)	-	-	**9657.52**	9553.38	9043.66	9677.14
% of EE CS	-	-	**100**	98.92	93.64	100.20

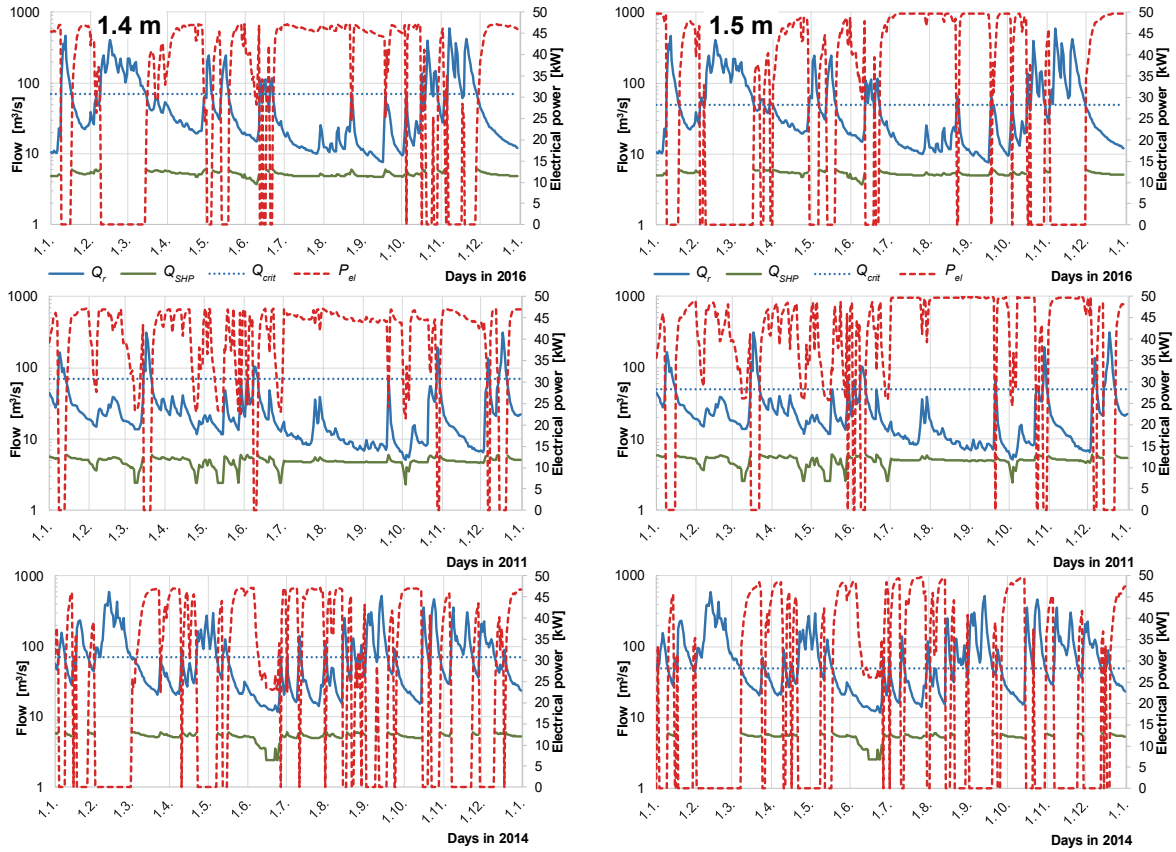

Fig. 5. SHP output electrical power, river flow and utilized flow for the year 2016, the droughtiest year 2011 and the wettest year 2014 for 1.4 m (left side) and for 1.5 m equipment (right side) at installation heights with nominal levels

6 CONCLUSION

Comparison of calculated EE for four variants reveals actual influence of the equipment size and its installation height on possible production. The sensitivity of EE production on installation height is not as strong as it would be expected dealing with the ultra-low head SHP. Displacement of the installation height for 3.5 % regarding the size of 1.4 m equipment at optimal installation height reduces total EE for only 1 %. If larger equipment is used at proper installation height practically the same value of EE is obtained. On the basis of simulation results it can be concluded that our speculation has realistic base and SHP equipment of the same size can be efficiently employed on sites with moderately different heads. With further simulations we will try to verify whether optimal installation height proposed by the experts actually provides the highest production.

REFERENCES

[1] Lashofer A, Kaltenberger F, Pelikan B. Wie gut bewährt sich die Wasserkraftschnecke in der Praxis?, Wasserwirtschaft 2011;7-8:2-7. https://doi.org/10.1007/978-3-658-00996-0_40.

[2] Williamson SJ, Stark BH, Booker JD. Low head pico hydro turbine selection using a multi-criteria analysis, Renew Energy 2014;61:43–50. https://doi.org/10.1016/j.renene.2012.06.020.

[3] Ak M, Kentel E, Kucukali S. A fuzzy logic tool to evaluate low-head hydropower technologies at the outlet of wastewater treatment plants, Renew Sustain Energy Rev 2017;68:727-737. https://doi.org/10.1016/j.rser.2016.10.010.

[4] Waters S, Aggidis GA. Over 2000 years in review: Revival of the Archimedes Screw from Pump to Turbine, Renew Sustain Energy Rev 2015;51:497-505. https://doi.org/10.1016/j.rser.2015.06.028.

[5] Kozyn A, Lubitz WD. A power loss model for Archimedes screw generators, Renew Energy 2017;108:260-273. https://doi.org/10.1016/j.renene.2017.02.062.

[6] http://vode.arso.gov.si/hidarhiv/pov_arhiv_tab.php?p_vodotok=Kolpa. Accessed 30.3.2018.

[7] Lyons M., Lab Testing and Modeling of Archimedes Screw Turbines, Master Thesis, University of Guelph, Ontario, 2014.

HYBRID RENEWABLE SYSTEM MANAGEMENT: CLUSTERING CORRELATIONS TO IMPROVE THE PERFORMANCES OFA MODEL PREDICTIVE CONTROL STRATEGY

L.Bartolucci[1], S.Cordiner[1], V.Mulone[1]

1. Department of Industrial Engineering, University of Rome Tor Vergata, Rome, IT; email: lorenzo.bartolucci@uniroma2.it

ABSTRACT

The advent of distributed renewable energy supply sources and storage systems has placed a great focus on the operations of the LV (low voltage) electricity distribution network. However, LV networks are characterized by much higher variability in time series demand meaning that matching production and demand profiles is a challenging goal. Energy Management System (EMS) based on Model Predictive Control (MPC) strategies have been proved to improve the matching of profiles thus enhancing the RES exploitation. However, the performance of the EMS depends on the capability of reliably forecasting the day ahead profiles. In order to improve those predictions, a novel approach based on a correlation clustering strategy has been implemented into a MPC - EMS in order to correct the forecasts thus improving the performance and the reliability of the EMS control actions. The new approach has been compared against the ideal conditions of perfect forecasting and the baseline of the uncorrected forecast in order to show the improvement due to the novel approach proposed. Results showed an improvement of the RES self-consumption and a better utilization of the Energy Storage System (ESS).

Keywords: Hybrid Renewable Energy System; Model Predictive Control; Energy Management System;

1 INTRODUCTION

The European goal to reduce greenhouse gas emissions by 80–95% by 2050 implies the development of the current energy system. Different actions have to be pursued, toward greater efficiency and lesser CO_2 emissions. This target may be achieved with a steep increase of power production from renewable sources (RES) [1]. This requires actions at every level of power chain from production to final user, through the distribution system. Storage systems have a pivotal importance, as well as a more efficient interaction between decentralized and centralized systems to maximize the exploitation of RES while operating efficiently large-scale powerplants.

In such a scenario the introduction of Hybrid Renewable Energy System (HRES) can effectively improve the interaction between local and centralized production. Several works have proved the capability of HRES to supply stand-alone distributed generation systems in remote areas [2-5]. However, the key aspect of a microgrid within the HRES concept for maximizing the exploitation is the implementation of a two-way communication between the grid operator and customers, as demonstrated by different studies [6-8].

Results obtained with optimization strategies of HRES are promising [9-12], in particular wih the use of Model Predictive Control (MPC) based approached. Bartolucci et al. in [13-14] showed the potential of MPC control strategy to improve the integration of the residential microgrid with the renewable sources available locally. This is due to smoothing out the energy demand profile and absorbing the peak of production from the photovoltaic and wind powerplants, in cases of high RES penetration. It was also shown how high RES penetration can be with Demand Side Management (DSM), taking advantage of predictive control logics. In fact, DSM with a storage system improves the stability reducing fluctuations both ways (network-wise and user-wise). The work highlighted also the role of weather and load forecast, whose availability and accuracy is crucial for an optimal deployment of MPC-based control strategies.

The study here proposed aims at extending the MPC strategy proposed in [13] in order to improve the effectiveness of both weather and load forecast. A clustering analysis approach is proposed: based on historical data, different clusters of load profiles and weather conditions have been defined; during run time operation, the actual profiles were associated with a specific class with a Neural Network approach. The forecast was updated with the specific class recognized and used for the minimization of the objective function within a Mixed Integer Linear Programming (MILP) framework. Results show how the extended model was able to improve the performances in terms of minimization of unbalances in energy exchanged with the grid and operating costs. Different scenarios have been tested to prove the capability of the proposed approach, dealing with different degrees of forecast, weather conditions, and load characteristics.

2 DESCRIPTION OF HRES

In this section a brief description of HRES is given [Figure 1 (left)]. The core of the system is the Micro Grid Central Controller (MGCC), calculating energy fluxes splitting rules based on information coming from the Residential Micro Grid, the Database and the Grid subsystems. In the MGCC the control strategy is implemented together with tools for profile/pattern management.

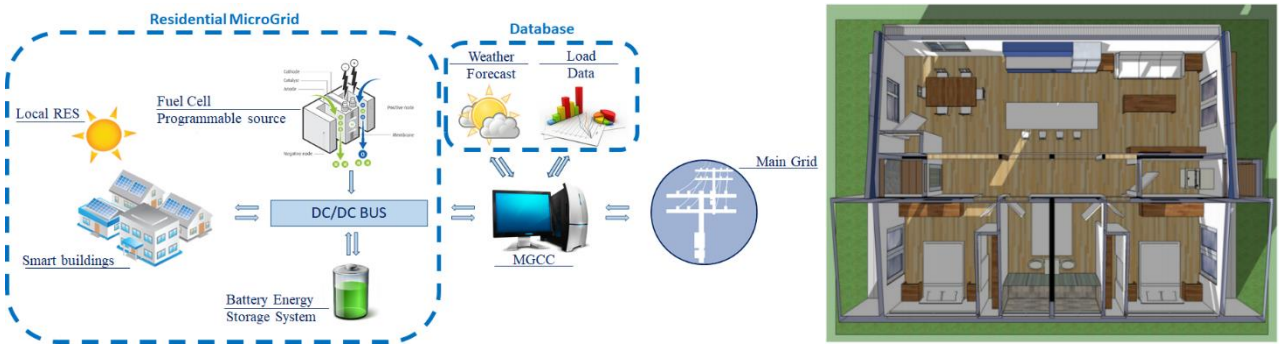

Figure 1 - Scheme of the Hybrid Renewable Energy System (left) - Sketch of the simulated apartment (right)

The Residential MicroGrid studied as application includes smart buildings featuring smart metering sensors and renewable source power supply systems (PV panels with a peak power of 5130 Wp per apartment). The smart buildings are connected via a DC/DC bus with the local programmable source, a fuel cell with a maximum power of 2400 W per apartment, and with a Battery Energy Storage System (BESS) with a total storage capacity of 280Ah@48V per apartment. 8 apartments have been considered for this study.

Special care has been given to the representation of the residential load, extending the stochastic model presented in [15] to describe the thermal load required by the house with dynamic effects. To that aim a model has been implemented linking dynamically Energy+ [16] and Matlab/Simulink codes. A sketch of the house considered is reported in Figure 1 (right). A period of 2 years has been studied, with real weather data collected at the weather station of the University of Rome Tor Vergata to generate a robust database for the residential load.

3 NUMERICAL APPROACH AND TEST CASES

Details on the implementation of the MPC for microgrid control has been treated extensively in [13], and thus in this section only a brief overview of the main concept is given with greater focus on the clustering analysis considered to improve the effectiveness of actions taken based on weather forecast. In general, MPC strategies are based on optimization procedures defining control commands to minimize – or maximize – objective functions defined with a model, representing the behavior of the system.

The controller evaluates a set of optimal control variables for a period of time from t (current state) and t+CP (where CP is the control period), based on the initial state and on an estimation of the external disturbance parameters (in this paper weather and load forecasts). These control actions are used to evaluate the evolution of the system at the time k+1 that is used as input for the forthcoming optimization process.

The effectiveness of the optimization process is highly dependent on the definition of the constraints and of the objective function. The first ones are needed in order to ensure the physical and technical feasibility of the optimal solution found. For example, constraints on the maximum power exchanged with the main grid or the maximum power obtainable from the local power generator have been implemented. A detailed description of the constraints implemented and the objective function used for the optimization process is presented in [13].

3.1 Forecast clustering analysis

In order to improve the accuracy of the load forecast a methodology based on the correlation clustering analysis has been implemented in the code. First of all, the load generated for the first year has been divided into sub-groups based on the actual power required at the beginning of the day which is mainly function of the ambient temperature. Then, for each sub-group, a correlation analysis has been performed looking at 9

specific parameters, namely for each daily time zone (3 zones *F1, F2, F3*) the value of the demand peak power (PP_{Fi}), the time at which the peak power occurs (hPP_{Fi}) and the overall energy consumed during the time zone (E_{Fi}). Correlation is calculated by the Pearson's correlation equation (1). The output of the equation will range from 0 to 1. A value of 1 describes a perfect correlation, while a value of 0 no correlation.

$$\rho(X,Y) = \frac{1}{n-1}\frac{\sum((x-u_x)(y-u_y)}{\sigma_x\sigma_y} \quad (1)$$

where ρ is the correlation coefficient, X, Y are vectors, n is the number of elements in each vector, x is an element within vector X, y is an element in vector Y, u_x is the mean of X, u_y is the mean of Y, σ_x is the standard deviation of X and σ_y is the standard deviation of Y. In order to assign the elements of the sub-group to a specific cluster, an iterative procedure has been performed. For each loop a different threshold value for the correlation has been used to complete the cluster, starting from a value of 0.98 below to a value of 0.95, which allowed for assigning all the elements to the generated clusters. Variable number of clusters and different number of elements per each cluster have been obtained by the analysis. Based on the elements of each cluster the mean representative profile has been calculated as average of each specific profile.

Once the clusters have been created, a Neural Network has been trained in order to recognize during run time operation the corresponding cluster. The output forecast used in the controller has been then evaluated as a weighted average between the demand forecast and the cluster mean profile. For this study a weight factor of 0.5 has been chosen.

In order to solve the MPC strategy with a sampling time of 15 minutes in a rolling horizon mode and an overall control period of 24 hours, a Mixed Integer Linear Programming (MILP) algorithm has been implemented into Matlab/Simulink along with the clustering analysis code.

3.2 Simulation specifications

Different simulations have been performed in order to analyze the performance of the model under different operating conditions and different scenarios. Extended MPC strategies have been tested for same HRES by varying forecasting accuracy. In particular, a reference scenario (IDEAL) has been considered for perfect weather and load forecast. With respect to this baseline reference, two different cases have been tested, and namely OLD MPC and NEW MPC models. The last two case differ only for the prediction stage of the control process. The system has been tested for two weeks in the 2015, the third week of January and June, representative of typical winter and summer weeks in Rome.

4 DISCUSSION OF RESULTS

Figure 2 shows the capability of the proposed model to improve the load forecast for a simulated summer week. In particular, the forecasted hourly profile with and without the correction based on the correlation clustering analysis have been reported respectively in blue and red and compared against the actual profile obtained during runtime. Looking at the details for a selected day an improvement in capturing the actual power demand profile, even though some discrepancies are still occurring. Integrating though the differences between the actual and the predicted profiles, the improvement is even more evident, with an overall corrected forecasted value less than the half of the corresponding forecasted without correction one.

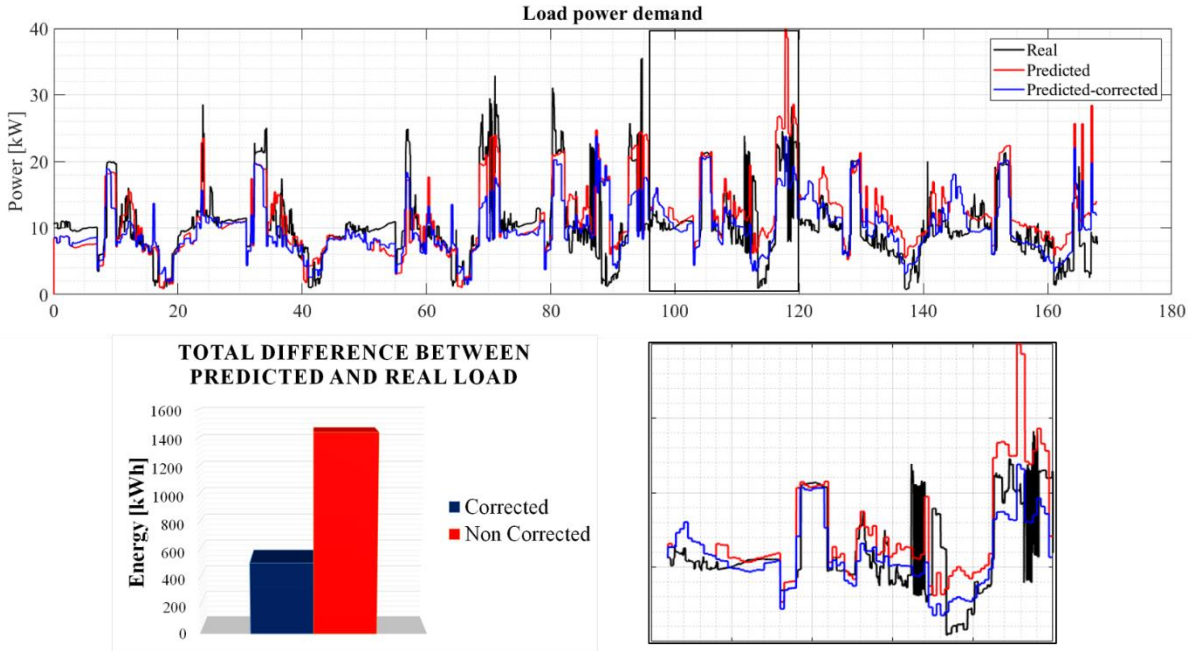

Figure 2 - Differences between Load predicted, Load predicted corrected and Load real during the simulated week of July (top) with details of the fourth day (bottom-right) and overall energy mismatch with respect to the real case (bottom - left).

Based on the improvement obtained in the forecasting of the load profile the analysis of the HRES system has been performed for two different weeks of January and July. It is worth noting that the selected to test the system under severe weather conditions. In fact, the differences between actual and forecasted weather (in particular the sun availability) were significant and adverse (Figure 3). More specifically, for the winter week high availability of RES was forecasted while not verified during the real time operation, and for the summer case the opposite situation occurred. Both situations are adverse with respect to the capability of the system to absorb RES fluctuation, in fact during the winter the ESS SoC is on average at low level and therefore capable of absorbing unpredicted greater availability, while not able to manage effectively unpredicted reductions. Opposite situations occur for the summer case.

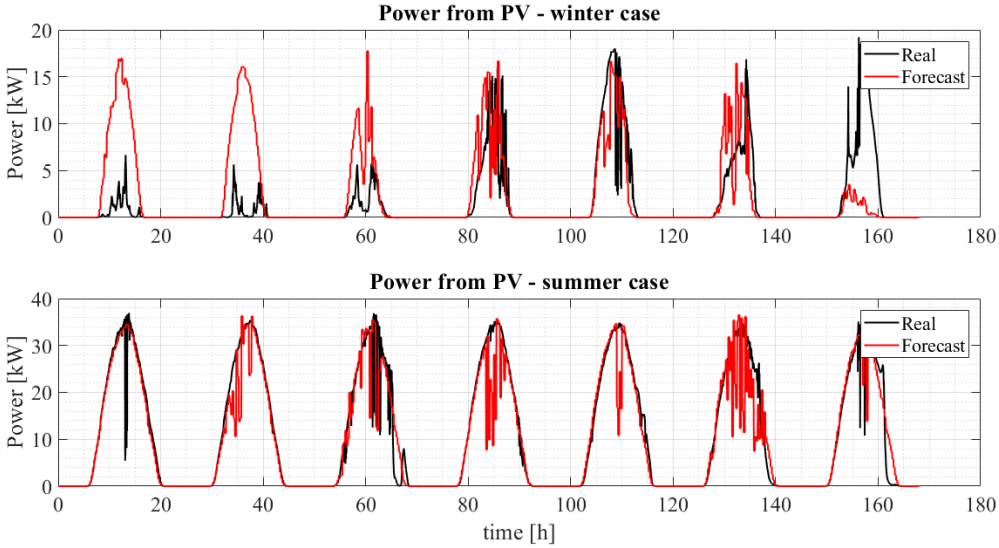

Figure 3 - Differences between actual and forecast PV production for the winter (top) and summer (bottom) cases

Although the challenging operating conditions, the improvement of the HRES systems in following the grid reference profile is evident. Figure 4 (top) shows the magnitude of the unbalance power profiles for the three simulated cases with details for the third day (bottom-right) for the summer case, confirming that accurate load forecasting can improve the capability of the HRES to attend a predefined load profile even under heavy RES availability variations. In fact, the unbalances were significantly lower for the IDEAL case and smoothed for the NEW MODEL with respect to the OLD one. This is confirmed also looking at the integrated unbalance

energy over the week (Figure 4 – bottom-left) were a reduction of about 15kWh has been achieved due to the improved load forecast obtained with the NEW MODEL with respect to the OLD prediction.

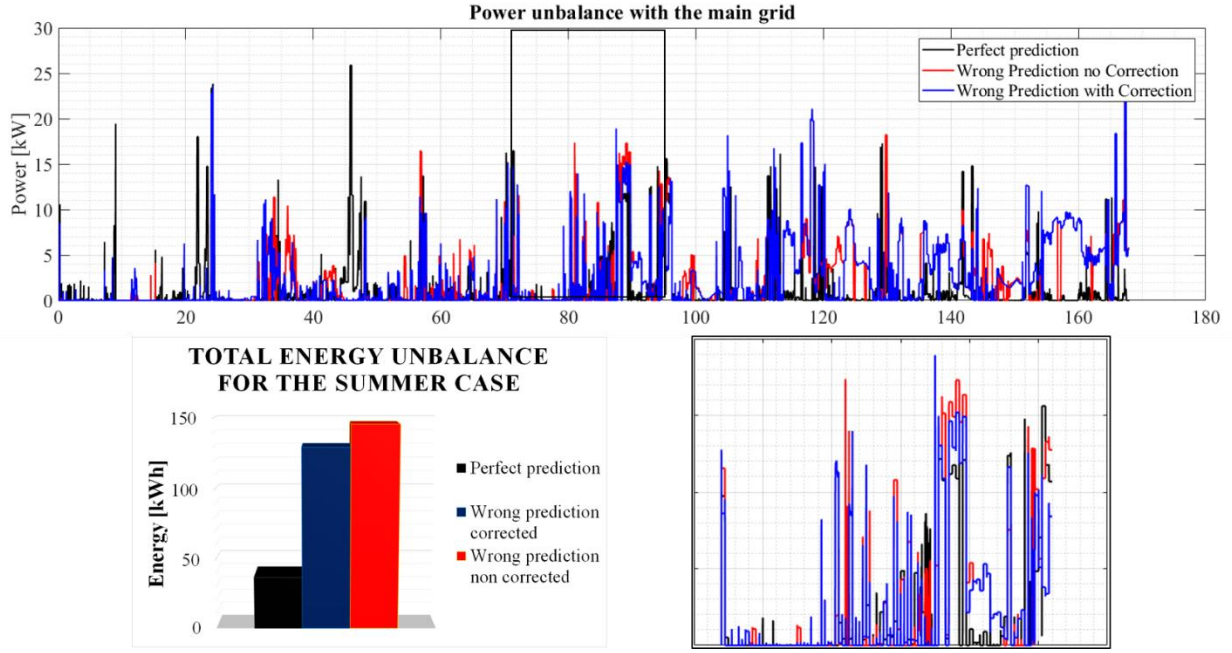

Figure 4 – Absolute value of the unbalance power profile for the three simulated cases (perfect prediction, wrong with no correction and wrong with correction during the simulated week of July (top) with details of the third day (bottom-right) and overall unbalance energy (bottom - left).

Similar consideration can be drawn also looking at the winter case (Figure 5). A general greater unbalances occurred for these operating conditions due to reduced capability of the ESS to adsorb the RES fluctuation when at low SoC. However, the system was able to reduce those oscillation transmitted to the main grid by means of the optimization process. Therefore, having a reliable prediction of the power demand is shown again to be essential to achieve consistent improvement toward the reduction of the total energy unbalance.

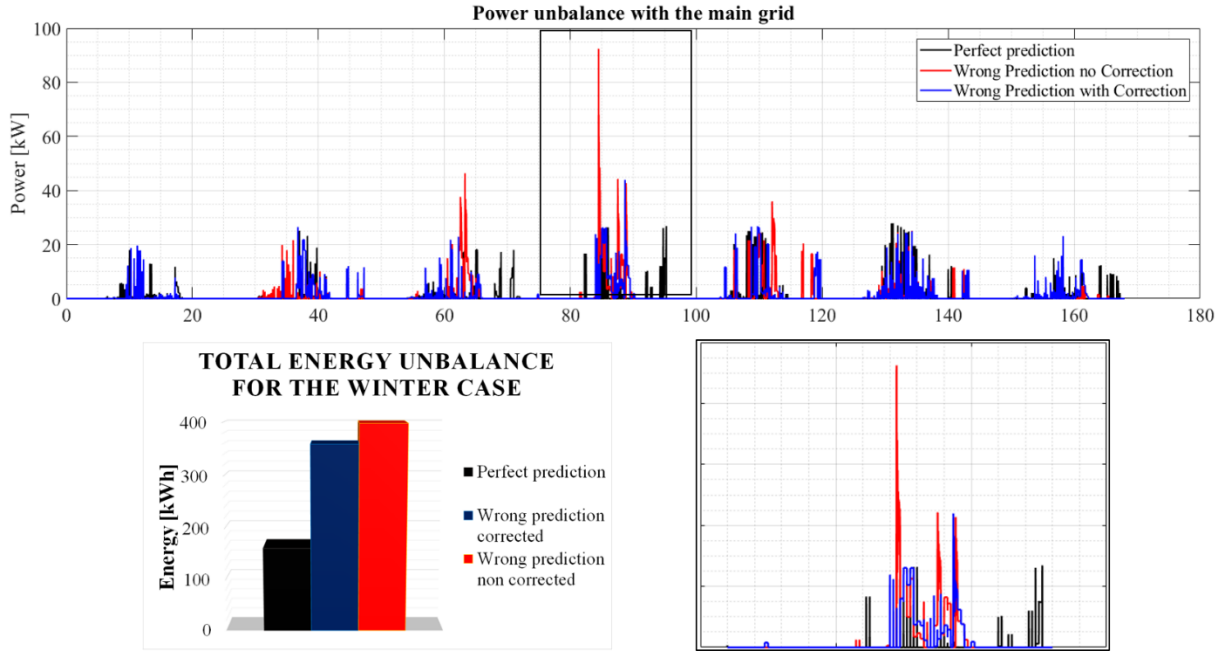

Figure 5 – Absolute value of the unbalance power profile for the three simulated cases (perfect prediction, wrong with no correction and wrong with correction during the simulated week of January (top) with details of the third day (bottom-right) and overall unbalance energy (bottom - left).

5 CONCLUSION

The proposed modification of the Model Predictive Control (MPC) approach for an Energy Management System (EMS) has been proved, that is capable of improving the performances of Hybrid Renewable Energy Systems (HRES) in terms of unbalances in the power exchanged with the grid.

Smoothening out the load profile with the Demand Side Management (DSM) of deferrable appliances and a more efficient use of the Battery Energy Storage System (BESS) together with an improved prediction of the foreseen load profile due to the implementation of the Correlation Clustering analysis have been found crucial to get the improvement.

A reduction of almost 40kWh and 15kWh in the energy withdrawn respectively for the winter and summer week has been achieved by means of the improved load forecast. This effect is also due to the maximization of the self-consumed local RES. Current fluctuations towards the grid were adsorbed by the BESS and FC sub-components allowing also the HRES to act as a voltage and frequency regulator in the main-micro grids interaction.

ACKNOWLEDGEMENTS

The authors would like to acknowledge MSc student Marina Santarelli for her essential contribution to the results shown in this paper.

REFERENCES

[1] European Commission, *Energy roadmap 2050*, Luxembourg: Publications Office of the European Union doi:10.2833/10759

[2] T.M. Tawfik, et al., *Optimization and energy management of hybrid standalone energy system: a case study*, Renewable Energy Focus, 25, June 2018, 48-56, https://doi.org/10.1016/j.ref.2018.03.004.

[3] Dimitrios Thomas, et al., *Optimal design and techno-economic analysis of an autonomous small isolated microgrid aiming at high RES penetration*, Energy, 116, 2016, 364-379, https://doi.org/10.1016/j.energy.2016.09.119.

[4] G. Bruni, et al., *Fuel cell based power systems to supply power to Telecom Stations*, International Journal of Hydrogen Energy, 39, 2014, 21767-21777, https://doi.org/10.1016/j.ijhydene.2014.07.078.

[5] S. Cordiner, et al., *Fuel cell based Hybrid Renewable Energy Systems for off-grid telecom stations: Data analysis from on field demonstration tests*, Applied Energy, 192, 2017, 508-518, ISSN 0306-2619, https://doi.org/10.1016/j.apenergy.2016.08.162.

[6] Sibo Nan, Ming Zhou, Gengyin Li, *Optimal residential community demand response scheduling in smart grid*, Applied Energy, 210, 2018, 1280-1289, https://doi.org/10.1016/j.apenergy.2017.06.066.

[7] M. S. Viana, et al., *Analysis of demand response and photovoltaic distributed generation as resources for power utility planning*, Applied Energy, 217, 2018, 456-466, https://doi.org/10.1016/j.apenergy.2018.02.153.

[8] Jianxiao Wang, et al., *Review and prospect of integrated demand response in the multi-energy system*, Applied Energy, 202, 2017, 772-782, ISSN 0306-2619, https://doi.org/10.1016/j.apenergy.2017.05.150.

[9] Allan R. Starke, et al., *Multi-objective optimization of hybrid CSP+PV system using genetic algorithm*, Energy, 147, 2018, 490-503, https://doi.org/10.1016/j.energy.2017.12.116.

[10] Samir M. Dawoud, et al., *Hybrid renewable microgrid optimization techniques: A review*, Renewable and Sustainable Energy Reviews, 82, 2018, 2039-2052, https://doi.org/10.1016/j.rser.2017.08.007.

[11] Motaz Amer, et al., *Optimization of Hybrid Renewable Energy Systems (HRES) Using PSO for Cost Reduction*, Energy Procedia, 42, 2013, 318-327, https://doi.org/10.1016/j.egypro.2013.11.032.

[12] G. Bruni, S. Cordiner, V. Mulone, V. Rocco, F. Spagnolo, *A study on the energy management in domestic micro-grids based on Model Predictive Control strategies*, Energy Conversion and Management, Volume 102, 2015, Pages 50-58, ISSN 0196-8904, https://doi.org/10.1016/j.enconman.2015.01.067.

[13] Lorenzo Bartolucci, Stefano Cordiner, Vincenzo Mulone, Vittorio Rocco, Joao Luis Rossi, *Renewable source penetration and microgrids: Effects of MILP – Based control strategies*, Energy, Volume 152, 2018, Pages 416-426, ISSN 0360-5442, https://doi.org/10.1016/j.energy.2018.03.145.

[14] L. Bartolucci, S. Cordiner, V. Mulone, V. Rocco, J.L. Rossi, *Renewable sources integration through the optimization of the load for residential applications*, Energy Procedia, Volume 142, 2017, Pages 2208-2213, ISSN 1876-6102, https://doi.org/10.1016/j.egypro.2017.12.590.

[15] Willy Bernal, Madhur Behl, Truong Nghiem, and Rahul Mangharam, *MLE+: A Tool for Integrated Design and Deployment of Energy Efficient Building Controls*, October 2012.

SYNTHESIS GAS PRODUCTION FROM A COMBINED BIOCHAR GASIFICATION AND ADSORPTION-CATALYSIS PROCESS

Suwimol Wongsakulphasatch [1], Supanida Chimplee [1], Supawat Vivanpatarakij [2], Thongchai Glinrun [3], Fasai Wiwatwongwana [3], Suttichai Assabumrungrat [4]

1 Department of Chemical Engineering, Faculty of Engineering, King Mongkut's University of Technology North Bangkok, Bangkok 10800, Thailand

2 Energy Research Institute, Chulalongkorn University, Phayathai Road, Wang Mai, Phatumwan, Bangkok Thailand

3 Department Chemical Engineering, Faculty of Engineering, Pathumwan Institute of Technology, Rama 1 Road, Wang Mai, Phatumwan, Bangkok, Thailand

4 Center of Excellence in Catalysis and Catalytic Reaction Engineering,

Department of Chemical Engineering, Faculty of Engineering, Chulalongkorn University, Bangkok 10330, Thailand

ABSTRACT

This research aims to evaluate a combined system of biochar gasification and adsorption-catalysis process for synthesis gas production. The effect of mangrove derived biochar gasification temperature, amount of water added as gasifying agent, adsorption-catalysis temperature, and the effect of CaO content in one-body multi-functional sorbent/catalyst material, Ni-CaO/$Ca_{12}Al_{14}O_{33}$, were studied in this work. Temperatures applied in biochar gasification process was evaluated in the range of 800-900°C. Addition of water in gasifying agent feed molar ratio was varied from 0-2, where the other compositions were fixed at CO_2:O_2:C = 0.25:0.25:1, and the temperatures of adsorption-catalysis reactor was varied from 450 to 650°C. Results were examined in terms of biochar conversion, gaseous product composition, and CO_2 emission. The results revealed that the temperature of 900°C provided the highest biochar conversion of ca. 92%. Synthesis gas production was found to depend upon amount of water added and temperature of the adsorption-catalysis reactor; higher amount of H_2 was observed with an increase of water and temperature. In term of process design, it was found that the hybrid adsorption-catalysis process using one-body multi-functional material offered greater amount of H_2 with similar amount of CO_2 emission when compared with separated sorbent/catalyst material.

Keywords: Gasification; sorption-enhanced water gas shift; multi-functional material

1 INTRODUCTION

Gasification of biomass is a technology that is used to convert biomass into synthetic gas or syngas, which consists of mainly H_2 and CO. Different compositions of H_2 and CO in the syngas can be applied for various downstream processes, i.e., electricity generation, synthetic gas production, H_2 production, chemical productions [1-3], etc. Biomass is a good representative of renewable resources for the production of syngas as it is carbon neutral [4]. Conversion of biomass via gasification could be made by using different gasifying agents such as oxygen, air, steam, carbon dioxide, and their mixtures [5-6]. These agents could yield different amount and product gas compositions [5, 7]. Although biomass gasification has been proved to be one of most efficient techniques for syngas production; however, the drawbacks of this technique is the accompanied production of CO_2 in the product stream. Purification of syngas by separation of CO_2 is therefore required and this process is known to be an intensive energy consumption [8]. In this work, we are therefore interested in improving efficiency of biomass gasification process in terms of reducing CO_2 emissions and utilizing the captured CO_2. Sorption-enhanced water gas shift (SEWG) reaction is an adsorption-catalysis hybrid process that applied to separate CO_2 from syngas after gasification. In this process, a high-temperature water gas shift catalyst and a CO_2 sorbent are combined in the same reactor to function simultaneously. As a consequence, this system allows an increase in CO conversion due to the removal of CO_2, leading to an enhancement of H_2 production.

2 MATERIALS AND METHODS

A multi-functional sorbent/catalyst material was prepared by firstly synthesising of calcium oxide, which was prepared by mixing a 100-ml of 2.5 M sodium carbonate solution with the same amount of 2.5 M calcium chloride under continuous stirring for 3 hr. Then, the solution was allowed to stand for 5 hr to yield precipitated solids. After 5 hr, the solids were dried at 30°C for 12 hr and calcined at 850°C for 30 min. To combine the sorbent and catalyst into one-body Ni/CaO-$Ca_{12}Al_{14}O_{33}$, the solution of aluminium nitrate ($Al(NO_3)_3{\cdot}9H_2O$ 3.79 g in 100 ml DI-water) was mixed with the solution of nickel nitrate (dissolved in 100 ml DI-water was mixed with the solution of nickel nitrate ($Ni(NO_3)_2{\cdot}6H_2O$ 3.03 g in 100 ml DI-water). Then 3.7 g of CaO was added into the solution and allowed to stir at room temperature for 3 hr. After that, the mixture was allowed to stand for 24 hr, dried in an oven at 120°C for 24 hr, and calcined at 900°C for 1.5 hr under dried air.

Syngas production was tested using two-connected fixed-bed reactors, one for biomass gasification and another one for sorption-enhanced water gas shift reaction. Gasification temperature was varied from 800-900°C and sorption-enhanced water gas shift reaction was varied from 500-650°C at atmospheric pressure. The pattern of sorbent and catalyst packed in sorption-enhanced water gas shift reactor was varied for 3 types as shown in Fig. 1. Gasifying agent was fed at fixed ratio of $CO_2/O_2/H_2O/C$ = 0.25/0.25/0.25/1.

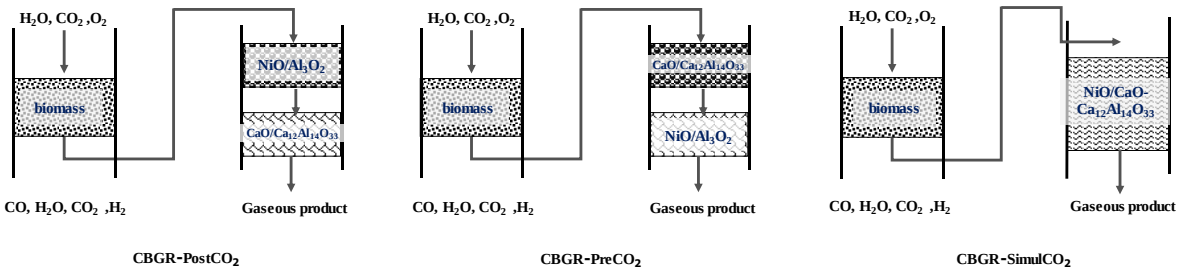

Fig. 1: Patterns of sorbent and catalyst packed in the SEWG reactor.

3 RESULTS AND DISCUSSION

3.1 Material Characterization

XRPD pattern of the synthetic material is shown in Fig.2. As seen, the result shows XRPD peaks correspond to CaO at 2θ = 32.204 and 53.856, $Ca_{12}Al_{14}O_{33}$ at 2θ = 18.052, 29.726, 33.280, 36.588 and 41.069, and NiO at 2θ = 30.259, 37.249 and 48.695.

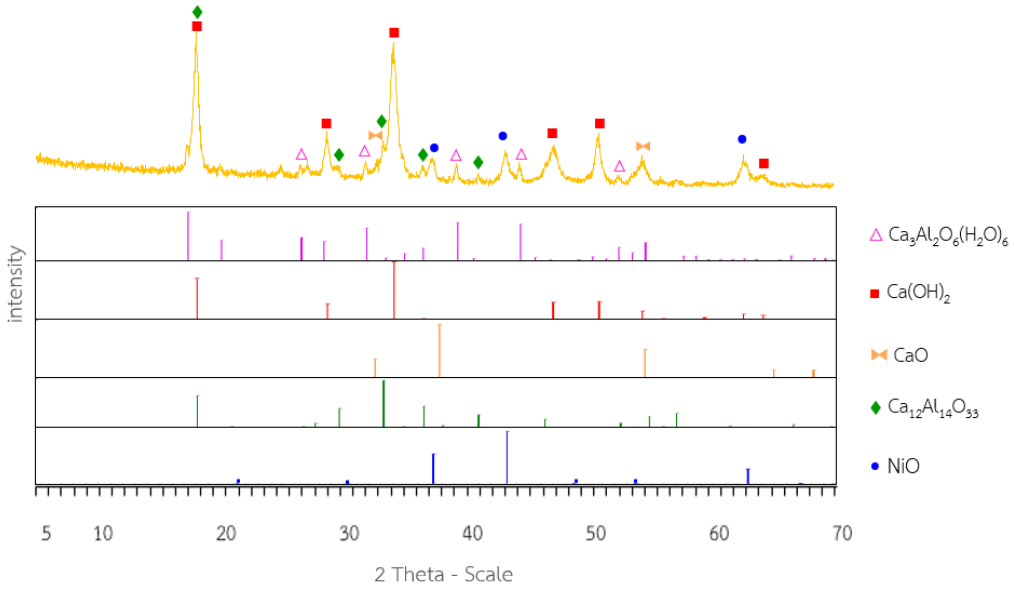

Fig.2: XRPD pattern of multi-functional material Ni/CaO-$Ca_{12}Al_{14}O_{33}$

3.2 Effect of gasification temperature

Gasification temperature of biochar was varied for two temperatures at 800 and 900°C. The results show that biochar conversion is only 30% for gasification temperature of 800°C; however, biochar conversion increases to ca. 92% when gasification temperature increases to 900°C.

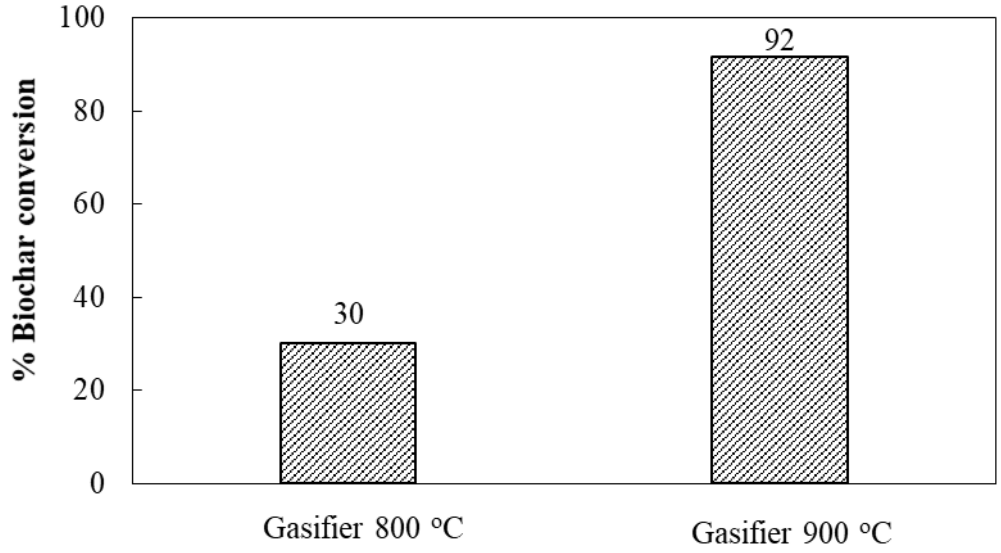

Fig. 3: % Biochar conversion at different gasifying temperatures.

Product compositions obtained from gasifier at different temperatures are shown in Fig. 4. The results show there are H_2, CO, and CO_2 observed in the product stream. Higher CO is observed instead of H_2, as a consequence converting of CO is required.

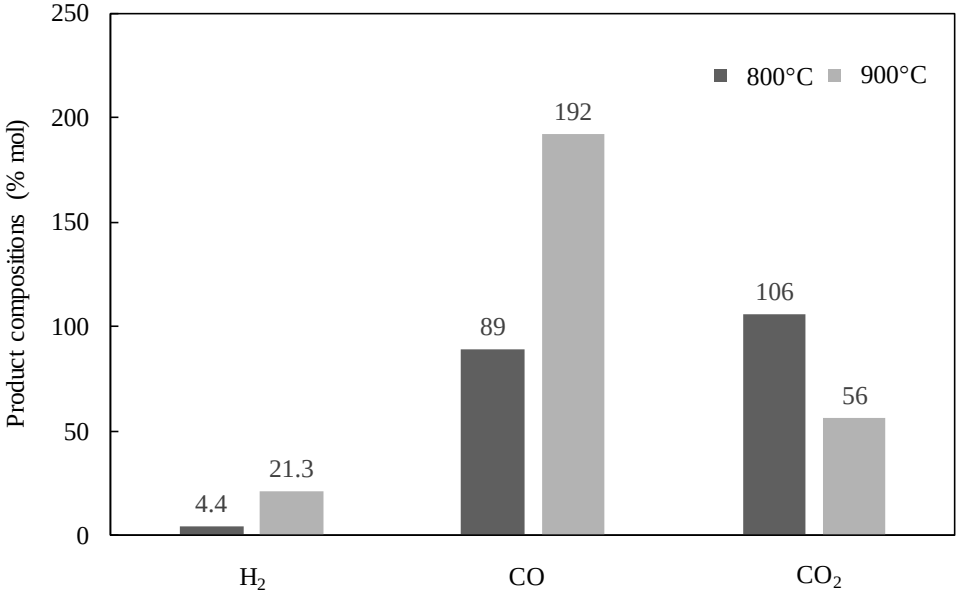

Fig. 4: Product composition at different gasifying temperatures.

3.3 Combined gasification and sorption-enhanced water gas shift reaction

To eliminate CO_2 and enhance H_2 production, sorption-enhanced water gas shift (SEWG) was added after gasification process. In the SEWG reactor, sorbent and catalyst was packed in the reactor with three different patterns as shown in Fig. 1. Results of produced syngas (shown as H_2/CO ratio) observed with different patterns of packed sorbent and catalyst is shown in Fig.5. As seen, combining sorption-enhanced water gas shift reaction could enhance H_2 production with lower CO_2 emission. However, the developed one-body

multi-functional material provides lower H_2 production than the pre-adsorption CO_2 before water gas shift reaction take places.

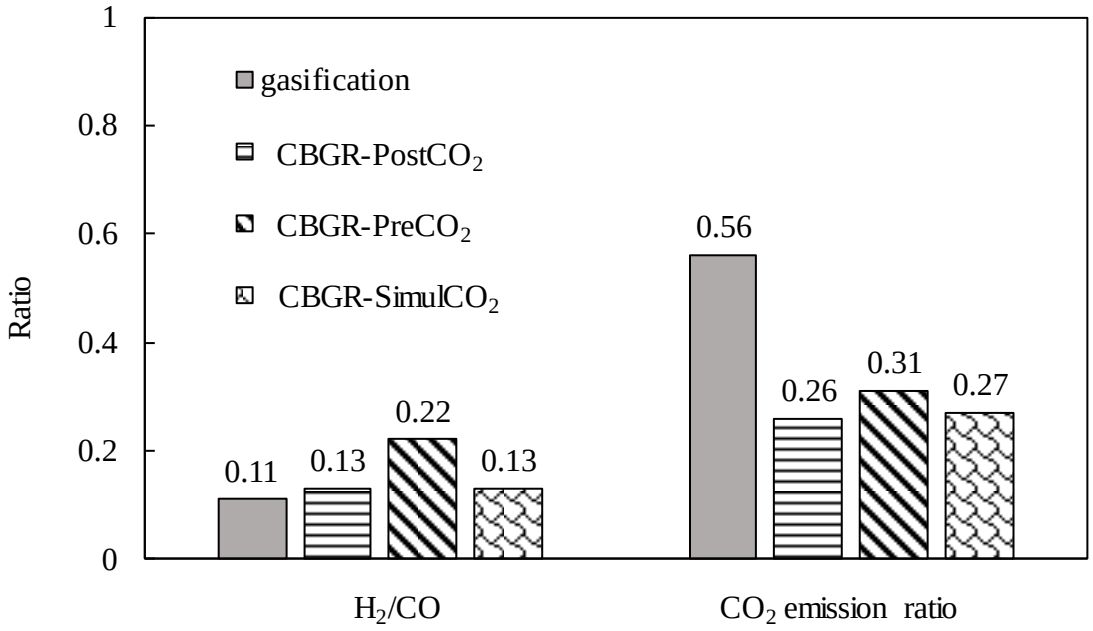

Fig. 5: H_2/CO and CO_2 emission ratio for different proposed systems.

4. CONCLUSIONS

Biochar could be gasified and converted into syngas and CO_2. By applying sorption-enhanced water gas shift into gasification of biochar system, the process could provide higher H_2 production and at the same time could reduce CO_2 emissions from the process.

ACKNOWLEDGEMENTS

The authors would like to thank the Ratchadapisek Sompoch Endowment Fund Chulalongkorn University 2016 (CU-59-003-IC) and the Thailand Research Fund (DPG5880003) for the supports.

REFERENCES

[1] M. Rodrigues, A.P.C. Faaij, A. Walter, Technol-economic analysis of co-fired biomass integrated gasification/combined cycle systems with inclusion of economies of scale, *Energy*, Vol. 28, pp. 1229-1258, 2003.

[2] C.N. Hamelinck, A.P.C. Faaij, H. den Uil, H. Boerrigter, Production of FT transportation fuels from biomass; technical options, process analysis and optimization, and development potential, *Energy*, Vol. 29, pp. 1743-1771, 2004.

[3] H. Liu, Y. Shao, J. Li, A biomass-fired micro-scale CHP system with organic Rankine cycle (ORC)-thermodynamic modelling studies, *Biomass Bioenergy*, Vol. 35, pp. 3985-3994, 2011.

[4] B. Acharya, A. Dutta, P. Basu, Chemical-Looping gasification of biomass for hydrogen-enriched gas production with in-process carbon dioxide capture, *Energy Fuels*, Vol. 23, pp. 5077-5083, 2009.

[5] J. Udomsirichakorn, P.A. Salam, Review of hydrogen-enriched gas production from steam gasification of biomass: The prospect of CaO-based chemical looping gasification, *Renewable and Sustainable Energy Reviews*, Vol. 30, pp. 565-579, 2014.

[6] P. Chaiwatanodom, S. Vivanpatarakij, S. Assabumrungrat, Thermodynamic analysis of biomass gasification with CO_2 recycle for synthesis gas production, *Applied Energy*, Vol. 14, pp. 10-17, 2014.

[7] P. Kraisornkachit, S. Vivanpatarakit, S. Amornraksa, L. Simasatitkul, S. Assabumrungrat, Performance evaluation of different combined systems of biochar gasifier, reformer and CO_2 capture unit for synthesis gas production, *International Journal of Hydrogen Energy*, Vol. 41, pp. 13408-13418, 2016.

[8] C. Song, Q. Liu, N. Ji, S. Deng, J. Zhao, Y. Li, Y. Song, Alternative pathways for efficient CO_2 capture by hybrid processes-A review, *Renewable and Sustainable Energy Reviews*, Vol. 82, pp. 215-231, 2018.

SUPPORTING THE RENEWABLE ENERGY SECTOR – THE ROLE OF ACADEMIA

Paul Blackwell[1], Simon Leslie[2], Dorothy Evans[3], Pauline Murray[4]

1. DMEM, University of Strathclyde, Glasgow, email: paul.blackwell@strath.ac.uk
2. Advanced Forming Research Centre, University of Strathclyde, Glasgow, email: simon.leslie@strath.ac.uk
3. DMEM, University of Strathclyde, Glasgow, email: dorothy.evans@strath.ac.uk
4. Advanced Forming Research Centre, University of Strathclyde, Glasgow, email: p.murray@strath.ac.uk

ABSTRACT

As is well known the renewables sector covers both a wide range of technologies and a wide range of companies that work in it, or supply to it. The paper considers the role of academia in supporting work across this sector drawing on an example using European Interregional funding via the SEUPB funding body. The recently established Renewable Engine programme supports twelve PhD's working on a variety of manufacturing and inter-linked technologies with the focus being on supporting companies in Western Scotland, Northern Ireland and the border counties of Ireland. The paper specifically details work being carried out at the Advanced Forming Research Centre; part of the University of Strathclyde, although the overall consortium includes a number of other academic establishments. The projects are diverse and include the use of augmented reality to support maintenance of off-shore wind farms, the development of novel energy storage systems and the development of software for the optimisation of choice regarding which balance of energy solutions is best for particular sites.

Keywords: Renewable Engine, SEUPB, academia, research

1 INTRODUCTION

The Renewable Engine programme, which started in January 2017 has been largely funded by the Special European Union Projects Board (SEUPB) under Interreg IV A covering the West of Scotland, Northern Ireland and the six Border Counties of the Irish Republic (see Figure 1). The total project value, including partner contributions, is €6.1 million with contributory funding coming from Mid Ulster council, Invest N.I. and the University of Strathclyde.

Figure 1. Geographical Area covered by the Renewable Engine project.

2 PURPOSE

The purpose of the programme is to develop a research supercluster based around a group of academic institutions within the region, to encourage and develop innovation within manufacturing companies operating within the renewables sector. The envisaged outcomes are increased cross-border collaboration and improved economic prospects for the regions. Initially the goal was to support eight projects, however, due to the quality of the project applications this was increased to twelve. The effort within academia is focussed on improving the technology readiness level (TRL) of these projects. Figure 2 illustrates the range of TRL's; the lower TRL's represent the zone of basic research carried out in Universities, while on the right hand side the higher TRL's represent processes / technologies that are ready for industrial or commercial implementation. Part of the purpose of the work being carried out under the Renewable Engine programme is to translate basic research into industrial solutions.

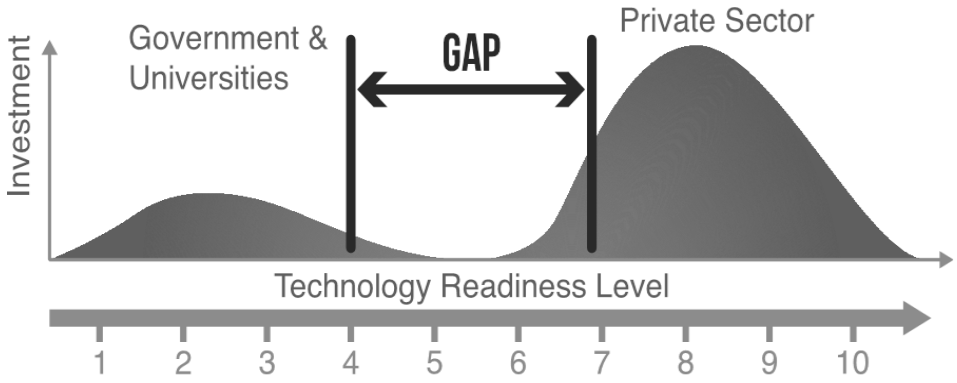

Figure 2. Technology Readiness Levels (TRL) scale

The programmes' main academic partners are South West College in Cookstown, Queens University, Belfast, Institute of Technology in Sligo and the Advanced Forming Research Centre (AFRC) at the University of Strathclyde.

Figure 3 sums up the overall programme management approach that was taken with regard to project definition and progression.

Figure 1. Process model for Renewable Engine programme [1].

Initially, there was an open call for companies within the prescribed geographical regions to apply for inclusion, this was done via trade shows and workshop events at each of the academic institutions and via advertisements through a website.

2.2 Project Selection

The project applications were put through a selection process and were scored by each of the academic partners independently before being reviewed by the Project Board, which has a range of internal and external stakeholders represented. Decisions were made either to approve the projects, ask for further clarification, or to reject. In some cases, projects were amalgamated where this gave increased benefits.

2.3 Project Implementation

One of the challenges in starting a programme of this kind is to recruit the required number of students with the skillsets necessary to support the research envisaged. Such recruitment was handled locally by the various academic institutions working with the selected industrial partners and twelve students were engaged.

2.4 Project Monitoring

Ongoing supervision of the individual projects is carried out as a partnership between the specific academic partner involved and the company, with both academic and company supervisors being in place to ensure that the project remains relevant to the requirements of both the companies involved and from an academic standpoint.

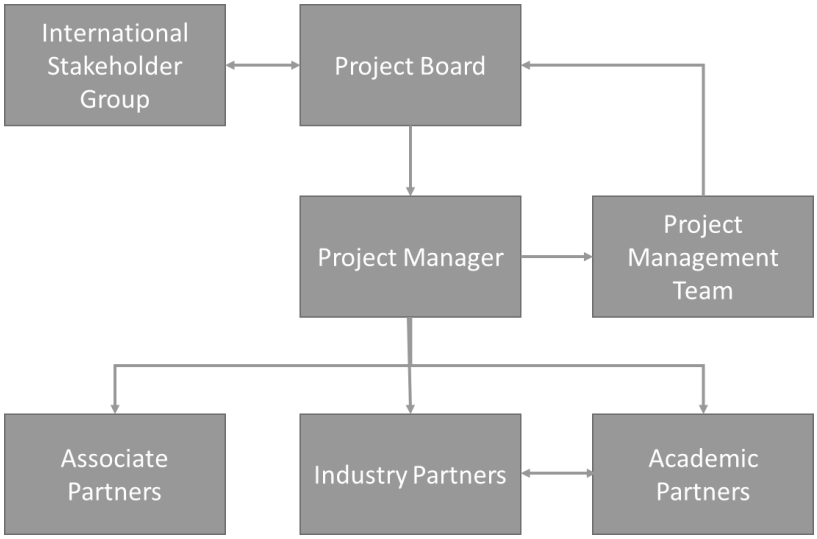

Figure.4. Overall governance structure for the Renewable Engine programme.

To further support the project, there is, as previously, noted a Project Board, a project management team and an International Stakeholder Group consisting of influential individuals from across the business community. Stakeholders were recruited from local, national and international business, government departments, advisory agencies and bodies with responsibility for the strategic direction of industry. The international stakeholder group meets formally twice per year. The overall governance structure for the project is shown in Figure 4.

2.7 Range of Projects

The 12 industry partners involved in the project are shown in Figure 5.

Figure 5. Industry partners of the Renewable Engine project

The programme portfolio currently consists of research into energy storage; energy generation and enabling technologies (Figure 6). The companies involved range from large multi-nationals such as Doosan Babcock to small SME's such as Soltropy.

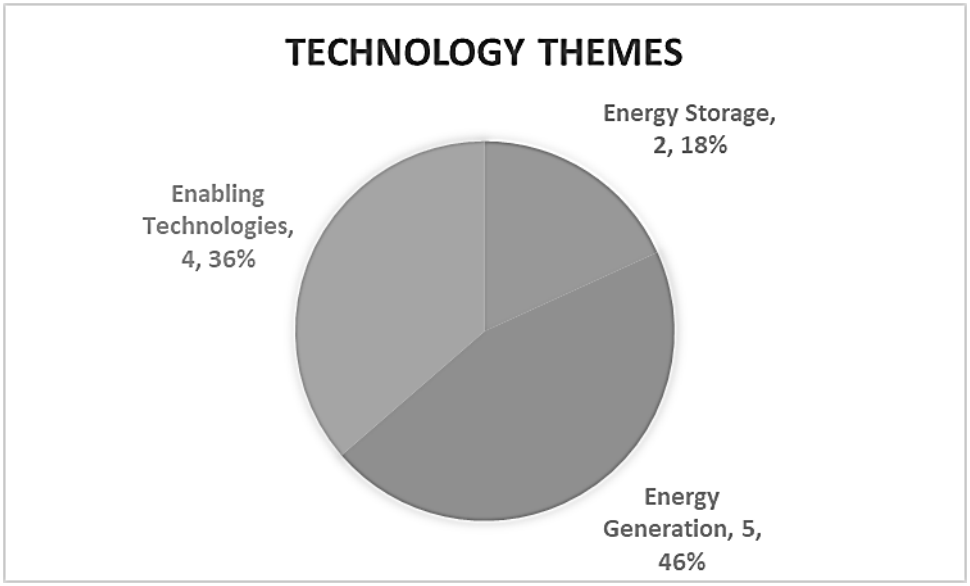

Figure 6. Breakdown of projects by renewable technology theme

3 Case Studies

3.1 Case Study: Booth Welsh

Booth Welsh are a process engineering company who work primarily in the pharmaceutical and chemical industries providing process solutions. They are a forward thinking innovative organisation who are seeking to utilise augmented reality within the renewables industry, namely maintenance of offshore wind turbines – this being the focus of the PhD research. The intent is to reduce maintenance time spent on the capital equipment and reduce risks to workers in dangerous offshore environments. Booth Welsh have embraced the concepts of Industry 4.0 with this project, the intention of which is to use virtual/augmented reality to allow technicians to be assisted in their work on offshore sites.

Working with the Renewable Engine partnership has allowed Booth Welsh to access a fully funded Doctoral student, the state of the art virtual reality suite at the AFRC and associated expertise. This has led to Booth Welsh being asked to join an influential steering group on virtual reality within the region.

3.2 Case Study: Doosan Babcock

Doosan Babcock are working in a number of areas including fuel cells which can run on hydrogen. Doosan's project proposal was for a software application development which will assist in the decision making process for what type or combination of renewable technologies will best suit a specific situation as energy distribution systems move to a more decentralised model

4 Discussion

Product and / or process development is frequently a challenge, even for larger companies and for many smaller enterprises can become a major stumbling block which holds back their ability to progress a product to a full prototype on which field trials can be run and which can in turn be used to define a method of manufacture for introduction to market. It is often the case that Universities, or other centres of research, can provide the skilled human resource and access to specialist equipment that might otherwise be beyond the reach of SME's in particular. There are also a number of, perhaps less obvious, advantages for companies working with academia:

- It is an opportunity to work with one organisation acting as a single point of contact to a wide range of expertise e.g. in manufacturing techniques, process modelling, material selection and failure analysis
- The academic partner can offer experience of supporting the commercialisation of innovations, intellectual property definition and market research
- Influence with policy setting organisations such as the devolved and UK governments
- Knowledge of funding sources, current policies and application process requirements
- Focus on long term economic innovation aspects, product lifecycle, closed loop production, industrial ecology and supply chain management

A specific area worth highlighting from the above list is that academic organisations can offer valuable support in defining pathways to funding that smaller organisations may be unaware of. It is generally the case that Universities / Colleges are experienced in the development of bids to a variety of funding organisations. The range of funding available can vary from a few thousand pounds for a scoping study, to much larger amounts assuming that the business case can be made. Generally, some level of matched funding will be required from the company itself, but it is useful to be able to leverage company investment with external financial support.

5 Summary

The Renewable Engine project provides a case study of how academia can support companies in the renewables sector through providing expertise and equipment to overcome barriers to eco-innovation; identifying value streams; social, economic and environmental, and linking commercial organisations to groups directly influencing policy and legislation on renewables and the environment.

The Renewable Engine programme model:

- Allows companies to access equipment and expertise which would otherwise be prohibitively expensive and time consuming for them to purchase, lease or hire

- Encourages collaboration between academic institutions which companies access for a greater range of expertise

- Provides funding for applied research projects that can be completed with industry partners to generate outcomes with practical application and academic impact

Acknowledgments

Funding for the Renewable Engine Programme is derived from the Special European Union Projects Board (SEUPB) under Interreg IV A with contributory funding coming from Mid Ulster council, Invest N.I. and the University of Strathclyde.

References

[1] J. Tidd & J. Bessant; *Managing Innovation: Integrating Technological, market, and organisational change,* Pub. John Wiley and Sons Ltd, Sussex, 4th Edition, 2009, p44.

MARKET DESIGN FOR SUCCESSFUL IMPLEMENTATION OF UAE 2050 ENERGY STRATEGY

S. Al Naqbi[1], I.Tsai[2] and T.Mezher[3]

1. Masdar Institute of Science and Technology, Khalifa University of Science and Technology, Abu Dhabi, UAE; email: salnaqbi@masdar.ac.ae
2. Masdar Institute of Science and Technology, Khalifa University of Science and Technology, Abu Dhabi, UAE; email: tmezher@masdar.ac.ae
3. Masdar Institute of Science and Technology, Khalifa University of Science and Technology, Abu Dhabi, UAE; email: itsai@masdar.ac.ae

ABSTRACT

In order to implement a RE strategy in any country, there is a need for a good market design in order to have successful outcomes. Market design depends of several factors such as Infrastructure, Human Capacity and Institutions. This thesis explored the literature on RE market design factors and sub-factors and selected the most acceptable framework for market design analysis. UAE 2050 Energy strategy calls for reduction on carbon dioxide emissions by 70%, increasing clean energy use by 50% (RE 44% and Nuclear 6%), and improve energy efficiency by 40% by the middle of the century. This will lead to an increase in savings of about 700AED billion. This thesis will analyse the current RE market design in UAE and proposes policies and mechanisms in order to achieve the proposed targets. In addition, it will look at the transitions needed from all relevant stakeholders especially the main UAE utilities, ADWEA and DEWA. The paper will show the business models of these utility companies that will help in the transition of UAE from fossil fuel economy to a harmonic fule mix with cleaner sources of energy.

Keywords: Market Design, Renewable Energy, Business Model, UAE

1 INTRODUCTION

The United Arab Emirates, an oil rich country, has embarked on the renewable energy (RE) journey when the Abu Dhabi Future Energy Company (Masdar) was created in 2006 [1]. Abu Dhabi took the leading role in adopting the first RE target, 7% of total power capacity by 2020 [2]. Since then Dubai, adopted an RE target to 5% by 2030 (ref, energy outlook, ASCE) and revised its target to 7% by 2020 and 25% by 2030 [3], [4], [5]. In 2018, UAE as a nation has decided to raise its clean energy target from 24 % to 27% by 2021 as part of its commitment to global efforts to fight climate change [6]. The country has great expectation in developing its RE economic sector in order to meet its ambitious RE targets. The total power capacity in 2021 for UAE is expected to be around 38 GW out of which 10.26 GW (27%) should come from clean energy, 5.6 GW from nuclear and 4.66 GW from RE. As of today, only a total of 323 MW (100 MW of CSP and 223 MW of PV), are installed and commissioned. Therefore, by 2021, additional capacity of 4.38 GW of RE should be installed. The main challenge will be to have the capability to install the targeted RE capacity in the next 3-4 years. The objective of this paper is to analyse the current market design for RE sector using an existing readiness framework which encompasses three major components: infrastructure, institutions, and human capacity [7], [8]. In addition, the paper will examine the current business model transitions of two major utilities in UAE: Abu Dhabi Water and Electricity Agency (ADWEA) and Dubai Electricity and Water Agency (DEWA).

2 MARKET ANALYSIS FRAMEWORK FOR UAE

The main factors that contribute for successful market design are infrastructure, institutions, and human capacity. The concept of renewable energy infrastructure refers to the physical capacity of the country to deploy those related technologies. These technologies are evaluated through the availability of natural resources (conventional fossil fuels and RE) such as the ability of the grid to transmit and distribute additional power or electricity generated from renewable sources to users. In addition, other factors are linked to infrastructure by developing RE technologies: market infrastructure consisting of the commodity market, reform of the power sector, RE technologies development, and power off-take attractiveness. And also another factor is the rate of access to electricity and the expected demand for electricity [7], [8].

Human capital is a critical engine for the sustainable development of RE technologies. In the perspective of RE readiness, human capital refers to the provision of human resources with the capacity to develop, manage, achieve, and maintain RE projects in a particular country. It is a standard for measuring the ability to select and operate the most appropriate technology towards sustainability. There is a need for factors such as technical and commercial skills, technology adoption and dissemination, as well as increasing consumer awareness of the positive value of RE in various areas for the development and promotion of human capital for the diffusion of RE technologies [8].

Institutional readiness provides an outline of the most important factors such as: the existing institutional framework, as well as main long-term policies, access to renewable energy financing and the microeconomic environment for the diffusion of RE technology. The importance of these factors is highlighted in the development of an effective and reliable clean energy policy for sustainable energy development in any country. In addition, they demonstrate the effectiveness of institutions in implementing targeted RE projects and their sustainable development to reach global targets. Public and private institutions related on RE, the quality of institutions has a strong impact on the development of relevant RE projects. Where the legal and administrative frameworks governing the public and private sectors represent the general institutional environment. In addition, institutions influence the development of sustainable development strategies as well as policy and investment decisions in the same field [8].
Table 1 below shows all the factors and sub-factors in designing a RE market in UAE. As can be seen, UAE is leading in many of these factors but lacking in others. The paper will later discuss the different challenges that will impact the potential RE market growth

Table 1. Factors Critical to RE Market Design in UAE

Factors	Sub-factors	UAE
Infrastructure	Natural resources	Solar, wind energy, and waste.
	Country overall infrastructure	UAE has the one of most advanced infrastructure in the world.
	Existing grid capacity	As of 2016, the grid capacity in UAE was around 29 GW.
	Market infrastructure	Still weak. In the past power generation, transmission, and distribution are publicly owned. Abu Dhabi was leading in allowing the public-private partnership in power generation and water production only. Recently, Dubai has followed similar model.
	Electricity access rate & projected demand	100 % Electrification and It is expected that power demand capacity in UAE to be around 38 GW.

Human Capacity	Technical & commercial skills	UAE is weak in this area and strongly needs human capacity to embrace renewable energy, including technical and commercial skills.
	Technology adoption & diffusion	RE companies through the RE value chain are operating in UAE including financial institutions. Science and Technology institutions are working with both public and private sector to improve RE technology transfer, adoption and development to meet local context.
	Awareness among consumers, investors & decision makers	The prestigious annual Zayed Future Energy Prize. The annual Abu Dhabi Sustainability Week which attracts national and international investors throughout the RE value chain. Annual Solar World Congress. Annual Emirates Energy Awards.
Institutions	Public or private institutions related on RE	Government: Ministry of Energy and Industry. Abu Dhabi & Dubai Energy Councils. Public utilities: ADWEA, DEWA, FEWA, SEWA. Major private player in RE: Masdar Company.
	Key policies	UAE key policy: 27 % of Clean Energy of the total energy mix by 2021. Abu Dhabi key policy: 7% of electricity from RE by 2020. Dubai key policy: 7% of electricity from RE by 2020, 25% of electricity from RE by 2025 and 75% of electricity from clean energy by 2050. In 2010 enactment of Estidama in Abu Dhabi, by requiring building & natural sustainability systems to reduce energy and water consumption by one-third and pricing reforms. in Dubai, establishment of 30 % demand reduction target by 2030 through a mix of pricing reforms, performance codes, and efficient investments
	Access to RE finance	Private and international banks and investors
	Macroeconomic environment	UAE has a stable and sustainable economy. Many sectors are growing in the country where RE industry can benefit from. Still, RE industry is growing slowly.

3 EXISTING AND PROJECTED RE PROJECTS IN UAE

For the solar projects, from 2006 until 2016, only 3 RE utility scale projects were built in UAE due to high LCOE for the solar technologies. Since 2016, the cost of LCOE went down dramatically to 2.42 USA cents/kwh as in the case in Nour 1 in Abu Dhabi, see Table 2. In addition, the latest numbers from Saudi Arabia indicate that LCOE bidding for PV projects is below the 2 cents mark. In addition, utility scale PV projects are shifting more toward public-private partnership IPP-PPA model in power generation only.

Table 2 Existing and Future RE Solar Projects in UAE

Dubai			Abu Dhabi		
13 MW PV built and operated by DEWA (EPC). Commissioned in 2013	200 MW PV. Auctioned. Public-Private partnership, IPP-PPA Model. LCOE 5.85 Cents/Kwh. Commissioned in 2017.	800 MW PV. Auctioned in 2017 and awarded. Public-Private partnership, IPP-PPA Model. LCOE2.99 Cents/Kwh. Under construction.	Masdar 10 MW. Build by Masdar Company. Net metering with ADWEA. Commissioned in 2010.	SHAMS 1 100 MW CSP. Auctioned. Public-Private partnership, IPP-PPA Model. Commissioned in 2013.	Nour 1 350 MW PV. Auctioned in 2017 and not awarded yet. Public-Private partnership, IPP-PPA Model. LCOE 2.42 Cents/Kwh.

Table 2 below shows existing and future RE solar projects in UAE. From waste to energy perspectives, Abu Dhabi, Dubai, and Sharjah are planning waste-to-energy plants utilizing gasification technology. The total capacity of waste-to energy is 195 MW generating around 1,366,560,000 Kwh starting 2020 [9], [10], [11].

4 THE BUSINESS MODEL OF UTILITIES IN UAE

The business model can be defined as a structural template that describes the organizational and financial structure of a company. The BM is a shift that determines how the organization provides value to customers, and frees customers from paying for value, and turns those payments into profit [12]. Table 3 below shows the Business models of DEWA and ADWEA in handling the new transition to different energy mix in the country.

Table 3 below shows the Business models of DEWA and ADWEA

BM Elements	Dubai DEWA Utility BM	Abu Dhabi ADWEA Utility BM
Customer Segments (Different groups of people/organizations that the organization aims to access & serve)	Residential, commercial and remaining economic sectors	Residential, commercial, Industrial, and agricultural sectors.
Value Propositions (A range of products and services that create value for a customer segments)	Fulfil energy and water needs. Supply of reliable electricity and water to customers including from Renewable energy technologies and desalination.	Fulfil energy and water needs. Supply of reliable electricity and water to customers including from Renewable energy technologies and desalination.
Channels (How the company communicates with & reaches the customer segments)	On-line, TVs, payment channels, etc. Support via customer service and call centers, metering & billing etc.	On-line, TVs, payment channels, etc. Support via customer service and call centers, metering & billing etc.
Customer Relationships (Relations between the company & customer segments)	Formal & standardized. Short-term supply contracts.	Formal & standardized. Short-term supply contracts.
Revenue Streams (The money generated by the company from each segment of customer segments)	Sale of metered units of delivered electricity and water. Trading of surplus electricity to other emirates in UAE. Government subsidies. Profits for public-private projects. Low-carbon financial incentives (e.g. Renewables Obligation Certificates)	Sale of metered units of delivered electricity and water. Trading of surplus electricity to other emirates in UAE. Government subsidies. Profits for public-private projects. Low-carbon financial incentives (e.g. Renewables Obligation Certificates)
Key Resources (The most important assets required to make the business model work)	Financial, technical and legal resources to develop large-scale, centralized decentralized (RE) generation, transmission and distribution infrastructure for electricity and water. Customer services activities. Fossil fuels. Centralized generation (decentralized RE), transmission & distribution technologies	Financial, technical and legal resources to develop large-scale, decentralized generation, and centralized transmission and distribution infrastructure for electricity and water. Customer services activities. Fossil fuels. Decentralized generation and centralized transmission & distribution technologies.

Key Activities (One of the most important things the company does to make its business model workable)	Owing the electricity and water generation (conventional fuel), supply, distribution, and transmission. Partnering with IPPs to generate energy from renewable and integration with the grid.	Partnering with IWPP for the electricity and water generation (conventional and RE), Owning distribution, and transmission channels.
Key Partners (A network of suppliers and partners that make the business model work)	Financial Institutions & Investors. Fuel supply networks. Dubai Supreme Energy Council. Dubai Regulatory and Supervisory Bureau. IPP companies.	Financial Institutions & Investors. Fuel supply networks. Abu Dhabi Supreme Energy Council. Abu Dhabi Regulatory and Supervisory Bureau. IWPP companies.
Cost Structure (All costs to run a business model)	Staff and contractors to implement projects. Marketing and communication. Operation & maintenance of infrastructure. Finance or investment repayments. Technical, financial and legal consultancy. Metering & billing. Generation technology and/or wholesale purchase of energy. Fuel. Premises & land acquisition for generation. Cost of RE power generation as stipulated in PPA.	Staff and contractors to implement projects. Marketing and communication. Operation & maintenance of infrastructure. Finance or investment repayments. Technical, financial and legal consultancy. Metering & billing. Generation technology and/or wholesale purchase of energy. Fuel. Premises & land acquisition for generation. Cost of RE power generation as stipulated in PPA.

BARRIERS/CHALLENGES FACING RE MARKET DESIGN AND LESSONS LEARNED:

Since the announcement of Abu Dhabi Government in 2009 of its 7% RE target for 2020, only few projects were implemented. The economic crisis in 2009 and the drop in oil prices slowed the momentum for RE investments. But the World Expo 2020 that will be held in Dubai brought back the momentum. Still that are many challenges that UAE needs to address in order to successfully build a RE sector. These challenges include: economics and financial challenges (subsidies are a major concern); market challenges; political, institutional/governance, regulatory and administrative challenges; cultural, behavioural and educational challenges; and technical/technological challenges.

5 WAYS FORWARD

It is evident that UAE has rebuilt its momentum in renewable energy especially in the power sector. UAE utility companies, totally publicly owned, have taken an important step in changing their business models from EPC to IPP-PPA in power and water generations and productions. This will help in achieving the future UAE RE targets but previously above mentioned challenges and barriers need to be carefully addressed because in order have a good market design and encourage local and international investments in the energy and water sector.
In summary, market design in UAE is measured by the readiness of its infrastructure, institutions, and human capacity; and the challenges mentioned previously could have serious impacts on the readiness of the country in RE deployment. The current power infrastructure in UAE is well build and up to date but it is based on fossil fuel technologies. More attention

should be given to building smart grid systems to be able to integrate RE power sources and manage power dispatch. The new systems should be well operated and maintained and equipped with high technical skills. At the institutional levels, the governance structure of UAE gives each emirate its own autonomy in running their economic activities. The Federal Government national energy strategy is based on the integration of the energy strategies from each emirate. Abu Dhabi and Dubai have in place the right governmental institutions which include all the energy related public sector stakeholders. More attention is need to the other five smaller emirates which need to have active participation in the national RE strategy.

6 REFERENCES

[1] T. Mezher, S. Tabbara and N. Al Hosany, "An Overview of CSR in the Renewable Energy Sector: Examples from Masdar Initiative in Abu Dhabi," *Management of Environmental Quality,* vol. 21, no. 6, pp. 744-760, 2010.

[2] T. Mezher, G. Dawelbait and Z. Abbas, "Renewable Energy Policy Options for Abu Dhabi: Drivers and Barriers," *Energy Policy Journal,* vol. 42, pp. 315-328, 2012.

[3] "UAE Ministry of Energy," National Communication Report, 2012.

[4] "RE map2030, A Renewable EnergyRoadmap: Renewable Energy Prospects: United Arab Emirates," IRENA, 2015.

[5] "UAE State of Energy Report 2016," 2016.

[6] B. Abdul Kader, "UAE Raises Clean Energy Target to 27% by 2021," Gulf News, 23 October 2016. [Online]. Available: www.gulfnews.com. [Accessed 2017].

[7] D. Hawila, A. Mondal, S. Kennedyr and T. Mezhe, "Renewable Energy Readiness Assessment for North African Countries," *ELSEVIER,* vol. 33, pp. 3-7, 2014.

[8] A. Mondal, D. Hawila, S. Kennedy and T. Mezher, "The GCC Countries RE-Readiness: Strengths and Gaps for Development of Renewable Energy Technologies," *ELSEVIER,* vol. 54, pp. 3-12, 2016.

[9] "Working Towards Zero Waste," Beeah, 2016. [Online]. Available: http://www.beeah.com/. [Accessed 2017].

[10] "TAQA and CWM Abu Dhabi to Develop Waste to Energy Plant," TAQA, 20 June 2012. [Online]. Available: [2]. TAQA (Abu Dhabi National Energy Company) (2012), TAQA and CWM Abu Dhabi to Dewww.taqaglobal.com. [Accessed 2017].

[11] "The Waste to Energy Project," Goverment of Dubau, 2015. [Online]. Available: www.login.dm.gov.ae. [Accessed 2017].

[12] M. Richter, "Business Model Innovation for Sustainable Energy: German Utilities," *Elsevier,* vol. 62, 8 July 2013.

MODELING GAS TO SOLIDS RATIO DURING CLARIFICATION OF ACTIVATED SLUDGE BASED ON ELECTROLYTIC HYDROGEN BUBBLES

K. Cho[1,*], J. S. Kim[1], S. C. Jung[2] and T.H. Chung[3]

1. Division of Environmental Science and Engineering, Pohang University of Science and Technology (POSTECH), Pohang 37673, Republic of Korea
2. Department of Environmental Engineering, Sunchon National University, 255 Jungang-ro, Sunchon, Jeonnam 57922, Republic of Korea
3. Professor Emeritus, Department of Civil and Environmental Engineering, Seoul National University, San 56-1, Sillim, Gwanak, Seoul 151-742, Korea

*Corresponding Author Tel:82-54-279-2289, Fax:82-54-279-8299, E-mail: kwcho1982@postech.ac.kr

ABSTRACT

Without a loss of chemical energy, electrolytic bubbles (dominantly molecular hydrogen) can be utilized for environmental applications such as separation of tiny suspended pollutants in terms of electroflotation (EF). We previously demonstrated that the EF can intensify its clarification efficiency for biological flocs in terms of a final clarification unit of an activated sludge process. This study further provides a theoretical approach for practical applications of EF, specifically in combination with the biological wastewater treatment processes. The Gas to solids (G/S) ratio could be adjusted linearly against current density, under quasi-constant current efficiency of hydrogen (~ 1) and oxygen (~0.4) evolution reactions on Ti/IrO_2 anode and Ti cathode, respectively. Together with size measurements for the bubbles (35 μm on average) and biological flocs (discrete size of 22.5, 40, 60, 135, and 150 μm), the limiting G/S ratio was predicted based on the rise velocities of floc-bubble aggregate. The calculation was further compared with the results of continuous EF experiments under varying G/S ratio and hydraulic loading rate. Apparent compatibility was observed with an initial collision-attachment efficiency of 0.2. The G/S ratio should be greater than 4.2×10^{-3} and 6.6×10^{-3} for stable clarification of activated sludge under hydraulic loading rate of 0.87 and 1.73 cm/min.

Keywords: Hydrogen; Activated sludge; Clarification; Electroflotation (EF); Gas to solids (G/S) ratio

1 INTRODUCTION

Flotation has occasionally been applied for solids-liquid separation during treatment of low-density colloids and fine particles [1] for drinking water treatment and polishing of wastewater effluent [2]. When applied to clarification of activated sludge [3-5], clear effluent was produced within a much shorter detention time than in sedimentation. In addition, the performance of flotation is relatively independent on the settling ability and physicochemical properties of the biological flocs [6, 7]. Dissolved air flotation (DAF) as a representative flotation method has been utilized with design and operation guidelines for air to solids (A/S) ratio, solids and hydraulic loading rates [8, 9] among others. The mass ratio of air to solids, would be the most important factor determining the average number of attached bubbles and rise velocity of the bubble-particle agglomerates [6, 9].

On the other hand, electrochemical water splitting can generate superfine bubbles as small as 10 μm [10] and, thus, electroflotation (EF) can separate tiny suspended solids (SS) from the mixed liquor. The concentration of bubbles can be controlled relatively simply by adjusting the current density (*j*) [3]. Therefore, flexible operations would be possible even under influent loading fluctuations and variations in sludge characteristics [5]. In our previous reports [3-5], excellent clarification and thickening of activated sludge were corroborated, which in-turn enhanced the performance of biological nutrient removal processes. The guidelines in DAF were inapplicable because of the different composition of electrolytic bubbles (H_2 and O_2). In this regard, a modeling approach is necessary for practical application of EF to come up with the wide operational variability in the activated sludge processes. Thus, in this study, a simple theoretical approach was employed to estimate the limiting value of gas to solids (G/S) ratio, an extended definition of the A/S ratio [3], under variable hydraulic loading rate in continuous EF. Experimental results were compared with the calculation to evaluate the robustness.

2 MATERIALS AND METHOD

2.1 Current efficiency of electrolytic bubble generation

One IrO_2-TiO_2-Ti DSA (dimensionally stable anode; DIOES, Korea) and two Ti cathodes were arranged in parallel as a monopolar electrode module with geometric surface area of 30 cm^2. The IrO_2 content of the anode was 50% in molar fraction, while the spacing among electrodes was 0.5 cm. In order to estimate the current efficiency (CE) of electrochemical water splitting, a gas-tight acrylic cylinder (working volume: 0.5 L) was prepared in connection to a mass flowmeter (Coleparmer, USA) with moisture removal apparatus. Before each measurement, the electrolyte was saturated with H_2 and O_2 by gas purging. The flow rates of produced gas were quantified in 5 mM NaCl solutions at j values of 1.7 – 26.7 mA/cm^2, with and without an oxygen removal column (Matheson, USA) in order to estimate the CE of H_2 (HER) and O_2 evolution reaction (OER) separately. Since the volumetric flow was determined by pressure drop across an internal restriction, calibration was performed based on viscosity of gas mixture using Sutherland formula and Wilke method. The CE values were estimated in reference to the theoretical rate given by Faraday's law:

$$\frac{60I}{nF} \times 24.4 \quad \text{(mL/min)} \qquad (1)$$

Where, I is current (mA), F is the Faraday's constant (96485.3 C/mol), n is the number of electrons involved in charge transfer (eq./mol); 2 for the H_2 and 4 for O_2.

2.2 Size distributions of bubbles and activated sludge flocs

An on-line particle counter (Hemtrac, USA) was used to measure the bubble size as in our previous reports [3, 4]. The device employs a light blockage volumetric method by infrared laser diode with dynamic range of measurement from 2 to 400 μm. Under potential bias, electrolyte was pumped into the particle counter at 100 mL/min and circulated back. Either tap water or 10 mM NaCl solutions were used after GF/C filtration (pore size: 0.45 μm). On the other hand, activated sludge samples were collected from a laboratory scale sequencing batch reactor receiving an artificial wastewater. The sludge volume index of the mixed liquor was measured to be 50 ± 5 mL/g. The size distribution of biological flocs was determined with a particle size analyser based on laser diffraction (Malvern Instruments Ltd., UK).

2.3 Continuous EF experiments

Acrylic cylinders (diameter: 7 cm, volume: 2 L) were initially filled with 5 mM NaCl solutions and, after start-up of electrolysis, mixed liquor samples was continuously introduced to the units by peristaltic pumps. The effluent which concurrently escaped from the bottom was collected for 15 minutes. The mixed liquor suspended solids (MLSS) concentration, influent flow rate, and current were varied to be 2 – 4 g/L, 2 – 4 L/h, and 60 – 1,420 mA, respectively. The solids loading rate was from 0.795 to 3.184 $kg/m^2 \cdot hr$. The concentrations of MLSS and effluent SS were measured based on the Standard Methods [11]. [Cl^-] was analysed by ion chromatography (Dionex, USA) using an AS4A column and a conductivity detector. Mixture of Na_2CO_3 (0.168 g/L) and $NaHCO_3$ (0.742 g/L) was used as the eluent at a flow rate of 1.2 mL/min.

3 THEORETICAL APPROACH

The G/S ratio would determine the number of attached bubbles to a floc (B_n) and the rise velocity of bubble-floc agglomerates (V_{bf}), with overall collision-attachment efficiency (α) [12, 13]. In a continuous EF, agglomerates escape with effluent if the rise velocity is lower than the downflow rate [14]. The V_{bf} was calculated based on the separation zone model widely accepted in DAF [14]:

$$\alpha = \alpha_0 \cdot \left(1 - \frac{B_n}{B_m}\right), \; B_m = \pi \cdot d_{fb}^{\,2}, \; V_{bf} = \left[\frac{(\rho_w - \rho_f) \cdot d_{fb}^{\,3} + (\rho_w - \rho_b) \cdot B_n}{(d_{fb}^{\,3} + B_n)^{1/3}}\right] \cdot \frac{g \cdot d_b^{\,2}}{18 \cdot \mu} \qquad (2)$$

B_m is the maximum B_n on flocs of size d_f, d_{fb} is the relative diameter of floc to bubble (d_f/d_b), α_0 is the initial value of α when no bubble is attached. Bubbles adhered to a floc would hinder subsequent attachments [13]. The density of water, flocs, and bubbles are denoted as ρ_w, ρ_f, and ρ_b, respectively. The ρ_b would be negligible to ρ_w but obviously determines B_n and V_{bf} at a given G/S ratio. The wet density of sludge floc (ρ_f) was assumed to be 1.04 g/cm^3 regardless of d_f. The α_0 value was reported to be near 0.3 [13] and 0.2 was employed in this study.

4 RESULTS AND DISCUSSION

4.1 Electrolytic bubble generation efficiency

The CE estimation is prerequisite for calculation of the G/S ratio and B_n under a fixed current. Since the density of H_2 (ρ = 0.09 g/L at 25 ºC) is far smaller than that of air (1.18 g/L), the G/S ratio would significantly be affected by the fraction of O_2 (1.43 g/L) in the produced gas mixture. The electrolyte was initially saturated with O_2 and H_2, as in the case of continuous operation of EF, so that molar transport between rising bubbles and bulk liquid could be negligible. Fig. 1(a) shows the CE values of HER and OER in 5 mM NaCl solutions which were almost constant near 1 (for HER) and 0.4 (for OER) at j values greater than 8 mA/cm^2. These observation was compatible with the previous estimation [3, 4] with overall gas production efficiency of 0.7 with assumed stoichiometric water splitting.

Despite a lack of electrocatalytic activity, the Ti cathode was found to show excellent selectivity for the HER and side reaction such as O_2 reduction reaction was minimal. In comparison, the CE for OER was observed to be much lower (*i.e.*, nonstoichiometric water splitting), largely due to a competition with chlorine evolution reaction (ClER). DSAs based on IrO_2 are known to exhibit not only high corrosion-resistant properties in acidic environment but also electrocatalytic activities for OER by a proper interaction with active oxygen [15]:

$$IrO_x + H_2O \rightarrow IrO_x{-}OH_{ads} + H^+ + e^- \rightarrow IrO_x{-}O_{ads} + 2H^+ + 2e^- \rightarrow IrO_x + 1/2\ O_2 + 2H^+ + 2e^- \qquad (3)$$

The $-OH_{ads}$ and $-O_{ads}$ are reaction intermediates of OER which are known to participate in ClER as well. The selectivity between the OER and ClER would depend on [Cl^-], overpotential, and the electrode materials [2]. The rates of charge transfer limited OER/HER would be proportional with j, whereas competing ClER is diffusion limited. A low surface coverage of electrodes by adhering bubbles could also lead to local supersaturation before mass transfer process into gaseous phase bubbles [16]. As a result, the CE values were much lower at j values smaller than 8 mA/cm^2. Similar nonlinear responses of CE to j were reported theoretically and experimentally [16, 17]. Given quasi-constant CE at higher j, nevertheless, G/S ratio can be controlled linearly with j, which is an important advantage of EF [6, 9].

4.2 Size distributions of electrolytic bubbles and activated sludge flocs

The number distributions of electrolytic bubbles were superimposable, regardless of j and electrolyte, with mean diameters in the range of 34 – 35 μm (Fig. 1(b)). The largest fraction (30-35%) was occupied by bubbles sized from 30 to 50 μm, whereas bubbles smaller than 10 μm was observed rarely. Therefore, EF may prove to generate finer bubbles than those from DAF with a wide size distribution up to 200 μm. A significant body of literature reported that the bubbles in EF are generally smaller than those in DAF [10, 18]. The size of electrolytic bubbles can be influenced by current density and ionic strength of electrolyte which in-turn affect the electrostatic attraction with the electrode surface [10]. However, these effects were marginal in this study owing to small variations in these parameters.

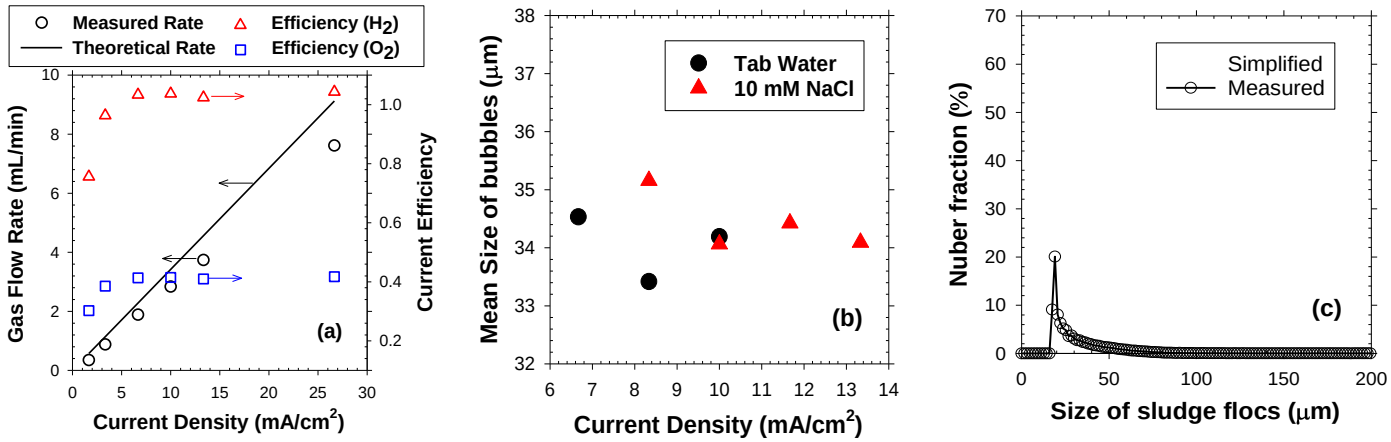

Figure 1. (a) CE of bubble generation together with size distributions of (b) electrolytic bubbles and (c) activated sludge flocs

On the other hand, the number distribution of flocs in the intact activated sludge sample showed a sharp peak at *ca*. 19 μm and broad tail up to 200 μm. Primary and colloidal particles smaller than 10 μm as well as macro-particles greater than 200 μm were hardly observed. Based on the measurements, uniform d_b of 35 μm was assumed for the theoretical calculation, whereas the size distribution of biological flocs was discretized into groups with d_f of 22.5, 40, 60, 135, and 150 μm. Further assuming identical ρ_f (1.04 g/cm^3), each group occupied about 5, 12, 15, 50, and 18% of total MLSS concentration, respectively.

4.3 Estimation of limiting G/S ratio at a given hydraulic loading

Although d_b significantly influences the flotation efficiency, an adjustment of d_b is practically infeasible [6], while the G/S ratio can be a control parameter. Compared to batch flotation, V_{bf} should be the primary consideration to estimate the separation efficiency in continuous flotation units. Fig. 2(a) shows that the rise velocity of agglomerates increased nonlinearly with B_n by combined elevations in effective size of aggregates and the buoyancy force.

In contrast to DAF with separate contact and separation zones, a continuous bubble generation in EF allowed collision/attachment and separation to occur in a single reactor. Our preliminary calculation based on white water bubble blanket model also suggests that the retention time in EF was sufficient for collision of bubble as a single collector of sludge flocs. Therefore, the limiting of G/S ratio could be calculated from the minimum B_n (B_n^{min} in integer form, Fig. 2(b)) to overcome the hydraulic loading rate, for variable d_f. The B_n^{min} was then converted into total required numbers of bubbles and the limiting G/S ratio by sequential multiplication of $1/\alpha$. If the B_n^{min} was greater than B_m (1.3, 4.1, 9.2, 46.7, and 57.7 for d_f of 22.5, 40, 60, 135, and 150 μm, respectively), B_m was used for the limiting G/S ratio calculation. The approach of this study might underestimate the limiting G/S ratio because, while the largest flocs are collected to reach their B_n^{min} (also the highest as readily expected), smaller particles would be attached to more bubbles than B_n^{min}.

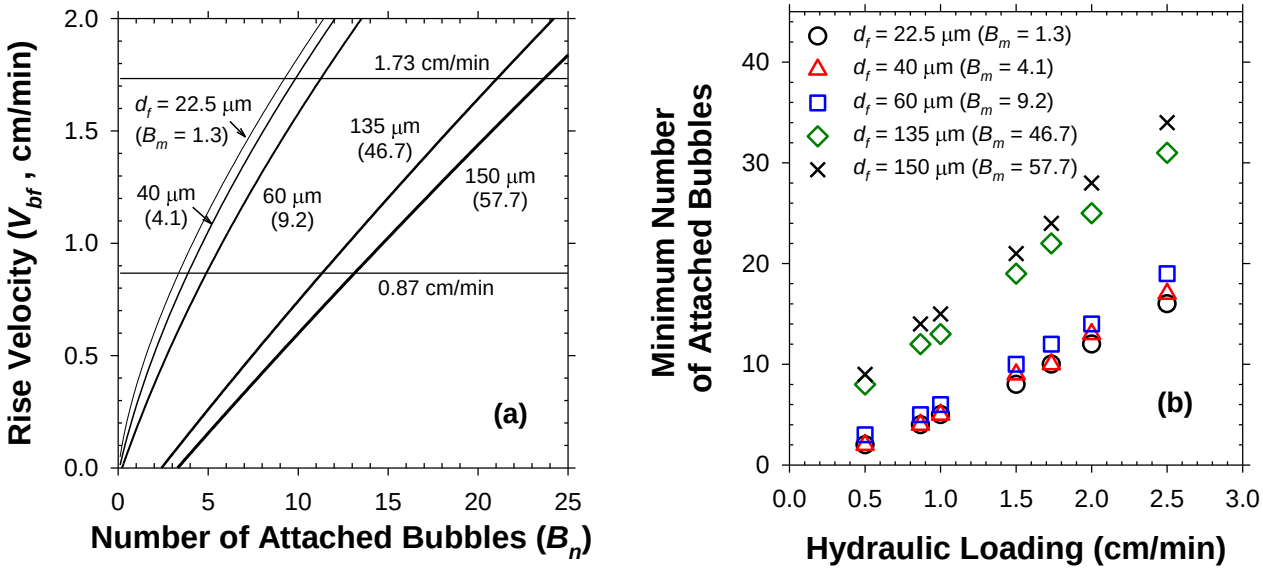

Figure 2. Relationship of (a) V_{bf} versus B_n, and (b) minimum B_n versus hydraulic loading

4.4 Effects of the G/S ratio and hydraulic loading on clarification

In continuous EF experiments, the effects of the G/S ratio on clarification efficiency were evaluated in terms of effluent SS concentration. A stable sludge blanket emerged quickly and the solids/liquid interface descended as the sludge bed extended. The incoming flocs, as well as the solids broken off from the upper bed, fell down to constitute the suspended solids in subnatant. The rising bubbles under the sludge bed capture the suspending flocs to prevent them from being dragged through with effluent. As suggested previously [3], excessive build-up of the sludge blanket was avoided to maintain the float stability especially under high G/S ratios. As clearly shown in Fig. 3, there were limiting G/S ratios for variable hydraulic loadings above which the effluent [SS] sharply decreased. In contrast, the MLSS concentration showed marginal influence on the clarification efficiency. The experimental results were in general agreement with the theoretical calculation with α_0 of 0.2. Evidences have been presented that the α_0 value could show a large

variation depending on the surface charge (zeta-potential) of flocs [19]. Further increase in G/S ratio would not raise V_{bf} infinitely due to the decline of the collision-attachment efficiency. When α value diminishes, other interactions such as bubble formation at floc surface and bubble entrapment would become significant [18]. The concomitant contact and separation in EF might further limit the operational range of hydraulic loading rate [13] in order to avoid a turbulent flow.

Eq. (2) can also give the maximum separation efficiency at a specific downflow rate. The minimum B_n exceeds B_m for particles with d_f of 22.5 μm at 0.87 cm/min. The volumetric fraction (~5%) of these flocs expected effluent [SS] greater than 100 mg/L (separation efficiency of 95%). At the loading of 1.74 cm/min, flocs with d_f of 40 μm were expected to escape as well, which leads to the separation efficiency of 83%. However, the observed clarification efficiencies were much greater than the predicted values, which would be ascribed to the averaged size of bubbles (d_b fixed at 35 μm) and neglecting finer bubbles. Incorporation of finer bubbles could bring about net increase in V_{bf} *via* large elevations in B_m and α [12, 19], although individual bubble has smaller buoyancy. Further study is necessary to consider the size distributions both for bubbles and flocs for more reliable estimation on the clarification efficiency.

Consequently, the G/S ratio needs be greater than 0.004 and 0.007 for stable clarification at the downflow rate of 0.87 and 1.73 cm/min, respectively. Considering the overall differences in gas density, these criteria correspond to 0.014 – 0.022 of A/S ratio, being in agreement with literature on the sludge clarification by DAF [6]. At G/S ratios exceeding the limiting value, the effluent [SS] was lower than 10 and 40 mg/L at 0.87 and 1.76 cm/min, respectively. As this study evinced, the buoyancy forces of electrolytic bubbles (primarily molecular hydrogen) could be employed for environmental remediation purposes. Even in the single compartment EF unit, the gaseous product is postulated to carry minimal amount of O_2 by aerobic respiration of the biological flocs, so as to be utilized for further energy conversion process.

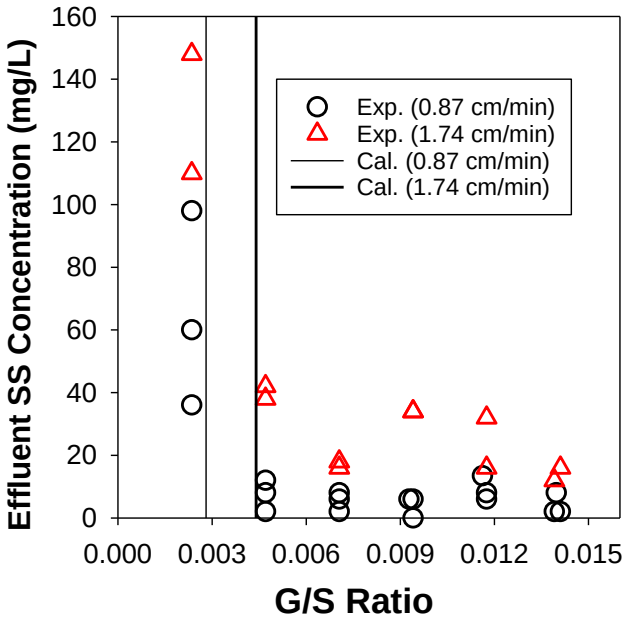

Figure 3. Relationship of effluent [SS] and G/S ratio in continuous EF experiments, in comparison with theoretical calculation.

5 CONCLUSION

The limiting mass ratio of electrolytic bubbles to solids, G/S ratio, was revisited theoretically and experimentally for clarification of activated sludge with a continuous CE. The observed size distributions of bubbles and biological flocs could be simplified to d_b of 35 μm and d_f of 22.5, 40, 60, 135, and 150 μm. At j values greater than 8 mA/cm^2, the CE was estimated to be unity for HER and 0.4 for OER so that about 80% of the electrolytic bubbles would be H_2. The G/S ratio and hydraulic loading ratio prove to be the primary factors of the clarification in continuous EF. A theoretical calculation properly predicted the limiting G/S ratio (4.2×10^{-3} and 6.6×10^{-3} at 0.87 and 1.73 cm/min, respectively), but underestimated the separation efficiency. The results of this study would broaden the usage of electrochemical water splitting for water treatment coupled with energy storage in water-energy nexus framework.

ACKNOWLEDGEMENTS

This work was financially supported by the Nano Material Technology Development Program through the National Research Foundation of Korea (NRF-2016M3A7B4908161).

REFERENCES

[1] A.A. Al-Shamrani, A. James and H. Xiao, Destabilisation of oil-water emulsions and separation by dissolved air flotation, Water Research, Vol. 36, pp. 1503-1512, 2002.

[2] M. Murugananthan, G.B. Raju and S. Prabhakar, Separation of pollutants from tannery effluents by electro flotation, Separation and Purification Technology, Vol. 40, pp. 69-75, 2004.

[3] K.W. Cho, Y.J. Kim, Y.G. Choi, S.W. Hong and T.H. Chung, Ratio of Electrolytic Bubbles to Solids as a Governing Parameter of Flotation for Activated Sludge, Environmental Engineering Science, Vol. 26, pp. 1131-1138, 2009.

[4] K.W. Cho, C.M. Chung, Y.J. Kim and T.H. Chung, Continuous clarification and thickening of activated sludge by electrolytic bubbles under control of scale deposition, Bioresource Technology, Vol. 101, pp. 2945-2951, 2010.

[5] K. Cho, C.M. Chung, Y.J. Kim, M.R. Hoffmann and T.H. Chung, Electroflotation clarifier to enhance nitrogen removal in a two-stage alternating aeration bioreactor, Environmental Technology, Vol. 34, pp. 2769-2776, 2013.

[6] J.R. Bratby and W.A. Ambrose, Design and Control of Flotation Thickeners, Water Science and Technology, Vol. 31, pp. 247-261, 1995.

[7] R. Gnirss and A. PeterFrolich, Biological treatment of municipal wastewater with deep tanks and flotation for secondary clarification, Water Science and Technology, Vol. 34, pp. 257-265, 1996.

[8] J. Haarhoff and L.R.J. Vanvuuren, Design Parameters for Dissolved Air Flotation in South-Africa, Water Science and Technology, Vol. 31, pp. 203-212, 1995.

[9] T.H. Chung and D.Y. Kim, Significance of pressure and recirculation in sludge thickening by dissolved air flotation, Water Science and Technology, Vol. 36, pp. 223-230, 1997.

[10] G.H. Chen, Electrochemical technologies in wastewater treatment, Separation and Purification Technology, Vol. 38, pp. 11-41, 2004.

[11] APHA, AWWA and WEF, Standard Methods for the Examination of Water and Wastewater, 20th ed., American Public Health Association, Washington, DC., 1998.

[12] J.K. Edzwald, Principles and Applications of Dissolved Air Flotation, Water Science and Technology, Vol. 31, pp. 1-23, 1995.

[13] K. Fukushi, N. Tambo and Y. Matsui, A Kinetic-Model for Dissolved Air Flotation in Water and Waste-Water Treatment, Water Science and Technology, Vol. 31, pp. 37-47, 1995.

[14] J.K. Edzwald, Dissolved air flotation and me, Water Research, Vol. 44, pp. 2077-2106, 2010.

[15] S. Trasatti, Electrocatalysis: understanding the success of DSA (R), Electrochimica Acta, Vol. 45, pp. 2377-2385, 2000.

[16] H. Vogt, On the gas-evolution efficiency of electrodes I - Theoretical, Electrochimica Acta, Vol. 56, pp. 1409-1416, 2011.

[17] H. Vogt, The Rate of Gas Evolution at Electrodes .1. An Estimate of the Efficiency of Gas Evolution from the Supersaturation of Electrolyte Adjacent to a Gas-Evolving Electrode, Electrochimica Acta, Vol. 29, pp. 167-173, 1984.

[18] J. Rubio, M.L. Souza and R.W. Smith, Overview of flotation as a wastewater treatment technique, Minerals Engineering, Vol. 15, pp. 139-155, 2002.

[19] M. Han, W. Kim and S. Dockko, Collision efficiency factor of bubble and particle (alpha(bp)) in DAF: theory and experimental verification, Water Science and Technology, Vol. 43, pp. 139-144, 2001.

ENERGY SITUATION AND RENEWABLES IN ALGERIA

I. Laib [1,2], A. Hamidat [3], M. Haddadi [1], K. Kaced [1], and A.G. Olabi [2]

1. Laboratory of Communication Devices and Photovoltaic Systems, Department of Electrical Engineering, National Polytechnic School, El-Harrach, Algeria; E-mail: ismail.laib@g.enp.edu.dz
2. Institute of Engineering and Energy Technologies, University of the West of Scotland, Paisley, UK; E-mail: Abdul.Olabi@uws.ac.uk
3. Centre de Développement des Energies Renouvelables, CDER, Algeria, E-mail : a.hamidat@cder.dz

ABSTRACT

The aim of this paper is to analyse briefly the Algerian energy situation, and the potential of renewable energy including, solar, wind biomass, hydro and geothermal and their applications.

Algeria is an energy producing-exporting country, the main energy sources are crude oil, flowed by natural gas. However, domestic fossil reserves are limited and harm the environment. In order to be less dependent on fossil fuel, meet the increasing energy demand and protect the environment, Algeria must diversify their energy resources. Indeed, the government gives particular importance for promoting renewable energy and improving energy efficiency, with the aim to produce 40% of electricity from renewable energy by 2030.

Solar energy is considered as a promising source in the improvement of the energy balance and the protection of the environment. In fact, it is clear that Algeria is endowed with good solar energy potentials. There is also optimism for wind and geothermal, but further work is required for comprehensive determination of geothermal and wind resources.

Despite the huge potential of renewable resources, the share of energy from renewable sources in energy balance is not significant.

Keywords: Algeria; Energy resources, renewable energy; Energy balance;

1 INTRODUCTION

The energy consumption in Algeria is increasing at a faster rate due to urban and economic development in constant progression. Energy demand could double by the year 2020 (60 MTOE, even 70 MTOE) by increasing uses of energy and activities. Statistics expect energy consumption to increase at about annual growth are of about 3.5% [1]. The use of energy in buildings represents a large share of this energy consumption and it is still in expansion. The Algerian energy strategy is decidedly towards sustainable development. In order to reduce the total energy demand and provide sustainable solutions the environmental challenges and to problems regarding the conservation of the energy resources of fossil origin, the state gives priority to the development of renewable energy.

This article presents an analysis of Algeria's energy situation, and the potential of renewable energy including, solar, wind biomass, hydro and geothermal and their applications.

The building sector, which ranks first in terms of electricity consumption for fossil fuels, is a key sector because it allows for an influence on demand, also a diagnosis of the current state of this sector shows that the importation of urban and architectural models not adapted to the Algerian climate and the intense use of mechanical means of thermal regulation led to an abuse and an energy consumption. Additionally, encouraged by the subsidy policy of electricity and gas implemented in Algeria since 1962, the national energy needs reached 55.9 Mtoe in 2015, representing an increase of 7.8% as compared to 2013 [2]. However, the economy of Algeria heavily depends on hydrocarbons export (oil and natural gas) and the current fall in oil prices caused an economic crisis, which prompted the government to review its energy policy.

2 CONVENTIONAL ENERGY

Energy plays a vital role in the economic and social development and in improving the quality of life. Much of the world's energy, however, is produced and consumed in a way that would not be viable in the long term if the technology did not evolve and the total quantities had to rise considerably.

In recent years, a great deal of research has been carried out with the objective of managing and controlling energy demand in all fields. To better understand the need for energy management, this study recalls Algerian energy context with particular attention to electrical energy.

2.1 Energy consumption

Algeria's total final consumption has steadily been increased in recent years, this increased significantly between 2005 and 2016. Fig.1 shows the evolution of energy consumption by category of sources. Like the national production, the petroleum products are the major source of energy in Algeria, followed by electricity and natural gas. According to MEM statistics for energy balance for 2016 [3], the total final energy use accounts for 55 Mtoe.

Oil and gas remain the main energy consumed by final consumers in Algeria (about 99%). Conversely, Renewable energies represent barely 0.1% of final consumption in Algeria; However, this figure is underestimated because it is often poorly known (Table1). Indeed, there is a figure of renewable energy consumption "officially" represents only a small small part of the total energy consumption.

Given the current distribution of energy consumption by sector of activity, 44% of Algeria's energy consumption is for the building sector. This is all the more worrying in view of the growth in the number of housing stock that is increasing year by year. According to the latest statistics, the latter has increased by more than two million dwellings during the last decade (Table2). The social progress and the increase in the quality of life of the Algerians were accompanied by an increase in the demands on the level of thermal comfort inside the houses. [4]

2.2 Energy production

Algeria has important potential from the point of view of proved natural gas and oil reserves, 12.2 thousand million barrels of oil and 4.5 trillion cubic meters of natural gas at the end of 2015. An analysis of Algeria's energy balance shows that the country's energy exports of petroleum and natural gas fell from 140 Million Tons Oil Equivalent (Mtoe) in 2010 to 150 Mtoe in 2016. This downward trend is related to a drop in Production, but mainly to the increase in national consumption, which rose from 38.9 Mtoe in 2010 to 54.6 Mtoe in 2016 Figure 1. [2]

In this year, Algeria produced approximately 68.5 Mtoe crude oil, of and 82.2 Mtoe of natural gas [5]. Algeria is one of the leading producer and exporter of oil and natural gas in the world. It is the fourth largest oil crude producer in Africa, and the sixth largest natural gas producer in the world [1]. Fig.1 shows the evolution of primary and derived energy production between 2005 and 2016 in Algeria.

Table 1. Algeria's energy consumption by source in 2015

Energy by source	Energy consumption (Mtoe)		
	2005	2010	2015
Oil	11.034	14.835	19.302
Natural Gas	20.904	23.683	35.118
Coal	0.594	0.310	0.179
Nuclear	0.000	0.000	0.000
Hydroelectricity	0.126	0.039	0.033
Renewables	0.000	0.002	0.018
total consumption	32.6583	38.8688	54.6495

Table 2. Evolution of the Algerian housing stock.

Year	1999	2008	2013	2015
Number of housings	5855584	6686124	7755584	8852378

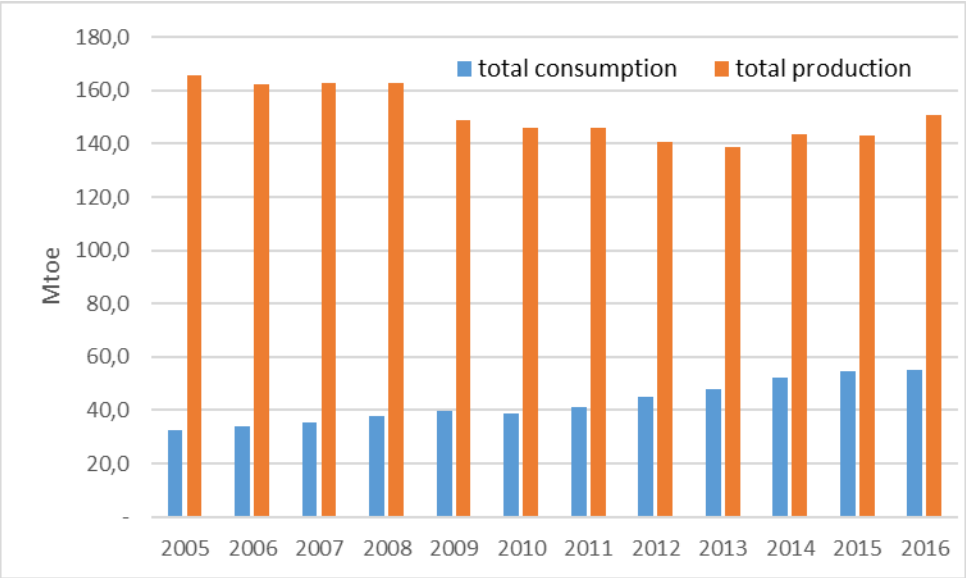

Fig.1: Production and domestic consumption of hydrocarbons in Algeria

2.3 Greenhouse gas emissions

The main cause of CO2 emissions in Algeria is fuel combustion, those emissions were just 52.73 Mt of CO2 in 1990 and reached 130.36 Mt of CO2 by 2016. Therefore, the CO2 emissions are increasing continuously.
The GHG emissions due to the final energy consumption in 2015 are 90 MT CO2, 2.357 T CO2 per capita. The total GHG emissions from primary energy consumption are 152.6 MT of CO2 [6]. These later are due mainly to petroleum products (60%) and gaseous products (40%). The transport sector is the highest producer GHG (49%) followed by residential sector by 31% and industrial sector (12%) and agriculture sector (7%). It can be noticed that the residential sector has the most important potential for GHG mitigation.

3 RENEWABLE ENERGY

As part of the implementation of the national energy policy and the development of renewable energies, Algeria is beginning a green energy dynamic. In 2011, the Algerian government launched an ambitious national program on renewable energies and energy efficiency
This program is characterized by a break with previous programs in the field of renewable energies by launching this program, Algeria is embarking on a new sustainable energy era. This strategic choice is motivated by the immense potential of solar energy. This energy constitutes the major axis of the program which devotes an essential part to the solar thermal and solar photovoltaic. Indeed, since the national potential in renewable energies is strongly dominated by solar power, Algeria regards energy as an opportunity and a lever for economic and social development,
This program is characterized by the program Grand Sud and the program of electrification of 20 villages in the south with solar photovoltaic energy. The main objectives of the current program are:

- ✓ Contribution of global and sustainable solutions to environmental challenges
- ✓ Diversification of energy sources and promotion of energy efficiency
- ✓ Preservation of fossil energy resources

3.1 Potentials:

Despite a range of efforts by the decision makers to increase access to modern energy sources in the country, the percentage of renewable energies in the national energy balance remains insignificant (0.006%) [7]. Energy policy advocates increasing the contribution of renewable energy in the national energy balance. The objective is to achieve a contribution of around 6% in the balance of power production by 2015 and 20 % by 2030. However, Algeria has a rich potential of renewable energy. The distribution of these potentials are [1]:

- ✓ Thermal solar: 169,440 TWh/year.
- ✓ Photovoltaic: 13.9 TWh/year.
- ✓ Wind energy: 35 TWh/year.

3.1.1 Solar energy

Solar energy is considered the potential source of renewable energy, the most of which is being naturally collected in the Sahara region. The insolation time over the quasi-totality of the national territory exceeds 2000 h annually and may reach 3900 h (high plains and Sahara) [8], as shown in Table 3.
The daily obtained energy on a horizontal surface of 1m2 is of 5 kWh over the major part of the national territory, or about 1700kWh/m2/year for the North and 2263 kWh/m2/year for the South of the country.

Table 3. Solar potential in Algeria

Areas	Coastal area	High plateau	Sahara
Surface (%)	4	10	86
Average duration of sunning (h/year)	2650	3000	3500
Received average energy(kWh/m2/year)	1700	1900	2650

3.1.2 Wind energy

Algeria has moderate wind speed (2 à 6 m/s), which is suitable for pumping water especially in high plateau. The annual average wind velocities in Algeria. The region of Adrar receives the most wind in the country judging from the results of the preliminary survey. Evaluations of powers recoverable at heights from 10 to 50 m could conclude in registering this region as a favorable site for the establishment of a windy farm. Other sites (North, High Plateaux) hide non-negligible energetic potentials.

3.1.3 Hydroelectricity

The overall flows falling over the Algerian territory are important and estimated to 65 billion cubic meters but of little benefit to the country: restrained rainfall days, concentration on limited areas, high evaporation and quick evacuation to the sea. In Algeria, more than 50 dams are currently operational, see Table 4.

Table 4. Hydroelectric production park [MEM, 2014]

Plant	Installed power (MW)
Darguina	71,5
Ighil Emda	24
Mansouria	100
Erraguene	16
oukEl DJEMAA	8,085
Tizi MEDEN	4,458
HZERNCHEBEL	2,712
GHRIB	7
GOURIET	6,425
BOUHANIFIA	5,7
OUED FODDA	15,6
BENI BEHDE	3,5
TESSALA	4,228

3.1.4 Geothermic energy

According to the study conducted by CDER on the geothermic energy potential in Algeria, there are more than 200 hot springs in North-East and North-West part of the country. One-third's temperatures are superior to 45 ◦C and the highest temperatures registered are 98 ◦C and 118 ◦C in Hamam El Maskhoutin and Biskra, respectively [9]. The Jurassic limestone of North Africa, which constitutes great geothermal reservoirs, is at the origin of these geothermal sources. This reservoir commonly called "Albian platform", is extended over several thousand m².

3.1.5 Biomass energy

The biomass potentially offers great promises with bearing of 3.7 millions of TEP coming from forests and 1.33 million of TEP per year coming from agricultural and urban wastes; however, this potential is not enhanced and consumed yet [10]. Biomass can be burnt directly or it can be converted into solid, gaseous and liquid fuels using conversion technologies such as fermentation to produce alcohols, bacterial digestion to produce biogas and gasification to produce a natural gas substitute. Industrial, agricultural livestock and forest residues can be used as a biomass energy source [11].
In Algeria, the current biomass potential coming from forests is about 37 Mtoe, however only 10% of this potential is recovered. The potential coming from agricultural and urban wastes is about 1.33 1.33 Mtoe.

3.2 Renewable energies applications:

The main renewable energy application are limited to electrification, pumping, telecommunication, public lighting and small refrigeration systems. The distribution of installed power per resources is shown in Table 5 and per application in Table 6 The overall installed power is 2.353MW.
Recently, the photovoltaic panels have been utilized for various applications in Algeria [10]. Some of these applications include:

- ✓ Electrification with solar power of 20 villages spread out among the four wilayas of the south: Tamanrasset, Tindouf, Illizi and Adrar. The solar energy produced by these systems is above 1.5 GWh.
- ✓ A solar hybrid (photovoltaic/diesel) power station of 13 kW in power station of 13 KW in Illizi, beaconing of 2300 km of roads.
- ✓ Supplying electricity for more than 100 telecommunications stations (650 kW).
- ✓ Electrification of more than 300 houses (550 kW), the total cost of this project was estimated at s115,000.
- ✓ 10 kW photovoltaic power station connected to the national grid.
- ✓ One oil station fed with solar energy (7 kW).
- ✓ NEAL Company: 150MW hybrid power station (solar/gas), with 34MW solar.
- ✓ Development of the market of solar energy water heater carried out by APRUE (Promotion of the Rational Use of Energy) to equip 5500 houses and 16,000 m2 in the tertiary sector.
- ✓ Rural electrification program: provide photovoltaic electricity to 16 villages with a total of 800 houses (0.5 MW).

Table 5. Distribution of installed power per resources

Resources	Installed power (Watt)	Percentage (%)
Solar	2.279.960	7
Wind	73,3	3
Total	2.353.260	100

Table 6. Distribution of installed power by application

Applications	Installed power (Watt)	Percentage (%)
Electrification	1.352.800	57,48
Pumping	288,4	12,25
Public lighting	48,43	2,05
Telecommunication	498	21,16
Others	165,63	7,03
TOTAL	2.353.260	100

4 CONCLUSION

In this paper, the energy situation of Algeria has been outlined and data for renewable energies are presented. Algeria is an energy producing-exporting country. The main energy sources is crude oil, flowed by natural gas. However, domestic fossil reserves are limited and harm the environment. In order to be less dependent on fossil fuel, meet the increasing energy demand and protect the environment, Algeria must diversify their energy resources. Indeed, government gives particular importance for promoting renewable energy and improving energy efficiency, with the aim to produce 40% of electricity from renewable energy by 2030.

Solar energy is considered as a promising source in the improvement of the energy balance and the protection of the environment. In fact, it is clear that Algeria is endowed with good solar energy potentials. There is also optimism for wind and geothermal, but further work is required for comprehensive determination of geothermal and wind resources. Despite the huge potential of renewable resources, the share of energy from renewable sources in energy balance is not significant.

REFERENCES

[1] A. Boudghene Stambouli, et al. Review on the renewable energy development in Algeria: Current perspective, energy scenario and sustainability issues. Renewable and Sustainable Energy Reviews 16(2012) 4445-4460.

[2] BP Statistical Review of World Energy, June 2016, website http://www.bp.com/statisticalreview

[3] I. Laib, A. Hamidat, M. Haddadi, N. Ramzan, A.G. Olabi," Study and simulation of the energy performances of a grid-connected PV system supplying a residential house in north of Algeria", Energy, Vol. 152, 2018, pp. 445-454. [3] BP Statistical Review of World Energy. June 2016.

[4] (APRUE). Agence Nationale pour la Promotion et la Rationalisation de l'Utilisation de l'Energie, Ministère de l'Energie et des Mines, Consommation Energétique Finale de l'Algérie, Année 2009, site Web: www.aprue.org.dz

[5] Ministère de l'énergie et des mines. Agence National pour la Promotion et la Rationalisation de l'Utilisation de l'Energie, APRUE. Consommation Energétique Finale de l'Algérie, Année 2007 (Edition 2009).

[6] Ministère de l'Energie et des Mines. Agence Nationale pour la Promotion et la Rationalisation de l'Utilisation de l'Energie. Consommation Energétique Finale de l'Algérie. Chiffres clés Année 2012.

[7] Ministère de l'Energie et des Mines. Bilan énergétique national 2013 (édition 2014). http://www.memalgeria.org/fr/statistiques/Bilan_Energetique_National_2013_edition_2014.pdf

[8] Amine Boudghene Stambouli, Promotion of renewable energies in Algeria: Strategies and perspectives. Renewable and Sustainable Energy Reviews 15 (2011) 1169 – 1181.

[9] Missoum, M., Hamidat, A., Imessad, K., Bensalem, S., Khoudja, A. Impact of a grid-connected PV system application in a bioclimatic house toward the zero energy status in the north of Algeria (2016) Energy and Buildings, 128, pp. 370-383.

[10] Y. Himri et al. Review and use of the Algerian renewable energy for sustainable development. Renewable and Sustainable Energy Reviews 13 (2009) 1584–1591.

[11] Mustafa Omer A. Renewable energy resources for electricity generation in Sudan. Renewable and Sustainable Energy Reviews 2007;11:1481–97.

POLICY AND FINANCIAL SUPPORT SCHEME FOR RENEWABLE ENERGY SOURCES UTILIZATION IN SLOVENIA

Marko Doric[1], Andreja Urbancic[2], Polona Lah[3], Fouad Al-Mansour[4], Matevz Pusnik[5], Boris Sucic[6], Leon Cizelj[7] and Andrija Volkanovski[8]

1. Energy Efficiency Centre, Jozef Stefan Institute, Slovenia; email: marko.djoric@ijs
2. Energy Efficiency Centre, Jozef Stefan Institute, Slovenia; email: andreja.urbancic@ijs.si
3. SID – Slovene Export and Development Bank Inc., Slovenia; email: polona.lah@sid.si
4. Energy Efficiency Centre, Jozef Stefan Institute, Slovenia; email: fouad.al-mansour@ijs.si
5. Energy Efficiency Centre, Jozef Stefan Institute, Slovenia; email: matevz.pusnik@ijs.si
6. Energy Efficiency Centre, Jozef Stefan Institute, Slovenia; email: boris.sucic@ijs.si
7. Reactor Engineering, Jozef Stefan Institute, Slovenia; email: leon.cizelj@ijs.si
8. Reactor Engineering, Jozef Stefan Institute, Slovenia; email: andrija.volkanovski@ijs.si

ABSTRACT

If properly planned the utilisation of renewable energy sources (RES) enables significant direct and indirect benefits and provides opportunities for technological development, employment and regional growth. However, from the implementation point of view, there is a need for initiatives and support schemes that will correct current energy market imperfections and promote concrete actions for exploiting RES for electricity generation. In a world of uncertain energy prices and rapid changes, effective support scheme for electricity generation from RES requires a clear vision of energy development strategy on a national level. The aim of this paper is to objectively evaluate the strengths and weaknesses of the support scheme for electricity generation from RES in Slovenia and to outline the most important targets and challenges for future development. Additionally, the research work described in this paper analyses the effects of the support scheme along with environmental, economic and societal benefits of RES utilisation in Slovenia. The future challenges of the RES utilisation in Slovenia are related to follow-up activities and continuous refinement of the support scheme to enable smooth transformation toward low carbon economy and creation of sustainable energy jobs.

Keywords: Sustainable energy, Renewable energy sources, Electricity generation, Support scheme mechanism, Low carbon economy

1 INTRODUCTION

Exploitation of renewable energy sources has traditionally played an important role in Slovenia's national energy policy. Slovenia has defined its national targets for RES in its National Renewable Energy Action Plan 2010-2020 (NREAP). According to [1], share of RES in Slovenia's gross final energy consumption has reach level of 22% and in order to fulfil EU's common environmental and energy Slovenia has to increase it in the next years. The NREAP has been adopted to meet the Slovenian obligation arising from the EU Directive 2009/28/EC and includes additional policies and measures to support smoother achievement of a 25% share of renewable energy sources in gross final energy consumption by 2020. To tackle the challenges and achieve the goals set, responsible policy makers will have to make some thorough energy policy adaptations as stated in [1] and [2].

The research field is very dynamic and interdisciplinary, hence a significant amount of research papers addressing challenges and obstacles of the utilisation of RES for electricity production (RES-E) have been published recently. Al-Mansour et al. [3] highlighted that in the Slovenian context exploitation of RES and energy efficiency were vital elements of long-term transition towards low-carbon society. Additionally, according to [3] the support scheme had a positive influence on the development of electricity production from solar (PV) and biogas from agricultural biomass in Slovenia. Optimal use of domestic biomass resources in Denmark are addressed in [4] with the objectives of minimizing global warming contribution. The subsidies for electricity generated from wind in Ireland are analysed in [5] and authors reported that overall wind power decreased system costs. The research work done by Taliotis et al. stated that RES technologies were cost-competitive in Cyprus, highlighting transmission – connected solar PV as the most competitive generation option [6].High-efficiency cogeneration of heat and power (CHP) is according to Jiménez Navarro et al. one of the key measures to improve the overall system efficiency and reduce total system costs and may increase

the penetration of renewable energy [7]. Slovenia has no specific targets for CHP but the high efficient cogeneration units on fossil fuels or renewable energy sources that are included in the support scheme have a potential to help Slovenia to achieve its goal of improving energy efficiency by 2020.
To accelerate the phasing-in of cleaner electricity generation technologies in EU, several types of RES utilisation supporting schemes have been launched, for example: feed-in tariffs, premium on capital remuneration, favourable dispatch and net metering or net billing systems [8]. Furthermore, feed-in tariff remuneration models have been analysed along with its own strengths and weaknesses in [9]. The future of the PV market in Germany and different scenarios regarding the feed-in tariff scheme have been analysed and discussed by Baur and Uriona [10]. The importance of long-time perspective of decisions on feed-in tariffs and alternative mechanisms are highlighted in [10], [11] and [12]. A renewable electricity certificate market scheme is analysed in [13]. The authors reported that the price of certificates depends largely on the behaviour of the market participants and that the possibility of overinvestment constitutes a threat to market stability. State of the art review on renewable electricity financing models has been done by Krupa and Harvey [14] and authors reported that interdisciplinary mind-sets would be essential to solving climate mitigation challenges, as finance was only one piece of the broader puzzle.
This paper analyses the effects of the support scheme for renewable energy sources utilization in Slovenia along with environmental, economic and societal benefits. Having in mind the framework of international and EU obligations, the real research question that arises in this context is: “How effective is the Slovenian financial support scheme for renewable energy sources utilization?

1.1 Structure of RES-E production in Slovenia

The total use of RES in 2016 in Slovenia was 1125 ktoe, which represents a 16.7% share of primary energy consumption. The two main renewable energy sources are hydro energy with a 6.1% share in primary energy or 411 ktoe, and wood with a 9.0% share in primary energy consumption or 608 ktoe. Other utilized renewable sources were biogas (from agriculture and wastes from households, restaurants, food and paper industry, sewage, landfill) with 0.4%, biofuels with 0.3%, solar energy (PV and thermal solar) with 0.2%, geothermal energy with 0.7% share of primary energy consumption and a minor contribution of wind energy. The share of RES-E production in Slovenia was 35.4% of all net electricity production in 2016. Variations in RES-E production are dependent on the hydrological situation in the country, since the majority of the electricity comes from hydropower plants. Their share in RES-E production is 89.8% of which 8.1% comes from small hydropower plants (up to 10 MW). Structure of electricity production from RES (large hydropower plants excluded) in Slovenia is presented in Figure 1.

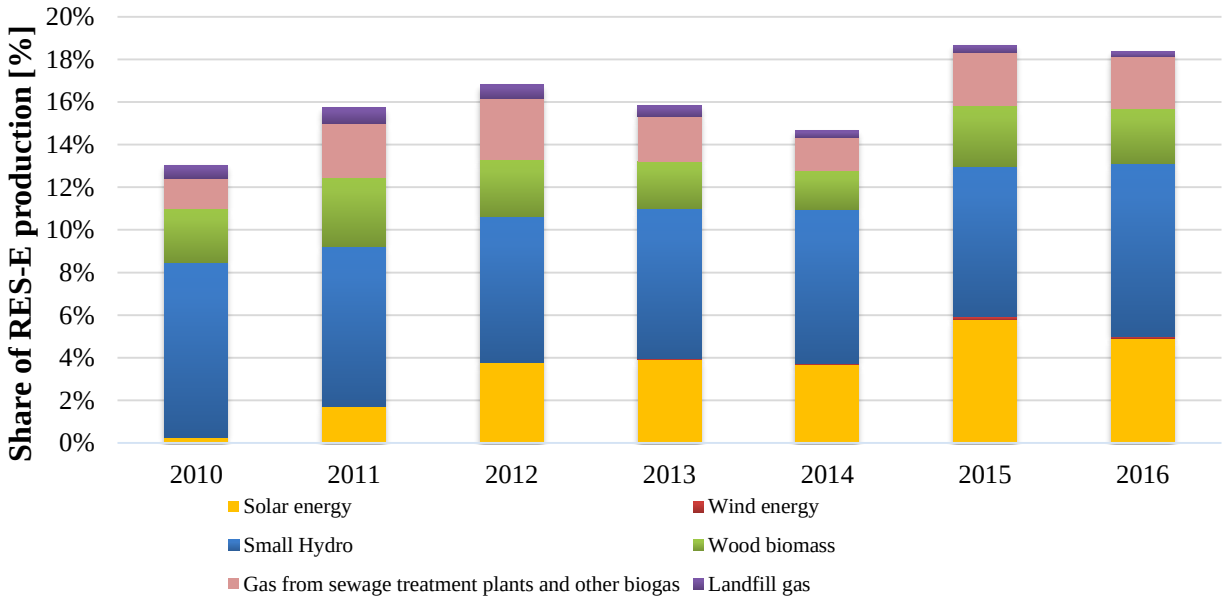

Figure 1: Structure of RES-E production (large hydro excluded) in Slovenia for the period from 2010 to 2016

Solar PV represents 5.0% of RES-E production, biogas (including landfill and sewage gas) represents 2.7% and wood biomass 2.6%. At this point, it has to be emphasised that in 2009 the share of solar PV electricity production was less than 0.1% of all RES-E production in Slovenia. Such development in recent years can be mostly attributed to the guaranteed purchase mechanism of support scheme for RES and high-efficiency CHP utilization.

2 METHODOLOGY

The feed-in support scheme is a support mechanism to subsidize renewable and high-efficiency CHP technologies for the production of electricity. According to [15], there are currently roughly 3900 power plants included in the scheme, predominantly solar PV and high-efficiency CHP. The total installed capacity is about 400 MW. The average support in 2017 (period from January to September 2017) amounted to 0.158 EUR/kWh.

The producers may opt for the support if the cost of electricity generation, including the normal market return on investment, exceeds the price that can be obtained for this type of electricity on the market. The scheme supports the production of electricity from various renewable energy sources, namely: water energy (small hydro), on shore wind, solar PV, geothermal, wood biomass, biogas originating from biomass and biodegradable waste, energy derived from landfill gas and gas derived from the sludge of treatment plants. For CHP, the support is intended exclusively for high-efficiency cogeneration of heat and power. All producers included in the scheme must issue and transfer to support centre (SC) guarantees of origin as proof of RES or CHP production.

The feed-in scheme is financed through dedicated add-on charges on the network fee bills of all users of electricity in Slovenia. To be more specific:

- contributions for RES and high-efficiency CHP, paid by all final consumers of electricity, natural gas and other gases used for network and district heating;
- contributions for the use of fossil fuels, paid by all final consumers of solid and liquid fossil fuels, liquefied petroleum gas, liquefied natural gas and heat from district heating systems;
- revenues generated by the RES and high-efficiency CHP support centre from the sale of electricity, which it has to buy from the recipients of the guaranteed purchase price.

Power plant owners have the option of choosing between two types of support [16]:

- *guaranteed purchase*, where SC takes over the electricity from the RES and high-efficiency CHP units and sells it to the market (the producer is thus included in the special balance group, operated by SC);
- *operating premium*, where the producer sells its energy on the market while SC only pays a premium as a difference between the full (guaranteed purchase) price and the market price, which is determined ex ante on a yearly level, based also on plant type.

Producers with power plants of installed capacity over 1 MW can only receive the *operating premium* type of support.

The calculation of the reference costs of electricity generation, which constitutes the upper limit of the electricity price that the electricity producer can offer in the application for the support scheme, is carried out in accordance with *Methodology for determining the price of electricity from production units and reference costs of electricity generation* [17]. In this, the methodology for calculating the reference costs of the CHP units takes into account the natural gas as the reference fuel and uses a general criterion of operating hours separating the CHP units into two groups: units with annual operating hours below 4000 and units with more than 4000 annual operating hours. The methodology [17] provided the legal and technical framework for the Slovenian Energy Agency to publish the first call for RES and CHP investment projects in late 2016. A total of 10 million EUR have been announced, and the funds were divided in the framework of a two-cycle competitive process.

For the purpose of this research work, we have obtained the technical declarations of generation units from Slovenian Energy Agency, whilst electricity generation for the specific unit has been obtained from Slovenian power market operator that administers the Slovenian electricity feed-in support scheme for RES and high-efficiency CHP. A yearly aggregate of technical declaration data of generation units has been used for the analysis. Slovenian power market operator collects the data on electricity production on monthly basis and for the purpose of this research work, a yearly aggregate has been used. According to Eisenhardt and Graebner, this represents an opportunity with unusual access to research [18].

The research work presented in this paper served as a statistical and analytical basis for the follow up assessment of national goals in the field of RES and CHP [19].

3 RESULTS AND DISSCUSSION

RES and high-efficiency CHP units that were included in the support scheme produced 1003.5 GWh of electricity in 2016. The majority of electricity was produced from natural gas, namely 31.5%, followed by solar PV with 25.9%, hydropower with 13.9% and wood biomass with 13.1% as presented in Figure 2. It is evident that high-efficiency CHP units on fossil fuels have contributed the largest share of the support scheme's total electricity production in the addressed year. Furthermore, in 2016, the total installed capacity of the production units included in the support scheme was 428 MW. Among the installed capacity the most represented ones were solar-powered installations with 60.0%, followed by natural gas with 19.2%, biogas with 6.6% (mostly from biomass) and hydropower with 6.4% as shown in Figure 2.

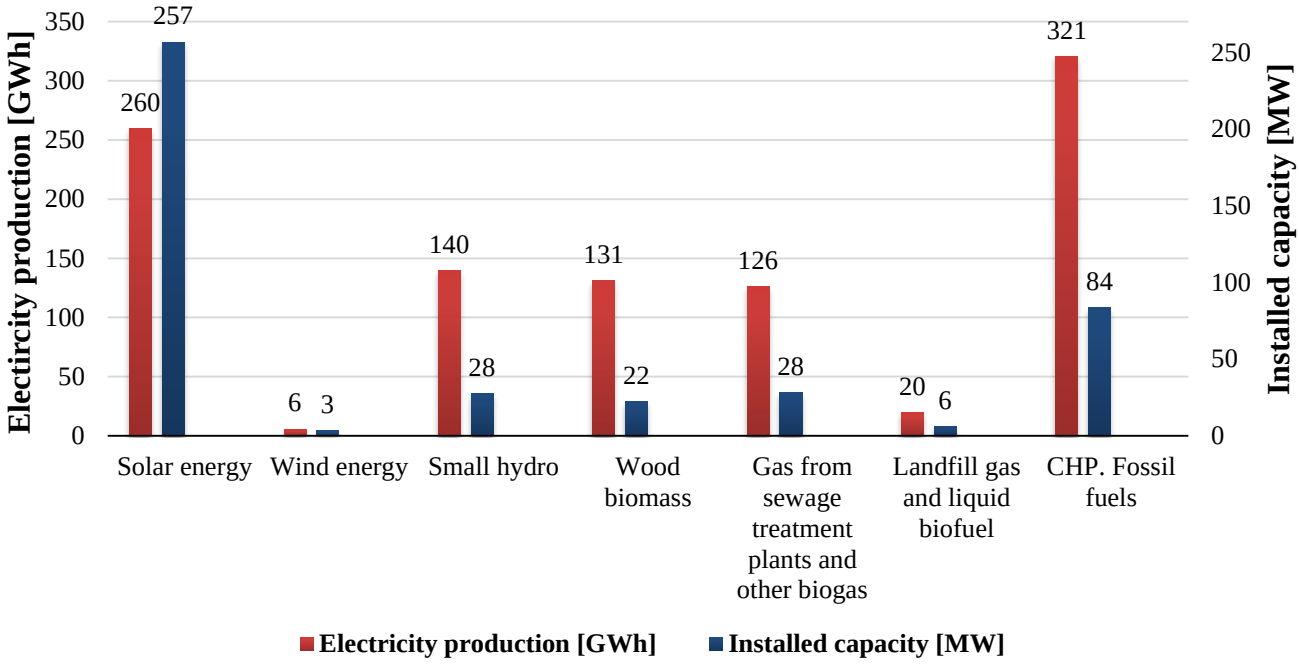

Figure 2: Electricity production and installed capacity of production units included in the support scheme in 2016

3.1 Economic impacts

The support scheme cost analysis shows that 139.2 million EUR were assigned as subsidies for electricity generation from RES and high-efficiency CHP as presented in Table 1. Most of the subsidies were allocated to solar plants, namely 63.9 million EUR and to cogeneration on fossil fuels, namely 31.1 million EUR. The structure of support costs in the existing scheme considerably varies over the years.

The structure of support recipients in 2016 is significantly different compared to the year 2010. Leading beneficiaries of subsidies have now become electricity producers from the solar, which accounted for 45.6% of all subsidies in the scheme (in 2010, 10.7%), followed by high-efficiency CHP units on fossil fuels with 22.3% (in 2010, 34.1%) and wood biomass with 13.5% (in 2010, 0%).

The share of subsidies for the production of electricity from RES and high-efficiency CHP units, in the total amount of overall subsidies in energy sector (e.g. excise duties relief on fuels, CO_2 tax relief, subsidies for energy efficiency and RES heat utilisation), is increasing. In 2010, the share of subsidies for the production of electricity from RES and high-efficiency CHP units was 24.3% and in 2015, it increased significantly to 48.2%. Although all subsidies invested in energy sector are increasing, the growth of subsidies from the support scheme is more rapid.

The costs of support for the production of electricity from RES and CHP with high efficiency in relation to GDP have been increasing over the years. In 2016, the value of support reached 0.35% of GDP. However, support for the electricity production from RES only is 0.27% of GDP which is below the EU average from year 2014 of 0.44% [20].

Table 1. Electricity production, support costs and electricity price per produced MWh for the period from 2010 to 2016

Production unit		2010	2011	2012	2013	2014	2015	2016
Solar PV	Production [GWh]	10	50	121	219	245	266	260
	Support cost [mio EUR]	3	16	34	55	59	64	64
	EUR/MWh	337	314	282	252	242	242	245
Wind energy	Production [GWh]	0	0	0	2	4	5	6
	Support cost [mio EUR]	0	0	0	0	0	0	0
	EUR/MWh	66	46	33	55	61	64	66
Hydro energy	Production [GWh]	122	94	101	131	157	120	140
	Support cost [mio EUR]	6	4	3	5	7	6	7
	EUR/MWh	50	41	34	42	47	51	53
Wood biomass	Production [GWh]	0	38	81	87	100	120	131
	Support cost [mio EUR]	0	5	9	11	14	17	19
	EUR/MWh	0	125	107	123	136	142	143
Gas from sewage TP and other biogas	Production [GWh]	84	124	125	109	106	112	126
	Support cost [mio EUR]	11	13	14	14	13	16	17
	EUR/MWh	125	105	109	126	127	141	133
Landfill gas and liquid biofuel	Production [GWh]	24	26	27	25	23	20	20
	Support cost [mio EUR]	1	0	0	1	1	1	1
	EUR/MWh	30	16	15	23	60	73	58
CHP fossil fuels	Production [GWh]	163	184	199	230	271	338	321
	Support cost [mio EUR]	11	14	17	23	27	34	31
	EUR/MWh	67	76	86	101	99	101	97
Total support cost [mio EUR]		32	52	78	109	122	139	139

3.2 Societal impacts

In 2016, the share of RES and high-efficiency CHP incentives in a typical household accounted for 17 % of its final electricity price. Due to the costs for promoting the production of electricity from RES and high-efficiency CHP, a typical household (annual consumption: 3500 kWh, connected load: 11 kW) had a monthly electricity cost increased by more than 8 EUR in 2016. For the industrial consumers, an exemption for the payment of the RES and high-efficiency CHP incentives was introduced in 2015 in accordance with the Act on support for the production of electricity from RES and high efficiency CHP [21]. In 2016, the share of RES and high-efficiency CHP incentives contribution for a typical industrial consumer (annual consumption: 50000 MWh, connected load: 10 MW) that did not meet the conditions for the exemption represented 20% of the final electricity price. Assessment of new jobs creation has been done only for installations in the support scheme, built in the period from 2010 to 2014. The analysis has shown that 270 new jobs were created for the operation, maintenance and fuel supply and 7114 one-year jobs were created for the construction and installation of those units.

3.3 Environmental impacts

Units in the support scheme have produced 59 ktoe of electricity and 32 ktoe of heat in 2016 or total 91 ktoe of energy from RES that equals 8.0% in final gross consumption of all RES. The electricity generation in the scheme accounted for 14.3% of the electricity produced from RES in that year. The support scheme has significantly contributed to the increase of the RES share towards the 25% target in 2020. In 2016, the contribution of the support scheme to the fulfilment of the national RES target increased, and the units receiving support contributed 1.8 percentage points to the 22% share of RES in the production of electricity and heat. Due to the operation of high-efficiency CHP units that were included in the support scheme, primary energy savings in 2016 were more than tripled (factor 3.3) in comparison to the year 2010, amounting to 51.2 ktoe. The support scheme also contributes to the achievement of Slovenia’s climate goals. Estimated savings in GHG emissions due to electricity generation in the support scheme and related heat production in high-efficiency CHP units in 2015 amounted to 535.5 kt CO_2 ekv that equals 3.04% of overall Slovenia's GHG emissions in same year.

4 CONCLUSION

The analysis of the support scheme for the promotion of electricity generation from RES and high-efficiency CHP has shown that the scheme has a significant impact on the fulfilment of Slovenia's international obligations in the field of RES utilization and energy efficiency. In 2016 the addressed scheme contributed 1.8% to the 22% share of RES in gross final energy and 51.2 ktoe of primary energy has been saved. The effectiveness of the scheme is slowly improving, reflecting the activities of previous years. The average support cost has stabilized, mostly due to lower energy prices on the market. RES and CHP utilization scheme has an important impact on the Slovenian economy as a whole and in order to increase overall effects of the addressed mechanism a stable and well-defined development environment is essential.

REFERENCES

[1] Draft Action Plan for Renewable Energy for the period 2010-2020 - update 2017, Ministry for Infrastructure, Republic of Slovenia, 2017.

[2] National Energy Efficiency Action Plan (NEEAP) for the 2017-2020 period, Ministry of Infrastructure, Republic of Slovenia, 2017.

[3] F. Al-Mansour, B. Sucic and M. Pusnik, Challenges and prospects of electricity production from renewable, *Energy*, vol. 77, pp. 73-81, 2014.

[4] D. Tonini, C. Vadenbo and T. F. Astrup, Priority of domestic biomass resources for energy: Importance of national environmental targets in a climate perspective, *Energy*, vol. 124, pp. 295-309, 2017.

[5] V. Di Cosmo and L. Malaguzzi Valeri, Wind, storage, interconnection and the cost of electricity generation, *Energy Economics*, vol. 69, pp. 1-18, 2018.

[6] C. Taliotis, E. Taibi, M. Howells, H. Rogner, M. Bazilian and M. Welsch, Renewable energy technology integration for the island of Cyprus: A cost-optimization approach, *Energy*, vol. 137, pp. 31-41, 2017.

[7] J. Jiménez Navarro, K. Kavvadias, S. Quoilin and A. Zucker, The joint effect of centralised cogeneration plants and thermal storage on the efficiency and cost of the power system, *Energy*, vol. 149, pp. 535-549, 2018.

[8] J. Pinho, J. Resende and I. Soares, Capacity investment in electricity markets under supply and demand uncertainty, *Energy*, vol. 150, pp. 1006-1017, 2018.

[9] T. Couture and Y. Gagnon, An analysis of feed-in tariff remuneration models: Implications for renewable energy investment, *Energy Policy*, vol. 38, no. 2, pp. 955-965, 2010.

[10] L. Baur and M. Uriona, Diffusion of photovoltaic technology in Germany: A sustainable success or an illusion driven by guaranteed feed-in tariffs?, *Energy*, vol. 150, pp. 289-298, 2018.

[11] M. García-Álvarez, L. Cabeza-García and I. Soares, Assessment of energy policies to promote photovoltaic generation in the European Union, *Energy*, vol. 151, pp. 864-874, 2018.

[12] G. Martinopoulos and G. Tsalikis, Diffusion and adoption of solar energy conversion systems – The case of Greece, *Energy*, vol. 144, pp. 800-807, 2018.

[13] M. Hustveit, J. S. Frogner and S. E. Fleten, Tradable green certificates for renewable support: The role of expectations and uncertainty, *Energy*, vol. 141, pp. 1717-1727, 2017.

[14] J. Krupa and L. D. D. Harvey, Renewable electricity finance in the United States: A state-of-the-art review, *Energy*, vol. 135, pp. 913-929, 2017.

[15] Borzen - Slovenian Power Market Operator, Slovenian Feed-in Support System for Electricity from RES and High-efficiency CHP - Periodic Report from 1.1.2017 to 30.9.2017, Borzen - Slovenian Power Market Operator, 2017.

[16] Borzen - Slovenian Power Market Operator, [Online]. Available: https://www.borzen.si/en. [Accessed 12 March 2018].

[17] S. Merse, D. Stanicic, F. Al-Mansour and P. Lah, Methodology for determining the price of electricity from production units and reference costs of electricity generation, Ministry for Infrastructure, Republic of Slovenia, 2016.

[18] K. M. E. a. M. E. Graebner, Theory Building From Cases: Opportunities And Challenges, *Academy of Management Journal*, vol. 50, no. 1, pp. 25-32, 2007.

[19] The Energy Agency, Follow up assessment of national goals in the field of RES and CHP for the period from 2015 to 2016, The Energy Agency, Republic of Slovenia, 2017.

[20] Status Review of Renewable Support Schemes in Europe, Council of European Energy Regulators, Brussels, 2017.

[21] Act on support for the production of electricity from RES and high efficiency CHP, Republic of Slovenia, 2015.

HOW TO MONITOR THE IMPACTS OF RENEWABLE ENERGY TECHNOLOGIES FOR NATURE AND LANDSCAPE PROTECTION

G. Erdmann[1] , M. Eichhorn[1] , G. Oehmichen[1] and D. Thrän[2]

1. Helmholtz-Centre for Environmental Research GmbH - UFZ, Department Bioenergy, Leipzig, Germany; email: georgia.erdmann@ufz.de; marcus.eichhorn@ufz.de; gunnar.oehmichen@ufz.de
2. German Biomass Research Centre – DBFZ, Department Bioenergy Systems, Leipzig, Germany; email: Daniela.thraen@dbfz.de

ABSTRACT

Renewable energies (RE) are the backbone of a sustainable energy supply in Europe. The related energy technology infrastructure (RETI) has been built up all over the countries (bioenergy, wind-turbines, water-power, photovoltaics, underground cables, aboveground lines) and leads to an increasing impact on nature and environment.

To ensure the detection and supporting the prevention of impacts of RETIs on subjects of conservation at an early stage we need a sound monitoring. We developed a concept for a threefold monitoring in Germany which gives information about (1) the achievements of targets concerning spatial efficiency of the RETIs, (2) the types and extent of conflicts of renewable energy technologies at a spatial scale and (3) the chronological effects of legal regulations on the expansion of RETIs. We developed 10 indicators according to the Drivers-Pressures-State-Impacts-Responses-scheme and evaluated the respective relevance, information value, feasibility and data availability. The strengths and weaknesses of the concept will be presented in detail.

The monitoring is continuously extendable and adaptable (to changing data availability and knowledge). The developed concept is a smart and extensive approach which can be easily adapted to other regions and countries to support the sustainable expansion of RETI.

Keywords: Renewable Energies, Renewable Energy Technology Impacts, Nature Conservation, Landscape, Monitoring Concept, Bioenergy, Wind-turbines, Water-power, Photovoltaics, Underground Cables, Aboveground Lines

1 INTRODUCTION

The transformation of the energy system is one of the great challenges. Renewable energies are a backbone of a sustainable energy supply. Different technologies are available to provide renewable power, such as wind turbines, photovoltaics, biogas and biomass plants and hydropower systems. Renewable energies have a lower energy density. While they lead to significant climate gas reduction, the expansion of renewable energy technologies and their accompanying infrastructure is related to increased land usage and leads to an increasing impact on nature and the environment. Effects may be induced directly or indirectly through construction, servicing and operation of RETIs and could have negative impacts on the preservation of habitats, populations, species and biodiversity. For example, effects are the collision of birds and bats with wind-turbines or aboveground lines [1, 2], barrier effects for aquatic fauna along dams [3] or the ploughing of grassland and related habitat loss due to crop cultivation for biogas plants [4]; the disturbance and displacement of birds by wind-turbines [5] or sedimentation and habitat loss due to reduced flow rates at dams [6].

Effects on nature and environment are manifold and multifactorial, the effects of RETIs are a part and their impacts are complex. The effects of RETIs are not yet fully explored and change dynamically. Previous developments are measured selectively so far. Therefore we need a regular and sound monitoring. Current monitorings in Germany are dealing with energy-economical aspects from the technology perspective [7] and with climate protection and nature conservation from the protective goods perspective e.g. [8, 9]. Effects of multiple RETIs and summarized effects are not under systematic and regular consideration.

Aim of our study was to develop a concept for a monitoring which includes informative, transparent, easy understandable and regularly computable indicators. It should build on (1) a comprehensive database on RETIs and their spatial location with regular updates, (2) a data base on proven effects of RETIs on nature and environment and (3) data on habitats and the spatial distribution of affected species and sensitivity of

populations. Conflicts from a legal (German Federal Nature Protection Law, EU Birds and Habitat Directive, EU Water-framework directive) as well as from an ecological perspective were considered.

2 CONCEPT

The general principle of a monitoring is the systematic and regular measurement or observation of processes or frameworks. To develop a monitoring system the first question is, what to monitor. Ideally there are clear political targets and the progress towards these targets is to be observed and assessed. For a monitoring of the effects of RETIs on nature and environment we need to go beyond: There are many spatial explicit conflicts to be considered and governed. We meet these challenges by creating a comprehensive RETI-data base and a threefold monitoring which gives information about (1) the achievements of targets concerning spatial efficiency of the RETIs (2) the types and extent of conflicts of renewable energy technologies at a spatial scale subdivided into a top-down and bottom-up approach and (3) the chronological effects of legal regulations on the expansion of RETIs. We developed 10 indicators according to the Drivers-Pressures-State-Impacts-Responses-scheme [10] and the respective relevance, information value, feasibility and data availability.

3 TARGET MONITORING

Nature protection agencies have declared selective goals and indicators to ensure the nature-compatible expansion of REs [11]. These objectives should be achieved in a monitoring system. They comprise of:

(1) primary energy consumption and proportion of renewable energy.
(2) proportion of energy from rooftop-photovoltaics to energy from photovoltaics in total
(3) land consumption per renewable energy unit (m²/MWh)
(4) proportion of bioenergy from residues and waste material to bioenergy in total
(5) further expansion and location of wind turbines in comparison to a target system of theoretical optimal locations

4 CONFLICT MONITORING

Monitoring the effects of RETIs on subjects of conservation should focus as much as possible on the direct effects on individuals, populations, species and habitats in order to obtain indicators with a high informative value. However, this approach is very limited due to the complexity of causes and effects in such a multifactorial interconnected system. Also, data availability of ecological data, species distribution and state of populations are restricted. Therefore, a standardised and transparent procedure to deduce systematically the most powerful, understandable and feasible indicators was developed following two tracks – the top-down and bottom-up approach based on the Drivers-Pressures-State-Impact-Response-scheme (DPSIR) [10].

The DPSIR-scheme is a framework to describe interactions between human impacts and the environment. The scheme differentiates between driving forces (Drivers) such as social and economic trends which results in strains (Pressures) such as pollution or land-use change and may change the situation (State) of protected goods such as water and soil quality, habitats, vegetation or species. These changes (Impacts), e.g. habitat fragmentation and biodiversity loss, may result in actions and implementations (Responses) e.g. legislation, technical and further measures [10]. Feedback-loops are inherent in the scheme, e.g. responses in form of changed legal situations will modify drivers, pressures, state and impacts on the environment.

Adapting the components of the DPSIR-scheme to the monitoring of effects of RETIs on the environment, the indicators comprises of (1) Drivers: energy policy and expansion targets (2) Pressures: spatial and technological features of the RETIs in relation to the subject of conservation, (3) State: state of subjects of conservation which are affected by RETIs, (4) Impact: changes in the state of subjects of conservation their sensitivity and (5) Response: changes in the involved legal framework and technical measures to minimise Drivers and /or enhance the State of the subject.

4.1 Top-Down Approach

The Top-Down approach takes the most important conflicts of RETIs on subjects of conservation under consideration. Aim is to describe indicators for each conflict and each of the five categories of the DPSIR-scheme.

In a first step, a literature review was done, extracting and listing all possible conflicts. In total, 54 conflicts were identified, too much to process all of them completely at high quality standards. Therefore, an expert survey was conducted and experts were asked about the importance of the conflicts and the confidence in

their assessment. The most important and reliable conflicts are caused by wind turbines, water power and bioenergy and are related to direct impacts on bats, birds and aquatic fauna and loss of grassland, fallow land and habitat changes in general (see top-ten list in table 1).

Table 1. Results of the expert survey: the most important and reliable conflicts of RETIs on subjects of conservation

Ranking of conflicts	Technology	Conflict
1	Wind turbines	Bat collision
2	Wind turbines	Bird collision
3	Water power	Barrier for aquatic fauna
4	Bioenergy	Biodiversity loss due to monoculture
5	Bioenergy	Water pollution due to waste water
6	Bioenergy	Grassland ploughing/intensification
7	Bioenergy	Loss of fallow land
8	Power lines	Impact on landscape
9	Water power	Habitat changes (sediments, flow)
10	Power lines	Bird collision

In the next step, indicators for each of the top-ten conflicts for the driver, pressure, state, impact and response category were defined. The methodology and all necessary data and their availability, accessibility and quality will be described for each indicator. From this information, the quality and feasibility of the five indicators for each conflict will be assessed according to informative value, comprehensibility, spatial and temporal resolution, data availability, accessibility and quality, effort for the calculation and regular calculability. The indicator with the highest rating in combination with data availability will be calculated for the respective conflict. Indicators with high informative values and comprehensibility but missing data will be described and missing points will be outlined. This allows pointing out flaws to decision-makers and may support closing data gaps in the future.
This stringent and systematic approach is applicable to all conflicts of RETIs on subjects of conservation and to comparable monitoring-projects in other countries

4.2 Bottom-Up Approach

The bottom-up approach does not start at the direct conflicts as the top-down approach, instead focussing on pressures. Aim is to give basic information about the spatial distribution, abundance and land consumption of RETIs in specific land use classes, their relation to protected areas and their pressure on the landscape. The quantification of pressures might indicate potential conflicts in a rather indirect way. However, our created data base of RETIs, their technological features and their location is comprehensive and profound. Land cover data are available from the CORINE-Project (Coordination of Information on the Environment) for the reference years 1990, 2000, 2006 and 2012 [12] and spatial data of protected areas such as conservation area, biosphere reserve, nature and national parks, special protection areas (EU Bird Directive and Habitat Directive) are available from the Federal Agency for Nature Conservation and the European Commission. Therefore, the bottom-up approach offers a high spatial and temporal resolution and results are (partially) comparable between different types of RETIs. Dramatic expansion of the number and land usage of RETIs in specific land use classes and decreased distances to protected areas can be detected and provide a data basis to discuss the dimension of negative impacts on subjects of conservation.

5 GOVERNANCE MONITORING

The governance monitoring considers and focusses on the feedback-loop of changed legal and governmental situations (Response) on all other components of the DPSIR-scheme.
In Germany, in the past 20 years, the Renewable Energy Act (EEG) guides the development of RETIs. Analyzing the effects of the EEG on the expansion of RETIs and taking environmental compatibility into account could help to identify and control key elements and to improve future legislations. The elements of the governance monitoring are currently under discussion.

6 DISCUSSION

With the presented approach we developed a comprehensive concept for the monitoring of RETIs and their effects on nature and environment. The complexity of effects of RETIs on the environment and the interaction with other factors, which affect nature and environment, the restricted data availability and quality, especially of ecological data was a great challenge. We solved the challenge by developing a threefold approach.

The Target Monitoring focusses on realistic and measurable objectives which are in the range of energy efficiency and spatial efficiency. Foci of the Conflict Monitoring were the direct effects of RETIs on individuals, populations, species and habitats. With the categorizing of indicators according to the DPSIR-scheme and a top-down approach from R (Response) to D (Drivers) we were able to deduce systematically the most feasible and significant indicators for the most important conflicts despite restricted data availability. The specification of target values for the Conflict Indicators requires intense discussion and debates. However, the Response Indicators may give hints for further recommendations for action. The Pressure Indicators from the bottom-up approach are easy to assess in comparison to the State, Impact, and Response indicators from the top-down approach. They provide data on the spatial and temporal development of RETIs in the landscape, in land use classes and in relation to protected areas. The discharge of impacts on subjects of conservation remains to discuss. The Governance Monitoring allows recommendations for action for the future, based on the analysis of past developments of installation of RETIs and the respective changes in legislation.

The three levels of the monitoring allow a transparent and adaptive monitoring system which is compatible with political needs (Target and Governance Monitoring) as well as taking the complexity of conflicts of RETIs on nature and environment into account (Conflict Monitoring with top-down and bottom-up approach).

ACKNOWLEDGEMENTS

The authors would like to thank the Federal Ministry for the Environment, Nature Conservation and Nuclear Safety for project funding and the Federal Agency for Nature Conservation for the support of the project.

REFERENCES

[1] Kuvlesky, William P., Jr.; Brennan, Leonard A.; Morrison, Michael L.; et al., Wind energy development and wildlife conservation: Challenges and opportunities, *Journal of Wildlife Management*, Vol. 71, pp. 2487-2498, 2007.

[2] Dudgeon, David; Arthington, Angela H.; Gessner, Mark O.; et al., Freshwater biodiversity: importance, threats, status and conservation challenges, *Biological Reviews*, Vol. 81, pp. 163-182, 2006.

[3] Drewitt, Allan L.; Langston, Rowena H. W., Assessing the impacts of wind farms on birds, *IBIS*, Vol 148, pp. 29-42. 2006.

[4] Popp, J.; Lakner, Z.; Harangi-Rakos, M.; et al. The effect of bioenergy expansion: Food, energy, and environment, Renewable and Sustainable Energy Reviews, Vol. 32, pp. 559-578. 2014.

[5] Kondolf, GM, Hungry water: Effects of dams and gravel mining on river channels, Environmental Management, Vol. 21, pp. 533-551, 1997.

[6] Federal Ministry for Economic Affairs and Energy. Statistical Report Renewable Energy Act, 2016.

[8] EEA / European Environment Agency, Progress towards the European 2010 biodiversity target – indicator fact sheets - EEA Technical report No 5/2009: 2009.

[9] Federal Statistical Office of Germany, Sustainable development in Germany: Indicator Report 2016. 2017.

[10] EEA / European Environment Agency. Environmental Indicators: Typology and Overview. 1999.

[11] Federal Ministry for the Environment, Nature Conservation and Nuclear Safety; http://www.bmu.de/fileadmin/Daten_BMU/Download_PDF/Naturschutz/5_punkte_energiewende_bf.pdf

[12] https://land.copernicus.eu/pan-european/corine-land-cover

ERROR ANALYSIS AND AUTO CORRECTION OF HYBRID SOLAR TRACKI NG SYSTEM USING PHOTO SENSORS AND ORIENTATION ALGORITHM

Junbin Zhang[1], Zhuojun Yin[1], Runze Cao[1], Xiujie Li[1], Chuangjun Huang[1], Peng Jin[1]

1. Green Lighting System Lab, School of Environment and Energy, Peking University Shenzhen Graduate School, Shenzhen, CHINA; email: jinpeng@pkusz.edu.cn

ABSTRACT

In order to further improve the efficiency of concentrating photovoltaic (CPV) or daylighting harvest systems, a high accuracy solar tracking system is required. The solar tracking error is the combined result of various sources, such as the azimuth rotational axis tilt, latitude and longitude position deviation, installation deviation, true north meridian deviation, algorithm calculation error and mismatch error of photo sensors, etc. Therefore, error compensations are critical for high precision solar tracking. In this paper, we designed and tested a dual-axis hybrid solar tracking system using both photo sensors and orientation algorithm. In addition, installation deviation of azimuth, elevation reference position error and true north meridian deviation for solar trajectory tracking accuracy are also analyzed and effectively compensated. The field test shows that the overall tracking accuracy of the system is improved after the correction.

Keywords: Daylight Harvesting, Error Correction, Dual-axis solarTracking, CPV

1 INTRODUCTION

Solar energy is the ultimate renewable and clean energy to solve the increasing energy demand while reducing the CO_2 emission[1]. Solar energy has been harnessed in various forms such as PV, solar thermal, CPV and concentrated solar power (CSP), etc[2]. Solar energy is intermittent due to the weather and sun movement, and some applications the energy conversion efficiency is higher when tracking the sun and concentrated solar beam hundreds time, such as CPV, CSP and our daylight harvesting system with concentration and tracking for indoor lighting[3, 4, 5, 6, 7]. As the concentration ratio increase, it will require higher angular tracking accuracy[8]. In addition, the reliability and cost of tracking system are also key factors in making those system competitive in the market. In low tracking accuracy requirement for a regular PV without concentration, an open loop single axis tracking method can be used, where the PV panel rotated automatically[9, 10]. In order to reach higher concentration of over 100 suns, the typical required tracking accuracy are in the range of $\pm 0.5°$ to $\pm 2°$, where dual axis tracking are needed[11]. For design of a cost-effective, precise sun tracking assembly, it requires that tracker should be able to withstand the weight of all components and wind loads, and compensate any system or random errors within certain tolerable bounds [12].

2 SOLAR TRACKING SYSTEM

The core of solar tracking system is composed of two main parts: tracking mechanism and tracking algorithm. The tracking mechanism is classified into single axis tracking and dual axis tracking. The single axis tracking application is limited to PV or Low concentration PV (LCPV), where solar concentration ratio is 2–10 suns[13]. Biaxial tracking is required with concentration ratio is over 10 suns[14]. The dual axis can be done purely using geological location and solar time algorithm, and coordinating the sun position by the latitude and longitude angles. The advantage of algorithm is running automatically without weather interference, while the disadvantage is the cumulative error over time. The photoelectric tracking is to detect a sun light direction by photoelectric sensors which requires direct solar radiation and can be affected by clouds.

We designed a horizontal dual axis structure as shown in the Fig.1, which used a hybrid tracking algorithm combining photoelectric tracking and orientation algorithm.

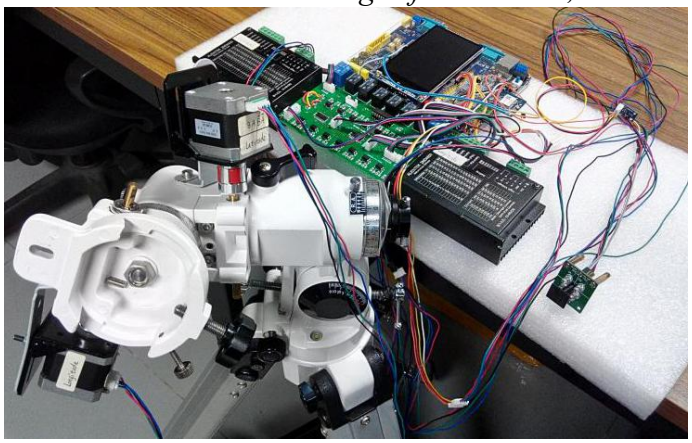

Fig.1 The hybrid dual axis tracking system

3 PHOTOELECTRIC TRACKING ERROR ANALYSIS AND CORRECTION

3.1 The Principle of Photoelectric Tracking

The photoelectric tracker uses four photodiodes, which are symmetrically placed on four quadrants as shown in Fig.2 (a). They are divided into two directions: X axis and Y axis. The O point is the center of photoelectric sensors which is seeking alignment with sunlight. A shade plate is used to block the sunlight forming a shadow as marked gray in the Fig.2 (b). The shadowing causes four photodiodes giving different current outputs and voltage reading $U_{1,2,3,4}$.

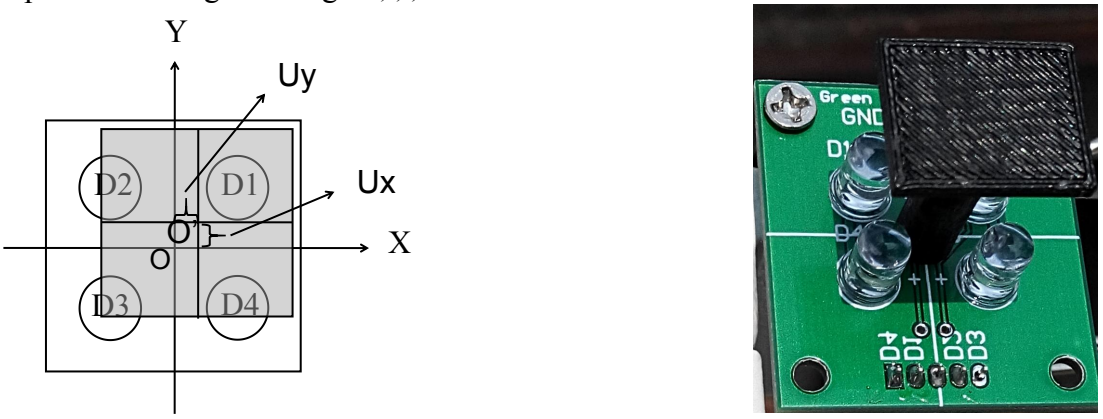

(a) Schematic diagram (b) Physical sample

Fig.2 The four-quadrant photoelectric sensor

As shown in Fig.2 (a), when the sunlight is obliquely incident on the photodiodes, the offsets of the shadow center O' deviation from the O point are U_x and U_y respectively[15]. When U_x=U_y=0, the O' coincides with the O point, indicating that the direction of sunlight is perpendicular to the photoelectric sensor. For a photodiode, the stronger the received light, the smaller the output voltage. Therefore

$$\begin{cases} U_x = U_1 - U_2 + U_4 - U_3 \\ U_y = U_1 - U_4 + U_2 - U_3 \end{cases} \quad (1)$$

In order to eliminate the influence of shadow's own power change on U_x and U_y, its needs to be normalized to E_x and E_y as shown in Equ. (2).

$$\begin{cases} E_x = \dfrac{U_1 - U_2 + U_4 - U_3}{U_1 + U_2 + U_3 + U_4} \\ E_y = \dfrac{U_1 - U_4 + U_2 - U_3}{U_1 + U_2 + U_3 + U_4} \end{cases} \quad (2)$$

3.2 Photodiodes Mismatch and Correction

The mismatch of photodiodes will cause the E_x and E_y to be none-zero even the solar ray is directly normal to the diodes plane. The mismatch reading of photodiodes can be from physical properties of diodes and

background lighting as well[16]. Therefore, we make the calibration on U_i when the light is the normal direction, when O' and the O points overlap. The normalized initial U_{i_init} values are in Equ. (3).

$$\begin{cases} U_{1\_init} = \dfrac{U_1}{U_1+U_2+U_3+U_4} \\ U_{2\_init} = \dfrac{U_2}{U_1+U_2+U_3+U_4} \\ U_{3\_init} = \dfrac{U_3}{U_1+U_2+U_3+U_4} \\ U_{4\_init} = \dfrac{U_4}{U_1+U_2+U_3+U_4} \end{cases} \tag{3}$$

During photoelectric tracking, the calibration value of the photodiodes data U'_i is calculated by Equ.(4). The after calibration value of $U_{i\_correct}$ is used to calculate Ex and Ey.

$$\begin{cases} U_{1\_correct} = \left(\dfrac{U_1^{'}}{U_1^{'}+U_2^{'}+U_3^{'}+U_4^{'}} - U_{1\_init} \right) \times \left(U_1^{'}+U_2^{'}+U_3^{'}+U_4^{'} \right) \\ U_{2\_correct} = \left(\dfrac{U_2^{'}}{U_1^{'}+U_2^{'}+U_3^{'}+U_4^{'}} - U_{2\_init} \right) \times \left(U_1^{'}+U_2^{'}+U_3^{'}+U_4^{'} \right) \\ U_{3\_correct} = \left(\dfrac{U_3^{'}}{U_1^{'}+U_2^{'}+U_3^{'}+U_4^{'}} - U_{3\_init} \right) \times \left(U_1^{'}+U_2^{'}+U_3^{'}+U_4^{'} \right) \\ U_{4\_correct} = \left(\dfrac{U_4^{'}}{U_1^{'}+U_2^{'}+U_3^{'}+U_4^{'}} - U_{4\_init} \right) \times \left(U_1^{'}+U_2^{'}+U_3^{'}+U_4^{'} \right) \end{cases} \tag{4}$$

4 SOLAR TRACKING ERROR ANALYSIS AND CORRECTION

4.1 Solar Tracking Error Analysis

The tracking error of the dual-axis solar automatic tracking system is caused by many factors, including installation error, positioning error, time error, calculation error, mechanical error, etc[17]. However repetitive and systematic in nature, those errors are still hard to fully eliminated. The calculation error can be reduced using the better algorithm. The mechanical error is the hardest to grasp. In the dual-axis tracking system, the azimuth axis should align with the geographical axis (or rotational axis). The pitch axis should perpendicular to the horizontal plane. This paper mainly analyzes the errors caused by installation and positioning, such as the horizontal deviation of the azimuth axis and the vertical deviation of the pitch axis installation.

For the solar trajectory tracking algorithm, the sun altitude angle h and azimuth angle γ calculation formula is

$$\sinh = \sin\varphi\sin\delta + \cos\varphi\cos\delta\cos\omega \tag{5}$$

$$\sin\gamma = \frac{\cos\delta\sin\omega}{\cosh} \tag{6}$$

In the Equ. (5) and Equ. (6), ω is the sun's hour angle, δ is the sun's declination angle, and φ is the local geographic latitude [15].

As shown in Fig.3 (a), assuming the pitching axis O is perpendicular to the horizontal plane, and the angle of the azimuth axis deviating from the S-N axis is α. This is due to the azimuth axis horizontal installation deviation from the S-N axis. The actual calculation of the solar azimuth angle can use Equ. (7) for compensation.

$$\gamma^{'} = \arcsin\gamma - \alpha \tag{7}$$

As shown in Fig.3 (b) , the azimuth axis is the S-N axis and the angle of the pitch axis deviating from the O axis is β, where the pitch axis not perpendicular to the horizontal plane. The actual calculation of the solar altitude angle h' can use Equ. (8) for compensation.

$$h^{'} = \arcsin h + \beta \tag{8}$$

In the installation of the tracking mechanism, it is difficult to ensure that the pitch axis and the azimuth axis are completely orthogonal, and angular errors, α and β, both exist.

（a）Azimuth axis horizontal deviation　　（b）Pitch vertical deviation

Fig.3 Schematic diagram of azimuth axis and pitch axis deviation

4.2 Solar Tracking Error Correction

The correction the solar tracking errors is in two steps. First, start with tracking using GPS and solar time algorithm, and record the altitude angle (Altitude_angle_GPS) and the azimuth angle (Azimuth_angle_GPS). Second, switch to calibrated photoelectric tracking. When the photoelectric tracking is aligned with the sun, the altitude angle (Altitude_angle) and the azimuth angle (Azimuth_angle) of the tracking mechanism are recorded, and calculated the correction value α and β are as below:

$$\alpha = \text{Azimuth\_angle} - \text{Azimuth\_angle\_GPS} \quad (9)$$

$$\beta = \text{Altitude\_angle} - \text{Altitude\_angle\_GPS} \quad (10)$$

α and β will be used to compensate the solar altitude and azimuth angle. Thus, the orthogonal deviation between the pitch axis and the azimuth axis, solar time algorithm and the GPS positioning errors can be partially corrected.

5 RESULTS AND DISCUSSION

We conducted the photoelectric tracking test from 09:45 to 12:00 on March 9-10, 2018 as shown in Fig.4. the zero-angle line in the graph is when the photodiodes are perfectly aligning with the sun. The results show that azimuth and altitude angle fluctuations are reduced after correction.

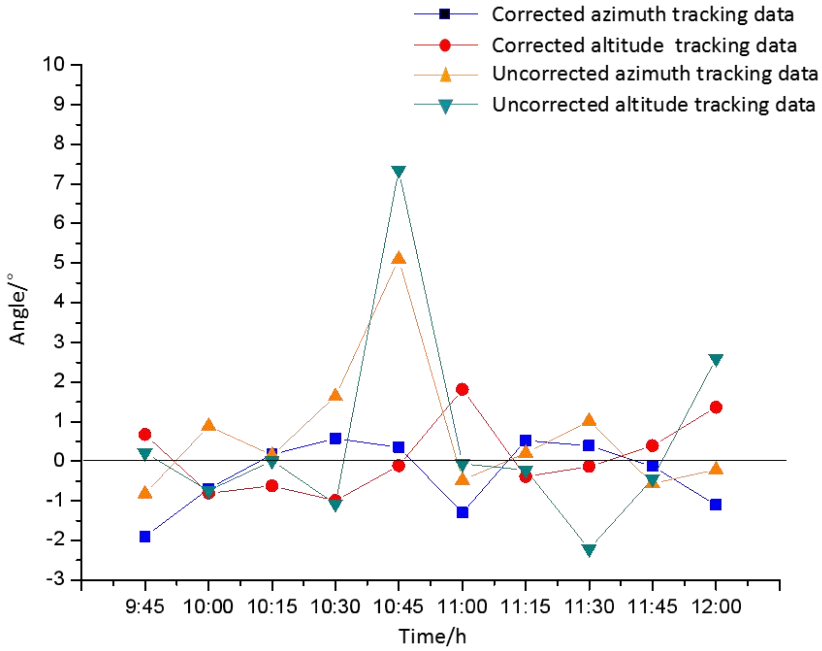

Fig.4 Photoelectric tracking data of March 9-10, 2018, in Shen Zhen, E 113° 58' and N 22° 35'

If photoelectric tracking is not corrected, it is obvious that the relative error of the altitude angle and azimuth angle are accumulating with time as shown in Fig.5 (a). Fig.5 (b) show that the data of the altitude angle and azimuth angle after the photoelectric sensor were corrected. The results show that the relative error of

azimuth angle is between -0.844° and 0.251°, and the relative error of altitude angle is between -0.498° and 0.576°.

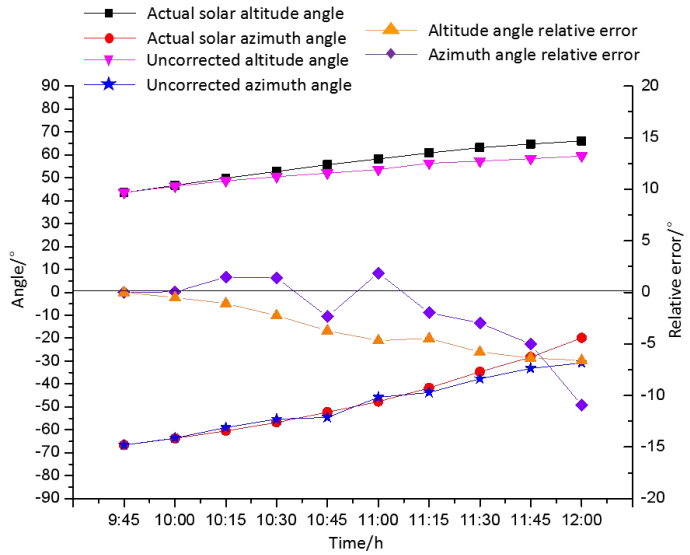

(a) Uncorrected data and relative error

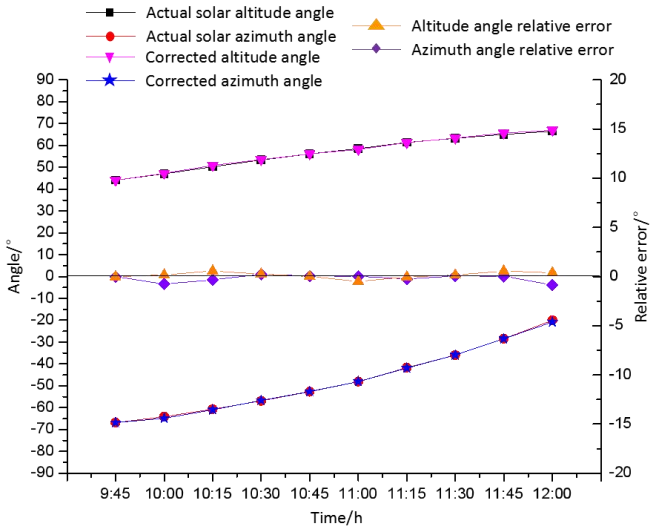

(b) Correction data and relative error

Fig.5 Photoelectric tracking data and relative error

We performed a solar tracking test from 09:00 to 16:00 on December 20, 2017. The latitude and longitude are E 113° 58' and N 22° 35'. Using the error correction method mentioned above, the system obtains the correction value of azimuth angle α is 5.716° and the correction value of altitude angle β is 2.184. As can be seen from Fig.6 (a), the uncorrected sun azimuth angle and actual azimuth angle relative error between 5.006° and 6.516°, and the corrected relative error decrease to within -0.71° and 0.8°, and the azimuth trajectory fits well with the actual solar azimuth trajectory. Fig.6 (b) shows the sun altitude trajectory and the relative error curves. The relative error between the corrected sun altitude angle and actual sun altitude angle is between 2.684° and 3.094°, and the corrected relative error decrease to within 0.5° and 0.91°. The corrected sun altitude trajectory fits well with the actual solar altitude trajectory.

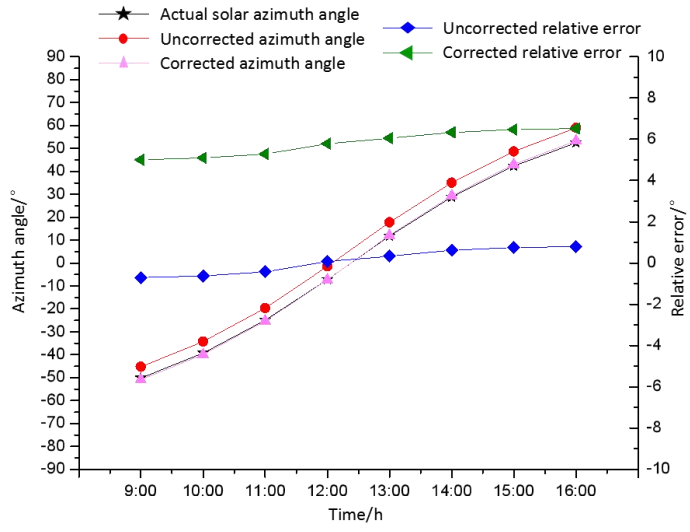

(a) Azimuth angle data and relative error

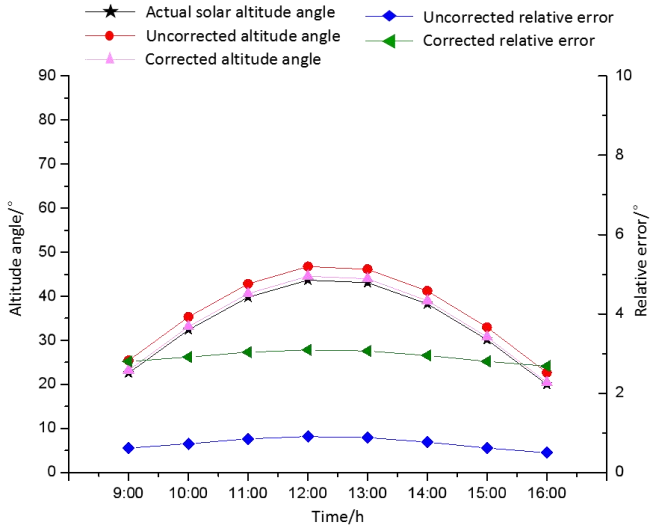

(b) altitude angle data and relative error

Fig.6 Solar tracking data and relative error

6 CONCLUSION

With increasing applications of solar tracking, the requirement for the tracking accuracy against weight and wind load directly related to the overall efficiency and cost of the system. We systematical analyzed the source of tracking errors, particularly, three type main errors - the orthogonal deviation between the pitch axis and the azimuth axis, solar time algorithm error - are studied and compensated using hybrid tracking.

The initializing calibration is proposed to correct the error caused by the mismatch of the photodiodes and background influence. For the horizontal axis deviation and pitch vertical deviation, combining solar time algorithm and the photoelectric tracking can obtain the compensation angles.
From our test results, after the correction of photoelectric sensor, the relative error of the azimuth angle is between -0.844° and 0.251°, and the relative error of the altitude angle is between -0.498° and 0.576°. After correction of shafting deviation, the sun altitude angle and azimuth angle of the tracking system are in good agreement with the actual solar trajectory.

ACKNOWLEDGEMENTS

This research is financially supported by Shenzhen Basic Research Fund - JCYJ20150529095551499 & JSGG 20170824094716462.

REFERENCES

[1] B. K. Widyolar, M. Abdelhamid, L. Jiang, R. Winston, E. Yablonovitch, G. Scranton, C. David, A. Hamid, K. Aleksandr, Design, simulation and experimental characterization of a novel parabolic trough hybrid solar photovoltaic/thermal (PV/T) collector. *Renewable Energy*, Vol.101, pp. 1379-1389, 2017.
[2] K. M. And, K. Domen, New Non-Oxide Photocatalysts Designed for Overall Water Splitting under Visible Light, *Journal of Physical Chemistry C*, Vol. 111, pp. 7851-7861, 2007.
[3] Xiujie Li, Zhuojun Yin, Peng Jin, Design and Analysis of an Active Daylight Harvesting System for Building, *Proc. Int. Conf. On Sustainable Energy & Environmental Protection*, Paisley, 2018.
[4] N. H. Vu, and S. Shin, A Concentrator Photovoltaic System Based on a Combination of Prism-Compound Parabolic Concentrators, *Energies,* Vol. 9, pp. 1-13, 2016.
[5] W. F. Hsu, Y. C. Hsu,Y. T. Shen, Orthogonal incidence method for efficient sunlight collection from asymmetric light couplers in tree-structured light guiding systems. *Applied Optics*, Vol. 52, pp. 6332-6343, 2013.
[6] K. Johnson, S. Selkowitz, Light guide design principles, *Energy Conservation Consumption & Utilization*, pp. 1-21, 1986.
[7] D. J. Carter, Developments in tubular daylight guidance system, *Building Research & Information*, Vol. 32, pp. 220-234, 2004.
[8] Peng Lei, Junyuan Lai, Jiong Ma, Peng Jin, Simulation and On-Site Performance of a Novel 3D Concentrator for Photovoltaic Application, *Applied Mechanics & Materials*, Vol. 457-458, pp. 1467-1473, 2014.
[9] Xiaonian Zheng, Qiaoyan Huang, Study on Sun-Tracking Methods and Application, *Energy Technology*, Vol. 24, pp. 149-151, 2003.
[10] C.S. Chin, A. Babu, W. McBride, Design, modeling and testing of a standalone single axis active solar tracker using MATLAB/Simulink, *Renewable Energy,* Vol. 36, pp. 3075-3090, 2011.
[11] A. Damiano, I. Marongiu, C. Musio, M. Musio, Concentrator photovoltaic standards: Experimental analyses of technical requirements, *Proc. Int. Conf. On Industrial Electronics Society*, IEEE, 2013.
[12] Minghui Tan, Kokkeong Chong, Rectifying structural deflection effect of large solar concentrator via correction of sun-tracking angle in the concentrator photovoltaic system, *Solar Energy*, Vol. 148, pp. 140-148, 2017.
[13] S. A. Sharaf Eldin, M. S.Abd-Elhady, H. A. Kandil, Feasibility of solar tracking systems for PV panels in hot and cold regions, *Renewable Energy*, Vol. 85, pp. 228-233, 2016.
[14] S. S. kouri, A. B. H. Ali, S. Bouadila, M. B. Salah, S. B. Nasrallah, Design and construction of sun tracking systems for solar parabolic concentrator displacement. *Renewable & Sustainable Energy Reviews*, Vol. 60, pp. 1419-1429, 2016.
[15] Pang Ying, The design and research of sun-tracking contol system based on STM32, *Yanshan University*, 2012.
[16] Cui Yang, Jian Zou, Dezhi Liu, Positioning error analysis of four quadrant detector, *Transducer and Microsystem Technologies*, Vol. 28, pp. 49-51, 2009.
[17] A. M. Bonanos, Error analysis for concentrated solar collectors, *Journal of Renewable & Sustainable Energy*, Vol. 4, pp. 146-150, 2012.

Materials for Solar cells

Tabbi Wilberforce[1], Abed Alaswad[2], A.G. Olabi[1]

1. Institute of Engineering and Energy Technologies, University of the West of Scotland, UK
2. Birmingham City University, School of Engineering and the Built Environment, UK

ABSTRACT

The world is currently aiming to depend on viable energy generation medium that is environmentally sustainable. Fossil fuels until the last few decades were the main energy generation medium in the world but the effects they have on the earth surface, variation in its prices and the general depletion of their reserves have urged researchers to consider renewable energy as an alternative for energy generation globally. Solar being the main hub on which the other forms of renewable energy revolves continue to be a beacon of light in the energy industry. This form of energy generation medium has seen massive and progressive transformation as in the last decades. It is generally abundant, cheap and environmentally friendly, which encouraged many researchers into exploring this scientific grey area as an alternative to fossil fuel. This investigation exposes the various generational stages in the solar cell industry and further compares the differences between these solar cells. The advantages and disadvantages of the solar cell types was equally explained. Some policies that could drive the solar cell industry further was finally discussed.

Keywords: Solar Energy, PV, Fossil fuel, Renewable Energy

1 INTRODUCTION

One of the most important issues in the 21st century is the prevention of energy crisis. This is simply because with increase in population and economic development, man requires more energy to create a conducive living environment [1]. Currently the world relies on fossil fuel as it's main energy source which has serious environmental implications such as climate change, global warming, air pollution and acid rain [2]. Efforts in reducing energy consumption and protecting the environment have led to scientist around the world researching on other suitable energy generation mediums [3]. It vividly shows energy as a necessity in any developing economy. It is therefore one of the major requirements for the production of almost all goods and services along with capital and labor. Studies conducted by a number of researchers all concluded to the fact that the buoyancy of any economy is highly dependent on it's energy generation medium [4-6]. All the investigations conducted by researchers around the globe concluded on how the economy and social development of any country is likely to suffer due to insufficient supply of energy. In 2010, 61.4% of total greenhouse gas emissions came from the energy sector [7, 8]. The Energy Information Agency projected that energy demand was likely to increase considerably in the years ahead [9-12]. They made some assumptions that most of the increase will occur in developing countries where the general energy consumption will rise from 46% to 58% between 2004 and 2040. Developing countries are also expected to see its consumption grow by 3% during that period. Demand for energy in developed countries is also anticipated to increase by 0.9% per year. Nonrenewable sources will be the bulk of the increase in energy consumption. Oil, coal and gas are principle sources of energy generation from renewable sources. The 21st session of the United Nations Conference of the Parties (COP21) held in December, 2015 was a major step in fighting climate change. According to the projections of the international Energy Agency(COP21), pledges to provide a boost to low carbon fuels and technologies, increasing the share of non-fossil fuels from 19% of the global energy mix today to 25% in 2040 (10). This analysis however does not show a clear picture of the rising global needs for energy in 2040. It projected that energy consumption will increase by one third as a result of high energy demand in Asia and Africa. The efficiency of the energy to be generated will play a critical role in reducing world energy demand growth to one third by 2040. The transition from traditional energy generation to renewable energy will help lower global emission [10 – 15]. The world in general has recently considered other alternate energy generation mediums and again drew attention to the fact that the future of the energy generation industry relates to how renewable sources are to be harnessed [14]. Another investigation also indicated that the world energy demand as being 10 terrawatts (TW) per year. It is expected that by 2050 this high demand for energy might increase to 30TW. The mid-century will require 20TW of non - CO_2 energy to stabilize the already existing amount of carbon dioxide in the atmosphere during that period [15]. The European Joint Research center predicted that energy harvested directly from sunlight would be 20% of the total energy consumption in 2050 and could be over 50% by 2100 [16]. A

researcher argued that that to stabilize the CO_2 in the atmosphere by mid-century, 10TW of electricity must be generated by photovoltaic and other renewables, hydrogen for transportation (10TW) and fossil fuels for residential and industrial heating (10TW) [17]. Solar energy from experiments and research works conducted so far is capable of generating emission free electricity [18, 19].

2.0 SOLAR ENERGY

French physicist, A. E, Becquerel in 1839 was the first to demonstrate photovoltaic properties experimentally [20]. The first photovoltaic cell was built in his father's laboratory whiles carrying out an experiment at age 19. The Effect of light on Selenium during the passage of an electric current was described by Willoughby Smith in an article that was published on 20 February 1873 issue of nature [21]. Mosser improved the concept of dye from photography to photo electrochemical cells using the dye erythrosine on silver halide electrode in 1887 [22]. The interest in photoelectron chemistry of semiconductors led to Wet – type PEC being discovered [23]. O'regan and Gra¨tzel then enhanced the idea of dye sensitized solar cells (DSSC) or commonly called Gratzel cell using organic dye molecules as a light absorber monolayer on a nano crystalline titanium dioxide (TiO_2), mesoporous network of wide band gap semiconductor [24]. The first solid state photovoltaic cell was built by Charles Frits who coated the semiconductor selenium with an extremely thin layer of gold to form the junctions. However, the invented device was only around 1% efficient. The first photoelectric cell based on sensitized solar cell (DSC or DSSC) was built by a Russian physicists Aleksandr Stoletov in 1888 [25]. This photoelectric cell was discovered by Heinrich Hertz earlier in 1887. The dye – sensitized solar cell (DSC or DSSC) stemmed from the study of photosynthesis. Researchers at Berkeley, while experimenting on chlorophyll extracted from plants noticed that electricity could be generated out of organic dyes at the oxide electrode of an electrochemical cell. During the experiment a conclusion was deduced that increasing the surface area of a charge collection was one of the best ways of improving the cell efficiency. French mathematician, August Mouchet suggested solar powered steam engines. With the help of Abel Pifre his assistant, the first sola powered engines were made. Parabolic dish collectors were manufactured as a result of the concept developed by Mouchet and Pifre. By 1980, the balometer was also invented by Samuel P Langley. This instrument aids in the measurement of light from the faintest stars and the sun's heat rays [26]. The progress on solar energy continued steadily till 1904 when Wilhelm Hallwachs discovered that combining copper and cuprous oxide is photosensitive. The following year 1905, Albert Einstein published his first paper on photoelectric effect. By 1950s the first office building using solar water heating and passive design was created by Architect Frank Bridgers. In 1956, William Cherry, of the US Signal Corps Laboratories approached RCA Lab's Paul Rappaport and Joseph Loferski about developing photovoltaic cells for proposed orbiting Earth satellites.

3.0 WORLD DEMAND FOR RENEWABLE ENERGY

Development of reliable and robust systems to harness energy from non – conventional energy resources has undergone thorough scientific research. Solar and wind power generation within the last ten years has experienced remarkable growth. The most plentiful resource on earth is the sun. Energy derived from the sun is solar energy. It is renewable, inexhaustible and environmentally friendly. Batteries charged by solar are able to store the energy and used later irrespective of the weather condition. Using the appropriate technology, approach and skill, large amount of power from solar radiation can be generated. Solar is very effective among all available renewable energy resources [31]. Solar is the most promising alternative source of energy and with time could help reduce the dependency on fossil fuels. In fact, solar energy, ie, Sunlight is the original source of energy for other energy mediums like fossil fuel, hydro and biomass.

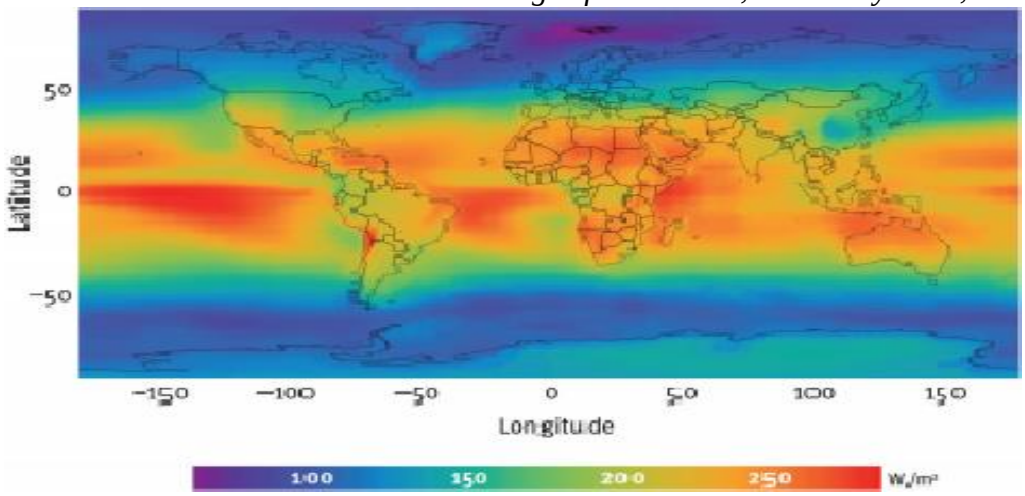

Fig. 1: Annual average intensity of radiation over the earth [31]

Solar energy falls on the Earth's surface at a rate of 120 petawatts, (1 petawatt = 1015 watt) [32]. In other research, it was concluded that 1.73 x 10^{17}J of energy is being radiated to the surface of the earth every second [32]. Fig. 1 clearly depicts the annual average intensity of radiation over the earth surface which is normally between around 100 and 250W/m^2 as a result of variation in the latitude and climate. Within a year the solar energy falling on the earth surface amount to about four million exajoules (1EJ = 10^{18}J). If it were possible to harvest 5 x 10^4 EJ, it would easily meet human primary energy demands of around 533EJ as of 2010 and projected figure of 782 EJ in 2035 based on current policies [33]. This stipulates that the energy demand for a period of twenty years could be achieved within one day from solar energy [34] if the world could make maximum use of the sun.

4.0 GENERAL OPERATION OF SOLAR CELLS

The word "photovoltaic (PV) is basically two words joined together. That is "photo" meaning light and "voltaic" meaning electricity. The scientific term is normally used to describe devices that convert solar energy into electricity and also generates electricity. The technology relies on a semi – conductor material capable of freeing electrons. The usual semi – conductor material used is silicon. Depending on their working principles, production techniques and material composition, photovoltaic cells can be divided into different categories [43, 44]. Photovoltaic cells are made up of two layers of such semi – conductors. One of these layers is positively charged whiles the other is negatively charged. DC current is generated when light shines on the semi – conductor. This phenomenon occurs due to the electric field across the junction between these two layers inducing electricity to flow. The higher the light intensity, the higher the flow of electricity generated. A photovoltaic system can even operate when sunlight is very minimal example on cloudy days [45]. Depending on the type of cloud, energy output can be produced even during unfavorable conditions. It is therefore possible that days with slight cloud can even generate higher energy as compared to days where there are absolutely no clouds. Solar energy is collected as packets of energy called photons [46]. These photons give up their energy to excite electrons when they are absorbed by a material. The electrons are normally in bonds with the atoms that form the material and once the bond becomes broken the electrons move to a state with higher energy. The energy can be captured and transformed to fuel, heat or electric power [47]. The conversion of solar energy can clearly be categorized into three areas: solar thermal, which is light energy being converted to heat; solar photovoltaic, which is light energy being converted to electrical work and solar chemical, which is light energy being transformed to stored chemical potential [50,51].

4.1 FIRST GENERATION SOLAR CELL

Photovoltaic production is currently 90% first generation solar cells that depend highly on expensive bulk multi crystalline or single crystal semiconductors. The first generation is mainly made up of silicon wafers that are reliable and durable but very expensive. This type of single – junction silicon wafers devices are known as the first generation (1G) technology. Most of them are produced based on screen printing devices as shown in Fig. 4.

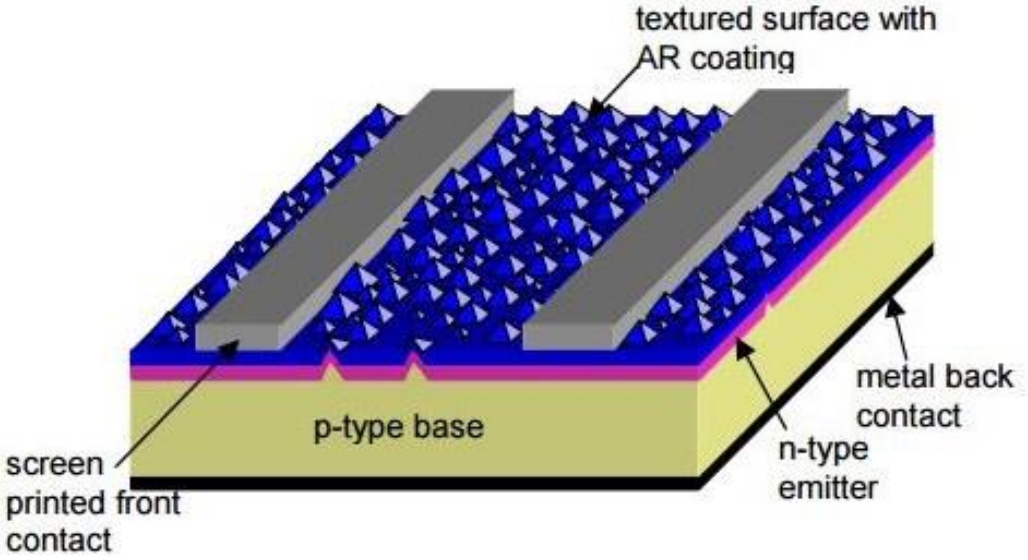

Fig. 4. Screen Printed single crystal solar cell

4. 2 SECOND GENERATION SOLAR CELLS (GENERATION II)

The second generation was formed by removing unnecessary material from the cost equation by using thin – film devices which in effect led to reduced $/W. They are single junction devices that aim to use less material whilst maintaining the efficiencies of 1G PV. The second generation solar cell led to the production of amorphous – Si (a – Si), CuIn(Ga)Se2(CIS), CdTe/Cds or Polycrystalline – Si (P- Si) deposited on low – cost substrates such as glass shown in Fig. 6.

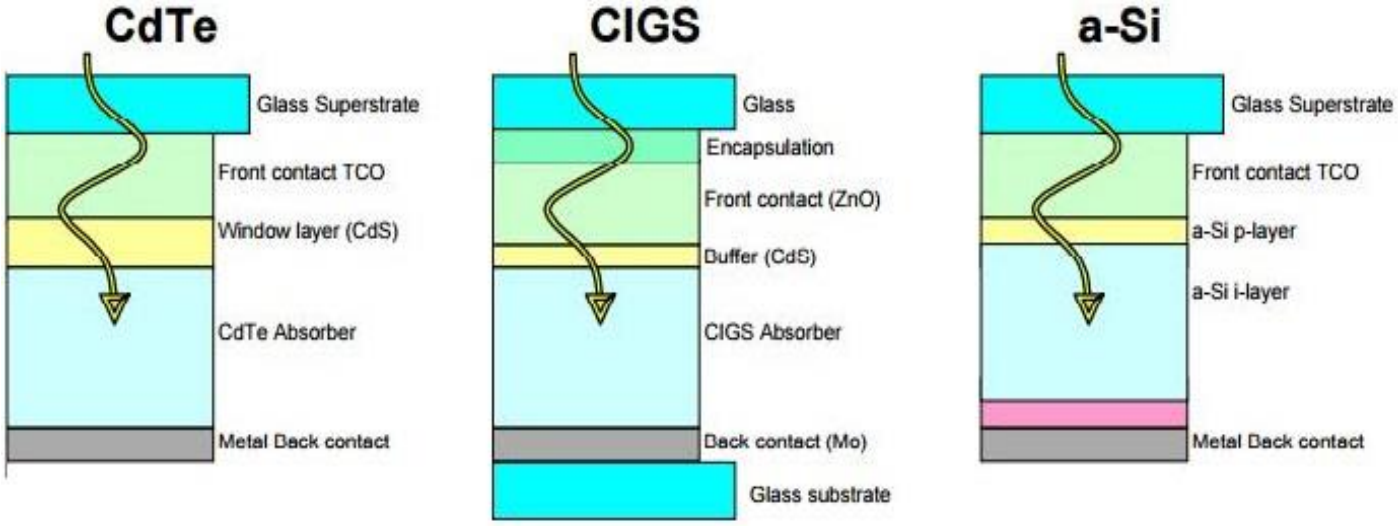

Fig. 6: Schematic diagrams of thin film CdTe, CIGS and a – Si thin film PV [35]

4.3 THIRD GENERATION SOLAR CELLS

The main objective of the third generation solar cells is to obtain high efficiency. In order to achieve such efficiency improvements, devices aim to circumvent the Shockley – Queisse limit for single bandgap devices that limits efficiencies to either 31% or 41% based on concentration ratio shown in Fig. 7.

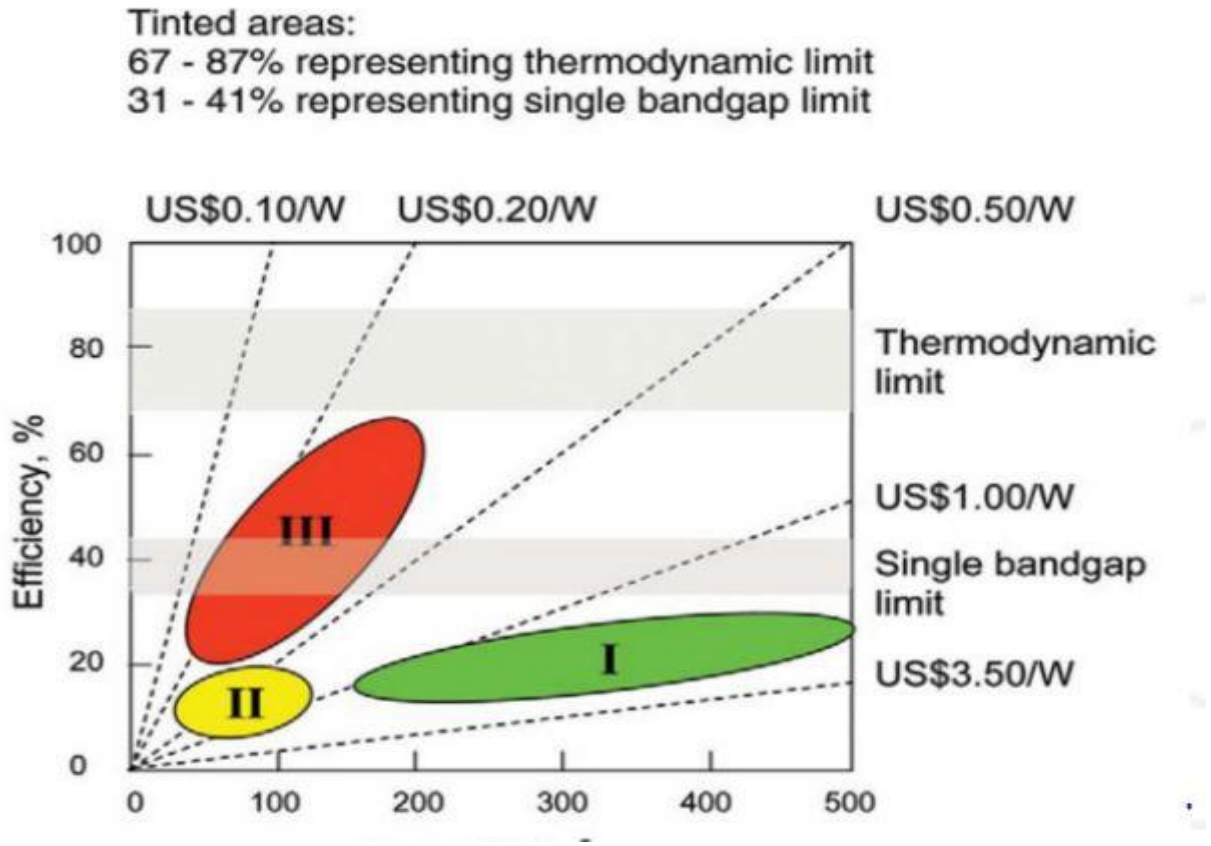

Fig. 7: Efficiency and cost projections for first- (I), second- (II), and thirdgeneration (III) PV technologies (waferbased, thin films, and advanced thin films, respectively) [36].

5.0 Conclusion

The world can meets its target of generating energy efficiently if more investigation is geared towards the solar industry to create other mediums for producing solar cells and PVs at a cheaper cost. This in effect would reduce the dependency of the world on fossil fuel and make the world a safe. The various stages encountered by the solar industry from the first to the third-generation solar cells vividly depict the progress in the industry, although much work is still needed.

Political will (high level positive attitude), pragmatic technology and a conducive financial environment are prerequisites for widespread adoption of solar energy technology. The growing exposition that anthropogenic CO_2 causes climate change in driving acceptance at all levels of government for the need to incorporate solar energy in the global energy supply [37]. Some legislated solar energy goals and incentives are positively influencing the financial environment in some countries and investment in solar energy technology is producing tangible outcomes like highly advanced solar cell. These factors are generic but apply equally to the applications of solar hydrogen-based electricity supply where there is no grid. Solar hydrogen-based systems have been proven in relatively controlled (quasi – laboratory) and relatively uncontrolled settings. Some of the major challenges that need to be surmounted to keep the advancement of the solar energy industry still progressing steadily are:

- The cost of solar energy systems components needs to be reduced to limit the payback time. This is very practical of the least mature component of any solar systems.
- An off grid, possibly remote, power supply system should be able to function unattended and reliable for long periods in unfavourable and widely variable situations.
- Optimal sizing of components according to the selected compromise between cost and availability of energy is necessary as over – sizing is expensive and under sizing compromise the ability to meet demand as well as reliability. The development of mathematical models for each individual system component and for simulating the operation of the entire system are therefore vital.
- Control algorithm is a major challenge that interacts with the sizing problem and maximizes the ability of energy whiles reducing the fluctuations in energy flow through vulnerable components to the point where their lifetimes are compromised.

- The degradation of performance with time, validated with environmental data from implemented installations need to be addressed for almost all components for solar systems.
- In many parts of the world, local regulations specific to solar energy technology do not exist and projects must conform with many disparate standards and regulations increasing the complexity and cost of the project.

6.0 References

1. Tabbi Wilberforce, A. Alaswad, A. Palumbo, A. G. Olabi. Advances in stationary and portable fuel cell applications. International Journal of Hydrogen Energy 41(37) March 2016.
2. Tabbi Wilberforce, Ahmed Al Makky, A. Baroutaji, Rubal Sambi, A.G. Olabi. Computational Fluid Dynamic Simulation and modelling (CFX) of Flow Plate in PEM fuel cell using Aluminum Open Pore Cellular Foam Material. Power and Energy Conference (TPEC), IEEE, Texas. 2017. DOI: 10.1109/TPEC.2017.7868285.
3. Tabbi Wilberforce, Ahmed Al Makky, A. Baroutaji, Rubal Sambi, A.G. Olabi Optimization of bipolar plate through computational fluid dynamics simulation and modelling using nickle open pore cellular foam material. International conference on reneable energies and power quality (ICREPQ'17), ISSN 2171-038X, No 15 April 2017.
4. Tabbi Wilberforce, A. Alaswad, J. Mooney,A.G.Olabi.Hydrogen Production for Solar Energy Storage. A Proposed Design Investigation.Proceedings of the 8th International Conference on sustainable Energy and Environmental Protection. ISBN: 978-1-903978-52-8.
5. Tabbi Wilberforce, F. N. khatib, O. Emmanuel, O. Ijeaodola, A. Abdulrahman, Ahmed al Makky A. Baroutaji, A.G. Olabi. Experimental study of operational parameters on the performance of pemfcs in dead end mode. Proceedings of SEEP2017, 27-30 June 2017, Bled Slovenia.
6. Tabbi Wilberforce, F. N. Khatib, Ahmed Al Makky, A. Baroutaji, A.G. Olabi Characterisation Of Proton Exchange Membrane Fuel Cell Through Design Of Experiment (DOE). Proceedings of SEEP2017, 27-30 June 2017, Bled, Slovenia.
7. Tabbi Wilberforce, Zaki, El-Hassan, F.N. Khatib, A. Al Makyy, A. Baroutaji, J. G. Carton and A. G. Olabi. Developments of electric cars and fuel cell hydrogen electric cars. DOI: 10.1016/j.ijhydene.2017.07.054
8. T. Wilberforce, Z. El-Hassan, F.N. Khatib, A. Al Makyy, A. Baroutaji, J. G. Carton and A. G. Olabi, Modelling and Simulation of Proton Exchange Membrane Fuel cell with Serpentine bipolar plate using MATLAB, International journal of hydrogen, 2017. DOI: 10.1016/j.ijhydene.2017.06.091.
9. Baroutaji, A., Carton, J, G., Stoke, J., Olabi, A, G., 2014. Design and Development of Proton Exchange Membrane Fuel cell using the Open Pore Cellular Foam as flow plate material. Journal of Energy Challenges and Mechanics. Volume 1 (2014) issue 3.
10. IRENA, 2015. Rethinking Energy: Renewable Energy and Climate Change, International Renewable Energy Agency, p. 44.
11. IRENA and C2E2, 2015. Synergies between Renewable Energy and Energy Efficiency, Working Paper. IRENA, Abu Dhabi and C2E2, Copenhagen.
12. Twidell, J., Weir, T., 2012. Renewable Energy Resources, second ed. Taylor & Francis, New York, USA.
13. Razykov, T. M., Ferekides, C. S., Morel, D., Stefanakos, E., Ullal, H.S., Upadhyaya, H. M ., 2011 . Solar Photovoltaic Electricity: Current status and future prospects.
14. European commissions, 2013. European Joint Research Centre .http://ec. europa.eu/dgs/jrc/index.cfm. (28 February, 2015).
15. Zweibel, K., 2005. The Terawatt challenge for thin film PV, In: Poortmans, J., Archipov, V. (Eds), Thin Film Solar Cells: Fabrication, Characterization and Application. John Wiley, pp. 18 – 22.
16. Zhang, L. H., Baeyens, J., Degreve, J., Caceres, G., 2013. Concentrated Solar Power Plants; Review and Design Methodology. Renew. Sustain, Energy Rev., 22(2013), pp 466 – 481.
17. Godson, J., Karthick, M., Muthukrishnan, T., and Sivagamasundari, M., S., 2013. Solar PV – Wind Hybrid Power Generation System. International Journal of Advanced Research In Electrical, Electronics and Instrumentation. Vol.2, Issue 11, November, 2013. ISSBN: 2320 – 3765.
18. Chopra, K.L., Paulson, P.D., Dutta, V., 2004. Thin-film solar cells: an overview. Prog. Photovoltaics Res. Appl. 12 (2–3), 69–92.

19. Shauddin, S, M., 2012 Comparison among various emerging PV cells with history, current states and future challenges.
20. Moser, J., 1887. Monatsh. Chemie 8, 373.
21. Gerischer, H., 1966. Electrochemical behavior of semiconductors under illumination. J. Electrochem. Soc. 113, 1174–1182.
22. O'regan, B., Gra¨tzel, M., 1991. A low-cost, high-efficiency solar cell based on dye-sensitized colloidal TiO2 films. Nature 353, 737–740.
23. Gevorkian, P., 2007. Sustainable Energy Systems Engineering: the complete green building design resource: McGraw – Hill Professional pp.498 -. ISBN 978 – 0 – 07 – 147359 – 0.
24. History Of Solar Energy In California - Go Solar California". *Gosolarcalifornia.ca.gov*. N.p., 2016. http://www.gosolarcalifornia.ca.gov/about/gosolar/california.php (Accessed: 15 Mar. 2016).
25. Willie, R, 2016. The History Of Solar Power - Experience.Com". *Experience.com*. N.p., 2016.https://www.experience.com/alumnus/article?channel_id=energy_utilities&source_page=additional_articles&article_id=article_1130427780670 (Accessed: 15 Mar. 2016.)
26. Jennings, C, E, Margolis, M, R., Bartlett, J, E, 2008. A historical Analysis of Investment in Solar Energy Technologies (2000 – 2007). Technical Report NREL/TP- 6A2 – 43602. http://www.nrel.gov/docs/fy09osti/43602.pdf (15/03/2016).
27. Aghaei, P, T., Meisen, P, 2014. Solar Electric and Solar Thermal Energy: A Summary of Current Technologies. Global Energy Network Institute. http://www.geni.org/globalenergy/research/solar-technology-summary/Solar-energy-and-technologies-2015-03-11.pdf (Accessed: 15/03/2016)
28. Jones, G., Boumane, L., 2012. A Business History Of Solar Energy. http://www.hbs.edu/faculty/Publication%20Files/12-105.pdf (Assessed: 15/3/16)
29. ABARE, 2010. Chapter 10 Solar Energy. In: Jaques, L., Bradshaw, M., Carson, L., Budd, A., Huleatt, M., Hutchinson, D., Lambert, I., LePoidevin, S., McKay, A., Miezitis, Y., Sait, R., Zhu, R. Hughes, M., Ball, A., Cuevas-Cubria, C., Copeland, A., Hogan, L., Lampard, M., Maliyasena, A., New, R., Penney, K., Petchey, R., Warr, S., McCallum, R., Sandu, S. (Eds.). Australian Energy Resource Assessment, Canberra, Australia: Australian Government Department of Resources, Energy and Tourism (RET), Geoscience Australia and Australian Bureau of Agricultural and Resource Economics (ABARE), pp. 261–284
30. Maslamani, M., T, Omer, I, A and Majid, M., A., 2014. Development of Solar Thermoelectric Generator. European Scientific Journal March 2014 edition vol.10, No.9 ISSN: 1857 – 7881 (Print) e - ISSN 1857-7431
31. Nelson, J., Gambhir, A., and Daukes, N., E., 2014. Solar Power for CO_2 mitigation. Grantham Institute for Climate change. Briefing paper no. 11.
32. World Energy Outlook, International Energy Agency, 2012
33. West, W., 1974. First hundred years of spectral sensitization. Photographic Sci. Eng. 18 (1), 35–48.
34. REN21. Renewables Global Status Report. Paris: REN21 Secretariat; 2014 ISBN 978-3-9815934-2-6.
35. EA, Energy technology perspectives 2012. Pathways to a clean energy system. ISBN 978-92-64-17488-7, 2012.
36. EC,Progress Reports. ⟨http://ec.europa.eu/energy/renewables/reports/reports_ en.htm⟩ 2014.
37. EC, Energy for the future: renewable sources of energy. White paper for a community strategyandactionplan,COM(97)599 final. 1997.
38. Council of the European Union, Presidency Conclusions, 7224/07. 2007.

SAHARAN ENVIRONMENTAL INFLUENCES ON THE PHOTOVOLTAIC ARRAY ENERGY PRODUCTION THROUGH LOAD-MATCHING MODEL: CASE STUDY GHARDAIA REGION, ALGERIA

Azzedine Boutelhig[1] and Salah Hanini[2]

[1]Unité de Recherche Appliquée en Energies Renouvelables, URAER, Centre de Développement des Energies Renouvelables, CDER, 47133, Ghardaïa, Algeria ; email: boutelhig@yahoo.com

[1]Laboratoire LBPT, ER,Université Yahia Farés, Médéa, Algeria; email: s_hanini2002@yahoo.fr

ABSTRACT

This paper examines the specific's influences of a desert area solar potential on the photovoltaic (PV) array energy production, through the application of load-matching model in PV water pumping system. Based on the global insolation data, recorded during two different seasons in Ghardaia, a desert area, the different influences have been investigated through the mono-Silicon PV modules fill factor and efficiency. The first determines the rate power that the PV array can provide from its total power capacity production and the second provides the real efficiency of such PV cell technology. Two months solar potential data have been used in such study. Following a characterization test, under an average of solar beam (564 W/m^2) and PV cell temperature (T=33.45°C), recorded in the coldest month (January), the PV module efficiency has achieved more than 12%, for an average energy production capacity (Fill factor) nexus 61.32%. However, in June the hottest month, for an average insolation (721 W/m^2) and PV cell temperature (T=54.98 °C), the efficiency has achieved only 10.5% for energy production capacity of about 66.5%. The obtained results were then applied by a Load-Matching Factor (LMF) model in PV water pumping system, it has been averred that the LMF tends close to 1 versus the decreased PV cell temperature values, in particular during the coldest periods.

Keywords: Saharan environmental, energy production, Fill factor, load-matching factor,

1 INTRODUCTION

Renewable energies, in particular solar energy are one of the main promising clean energy sources in the future of the world as an alternative for a global energy supply. The challenges facing the present world energy supply are the decline of fossil fuel resources, climate change by carbon dioxide emission; insecurity by nuclear weapon competence and radioactive materials. With a total surface of about 36 million km2 and an average yearly global irradiance of about 2.2 Tera-Watt-hour (TWh/km^2/years), the Sahara areas are the most efficient places to harvest solar energy in large amount. The technology of Photovoltaic PV is always on continuous developing in many applications, so it is electricity generator without effect on environment. However, In spite the availability of the huge quantity of solar radiation covering the large land of the great Sahara so called the solar belt area or (south Mediterranean belt region), different studies of the solar potential energy averred many specific parameters, that influence on the photovoltaic array energy production, which has a consequences on the load-matching of the PV systems. Many works have examined this subject, accordingly. A local study has adopted the solar potential in Algeria [1]. Over the major part of the territory, solar energy represents a significant potential (1700 kW h/m^2/year in the north and 2263 kW h/m2/year in the south of the country) [2]. Throughout the period from February to May, the windy storm is one of the specific events of the climatic characteristics closed to the desert area, which has a significant on the gradual decrease of PV power, since it has a great influence on the PV cell production, consequently on PV array load-matching [3]. The sandy dust accumulation affects both the solar energy production and the degradation cycle life of the PV module and systems, so this subject has been treated by many authors [4], [5]. During this period, shadow has an important factor on the drop of the solar beam and some works have been studied in this context [6]. Algeria aims to generate about 40% of its total electricity production from renewable sources by the year 2030, within the world target to reach the 100% renewable energy [7, 8]. Researches interested in PV water pumping to provide the performances of the PV array conversion, according to different topics; optimization [9] and sizing in sizing [10,11]. Solar irradiation impact on PV array has been investigated, through the performance of different water pumping systems, whereas, many combinations of models have been tested [12, 13]. Recent methods have been adopted in improving the PV

efficiency [14-15]. New strategies and methodologies have been proposed to alleviate the influence of the arid climates on the PV conversion [16, 17]. In this paper, a new load-Matching Model has been tested in PV water pumping system to highlight the influence of the specific desert characteristics on the PV output energy. The solar radiation and temperature data of two different seasons have been used in the load-matching model. The obtained plots averred that the efficiency of the pump is influenced, particularly by the temperature of the site, whereas sandy storms averred a significant depletion on the system efficiency.

2 SOLAR POTENTIAL IN ALGERIA

Algeria is an ideal environment for photovoltaic system applications, especially in the water pumping according to its geographical situation; it holds one of the highest solar reservoirs in the world. Indeed, the Algerian area receives more than 3000 h of sunshine per year with a high level of radiation. The yearly average of daily solar irradiation ranges from 5 to 7 kWh/m^2/day as far as tilted surfaces at optimum angles are considered [2].The insolation time over the quasi-totality of the national territory exceeds 2000 hours annually and may reach 3900 hours (high plains and Sahara). The daily irradiation potential distribution in Algeria is shown in the Table1.

Table 1. Solar energy potential in Algeria

Areas	Costal area	High land plates	Sahara
Surface (%)	4	10	86
Average sun shine hours (Hours/year)	2650	3000	3500
Average energy received (kWh/m^2/year)	1700	1900	2650

3 LOAD-MATCHING MODEL IN PV WATER PUMPING SYSTEM

In direct PV water pumping system, the PV array load-matching factor (LMF) depends on the comparison of the maximum operating point of DC motor-pump and the maximum power MPP provided by the PV array at the same solar intensity, and it is given by the equation (1).

$$LMF = \frac{P_{pm}}{P_{pvm}} \qquad (1)$$

From the motor-pump efficiency model (4), the pump power model at certain solar intensity level and PV cell temperature has been deduced and is shown by the equation (2).

$$P_{pm} = V_{pm} I_{pm} = \frac{C_H HQ}{\eta_P} \qquad (2)$$

Where,

E_h is the hydraulic energy, C_h is the hydraulic constant, H the Total Mano-metric Head (TMH) and Q(m^3/h) is the hourly flow-rate.

From the PV array efficiency model (2), the PV power model at certain solar intensity level and PV cell temperature has been concluded and is shown by the equation (3).

$$P_{pvm} = V_{pvm} I_{pvm} = \eta_{PV} A_{pv} E_i \qquad (3)$$

3.1 DEPENDENCY OF SOLAR IRRADIANCE

The PV array efficiency is obtained by the comparison of the maximum output power presented by its instantaneous maximum I-V characteristics and the product of its front area and the irradiance , and then is given by equation (4).

$$\eta_{pv} = \frac{V_{pvm} I_{pvm}}{A_{PV} E_i} \qquad (4)$$

Where,

A_{pv} (m) and E_i (W/m^2) are the PV front surface and the solar intensity level (irradiance) falling on the PV array.

3.2 DEPENDENCY OF THE PV CELL TEMPERATURE

In the reality the overall efficiency of such PV system varies according to the outdoor conditions. Let's talk by the influence of the ambient temperature via the PV cell temperature. In the following we consider that the pump efficiency is constant and only the PV array efficiency is variable throughout the environment change. By referring to the theoretical model of the PV array efficiency which is presented by the model (5):

$$\eta_{pv} = \eta_{ref}\left[1 - \beta(Tcell - Tcell,ref) + \gamma \log\left(\frac{E_i}{E_{i,ref}}\right)\right] \qquad (5)$$

Where,

η_{ref}, $T_{cell,ref}$, $E_{i,ref}$ are the PV module efficiency reference, PV cell Temperature reference and the incident solar intensity reference, respectively.

β and γ are coefficients.

Electrical energy: The provided and consumed powers are instantaneous, by consequence the load-matching factor LMF is recorded at each measurement at certain solar intensity (insolation) level. The two power models are converted into energy model expressions throughout the day. The energy provided by the PV array during the day can be found by the following expressions (6) and (7), respectively:

$$E_{pv} = \eta_{pv} A_{PV} \int_{t_{SR}}^{t_{SS}} E_i \, dt = \eta_{pv} A_{PV} E \qquad (6)$$

Where,

t_{sr} is the sunrise time and t_{ss} is the sunset time. E is the daily global solar irradiation in (Wh/m^2), received on tilted PV array closed the latitude of the site.

$$E_e = \frac{C_H H \int_{t_{SR}}^{t_{SS}} Q dt}{\eta_P} \Rightarrow E_e = \frac{C_H H Q_d}{\eta_P} \qquad (7)$$

Where, Q_d (m^3) is the daily water discharge flow-rate.

The new Load-Matching Factor expression is then obtained by replacing the new energy expression equations. We consider that the overall system efficiency is constant and the load-matching factor depends only on the daily average solar radiation energy. The new model is presented by the expressions (8) and (9), respectively:

$$LMF = \frac{E_e}{E_{pv}} \qquad (8)$$

The model becomes as follows;

$$LMF = \left(\frac{C_H HQ_d}{\eta_p \eta_{pv} A_{pv}} \right) * 1/E \qquad (9)$$

4 LOAD-MATCHING APPLICATION

Through the manufacturer performance references of the mono-silicon PV modules Isofoton (130/24), the DC Grundfos pump (1.4 kW) and the solar potential data recorded on outdoor of the site. A theoretical investigation of the load-matching has been studied on cold and hot months including the windy storm seasons to determine the characteristic influences of the solar potential on the PV array energy production. The PV array consists of two parallel strings, in each strings is composed of 7 Isofoton (130/24) PV modules connected in serial. The nominal characteristics of the PV array and the DC Grundfos pump are presented in the table 2 and the table 3, respectively:

Table 2: Nominal characteristics of the PV array

Charact-eristic	P_m (W)	I_{SC} (A)	V_{OC} (V)	I_m (A)	V_m (V)	Area (m^2)	$\eta_{PV\ (\%)}$
PV module Isofoton (130/24)	110 + 10%	3.94	43.2	3.76	34.6	0.96	12.65
PV array (2X7)	1820	7.88	302.4	6.32	242.2	12.90	12.65

Table 3: Nominal characteristics of the DC pump

Motor-pump type	Nominal power	Max. DC voltage	Max. AC voltage	Im (A)	ηp (%)
Grundfos (1.4 kW)	1400 W	30–300 V	1x90 – 240 V	8.4	0.44

By mean of the irradiance data and the calculated mono-silicon PV cell temperature data of different months of different seasons, the solar potential and the obtained PV cell efficiency of the coldest month (January), the medium month (March) and the hottest month (June) are illustrated in the following figs. 1-6, respectively (See the Annex).

Fig.1: presents the average daily irradiance and PV cell temperature recorded during the coldest month (January) of the year. The curves show that the maximum recorded irradiance is between 800 W/m2 and 850 W/m2 and the PV cell temperature is between 20°C and 35 °C. Fig.2: Shows the calculated efficiency of the mono-silicon PV cell, through the solar potential data of the coldest month (January), the calculated PV cell efficiency is obtained between 13.5% and 14.5%. So less solar intensity but a significant PV cell efficiency. Fig.3: During a medium climate month (March), the irradiance reached the normal average of about 1000 W/m^2, however the PV cell temperature varies between 20°C and 50 °C. Indeed, during this period (spring), the irradiance varies with the influence of the sandy storm. Fig.4: The PV cell efficiency during March is between 13% and 14% and this is a medium obtained efficiency value in this month. Fig.5: In the hottest month (June), the solar intensity exceeds the average of about 1100 W/m^2. The PV cell temperature is between 45°C and 65°C. Fig.6: During the hottest month, the PV cell efficiency decreases and the average is between 12% and 13%, as shown in the plot. So this is less significant obtained efficiency.

The plots illustrated by the figs. 7a - 7f, averred load-matching factor convergence to the value 1. The most significant load-matching factor is illustrated in the plots of the figs.7e -7b for both coldest months (January and December), where the PV cell temperature and the windy storms are insignificant. The load-matching values calculated at the pump efficiency more than 40%, are not with significant purpose. These plots show that the variation of the pump efficiency has reached the same value for all the months of the year. In other hand, to obtain an accurate load-matching model the pump efficiency as well as the PV cell efficiency must vary each month.

5 CONCLUSIONS

The desert specific outdoor characteristics conditions that influence on the solar potential received on PV array module have been investigated to determine a load-matching model. From the different study of the PV cell and load (pump) efficiency variation under different climate change closed to desert specific weather, it can be concluded the variation of the solar intensity and the PV cell temperature during the windy storm seasons are perturbed consistently according to the climate change of the desert. The wind and the sandy dust as well as the suddenly daily temperature variation should be taken into consideration. Our obtained load-matching model needs to be more investigated through the investigation of the load efficiency variation versus the temperature.

REFERENCES

[1] A. Maafi. A survey on photovoltaic activities in Algeria. *Renewable Energy* 20 (2000) 9±17.

[2] Maafi A. Tilted surfaces iso-radiation maps for Algeria. *Proceedings* WREC III, 3rd World Renewable Energy Congress, Reading UK, 11±16 September 1994.

[3] A. O. Mohamed, A. Hasan. Effect of Dust Accumulation on Performance of Photovoltaic Solar Modules in Sahara Environment. *Journal of Basic and Applied Scientific Research*. 2(11)11030-11036, 2012.

[4] Monto Mani *, Rohit Pillai " Impact of dust on solar photovoltaic (PV) performance: Research status, challenges and recommendations" *Renewable and Sustainable Energy Reviews*, 14 (2010) 3124–3131.

[5] R. E. Cab anillas, H. Munguı´a "Dust accumulation effect on efficiency of Si photovoltaic modules» *Journal of renewable energy and sustainable energy* 3, 043114 (2011).

[6] A. Ibrahim «Effect of Shadow and Dust on the Performance of Silicon Solar Cell" J. Basic. *Applied Scientific Research*. (2011), 1(3)222-230.

[7] Brian V. Mathiesen, Henrik Lund, Kenneth Karlsson. 100% *Renewable energy systems, climate mitigation and economic growth*. *Applied Energy* 88 (2011) 488–501.

[8] A.G.Olabi. States of the Art on renewable and sustainable energy edit. *Energy* 61 (2013) 2- 5.

[9] Ceyda Olcan. Multi-objective analytical model for optimal sizing of stand-alone photovoltaic water pumping systems. Energy Conversion and Management 100 (2015) 358–369.

[10] Dhiaa H. Muhsen, A.B. Ghazali, T. Khatib. Multi-objective differential evolution algorithm-based sizing of a standalone photovoltaic water pumping system. Energy Conversion and Management 118 (2016) 32–43.

[11] Renu, Birinchi Bora, Basudev Prasad, O.S. Sastry, Atul Kumar, Manander Bangar. Optimum sizing and performance modeling of Solar Photovoltaic (SPV) water pumps for different climatic conditions. Solar Energy 155 (2017) 1326–1338.

[12] Azzedne Boutelhig, Amar Hadj Arab and Salah Hanini. New approach to exploit optimally the PV array output energy by maximizing the discharge rate of a directly-coupled Photovoltaic water pumping system (DC/PVPS). Energy Conversion and Management 111 (2016) 375–390.

[13] Azzedine Boutelhig, Salah Hanini and Amar Hadj Arab. Performances' investigation of different photovoltaic water pumping system configurations for proper matching the optimal location, in desert area. Energy Conversion and Management 151 (2017) 439–456.

[14] Fabio Schiro, Alberto Benato, Anna Stoppato and Nicola Destro. Improving photovoltaic efficiency by water cooling: Modeling and experimental approach. Energy 10823 (2017).

[15] Mohsen Mirzaei, Mostafa Zamani Mohiabadi. A comparative analysis of long-term field test of monocrystalline and polycrystalline PV power generation in semi-arid climate conditions. Energy for Sustainable Development 38 (2017) 93–101.

[16] Dhiaa Halboot Muhsena, Tamer Khatib & Farrukh Nagi. A review of photovoltaic water pumping system designing methods, control strategies and field performance. Renewable and Sustainable Energy Reviews 68 (2017) 70–86.

[17] Billel Talbia, Fateh Krim, Toufik Rekioua, Saad Mekhilef, Abdelbaset Laiba, Abdesslam Belaouta. A high-performance control scheme for photovoltaic pumping system under sudden irradiance and load changes. Solar Energy 159 (2018) 353–368.

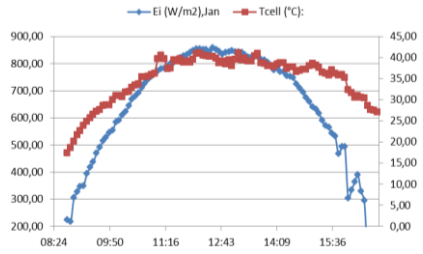

Fig.1: Irradiance & temperature in Jan.

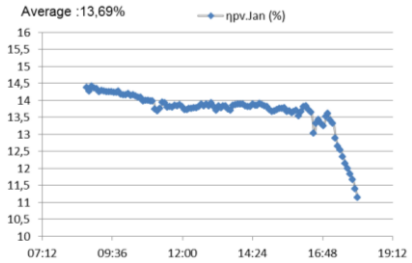

Fig.2: PV cell efficiency in Jan.

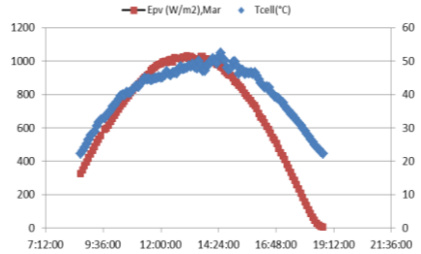

Fig.3: Irradiance & temperature of Mar.

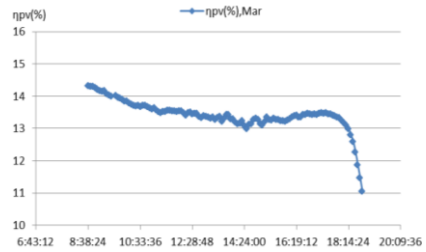

Fig.4: PV cell efficiency in Mar.

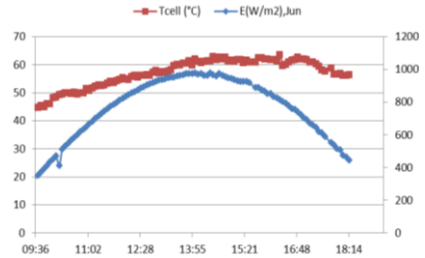

Fig. 5: Irradiance & temperature of Jun.

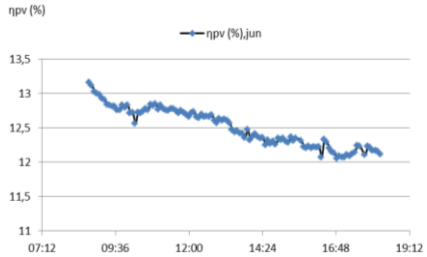

Fig.6: PV cell efficiency in Jun.

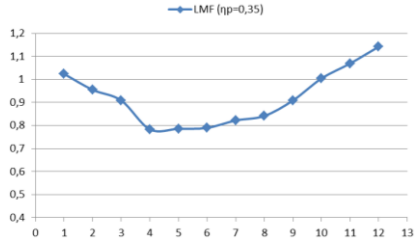

Fig. 7a

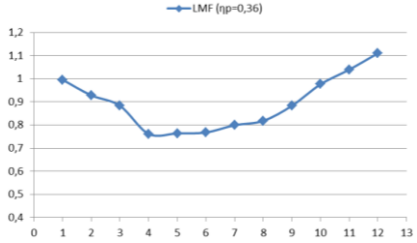

Fig. 7b

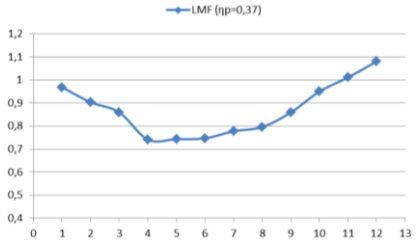

Fig. 7c

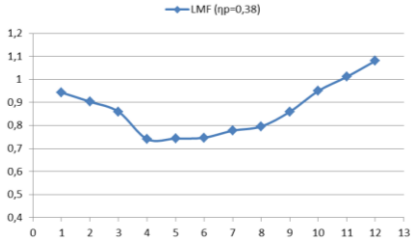

Fig. 7d

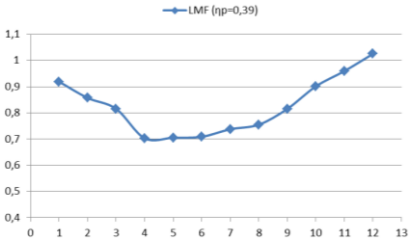

Fig. 7e

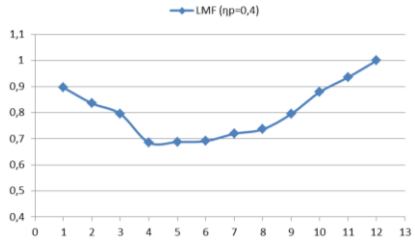

Fig. 7f

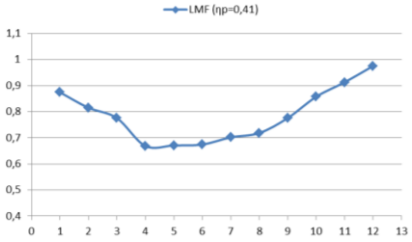

Fig. 7g

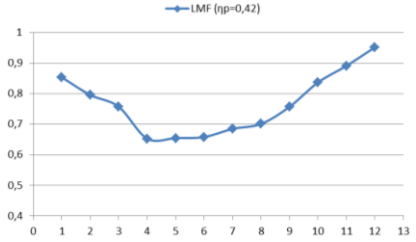

Fig. 7h

ECONOMIC ANALYSIS OF PHOTOVOLTAIC CHARGING STATION WITH SECOND LIFE ELECTRIC VEHICLE BATTERIES AS STORAGE SYSTEM

Bo BAI[1] and Siqin XIONG[2]

1. Engineering Laboratory of Energy Conservation and Emission Reduction Data and Modeling, School of Environment and Energy, Peking University Shenzhen Graduate School, Shenzhen 518055, China; email: baibo.pku@foxmail.com
2. Engineering Laboratory of Energy Conservation and Emission Reduction Data and Modeling, School of Environment and Energy, Peking University Shenzhen Graduate School, Shenzhen 518055, China; email: xiongsq95@163.com

ABSTRACT

The rapid development of electric vehicles leads to a growing demand for charging stations, nonetheless a large number of charging points will impose a significant impact on the electric grid. Photovoltaic based electric vehicles charging stations can not only provide clean energy, but also reduce the load on the electric grid. Moreover, second life batteries retired from electric vehicles provide another option for storage systems. A photovoltaic based charging station, with second life electric vehicle batteries as storage system located along the expressway is studied in this research. By focusing on the latest national subsidy policy, our results show that PV charging station is more economically efficient than traditional charging station located in each cities and provinces in China. When the price of second use traction batteries drops to 200¥/kWh, 83% provinces and cities could use battery energy storage system to achieve higher economic benefit.

Keywords: Photovoltaic, Charging station, Second life batteries, Economic analysis

1 INTRODUCTION

Ever since global warming was proposed by some scholars in 1800s, increasing amount of attention has been paid to the issue of climate change. One of the crucial sectors which contributes significantly to greenhouse gas emission is transportation, 95% of which depends on fossil fuels[1]. Under this circumstance, plug-in hybrid electric vehicles(PHEVs) and electric vehicles(EVs) are becoming popular due to their potential for oil consumption and greenhouse gases emission reduction by improving the overall fuel efficiency and cleanliness of light vehicles[2].To accompany for the PHEVs and EVs trends, a highly capable electricity infrastructure is required, while a large number of charging points may impose a significant impact on the electric grid. Photovoltaic(PV) based EVs charging stations, which could increase the penetration of renewable energy sources into the transportation sector, will not only provide clean energy, but also mitigate the dependence and impacts on power grid[3]. In the meantime, energy storage is essential for the development of renewable energy, since it appears to be the only solution to the problem of intermittency of production.[4]. For PV powered charging stations, small sized storage system can assist in mitigating the day-day solar variations and reduce the grid energy exchange [5]. Li-ion batteries present attractive features when adopted in energy storage applications except for its expensive cost[6]. However, second-use EV batteries can be reutilized at a sufficiently low cost[7].

Economics of PV powered workplace parking garage charging station has been studied in [8]. Through hourly simulations model, the results show that the garage owner will get the payback of installations and maintenance cost and make extra profit within the life of the PV panels. In this paper, we exam the economic benefits of PV charging stations with second life electric vehicle batteries as storage system for 30 provinces and regions in China under the assumption that the PV charging stations locate along the expressway instead of the workplace location assumption.

PV charging station along expressway can be exploited to deal with the difficulties of long-distance trip for EVs. After taking shape, it can support the layout of intercity charging grid, as well as act on peak shaving and valley filling for electric network. The demonstration project of PV charging station with second life electric vehicle batteries as storage system has been established at expressway service area in Tianjin, China. In this paper, economic benefits are evaluated via the comparison between PV charging station and traditional charging station. Net present value (NPV) and levelized cost of energy(LCOE) are applied as the economic measures.

2 METHODOLOGY

2.1 Policy and Subsidy

On August 30th, 2013, the NDRC (National Development and Reform Commission) issued the *Notice to Play the Role of the Leverage of Electricity Tariff to Promote the Healthy Development of Solar PV Industry*, which stated that the central government grants a subsidy of CNY0.42/kWh of each output from distributed solar PV(DPSV) projects[9]. And the nationwide PV power generation was divided into three level resource areas, with different feed-in tariff implemented[10].

On December 22nd, 2017, NDRC decreased the subsidy of DPSV projects to CNY0.37/kWh, and the feed-in tariff was reduced to CNY0.55/kWh for the first resource area, CNY0.60/kWh for the second resource area and CNY0.65/kWh for the third.

2.2 Data and Assumptions

The following study concentrates on a 15kWh installed capacity of PV charging station. According to the market investigation in China, the prevailing price of PV module is 3150 ¥ /kWh, and the soft cost of installation fee such as labor cost is supposed to be 2000 ¥ /kWh[11]. Market price of either converter or inverter is 650 ¥ /kWh. The degradation rate of PV module introduces only a small change of around 0.7%/year[12]. The lifetime of PV module is supposed to be 20 years[13], whereas the lifecycle of converter and inverter is considered to be 10 years, hens the replacement cost would take place at the end of first ten years.

[14] provides great convenience for us in terms of the evaluation of the PV module output. Taking consideration of irradiation data, dry bulb temperature, wind speed, and standardized setting of inverter and array, they develop provincial solar output profile in China by utilizing 10-year hourly solar irradiation data from 200 presentative locations.

2.3 Economic Evaluation

Economic performance of the project on condition of existing technology, market and policies will directly affect investors' willingness to invest [15], therefore, it is an important indicator to evaluate the development of PV charging station in China.

PV Charging Station

Grid-connected PV charging station is realizable since electricity is available in most service area along the expressway. In case where the PV is able to deliver certain portion of energy instead of full amount, the grid can help to deliver the rest portion, which means that both the PV and grid contribute to the charging[16]. Some infrastructure cost and revenue stream derived from PV charging station is similar with the cost and revenue stream derived from traditional charging station, in this case we only focus on the situation where PV panel is installed on an existing charging station, when doing the economic evaluation.

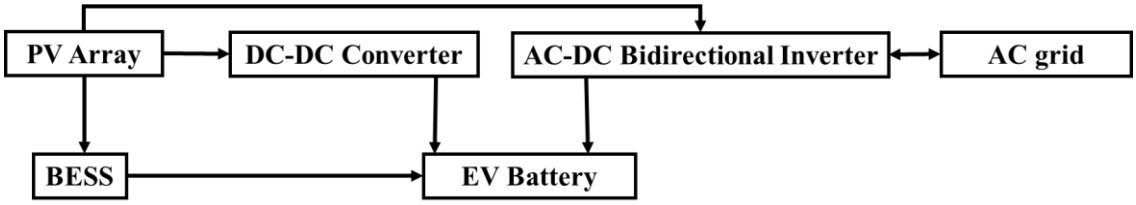

Figure 1. The structure of PV charging station with BESS.

Net present value which is calculated out of initial cost and all the future discounted cash flow over a period is applied to evaluate the economic benefit.

$$\mathrm{NPV} = -C_{initial} + \sum_1^n \frac{(CF_{in} - CF_{out})}{(1+i)^n}$$

$$= -\left(Ex_{pv} + Ex_{con}\right) + \sum_1^n \frac{((E_{sc}\cdot(p_{pur}+sub) + E_{grid}\cdot(p_{sold}+sub) - OpEx_{PV} - OpEx_{con} - OpRe)}{(1+i)^n}) \quad (1)$$

Where, $C_{initial}$ refers to initial investment cost which includes the cost of PV(Ex_{pv}), converter and inverter(Ex_{con}). The annual cash inflows (CF_{in}) is realized from the energy generated from PV for direct self-consumption (E_{sc}) and feeding back to the grid (E_{grid}). The electricity price for commercial sector (p_{pur}) and desulfurization benchmark price (p_{sold}) is collected manually from provincial *Development and*

Reform Commission, and sub refers to subsidy based on the national level. The annual O&M (operational and maintenance) cost for PV system ($OpEx_{PV}$) and inverter and converter ($OpEx_{con}$) is assumed to be 3% of its initial price[17]. $OpRe$ refers to the replacement cost of converter and inverter. n is the lifetime of PV. The interest rate of 5-year national debt (4.17%) in 2017 is used as the discounted rate(i).

The levelized cost of energy(LCOE) is a useful indicator to quantify the price of energy generated by the renewable energy project[18]. LCOE is normally measured as the ratio of the total cost over its lifetime and total energy output, which can be viewed as the minimum cost at which electricity must be sold to break-even over the lifetime of the project.

$$LCOE = \frac{C_{initial}+\sum_{n=1}^{Y}\frac{OpEx_{PV}+OpEx_{con}}{(1+i)^n}+OpRe}{\sum_{n=1}^{Y}\frac{E_{sc}+E_{grid}}{(1+i)^n}} \quad (2)$$

Battery Energy Storage System(BESS)

BESS could improve the share of self-consumption significantly, so we would like to examine whether installing BESS is economically efficient or not. The cost of installing BESS is determined as follow:

$$Ex_{BESS} = \frac{E_s}{DOD} \cdot p_{BESS} \quad (3)$$

Where Ex_{BESS} is the initial investment of BESS, which is the product of battery sizing and per unit cost(p_{BESS}). To determine the sizing of battery, we take the allowable depth of discharge(DOD) into consideration which equals to 80%. E_s refers to the energy to be stored.

The cash inflow of BESS is generated from the increasing percentage of self-consumption, and a total of 85% round-trip efficiency is assumed for reused batteries[19]. The cash outflow consists of O&M ($OpEx_{BESS}$) which is 2% of the initial investment, and replacement cost ($ReEx_{BESS}$). Since the lifetime of second-used batteries is supposed to be 5 years, replacement cost would incur at every 5 years.

3 RESULTS AND DISCUSSION

Firstly, by evaluating the incremental cost and benefit derived from PV charging station compared with traditional charging station, our results show that under the latest subsidy policy, PV charging station is more economically efficient than traditional charging station located in each cities and provinces, no matter how much self-consumption is accounted for, as shown in Table 1. Moreover, increasing self-consumption can further improve the economic performance, and the enhanced amount of NPV due to increased self-consumption is highly related to the difference between local electricity price and desulfurization benchmark price. Aside from shares of self-consumption, solar irradiation as well as local electricity price also plays important role in determining the NPV. As for the environmental performance, by avoiding the consumption of thermal power, the amount of CO_2 emission reduction is shown in Table 1. Qinghai gains both the highest economic benefit and environmental benefit from adding PV program, which is mainly derived from its high solar irradiation.

Table 1. NPV under different shares of self-consumption, and the LCOE, as well as CO2 emission reduction in each provinces and cities.

	NPV in thousands RMB, 15kWh						LCOE ¥/kWh	CO_2 emission reduction(kg)
w(self.c)	100%	80%	60%	40%	20%	0%		
Xinjiang	147.74	131.93	116.11	100.29	84.48	68.66	0.39	21316.66
Ningxia	129.34	109.94	90.55	71.15	51.75	32.35	0.49	16592.50
West Inner Mongolia	164.79	143.51	122.23	100.95	79.66	58.38	0.43	24677.71
Gansu	191.12	165.68	140.25	114.81	89.38	63.94	0.43	19111.66
Qinghai	704.88	628.17	551.45	474.74	398.03	321.31	0.18	51821.02
East Inner Mongolia	331.09	292.52	253.94	215.37	176.80	138.22	0.31	34548.79
Shanxi	192.06	172.28	152.49	132.70	112.92	93.13	0.39	22190.09
Shaanxi	137.21	118.72	100.22	81.72	63.23	44.73	0.52	16255.21
Yunnan	147.74	131.93	116.11	100.29	84.48	68.66	0.39	29419.70
Tianjin	187.73	163.98	140.23	116.48	92.73	68.98	0.46	17536.68

Beijing	229.31	201.04	172.78	144.51	116.25	87.98	0.42	11268.05
Hebei	155.16	139.61	124.06	108.51	92.96	77.42	0.44	20055.14
Liaoning	193.54	170.98	148.42	125.86	103.30	80.74	0.44	23640.54
Jilin	222.87	195.15	167.43	139.71	111.99	84.28	0.43	26071.13
Heilongjiang	191.38	167.84	144.29	120.75	97.20	73.66	0.46	20861.55
Sichuan	186.55	165.37	144.18	122.99	101.80	80.61	0.46	21645.87
Guizhou	88.59	74.87	61.15	47.43	33.72	20.00	0.62	11768.53
Henan	120.84	104.81	88.78	72.75	56.72	40.69	0.55	15087.98
Anhui	136.19	118.56	100.92	83.29	65.66	48.02	0.52	15040.59
Shandong	175.35	156.77	138.18	119.59	101.00	82.42	0.45	17175.74
Fujian	145.88	129.49	113.10	96.72	80.33	63.94	0.49	15943.30
Jiangsu	156.79	137.15	117.50	97.85	78.21	58.56	0.51	13502.63
Chongqing	103.35	88.38	73.40	58.43	43.46	28.48	0.62	14131.13
Hubei	130.34	112.27	94.21	76.15	58.09	40.03	0.58	13120.77
Jiangxi	90.67	77.50	64.33	51.15	37.98	24.81	0.65	12109.27
Shanghai	205.29	181.45	157.61	133.77	109.92	86.08	0.45	16939.03
Guangxi	97.39	83.10	68.82	54.53	40.25	25.96	0.65	11749.13
Zhejiang	174.40	153.35	132.30	111.26	90.21	69.16	0.49	13532.09
Hainan	348.22	315.77	283.32	250.87	218.42	185.97	0.31	23634.14
Hunan	115.16	99.85	84.55	69.24	53.93	38.62	0.62	12790.37
Guangdong	144.51	128.23	111.95	95.67	79.39	63.11	0.53	13743.70

Secondly, the increased self-consumption, which can be realized via installing BESS, will promote the economic perform significantly. However, whether installing BESS is economically efficient or not depends on the benefit from increased self-consumption and the cash outflow generated from BESS, thus we compared the cost of BESS when increasing certain amount of self-consumption with the revenue generated from the increased self-consumption, and then calculated the break-even price. Figure 2 illustrates that the higher the price of second use EV batteries as BESS can be accepted, the larger difference between local electricity price and desulfurization benchmark price, because larger difference means higher enhanced amount of NPV can be obtained from increasing self-consumption. However, Qinghai is an exception, since the energy loss from BESS is relatively large under its pretty high solar irradiation. When the price of second use battery drops to 200 ¥/kWh, 83% provinces and cities would use BESS to achieve higher economic benefit.

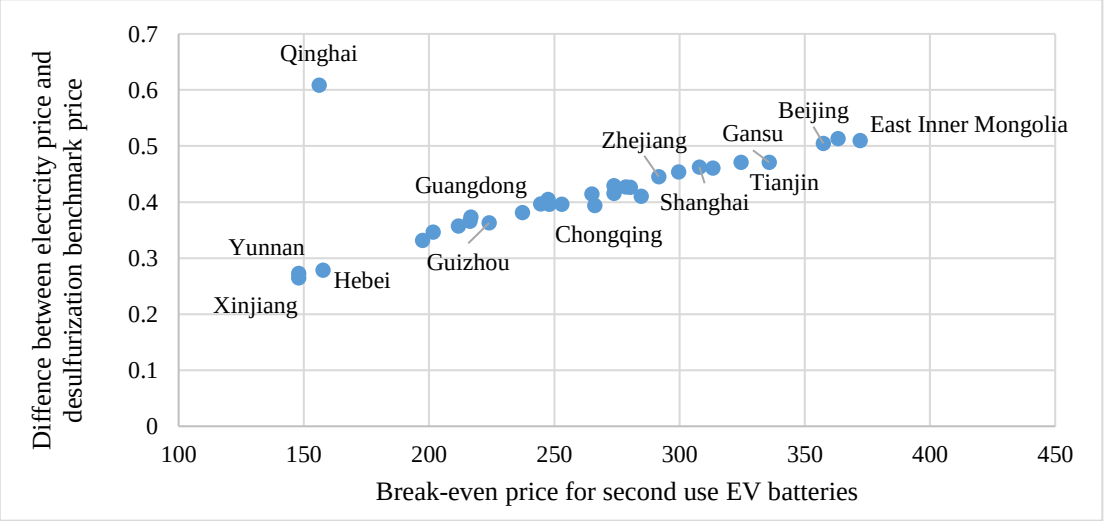

Figure 2. The difference between electricity price and desulfurization benchmark price against break-even price for second use EV batteries.

Thirdly, it appears meaningful to investigate whether the PV charging station is profitable in an environment without policy support. Supposing without the 0.37¥/kWh subsidy, our results reveal that the NPV of PV charging station is negative when the proportion of self-consumption is low in most areas as shown in Figure 2. Only Hainan and Qinghai can maintain positive NPV even the proportion of self-consumption is zero. Without BESS, when the direct shares of self-consumption can reach 50%, 80% provinces and cities could benefit from installing PV even without subsidy. The prevailing price of second use EV batteries is about ¥300/kWh in China, thus only East Inner Mongolia, Jilin, Beijing, Gansu, Tianjin, Heilongjiang and Shanghai can benefit from BESS so far.

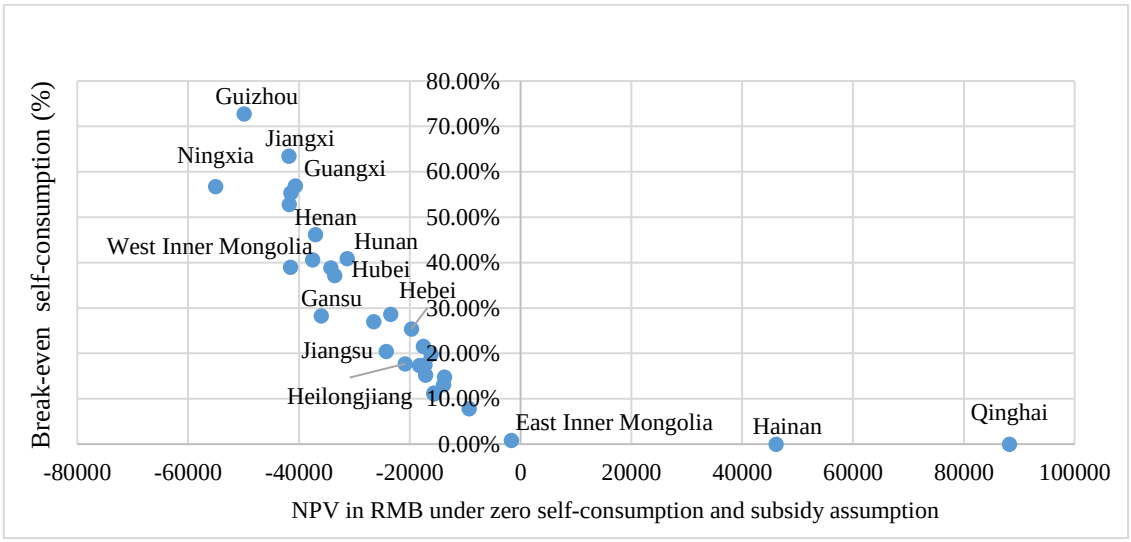

Figure 3. Without subsidy, the minimum self-consumption (%) required to achieve break-even against NPV with zero self-consumption.

Fourthly, since one of the main benefits for PV charging station is to mitigate the impact on grid, higher proportion of self-consumption helps to minimize the grid dependency. Thus we exam the economic performance of PV charging station when all the generated energy is used for self-consumption with the help of BESS. Under this circumstance, when the direct self-consumption is 40%, 60% of the energy will be stored. Illustrate by the case of Beijing, with current subsidy the NPV is ¥153134.34, while without the subsidy is ¥58852.88. As for Guizhou, where requires the highest self-consumption to avoid negative NPV without subsidy, the NPV is ¥39727.08 with subsidy, while -¥23912.91 without subsidy. So under the current price of reused batteries, some regions still cannot benefit from PV charging station without subsidy.

4 CONCLUSIONS AND SUGGESTION

To investigate the current feasibility and future application potential of PV charging station, this paper examines the economic performance of PV charging station in 30 provinces and cities by evaluating the incremental cost and benefit of PV charging station compared with the traditional charging station. The main results drawing from this paper are, based on existing technology, market and the latest policies, the economic performance of PV charging station is relatively attractive in each cities and provinces, no matter how much self-consumption is accounted for. Two primary means are pointed out that can help PV charging station to improve its economic performance, one of which is government subsidy. Without the ¥0.37/kWh government subsidy, only Qinghai and Hainan can achieve positive NPV under all electricity power consumption situations. When the direct shares of self-consumption reach 50%, 80% provinces and cities could benefit from installing PV. Thus the other way is to increase self-consumption, which can be achieved through installing BESS. When the price of second use EV batteries drops to 200¥/kWh, over 83% provinces and cities would use BESS to increase their self-consumption to gain higher economic benefit. Caused by different solar radiation and electricity price, the economic performance of PV charging station varies from region to region. To mitigate the impact of grid from charging EVs, as well as develop clean energy, government should allocate more funds to support the research and development of PV charging station. To promote the research and development, two types of regions should be paid more attention to. One is the area with abundant solar energy resources, where nature resource can be taken full advantage of

to gain high economic performance. Another one is the developed area in China, especially for those with high EVs penetration, which indicates potentially high self-consumption proportion. Under current subsidy policy, PV charging station is economically efficient, however, without the uniform subsidy for distributed solar PV, part of the regions cannot benefit from PV charging station. To promote the development, government subsidy for PV charging station should be differentiated instead of uniform, due to the variation of the economic development and solar irradiation resource. Moreover, the decreasing price of EV batteries should also be taken into consideration as one critical factor that may influence the economic performance.

REFERENCES:

[1] Bicer, Y. and I. Dincer, Comparative life cycle assessment of hydrogen, methanol and electric vehicles from well to wheel. *International Journal of Hydrogen Energy*, Vol. 42(6), pp. 3767-3777, 2017.
[2] Neubauer, J. and A. Pesaran, The ability of battery second use strategies to impact plug-in electric vehicle prices and serve utility energy storage applications. *Journal of Power Sources*, Vol. 196(23), pp. 10351-10358, 2011.
[3] Hung, D.Q., Z.Y. Dong and H. Trinh, Determining the size of PHEV charging stations powered by commercial grid-integrated PV systems considering reactive power support. *Applied Energy*, Vol. 183, pp. 160-169, 2016.
[4] Bermúdez, J.M., et al., New concept for energy storage: Microwave-induced carbon gasification with CO2. *Energy Conversion and Management*, Vol. 78, pp. 559-564, 2014.
[5] Chandra Mouli, G.R., P. Bauer and M. Zeman, System design for a solar powered electric vehicle charging station for workplaces. *Applied Energy*, Vol. 168, pp. 434-443, 2016.
[6] Heymans, C., et al., Economic analysis of second use electric vehicle batteries for residential energy storage and load-levelling. *Energy Policy*, Vol. 71, pp. 22-30, 2014.
[7] Assunção, A., P.S. Moura and A.T. de Almeida, Technical and economic assessment of the secondary use of repurposed electric vehicle batteries in the residential sector to support solar energy. *Applied Energy*, Vol. 181, pp. 120-131, 2016.
[8] Tulpule, P.J., et al., Economic and environmental impacts of a PV powered workplace parking garage charging station. *Applied Energy*, Vol. 108, pp. 323-332, 2013.
[9] Zhang, S., Analysis of DSPV (distributed solar PV) power policy in China. *Energy*, 2016. 98: p. 92-100.
[10] Zhi, Q., et al., China's solar photovoltaic policy: An analysis based on policy instruments. *Applied Energy*, Vol. 129, pp. 308-319, 2014.
[11] Zhang, F., et al., Analysis of distributed-generation photovoltaic deployment, installation time and cost, market barriers, and policies in China. *Energy Policy*, Vol. 81, pp. 43-55, 2015.
[12] Rodrigues, S., X. Chen and F. Morgado-Dias, Economic analysis of photovoltaic systems for the residential market under China's new regulation. *Energy Policy*, Vol. 101, pp. 467-472, 2017.
[13] Zou, H., et al., Large-scale PV power generation in China: A grid parity and techno-economic analysis. *Energy*, Vol. 134, pp. 256-268, 2017.
[14] He, G. and D.M. Kammen, Where, when and how much solar is available? A provincial-scale solar resource assessment for China. *Renewable Energy*, Vol. 85, pp. 74-82, 2016.
[15] Zhao, X., Y. Zeng and D. Zhao, Distributed solar photovoltaics in China: Policies and economic performance. *Energy*, Vol. 88, pp. 572-583, 2015.
[16] Bhatti, A.R., et al., Electric vehicles charging using photovoltaic: Status and technological review. *Renewable and Sustainable Energy Reviews*, Vol. 54, pp. 34-47, 2016.
[17] Gur, K., et al., The reuse of electrified vehicle batteries as a means of integrating renewable energy into the European electricity grid: A policy and market analysis. *Energy Policy*, Vol. 113, pp. 535-545, 2018.
[18] Akter, M.N., M.A. Mahmud and A.M.T. Oo, Comprehensive economic evaluations of a residential building with solar photovoltaic and battery energy storage systems: An Australian case study. *Energy and Buildings*, Vol.138, pp. 332-346, 2017.
[19] Ahmadi, L., et al., Energy efficiency of Li-ion battery packs re-used in stationary power applications. *Sustainable Energy Technologies and Assessments*, Vol.8, pp. 9-17, 2014.

LONG-TERMP MODEL ANALYSIS FOR DIFFERENT PHOTOVOLTAIC MODULE TECHNOLOGIES AT DIFFERENT SITES

I. Hadj Mahammed[1,2], A. Hadj Arab[3], S. berrah[1] and Y. Bakelli[3]

1. Electronics Lab/ Faculty of Electronics, A. Mira University, Bejaia, Algeria, e-mail: hmidriss65@yahoo.fr, e-mail: sberrah@yahoo.fr
2. Unité de Recherche Appliquée en Energies Renouvelables, URAER, Centre de Développement des Energies Renouvelables, CDER, 47133, Ghardaïa, Algeria,
3. Centre de Développement des Energies Renouvelables, CDER, 16340, Algiers, Algeria , email: hadjarab@hotmail.com, e-mail:bakelliy@gmail.com

ABSTRACT

The present work shows the results of electrical performance measurements of 153 crystalline silicon PV modules following long-term outdoor measurements. 90 PV modules consist of a continuous PV array of the first grid-connected PV system in Algeria, installed at CDER site of Mediterranean coast, Bouzareah, Algiers, along with 63 PV modules whose measurements have been collected from different applications, undertaken in the arid area of the desert region of Ghardaïa site, about 600 km south of Algiers. Following different characterization tests, it turned out that the all tested PV modules keep their power generating rate except a slight reduction. Accordingly, a mathematical model has been adopted to carry out the PV module testing at different irradiance and temperature levels. Hence, different PV module parameters have been computed based on the recorded values of the open-circuit voltage, the short-circuit current, the voltage and current at maximum power point. The electrical measurements have showed different degradations of current-voltage parameters. All the PV modules averred a decrease in the nominal power, which is variable from one module to another.

Keywords: Photovoltaic module, degradation, ageing, performance, PV array

1 INTRODUCTION

The reduction in the cost of crystalline silicon photovoltaic (PV) modules is noticeable and holds a great promising future hides a promising future). However, this raises the question of whether weather conditions can have an impact on these PV modules. Especially in terms of the impact weather conditions on PV modules. The manufacturers deploy efforts to improve the PV modules lifetimes, even under hard operating conditions. Therefore, the acceleration and qualification tests procedures have been undertaken to the aging mechanisms, and to establish reasonable standard quality. A purchased PV-module is often accompanied with a warranty of more than 20 years, which is based on a type certificate IEC 61215" and processed with a number of accelerated lifetime tests. It is of a great importance to support the accelerated tests data with data from field-testing to convince the customers that a warranty of more than 20 years is valid. Significant progress has been achieved, however more research is needed and then manufacturers will have to establish serious standard quality control in order to fulfil the long-term goals. So, as to predict lifetime, mainly in remote areas, it is necessary to study the aging of the photovoltaic modules in various climatic areas. Ndiaye et al. [1] have evaluated the performance degradation of four Photovoltaic modules after a few years of operation in a tropical environment. The global degradation and the degradation rate of electrical characteristics such as Current-Voltage and Power-Voltage curves, open-circuit voltage (Voc), short-circuit current (Isc), maximum output current (Imax), maximum output voltage (Vmax), maximum power output (Pmax) and fill factor (FF) have been evaluated at standard test conditions (STC). They concluded that Pmax, Imax, Isc and FF are the most degraded performance characteristics common to all PV modules. A PV system reliability and lifetime depend essentially on the energy performance of PV modules, as well as on their different degradation modes. Therefore, research must emphasize on the photovoltaic modules degradation. Ndiaye et al. [2] reviewed recent literature about different types of degradation They have also given models associated with the PV modules degradation that can help to overcome the obstacle in the long-term experiments in order to study PV modules degradation, under real conditions. Chandel et al. have inventoried the main defects observed in PV modules, and degradation is quantified by measuring PV

parameters under indoor and outdoor conditions [3]. The Schatz Energy Research Center (SERC) has performed a PV array employed in a cool, marine environment [4-5]. Two modules that were in work for more than 30 years in the Libyan climate have undergone outdoor and indoor measurements by M. A. S. Alshushan and I. M. Saleh [6]. Singh et al. [7] have discovered that most of the modules tested in this hot-dry climate do not go with the guarantee expectations, which is limited to 20% degradation of the nominal power over 20 years. Kichou et al. [8] have studied the degradation of the micromorph solar cells of the TFPV modules in a relatively dry and sunny inland site with a Continental-Mediterranean climate in Jaén, Spain. They have noted the reduction of the DC output power of about 12.51% after the first month of exposure under outdoor conditions. Furthermore, the stabilization period was observed to start after four months of operation with a total reduction of the PV array DC output power of 16.66%. Kahoul et al. [9] have studied the electrical performance degradation of local manufacturing PV modules (UDTS-50), in Algeria. Results reveal the degradation of some PV modules up to 12% compared to their original state. As for us, we aim at evaluating the degradation of the electrical characteristics of 153 PV modules of different technologies, tested at different sites. 90 PV modules of monocrystalline silicon technology operating, at CDER, Bouzareah of Mediterranean climate condition, and 63 modules of mono and polycrystalline at Ghardaïa site of arid climate. The period of exposure of these modules is the same in both sites, 2004-2015.

.

2 PHOTOVOLTAIC ARRAY

The total number of the PV modules previously mentioned forming the four PV generators (PVG) and operating for different applications have been put into test according to the type of use, as follows:

2.1 Photovoltaic Array PVG1

The PV array consists of 90 PV 106 Wp crystalline silicon modules. It is composed of three sub-arrays of 30 modules each. The sub-array configuration is 15sx2p. Each sub-array is connected to a 2.5 kVA inverter [11].

2.2 Photovoltaic Array PVG2

Similar to the PVG1, the current PVG2 array, which consists of 30 PV modules of the same technology, was installed on a roof at URAER (Applied Research Unit for Renewable Energy) building (Ghardaïa). The station latitude is 32.4 °. The common tilt angle was close to the latitude angle of Ghardaïa. This site is characterized by huge irradiances and temperatures. The PV array consists of the two following sub systems:

- Subsytem1 consists of 10 PV modules of 100 Wp, connected in (2SX5P).
- The subsystem 2 consists of 20 PV modules of 50 Wp configured in (2sx10p).

All the subsystems are connected to a 2 kVA inverter and supply a PV standalone system.

2.3 Photovoltaic Array PVG3

This PV array was installed at URAER site (Ghardaïa). As PVG1, it is the result of collaboration between CIEMAT and CDER, The station latitude is 32.4 °. The unique tilt angle considered of the PV array is equal to the latitude angle of Ghardaïa, situated in the Sahara region, which is characterized, by higher irradiances and temperatures [10].

2.4 Photovoltaic Array PVG4

This PV array was installed at URAER site of Ghardaïa as part of a National Research project (NRP). As the previous one, it is inclined to the latitude angle of the Ghardaïa site. The PV array consists of 8 PV modules of 110 Wp, polycrystalline silicon, mounted in 2sx4p configuration. All these modules are connected to a 1.5 kVA inverter to supply a solar house.

3 DEGRADATION RATE

In order to quantify the degradation rate (DR) of the maximum power output (Pmax) of the PV modules, measured standardized values are compared to the reference ones given by the manufacturer's data of the PV module. The difference in percentage represents the reduction of the parameter. The degradation rate of parameters is given respectively by the following equation [1]:

$$DR(\%) = \left(\frac{P\max_0 - P\max}{P\max_0} \right) \times 100 \qquad (1)$$

Where: Pmax0 and Pmax are respectively the maximum power given by the manufacturer and the maximum measured power.

4 RESULTS AND DISCUSSIONS

4.1 Results For PVG 1

Table 1. presents a detailed estimation of modules degradation for the three subarrays

Table 1. Degradation factors of the tested pv modules of pvg1 subarrays

Module	**Sub-array 1**		**Sub-array 2**		**Sub-array 3**	
	String 1	String 2	String 1	String 2	String 1	String 2
M1	1.20	2.42	3.33	6.12	3.27	10.77
M2	2.35	7.21	4.39	6.84	3.88	6.22
M3	4.47	5.74	9.31	7.37	7.28	13.75
M4	3.33	5.20	6.80	7.98	7.21	10.37
M5	1.52	7.11	7.52	5.25	9.19	9.97
M6	1.30	5.81	6.78	6.09	7.88	13.24
M7	4.99	1.14	3.79	8.60	9.54	9.89
M8	1.48	4.29	2.55	5.05	7.00	7.55
M9	2.90	3.87	2.70	6.82	7.10	8.65
M10	0.53	6.36	7.87	10.12	6.64	10.29
M11	1.00	3.85	4.91	3.28	9.82	7.71
M12	4.87	4.51	2.34	9.27	11.25	6.81
M13	4.01	5.96	4.24	5.33	10.56	6.56
M14	7.93	2.11	4.10	4.81	11.66	7.83
M15	6.15	3.99	8.69	3.98	8.66	5.02
Mean DR	**3.20**	**4.64**	**5.29**	**6.46**	**8.06**	**8.98**
Subarray mean DR	**3.92**		**8.52**		**5.87**	

Table 2 summarizes the minimum, average and maximum performance of all modules of the installed grid connected PV system. It provides the maximum power modules for different performances reported at STC conditions: their degradation rates and their positions in the PV generators. Thus, the best performance is allotted to a module from the sub array1, also the medium to one module of the third sub array3 and the worst performance to one belonging to the second sub array2.

Table 2. Performance of all modules of the installed grid connected PV system

Parameters	**Minimal Performance**	**Average performance**	**Maximal performance**
Pmax (W)	91.43	99.54	105.44
DR (%)	13.75	6.10	0.53

4.2 Results For PVG 2

It can be seen that the majority have moderate degradation, except for one module of this array which has high degradation with 16.25 % of DR. But 90% of this array has average degradation betwween 5.07% and 8.32 % of DR wich is inferieur to 0.8 % DR /year. (See Table 3). From Table 3, 7.19% of DR is observed. This degradation can be divided into three categories as follows: 20% of moderate, 20% of medium and 60% of high degradation.

Table 3. Degradation factors of the tested PV modules of the sub- array1 of PVG2.

Sub-array1 PVG2		**Sub-array2 PVG2**			
	M 1		M 1	M2	String Mean DR
S1	5.65	S1	5.96	10.67	8.315
S2	8.32	S2	5.11	4.72	4.915
S3	16.25	S3	7.91	7.31	7.61
S4	7.03	S4	5.01	1.93	3.47
S5	6.74	S5	21.88	6.5	14.19
S6	7.39	S6	12.95	12.67	12.81
S7	7.37	S7	5.86	2.04	3.95
S8	5.79	S8	5.28	5.73	5.505
S9	5.62	S9	1.08	8.79	4.935
S10	5.07	S10	6.86	5.58	6.22
Mean DR	7.52		7.192		

4.3 Results For PVG 3

It can be seen that 80 % of them have average degradation, 12 % have moderate degradation and only 8% have high degradation. with 1.7% /year (Table 4).

Table 4. Degradation factors of the tested PV modules of PVG3

Sub-array PVG3	**Module**				
	Row				
Column	17.48	16.22	17.62	18.82	18.74
	14.81	16.87	15.65	16.91	20.02
	18.03	15.22	14.59	18.01	18.89
	19.18	21.86	14.79	16.05	17.18
	19.22	17.37	18.37	18.23	15.89
Mean DR	17.44				

4.4 Results For PVG 4

It can be seen that 62.5% have average degradation. Unlike the other PV arrays, it presents the lower DR 0.6%/year (Table 5.

Table 5. Degradation factors of the tested PV modules of PVG4

Sub-array PVG2	**Module**		
	M1	M2	Mean DR
S1	4.77	7.29	6.03
S2	7.67	0.34	4.00
S3	6.81	9.08	7.95
S4	5.13	4.39	4.76
Subarray mean DR	5.69		

5 CONCLUSION

The degradation of the PV modules of the different PV systems installed since 2004 in two different regions was presented in this work. The outdoor testing was carried out on the 153 modules, which were manufactured and installed in 2004, have been measured after this period of outdoor exposure in the two different climates. The results are translated and compared with the characteristics given by the manufacturers of the tested modules. The modules have an average peak power degradation between 3.92% and 17.44% lower than the average value measured before exposure. It can be noted that the modules are not only exposed but still working since 2004. However, we noticed that the degradation is not homogeneous; the modules located in the middle of the 90 modules of the grid-connected system were the most affected by degradation, this is probably due to the lack of natural ventilation despite the fact that the modules are exposed to the sea. Furthermore, the degradation varies from 0.5 to 25 %. However, the highest degradation was observed on the system installed in semiarid climate, which is characterized by a hostile climate, particularly the PV array of the solar pumping system that is installed on the floor unlike those installed on the roof.

REFERENCES

[1] Ndiaye A., Kébé C. M. F., Charki A., Ndiaye P. a., Sambou V., et Kobi A., Degradation evaluation of crystalline-silicon photovoltaic modules after a few operation years in a tropical environment 2014, Sol. Energy;103: 70–77.

[2] Ndiaye A., Charki A., Kobi A., Kébé C. M. F, Ndiaye P. A., et Sambou V., Degradations of silicon photovoltaic modules: A literature review, Sol. Energy 2013; 96: 140–151.

[3] Chandel S. S., Nagaraju Naik M., Sharma V., et Chandel R., Degradation analysis of 28 year field exposed mono-c-Si photovoltaic modules of a direct coupled solar water pumping system in western Himalayan region of India, Renew. Energy 2015 ;78: 193–202,.

[4] Reis A. M., N. Coleman T., Marshall M. W., Lehman P. A., et Chamberlin C. E., Comparison of PV module performance before and after 11-years of field exposure. In: Conference Record of the Twenty-Ninth IEEE Photovoltaic Specialists Conference 2002; 19-24 May 2002; Hyatt regency New Orleans, New Orleans, Louisiana USA: pp1432-1435.

[5] Chamberlin C. E., Rocheleau M. A., Marshall M. W., Reis A. M., Coleman N. T., Lehman P. A. Comparison of PV module performance before and after 11 and 20 years of field exposure, In: 37th IEEE Photovoltaic Specialists Conference (PVSC) 2011; 19-24 June 2011; Seattle, Washington, USA:IEEE. pp. 000101-000105.

[6] Alshushan M. A. S., Saleh I. M., Power degradation and performance evaluation of PV modules after 31 years of work, In: 39th IEEE Photovoltaic Specialists Conference (PVSC) 2011; 16-21 June 2013; Tampa, Florida, USA: pp. 2977–2982,

[7] Singh J., Belmont J., et TamizhMani G. Degradation analysis of 1900 {PV} modules in a hot-dry climate: {Results} after 12 to 18 years of field exposure. In: 39th IEEE Photovoltaic Specialists Conference (PVSC) 2011; 16-21 June, 2013; Tampa, Florida, USA: IEEE pp. 3270–3275.

[8] Kichou S., Abaslioglu E., Silvestre S., Nofuentes G., Torres-Ramírez M., Chouder A. Study of degradation and evaluation of model parameters of micromorph silicon photovoltaic modules under outdoor long term exposure in Jaén, Spain. Energy Convers. Manag., 2016; 120: 109-119.

[9] Kahoul N., Houabes M., et Sadok M. Assessing the early degradation of photovoltaic modules performance in the Saharan region, Energy Convers. Manag.2014; 82: 320-326.

[10] Hadj Arab A., Ait Driss B., Amimeur R., et Lorenzo E. Photovoltaic systems sizing for Algeria. Sol. Energy.1995; 54,no 2: 99-104.

[11] Hadj Arab A., Cherfa F., Chouder A., Chenlo F. Grid-Connected Photovoltaic System at CDER-Algeria. In: 20 th European Photovoltaic Solar Energy Conference and Exhibition 2005; 06-10 June 2005; Barcelona, Spain: pp.6-10.

[12] Boutelhig A., Hadj Arab A., Hanini S. New approach to exploit optimally the PV array output energy by maximizing the discharge rate of a directly-coupled photovoltaic water pumping system (DC/PVPS), Energy Convers. Manag. 2016; 111: 375-390.

[13] Hadj Arab A., Chenlo F., Benghanem M., Loss-of-load probability of photovoltaic water pumping systems, Sol. Energy 2004; 76, no 6: 713-723,

[14] Bandou F., Hadj Arab A., Belkaid M. S., Test Performance Electrical of the Photovoltaic Module in Two Different Environments. Energy Procedia 2013; 36: 1018-1024.

OPTICAL AND THERMAL ENHANCEMENT OF ALUMINUM SUBSTRATES WITH AIR BLASTED GRAPHENE DEPOSITS FOR POTENTIAL SOLAR THERMAL APPLICATIONS

Abdul Hai Alami[1,2] and Kamilia Aokal[2]

1. Sustainable and Renewable Energy Engineering Department, University of Sharjah, P.O. Box 27272, Sharjah, United Arab Emirates, aalalami@sharjah.ac.ae

2. Centre for Advanced Materials Research, University of Sharjah, P.O. Box 27272, Sharjah, United Arab Emirates, k_aokal@outlook.com

ABSTRACT

As a material with interesting properties, graphene has been the center of attention for various applications on the micro- and nano-scale. This work presents a facile process with which pure graphite powder is air blasted on substrates with large surface areas to generate an adherent graphene layer. The process is chemical-free and carried out at atmospheric pressure and temperature. The resulting graphene deposits are then characterized with Raman spectroscopy and scanning electron microscopy to determine its quality and number of layers produced. The aluminium substrates with graphene deposits are then assessed for the enhancement of their optical and thermal properties compared with a bare aluminium reference. The proposed process promises simultaneous graphene synthesis and deposition on large absorber plates of thermal solar collectors. The process is amenable for automation and is expected to drive down the costs of graphene coats application with all the attractive properties offered by such material.

Keywords: Bulk graphene deposition, solar thermal materials, optical enhancement

1 INTRODUCTION

Metallic substrates offer a wide range of applications across many different fields. In order to maintain their physical surface properties, surface coatings are required to prolong the material lifecycle and reduce process maintenance.

Evidently, graphene is a material that achieved prominence shortly after its discovery in 2004, and has attracted researchers to understand and exploit its superior optical, thermal, physical, electrical and structural properties to a wide spectrum of applications [1-3]. Its high conductivity and broadband light absorption of 2.3%. demonstrates graphene as a good candidate for optical modulation. However, graphene's optical and thermal properties are extremely sensitive to the number of layers and structural defects present, and for practical high-performance photodetectors for example, tuning its synthesis routes and conditions is relatively important [4, 5, 6].

Historically, graphene has been produced by various exfoliation techniques that are now well established and documented, including mechanical and chemical exfoliation [7-12]. In addition to that, graphene has also been grown on different substrates, such as catalytic metals, silicon carbide, etc. through chemical vapor deposition (CVD) and plasma enhanced CVD, among other reported procedures [13-16]. While existing synthesis approaches such as chemical vapor deposition (CVD) on copper substrates and epitaxial growth on silicon carbide can produce highly ordered graphene layers, the costly high temperature and/or high vacuum process prohibit the widespread usage, and the subsequent need for transferring graphene from the growth substrates prove to be challenging. As a result, simple and low-cost alternatives addressing both the synthesis and deposition of graphene films are highly desirable.

Very rarely has high throughput mechanical exfoliation techniques been put forward, although some have succeeded by the use of high-energy centrifugal milling [17, 18]. Therefore, exfoliation methods with higher yields are still of critical interest.

This work presents a novel process of exfoliating high purity graphite to produce few-layer graphene material by high pressure graphite blasting. The process is fully automated, and relies on allowing the blasting nozzle to traverse the specimen a pre-set number of times to introduce graphene on the surface. The specimens are then characterized, and tested to assess the optical and thermal enhancements of the graphene layer. The sought application is to cover the surface of the absorber section of solar thermal collectors with such material, to enhance its absorbance in the visible and near infrared regions of the solar spectrums. The

process shows good promise of applying graphene on large substrates with minimal energy expenditure and controlled results.

2 EXPERIMENTAL

2.1 Sample preparation

A standard sand blasting gun with a detachable 500 ml reservoir (to be filled with graphite powder) is used in conjunction with a high pressure air compressor. The graphite used is 4N pure (99.99%) obtained as a rod, with small pieces cut off and ground in a ball milling machine to arrive at a fine powder no more than 125 μm in size (sieved). Larger particles will not pass through the nozzle area. For the current procedure, the distance between the sample surface and the blasting gun was varied between 20cm and 40 cm apart. To ensure proper control over the deposition process, a Shapeoko2 CNC machine (www.inventables.com) shown in Figure 1 was used to control the z-location of the nozzle from the samples, while moving it in the x-y planes as accurately as possible.

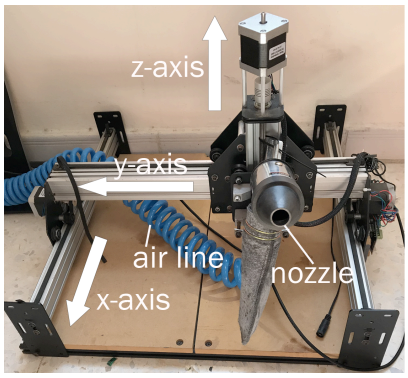

Fig. 1. CNC machine with fitted high air pressure nozzle

The machine was programmed to reciprocate in the y-direction to fix the deposition rate at one, two or three passes. The linear velocity of the machine was kept at a constant 0.1m/s throughout the experiments, while the blasting pressure of the graphite-rich air was set to 8 bar. The 0.35mm thick aluminum substrates had their surfaces ground with 120 grit sand paper to unify the surface conditions. The samples were then rinsed with deionized water and placed on the CNC machine for deposition.

2.2 Sample characterization

Raman spectroscopy and Scanning Electron Microscopy (SEM)

Raman spectroscopy is utilized as a verification tool of the presence and quality of graphene pertinent to the deposition process. This is done by identifying the typical peaks of graphene known as the D, G and 2D peaks corresponding to wavenumbers of ~1350, ~1580 and ~2700 cm-1, respectively. The Raman spectra are measured at room temperature in the back scattering configuration with a Renishaw inVia Raman microscope its visible 514nm laser. Random locations were scanned with 10-50% laser intensity with an illuminated area of around 1 μm. The spectral dataset was then normalized with its baseline subtracted and was scanned along a 200 μm2 area for G-band areas larger than 1581.6 to provide a mapped image for analysis on deposition coverage. The samples were characterized using a VEGA3 XM TESCAN scanning electron microscope (SEM), operating at 30 kV acceleration voltage.

Optical tests

Spectral reflection of the sheets is carried out via Maya 2000-Pro high-resolution spectrometers (from OceanOptics). A dedicated Vis-NIR range (375-850 nm) spectrometer has a resolution of 0.2 nm and has 300 lines per mm diffraction gratings and 10-μm entrance slit. The signals are transported via a fiber optic cable 2-m long, and of a 200-μm-core diameter. The integrating sphere (OceanOptics ISP-REF, with a sample aperture of 0.4 inch) has a built-in tungsten halogen light source (Ocean Optics LS-1-LL) and is capable of measuring specular and diffuse reflectance. A reference surface of a roughened aluminum is used to store baseline reflectance (100 %) spectra to facilitate comparison between the various compositions.

Thermal tests

Thermal testing was carried out on 1 cm2 sample surface areas using a 750W heating plate from Semco with k-type thermocouples occupying a circular surface contact 0.1mm in diameter. The samples were heated until steady state and were cooled back to room temperature.

3 RESULTS AND DISCUSSION

3.1 Raman spectroscopy and SEM results

Raman spectroscopy is a valuable tool in determining the existence and quality (number of layers) of the produced graphene material. The graphs of Figure 2 show the results of samples with one, two and three deposition passes. In the two and three pass samples analyzed, the line width of the 2D peak, along with its perfect symmetry, is found to be about 60 cm^{-1}. Figure 2(b) shows a distinct bulge to the left of the 2D band of the single-pass sample indicating the presence of multi-layer graphene (MLG) of more than 5 layers.

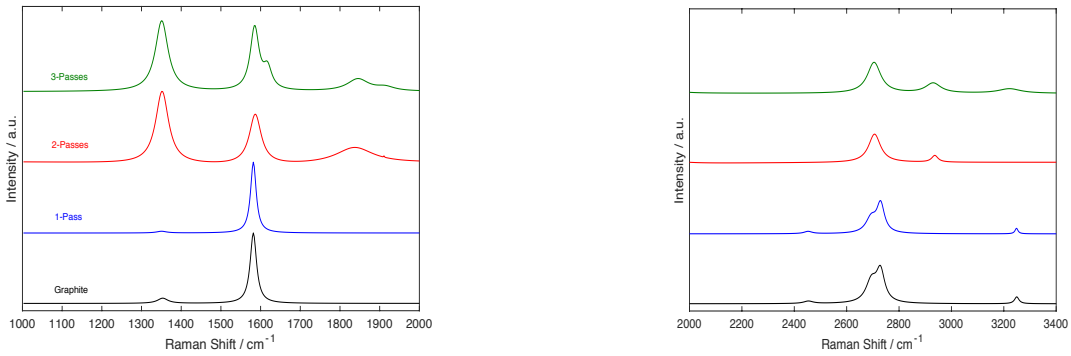

Fig. 2. Raman Spectroscopy of sandblasted samples

This is better presented by correlating the G band position with the number of layers using the following Equation:

$$\omega_G = 1581.6 + \frac{11}{n^{1.5}} \quad (1)$$

where ω_G is the observed Raman shift that correlates to the *G*-peak, while *n* determines the number of layers present. A summary of the results is shown in Table 1, which also includes the expected peaks of graphite for comparison.

Table 1. G peak analysis for specimens at 20cm distances from nozzle

Sample	G peak [cm^{-1}]	2D peak [cm^{-1}]	I_D/I_G	L_a / nm	Number of layers
Graphite Powder	1580	2720	0.084	89.11	-
Single pass	1582	2727	0.033	507.63	>5
Two passes	1585	2707	1.38	12.14	2
Three passes	1585	2706	1.092	15.34	2

A mapping image was created for the samples where the spectral dataset was normalized with its baseline subtracted and was scanned along a 200 μm2 area for G-band areas larger than 1581.6 (the resulting peak from graphite). Figure 3 shows better homogeneity in the triple-pass samples. The samples have been further characterized via optical and microstructural techniques as will be described in the following paragraphs.

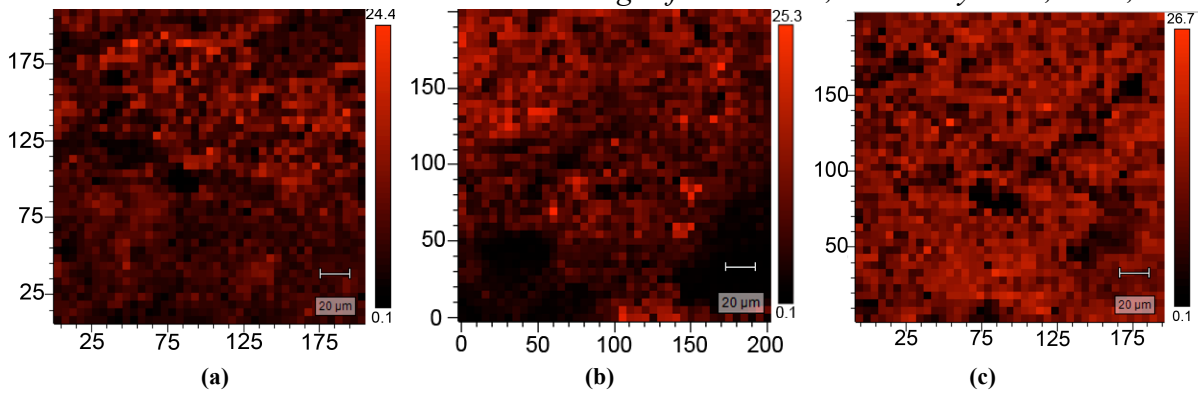

Fig. 3. Raman mapping figure a) one and b) two and c) three passes

Figure 4 (b-d) shows the SEM images taken for the one, two and three passes, respectively against the bare aluminium reference in Figure 4 (a).

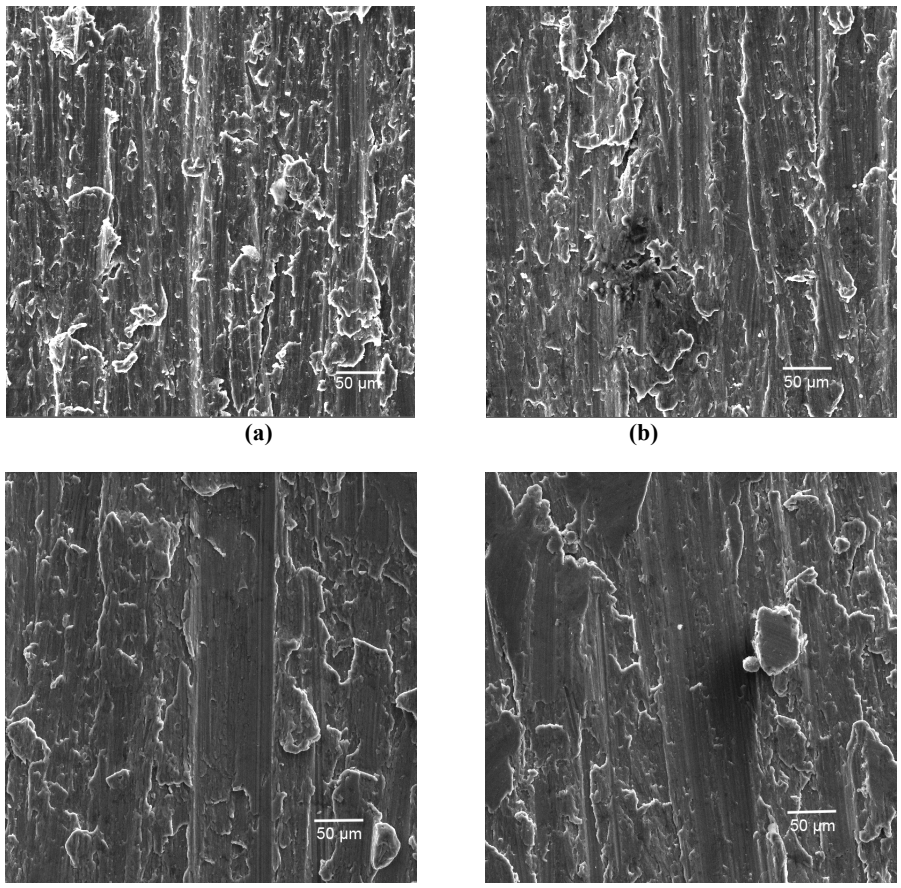

Fig. 4. SEM images for (a) bare aluminum and specimens with (b) one, (c) two and (d) three deposition passes

The transparent nature of the graphene deposits expose the ground surface details as the homogeneity of the coverage is enhanced with two and three passes (Figures (c) and (d)). As will be discussed later, this optical translucency is coupled with the thermal properties of graphene to create an attractive effect that will enhance the in-plane heat transfer of substrates with graphene deposits.

3.2 Optical test results

The samples were also subjected to a reflectivity test to investigate the effect of the graphene deposition on their optical performance. Figure 5 shows the reflectivity test results for the single-pass, double-pass and triple-pass samples. For the single-pass, reflectivity is seen to decrease towards the visible range and picks up at around 600 nm. In the visible and near infrared range, transparent monolayer graphene corresponds to an absorption value of 2.3%, due to its fine structure constant.

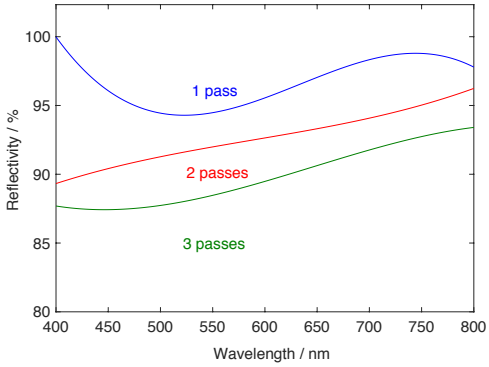

Fig. 5. Sample Reflectivity for specimens with two and three passes against the untreated aluminum reference.

The triple-pass sample showed the highest absorbance value when compared to single-pass samples. The spectra for the triple-pass sample consistently showed a 7% increase in absorption when compared to the single-pass sample. This is due to the ability of the light to pass through the fewer layers of graphene more efficiently than with the multi-layer graphite. Note that the surfaces were not painted with black-mat paints, and thus their reflectivity remains large compared with darkened specimens prepared for better absorbance.

3.3 Thermal test results

Thermal testing of the specimens shows the enhanced thermal conductivity of the sheets with increased passes as shown in Figure 6. Since the number of graphene layers is inversely proportional to the number of deposition passes, the thermal conductivity of aluminum sheets is increased around 22% for specimens with two graphene layers compared to the bare aluminum reference. The difference is also pronounced when comparing the two-layer graphene specimens with ones having more than 5 layers (around 10% larger for the two-layer graphene sample).

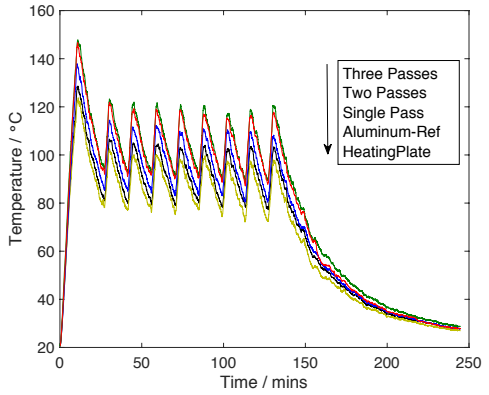

Fig. 6. Thermal analysis for specimens with one, two and three passes vs. vs. the untreated aluminum reference

The heating plate thermostat maintains the temperature between 80 and 100˚ C, and hence the fluctuation in temperature measurement with time. It is interesting to note how adding the aluminum sheets enhances the local thermal conductivity of the plate, and hence adding the graphene layer is analogous to adding fins to the surface but without complex inclusion of metallic protrusions. This opens up applications in heat dissipation for electronic circuits without the need for cumbersome heat sinks and fins.

CONCLUSION

This paper introduced a novel method of simultaneously synthesizing and depositing graphene from pure graphite powder directly onto an aluminium substrate. The depositing nozzle, operating at 8 bar pressure, blasted the graphite powder which in turn was mechanically exfoliated into adherent graphene layers. The effect of depositing such layers on the optical and thermal properties of pure aluminium substrates was experimentally proven. With an inverse relationship between the number of deposition passes and number of graphene layers produced, the three pass deposition setting was found to result in a homogenous two-layer graphene coverage. Optically, the specimens with three passes exhibited the best spectral absorptivity (corresponding to the least spectral reflectivity) between 450-800 nm. The specimens have also exhibited the

best enhancement in thermal conductivity compared with the bare aluminium reference. These results confirm the suitability of the process in producing large absorbers for thermal solar collectors that have enhanced optical and thermal properties. The relative ease of this automatic deposition process makes it attractive for large-scale applications that can benefit from an added graphene layer, with all the enhancements it provides.

REFERENCES

[1] HO. Pierson, Handbook of carbon, graphite, diamond and fullerenes. NJ, USA: Noyes; 1993.

[2] A. Ferrari, J. Meyer, V. Scardaci, C. Casiraghi, M. Lazzeri, F. Mauri, S. Piscanec, D. Jiang, K. Novoselov, S. Roth and A. Geim, "Raman Spectrum of Graphene and Graphene Layers", Physical Review Letters, vol. 97, no. 18, 2006.

[3] A. Ferrari and J. Robertson, "Interpretation of Raman spectra of disordered and amorphous carbon", Physical Review B, vol. 61, no. 20, pp. 14095-14107, 2000.

[4] B. Machado and P. Serp, "Graphene-based materials for catalysis", Catal. Sci. Technol., vol. 2, no. 1, pp. 54-75, 2012.

[5] J.Malig,N.Jux andD.Guldi,"Toward Multifunctional Wet Chemically Functionalized Graphene-Integration of Oligomeric,Molecular,and Particulate Building Blocks that Reveal Photoactivity and Redox Activity",AccountsofChemical Research,vol.46,no.1,pp.53-64,2012.

[6] N. Sahoo, Y. Pan, L. Li and S. Chan, "Graphene-Based Materials for Energy Conversion", Advanced Materials, vol. 24, no. 30, pp. 4203-4210, 2012.

[7] K. Novoselov, V. Fal′ko, L. Colombo, P. Gellert, M. Schwab and K. Kim, "A roadmap for graphene", Nature, vol. 490, no. 7419, pp. 192-200, 2012.

[8] D. Abergel, V. Apalkov, J. Berashevich, K. Ziegler and T. Chakraborty, "Properties of graphene: a theoretical perspective", Advances in Physics, vol. 59, no. 4, pp. 261-482, 2010.

[9] W. Wei and X. Qu, "Extraordinary Physical Properties of Functionalized Graphene", Small, vol. 8, no. 14, pp. 2138-2151, 2012.

[10] Z. Sun, D. James and J. Tour, "Graphene Chemistry: Synthesis and Manipulation", The Journal of Physical Chemistry Letters, vol. 2, no. 19, pp. 2425-2432, 2011.

[11] X. Huang, X. Qi, F. Boey and H. Zhang, "Graphene-based composites", Chem. Soc. Rev., vol. 41, no. 2, pp. 666-686, 2012.

[12] V. Singh, D. Joung, L. Zhai, S. Das, S. Khondaker and S. Seal, "Graphene based materials: Past, present and future", Progress in Materials Science, vol. 56, no. 8, pp. 1178-1271, 2011.

[13] C. Lee, C. Cojocaru, W. Moujahid, B. Lebental, M. Chaigneau, M. Châtelet, F. Normand and J. Maurice, "Synthesis of conducting transparent few-layer graphene directly on glass at 450 °C", Nanotechnology, vol. 23, no. 26, p. 265603, 2012.

[14] A. Guermoune, T. Chari, F. Popescu, S. Sabri, J. Guillemette, H. Skulason, T. Szkopek and M. Siaj, "Chemical vapor deposition synthesis of graphene on copper with methanol, ethanol, and propanol precursors", Carbon, vol. 49, no. 13, pp. 4204-4210, 2011.

[15] P. Sutter, J. Sadowski and E. Sutter, "Graphene on Pt(111): Growth and substrate interaction", Physical Review B, vol. 80, no. 24, 2009.

[16] X. Li, W. Cai, J. An, S. Kim, J. Nah, D. Yang, R. Piner, A. Velamakanni, I. Jung, E. Tutuc, S. Banerjee, L. Colombo and R. Ruoff, "Large-Area Synthesis of High-Quality and Uniform Graphene Films on Copper Foils", Science, vol. 324,no. 5932,pp.1312-14,2009.

[17] A. Alami, K. Aokal, M. Assad, D. Zhang, H. Alawadhi and B. Rajab, "One-step synthesis and deposition of few-layer graphene via facile, dry ball-free milling", MRS Advances, vol. 2, no. 15, pp. 847-856, 2017.

[18] V. León, M. Quintana, M. Herrero, J. Fierro, A. Hoz, M. Prato and E. Vázquez, "Few-layer graphenes from ball-milling of graphite with melamine", Chemical Communications, vol. 47, no. 39, p. 10936, 2011.

NUMERICAL STUDY OF A HYBRID PHOTOVOLTAIC THERMAL DESALINATION SYSTEM

C. Noble[1] and A. Madhlopa[2]

1. Energy Research Centre, Department of Mechanical Engineering, University of Cape Town, Cape Town 7701, South Africa; email: amos.madhlopa@uct.ac.za
2. Energy Research Centre, Department of Mechanical Engineering, University of Cape Town, Cape Town 7701, South Africa; email: cole.d.noble@gmail.com

ABSTRACT

Photovoltaic (PV) systems are emerging as a potential off-grid alternative to the traditional means of electricity generation from fossil fuels. However, their widespread deployment is partially inhibited by their diminished efficiency (<20%). One way of improving the system efficiency is through hybridization of PV and thermal (T) desalination subsystems. In previous studies, PV/T systems have been modelled for the purpose of performance optimisation but most of them do not account for the optical view factor of the still. The objective of this study was to develop a numerical model with view factor for a hybrid PV/T desalination system. The modelling process was performed in MATLAB software and validated against empirical data using Root Mean Square Error (RMSE) analysis. It was found that the view factor reduced the RMSE of hourly water yield from 28.9% to 22.0%. It is concluded that the incorporation of view factors improves the accuracy of modelling hybrid PV/T desalination systems.

Keywords: efficiency, view factor, model validation

1 INTRODUCTION

A hybrid photovoltaic thermal (PV/T) desalination system is a combination of photovoltaic (PV) module with collector and solar still subsystems [1], as shown in Figure.1. In a simple PV/T system, a glass cover is fitted in front of the PV module to allow transmission of solar radiation onto the PV plate which is joined together with a flat plate collector by using an adhesive material. Basically, the collector comprises an absorber and a tube. Part of the solar radiation is absorbed and converted into electricity and heat by the PV plate. Heat then flows towards the water in the tubes by traversing through the PV plate, adhesive layer, absorber and tube [2]. This hot water can then be pumped or thermosyphoned into a solar still [3].

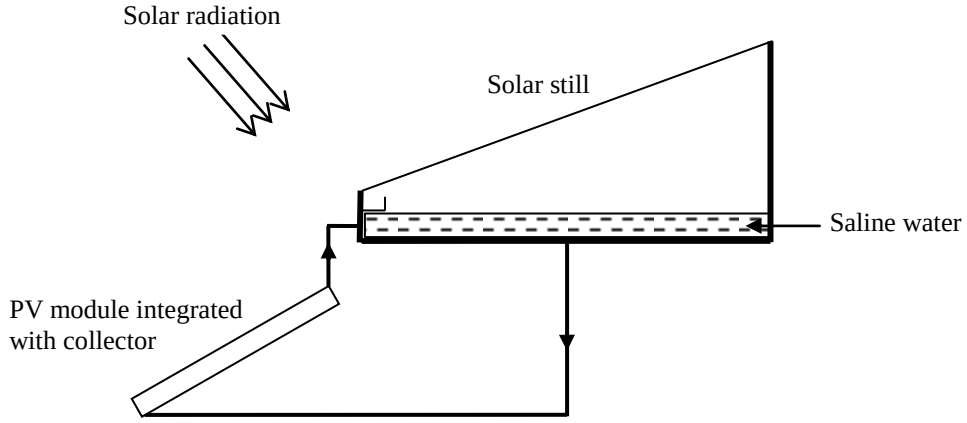

Figure1: Schematic view of a photovoltaic thermal desalination system.

A conventional solar still consists of a chamber with a thin layer of saline water in a basin. The top part of the chamber is covered by a sloped transparent film which allows incident solar radiation to heat the water. Some of the heated water then evaporates, and the vapour rises and condenses as it comes into contact with the inclined transparent cover. The distillate is then funnelled into a collection tray [4], with the temperature difference between saline water and the condensing surface largely determining the extent of the system yield [5].

In previous work on hybrid PV/T desalination systems, Kumar and Tiwari [3] compared the performance of passive and active PV/T solar stills with various water depths (0.05, 0.10 and 0.15m). Kumar and Tiwari [1] further investigated the economic advantage of using passive over active hybrid PV/T desalination systems.

Kumar et al. [6] performed an experiment to determine the empirical relationship between basin water, ambient and the PV glass cover temperatures in a hybrid PV/T desalination system. However, information is scarce on studies that incorporated the optical view factor into hybrid PV/T desalination models. The aim of this study was to develop a numerical model of a hybrid PV/T desalination system.

2 METHODOLOGY

2.1 System description

For the configuration of the PV module integrated with a collector, a sheet-and-tube type design [2] with a single glass cover was selected because this design is reported to have the best electrical efficiency [7]. In addition, the performance of such systems is well documented [2, 8]. This design consists of a PV module (Polycrystalline Silicon) which is fitted to part of the absorber plate with a thin adhesive layer (Figure 2). A glass cover is fitted over the PV panel and collector to protect the panel and to improve the thermal efficiency of the system [9].

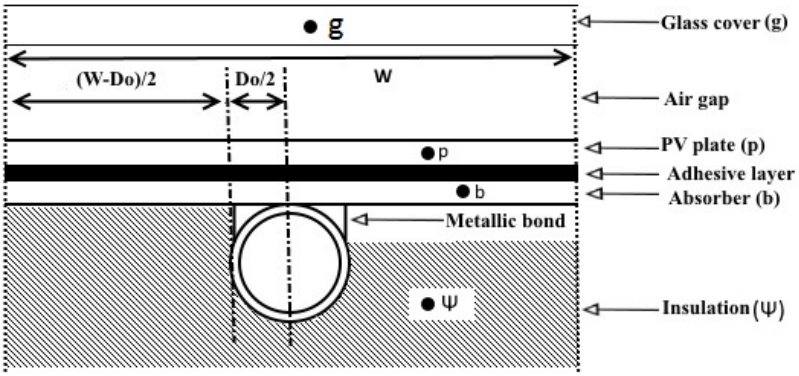

Figure 2: Side view of PV panel configuration [2].

Available solar radiation, over the course of the year, can be maximised by setting module tilt to the angle of latitude [10]. So, a module and collector tilt angle of 34˚ was chosen to optimize transmission of solar radiation at Stellenbosch weather site (33.935°S, 18.7817°W) in South Africa. Tubes link up the PV and collector to a basin type solar still. To minimise minor head losses in the system, fittings with a small frictional resistance were chosen [11].

The solar still consists of a square chamber, with a blackened absorptive floor, and its dimensions are given in Table 1. The still has a saline water inlet and outlet which are situated at the mid-point front wall and the midpoint of the rear wall respectively. As with the PV and collector component of the system, the tilt angle of the cover is optimal when it is near the latitude of the site [12].

Table 1: Dimensions of a basin type solar still.

Component	Value
Still Length	1m
Still Breadth	1m
Cover Length	1.16m
Cover Breadth	1m
Cover Thickness (δ_g)	0.004m
Back height	1.07m
Front height	0.4m
Basin thickness	0.01
Depth of water (δ_k)	0.2m
Tilt angle (β_p)	34°

2.2 Mathematical model

PV and collector subsystem

The subsystem of a PV module integrated with a flat plate collector comprises glass cover, PV, absorber, tube, insulation and water components. Assuming a uniform temperature distribution within a given component, then each component can be represented by one thermal node. For example, the glass cover of the PV module absorbs part of solar radiation and it also receives heat through the air gaps from the PV plate and collector beneath it. The energy balance for this glass node can be given by Eq. (1) [2].

$$m_g C_g \frac{dT_g}{dt} = A_g \alpha_g G_g + h_{p-g} A_g (T_p - T_g) + h_{q-g} A_g (T_q - T_g) - h_{c,g-a} A_g (T_g - T_a) - h_{r,g-s} A_g (T_g - T_s) \quad (1)$$

Equation symbols have been defined in the nomenclature section at the end of this paper. Other components of the PV module and collector subsystem were modelled likewise. Details of the component equations can be found in Chow [2].

Solar still

Similarly, the solar still subsystem comprises glass cover, water and basin components. The glass cover of the solar still has outer and inner nodes. The outer node experiences heat input by absorbing incident solar radiation directly, and its energy balance can be given by Eq. (2).

$$Q_k A_k + h_{ki-ko} A_k (T_{ki} - T_{ko}) = h_{c,ko-a} A_k (T_{ko} - T_a) + h_{r,ko-s} A_k (T_{ko} - T_s) \quad (2)$$

The inner node of the glass still cover is given in Eq.(3). Heat is gained from the water surface and is lost through conduction to the top cover of the glass [5].

$$h_{w-ki} A_{bb} (T_w - T_{ki}) = h_{ki-ko} A_k (T_{ki} - T_{ko}) \quad (3)$$

In Eq.(3), the overall heat transfer coefficient (h_{w-ki}) is the sum of the convective, evaporative and radiative heat transfer coefficients, which were computed according to Madhlopa [9].

The node of the saline water (in the basin) is represented by Eq. (4) [5, 13]. In this equation, energy flows into the water from the moving water mass ($\dot{m}_w$). In addition, solar flux (Q_w) is absorbed directly by the saline water [5].

$$m_w C_w \frac{dT_w}{dt} = \dot{m}_w C_w (T_{w2} - T_w) + Q_w A_{bb} - h_{b-w} A_{wb} (T_w - T_b) - h_{w-ki} A_{bb} (T_w - T_{ki}) \quad (4)$$

The basin (liner) receives heat from the hot water contained within it and from incident solar radiation which reaches the basin floor after traversing through the water. This component loses heat through the floor and side walls. The basin node has an energy balance equation as shown by Eq. (5) [5].

$$m_{bs} C_{bs} \frac{dT_{bs}}{dt} = Q_{bs} A_{bb} - h_{w-b} A_{wb} (T_w - T_{bs}) - h_{bb} (T_{bs} - T_a) - h_{bd} A_{bb} (T_{bs} - T_a) \quad (5)$$

In Eq.(5), the thermal resistance from the bottom of the basin towards the air (h_{bb}) is given by a series combination of the thermal resistances of the basin bottom with the parallel convective and radiative thermal resistances from the bottom of the basin. The heat transfer coefficient from the basin side wall (h_{bd}) is expressed as a ratio of the area of the side wall exposed to water to the area of the basin floor, as shown by Eq. (7). This term can be neglected if the area of water in contact with the side wall is small compared to the bottom area of the basin [5].

$$R_{bb} = \frac{1}{\frac{k_{bs}}{L_{bs}} A_{bb}} + \frac{1}{(h_{c,bs-a} + h_{r,bs-s}) A_{bb}} \quad (6)$$

$$h_{bd} = \frac{A_{bd}}{A_{bb}} h_{bb} \quad (7)$$

Solution procedure

Euler Method was used to iteratively determine the nodal temperatures of the system. This method relies on initial conditions and the chosen timestep (Δt) to determine successive approximations of the function outputs. An example is given by Eq. (8), for the temperature of water (T_w) [14]. The Gauss-Seidel iteration method [15] was used to speed up the estimation process.

$$T_w(t+1) = T_w(t) + (\Delta t)\frac{T_w}{dt} \quad (8)$$

Models 1 (with view factor) and 2 (without view factor) were validated against empirical data reported by Kumar and Tiwari [16]. The same system design appears in another study by the same author where the values of other design parameters essential for validation are reported [17]. For model validation, some dimensions and properties of the PV module integrated with a collector are presented in Table 4.

Table 4: Experimental PV and collector dimensions and properties [18].

Parameter	Value
Total area of glass cover (A_g)	2× (1.9m×1.25m)
Glass cover thickness	0.004m
Absorber plate area (A_b)	1.25m×0.55m
Insulation thickness (δ_Ψ)	0.01m
Number of tubes per collector	10
Number of collectors	2
Power output (E_p)	75W
Tilt angle (β_p)	45°

Analysis of the root mean square error (RMSE) was used to establish the difference between theoretical and experimental results of hourly water output [19-21]. All the computations were performed in MATLAB.

3 RESULTS AND DISCUSSION

The hourly water yields of the experiment, Model 1 (with view factor) and Model 2 (without view factor) are shown in Figure 3. As can be seen from this graph, Model 1 track the experimental water yield more closely than Model 2, probably due the effect of the view factor.

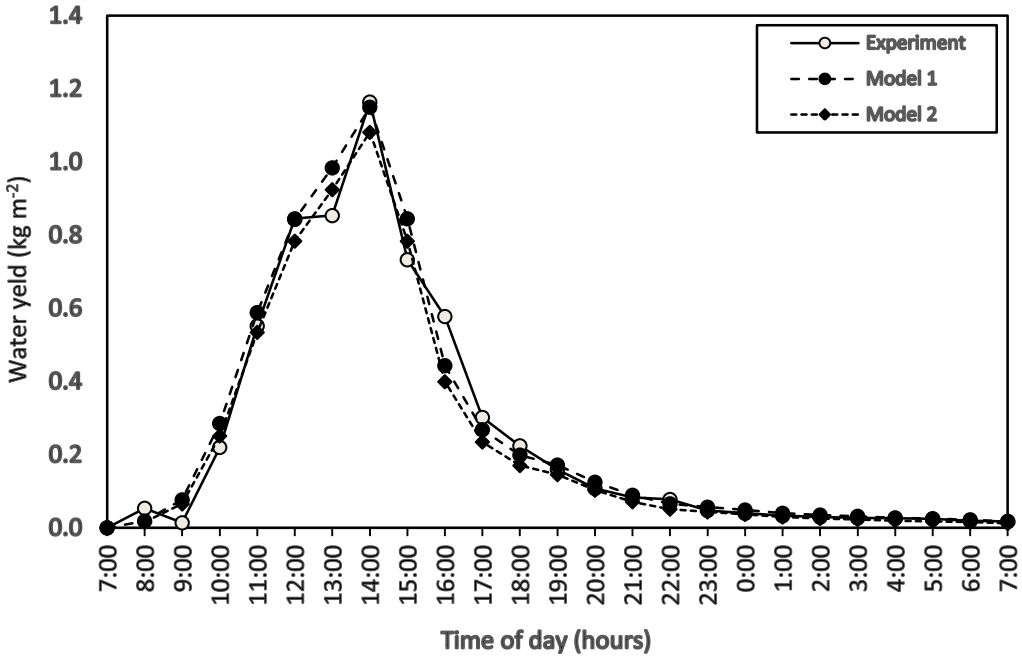

Figure 3: Hourly water yields for experimental data [19] and Model 1and Model 2.

The accuracy of both models is statistically analysed using RMSE as shown in Table 5**.** As can be seen from this table, the RMSE values are 22.0 % and 28.9% for Models 1 and 2, respectively. Previous studies report a range of RMSE values that give an indication of the present accuracy in predicting the hourly water productivity of a solar still. For example, some studies on solar distillation found RMSE values of 48.5% [21] and 32.1% [22]. For a study of a solar still coupled with evacuated tubes, a RMSE value of 39.7% was

reported [22]. In literature, data is scarce on RMSE values for a hybrid PV/T desalination system. However, these values from similar studies indicate that the present values are reasonable.

Table5: RMSE values for water yield.

Model	RMSE (%)
Model 1	22.0
Model 2	28.9

4 CONCLUSIONS

A hybrid photovoltaic thermal (PV/T) desalination system has been studied numerically. The desalination subsystem was a basin type solar still. A mathematical model of the energy balance of the system was developed. In this model, the coefficient of internal radiative heat transfer was computed with (Model 1) and without (Model 2) the view factor between the water and surrounding surfaces of the solar still. A code was written in MATLAB to solve energy balance equations, and the model was validated against experimental data from previous work. The Root Mean Square Error (RMSE) was used to determine the accuracy of the model. Results show that the values of RMSE are 22.0% and 28.9% for Models 1 and 2 respectively. Consequently, it can be concluded that the accuracy of modelling a hybrid PV/T desalination system can be improved by accounting for the view factor within the solar still.

ACKNOWLEDGEMENTS
Authors would like to acknowledge the National Research Foundation for the financial assistance through grant number 95689.

REFERENCES

[1] S. Kumar and G. Tiwari, *Life cycle cost analysis of single slope hybrid (PV/T) active solar still*, Applied Energy, Vol. 86, pp. 1995-2004, 2009.
[2] T. Chow, *Performance analysis of photovoltaic-thermal collector by explicit dynamic model*, Solar Energy, Vol. 75, pp. 143-152, 2003.
[3] S. Kumar and A. Tiwari, *An experimental study of hybrid photovoltaic thermal (PV/T)-active solar still*, International Journal Energy Research, Vol. 32, pp. 847-858, 2008.
[4] A. Madhlopa and J. Clarke, *Computation of irradiance in a solar still by using a refined algorithm*, Renewable Energy, Vol. 51, pp. 13-21, 2013.
[5] G. Tiwari and A. K. Tiwari, *Solar Distillation Practice for Water Desalination Systems*. Anshan Pub, 2008.
[6] S. Kumar, G. Tiwari and M. Gaur, *Development of empirical relation to evaluate the heat transfer coefficients and fractional energy in basin type hybrid (PV/T) active solar still*, Desalination, Vol. 250, pp. 214-221, 2010.
[7] H. A. Zondag, D. W. de Vries, W. G. J. van Helden, R. J. C. van Zolingen and A. A. van Steenhoven, *The yield of different combined PV-thermal collector designs*, Solar Energy, Vol. 74, pp. 253-269, 2003.
[8] S. Dubey and G. Tiwari, *Thermal modeling of a combined system of photovoltaic thermal (PV/T) solar water heater*, Solar Energy, Vol. 82, pp. 602-612, 2008.
[9] S. A. Kalogirou and Y. Tripanagnostopoulos, *Hybrid PV/T solar systems for domestic hot water and electricity production*, Energy Conversion and Management, Vol. 47, pp. 3368-3382, 2006.
[10] A. K. Yadav and S. S. Chandel, *Tilt angle optimization to maximize incident solar radiation: A review*, Renewable and Sustainable Energy Reviews, Vol. 23, pp. 503-513, 7, 2013.
[11] J. R. Welty, C. E. Wicks, G. Rorrer and R. E. Wilson, *Fundamentals of Momentum, Heat, and Mass Transfer*, John Wiley & Sons, 2007.
[12] A. J. N. Khalifa, *On the effect of cover tilt angle of the simple solar still on its productivity in different seasons and latitudes*, Energy Conversion and Management, Vol. 52, pp. 431-436, 2011.
[13] S. Kumar and A. Tiwari, *An experimental study of hybrid photovoltaic thermal (PV/T)-active solar still*, International Journal of Energy Research, Vol. 32, pp. 847-858, 2008.

[14] A. Jones and C. Underwood, *A thermal model for photovoltaic systems*, Solar Energy, Vol. 70, pp. 349-359, 2001.
[15] J. H. Mathews and K. D. Fink, *Numerical Methods using MATLAB*, Prentice hall, 1999.
[16] S. Kumar and A. Tiwari, *An experimental study of hybrid photovoltaic thermal (PV/T)-active solar still*, International Journal of Energy Research, Vol. 32, pp. 847-858, 2008.
[17] R. Dev and G. Tiwari, *Characteristic equation of a hybrid (PV-T) active solar still*," Desalination, Vol. 254, pp. 126-137, 2010.
[18] S. Kumar and A. Tiwari, *Design, fabrication and performance of a hybrid photovoltaic/thermal (PV/T) active solar still*, Energy Conversion and Management, Vol. 51, pp. 1219-1229, 2010.
[27] K. Sampathkumar, T. Arjunan, M. Eswaramoorthy and P. Senthilkumar, *Thermal Modeling of a Solar Still Coupled with Evacuated Tube Collector under Natural Circulation Mode—An Experimental Validation*, Energy Sources, Part A: Recovery, Utilization, and Environmental Effects, Vol. 35, pp. 1441-1455, 2013.
[28] E. Deniz, *An Experimental and Theoretical Analysis of a Vacuum Tube Solar Collector-assisted Solar Distillation System*, Energy Sources, Part A: Recovery, Utilization, and Environmental Effects, vol. 34, pp. 1637-1645, 2012.
[29] A. K. Tiwari and G. Tiwari, *Thermal modeling based on solar fraction and experimental study of the annual and seasonal performance of a single slope passive solar still: the effect of water depths*, Desalination, Vol. 207, pp. 184-204, 2007.
[30] R. Tripathi and G. Tiwari, *Performance evaluation of a solar still by using the concept of solar fractionation*, Desalination, Vol. 169, pp. 69-80, 2004.

NOMENCLATURE

A	surface area (m^2)
C	specific heat (J $kg^{-1}K^{-1}$)
G	solar radiation flux (W m^{-2})
h	heat transfer coefficient (W m^{-2} K)
k	thermal conductivity (W $m^{-1}K^{-1}$)
m	mass (kg)
$\dot{m}$	mass flow rate (kg s^{-1})
Q	energy flux (W)
R	thermal resistance (K W^{-1})
t	time (s)
T	temperature (°C)
T_w	temperature of water in basin (collector inlet) (°C)
T_{w1}	average temperature of water in the tube (°C)
T_{w2}	temperature of water from the collector output (°C)

Greek symbols

α	absorptance (dimensionless)
β	tilt angle of surface (to horizontal) (°)
δ	thickness or depth (m)

Subscripts

a	air
b	absorber plate
bb	basin bottom
bd	basin side
bs	basin
c	convective
g	glass cover
i-j	from i^{th} component to j^{th} component
p	PV plate
r	radiation
s	sky
w	water
κ	cover of the solar still
κi	inner side of cover of the solar still
κo	outer side of cover of the solar still
Ψ	insulation material

TECHNO-ECONOMIC EVALUATION OF BUSINESS MODELS IN MULTI-ENERGY COOPERATIVE UTILIZATION: A CASE STUDY OF SOLAR-HEAT PUMP WATER HEATER

Zhuoran Li, Linwei Ma, Zheng Li, Weidou Ni

State Key Laboratory of Power Systems, Department of Energy and Power Engineering, Tsinghua University, Beijing, China; email: lizr17@mails.tsinghua.edu.cn

ABSTRACT

The commercialization of technologies in multi-energy cooperative utilization is facing the challenge of economic weakness at present, and business models have great influences on the techno-economic performance of the technologies. Taking solar-heat pump water heater as a typical case, this paper attempts to develop a quantitative model to evaluate and compare the techno-economic performance of multi-energy cooperative utilization under different business models. The results indicate that, in the model of no third party intervention, which means only rely on a single enterprise operation, this technology is difficult to have investment value from the user's point of view. Therefore, it needs the government to grant a high ratio of subsidies. When Energy Service Companies are involved in the transaction, it can not only help users avoid high initial investment costs, but also improve economic of the project by providing value-added services for users. Under this circumstances, only with a reasonable government subsidy ratio, the project is expected to have investment value.

Keywords: Multi-energy cooperative utilization, Solar-heat pump water heater, Business model, Techno-economic evaluation

0 INTRODUCTION

In the early twenty-first Century, China's original plan was to double the energy demand in 2020. That is, the total energy consumption of 1 billion 500 million tce in 2000 would be increased to 3 billion tce in 2020 [1]. However, the total energy consumption in 2016 has reached 4 billion 360 million tce. The continuous and large consumption of energy, while providing impetus for economic growth, has also brought serious challenges to ecological environment and energy security. Optimizing the energy industry structure and energy diversity have become an important development direction, which bring the need for multi-energy. Multi-energy cooperative utilization refers to the comprehensive utilization on different kinds of energy according to their own characteristic [2]. Result from the feature of energy industry chain, multi-energy cooperation utilization includes not only the cooperation on different kinds of energy resource, but also the coordination in transformation, storage and terminal utilization process.

In the previous studies, Yongbin Han [3] has proposed renewable energy access technology, integration and complementary utilization of fossil energy to achieve multi-energy cooperation. It is suggested that China should strengthen the multi-energy complementarity, construct optimization pattern where primary energy and secondary energy are used in common. Cheng Lin [4] also pointed out that nowadays the technology of new energy in China are not mature yet. Some energy sources are intermittent so that lead to greater interference when merged into energy supply net. Therefore, coordinated use of multiple energy is considered as potential development direction.

At present, the comprehensive commercialization of multi-energy cooperative utilization has not been realized. Main reason is the difficult implementation, high cost and it involves complex relationship of multiple subjects. In order to provide solutions for the difficulties encountered, it is necessary to consider flexible business models based on multiple subjects, and research on economic and influencing factors of different business models.

This paper takes solar-heat pump water heater as an example, and evaluates the business models based on techno-economic method. In the research, system structure are firstly analyzed, which performs physical modeling. Next, economic modeling is based on the techno-economic method. Finally, three types of business model are considered, and investment value is evaluated under every business model. It tries to develop a set of quantitative models through the analysis process, which will provide useful inspiration for the commercialization of multi-energy cooperative utilization.

1 METHOD AND DATA

1.1 Physical Modeling

Solar-heat pump water heater utilizes a combination of solar energy and a small amount of electric energy, which can be divided into two parts: the solar subsystem and the air source subsystem. The two subsystems are respectively responsible for the different period of task to heat cold water. When sunlight is sufficient, the solar subsystem is mainly used to heat the water. In a cloudy day or at night, the heat pump (air source subsystem) is mainly used with a small amount of electricity.

In order to establish a simplified physical model for the system, a hot water system in a normal family of Beijing is used as a case. It is assumed that the volume (V) of annual hot water for each family is 21000 L, and the corresponding mass equals to 21000 kg. Formula as follows (Where ρ refers to density of water, 1 tons / liter):

$$m = \rho V = 21000 \quad (\mathrm{kg}) \tag{1}$$

According to the situation in Beijing, make following assumptions: water is heated from 20 celsius to 52 celsius; Percentage of heating load in solar subsystem equals to 75%. COP (coefficient of performance) of heat pump equals to 2.5. The annual income B of solar-heat pump water heater can be estimated by using the saved power cost compared with the electric water heater. Formula as follows:

$$B = \frac{C_p m \Delta t \beta P_e}{3.6 \times 10^6 \eta_e} + \frac{C_p m \Delta t (1-\beta) P_e}{3.6 \times 10^6 \eta_e}\left(1 - \frac{1}{COP}\right) \tag{2}$$

Where: Cp is the specific heat capacity of water (J/ (kg ·℃)). m represent mass of water (kg), Δt represent the temperature rise of water (°C). β is load percentage of solar subsystem(%). Pe is the electricity price in Beijing (RMB/kWh). ηe represents the electric heating efficiency.

1.2 Economic Modeling

NPV Method

Net present value (NPV) method is a common method to evaluate engineering and technical projects [5], which can judge the investment value of a project. The main principle is to predict the cash flow that the project should generate in the future. Combined with the discount rate, we can discount cash flow to get present value, and then get the net present value by adding them up. Assuming that working life of a water heater is 15 years, formula is as follows:

$$NPV = \sum_{i=0}^{14} (B_i - C_i)(1+r)^{-i} \tag{3}$$

Where: Bi is revenue of year i. Ci is cost of year i. (1+r)^(-i) is discount factor. The discount rate is r. In this study, Bi is selected as the savings of using a solar-heat pump water heater compared with electric water heater. Ci is annual expenditure.

Payback Period Method

The payback period method is also one of the main methods for techno-economic evaluation. Economic status of the project is judged through the comparison between payback period and working life of the item [6]. If the payback period is larger than working life, that is the initial investment can not be recovered within working life, the item does not possess investment value. The formula is as follows:

$$n = \frac{\log(B-C) - \log(B-C-r\times p)}{\log(1+r)} \tag{4}$$

Where: P is the cost of initial purchase. B is the savings of the item while C is annual expenditure.

IRR Method

Internal rate of return refers to the discount rate when NPV=0. Internal rate of return is often used to assess the economy of project. When internal rate of return is greater than discount rate, the project is worth investing.

1.3 Business Model Design

Three types of business models have been designed. The first type is a model in which retailer contacts with the user directly and complete transaction, which can be called no third-party intervention model. The

second type of model is to consider the subsidy from government, which can be called government intervention model. The third type is to consider professional third-party company such as energy service companies in addition to government.

2 RESULTS AND DISCUSSIONS

2.1 No Third-party Model

This type of business model is to explore the techno-economic situation of solar-heat pump water heater without any third-party intervention [7]. In this study, the purchase cost for solar-heat pump water heater is 4900 RMB. Installation fee is 60 RMB. Spare parts is 200 RMB. Transportation cost is 100 RMB. So initial total investment is 5260 RMB. The annual maintenance cost is calculated as 1% of initial investment.

In this case, select Cp=4200 (J/ (kg ·℃)), m =21000 kg, Δt =32 ℃, β=0.75, ηe=90%, Pe=0.48RMB/KWh. The annual revenue of solar-heat pump water heater is 376 RMB from (2). Discount rate r=4.35%. Assume that the water heater has a working life of 15 years. The estimated net salvage value at the end of the 15th year is 100 RMB. The capital budget is as follows:

Table 1. Capital budget of the first model (Solar-heat pump water heater)

Year	Cost (RMB)	Revenue	Cash flow	Discount factor	Present value
0	5312.6	376	-4936.6	1	-4936.6
1	52.6	376	323.4	0.958	309.9
2	52.6	376	323.4	0.918	297.0
3	52.6	376	323.4	0.880	284.6
4	52.6	376	323.4	0.843	272.7
5	52.6	376	323.4	0.808	261.3
6	52.6	376	323.4	0.774	250.4
7	52.6	376	323.4	0.742	240.0
8	52.6	376	323.4	0.711	230.0
9	52.6	376	323.4	0.681	220.4
10	52.6	376	323.4	0.653	211.2
11	52.6	376	323.4	0.626	202.4
12	52.6	376	323.4	0.599	194.0
13	52.6	376	323.4	0.574	185.9
14	-47.4	376	423.4	0.550	233.2

Add the present values to get NPV=-1543＜0. Next, we calculate net present value of the electric water heater. Purchase cost equals to 1000 RMB. Installation cost is 60 RMB. Spare parts are 50 RMB. Transportation cost is 100 RMB. So the initial total investment equals to 1210 RMB. The cost of maintenance is 12.1 RMB per year（1% of the initial investment）. Annual revenue of the electric water heater (relative to the electric water heater) is 0 RMB, and other conditions are not changed.

Table 2. Capital budget of the first model (Electric water heater)

Year	Cost (RMB)	Revenue	Cash flow	Discount factor	Present value
0	1222.1	0	-1222.1	1	-1222.1
1	12.1	0	-12.1	0.958	-11.59
2	12.1	0	-12.1	0.918	-11.11
3	12.1	0	-12.1	0.880	-10.64
4	12.1	0	-12.1	0.843	-10.20
5	12.1	0	-12.1	0.808	-9.77
6	12.1	0	-12.1	0.774	-9.37
7	12.1	0	-12.1	0.742	-8.98
8	12.1	0	-12.1	0.711	-8.60
9	12.1	0	-12.1	0.681	-8.24
10	12.1	0	-12.1	0.653	-7.90
11	12.1	0	-12.1	0.626	-7.57
12	12.1	0	-12.1	0.599	-7.25

13	12.1	0	-12.1	0.574	-6.95
14	-87.9	0	87.9	0.550	48.42

By adding the present value we get NPV= -1292. So NPV of electric water heater is higher. No third-party model only involves user's personal behavior. Under the premise of choice, project with higher net present value is better for rational consumers. Thus, we conclude that solar-heat pump water heater does not have advantage, which is consistent with current situation in the market.

The payback period calculated equals to 29.4 years, while working life of item is about 15 years. So the project's economy is poor.

2.2 Government Intervention Model

Since electricity savings are the main revenue, changes in electricity prices will have an impact on the investment value. Therefore, we consider the government's adjustment on electricity price first [8]. Since the third party's intervention make it no longer a personal behavior of consumers, the project with positive NPV has investment value. Assume that the government makes different adjustments on electricity price and maintains it in the project cycle. NPV is showed as follows:

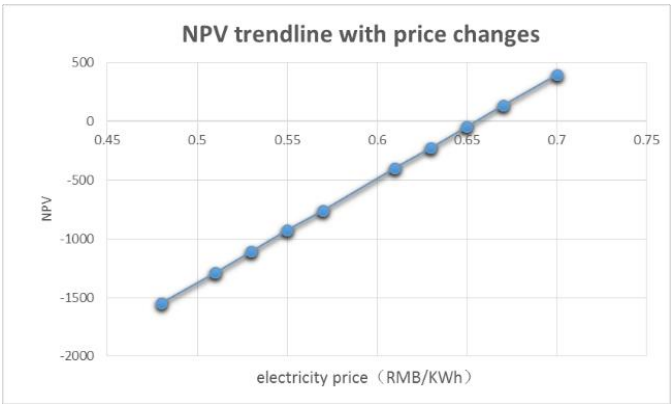

Figure 1. Trendline with price changes

From above results, project starts to exhibit a positive NPV value when the price of electricity is raised to about 0.655 RMB/KWh (previously 0.48 RMB/KWh).

Next, we will research the case of government subsidies to intervene in transactions. That is, users who purchase solar-heat pump water heaters can enjoy a percentage of subsidies. First assume that the proportion of government subsidies is 10%. With a 10% subsidy, the initial total investment is 4734 RMB. Capital budget is as follows:

Table 3. Capital budget with 10% government subsidy

Year	Cost (RMB)	Revenue	Cash flow	Discount factor	Present value
0	4786.6	376	-4410.6	1	-4410
1	52.6	376	323.4	0.958	309
2	52.6	376	323.4	0.918	297
3	52.6	376	323.4	0.880	284
4	52.6	376	323.4	0.843	272
5	52.6	376	323.4	0.808	261
6	52.6	376	323.4	0.774	250
7	52.6	376	323.4	0.742	240
8	52.6	376	323.4	0.711	230
9	52.6	376	323.4	0.681	220
10	52.6	376	323.4	0.653	211
11	52.6	376	323.4	0.626	202
12	52.6	376	323.4	0.599	194
13	52.6	376	323.4	0.574	185
14	-47.4	376	423.4	0.550	233

From table above, we can see that the project's NPV = -1022 < 0 when subsidy ratio is 10%. So that there is still no investment value. Next, we continue to analyze the NPV changes under different subsidy ratios. The results are as follows:

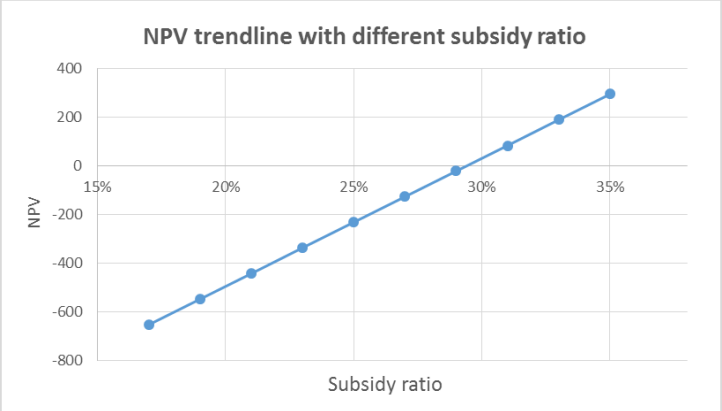

Figure 2. Trendline with different subsidy ratio

As can be seen, NPV = 0 when subsidy ratio equals to approximately 29.4%. That is, in order to make investment value positive, subsidy ratio is at least 29.4%, about 1440 RMB. At this point the project has a good investment value. But for government, excessively high subsidy will bring huge financial expenditures.

2.3 ESCO Intervention Model

Energy service company (ESCO) is different from traditional energy equipment manufacturers and suppliers. It is a type of energy companies which is dedicated to providing a series of energy services such as equipment purchase, maintenance testing, cost estimation, and etc [9].

The preconditions are unchanged. Assume that ESCO purchases a solar-heat pump water heater for users and bears the costs of transportation, installation and etc. The electricity price in Beijing increases in accordance with the natural growth trend. Users need to pay ESCO the savings and an additional 10% of the savings as service fee. Calculate the internal rate of return (IRR) by calculating the NPV at different discount rates. Calculation results are shown as follows:

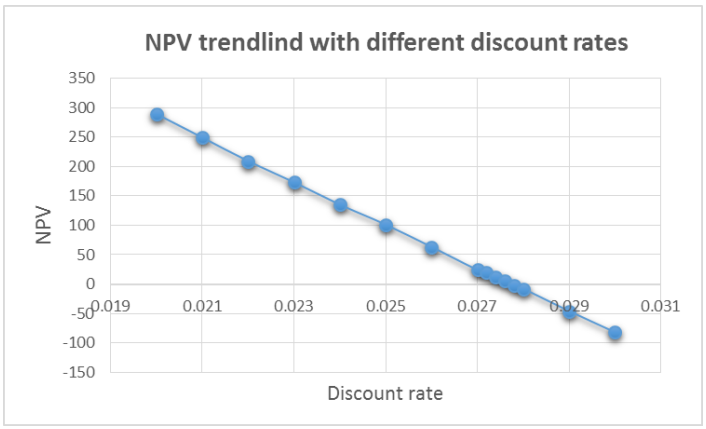

Figure 3. Trendline with different discount rate

It can be obtained that IRR=2.77%. Discount rate in real market equals to 4.35%. IRR is less than discount rate. According to the principle of IRR method, this project does not have investment value for ESCO. Entering this market will not bring significant benefits.

Continue to assume that government subsidies and ESCO are involved at the same time. Discount rate is still r=4.35%. Other assumptions do not be changed. Then relationship between NPV and subsidy ratio is as follows:

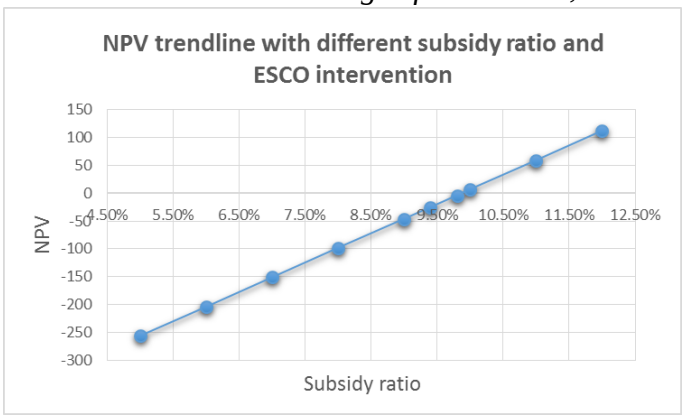

Figure 4. Trendline with different subsidy ratio and ESCO

It can be obtained that it will have an investment value for ESCO when subsidy ratio is more than 10%. 10% subsidy is also within an acceptable range for government. Therefore, when government and ESCO are involved at the same time, users are positively motivated by the large-scale transfer of risk. ESCO have also realized long-term profitability because users have created value-added services and they can get subsidies from government. For government, 10% subsidy ratio is relatively reasonable.

Therefore, under this business model, the profit or expenditure of every stakeholders can be maintained at a reasonable level and it possesses the conditions for forming a short-term equilibrium.

3 CONCLUSIONS AND SUGGESTIONS

This paper selects solar-heat pump water heater as a typical case of multi-energy cooperative utilization. Use NPV method, payback period method and IRR method to research on the economics of solar- heat pump water heater under three types of business model.

The results show that solar-heat pump water heater is less competitive under current market conditions with no third-party intervention. Government needs to increase electricity prices largely, or provide high subsidies to make item possess good investment value. But it will bring a heavy financial burden. When an ESCO intervenes alone, an effective incentive can be formed for users, but incentive for ESCO is poor. When ESCO and government are involved together, effective incentives for each stakeholders can be achieved, which is a more promising business model. Therefore, it is recommended to strengthen the construction of business model in which government and ESCO are involved jointly. It is also proposed to conduct deep analysis on more different types and more large-scale multi-energy cooperative utilization cases in the future research.

REFERENCES

[1]Weidou Ni, Zhen Chen, Linwei Ma, Feng Fu, Zheng Li. Several strategic guiding ideas about energy saving in China [J]. China's energy, 2009, 31(07):5-11.

[2]Weidou Ni. Discussion on the sustainable energy system in China [J]. Energy and Energy Saving, 2011(06):1-5.

[3]Yongbin Han, Hongmei Cao. Technical approaches and policy recommendations for the coordinated development of fossil energy and renewable energy in China [J].China's energy, 2014, 36(04):25-29.

[4]Lin Cheng, Chen Liu, Shouzhen Zhu. Research on Energy Interconnection Micronet Based on Multi-energy Cooperative Strategy [J]. Power grid technology, 2016, 40(01):132-138.

[5]Jiaxing Yang, Chunhua Luo. Economic analysis and evaluation of solar heat pump water heater [J]. Heilongjiang Science and Technology Information, 2010(16):35.

[6]Kehong Wang, Daiqing zhao. Analysis on environmental and economic benefits of solar water heater and electric water heater [J]. Energy Engineering, 2006(05):4-8.

[7] Nicholas Good, Eduardo A. Martínez Ceseña. Techno-economic and business case assessment of low carbon technologies in distributed multi-energy systems [J]. Applied Energy, 2016, 167: 158–172.

[8] Ming-Lang Tseng, Anthony S.F. Chiu, Dong Liang. Sustainable consumption and production in business decision-making models [J]. Resources, Conservation and Recycling, 2018, 128: 118-121.

[9]Guiwen Liu, Bo Lei. Enlightenment of European Energy Service Companies' development to China [J]. Energy saving and environmental protection, 2009(09):25-28.

FAST LAYOUT DESIGN FOR COMMERCIAL SOLAR POWER PLANTS

F.J. Collado[1] and J. Guallar[2]

1. Department of Mechanical Engineering, EINA, Universidad de Zaragoza, Zaragoza, Spain; email: fjk@unizar.es
2. Department of Mechanical Engineering, EINA, Universidad de Zaragoza, Zaragoza, Spain; email: jguallar@unizar.es

ABSTRACT

Solar power tower (SPT) is nearly a mature technology with several projects at a commercial scale (>100 MWe) already operational. Many of these commercial scale projects consist of a surrounding heliostat field with a receiver atop of the tower. However, the optimal layout of thousands of heliostats remains a rather difficult and time-consuming problem. Recently, the authors have presented elsewhere some preliminary results about the layout optimisation for Noor III 150 MWe project, with 7400 heliostats, in Morocco. Based on their own analysis, developed through campo code, it has been shown that it is possible a fast selection of the most efficient layout. The heliostat field is divided in three zones, in which the first one, the closest to the tower, always has the maximum density. Therefore, the layout definition is only based on three parameters namely, the number of heliostats of the first row in the first zone, and the non-dimensional constant radial increments between rows in zone 2 and zone 3 i.e., Δr_2, and Δr_3, respectively. The optimum layout would fulfil that Δr_3 be of the order of twice Δr_2 thus easing considerably the problem. Based on a Noor III-like plant, a full analysis is performed with campo code in order to support this new result.

Keywords: Solar Tower, Optimum layout, Campo Code

1 INTRODUCTION

Currently, solar power tower (SPT) plants are nearly a mature technology with several projects at a commercial scale (>100 MWe) already fully operational [1], in which the levelised cost of energy (LCOE) are getting closer to those of fossil power plants [2]. The collector field of SPT systems, with thousands of heliostats, or giant mirrors, concentrating sunlight onto a receiver atop a tower, is a subsystem of major importance as it can represent around the 50% of the total investment and can generate about the 40% of solar energy losses in the system [3]. Therefore, any improvement of the heliostat field performance will certainly reduce the LCOE.

The instantaneous optical efficiency of a heliostat η_{opt} is

$$\eta_{opt}(x,y,t) = \rho \cos\omega(x,y,t)\, f_{att}(x,y)\, f_{int}(x,y,t)\, f_{sb}(x,y,t,neighbours), \qquad (1)$$

where ρ is the effective mirror reflectivity, $\cos\omega$ is the cosine of the incidence angle between the sun rays and the heliostat normal, f_{att} is the atmospheric attenuation factor, f_{int} is the intercept factor i.e., the fraction of the energy spot sent by the heliostat that hits onto the receiver surface, and finally f_{sb} is the shadowing (of the incident sunlight by neighbour mirrors) and blocking (of reflected sunlight by adjacent heliostats) factor.

The optimized design of heliostat fields usually has as figure of merit the field efficiency η_{field}, which is the entire field average of the single annual-averaged optical efficiencies.

However, to find the optimum field layout for a given number of heliostats in a commercial scale SPT plant is rather complex because we should check a huge amount of heliostat distributions, with thousands of heliostats, to find the one that yielded the highest η_{field}. On the other hand, there are nor standard procedures to calculate the optical efficiency, Eq. (1), or even to select the most convenient layout pattern. Therefore, numerous software tools to tackle this complex problem have been proposed. A recent and extensive review [4] of software for optical analysis and optimization of heliostat fields include no fewer than twenty-eight codes. For example, the calculation of the intercept factor in Eq. (1) may be done through flux images resulting from convolution methods, as classic codes DELSOL3 [5] and HFLCAL [6], or by ray-tracing see, e.g. Biomimetic [7] or Tonatiuh [8].

About the most convenient layout pattern, theoretically, the global optimum should be found through a pattern-free optimization since it utilizes larger design search domain than pattern-based optimizations. However, in commercial scale plants involving thousands of heliostats, this pattern-free searching implies

very long computational times. Thus, generation field algorithms based on patterns are more likely to be implemented in real plants [9], such as the classic radial staggered pattern used by codes as DELSOL3 or HFLCAL.

1.1 Optimization of Gemasolar Plant with CAMPO Code

The authors, using CAMPO code, have recently presented [10] an optimized design of the radial staggered collector field for a Gemasolar-like [11] solar power tower plant with 20 MWe, 2650 heliostats and 15 h of storage. The Sener HE35 heliostat model has a mirror area of 115.72 m^2, and an assumed heliostat diagonal DM=15.7 was used in the analysis. This optimization intends to select the location of thousands of heliostats, the tower height (THT) and the receiver dimension, its radius RR, with the lower LCOE. Due to the complexity of the problem, the optimisation is broken down into two steps. The first optimization stage seeks the best heliostat field layout i.e., supplying the maximum annual incident energy, or maximum field efficiency, for all the checked combinations of receiver radius and tower height (THT, RR). Then, the figure of merit of the main (second) optimization is the LCOE, which is calculated for every explored design of the collector field (THT, RR, optimized layout).

The present work is centred in the first stage optimization, i.e. the searching of layouts with the highest efficiency but now for huge fields of commercial plants with much more mirrors than Gemasolar. Point out that this optimisation layout is rather cumbersome because we have to calculate, for every explored couple (THT, RR), the field efficiency of all the possible combinations of the variables defining the layout. Therefore, the number of variables defining the layout is crucial.

In CAMPO, the number of layout variables has been reduced to only three ones [10] namely, the number of heliostats of the first row in the first zone $Nhel_1$, and the non-dimensional constant radial increments of zone 2 and zone 3, Δr_2 and Δr_3, respectively. The actual radial distance between sequential rows in any zone is ΔR_i, which is constant throughout the zone. Then, the non-dimensional radial increment for any zone is $\Delta r_i=\Delta R_i/DM$, DM being the diagonal of the heliostat, which is the diameter of the circle representing the maximum heliostat footprint. For zone 1, which is the closest one to the tower, the optimum radial increment always resulted in the minimum distance i.e., maximum density in a radial staggered layout [10], $\Delta R_1=\cos 30^{\circ} DM=0.866$ DM, i.e. $\Delta r_1=0.866$. This is maintained in this work.

1.2 Preliminary Optimization of Noor III

Quite recently, the authors [12] have also presented some annual energy evaluations for a Noor III-like plant [13], which is under construction in Morocco, also using CAMPO code. Noor III 150 MWe project, with 7400 heliostats, surrounding field and 7.5 hours of molten salt storage is a full commercial solar power tower plant. Besides, the Sener HE54 heliostat used in Noor III has 178.5 m^2 of mirror area and the assumed DM in the calculations is 19.67 m. In order to obtain the field annual efficiency and under the lack of meteorological data for Noor-III, the TMY for Almería-PSA from the GAST project [14] has been used. A relevant result of this preliminary analysis is that is perfectly possible to place 7400 heliostats or more in three zones while the non-dimensional radial increments are of the same order of magnitude than in Gemasolar (with only 2650 mirrors). After a rather limited number of annual energy evaluations for only one height (THT=250 m), it would seem that an approximated rule of thumb for optimum radial staggered layouts could be the following: zone 1 with maximum density $\Delta r_1= 0.866$, zone 2 $\Delta r_2\approx 1.0$ and zone 3 $\Delta r_3\approx 2.0$. Hence, the optimum Δr_3 would be of the order of twice Δr_2. Highlight that similar results were found for the Gemasolar analysis, see Table B1 in [10].

In this work, after briefly reviewing the optical efficiency model and the generation of the radial staggered layout proposed [10], the full layout optimization procedure for a Noor-III like plant is presented. Thus, for every couple (THT, RR) scanned, the layouts (Δr_2, Δr_3) supplying the highest η_{field} are sought. If the order of magnitude of the non-dimensional settings for the optimum layouts were confirmed, this would substantially reduce the computational load of the first stage optimization avoiding the review of a large number of alternative layout designs. Thus, it would allow that the optimization process could centre mainly in the second stage namely, the dependence of LCOE on tower height and receiver dimensions.

2 OPTICAL EFFICIENCY MODEL

The major factors that make up the optical efficiency, Eq. (1), are the intercept factor and the shadowing and blocking factor. CAMPO code includes the HFLCAL analytic flux density [6] model whose intercept factor results in an analytical expression. The HFLCAL attenuation model is also used. The standard average

deviations of the usual Gaussian error functions selected for the HFLCAL flux model are the following. The average standard deviation of the slope error used in the preliminary analysis of Noor III [12] was σ_s=0.94 mrad although this value was indeed derived for the Sener HE35 heliostat [10]. In this work, as the Sener HE54 model used in Noor III is much bigger, σ_s is set to 1.53 mrad based on [14]. Under the lack of data, the tracking error deviation σ_t is given the same value whereas the sun shape standard deviation is σ_{sun}=2.51 mrad [10]. Besides, a more recent estimation [14] of the effective mirror reflectivity is chosen i.e., 0.9x0.99.
Finally, the shadowing and blocking factor has been calculated through the Sassi procedure [15]. The heliostat problem is divided into several vertical stripes, and only the centre of the affecting heliostats (assumed parallel to the heliostat problem) is projected, following the sun or tower unit vectors, onto the surface of the analysed heliostat. The highest intersection for each strip gives the boundary of the shaded or blocked area.

3 CAMPO GENERATION OF RADIAL STAGGERED HELIOSTAT FIELDS

The most recent and simple procedure followed by CAMPO to generate a regular radially staggered layout with three parameters has been explained in detail elsewhere [10]. Thus, only the more relevant assumptions are briefly explained here. The field generation proceeds from the tower outwards. The number of heliostats of the first row in the first zone, closest to the tower, is $Nhel_1$, whose footprint circles are tangential each other. So, the radius of the first heliostat row i.e., the radial distance between the tower axis and the first row, is

$$R_1 = \left(DM \cdot Nhel_1\right)/2\pi, \tag{2}$$

whereas the azimuth angular spacing for zone 1 is

$$\Delta az_1 = 2\pi/Nhel_1. \tag{3}$$

As we have commented above, the non-dimensional radial increment for zone 1 is Δr_1=0.866. In order to maintain the radial staggered pattern, the azimuth angular spacing is kept constant in the zone. Then, the number of heliostats per row for any zone does not change along the optimisation.
However, the length of the azimuth spacing (metres) between adjacent heliostats will accordingly increase with the radius of the row. This gives a criterion to finish any zone: when an extra heliostat can be placed between two adjoining mirrors in the same row. Thus, the azimuth angular spacing of the outer next zone will be half the previous one whereas the number of heliostats per row will be doubled.

$$\Delta az_2 = \Delta az_1/2, \tag{4}$$

$$Nhel_2 = 2Nhel_1. \tag{5}$$

This also defines the radius of the first row of zone 2 then the number of rows of zone 1,

$$Nrows_1 = round\left(R_1/\Delta R_1\right), \tag{6}$$

where the quotient is rounded off to the next lower integer because $Nrows_1$ is an integer.
Assuming again a maximum density field, in which the non-dimensional radial increase for any zone is the minimum one (Δr_2 =0.866 and Δr_3=0.866), it is easy to define the number of rows of zones 2 and 3.

$$Nrows_2 = round\left(2R_1/\Delta R_1\right); \quad Nrows_3 = round\left(4R_1/\Delta R_1\right), \tag{7}$$

whereas the number of heliostats of zone 3 will be $Nhel_3 = 2Nhel_2$.

Highlight that the number of rows per zone $Nrows_i$ and the number of heliostats per row for each zone $Nhel_i$ have been calculated above for the densest field. As long as $Nhel_1$ does not change, they will not vary along the optimisation process. However, in order to improve the field efficiency, the radial increments will be increased, i.e. Δr_2 >0.866 and Δr_3>0.866 so the field will be expanded along the optimisation. In turn, the azimuth spacing will also naturally grow due to the radial staggered layout. Clearly, when Δr_2 and/or Δr_3 be greater than the minimum value, the circular heliostat footprints of the first row in zone 2 and/or zone 3 will not be tangential each other so naturally increasing the azimuth spacing. Then, it is not necessary to include some extra separation distance in the mirror footprint.
Finally, about the transition between consecutive zones, the radial distance between the last row of zone 1 and the first row of zone 2 is set to ΔR_2 as well as the radial increment between the last row of zone 2 and the first row in zone 3 is ΔR_3. In conclusion, we only need three variables to completely define the thousands

of coordinates of a heliostat field namely, $Nhel_1$, Δr_2 and Δr_3, which will be varied along the optimization. Notice that in this work, based on [12], $Nhel_1 = 60$, which is coherent with DELSOL advices.

4 RESULTS

Table 1 shows the optimum layouts, giving the maximum η_{field}, for the (RR, THT) couples scanned whilst Figure 1 gathers the optimum field efficiencies vs. the receiver radius for the four tower heights explored.

Table 1. Optimum layouts (Δr_1=0.866) for the (THT, RR) options scanned. (N_{hel}=7400, Noor III)

RR (m)	THT=200 m	THT=225 m	THT=250 m	THT=275 m
7.0	Δr_2=0.866 Δr_3=1.8	Δr_2=0.866 Δr_3=1.6	Δr_2=0.866 Δr_3=1.6	Δr_2=0.866 Δr_3=1.4
8.0	Δr_2=0.866 Δr_3=1.8	Δr_2=0.866 Δr_3=1.8	Δr_2=0.866 Δr_3=1.6	Δr_2=0.866 Δr_3=1.6
9.0	Δr_2=1.0 Δr_3=2.0	Δr_2=0.866 Δr_3=1.8	Δr_2=0.866 Δr_3=1.8	Δr_2=0.866 Δr_3=1.6
10.0	Δr_2=1.0 Δr_3=2.0	Δr_2=1.0 Δr_3=1.8	Δr_2=0.866 Δr_3=1.8	Δr_2=0.866 Δr_3=1.6
11.0	Δr_2=1.0 Δr_3=2.2	Δr_2=1.0 Δr_3=2.0	Δr_2=0.866 Δr_3=1.8	Δr_2=0.866 Δr_3=1.6

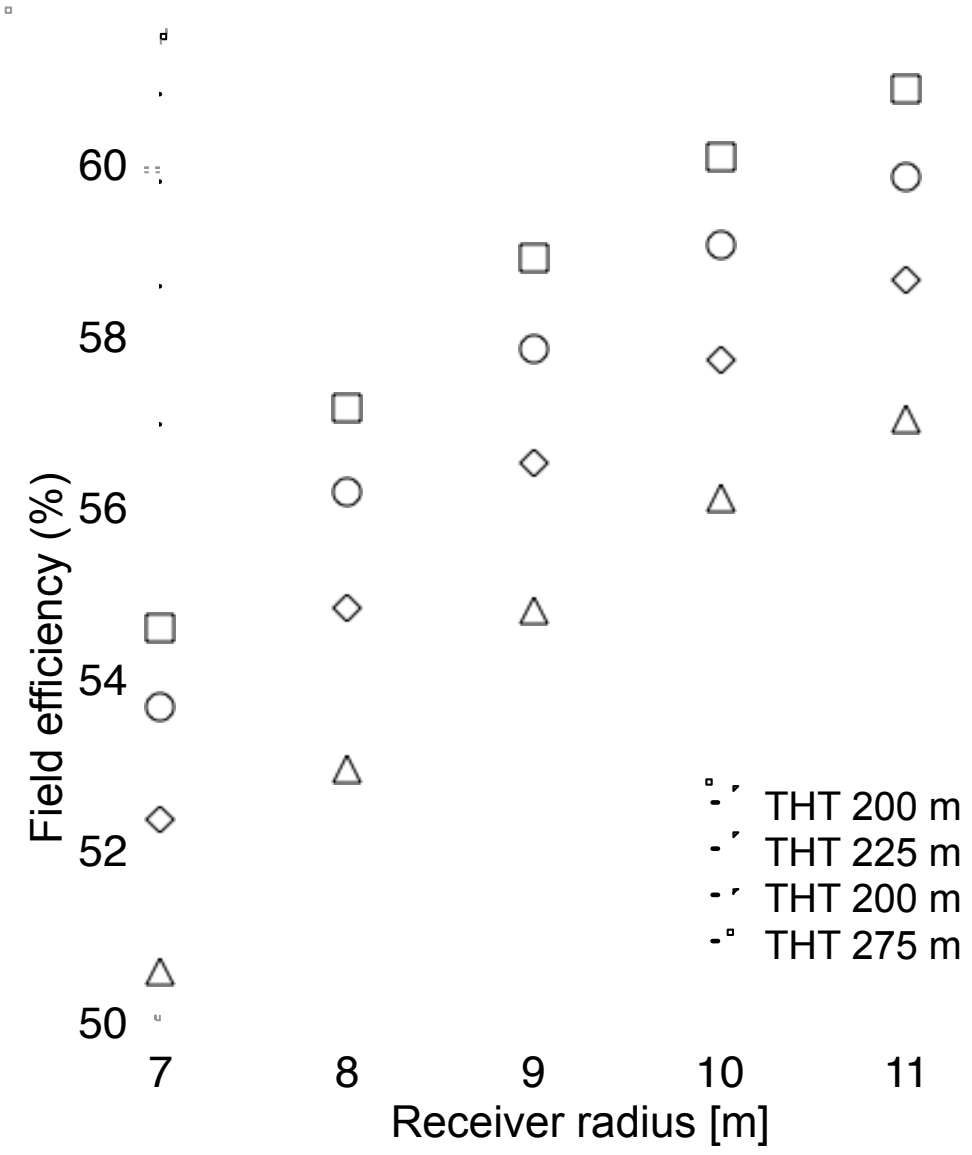

Figure 1. Field efficiency vs. receiver radius and tower height for optimum layouts (Noor III)

Highlight that the sensitivity of η_{field} to moderate changes of the layout parameters is quite smooth provided that Δr_3 be of the order of twice Δr_2. As we have already commented above, this rule of thumb is also verified in Table B1 in [10] for the Gemasolar analysis. This would confirm the appropriateness of the survey points range chosen as well as the steps between the non-dimensional radial increments. Namely, Δr_2=(0.866, 1.0, 1.1) and Δr_3=(1.6, 1.8, 2.0).
The results shown in Table 1 also exhibit internal consistency as those of Table B1 [10]. Since the larger the receiver, the field is less dense i.e., with higher radial increases between heliostat rows. Thus, reducing the shadowing and blocking factor f_{sb}, Eq. (1), but without worsening the intercept factor f_{int} because a larger receiver can fit in larger energy spots sent by further heliostats.
The tower optical height (THT) shows a similar trend. The higher the tower, the lower the radial distance, since shadings and blockings will be reduced as tower grows. Moreover, f_{int} will improve too because, in reducing radial distances between rows, heliostats become closer to the tower and the energy spot will be smaller.
Figure 1 also presents consistency. With small receivers, η_{field} is low. At the beginning, as long as the receiver radius increases, the field efficiency grows fast. However, as the receiver is ever bigger, the growing rhythm is reducing. This indicates that the receiver size range and the steps between the points chosen are appropriate because the optimum size will be there. The tower height shows a similar trend i.e., the vertical distance between the curves is ever shorter as the height increases. Again, the size range and the steps between the survey points seem correct.
Finally, comment that Figure 1 is the starting point to the second stage of the full thermo-economic optimization of the collector field [10].

5 CONCLUSIONS

For a given number of heliostats, CAMPO code [10] could be able to perform the full thermo-economic optimization of the collector field of a commercial tower power solar plant as bigger as Noor III, 150 MWe and 7400 heliostats, dividing the process into two stages.
The first stage, analysed in this work, seeks the optimum layouts for every couple receiver radius and tower optical height (THT) scanned. Thereafter, although not treated in this work, it is possible to find the best collector field (RR, THT, optimised layout) with the highest LCOE.
One of the key points of process is the simple, yet powerful, layout characterization of a radial staggered heliostat field by only three parameters. Namely, the number of heliostats of the first row in the first zone $Nhel_1$, and the non-dimensional constant radial increments of zone 2 and zone 3, Δr_2 and Δr_3, respectively.
A significant result of this work is the confirmation of a rule of thumb about the values of the optimum Δr_2 and Δr_3 namely, $\Delta r_2 \approx 1.0$ whereas Δr_3 is around twice Δr_2.
This approximated relationship has been verified, see Table B1 in [10], not only for a medium solar tower power plant as Gemasolar 20 MWe (THT=140 m [11]) with the HE35 Sener heliostat (DM≈15.7 m) but also for a 150 MWe full commercial plant as Noor III (THT=250 m [13]) and equipped with the HE54 Sener heliostat (DM≈19.67 m).
The suggested ranges chosen for the Δr_2 and Δr_3 survey points and the steps between them allows to quickly find the optimum layouts supplying the highest η_{field}. Furthermore, the field efficiency sensitivity to moderate changes of the layout parameters is smooth provided the above rule of thumb is observed.
Moreover, for a surrounding heliostat field, the ranges and steps suggested for the receiver size and the tower height could be quite appropriate since the profiles of the curves η_{field} vs. receiver radius and tower height exhibit some saturation at the end so suggesting that the trade-off between equipment cost and energy capture efficiency is coming to an equilibrium.
Finally, these results could accelerate the complex problem of the full thermo-economic optimization for the huge collector field of full commercial solar tower power plants.

ACKNOWLEDGEMENTS

The authors want to thank the Spanish Minister of Economy and Competitiveness, and the European Fund for Regional Development for the funding of this research through the research project ENE2015-67518-R (MINECO/FEDER)

REFERENCES

[1] New Energy Update: CSP, http://analysis.newenergyupdate.com/csp-today, 2018.
[2] NREL, SolarPACES, https://www.nrel.gov/csp/solarpaces/power_tower.cfm, 2018.
[3] G. J. Kolb, An evaluation of possible next-generation high-temperature molten salt power towers, SAND2011-9320, 2011.
[4] N. C. Cruz, J. L. Redondo, M. Berenguel, J. D. Alvarez and P. M. Ortigosa, Review of software for optical analysing and optimizing heliostat fields, *Renewable and Sustainable Energy Reviews*, Vol. 72, pp. 1001-1018, 2017.
[5] B. L. Kistler, A user's manual for DELSOL3: a computer code for calculating the optical performance and optimal system design for solar thermal central receiver plants, SAND86-8018, 1986.
[6] P. Schwarzbölz P, M. Schmitz and R. Pitz-Paal, Visual HFLCAL–a software tool for layout and optimization of heliostat fields, *Proc. Int. Conf. on Concentrating Solar Power and Chemical Energy Systems*, Berlin, 2009
[7] C. J. Noone, M. Torrilhon, and A. Mistos, Heliostat field optimization: a new computationally efficient model and biomimetic layout, *Solar Energy*, Vol. 86, pp. 792-803, 2012.
[8] https://github.com/iat-cener/tonatiuh, 2018.
[9] J. G. Barberena, A. Mutuberria-Larrayoz, M. Sanchez and A. Bernardos, State of the art of heliostat field layout algorithms and their comparison, *Energy Procedia*, Vol. 93, pp. 31-38, 2016.
[10] F. J. Collado and J. Guallar, Two-stages optimised design of the collector field of solar power tower plants, *Solar Energy*, Vol. 135, pp. 884-896, 2016.
[11] S. Relloso and E. Garcia, Tower technology cost reduction approach after Gemasolar experience, *Energy Procedia*, Vol. 69, pp. 1660-1666, 2015.
[12] F. J. Collado and J. Guallar, Scaling campo code to commercial solar tower plants, *Proc. Int. Conf. on Concentrating Solar Power and Chemical Energy Systems*, Santiago de Chile, 2017.
[13] S. Relloso and Y. Gutierrez, SENER molten salt tower technology. Ouarzazate NOOR III case, SolarPACES 2016, AIP Conference Proceedings 1850, edited by A. Al Obaidli et al. (American Institute of Physics, Melville, NY, 2017), No.030041.
[14] W. Meinecke, IAS-RL-100200-028, 1982.
[15] NREL, System Advisory Model (SAM), https://sam.nrel.gov, 2018.
[16] G. Sassi, Some notes on shadow and blockage effects, *Solar Energy*, Vol. 31, pp. 331-333, 1983.

ASSESSING SOLAR POTENTIAL AND BATTERY INSTALMENT FOR SELF-SUFFICIENT BUILDINGS WITH SIMPLIFIED MODEL

M. Kovač[1], G. Stegnar, M. Česen and S. Merše

1. Energy Efficiency Center, Institute Jožef Stefan, Ljubljana, Slovenia; email: marko.kovac@ijs.si

ABSTRACT

A high penetration rate of individual photovoltaic installations in the recent years is concentrating on maximizing overall solar power production with not enough regards towards other power system parameters. This is mainly guided by energy policies and economic models, which were adequate for relative low share of solar power within entire energy mix. However, these models are becoming more disruptive as the share of solar power increases and therefore prompt for additional models for calculating solar technical and economic potential can offer valuable data for planning future energy sources. This paper presents a simplified model to assess energy needs of typical households and analyses the potential for individual roof-top solar installation in combination with battery storage, which can be also used by home-owners. This model accounts for the main influences: the weather pattern, load curve and roof orientation. Typical applications and main benefits of the proposed model are discussed and critically reviewed.

Keywords: Photovoltaic, Battery Storage, Numerical Modeling

1 INTRODUCTION

Use of photovoltaic (PV) panels for the domestic self-powering is seen as somewhat disruptive technology for energy providers and home owners alike. The first cannot afford the impact of PV to disrupt the equilibrium of power grids, while the latter have limited information and experiences how is going to impact their overall costs. In the past a lot of quite refined studies were made (e.g., [1, 2]), which covers this in details, however while this deep approach is requested within academic world it seems an overkill for home-owners. Due to extensive PV support through feed-in schemes within years 2010 and 2013, the PV in Slovenia made quite an impact, covering an almost 2% of total electricity needs [3]. However, the number of installation was driven by the support scheme and not by overall economics. From that period, the number of new PV installation in Slovenia has fallen significantly since more of the cost is now covered by home-owners and less by tax payers through the support schemes [3]. Rapidly decreasing PV prices are also improving cost efficiency of installation without the support schemes at end-user level.

Furthermore, with the decreasing prices of battery storage, adding a storage unit to PV is quite affordable and viable option, which eliminates the main drawback of PV as an energy source – reliance on the daytime clear weather [4]. However, attaching complementary component into the small-scale system to make it self-sufficient demands its careful pre-analysis to optimize its performance. Sophisticated numerical tools were developed in the recent years [5, 6], however while they are more and more academically complex, they are not necessary best suitable for home owners. For the purpose of energy literacy [7], a somewhat simplified approach to model for PV energy input and battery storage is needed, which should be home owners friendly while accurate enough.

Simplified model is also suitable since the technologies (e.g., different types of electricity storage) and economic parameters are changing quite rapidly [4]. The falling prices of home PV and battery installations are pushing technology from the hands of tech-enthusiasts towards less knowledgeable investors, where quick (and adequate) models are essential to reduce the chances of costly energy misinvestments. Another benefit of this approach is that it could be done with simple spreadsheet computer tools, which home investors are probably already using.

Figure 1 shows the main influences on household energy budget on any given moment. The energy depends on PV and battery power outputs: The Sun position (azimuth and elevation), PV position (azimuth and elevation), the size and efficiency of PV panel (with efficiency of add-ons like inverter etc.), weather, local surroundings (especially shading), battery size, state and efficiency, household consumption (loading curve), outside and desired inside temperature (for heating) to name a few.

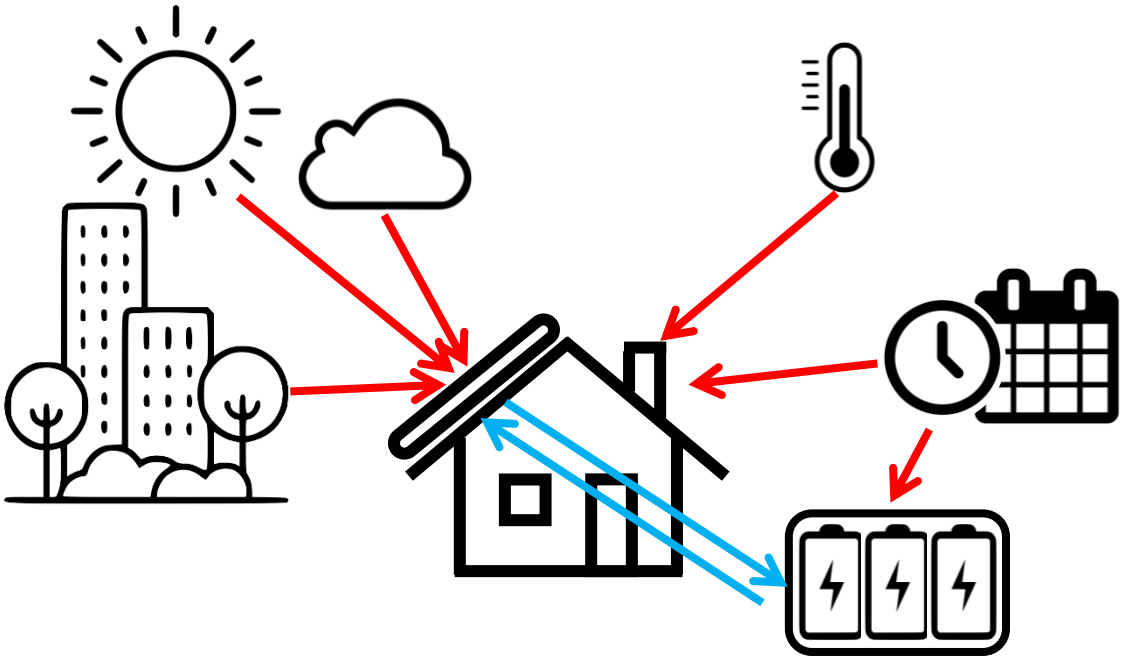

Figure 1: Schematics of influences on the photovoltaic energy production and battery usage in common household

The main disadvantage of photo voltaic electricity production is its reliance to sun cyclic (daily and yearly) pattern. This could be overcome by storage system. While short term storage is economical feasible, long term (i.e., yearly) one is often not practical [8]. Therefore, the effort on the improvement of PV efficiency should be on ensuring higher outcome in critical times, when the sunlight is sparse (i.e., winter in areas of moderate to extreme geographic latitude and/or bad weather).

2 DATA AND MODEL

For the purpose of this paper two typical new households with location of Ljubljana, Slovenia were used. The main reasons for this are availability of the data and the weather pattern, which is a bit demanding, with relatively cold and cloudy weather during late fall and winter, which impairs PV electric production and enhances demands for the battery storage. Figure 2 shows outdoor temperature (left) and solar radiation (right) [9] for the test reference year. This takes into account measures of selected parameters in the space of 30 years and thus presents historical digital data set that represents measured 365-day values of the selected meteorological variables on the hourly basis. The sequence is synthetically constructed using monthly values selected from a multiple year data set for a given location so the resulting test reference year is typical for the location. The heating demand is calculated as a linear function of temperature shortage, however no additional sources (solar radiation and internal heat gains, transmission and ventilation losses) were taken into account due to simplification.

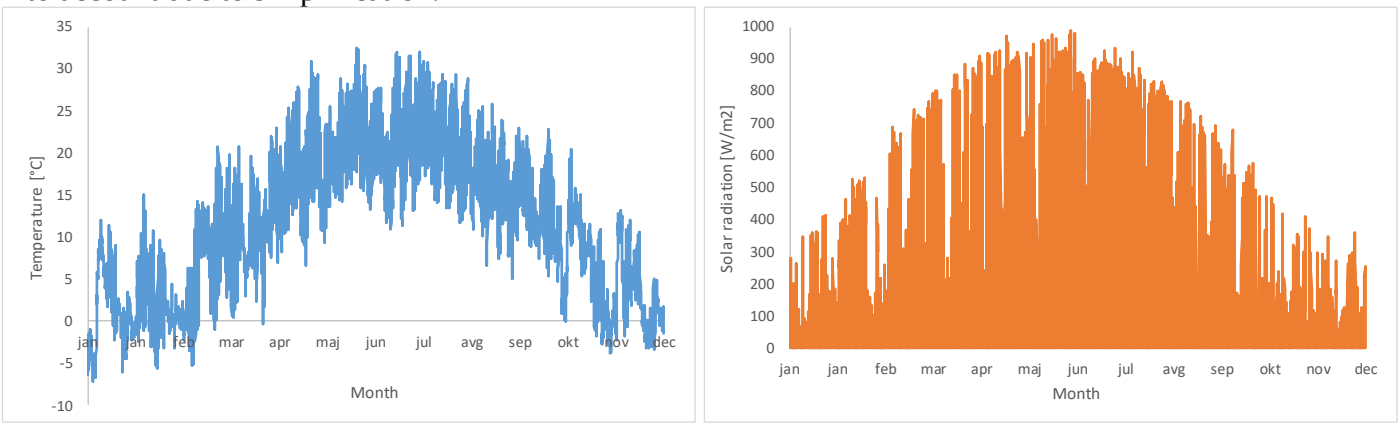

Figure 2: Outdoor temperature of selected model year (left) and solar radiation (right)

The calculation of solar position was adapted from the calculation procedure by NOAA [10] and [11]. An optimal position of photovoltaic panel with maximum total energy output for selected location is elevation of

32° and azimuth of -2° [12]. However, this approach with relatively narrow spikes in solar electricity production causes duck-curve phenomena [4], which averts even wider acceptance of photovoltaic and hence renewable electricity production. With rising prices of power grid fees [3], the push towards electric energy independence will grow further. In this case PV panel should be assisted with battery, which are slowly gaining popularity. To enable electric energy independence – the combination of produced electricity and storage energy should be enough to power an individual building at any hour.

The used model of domestic electric energy consumption and production is intentional simplified to obtain just rough indications regarding the problematic issues. The production of electric energy by photovoltaic is hence defined by time (due to orientation of the sun ω_{sun}, orientation of the PV panel ω_{PV}, solar radiation *sol_rad* and also the state of battery). The latter can fulfill the electric energy demand only if not thoroughly depleted. The demand P_{demand} should be outweighed by production $P_{production}$ and reserve from battery storage $P_{battery}$ at any time:

$$\forall t; P_{production}\left(\omega_{sun}(t), \omega_{PV}, sol\_rad(t)\right) + P_{battery}(s) \geq P_{demand}(t,T) \qquad (1)$$

The calculation of electric production from PV at the time does not account for shading, which needs case-by-case approach for each rooftop. Some ideas how to overcome this limitation are addresses in other literature [13, 14].

Electric energy demand $P_{demand}(t,T)$ is a sum of general demand $P_{gen}(t)$ (e.g., lighting, home appliances), which varies over time of the day, and demand for heating $P_{heat}(T(t))$, which depends on the outside temperature (if that is lower than desired):

$$P_{demand}(t,T) = P_{gen}(t) + P_{heat}\left(T(t)\right) \qquad (2)$$

$$P_{gen}(t) = P_{ave} \cdot \beta(t) \text{ and } P_{heat}\left(T(t)\right) = \Delta T^{*}(t) \cdot C^{*}, \qquad (3)$$

where P_{ace} is average generated power. Temperature deficit $\Delta T^{*}(t)$ and specific heating demand C^{*} are defined by:

$$\Delta T^{*}(t) = min\{T_{out}(t) - T_0, 0\} \text{ and } C^{*} = \frac{Q_{heat,year}}{\sum_t \Delta T^{*}(t)}. \qquad (4)$$

Figure 3 left shows demand for electricity in households relative to average consumption [15] – noted as β in equation (3) plotted against daily hours, where the morning and afternoon/evening peaks are clearly visible. Figure 3 right shows the outside temperature (red line, left-side scale) and heating demand $P_{heat}(T(t))$ (blue line, right-side scale) for 60-day period of model year – from the late February to the late April. The demand for heating noticeably decreases as outside temperatures start to rise due to the spring weather.

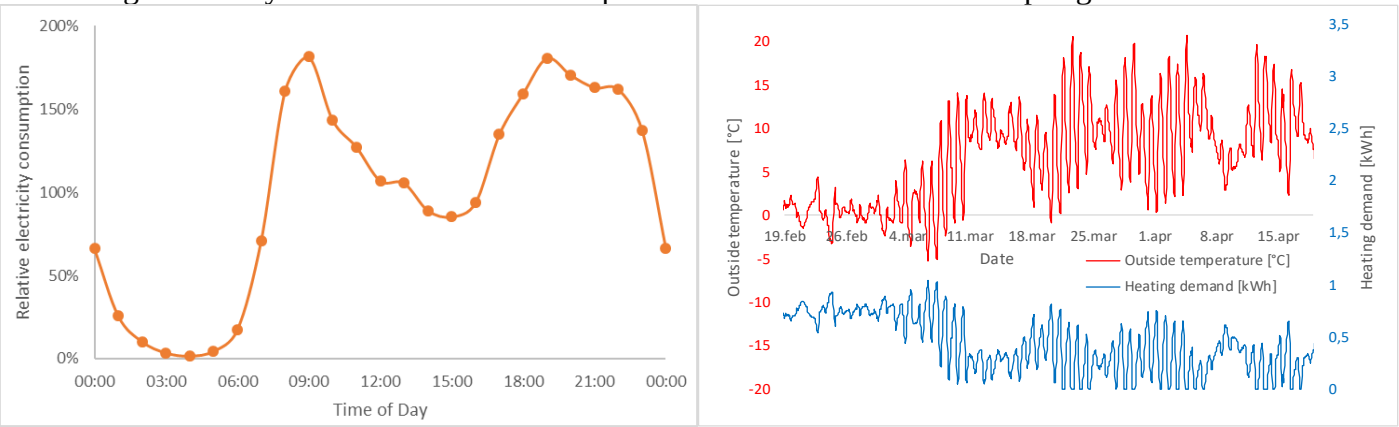

Figure 3: Relative electric energy consumption (left) and outside temperatures and temperature deficit (right)

3 CALCULATION

Two showcases are used for model demonstration: (a) a small cabin with area of around 50 m^2 and electricity needs of 2500 kWh per year and heating needs of 1000 kWh per year and (b) normal passive residential house with area of 150-200 m^2 with electricity needs of 3000 kWh per year and heating needs of 2500 kWh per year [3]. The showcases were calculated using a PV panel ranging between 3 – 9 kW_{el} and battery storage with capacity of 5-40 kWh, which at the beginning of calculation was holding a half of its capacity. It was reasonably assumed that the discharge current capability of the used battery storage is

sufficient to power the household at any time. Due to availability of meteorological data, one-hour time slot was used for the calculation.
Tables 1 and 2 show the minimum energy balance of calculated showcases (a) and (b), respectively. Negative results are sign that the whole combination of PV facility and battery storage are not enough to cover the energy needs. The minimum usually occurs during longer times of bad weather during winter periods.

Table 1: The minimum energy balance of calculated case (a) P_{gen} = 2500 kWh, P_{heat} = 1000 kWh

		Power of PV [kW_{el}]				
		3.0	4.5	6.0	7.5	9
Battery capacity [kWh]	5	-43.3	-18.0	-13.1	-11.8	-10.3
	10	-38.3	-13.0	-8.1	-6.7	-5.3
	15	-31.4	-8.0	-3.1	-1.7	0.3
	20	-26.7	-3.0	1.9	3.25	4.7
	25	-21.4	2.0	6.9	8.2	9.7
	30	-16.8	7.6	11.9	12.3	12.3

Table 2: The minimum energy balance of calculated case (b) P_{gen} = 3000 kWh, P_{heat} = 2500 kWh

		Power of PV [kWel]			
		4.5	6.0	7.5	9.0
Battery capacity [kWh]	15	-40.9	-14.3	-5.3	-2.0
	20	-24.2	-6.5	0.6	3.0
	25	-20.5	-0.4	5.6	8.0
	30	-15.9	3.3	10.9	13.0
	35	-12.3	8.2	15.6	16.7

The results show that the energy self-sufficient household can be achieved using proper combination of PV panels and battery storage. For the showcase (a) the battery storage should be above 20 kWh and installed PV power above 4.5-6 kW_{el}. The more demanding showcase (b) needs at least somewhat similar capacity of storage with PV panels capable of reaching 7.5 kW_{el}. Of course, this means also that any other combination with larger capacity will also be more than enough to power the household. On the other hand, this abundance of combinations allows us to hint at cost optimization.
Another interesting observation is the optimal orientation of the PV panel to obtain the most self-sufficient energy balance as shown in Figure 3, where orange circles represent combinations with positive balance and white with negative ones, while the size determines amplitude. An average azimuth is 178° (i.e., South), however the elevation is 69°, which is much more suitable for winter time with low sun. This is also an economical case for PV panels mounted on the house façades or into windows.

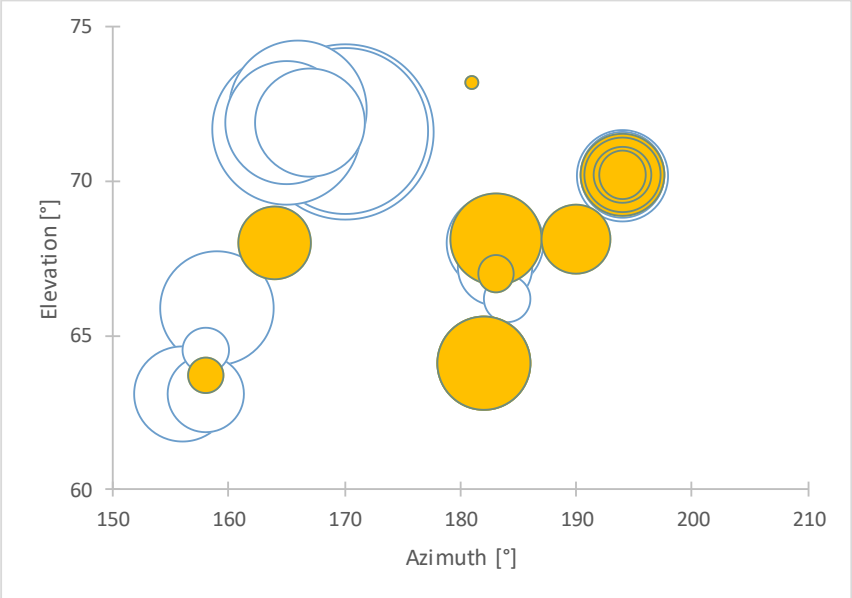

Figure 3: Optimal orientation of PV for different combination of PV and battery storage

From the data obtained [16], the current prices of installed battery storage are around 325 €/kWh for small units (up to 50 kWh). The prices for PV installation up to 50 kW_{el} are around 2700 €/kW_{el}, which includes the cost of modules and installation. Using the price assumptions, the different combinations presented in Tables 1 and 2 can be estimated for cost. Figure 4 shows minimum energy balance plotted against installation costs for both showcases (a) and (b). The approximation curves with coefficient of determination R^2-values are also shown.

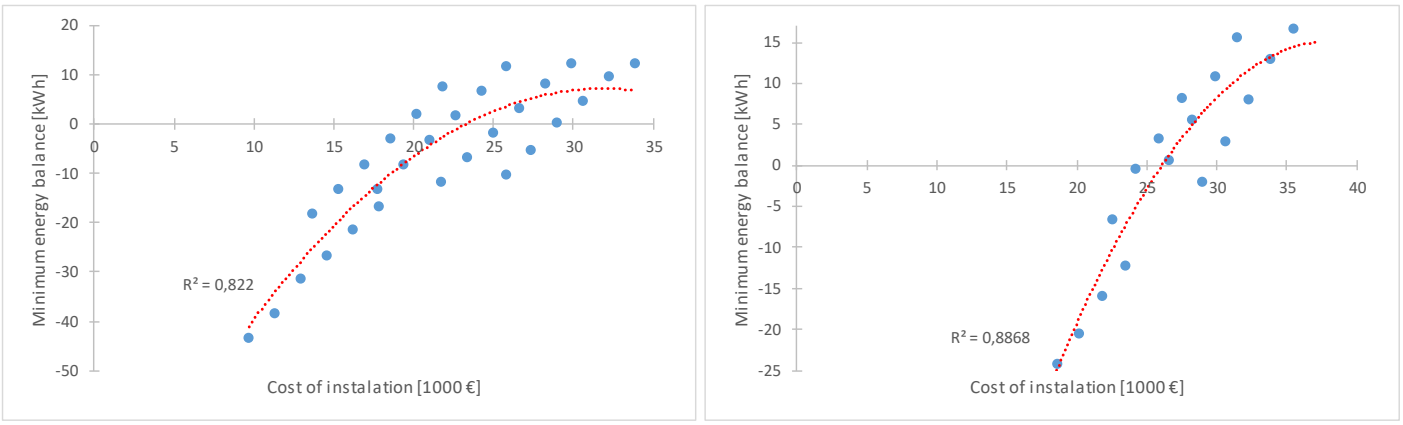

Figure 4: Minimum energy balance plotted against installation costs for showcase (a) on the left and showcase (b) on the right

The approximation shows that the price for self-sufficient installation of PV panels and battery storage for typical household (showcase (b)) are in order of 26,000 €. For somewhat smaller house (showcase (b)), the price of installation is around 23,000 €, which is surprisingly close to the first results especially since our economic model did not account for difference in installation relative cost regarding energy output.

The results shown above do not account for different lifespans of PV panels and batteries. The former is around 25 – 30 years, the lifespan of the latter much depends on the number of cycles and wholesome energy throughput. The presented cases had 400 – 525 battery cycles per year with the cumulative energy flow of 4.6 MWh. Based on data from literature [17] and from some of the manufacturers [18], the expected economical lifespan varies, however an assumption of 8 years is reasonable. This is somewhat 3-times shorter than PV, therefore total cost over longer time period should also include multiple batteries packs.

4 CONCLUSION AND FUTURE WORK

The presented results of simplistic approach were useful towards electricity econometrics, which allows quick evaluation of combination of PV panels with energy storage. This is especially important since the understanding of governing principles goes hand-in-hand with technology penetration within an ordinary consumer life. The feasibility of the self-sustained household in moderate climate (as Slovenia) was shown

with somewhat affordable price. With the decreasing prices of PVs and batteries the feasibility will importantly increase in the future.

The future work should be related to obtain more automatic solution and hence improve the accuracy of the method. Furthermore, additional influences such as surrounding shading (building, vegetation, local relief) should be addressed. More emphasis should be given to the economic part of the evaluation to account for a rapidly changing prices of installation (and also electricity). The showcases used one orientation of PV, however results with high angles of elevation show that multi-panel approach might be of use.

REFERENCES

[1] Lukač, Niko. *Algoritem za celostno vrednotenje fotovoltaičnega in vetrnega potenciala večjih geografskih območij*. Maribor. Fakulteta za elektrotehniko, računalništvo in informatiko, Univerza v Mariboru, 2016.

[2] *Buildings roofs photovoltaic potential assessment based on LiDAR (Light Detection and Ranging) data*. Lukač, Niko, et al.: Elsevier Ltd., 2014, Energy, Issue. 66, pp. 598-609.

[3] Ministry of Infrastructure of Republic of Slovenia. *Portal Energetika. Električna energija - količine*. 14. 12 2017. www.energetika-portal.si/statistika/statisticna-podrocja/elektricna-energija-kolicine.

[4] Wirth, Harry et al. *Recent Facts about Photovoltaics in Germany*, Fraunhofer ISE, Freiburg, January 2018

[5] Hassan, Abubakar Sani, Cipcigan, Liana and Jenkins, Nick. O*ptimal battery storage operation for PV systems with tariff incentives*. Applied Energy. 2017, Vol. 203.

[6] Merei, Ghada, et al. *Optimization of self-consumption and techno-economic analysis of PV-battery systems in commercial applications.* Applied Energy. 2016, Vol. 168.

[7] Office of Energy Efficiency & Renewable Energy. *Energy Literacy: Essential Principles and Fundamental Concepts for Energy Education*. Energy.gov. 2018. www.energy.gov/eere/education/energy-literacy-essential-principles-and-fundamental-concepts-energy-education.

[8] Komarnicki, Przemyslaw, Lombardi, Pio in Styczynski, Zbigniew. *Electric Energy Storage Systems: Flexibility Options for Smart Grids*. Berlin: Springer-Verlag, 2017. ISBN 978-3-662-53274-4.

[9] *Državna meteorološka služba. meteo.si.* Državna meteorološka služba. Agencija RS za okolje, 2017. meteo.arso.gov.si/met/sl/climate/.

[10] Cornwall, Chris, Horiuchi, Aaron and Lehman, Chris. *NOAA ESRL Sunrise/Sunset Calculator.* National Oceanic and Atmospheric Administration. NOAA , 2018. www.esrl.noaa.gov/gmd/grad/solcalc/sunrise.html.

[11] Pelletier, Greg. *Models and tools for water quality improvement.* Washington State Department of Ecology. 2017. ecology.wa.gov/Research-Data/Data-resources/Models-spreadsheets/Modeling-the-environment/Models-tools-for-TMDLs.

[12] *Sončno obsevanje v Sloveniji*. PV Portal. 2017. pv.fe.uni-lj.si/ObsSLO.aspx.

[13] Gagnon, Pieter, et al. *Rooftop Solar Photovoltaic Technical Potential in the United States: A Detailed Assessment*. NREL. Golden, CO, ZDA: National Renewable Energy Laboratory, January 2016. NREL/TP-6A20-65298.

[14] Mathiesen, B. V., et al. *The role of Photovoltaics towards 100% Renewable energy systems*. Aalborg: Department of Development and Planning, Aalborg University, 2017.

[15] Torriti, Jacopo et al. *Peak residential electricity demand and social practices: Deriving flexibility and greenhouse gas intensities from time use and locational data.* Indoor and Built Environment. Volume: 24, pp: 891-912.

[16] IRENA, *Electricity Storage and Renewables: Costs and Markets to 2030*, International Renewable

[17] Bartlett, Dennis et al.: *Business Models for Extracting More Useful Life from Lithium Ion Battery Systems*, Duke University, 2017.

[18] *Tesla Powerwall Limited Warranty*, Applies to: 13.5 kWh Powerwall 2 AC, April 2017, CA, USA

ONE-STEP HYDROTHERMAL SYNTHESIS OF Ag@TiO_2 NANOPARTICLE TOWARDS DYE-SENSITIZED SOLAR CELL APPLICATION

Yong Xiang Dong[1], Dao Yong Wan[1], Zhi Yu Fan[1], En Mei Jin[1], Sang Mun Jeong[1,*], See Hoon Lee[2]

[1]Department of Chemical Engineering, Chungbuk National University, 1 Chungdae-ro, Seowon-Gu, Cheongju, Chungbuk,. Republic of Korea; email: smjeong@chungbuk.ac.kr

[2]Department of Mineral Resources & Energy Engineering, Chonbuk National University, 567 Baekje-daero, Deokjin-gu, Jeonju , Jeonbuk, 54896, Republic of Korea; email: donald@jbnu.ac.kr

ABSTRACT

Recently, great efforts have been directed at developing efficient visible light-activated photovoltaic materials. In this work, Ag@TiO_2 nanoparticles synthesized by the hydrothermal method exhibited significantly increased visible light absorption and improve photovoltaic activity, compare with anatase TiO_2. TiO_2 nanoparticles were doped with different concentrations of Ag to improve their photovoltaic properties. All as-prepared TiO_2 and Ag@TiO_2 particles showed a pure anatase crystalline structure, and in comparison to non-doped TiO_2, the absorption edge of Ag-doped nanoparticles were broader and shifted to higher wavelength. This indicated that UV-Vis absorption closely related to doping metal ions and non-metal atoms. The solar conversion efficiency (η) of 0.1M Ag-doped ($Ag_{0.1}$@TiO_2) nanoparticle-based dye-sensitized solar cells (DSSCs) was 6.44%, which showed an improvement of ~ 22% compared with TiO_2 nanoparticle-based DSSCs (η of 5.05%).

Keywords: Hydrothermal reaction, Ag@TiO_2, photon energy, dye-sensitized solar cell

1 INTRODUCTION

Nanostructured titanium dioxide (TiO_2) has been of significant interest to researchers due to its unique physical and chemical properties, as well as for its great potential applications in a wide range of fields including catalysis, photocatalysis, gas sensor, photoluminescence, fuel cell, and solar cells [1]. The unique physical and chemical properties of TiO_2 depend on various characteristics, such as the crystalline phase, particle size, particle shape, etc. For example, TiO_2 with different crystalline structure exhibits different band gaps (2.98 eV for rutile TiO_2, 3.05 eV for anatase TiO_2, 3.26 eV for brookite TiO_2), which determine the photocatalytic activity of TiO_2 [2-4]. Various techniques such as sol-gel, microwave-driven polyol, and hydrothermal method have been proposed to synthesize TiO_2 nanoparticles [3-7]. Among those methods, the hydrothermal reaction is intended to crystallize material from aqueous solution at relatively low temperatures and high pressures. The hydrothermal reaction also allows easy synthesis of high-purity crystals. In this work, TiO_2 nanoparticles were synthesized by the hydrothermal reaction and Ag metal was doped into TiO2 to improve the photovoltaic properties. As-prepared TiO_2 and Ag@TiO_2 nanoparticles were applied to photoelectrode of dye-sensitized solar cells (DSSC).

2 EXPERIMENTAL

TiO_2 and Ag@TiO_2 nanoparticles were synthesized by hydrolysis of titanium isopropoxide(TTIP, 99.9%, Aldrich). Typically, TTIP was dissolved in distilled water under stirring for a few minutes and then, NH_3 (28-30%, SAMCHUN) was added into the solution. Then, $AgNO_3$ (≥99%) was added at different concentrations (0.05M - 0.2M) for Ag-doping. After continuous stirring for 2 h, the mixture solution was heated in an autoclave at 200°C for 5 h. The obtained precipitate of TiO_2 was washed by ethanol and it was vacuum-dried. The as-synthesized TiO_2 and Ag@TiO_2 was treated by nitric acid to enhance dispersion of particles as reported in our previous report [7]. For the fabrication of photoelectrode for DSSC, TiO_2 or Ag@TiO_2 powders, acetylacetone (99%, Aldrich), hydroxypropyl cellulose (99%, Aldrich) and distilled water were mixed to prepare a paste. The prepared paste was coated on a fluorine-doped tin oxide substrate (FTO, 8 Ω/cm^2, Pilkington), which was subsequently sintered at 450 °C for 0.5 h. Then, the film (active cell area: 0.25 cm^2) was immersed in 0.5 mM ethanol solution of N719 dye (cis-bis(isothioxyanato)bis(2,2'-bipyridyl-4,4'-dicarboxylato)-ruthenium(II)bis-tetrabutylammonium) for 5h. The DSSC was assembled by as-prepared TiO_2 or Ag@TiO_2 photoelectrode and Pt counter electrode as sandwich-type. The electrolyte, 0.5M LiI, 0.05 M I_2, 0.5 M 4-tert-butylpyridine, 0.6 M DMPII in 3-methoxypropionitrile was introduced into the cell.

The crystal structures and morphologies of the synthesized materials were characterized by X-ray diffraction analysis (XRD, Rigaku, Japan) and field emission transmission electron microscope (FE-TEM, 200KV, JEM 2100F, JEOL). Surface area and pore characterization system (ASAP2020, Micromeritics), X-ray photoelectron spectroscope (XPS, ESCALAB 210, VG Science), and UV-Vis spectrum (S-3100, Scinco). Photovoltaic properties of the DSSCs were measured by recoding the current density-voltage characteristics under illumination with a Polaronix K201 (McScience, Korea) equipped with a K401 CW150 lamp power supply and an AM 1.5G filter (100 mW/cm^2).

3 RESULTS AND DISCUSSIONS

The XRD patterns of the TiO_2 and $Ag@TiO_2$ nanoparticles are shown in Fig. 1. In the XRD pattern, all diffraction peaks of the TiO_2 and $Ag@TiO_2$ nanoparticles match well with the crystal structure of the anatase TiO_2 phase (space group $I4_1/amd$, card no. 21-1276 in the JCPDS database), the sharp and intense peaks at 25.3˚, 37.9˚, 48.1˚, and 53.5˚ are representative of the (101), (004), (200), and (211) diffraction planes, respectively. The (101) peak intensity of $Ag@TiO_2$ nanoparticles was smaller than for non-doped TiO_2 nanoparticles, and as the Ag-dopant concentration increased, the intensity of the (101) peak increased as well. It can be seen that anatase crystallinity was hindered as it was doped with Ag. In addition, the lattice parameters *a* and *c* decreased with increasing Ag-dopant concentration, confirming the presence of dopant inside the TiO_2 lattice. The variations in the lattice parameters were calculated by the Rietveld refinement method and the results are provided in Table 1.

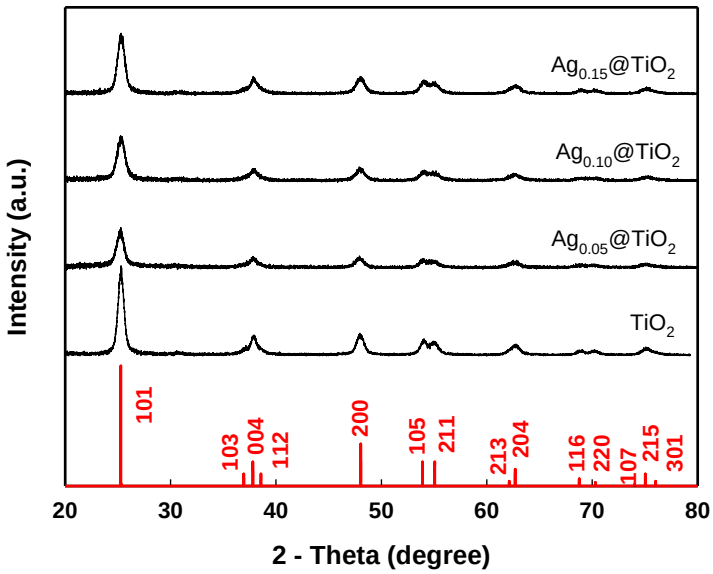

Figure 1. XRD patterns of TiO_2 and $Ag@TiO_2$ nanoparticles.

Table 1. Physico-chemical and photovoltaic properties of TiO_2 and $Ag@TiO_2$ nanoparticles.

Samples			TiO_2	$Ag_{0.05}@TiO_2$	$Ag_{0.10}@TiO_2$	$Ag_{0.15}@TiO_2$	$Ag_{0.20}@TiO_2$
Lattice parameter	*a*	(Å)	3.7908	3.7894	3.7887	3.7850	3.7841
	c	(Å)	9.4826	9.4917	9.4640	9.4710	9.4910
	v	(Å^3)	136.2665	136.2966	135.8486	135.6837	135.9055
Surface area		(m²/g)	64.44	-	100.29	-	-
Pore volume		(cm³/g)	0.25	-	0.27	-	-
Photon energy		(eV)	3.22	3.20	3.18	3.12	3.09
Photovoltaic properties	V_{oc}	(V)	0.69	0.67	0.67	0.67	0.67
	J_{sc}	(mA/cm^2)	13.25	15.48	17.20	14.45	14.11
	FF	(%)	55.23	56.14	55.92	56.37	56.28
	η	(%)	5.05	5.82	6.44	5.46	5.32

To determine the particle size and morphologies of TiO_2 and $Ag_{0.10}@TiO_2$ nanoparticles, the FE-TEM images were analysed as shown in Fig. 2. The morphology of the nanoparticles is that of a pseudo-cube shape, with an average particle lengths of 18 nm for TiO_2 and 14 nm for $Ag_{0.10}@TiO_2$ nanoparticles, respectively. The particle size of $Ag@TiO_2$ was smaller than that of non-doped TiO_2. In the Fig. 2 (c) and (d), magnified FE-SEM images for TiO_2 and $Ag_{0.10}@TiO_2$ nanoparticles are shown. An interplanar spacing of d=0.35 nm was found for the TiO_2 nanoparticles, which corresponds to the (101) plane of anatase TiO_2. In the $Ag_{0.10}@TiO_2$ nanoparticles, the cubic phase of silver was identified by the interplanar spacing of d=0.23 nm and indexed as the (111) plane, indicating that Ag is doped into TiO_2 structure.

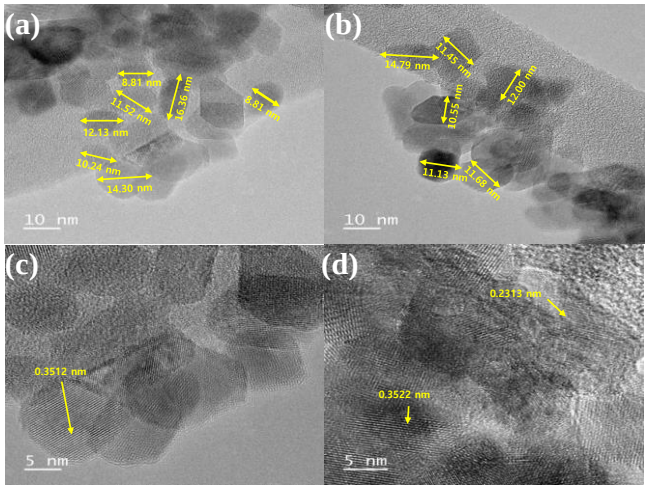

Figure 2. HR-TEM images of (a) TiO_2, (b) $Ag_{0.10}@TiO_2$, magnification TEM images of (c) TiO_2, and (d) $Ag_{0.10}@TiO_2$ nanoparticles.

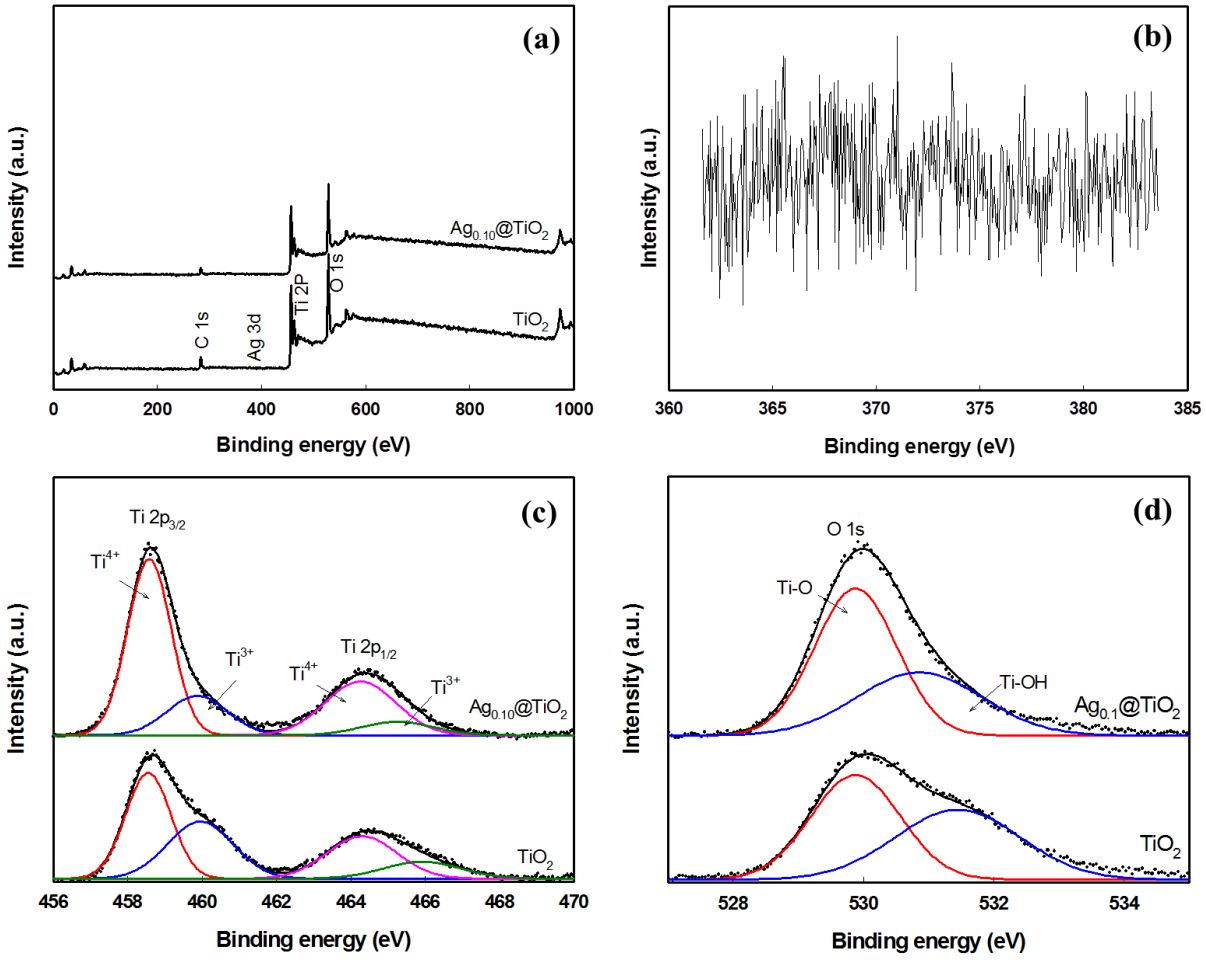

Figure 3. (a) The survey spectra, (b) Ag 3d spectra of $Ag_{0.10}@TiO_2$ nanoparticles, (c) Ti 2p, and (d) O 1d core levels of the TiO_2 and $Ag_{0.10}@TiO_2$ nanoparticles according to XPS spectra.

The chemical composition and surface properties of TiO_2 and $Ag_{0.10}@TiO_2$ nanoparticles were determined by XPS studies. Fig. 3 shows the XPS spectra of TiO_2 and $Ag_{0.10}@TiO_2$ nanoparticles. The fully scanned spectra (Fig.3 (a)) show that the Ti, O, and C elements exist on the surface of the pure TiO_2 and $Ag_{0.10}@TiO_2$ nanoparticles. In general, the chemical bonds corresponding to AgO (Ag^{2+}), Ag_2O (Ag^{+}) and Ag (Ag^{0}) can be found around at 367.4 eV, 367.8 eV and 368.2 eV, respectively [8]. However, the Ag element peaks are only slightly distinguishable in $Ag_{0.10}@TiO_2$ nanoparticles as shown in the Fig. 3 (b). This will be related to the small amount of doping Ag present. According to Chen's report, the Ag3d bond peaks could be observed clearly when more than 0.5 wt% of Ag was doped into TiO_2 [9]. The presence of elemental C can be ascribed to contamination on sampling or testing. The XPS peak fitting program (PeakFit, Version 4, Jandel) was used to analyze the XPS data. The high-resolution of Ti2p also consists of two kinds of peaks for $Ti2p_{3/2}$ and $Ti2p_{1/2}$. The peaks located at 458.6eV and 464.3eV are attributed to Ti^{4+}, and the peaks located at 460.0eV and 465.9eV are attributed to Ti^{3+}. The peak position for Ti2p in the $Ag_{0.10}@TiO_2$ nanoparticles is almost similar to TiO_2 nanoparticles. However, the Ti^{3+} peak area of $Ag_{0.10}@TiO_2$ nanoparticles is increased because of Ag taking electrons from isopropyl radicals ($C_3H_7^{-}$) during the hydrothermal reaction and the electron migrating to Ti^{4+} to form Ti^{3+} ($Ag+e^{-}\rightarrow Ag^{-}$, $Ag^{-}+Ti^{4+}\rightarrow Ti^{3+}$) [10]. The O1s XPS peak at 529.82 eV is characteristic of the lattice oxygen of TiO_2 (Ti-O) and the peak locates at 531.4 eV is assigned to the surface hydroxyl groups (OH^{-}).

Fig. 4. shows the obtained nitrogen adsorption-desorption isotherm results analyzed by BET method for surface area and Barrett-Joyner-Halenda (BJH) pore size distribution as insert. The relative isotherms of the TiO_2 and $Ag_{0.10}@TiO_2$ nanoparticles were of type IV, which is characteristic of mesoporous materials with an H2-type hysteresis loop indicating the presence of mesoporous (2-50 nm) [11]. The surface area of TiO_2 and $Ag_{0.10}@TiO_2$ nanoparticles were 64.44 m^2g^{-1} and 100.29 m^2g^{-1}, denoting a significant increase in the surface area compared to commercial P25 (51 m^2g^{-1}) [12]. Such large surface area might improve the absorption capacity for dye molecules, the charge transfer and solar conversion efficiency. The pore size distribution can be calculated from the desorption branch of the N_2 isotherm by the BJH method (Fig. 4 (b)), evidenced an average pore diameter of about 17 nm for TiO_2 and 12 nm for $Ag_{0.10}@TiO_2$ nanoparticles. This porous structure has a significant impact on the on the photoelectric response of dye-sensitized solar cells, because it facilitates the loading of the dye molecule on the TiO_2 surface and diffusion of electrolyte in dye-sensitized solar cells.

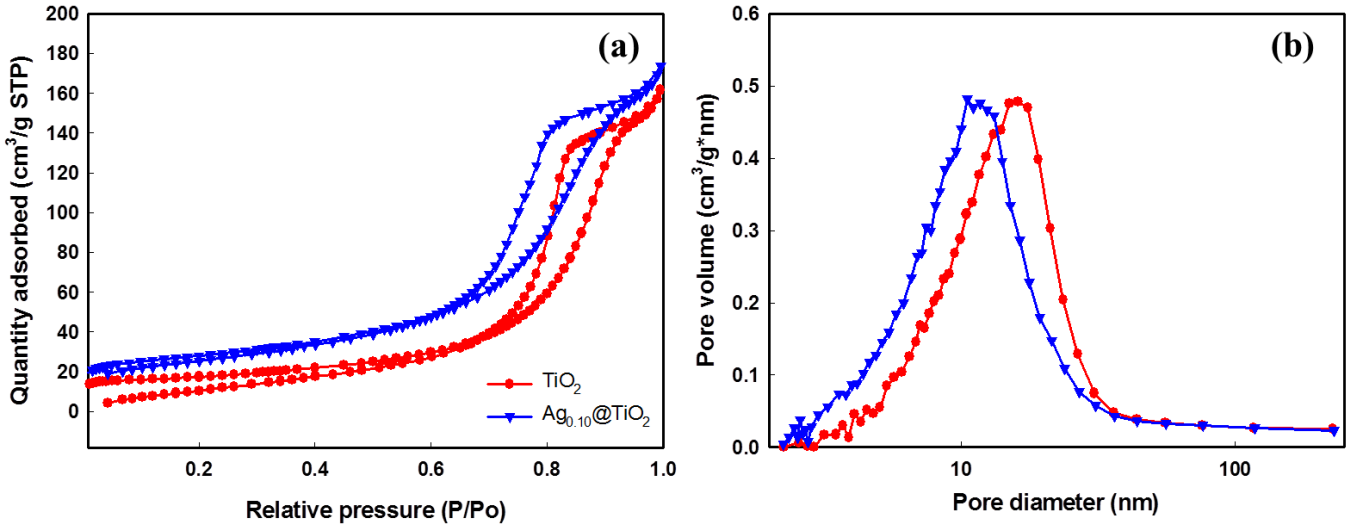

Figure 4. (a) Nitrogen adsorption-desorption and (b) pore size distribution.

UV-Vis absorption spectra of TiO_2 and $Ag@TiO_2$ nanoparticles are shown in Fig. 5. The absorption curve of TiO_2 (Fig. 5 (a)) indicates that pure TiO_2 hardly absorbs light at a wavelength of 430 nm or more. On the other hand, the absorption capabilities of $Ag@TiO_2$ nanoparticles were markedly improved in a range of 400-800 nm due to both the surface plasmon resonance (SPR) and the interference effect caused from the electromagnetic field of the conduction electrons released from Ag dispersed on the TiO_2 matrix [13]. Such an enhanced absorption could lead a greater photovoltaic efficiency of $Ag@TiO_2$. The plot of $(\alpha hv)^{1/2}$ *vs.*

photon energy was obtained by Tauc's formula, as shown in Fig. 5 (b). The photon energy values were found to be 3.22, 3.20, 3.18, 3.12, and 3.09 eV for TiO_2, $Ag_{0.05}@TiO_2$, $Ag_{0.10}@TiO_2$, $Ag_{0.15}@TiO_2$, and $Ag_{0.20}@TiO_2$, respectively.

Fig. 6 shows the photocurrent density-voltage curves for different nanoparticles used in dye-sensitized solar cells (DSSCs). $Ag@TiO_2$ leads to an increase in photocurrent density (J_{sc}) and solar conversion efficiency (η). The best J_{sc} (17.20 mA cm^{-2}) and η (6.44 %) were observed with $Ag_{0.10}@TiO_2$ nanoparticles because the large surface area of $Ag_{0.10}@TiO_2$ nanoparticles can adsorb more dye molecules and a greater absorption of visible light can improve the utilization of sunlight. However, the open circuit voltage (V_{oc}) was slightly decreased after Ag-doping. This can be explained though consideration of the band edge diagram for the $Ag@TiO_2$. The results of photovoltaic properties for TiO_2, and $Ag_{0.10}@TiO_2$ nanoparticles were provided in Table 1.

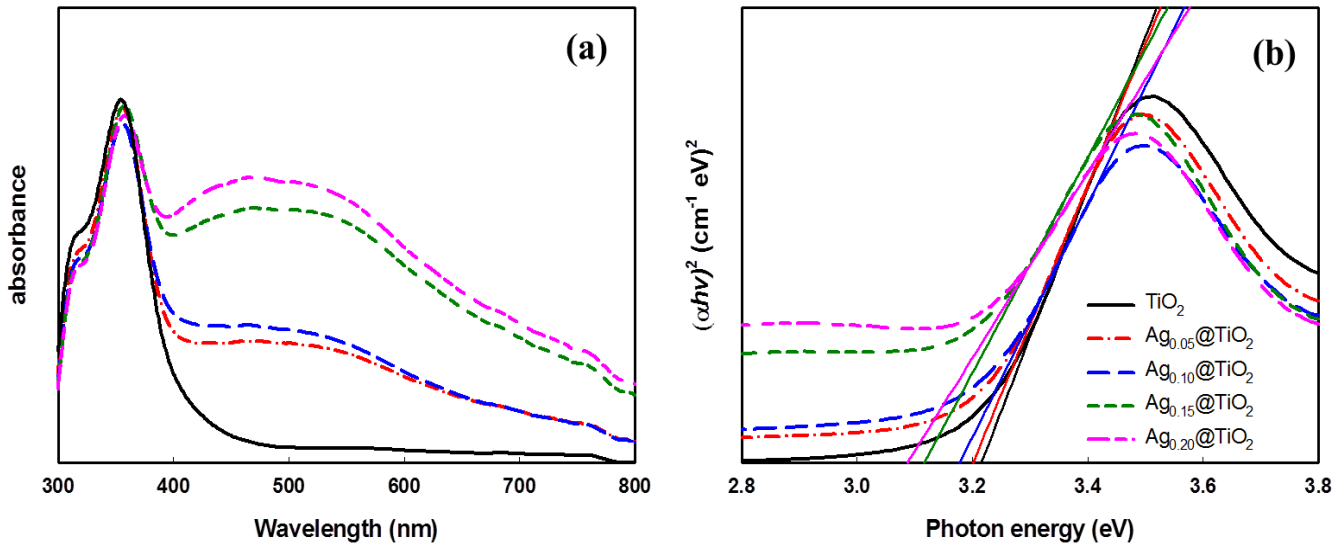

Figure 5. (a)The plot of $(ahv)^2$ *vs*. photon energy and (b) UV-vis diffuse reflectance spectra.

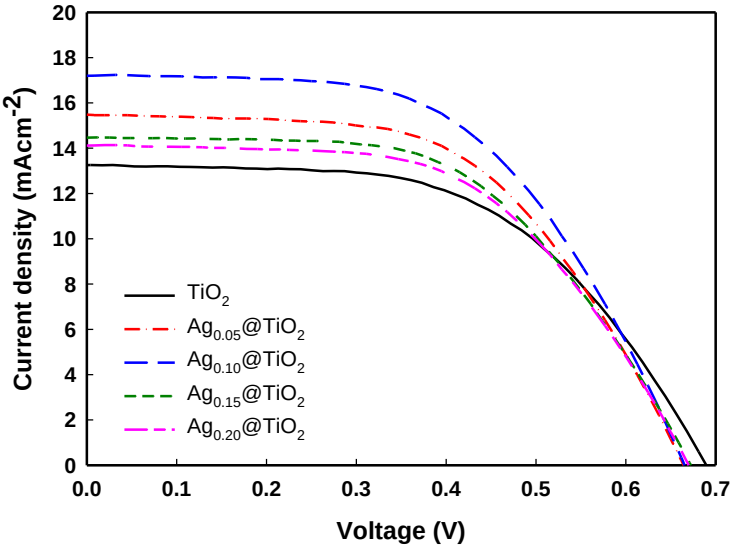

Figure 6. Photocurrent density-voltage curves of DSSCs made of TiO_2 and $Ag@TiO_2$ photoelectrode.

4 CONCLUSIONS

TiO_2 and $Ag@TiO_2$ were synthesized using hydrothermal reaction, and their surface area and visible light absorption were improved by Ag-doping. All as-prepared TiO_2 and $Ag@TiO_2$ particles showed the pure

anatase crystalline structure and, in comparison to non-doped TiO_2, the absorption edge of Ag-doped nanoparticles were broader and shifted to a higher wavelength. The higher surface and wide visible light absorption region allows us to determine that the $Ag_{0.10}@TiO_2$ nanoparticles-based DSSC gave the best η of 6.44%. Compared with TiO_2-NP photoelectrode based DSSCs (with a value for η of 5.05%), the $Ag_{0.10}@TiO_2$ exhibited an improvement of ~22% in η.

ACKNOWLEDGEMENTS

This work was funded by the MOTIE/KIAT. [R0004144]. Also, this research was supported by Basic Science Research Program through the National Research Foundation of Korea (NRF) funded by the Ministry of Education (2017R1D1A1B03031989).

REFERENCES

[1] A.R. Dalod, L. Henriksen, T. Grande, M.A. Einarsrud, Functionalized TiO_2 nanoparticles by single-step hydrothermal synthesis: the role of the silane coupling agents, *Beilstein Journal of Nanotechnology*, Vol. 8, pp. 304-312, 2017.

[2] A. Di Paola, M. Bellardita, L. Palmisano**,** Brookite, the Least Known TiO_2 Photocatalyst, *Catalysts*, Vol. 3, pp. 36-73, 2013.

[3] T. Yamamoto, Y. Wada, H. Yin, T. Sakata, H. Mori, S. Yanagida, Microwave-Driven Polyol Method for Preparation of TiO_2 Nanocrystallites, *Chemistry Letters,* Vol. 31, pp. 964-965, 2002.

[4] I. Jang, H.J. Leong, S.G. Oh, Effects of surfactants on the preparation of TiO_2 nanoparticles in microwave-assisted sol-gel process and their photocatalytic activity, *Korean Journal of Chemical Engineering*, Vol. 33, pp. 1647-1652, 2016.

[5] L. Natarajan, P. Singh, H.C. Bajaj, R.J. Tayade, Facile synthesis of $TiO_2/ZnFe_2O_4$ nanocomposite by sol-gel auto combustion method for superior visible light photocatalytic efficiency, *Korean Journal of Chemical Engineering*, Vol. 33, pp. 1788-1798, 2016.

[6] N. Liu, X. Chen, J. Zhang, J.W. Schwank, A review on TiO_2-based nanotubes synthesized via hydrothermal method: Formation mechanism, structure modification, and photocatalytic applications, *Catalysis Today*, Vol. 225, pp. 34-51, 2014.

[7] E.M. Jin, S.M. Jeong, H.-C. Kang, H.-B. Gu, Photovoltaic effect of metal-doped TiO_2 nanoparticles for dye-sensitized solar cells, *ECS Journal of Solid State Science and Technology*, Vol. 5, pp. Q109-Q114, 2016.

[8] J.F. Moulder, *Handbook of X-ray photoelectron spectroscopy: A Reference Book of Standard Spectra for Identification and Interpretation of XPS Data*, 1995.

[9] H.W. Chen, Y. Ku, Y.L. Kuo, Photodegradation of o-Cresol with Ag Deposited on TiO_2 under Visible and UV Light Irradiation, *Chemical Engineering & Technology,* Vol. 30, pp. 1242-1247, 2007.

[10] T.-D. Pham, B.-K. Lee, Feasibility of silver doped TiO_2/glass fiber photocatalyst under visible irradiation as an indoor air germicide, *International Journal of Environmental Research and Public Health,* Vol. 11, pp. 3271-3288, 2014.

[11] K.S. Sing, Reporting physisorption data for gas/solid systems with special reference to the determination of surface area and porosity (Recommendations 1984), *Pure and Applied Chemistry,* Vol. 57, pp. 603-619, 1985.

[12] B. Wang, L. Guo, M. He, T. He, Green synthesis of TiO_2 nanocrystals with improved photocatalytic activity by ionic-liquid assisted hydrothermal method, *Physical Chemistry Chemical Physics,* Vol. 15, pp. 9891-9898, 2013.

[13] E.Albiter, M.A. Valenzuela, S. Alfaro, G. Valverde-Aguilar, F.M. Martínez-Pallares, Photocatalytic deposition of Ag nanoparticles on TiO_2: Metal precursor effect on the structureal and photoactivity properties, *Journal of Saudi Chemical Society*, Vol. 19, pp. 563-573, 2015.

NUMERICAL COMPARISON BETWEEN FREE AND FORCED CONVECTION IN COOLING PV PANELS

T. Ibrahim[1], F. Hashem[1], M. Ramadan[1,2 *] and M. Khaled[1,3]

[1] School of Engineering, International University of Beirut, PO Box 146404 Beirut, Lebanon.
[2] Associate member at FCLAB, CNRS, Univ. Bourgogne Franche-Comte, Belfort cedex, France.
[3] Univ. Paris Diderot, Sorbonne Paris Cité, Interdisciplinary Energy Research Institute (PIERI), Paris, France

ABSTRACT

Solar panels produce electricity when exposed to sunrays. That said, a part of the solar irradiation is transformed into electricity another part is reflected by the PV's frontal surface while the remaining portion is transformed into heat and is stored in the PV which increases its temperature. In order to increase its output power and efficiency, PV's temperature should be decreased. This paper studies numerically the effect of free and forced convection combined with a rectangular finned plate in cooling PV panels. Three different techniques were compared, finned plate-forced convection, finned plate-free convection and forced convection without finned plate. Results show that the optimum number of fins in the rectangular finned plate was 24 fins. On the other hand, an average temperature decreas of 47.8 is obtained when finned plate is used along with a finned plate.

Keywords: Photovoltaic panels, air cooling, rectangular finned plate, numerical analysis.

1. INTRODUCTION

Because of the negative impacts of non-renewable energy resources [1-2] huge effort is being performed to find new techniques and methods to produce energy. Renewable energy resources [3-5] and heat recovery systems [6-12] form a substitute to fossil fuel energy [13-14] production. Renewable energy resources are characterized by their ability to produce a clean and sustainable energy [15-18]. The main renewable energy sources are solar energy [19-20], wind energy, biofuel [21-22] and geothermal energy [23-24]. Having said that, studies show that solar energy have reached a major growth rate especially through PV panels [25]. Yet the biggest obstacle that faces PV panels is the rise in their temperatures due to the constant absorption of solar irradiation and high ambient temperatures. Panel's power production may reach 15-20% depending on the type of the PV panel while the rest of the power are transformed into heat. That is why, huge effort is performed to test different cooling techniques for photovoltaic panels. Hachem et al [26] experimentally cooled the PV panel by using pure and combined PCM. It was shown that the use of combined PCM in cooling increased the efficiency of the PV by an average of 5.8% while the use of pure PCM increased the efficiency by an average of 3%. Furthermore, El Mays et al [27] experimentally increased the efficiency of the PV panel by 1.75% using heat sinks under free convection. Rosa-Clot et all [28] experimentally increased the efficiency of a PV panel by about 10% through submerging it by water. Chandrasekar et al. [29] increased the efficiency of PV by 10% by the use of cotton wick structure with the combination of water and nano-fluid. In the present study three cooling techniques were used to study the effect of free and forced convection in cooling PV panels along with the use of finned plate.

2. NUMERICAL APPROACH

2.1. Model Geometry

The simulated model is illustrated in figure 1. A rectangular finned plate made of aluminium) was attached to a PV panel of 35 cm width and 69 cm length.

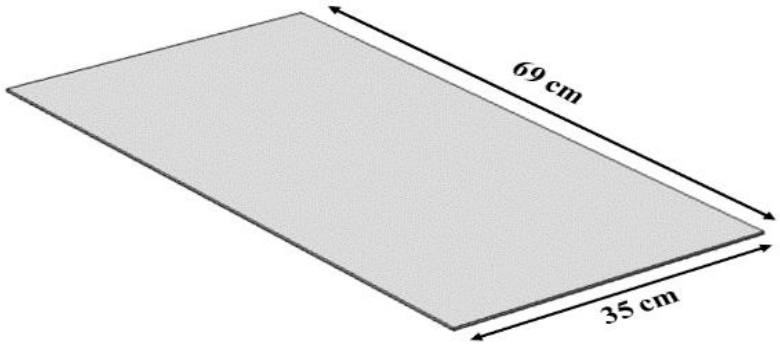

Figure 1. Simulated model and its dimensions

The PV panel is made of six different layers with different thermal conductivities and thicknesses. Table 1 illustrates the different layers of a the PV.

Table 1. PV's different layers (30)

Layer	Thickness (m)	Thermal Conductivity, (W/m.k)
Glass	0.003	1.8
ARC	100×10^{-9}	32
PV cell	225×10^{-6}	148
EVA	500×10^{-6}	0.35
Rear contact	10×10^{-6}	237
Tedlar	0.0001	0.2

The rectangular finned plate is made of aluminium with a thermal conductivity of 237 W/m.K, a density of 2770 Kg/m^3 and a heat capacity at constant pressure of 1250 J/kg.K. It is placed at the back surface of the PV panel in order to increase the surface area to ensure an increase of heat transfer by convection between the passing fluid and the PV panel. Finned plate dimensions were chosen according to standard conditions found in the market, however, simulation focus was on the number of fins and their effect on the temperature varaiation.

2.2. Assumptions

Numerical simulations are performed with the following assumptions:

- Steady state, incompressible and uniform flow.
- Steady state heat transfer.
- Perpendicular solar irradiation entering the PV.
- No internal heat generation.
- One dimensional conduction.
- Uniform cross-sectional area.
- Uniform convection across the surface area.
- Ideal contact between the finned plate and the PV panel.

3. RESULTS

In this study, three PV panels were examined to study the effect of forced and free convection in cooling in addition to a reference PV panel for comparison. The first PV panel was studied under free convection with the construction of a rectangular finned plate at its back surface. The back surface of the

second PV was exposed to a forced convection. While the rectangular finned plate of the third PV panel was exposed to a forced convection.

The tilt angle for the PV panels under study was 30 degrees with the horizontal, at an ambient temperature of T_{amb}=35 °C, and at a constant thermal irradiation flux of q=700 W/m^2.

3.1. Optimum fins number

In order to indicate the optimum number of fins for a rectangular finned plate, a study was made on different number of fins under free and forced convection. This study was illustrated in figure 2.

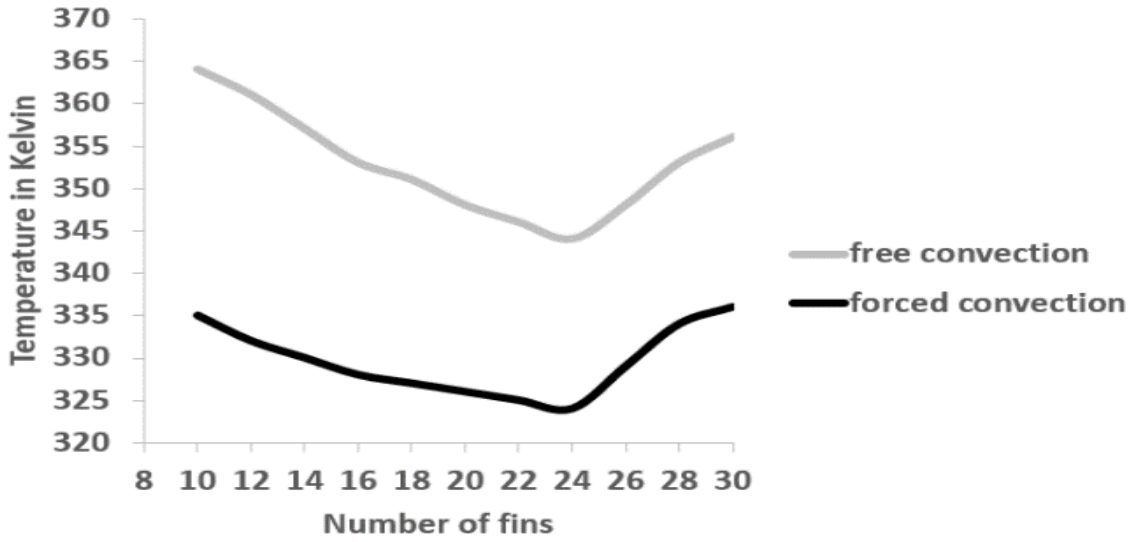

Figure 2. Temperature variation versus number of fins

Figure 2 shows the temperature variation with respect to the number of fins in a finned plate. As shown in the following figure, the temperature of a PV panel under free and forced convection decreases until the number of fins reaches 24 fins in a finned plate, then the temperature increases for further increase in fin number. This shows that the optimum number of fins that should be used is 24 fins.

3.2. Temperature variation

Contour plots of the three cooling methods are shown in figures 3-5.

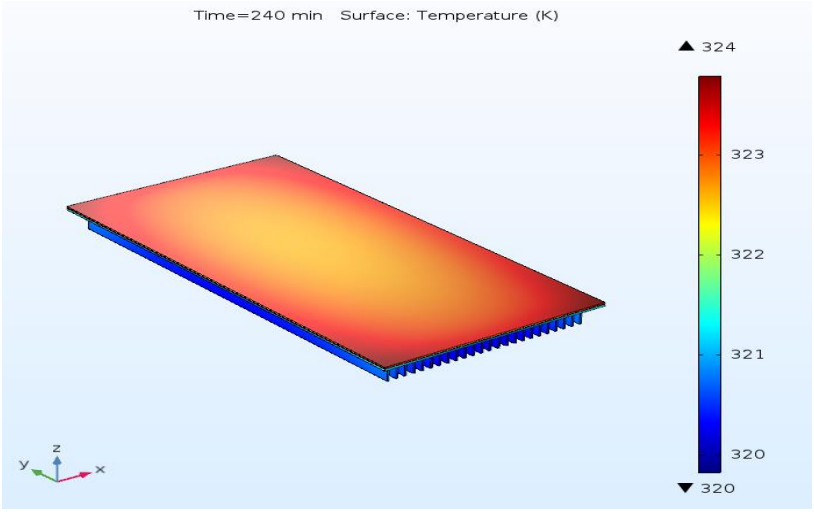

Figure 3. Contour plot of the forced convection with fins PV

In the case of forced convection-finned plate combination, the PV panel maintained a temperature range of 322-325 K (see figure 3) while the temperature of the finned plate increased from ambient temperature to reach approximately 320 K after 240 minutes of simulation.

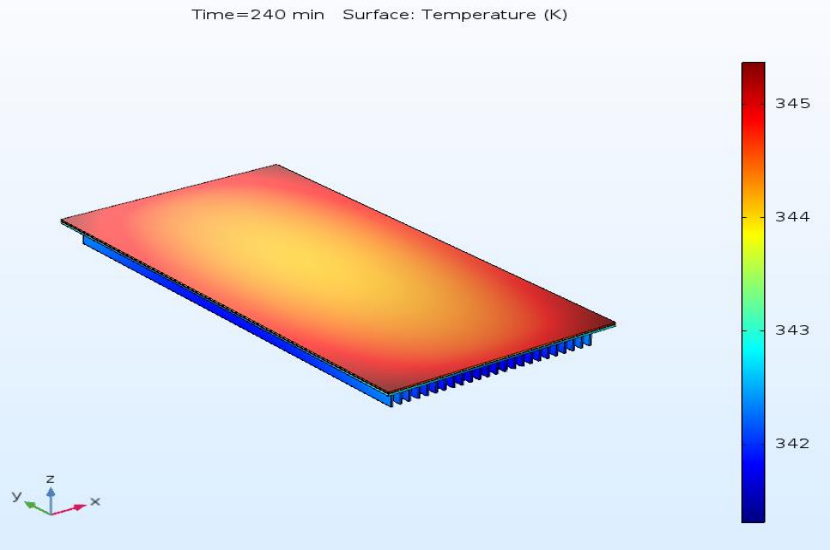

Figure 4. Contour plot of the free convection with fins PV

On the other hand, when free convection is used (figure 4), the PV panel maintained a temperature between 344 and 345 K while the temperature of the finned plate has increased from the ambient temperature to reach approximately 342 K after 240 minutes of simulation.

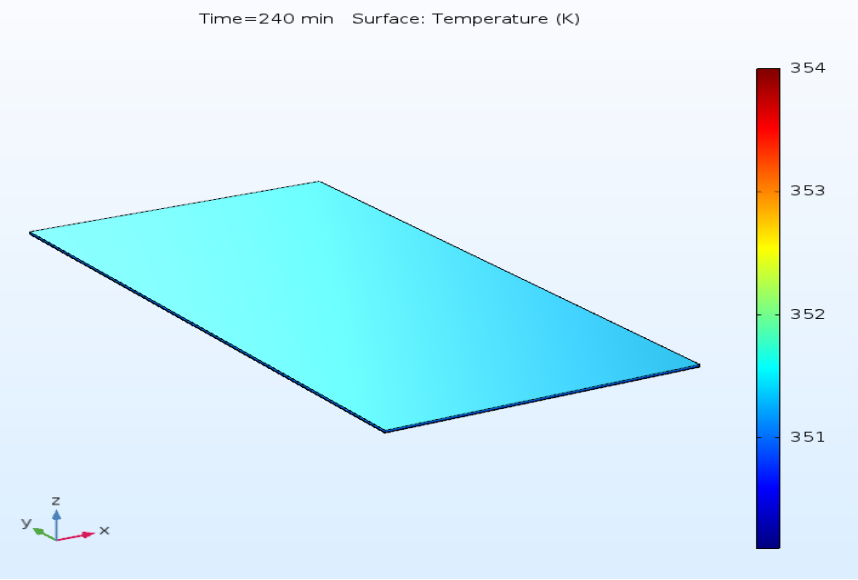

Figure 5. Contour plot of the forced convection PV

The PV panel under forced convection showed the highest temperature range between the three simulated PV panels with a range between 351-352 K after 240 minutes of simulation. Results of the three configurations are presented in figure 6.

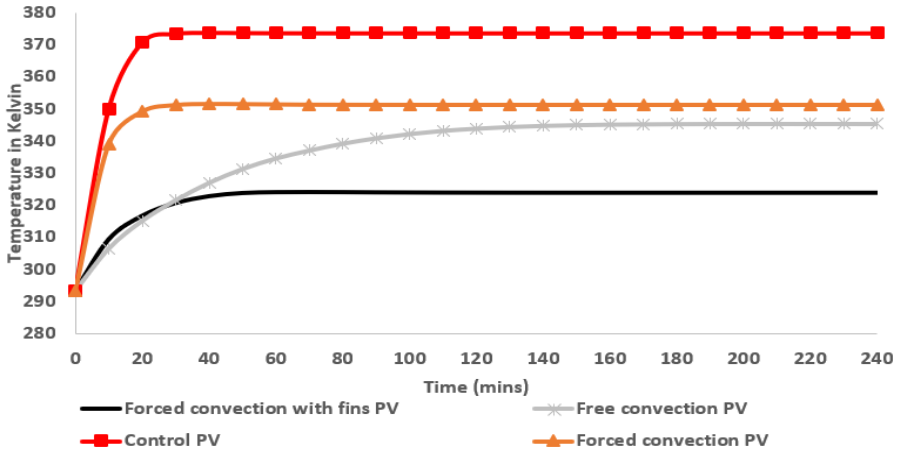

Figure 6. Temperature of the four PV panels versus time

Indeed, forced convection with fins maintained a lower temperature than free convection with finned plate and forced convection. The forced convection PV panel increased gradually from 293 K at the beginning of the simulation to reach a nearly constant value of 324 K after 70 minutes. While the temperature of the PV under free convection increased gradually from 293 K at the beginning of the simulation and reached a constant value of nearly 345 K after 150 minutes. Moreover, the temperature of the forced convection PV panel increased gradually from 293 K to reach a constant value of 351 K after 30 minutes. The reference PV panel reached a constant temperature of 373 K after 20 minutes of the simulation process.

4. CONCLUSION

To decease the temperature of PV, two main strategies could be used. Either increasing the surface of contact between the PV and the cooling fluid or increasing the velocity of the cooling fluid by using a forced convection. Finned plate increases the total area of the back surface of the PV panel, which increases the

surface exposed to convection and as a matter of fact the dissipated heat decreases. Three different cooling techniques were studied numerically. The first one consists in using a finned plate installed at the lower side of the PV. The second one consists in applying a forced convection to the PV. The third technique is a combination of the first two techniques where a finned plate is used along with a forced convection. Results show that the best cooling technique is provided by the combined forced convection–finned plate technique. Indeed, this technique offered an average temperature drop of 47.8 °C compared to the reference PV.

REFERENCES

1. T.K. Baul, D. Datta, A. Alam, A comparative study on household level energy consumption and related emissions from renewable (biomass) and non-renewable energy sources in Bangladesh,Energy Policy, Volume 114, 2018.
2. Samuel Adams, Edem Kwame Mensah Klobodu, Alfred Apio,Renewable and non-renewable energy, regime type and economic growth, Renewable Energy, Volume 125, 2018.
3. Tauseef Aized, Muhammad Shahid, Amanat Ali Bhatti, Muhammad Saleem, Gabrial Anandarajah, Energy security and renewable energy policy analysis of Pakistan, Renewable and Sustainable Energy Reviews, Volume 84, 2018.
4. Yu-Ching Tsai, Yea-Kuang Chan, Fu-Kuang Ko, Jing-Tang Yang, Integrated operation of renewable energy sources and water resources, Energy Conversion and Management, Volume 160, 2018.
5. Zafar Said, Abdulla A Alshehhi, Aamir Mehmood, Predictions of UAE's renewable energy mix in 2030, Renewable Energy, Volume 118, 2018.
6. Ramadan M, Lemenand T, Khaled M. Recovering heat from hot drain water—Experimental evaluation, parametric analysis and new calculation procedure. Energy and Buildings 2016; 128: 575-58.
7. Ramadan M, Gad El Rab M, Khaled M. Parametric analysis of air-water heat recovery concept applied to HVAC systems: Effect of mass flow rates. Case Studies in Thermal Engineering 2015; 6: 61-68.
8. Khaled M, Ramadan M, El Hage H. Parametric analysis of heat recovery from exhaust gases of generators. Energy Procedia 2015; 75: 3295-6.
9. Khaled M, Ramadan M, Chahine K, Assi A. Prototype implementation and experimental analysis of water heating using recovered waste heat of chimneys. Case Studies in Thermal Engineering 2015; 5: 127-7.
10. Jaber H, Khaled M, Lemenand T, Ramadan M. Short review on heat recovery from exhaust gas. AIP Conference Proceedings 2016; 1758: 10.1063/1.4959441
11. Herez A, Ramadan M, Abdulhay B, Khaled M. Short review on solar energy systems. AIP Conference Proceedings 2016; 1758: 1- 10.1063/1.4959437.
12. Ramadan M, Khaled M, El Hage H. Using Speed Bump for Power Generation –Experimental Study. Energy Procedia 2015; 75: 867-6.
13. Jianglong Li, Chuanwang Sun, Towards a low carbon economy by removing fossil fuel subsidies? China Economic Review, 2018.
14. Arjan Trinks, Bert Scholtens, Machiel Mulder, Lammertjan Dam, Fossil Fuel Divestment and Portfolio Performance, Ecological Economics, Volume 146, 2018.
15. Ahmed Shata Ahmed, Wind energy characteristics and wind park installation in Shark El-Ouinat, Egypt, Renewable and Sustainable Energy Reviews, Volume 82, Part 1, 2018.
16. Bikash Kumar Sahu, Wind energy developments and policies in China: A short review, Renewable and Sustainable Energy Reviews, Volume 81, Part 1, 2018.
17. Zhenyu Li, Afreen Siddiqi, Laura Diaz Anadon, Venkatesh Narayanamurti, Towards sustainability in water-energy nexus: Ocean energy for seawater desalination, Renewable and Sustainable Energy Reviews, Volume 82, Part 3, 2018.
18. I. Prieto-Prado, B. Del Río-Gamero, A. Gómez-Gotor, S.O. Pérez-Báez,Water and energy self-supply in isolated areas through renewable energies using hydrogen and water as a double storage system, Desalination, Volume 430, 2018.
19. Ehsanul Kabir, Pawan Kumar, Sandeep Kumar, Adedeji A. Adelodun, Ki-Hyun Kim,Solar energy: Potential and future prospects, Renewable and Sustainable Energy Reviews, Volume 82, Part 1, 2018.

20. Sunil Kumar Sansaniwal, Vashimant Sharma, Jyotirmay Mathur, Energy and exergy analyses of various typical solar energy applications: A comprehensive review, Renewable and Sustainable Energy Reviews, Volume 82, Part 1, 2018.
21. Floris Dalemans, Bart Muys, Anne Verwimp, Goedele Van den Broeck, Babita Bohra, Navin Sharma, Balakrishna Gowda, Eric Tollens, Miet Maertens,Redesigning oilseed tree biofuel systems in India, Energy Policy, Volume 115, 2018.
22. Sara A. Shields-Menard, Marta Amirsadeghi, W. Todd French, Raj Boopathy, A review on microbial lipids as a potential biofuel, Bioresource Technology, 2018.
23. Kh.R. Dione, H. Louahlia, M. Marion, J.L. Berçaits, Evaporation heat transfer and pressure drop for geothermal heat pumps working with refrigerants R134a and R407C, International Communications in Heat and Mass Transfer, Volume 93, 2018.
24. Hossein Yousefi, Halldór Ármannsson, Soheil Roumi, Sanaz Tabasi, Hamed Mansoori, Mehdi Hosseinzadeh, Feasibility study and economical evaluations of geothermal heat pumps in Iran, Geothermics, Volume 72, 2018.
25. Peter Atkin, Mohammed M. Farid. Improving the efficiency of photovoltaic cells using PCM infused graphite and aluminium fins. Solar Energy 2015; 217–228.
26. Farouk Hachem, Bakri Abdulhay, Mohamad Ramadan, Hicham El Hage, Mostafa Gad El Rab, Mahmoud Khaled, Improving the performance of photovoltaic cells using pure and combined phase change materials – Experiments and transient energy balance, In Renewable Energy, Volume 107, 2017, Pages 567-575, ISSN 0960-1481
27. Ahmad El Mays, Rami Ammar,Mahamad Hawa, Mahamad Abou Akroush, Farouk Hachem, Mahmoud Khalid and Mohamad Ramadan. International Conference on Technologies and Materials for Renewable Energy, Environment and Sustainability. Energy Procedia 2017.
28. M. Rosa-Clot, P. Rosa-Clot, G.M. Tina, P.F. Scandura, Submerged photovoltaic solar panel: SP2, Renewable Energy, Volume 35, Issue 8, 2010.
29. M. Chandrasekar, S. Suresh, T. Senthilkumar, M. Ganesh karthikeyan, Passive cooling of standalone flat PV module with cotton wick structures, Energy Conversion and Management, Volume 71, 2013.
30. [19] S. Armstrong, W.G. Hurley. A Thermal Model for Photovoltaic Panels under Varying Atmospheric Conditions. Power Electronics Research Centre, Electrical and Electronic Engineering, National University of Ireland, Galway, Ireland.

A Roadmap for c-Si Solar Panel End-of-Life Treatment

Sydney Edwards[1]

1. Department of Electrical and Computer Engineering; University of Maryland, College Park; email: sydneyedwards72@gmail.com

ABSTRACT

As the installation of PV systems grows to promote a path for sustainable energy generation, solar panel recycling and end-of-life procedures have become areas of increasing concern. Given the post-2000s boom in PV installation, and the 25-30 year lifetime of a PV plant, the new industry created by this anticipated 20,000 tons of solar panel waste will be worth upwards of 112 million dollars by 2025 [3]. Building upon research that explores the limitations of Solar Panel Recycling (SPR) methodologies and economics, this paper will identify new factors for assessing the potential of this upcoming industry. These factors will support that SPR technology will be increasingly favorable than past research suggests. To begin forming a roadmap that outlines all necessary considerations for SPR infrastructure, a system dynamics approach will be used. Using a framework based on SPR technological limitations and economics, a closed-loop model will be created to demonstrate industry potential.

***Keywords**:* Solar Panels, Recycling, Silicon, Photovoltaic, End-of-Life Treatment

1. Introduction

The rapid expansion of the solar photovoltaic (PV) industry has resulted in solar playing a crucial role for the future of power generation systems. PV technology is considered to be a sustainable power generation process as it generates electricity directly from the sun and avoids fossil fuel consumption and greenhouse gas emission. Over the last decade, the technology has proven the ability to become a major generator for the world, with robust and continuous growth even during times of financial and economic crisis. Significant research and industry spending has gone into creating more efficient solar panel manufacturing, installation, and operations/maintenance procedures. An aspect of the technology that is often left out, however, is the End-of-Life Treatment (EoLT) of these solar power plants. SPR by nature can be used to reduce PV waste, utilize recycled raw materials, and create a closed-loop life cycle specifically for the U.S. solar industry. Up until now, there has not been a way of modelling factors in the SPR industry to draw conclusions on what a roadmap to designing it would require. However, through the SPR infrastructure model discussed in this paper, we are now able to explore how the industry will be affected by the following aspects: Number of installations per year in a given area, Rate of decommissioning for an average panel, Cost efficiency of recycling vs. landfill disposal rates, Previously developed SPR infrastructure, and Importance of SPR Awareness. It should be noted that within the context of this paper, “decommissioned” will refer to solar panels that are now ready to be disposed of per the end of their useful lifetime.

To date, lack of awareness and concern about this issue is a result of very few panels having reached the point of decommissioning. Solar power plants have a technical lifetime of 25-30 years, with installation of these plants occurring exponentially since the 2000s [6]. Currently, most PV modules that have reached their decommissioning date have either been defects during production, damaged during

transportation and installation, or malfunctioned during their first year of operation. Based on the timeline established, and further research that will be provided below, the date when entire solar power plants will need to be decommissioned is quickly approaching. In order to insure that these panels are efficiently recycled and not disposed of in landfills, an infrastructure must be created in the U.S. to support a closed loop cycle for the solar industry that keeps the promise of sustainable power generation.

2. Economics of the SPR Industry

Based on past research, development of the SPR industry has already suggested strong economic validity. A study conducted by N.C. McDonald found the estimated total cost of collection and recycling of c-Si panels to be in the range of $0.08-0.11 / W. This is compared to the $23.96-23.99 per panel landfill disposal cost sited in the same study, meaning landfill disposal of a 300 watt solar panel would cost roughly $0.08 to decommission. At these comparable costs, it was determined at the time of the study, in 2010, that SPR was economically comparable with landfill rates. The average price to dispose of a ton of municipal solid waste in a U.S. landfill, however, has reported to be continuously rising. An IBISWorld Procurement Research study shows that from 2013 to 2016, the prices of landfill and solid waste collection services have increased at an estimated average rate of 1.7-2.9% per year. From 2016 to 2019, IBISWorld says it expects the prices of solid waste collection and disposal services to increase at a moderate annualized rate of 2.0%. The reasons behind this increase will not be explored in the scope of this paper, however, a parallel can easily be made to landfill disposal costs overall. These factors suggest SPR may be more economically viable compared to landfill disposal with the passage of time based on cost efficiency.

3. A Closed-Loop SPR Infrastructure Model

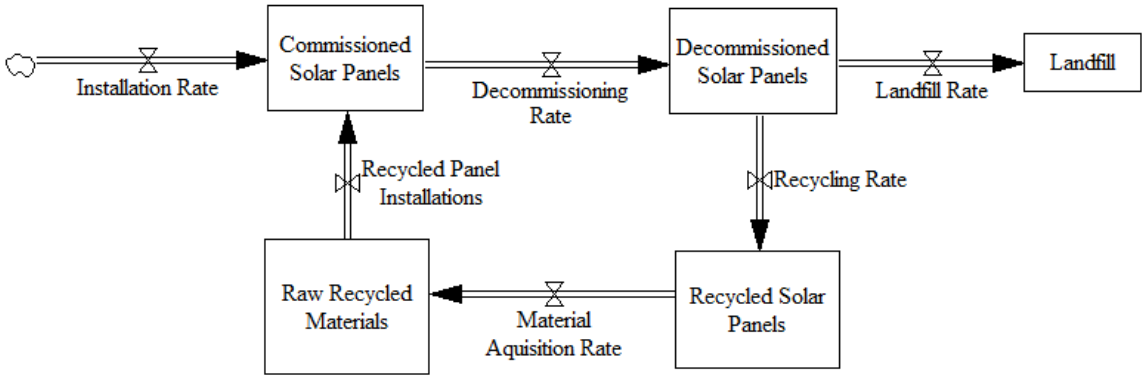

(1) SPR Infrastructure Feedback Loop

To map how the previously discussed aspects of the solar industry connect to development of a SPR infrastructure, the following model was developed using system dynamics software. The model is structured as follows. The input for the system is the number of installed c-Si solar panels in a region by year. This data was pulled from a report released by the U.S. Department of Energy in July 5th 2017. The report outlines, the kWhr/month of solar power generation in the U.S from 1998-2017. From this data, a function where the input is a time step, called “Time”, starts at zero and models the number of installed

panels per year in the U.S. Using the assumption that an average panel is 300 watts, with 5 average sun hours/day of exposure for an average of 30 days per month, one solar panel was determined to be roughly 45,000 kWhr/month. This made it simple to divide the function by this number and determine a function input for the number of panels per year installed from 2008 onwards, titled *Installation Rate* (2).

$$Panels/Year = -0.4303 \times Time^6 + 26.329 \times Time^5 - 568.35 \times Time^4 + 5597.2 \times Time^3 - 26034 \times Time^2 + 52239 \times Time - 21822 \quad (2)$$

The *Installation Rate* has an error due to the fact it is produced using a function versus specific data points per year. This error has been tracked in figure 3.

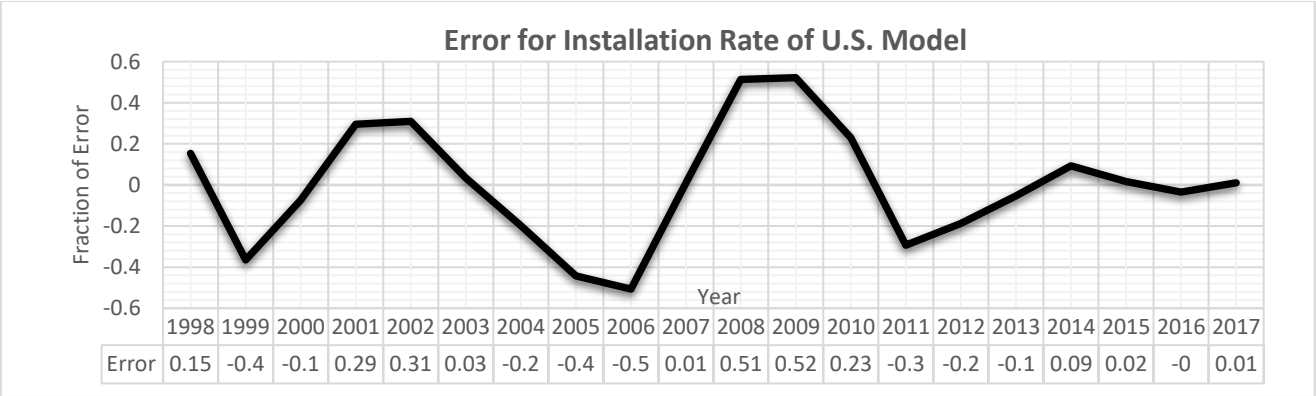

	1998	1999	2000	2001	2002	2003	2004	2005	2006	2007	2008	2009	2010	2011	2012	2013	2014	2015	2016	2017
Error	0.15	-0.4	-0.1	0.29	0.31	0.03	-0.2	-0.4	-0.5	0.01	0.51	0.52	0.23	-0.3	-0.2	-0.1	0.09	0.02	-0	0.01

(3) Error Calculation for Installation Rate function for the U.S. SPR Infrastructure Model

Although this error is relatively high initially, which we've been able to adjust using an adjustment ratio, a function is necessary instead of actual data values because it allows flexibility of the model for adjustments per region. After calibrating the model, the percentage of error decreases towards zero as time progresses, where it will effectively become more accurate for larger stretches of time modelled.

The next rate to consider is the *Decommissioned Rate*. This rate is based on how many panels need to be disposed of before the 25-30 year plant life concludes, and all the remaining panels are disposed of. It is based on the average number of panels that experience malfunctions or breakage based on what stage in their lifetime this has been shown to happen. Estimating this rate was based on a study done by Fthenakis, V.M. From it, the average delay of when commissioned solar panels need to be disposed of can be extrapolated. For the first year, 10% of the panels will need to be disposed of, whether this be to accidents, technological failures, etc. Then, from the 2^{nd}-10^{th} year 4.5% of panels will need disposal, and for the 10^{th}-29^{th} 0.05% respectively. At the 30^{th} year it was assumed that all panels will be decommissioned based on the U.S. standard. The function created for the *Decommissioning Rate* reflects all these delays. Lastly, the *Recycling Rate*, controlled by the *Recycling Ratio* shown in figure 5, was established by determining the three main factors that effect it, multiplied together:

1. Awareness: The knowledge of SPR in the solar industry, as well as a strong public understanding of the technical and economic aspects of it.
2. Infrastructure: The amount of facilities in a region with the ability to recycling solar panels in a sustainable closed-loop process.
3. Cost Efficiency: How competitive SPR costs are with landfill disposal costs.

Awareness in this model is reflected using a 0 or 1 function. This assumes that awareness of the ability to recycle one's solar panels is the first step to recycling them. Without this, no panels get recycled, hence an

overall *Recycling Rate* of 0. Per the definition of infrastructure above, infrastructure in the model is calculated based on the number of facilities in an area times the amount of panels that a SPR facility should be able recycle in a year. Each solar recycling facility should be able to handle a rated number of solar panels per year based on its capacity. Therefore this number of solar panels is multiplied by the number of facilities. Then, cost efficiency refers to the cost of solar recycling being competitive with landfill costs. This is also a 0 or 1 function. This will be assessed in terms of solar panel recycling legislation. Currently, there is only a 1-2 cent difference between the costs of solar panel recycling and landfill rates, as discussed more thoroughly above. Therefore, this function is controlled by the user of the model, and based on the arguments made previously, it was set to 1 for our model.

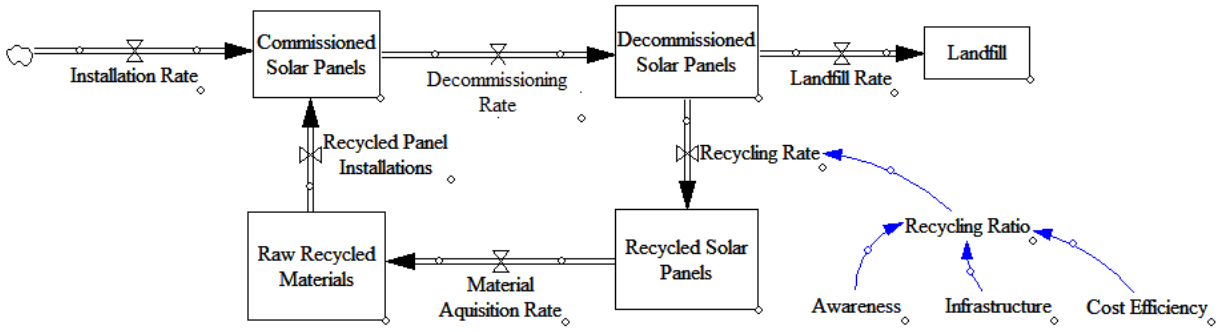

(5) SPR Infrastructure Feedback Loop with Recycling Ratio displayed

The subsequent stocks and flows in the model are determined by calculating how many raw materials can be recycled from a solar panel and how much raw material is needed to remake a new panel. It was determined that 1/0.015 of a ton of these raw materials can be used to make a new solar panel based on the average weight and recyclable material from a panel. This is also presuming reuse of 90% of the panel as demonstrated by PV Cycle [7]. These values are then used to complete a full lifecycle roadmap. The output of our model is shown in figures 6 and 7. For these graphs, time 0 represents the year 1998 and Time 30 represents the year 2038.

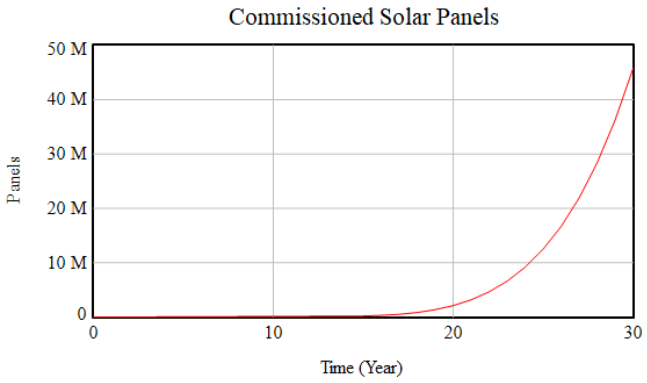

(6) Commissioned Solar Panels

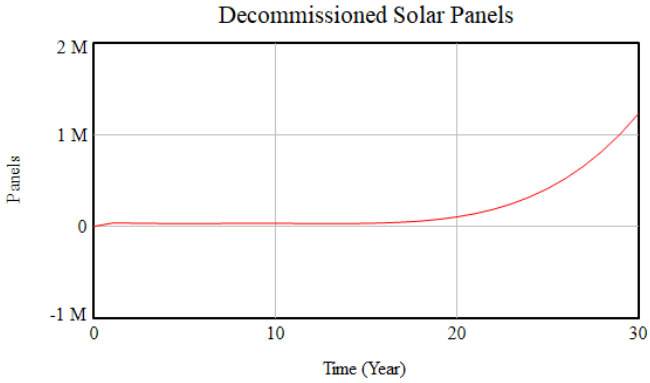

(7) Decommissioned Solar Panels

Based on this model, we now have a way of demonstrating the effects and potential of a full lifecycle SPR industry infrastructure that can be adjusted based on various considerations. This model is important in determining how fluctuations in SPR economics and legislation effect the capacity of the technology.

4. Conclusion

By combining past research with the new considerations mentioned in this paper, we are now able to accurately predict the number of decommissioned panels that will be available by a certain date within any given region. This information will help to provide a roadmap for the SPR infrastructure needed in the U.S. This is essential as end-of-life considerations for solar power plants will become a significant concern in the next decade as more plants reach their decommissioning dates. The capacity of this new industry can now be predicted using a systems dynamics approach. The model itself uses discussed inputs such as installation rate of an area, awareness, infrastructure, and cost efficiency, along with background research to create a versatile means for prediction. This research and data will help the industry prepare for the oncoming boom of decommissioned solar panels in the next decade.

ACKNOWLEDGEMENTS

I would like to thank the Snider Program through the Robert H. Smith School of Business at University of Maryland for initial funding of the project and continued support of my research. I would also like to thank Dr. Qingbin Cui for mentoring and guiding the project into life.

REFERENCES

[1] Fthenakis, V.M., (2000). End-of-life management and recycling of PV modules. Environmental & Waste Technology Group. *Department of Advanced Technology, Brookhaven National Laboratory.*

[2] N.C. McDonald and J. M. Pearce, (2010). Producer responsibility and recycling solar photovoltaic modules. *Energy Polic*y 38, pp. 7041-7047.

[3] GM Insights, (2016). Solar Panel Recycling Management Market Size By Process (Thermal, Mechanical, Laser), By Product (Monocrystalline, Polycrystalline, Thin Films PV Cells), By Shelf Life (Early Loss, Normal Loss), Industry Analysis Report, Regional Outlook (U.S.), Application Potential, Price Trends, Competitive Market Share & Forecast, 2016 – 2024.

[4] Smith, Deonta, (2016). Avoiding the Red when Going Green. *IBISWorld.*

[5] U.S. Department of Energy, (2018). Electric Power Monthly with Data for January 2018. Available at https://www.eia.gov/electricity/monthly/current_month/epm.pdf

[6] SEIA, (2018). Solar Industry Research Data. Accessed 1 March, 2018. Available at: https://www.seia.org/solar-industry-research-data

[7] PV Cycle, (2009). Making Photovoltaics “Double Green”, Accessed 6 December, 2009. Available at http://www.pvcycle.org/index.php?id=4

PERFORMANCE EVALUATION OF COILED TUBE RECEIVER CAVITY FOR A CONCENTRATING COLLECTOR

Kuldeep Awasthi[1] and Mohd. Kaleem Khan[2]

1. Department of Mechanical Engineering, Indian Institute of Technology Patna, Patna, India; email: kuldeep.pme16@iitp.ac.in
2. Department of Mechanical Engineering, Indian Institute of Technology Patna, Patna, India; email: mkkhan@iitp.ac.in

ABSTRACT

In the present work, a special coiling arrangement of helical-spiral coiled copper tube has been employed as the conical receiver cavity for a point focus solar concentrator. A computational model based on finite volume method for the laminar flow of water through the proposed receiver cavity with constant heat flux has been developed using commercial software ANSYS-FLUENT. Its performance has been compared with helically-coiled copper tube (i.e. cylindrical cavity) of the same length. The model has been validated with Manlapaz and Churchill's [10] correlation for helically coiled tube. The conical cavity has been tested with both upright and inverted arrangements. In upright arrangement, the coil is exposed to constant heat flux from inside of the conical cavity whereas it is subjected to constant heat flux from outside of the cavity in case of inverted arrangement. It has been found that it is beneficial to use conical receiver cavity instead of cylindrical cavity as far as heat transfer characteristics is concerned. In fact, it is always preferable to use conical cavity in an inverted position as it gives nearly 14% average increase in Nu compared for entire range of Re (250-1500) compared to the conical cavity in upright position.

Keywords: solar collector, receiver cavity, helical-spiral, Nusselt number

1 INTRODUCTION

A solar concentrating collector intensifies the solar insolation at its focal area where a receiver cavity is placed. The receiver cavity is designed to extract heat from the solar radiations as much as possible. Efficient receiver cavity design has always been a challenging task in the design of water heating system based on solar concentrating collector. One of the ways to remove heat is to employ coiled copper tube as receiver cavity [1-3]. Coiling makes the design compact enabling high heat removal rate from the small focal area. There can be different coiling arrangements such as spiral, helical and helical-spiral. The spiral and helical coiling of copper tubes are common designs whereas helical-spiral is a recent development [4-9]. For a given aperture area, both spiral and helical coiling arrangements have limitations. In case of spiral coiling, only a fraction of focal area will be under the concentrated beam or coil has to be placed in between focus and the concentrator under reduced intensity whereas in helical coiling, there will be uneven interception of concentrating solar beam along its height. The above comparison between spiral and helical coiling is valid for same diameter and length of copper tube used in coiling. Kurnia et al. [5] have numerically investigated the heat transfer and entropy generation of laminar flow in helical tubes with circular, ellipse and square cross-sections. Effect of different parameters like geometry, wall temperature, Reynolds number and heating/cooling mode was evaluated at constant wall temperature.

To utilize the merits of both spiral and helical arrangements, it is proposed to employ helical-spiral coiled tube as receiver cavity. This arrangement has the advantage of intercepting the concentrating beam uniformly throughout its height. It is worth mentioning here that Xie et al. [6] have already carried out research on conical cavity (i.e. helical-spiral coiling arrangement). In fact, they have investigated thermal performance on conical, helical and spherical coiling arrangements of copper pipes as receiver and Fresnel lens as concentrator. Numerical and experimental investigations have been conducted to obtain temperature distributions over receiver area. Conical cavity receiver was found to give the optimum performance compared to other two receiver cavities. It should be noted that Xie et al. [6] have used an upright arrangement for conical cavity. None of the researchers have tested the conical cavity in an inverted position, i.e. the outer surface of the cavity is exposed to the concentrating beam. The inverted conical cavity has the advantage of utilizing outer surface area which is obviously larger than its inner surface area. It is

proposed to numerically investigate the laminar flow of water through the inverted helical-spiral (conical) cavity subjected to constant heat flux at outer surface of conical cavity using ANSYS FLUENT version 17.2. The inner surface of the conical cavity is insulated to minimize the heat loss due to convection.

2 GOVERNING EQUATIONS AND SOLUTION METHODOLOGY

In this study, different coil arrangements are simulated as shown in Figure 1. The copper tube, used in each coiling arrangement, has internal diameter 6.35 mm and length 1586 mm. The aperture diameter (maximum coil diameter) of cavities is 85 mm. Vertex angle of cross-section through symmetric axis of conical cavity is 30°. Water flows from bottom to top in all the cases.

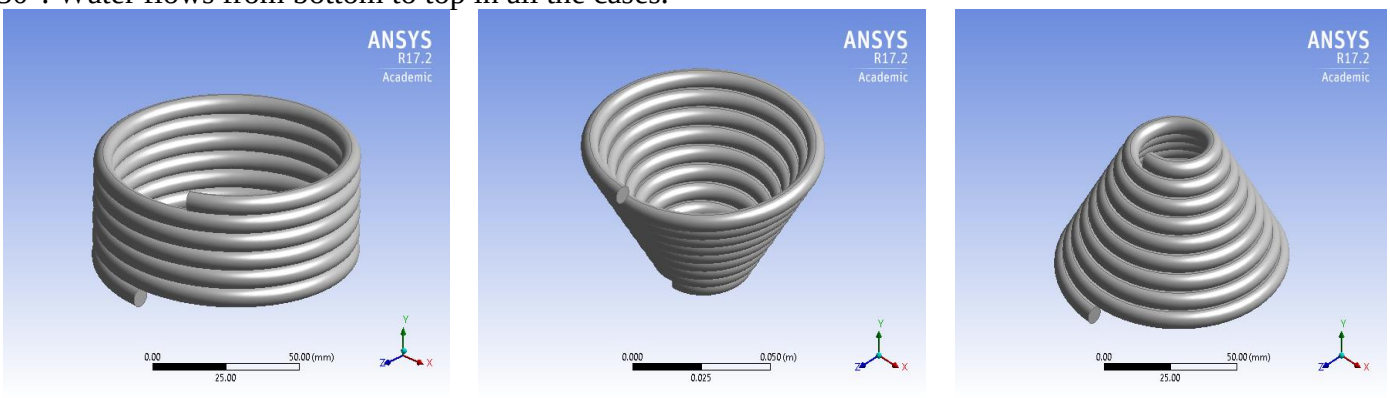

(a) (b) (c)

Figure 1. Cavity receivers (a) Cylindrical (b) Upright conical (c) Inverted conical

The simulation of inverted conical cavity with inner surface insulated is the main objective for the present research. The results of simulation of upright cavity with outer surface insulated are used for the sake of comparison. It should be noted that cylindrical cavity has been simulated for the purpose validation with well-known Manlapaz and Churchill's correlation [10]. Outer and inner surfaces are subjected to constant heat flux conditions for cylindrical and upright conical cavities.

Following are the assumptions in the present numerical study:

- Steady and fully developed laminar flow
- Pipe wall is thin, so conduction losses can be neglected.
- Thermo-physical properties of water are assumed as constant.

The solutions are obtained by solving the governing equations (Continuity, Momentum, Energy equation) for steady flow of water through cavity.

Continuity equation:

$$\nabla \cdot V = 0 \tag{1}$$

Momentum equation:

$$\rho \frac{DV}{Dt} = -\nabla P + \mu \nabla^2 V \tag{2}$$

Energy equation:

$$\rho C_p \frac{DT}{Dt} = k \nabla^2 T \tag{3}$$

The governing equations have been solved using the following boundary conditions for present model as shown in Table 1.

Table 1: Operating parameters

Operating parameters	Boundary condition	Value
Inlet	Mass flow rate inlet	4.48 – 26.89 kg/hr
Outlet	Pressure outlet (gauge)	0
Pipe wall	Constant heat flux	5000 W/m^2
Other walls	Insulated	-

The inlet temperature of water entering the cavity is 300 K and Reynolds number is varied in the range 250-1500. No slip condition with constant heat flux has been applied to pipe wall. The constant atmospheric pressure outlet condition is applied.

Nusselt number is considered for evaluating heat transfer characteristics. The Nusselt number along the tube is calculated as:

$$Nu = \frac{hd}{k} \tag{4}$$

The heat transfer coefficient h has been calculated using temperature data of numerical model.

$$h = \frac{q_w}{(T_w - T_m)} \tag{5}$$

where q_w is wall heat flux, d is tube diameter.

T_w is average wall temperature.

T_m is mean temperature and is calculated as

$$T_m = \frac{\int_{A_c} uTdA_c}{\int_{A_c} udA_c} \tag{6}$$

where A_c is cross-sectional area of copper tube.

Reynolds number is calculated as:

$$\mathrm{Re} = \frac{\rho U_m d}{\mu} \tag{7}$$

3 NUMERICAL METHODOLOGY

A computational code based on finite volume method has been developed using ANSYS FLUENT 17.2 CFD code. The governing equations are solved using steady pressure based solver. Second order upwind scheme is used to discretize the momentum and energy equations. A double precision SIMPLE (Semi Implicit Pressure Linked Equation) algorithm has been used for coupling of pressure with velocity. The numerical computation is contemplated converged when sum of residual mass is less than 10^{-5} and sum of residual energy is less than 10^{-7}. A non-uniform grid with structured quadrilateral elements has been employed. A grid independency test has been performed by increasing number of elements from 960336 to 4512105. The mesh independency criterion is: the deviation in Nu should be less than 1%. Figure 2 illustrates the results (plots of Nu versus Re) of mesh independency tests of helical coiled tube. Based on the results, it is revealed that mesh with elements of 2834164 was adequate to solve the present numerical model.

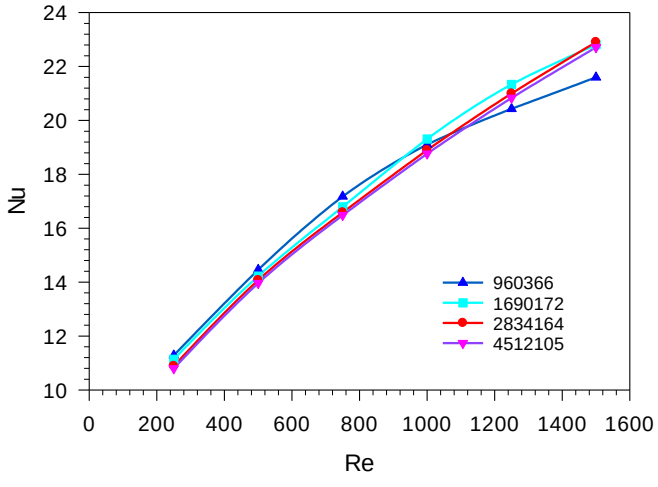

Figure 2. Grid independency results for cylindrical cavity

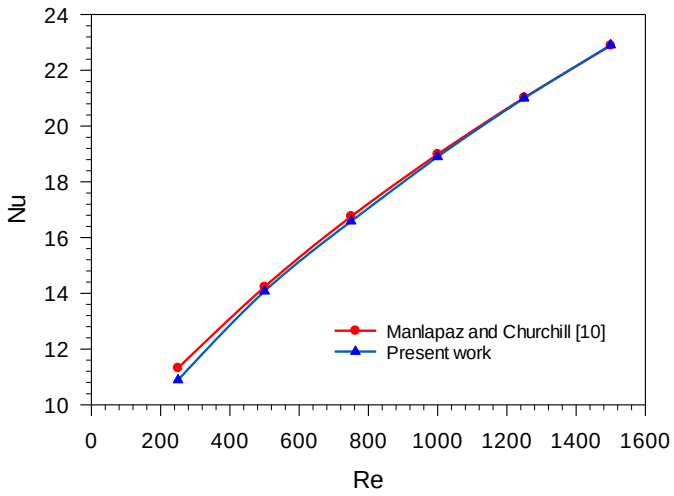

Figure 3. Validation with Manlapaz and Churchill's correlation [10]

4 RESULTS AND DISCUSSION

The present CFD model has been validated for cylindrical cavity (helical coil) by comparing computed Nusselt number with Nusselt number obtained from Manlapaz and Churchill's [10] correlation for Reynolds number ranging from 250 to 1500. Manlapaz and Churchill's [10] correlation is given by:

$$Nu = \left[\left(4.364 + \frac{4.636}{\left(1 + \frac{1342}{De^2 \,\mathrm{Pr}}\right)^2} \right)^3 + 1.816 \left(\frac{De}{1 + \frac{1.5}{\mathrm{Pr}}} \right)^{\frac{3}{2}} \right]^{\frac{1}{3}} \tag{8}$$

The validation results are shown as the variation of Nusselt number with Reynolds number in Fig. 3. As mentioned earlier, the helical coil is subjected to constant heat flux from both inside and outside. The computed values of Nusselt number are in excellent agreement with the predictions of Manlapaz and Churchill's [10] Nusselt number correlation with maximum deviation of 3.82% at lowest Re = 250.

In Figure 4, a comparison of the results for cylindrical and conical cavities, subjected to constant heat flux condition at both inner and outer surfaces, has been presented. The Nusselt number is significantly higher for conical cavity for the entire range of Reynolds number. The average percentage increase in Nusselt number is found to be 10.2%.

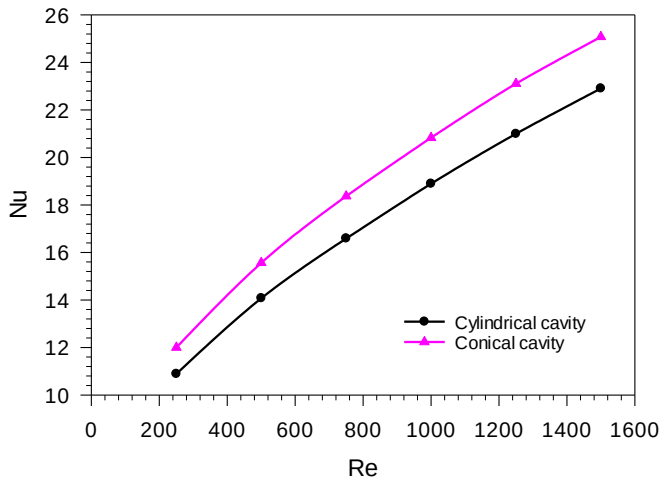

Figure 4. Nu versus Re for cylindrical and conical cavities constant heat flux condition throughout tube periphery

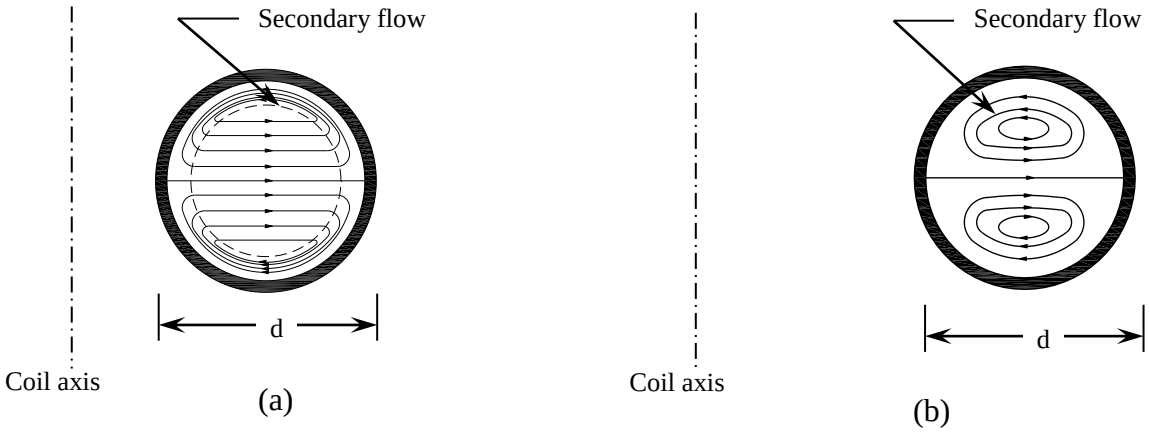

Figure 5. Secondary flow (a) large curvature (b) small curvature

This increase in Nusselt number is due to different coiling patterns in helical (cylindrical) and helical-spiral (conical). In helical-spiral (conical) configuration, the curvature keeps on increasing from base to vertex whereas curvature is constant throughout for helical (cylindrical) configuration. It is known that coiling causes the formation of two oppositely rotating vortices (known as secondary flows) inside tube cross-section. The strength of secondary flow increases with the increase in tube curvature. The effect of curvature on secondary flows has been demonstrated in Figure 5. In fact, a straight tube can be perceived as a coil of infinite radius of curvature. As a matter fact, there is no secondary flow in a straight tube. One can conclude that stronger the secondary flow higher will be the rate of convective heat transfer. Thus, conical cavity has higher Nusselt number compared to the cylindrical cavity.

Figure 6 shows the comparison of Nusselt number for inverted and upright helical-spiral coils. The inner surface of inverted helical-spiral coil and outer surface of upright helical-spiral coil are insultated whereas outer surface of inverted helical-spiral coil and inner surface of upright helical-spiral coil are subjected constant heat flux. These conditions simulate an actual receiver cavity of a solar concentrating collector. It can be seen from the figure that invertted cavity gives a better heat transfer performance for the entire range of Reynolds number. In fact, the increase in Nu is higher for lower range of Re. The maximum increase in Nu is 24.7% at Re = 500 and an average increase in Nu is 14.2% for the entire range of Re. The reason for increase in heat transfer rate is that the inverted helical-spiral coil has the advantage of utilizing heat transfer from outer surface area which is obviously greater than its inner surface area. Total heat input to inverted helical-spiral coil is much larger than the upright helical-spiral coil. It has also been reported that at low Re, strength of vortices is low. However, flow velocities are higher at the outer periphery of the coil compared to that at the inner periphery of the coil. Thus, at low Re the inverted helical-spiral coil will have higher heat transfer coefficient at the outer periphery, as heat flux as well as high velocity stream are on same side, i.e. at the outer periphery. At high Re, strength of vortices increases in either coil leading to increased mixing and reduced difference in Nusselt numbers in two cavities.

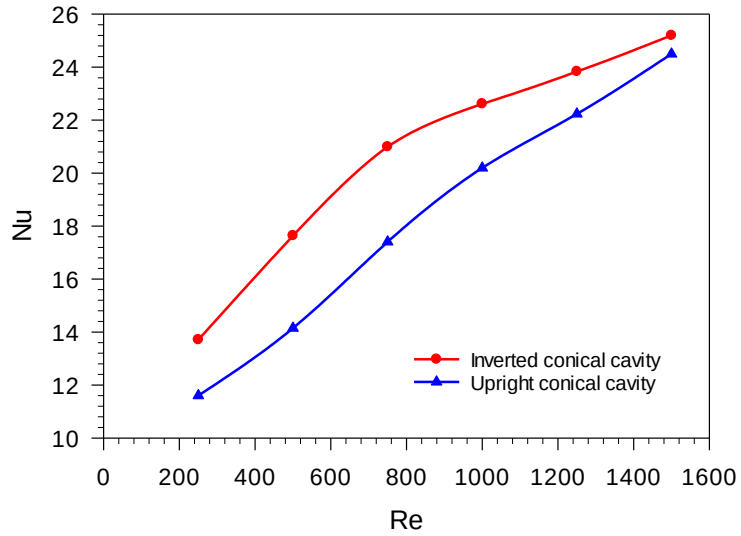

Figure 6. Nu versus Re for inverted and upright conical cavities

5 CONCLUDING REMARKS

In the present work, various configuration of coiled tubes used as receiver cavity in a solar concentrator have been simulated using ANSYS-FLUENT. Following conclusions can be drawn:

- The results of simulation are in excellent agreement with Manlapaz and Churchill's correlation [10].
- Conical cavity has a significantly higher heat transfer performance than cylindrical cavity with 10.2% average increase in Nusselt number.

- Inverted conical cavity has superior heat transfer characteristics than upright conical cavity with 14.2% average increase in Nusselt number.

NOMENCLATURE

d (m)	coil tube diameter	V (m s^{-1})	velocity vector of fluid element
A_c(m^2)	cross-sectional area of tube	ρ (kg m^{-3})	density
T_w(K)	pipe wall temperature	μ (Pa s)	dynamic viscosity
T_m(K)	mean temperature	t (s)	time
Nu	Nusselt number	P (Pa)	fluid pressure
Re	Reynolds number	c_p (J kg^{-1} K^{-1})	specific heat capacity
Pr	Prandtl number	k (W m^{-1} K^{-1})	thermal conductivity
De	Dean number	T(K)	temperature
h (W m^{-2} K^{-1})	heat transfer coefficient	U_a (m s^{-1})	axial velocity
q_w (W m^{-2})	heat flux	U_m (m s^{-1})	mean velocity

REFERENCES

[1] J. A. Duffie and W. A. Beckman, *Solar engineering of thermal processes,* John Wiley & Sons, 2013.

[2] S. A. Kalogirou, Solar thermal collectors and applications, *Progress in energy and combustion science*, Vol. 30(3), pp.231-295, 2004.

[3] S. Suman, M. K. Khan and M. Pathak, Performance enhancement of solar collectors—A review, *Renewable and Sustainable Energy Reviews*, Vol. 49, pp.192-210, 2015.

[4] M. Prakash, S. B. Kedare, and J. K. Nayak, Investigations on heat losses from a solar cavity receiver, *Solar Energy*, Vol. *83*(2), pp.157-170, 2009.

[5] J. C. Kurnia, A. P. Sasmito, T. Shamim and A. S. Mujumdar, Numerical investigation of heat transfer and entropy generation of laminar flow in helical tubes with various cross sections. *Applied Thermal Engineering*, Vol. 102, pp.849-860, 2016.

[6] W. T. Xie, Y. J. Dai and R. Z. Wang, Numerical and experimental analysis of a point focus solar collector using high concentration imaging PMMA Fresnel lens, *Energy Conversion and Management*, Vol. 52(6), pp.2417-2426, 2011.

[7] A. Tohidi, S.M. Hosseinalipour, M. Shokrpour, A.S. Majumdar, Heat transfer enhancement utilizing chaotic advection in coiled tube heat exchangers, *Applied Thermal Engineering*, Vol. 76, pp.185-195, 2015.

[8] J.S. Jayakumar, S.M. Mahajani, J.C. Mandal, K.N. Iyer, P.K. Vijayan. CFD analysis of single phase flows inside helically coiled tubes, *Computers and Chemical Engineering*, Vol. 34, pp.430-446, 2010.

[9] J.S. Jayakumar, S.M. Mahajani, J.C. Mandal, K.N. Iyer, P.K. Vijayan, Rohidas Bhoi, Experimental and CFD estimation of heat transfer in helically coiled heat exchangers, *Chemical Engineering Research and Design*, Vol. 86, pp.221-232, 2008.

[10] R. L. Manlapaz and S. W. Churchill, Fully developed laminar flow in a helically coiled tube of finite pitch, *Chemical Engineering Communications*, Vol. 7(1-3), pp.57-78, 1980.

A SIMPLIFIED FRAME DESIGN FOR SCHEFFLER REFLECTOR

Desireddy Shashidhar Reddy[1] and Mohd. Kaleem Khan[2]

1. Department of Mechanical Engineering, Indian Institute of Technology Patna, Patna-801106, India; email: desireddy.pme16@iitp.ac.in
2. Department of Mechanical Engineering, Indian Institute of Technology Patna, Patna-801106, India; email: mkkhan@iitp.ac.in

ABSTRACT

This paper presents a new and simple design methodology for the error-free Scheffler reflector profile. The input parameters required for design methodology are aperture area and focal length whereas the output design parameters are section plane angle, and dimensions of crossbars. It has been found that the choice of inclined sectional plane angle can be made either in the range 42° to 43.86° or 43.86° to 44.9°, which will depend upon the application for which the Scheffler reflector is to be designed. Low range helps in higher concentration and lower cost whereas its higher range will decrease the concentration and increase cost with an advantage of focusing light at a relatively far away point.

The existing crossbar design is complicated and monotonous. To ease the overall design process, a chart is presented which can be used to design the Scheffler reflector of any size. It is proposed that existing circular crossbars can be replaced by the new and exact circular crossbars, which are the parts of circle having centres along the axis of paraboloid and lie in the planes perpendicular to it. The proposed new design involves generating the circular crossbars by intercepting paraboloid with planes normal to its axis, hence eliminating the need for approximation of the crossbars suggested by researchers earlier. The proposed crossbar design is simple and has the potential for mass production.

Keywords: Scheffler reflector, crossbars, design charts, parabolic

1 INTRODUCTION

Climate change is a global concern and has always been a trending hot topic. The improved standard of living increased the consumption of fossil fuels. This came at a heavy price in the form of environmental pollution. In such a crisis, solar energy, which is free and renewable seems to be an attractive alternate to fossil fuels [1-2].

Scheffler reflector is one among many concentrated solar power (CSP) technologies which is becoming popular among solar kitchen community due to its unique features such as non-moving focal area, flexible surface curvature and shadow-less concentration [3]. It is essentially a lateral part of the paraboloid formed by its interception with an inclined plane. Though it was invented by Scheffler [4] with main intention of providing a comfortable solar kitchen, researchers have successfully demonstrated that it can be used for many other wide varieties of applications such as baking ovens, cooking food, sterilizing, distillation, processing of plants for oil, cremation of dead people, solar refrigeration etc. [5-10]. Scheffler and Fresnel reflectors are the only CSP technologies than can provide non-moving focal area. Scheffler reflector has an advantage over Fresnel reflector as it provides the non-moving focus at ground level which helps in easy maintenance. Also, the tracking mechanism of Scheffler reflector is much simpler than that of Fresnel reflector as it requires only a single motor.

The manufacturing of Scheffler reflector is a complex and monotonous process, which involves lot of approximations introducing small error in its profile. Its fabrication requires attaching mirrors/reflecting film to the supporting frame, which consists of an elliptical rim, a central parabolic support and a number of elliptical crossbars. The existing design approximates elliptical crossbars by circular crossbars as generating elliptical crossbars is a costly and time-consuming affair. This approximation introduces a small error in reflector profile. Till date, only Munir et al. [11] and Reddy et al. [12] presented design principles and design charts for the construction of Scheffler reflector. The paper provides a novel design for crossbars that can generate error free Scheffler reflector profile. The new design replaces approximated circular crossbars by

exact circular crossbars in a plane perpendicular to the axis paraboloid. The design is simple and has the potential for mass production.

2 REFLECTOR DESIGN

Scheffler reflector is essentially a lateral portion of paraboloid formed by intersection of an inclined plane. This inclined sectional plane and paraboloid can be represented by an inclined line (E1E2) and a parabola respectively in a 2D plane as shown in Figure 1. The most important step in the designing of Scheffler reflector is the choice of sectional plane, which is characterised by its slope α and x-intercept x_i.

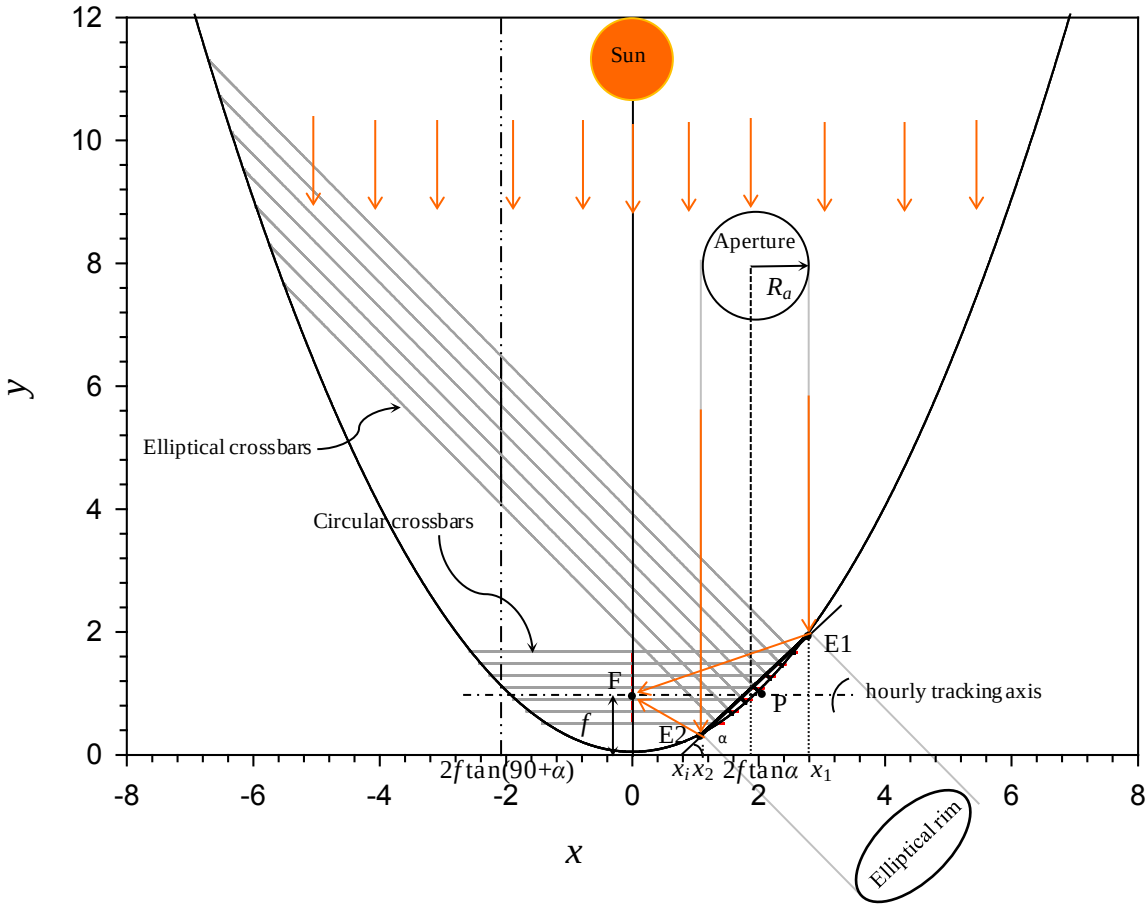

Figure 1 Details of Scheffler reflector

The contour generated as a result of intersection of an inclined section plane and a paraboloid is an ellipse, which represents the rim of the Scheffler reflector. The details are shown in Figure 1.

In 2D, the equation of paraboloid with its vertex at origin is given by

$$x^2 = 4fy \tag{1}$$

The equation of inclined planeE1E2 in 2D with slope α and x-intercept x_i is given by

$$y = \tan\alpha(x - x_i) \tag{2}$$

If E1 (x_1, y_1) and E2 (x_2, y_2) are the points of intersection of line E1E2 and parabola, the radius of aperture of Scheffler reflector, is given by

$$R_a = \frac{x_1 - x_2}{2} \tag{3}$$

From Equations (1), (2) and (3), x_1 and x_2 can be represented by

$$x_1 = 2f\tan\alpha + R_a \tag{4}$$

$$x_2 = 2f\tan\alpha - R_a \tag{5}$$

For minimizing the torque required for rotating the Scheffler reflector for hourly tracking of the sun, the point P (2*f*, *f*) should lie at the center of the parabolic curve (Scheffler profile E1-P-E2). Thus, length E1P along the parabola must be equal to PE2, i.e.

$$\int_{x_2}^{2f} \sqrt{1+\left(x/2f\right)^2}\,dx = \int_{2f}^{x_1} \sqrt{1+\left(x/2f\right)^2}\,dx \qquad (6)$$

For a Scheffler reflector of aperture radius R_a and focal length f, the value of α must satisfy Equation (6). Reddy et al. [12] found that α can have values within the limits 42° and 44.9°. A code has been developed in MATLAB to evaluate α by solving Equations (4)-(6) iteratively for a given R_a and f. As the difference between the terms in left hand and right hand sides in Equation (6) is less than 0.01 mm, the convergence criterion is satisfied.

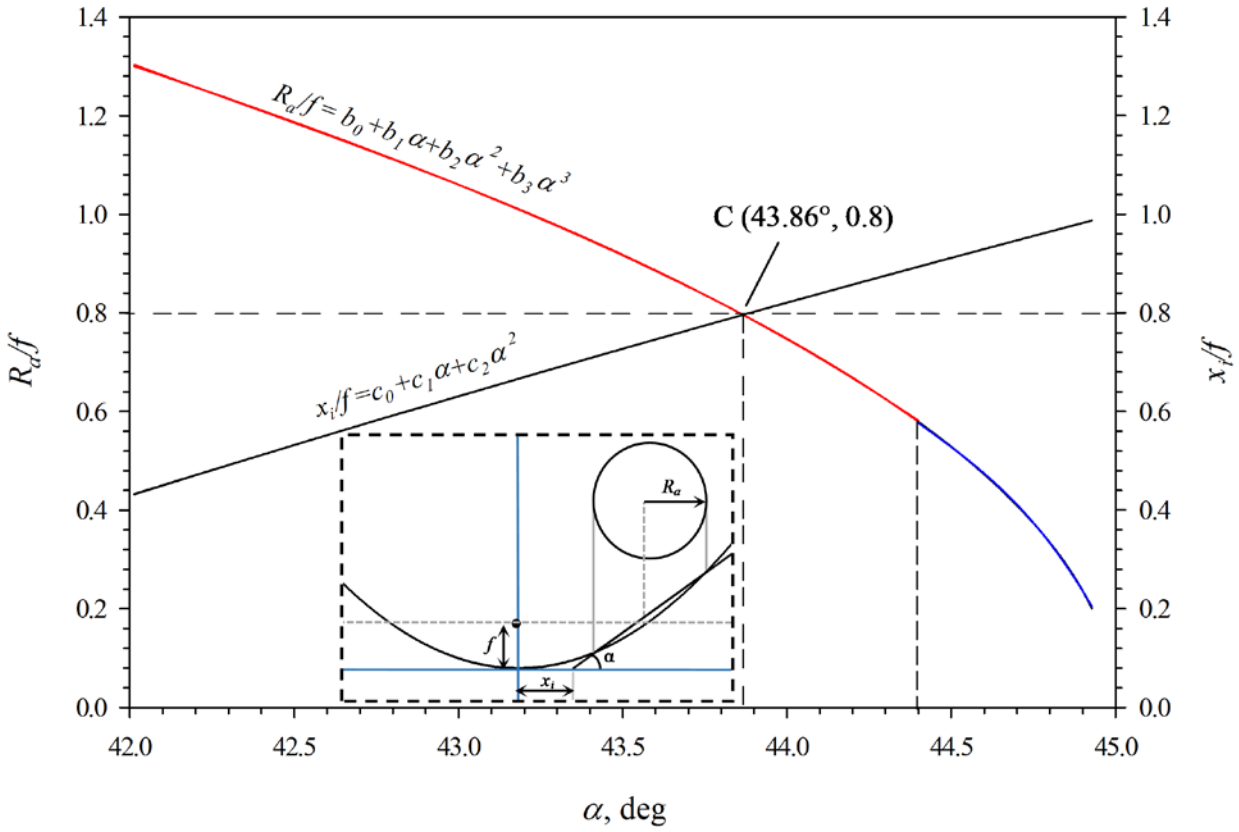

Figure 2 Variation of aperture radius and x-intercept with inclination angle

Depending upon the application, the size of the Scheffler reflector may vary. A non-dimensional scaling factor R_a/f is chosen to make the design independent of size. Since all the parabolas are geometrically similar and can be scaled up or down to match one another. In the same way, all reflectors with same value of α can be grouped into one category which can be represented by the ratio R_a/f. For the same reason x-intercept has also been non-dimensionalzed by dividing it by focal length, i.e. x_i/f. A chart, shown in Figure 2, is prepared for these scaling factors R_a/f and x_i/f for α ranging from 42° and 44.9°.

To simplify the design process for the determination of R_a and x_i, curve fitting based on least square method has been carried out and equations have been evolved. The prediction equations have been evolved to simplify the complicated design process, which involved iterative solution procedure as explained previously. The details are presented in Table 1. Further, the R_a/f versus α plot has been divided into two parts, shown by red and blue colours, to obtain the accurate prediction equations for entire range of α from 42° to 44.9°. This is evident from the value of determination coefficient, R^2.

It can be seen from Figure 2 that the two curves, i.e., R_a/f versus α and x_i/f versus α intersect each other at point C (43.86°, 0.8). This point C has a remarkable significance in the design of the Scheffler reflector as it divides the entire range of inclination angle α into two parts- 42° to 43.86° and 43.86° to 44.9°. At this point,

radius of aperture is equal to the x-intercept, which is 0.8 times the focal length *f*. Choosing inclination angle less than 43.86° means larger aperture area (higher concentration ratio) and lower x-intercept (nearer focal point) whereas if α is greater than 43.86°, the concentration ratio is less and focus is distant away. Further, for lower α-values the Scheffler reflector curvature will be more and manufacturing tolerances can be relaxed leading to lower fabrication costs. On the other hand, if α-values are greater than 43.86°, the light can be concentrated at a larger distance from the reflector with low concentration ratio. Since curvature is less, it requires tighter tolerances resulting in increased manufacturing costs.

Table 1 Correlations for aperture radius and x-intercept

Radius of aperture	**Coefficients**				**Range of Inclination angle**	**Determination coefficient**
$R_a / f = b_0 + b_1\alpha + b_2\alpha^2 + b_3\alpha^3$	b_0	b_1	b_2	b_3	α	R^2
	1237.144	-87.144	2.0538	-0.0162	$42^o \le \alpha \le 44.4^o$	1
	71038.654	-4798.786	108.0671	-0.8113	$44.4^o < \alpha \le 44.9^o$	0.9997
x-intercept						
$x_i / f = c_0 + c_1\alpha + c_2\alpha^2$	c_0	c_1	c_2		α	R^2
	-17.9925	0.6707	-0.0055		$42^o \le \alpha \le 44.9^o$	1

3 CROSSBARS DESIGN

Crossbars are the supporting rods for mirrors or reflective sheets and are attached to the elliptical rim. They take the shape of the paraboloid, as shown in Figure 3. Munir et al. [11] suggested using the crossbars (shown in Figure 3) that lie in the plane perpendicular to E1E2. These crossbars are the portions of ellipses intercepted by inclined sectional plane between E1 and E2. The centres of these ellipses lie on a vertical line passing through a point having coordinates (2*f* tan (90+α), 0). Since these elliptical crossbars are difficult and costly to manufacture, Munir et al. [11] suggested using 3 point approximated circular crossbars which are easy to manufacture and are cost effective in place of elliptical crossbars. These approximated circular crossbars are also perpendicular to E1E2 (shown in yellow of Figure 3). Due to this approximation, a small error in the profile of Scheffler reflector [12] is introduced.

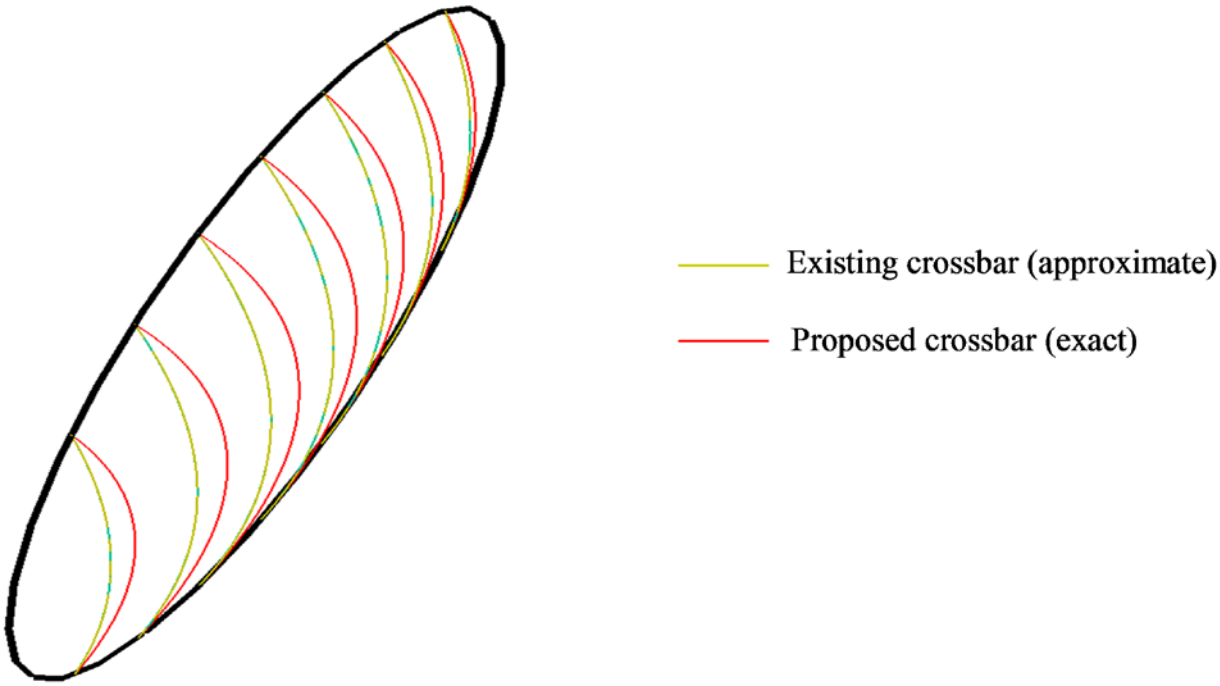

Figure 3 Existing and proposed crossbar designs

Instead of constructing a Scheffler reflector with approximated circular crossbars that are perpendicular to E1E2, new and accurate method of choosing the circular crossbars is proposed in this section. The new

circular crossbars are essentially the arcs that are formed at the intersection of paraboloid and the planes normal to its axis. These arcs are inclined at an angle α to the line E1E2.
If n number of crossbars that are placed equally apart between the points E1 and E2 are to be designed, then the radius of any crossbar cb_m is given by

$$R_m = \sqrt{4f \tan\alpha (x_m - x_i)} \tag{7}$$

Where x_m is given by

$$x_m = x_2 + \frac{m}{n+1}(x_1 - x_2) \tag{8}$$

The width of the crossbar cb_m is given by,

$$W_m = 2\sqrt{R_m^2 - x_m^2} \tag{9}$$

The angle subtended by the circular crossbar cb_m at its centre is,

$$\theta_m = 2\cos^{-1}\left(x_m / R_m\right) \tag{10}$$

From equation (7) and (10), the length of the circular crossbar can be found out as,

$$L_m = R_m \times \theta_m \tag{11}$$

With the help of the radius, width and length form Equations (7), (9) and (11), new circular crossbars can be designed easily. These circular crossbars when attached to the elliptical rim at an angle α can accurately define the shape of the Scheffler reflector. In fact the Scheffler profile and the two types of crossbars, shown in Figure 3, are generated from the MATLAB code.

4 CONCLUSIONS

With its unique features such as shadow-less concentration, non-moving focus and flexible curvature, the Scheffler reflector has been gaining acceptance among masses. Following conclusions can be drawn from the present work:

- The existing crossbar design is complicated and monotonous. To ease the overall design process, a chart is presented which can be used to design Scheffler reflector of any size. Further, the prediction equations have also been developed with aperture radius and x-intercept as function of inclination angle.
- It has been found that the choice of inclined sectional plane angle can be made either in the range 42° to 43.86° or 43.86° to 44.9°, which will depend upon the application for which the Scheffler reflector is to be designed. Low range helps in higher concentration and lower cost whereas its higher range will decrease the concentration and increase cost with an advantage of focusing light at a relatively far away point.
- It is proposed that existing circular crossbars can be replaced by the new and exact circular crossbars, which are the parts of circle having centres along the axis of paraboloid and lie in the planes perpendicular to it. The proposed crossbar design eliminates the approximations and eases the fabrication process and, thus, has the potential for mass production.

REFERENCES

[1] J. A. Duffie and W. A. Beckman, *Solar engineering of thermal processes*, Wiley, 2013.
[2] S. Suman, M. K. Khan, M. Pathak, Performance enhancement of solar collectors - A review,*Renewable and Sustainable Energy Reviews*,Vol. 49, pp. 192–210, 2015.
[3] W. Scheffler, S. Bruecke, G. von Werdenbergstr, Introduction to the revolutionary design of Scheffler reflectors, *Sol. Cookers Food Proc. Int. Conf*, Spain,2016.
[4] U. Oelher, W. Scheffler, The use of indigenous materials for solar conversion, *Solar Energy Materials and Solar Cells*, Vol.33, pp. 379-387, 1994.
[5] A. Afzal, A. Munir, A. Ghafoor, J. L. Alvarado, Development of hybrid solar distillation system for essential oil extraction, *Renewable Energy*, Vol. 113, pp.22-29, 2017.

[6] G. Agrisani, K. Bizon, R. Chirone, G. Continillo, G. Fusco, S. Lombardi, F. S. Marra, F. Miccio, C. Roselli, M. Sasso, R. Solimene, F. Tariello, M. Urciuolo, Development of a new concept solar-biomass cogeneration system, *Energy Conversion and Management*, Vol. 75, pp. 552-560, 2013.
[7] A. Z. Hafez, A.Soliman, K. A. El-Metwally, I. M. Ismail, Design analysis factors and specifications of solar dish technologies for different systems and applications, *Renewable and Sustainable Energy Reviews*, Vol. 67, pp. 1019-1036, 2017.
[8] A. Z. Hafez, A.Soliman, K. A. El-Metwally, Ismail, Solar parabolic dish Stirling engine system design, simulation and thermal analysis, *Energy Conversion and Management*, Vol. 126, pp. 60-75, 2016.
[9] A. Munir, O. Hensel, On-farm processing of medicinal and aromatic plants by solar distillation system,*Biosystem Engineering*,Vol. 106(3), pp. 268-277, 2010.
[10] H. Naik, P.Baredar, A. Kumar, Medium temperature application of concentrated solar thermal technology: Indian perspective, *Renewable and Sustainable Energy Reviews*,Vol. 76, pp. 369-378, 2017.
[11] A. Munir, O. Hensel, W. Scheffler, Design principle and calculations of a Scheffler fixed focus concentrator for medium temperature applications,*Solar Energy*, Vol. 84(8), pp. 1490-1502, 2010.
[12] D. S.Reddy, M.K. Khan, M.Z. Alam, H. Rashid, Design charts for Scheffler reflector, *Solar Energy*, Vol. 163, pp. 104-112, 2018.

POTENTIAL OF THE PARABOLIC TROUGH COLLECTORS USE IN THE INDUSTRY OF CYPRUS: CURRENT STATUS AND PROPOSED SCENARIOS

P.K. Ktistis[1], R.A. Agathokleous[2], S.A. Kalogirou[3]

1. Ktistis K. Panayiotis, Department of Mechanical Engineering and Materials Science, Cyprus University of Technology, Limassol, Cyprus, email: panayiotis.ktistis@cut.ac.cy
2. Agathokleous A. Rafaela, Department of Mechanical Engineering and Materials Science, Cyprus University of Technology, Limassol, Cyprus, email: rafaela.agathokleous@cut.ac.cy
3. Kalogirou A. Soteris, Department of Mechanical Engineering and Materials Science, Cyprus University of Technology, Limassol, Cyprus, email: soteris.kalogirou@cut.ac.cy

ABSTRACT

Cyprus is the worldwide leader country for the use of solar water heating systems per capita, which are of the thermosiphon solar water heating type. In this paper, an investigation of the prospects to start using parabolic trough collectors (PTC) in industry is carried out. Although the industrial market of Cyprus is small in comparison with other countries, the industry sector is a big energy consumer. The large amount of incident solar radiation through a year and the need of the people to reduce their energy needs, makes the idea to adopt PTC collectors for energy production in industry very attractive. This study presents an investigation carried out to evaluate the current status of the industrial energy needs as well as the systems currently used for energy production. To achieve this, an extensive research is carried out to collect all the information directly from the industries or through statistical data. This is focused on the energy consumption of industry sector, fuel use by industry sector as well as its energy needs. Accordingly, an examination of the PTC systems is done in order to study the feasibility of installation in the industrial sector of Cyprus. The feasibility study is done considering the energy production, the cost of installation, the cost of energy savings and the CO_2 emissions reduction. The investigation of the system is carried out with TRNSYS simulation software, and F-chart optimization method for the thermal analysis and economic analysis respectively.

Keywords: PTC, industry, thermal, solar, Cyprus, food and beverage industry.

1 INTRODUCTION

Solar energy is the most used source of energy among the other renewable energy sources. Every year there is an increase in the total installed capacity of the solar energy systems worldwide.

Cyprus is the third largest island in the Mediterranean region at 35° north latitude and 33° longitude, and it is among the most insolated countries in the EU, as the average global solar radiation exceeds the value of 2000 kWh/m^2. The climate is Mediterranean with warm and dry conditions from May until the end of September and mild from October to April. There is sunshine for 11,5 hours per day on average throughout the year.

Although solar energy production has a great potential on the island, currently the energy system is mostly dependent on energy from fossil fuels. The island has a small and isolated energy system which is not connected with other energy networks there are no fossil fuel resources, which have been utilized so far, on the island [1]. Thus Cyprus is very dependent on imported fuels and 94% of the country's energy needs is covered by oil [2]. The abundance of solar radiation in combination with the energy needs of the island and the fact that there are no supplies from the local fossil fuels reserves yet, creates favorable conditions for the exploitation of solar energy in the island.

During the last years, the EU promotes a series of measures for environmental protection, energy consumption mitigation and increase of renewable energy sources for energy generation. Thus, all the EU countries have to achieve various targets. The solar energy potential makes Cyprus one of the promising candidates for meeting its energy needs based on solar energy in the future and meet the targets set by the EU for the renewable energy Directives and the energy efficiency targets. Cyprus achieved the target of energy consumption reduction by achieving the energy saving target of 242317 ktoe by 2016, as well as the primary energy consumption reduction target for the years 2013, 2014 and 2015 [1]. However, energy consumption is proved historically that is related with the national income. Thus, the reduction in energy consumption in the island for these years coincides with the financial crisis period.

Figure 1 shows the final energy consumption by sector in 2015. As can be observed the biggest consumer is the transport sector and then the residential. The government proposes various measures and grants to reduce the energy consumption of the buildings sector, based on the EU targets of the 20-20-20 Directive [3]. Regarding the energy consumption in the buildings sector, it is worth mentioning that Cyprus is the worldwide leader country for the use of solar water heating systems per capita, which are of the thermosiphon solar water heating type. The total capacity of glazed water collectors in 2013 was 423,3 kW_{th} per 1000 inhabitants, making Cyprus the leading country, followed by Austria with installed capacity of 382,2 kW_{th} per 1000 inhabitants [4]. For Cyprus, this capacity was around 3 % of the energy required in the building's sector in 2013.

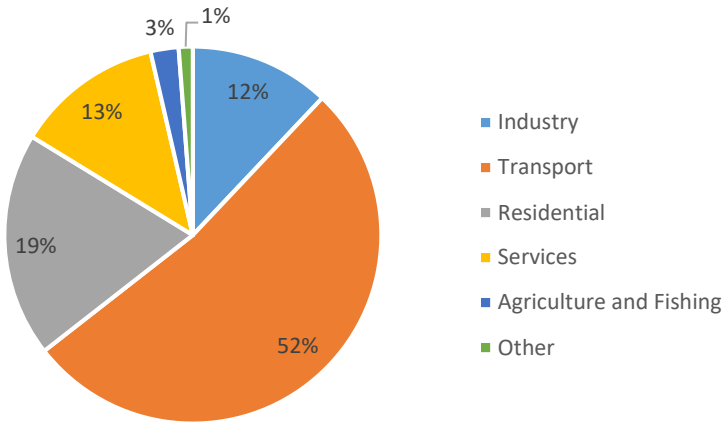

Figure 1. The final energy consumption by sector in 2015.

However, the flat plate water collectors are used for domestic hot water and in hotel units for services. Taking into account the markets that should implement solar energy systems for electricity or heat energy generation, it can be seen that there is a great potential for the industrial sector. In 2015, nearly 150000 toe were used by the industrial sector [5] for heat energy production which could be covered by solar energy.

Looking at the required amount of oil to cover the heat energy needs of the industrial sector, an important market potential exists for high temperature solar heaters. For the industrial sector, the flat plate solar collectors already in use in the building's sector are not the best option since higher temperatures are required. The most appropriate system to cover these needs would be a parabolic trough collector (PTC) system, which can work at elevated temperatures with good efficiency. Thus, parabolic trough collector systems could be a sustainable, profitable and dispatchable technology, especially for the Cypriot industries.

In this paper, the analysis is focused on the industrial sector which consumes 12% of the total energy, and especially in the food and beverage industry which is the second largest consumer of oil for heat energy supply, after the non-metallic mineral products industry. This study presents an investigation carried out to summarize the current status of the industrial energy needs as well as the systems being used for energy production. To achieve this, an extensive research is carried out to collect all the information directly from the industries or through statistical data. This is focused on the energy consumption of the industry sector, fuel use by industry sector as well as its energy needs. Subsequently, one scenario is examined, and a feasibility analysis of using a PTC system is carried out considering the energy production, the cost of installation and cost of energy savings as well as the CO_2 emissions reduction for a particular industry. The investigation of the system is carried out with TRNSYS simulation software, and F-chart optimization method for thermal analysis and economic analysis respectively.

2 LITERATURE REVIEW

There are various studies carried out on the performance of the PTC and their use to cover the heat energy needs of the industrial sector and mainly the food industry which requires more heat for its various processes [6], [7]. Additionally, there are various studies investigating the feasibility to use these systems for heat energy production in industry [8], [9] in terms of economics and design optimization.

Cotrado et al. [10] presented a dynamic simulation model and monitoring data of a large scale solar plant for industrial process heat for a meat factory in Austria. The dynamic model is developed in TRNSYS and the simulation results are in agreement with the measured monitoring data of the field. However, a complete validation of the model was not possible because there were not enough experimental data for one year by that time. From the economic analysis it was concluded that 50,7 m^3 of oil can be saved every year when the energy is covered by the solar system. This corresponds to 26,9% of the total oil required by the factory and cost savings of approximately €507093. The heat from the solar system is employed for drying air conditioning systems (21%) and for feed water preheating for the steam boiler.

Biencinto et al. [11] presented a simulation model for direct steam generation in PTC validated with real experimental data obtained from the DIrect Solar Steam (DISS) solar test loop in Spain [12]. The simulation model is developed in TRNSYS simulation tool and the simulation data are compared with experimental data measured over more than 20 days from 2000 to 2003. In order to allow reliable evaluation of the model performance, the authors selected three significant days of different working pressure at 3, 6 and 10 MPa.

Cundapi et al. [13] carried out a thermo-hydraulic study of water-steam flow of a small sized parabolic trough collector for industrial process heat applications and an analysis to investigate the effects of inlet temperature and pressure. The model of this study was not validated with experimental data since the system was not built by the time that the study was made and it was thus decided to validate the code by comparing the results with experimental data from the DISS PTC system [14].

Ghazzani et al. [15] carried out a dynamic simulation of a small sized parabolic trough collector plant using TRNSYS software. The PTC plant generates heated air for an industrial food factory which requires heated air at 150°C from 8:30 to 00:00 daily throughout the year. The results of the simulation model are analyzed in terms of the energetic and exergetic performance data and the environmental impact analysis determined that up to 57% of CO_2 emissions can be avoided annually with the use of a solar plant.

Kalogirou [16] investigated the viability of using a parabolic trough collector system for industrial heat generation in Cyprus. The system is investigated thermally and economically in TRNSYS for TMY data for Nicosia, Cyprus. The present study is similar with the study presented in [16] considering the same location but in this study more

focus is paid on real factories as case studies for the feasibility analysis. It is worthy to be mentioned that Kalogirou [16] in 2002 concluded that the opportunities for the application of PTC solar energy systems for industrial process heat are enormous in Cyprus and should be utilized. However, 16 years later, there is still no implementation of these systems in Cyprus, although there is great potential of their utilization.

3 ENERGY CONSUMPTION BY THE INDUSTRIAL SECTOR

3.1 Electricity and Heating Consumption

Separating the electricity needs from the heat needs, the electricity and oil consumption breakdown by industry in 2017 are shown in Figure 2 and Figure 3 respectively. As can be seen, the industrial sector is the third biggest consumer of electricity and the second biggest in oil consumption for heat energy.

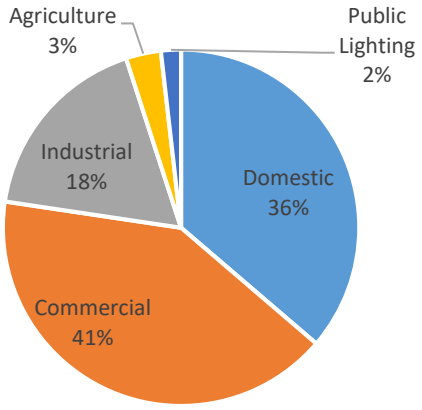

Figure 2.Electricity consumption by sector [5].

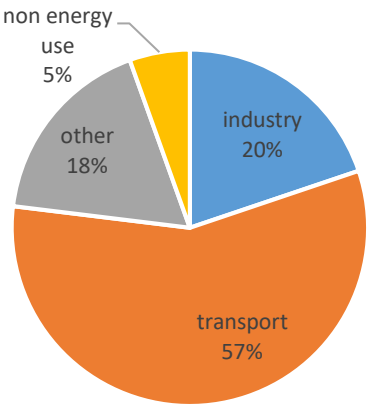

Figure 3. Oil consumption by sector [5].

The industry of Cyprus deals with food and beverage, textile and leather, paper, pulp and print, chemical and petrochemical, wood and iron and steel. Most of the industries use thermal and electrical energy for their various processes, with the biggest consumer to be the non-metallic minerals industry (glass, pottery and building materials) and the second bigger consumer is the food industry. The latter requires large amounts of thermal energy which could be provided by a PTC since the required temperatures are 100°C - 300°C which is a very common range of temperatures for such systems. For the years 2011 to 2014, the food and beverage industry and the non-metallic mineral products industry were the main oil consumers of the industrial sector [17]–[21]. In the food industry, the heat is used mainly for drying, cooking and cleaning.

3.2 Energy Demand for Industrial Process Heating

Table 1 shows the thermal energy demand of various Cyprus factories of the food and beverage industry and the non-metallic minerals industry as well, showing the temperature range per process as well as the average daily load flow.

As can be observed, the thermal load of these factories can be classified in relation to the required temperature range as follows:

- Low temperature (until 100^{o}C)
- Medium temperature (100^{o}C – 300^{o}C)
- High temperature (more than 300^{o}C)

Table 1. Thermal demand of various factories from the food and beverage industry in Cyprus.

Factory	Process	Temperature range (°C)	Hot water/ steam	Average load (t/h)
Wine	Sterilization	90	Hot Water	1,5
Milk & Dairy products	Sterilization	120	Steam	2,2
	Drying			
Soft drinks	Pasteurization	95	Steam	3,5
	Cleaning / disinfecting process	150	Steam	
Meat	Cooking	90-100	Steam	1
Beer	Cleaning / disinfecting process/ hot water	80-90	Steam	5
Plastics	Separation	200-220	Steam	2
	Drying	180-200	Steam	
	Blending	120-140	Steam	
Bricks and blocks	Curing	60-140	Steam	4

4 THERMAL ENERGY BY PTC SYSTEM & CASE STUDY

This study is focusing on the food and beverage industry and examines the potential use of the PTC systems in a soft drinks factory. As shown in Table 1, the food and beverage sector requires temperatures from 100-200°C which can be easily obtained from PTC systems. A PTC system comprises of various parts responsible for different operations such as the collectors, storage tank, pumps, heat exchangers and auxiliary boilers. A schematic representation of a typical industrial PTC system is shown in Figure 4.

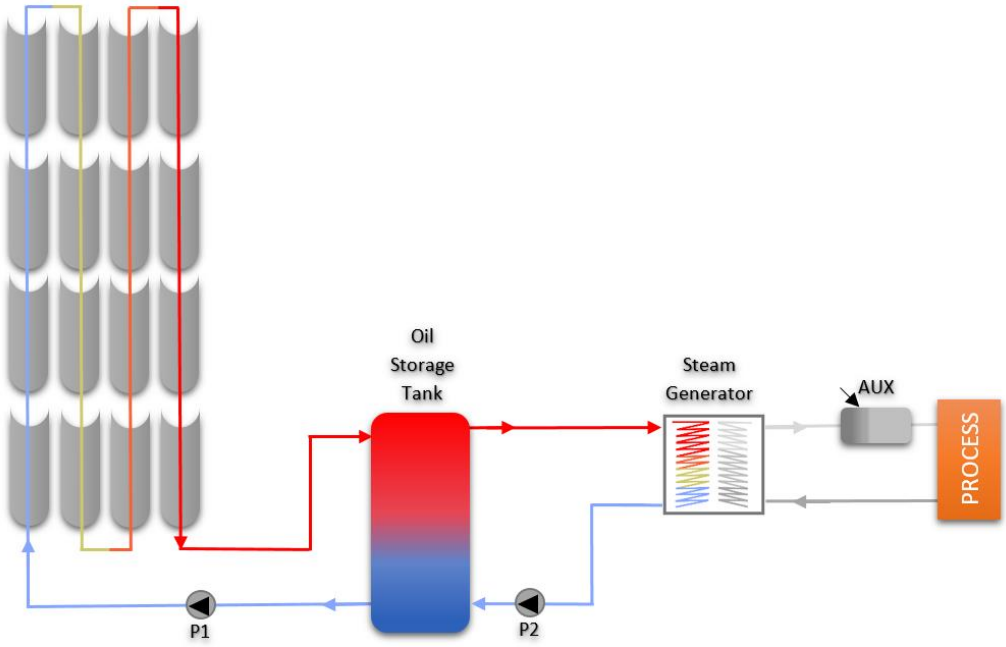

Figure 4. Schematic representation of an industrial PTC system.

A parabolic trough collector consists of the reflector structure where incident rays are reflected on the absorber tube placed at the focal line of the collector. The concentrated rays falling on the absorber tube heat the working fluid. The fluid, called heat transfer fluid (HTF), is circulated by a pump through the system. In this analysis, a number of PTC are simulated with the use of Therminol 66 as the HTF, for a temperature up to 300°C to charge

the storage tank. The HTF is then circulated back to the collectors with an oil pump (P1) and additionally, it is fed to a steam generator and delivered back to the storage tank by an oil pump (P2). If the steam is not enough to cover the thermal load, then an auxiliary system is employed in a series configuration. The steam is provided to the process and it is circulated back to the steam generator. Moreover, simple and differential thermostats are involved in order to control the operation of the system.

As mentioned earlier, a feasibility study is carried out to investigate the potential to use PTC systems in specific industries of Cyprus. Thus, to assess the feasibility of the system, a particular industry is selected as a case study. This is a factory from the drinks and beverages industry, located in Limassol, Cyprus, with thermal demand of 500 kW_{th}. The industry needs steam at 150°C for 10 hours per day and seven days per week.

5 PTC USE ASSESSMENT FOR THE CASE STUDY: SIMULATION DYNAMIC MODELING

The case study mentioned above together with the PTC system are modelled, to represent a real industrial PTC system. A dynamic model is developed in TRNSYS simulation software to investigate the energy production of the system under various configurations and in combination with the F-chart financial analysis to propose the best system for the specific factory, with the higher contribution of solar energy and the smaller payback period.

The F-chart optimization method is based on the life cycle cost method. This method takes into account the time value of money. If the system has a cycle life of 20 years, and the industry paid 20% of the system cost in advance and the 80% the next 20 years with interest rate of 7%, the payback period time is calculated by summing the costs and the financial gain of the system for 20 years of operation.

The purpose of the simulation analysis is to examine a PTC system in terms the solar fraction, investigating the number of collectors required and the volume of the storage tank. Thus, five different volumes of the storage tank are examined; 15, 20, 25, 30 and 35 m^3, and seven different numbers of collectors, from 100 to 160 in steps of 10. Accordingly, a total of 35 cases are examined. The TRNSYS simulation model is shown in Figure 5.

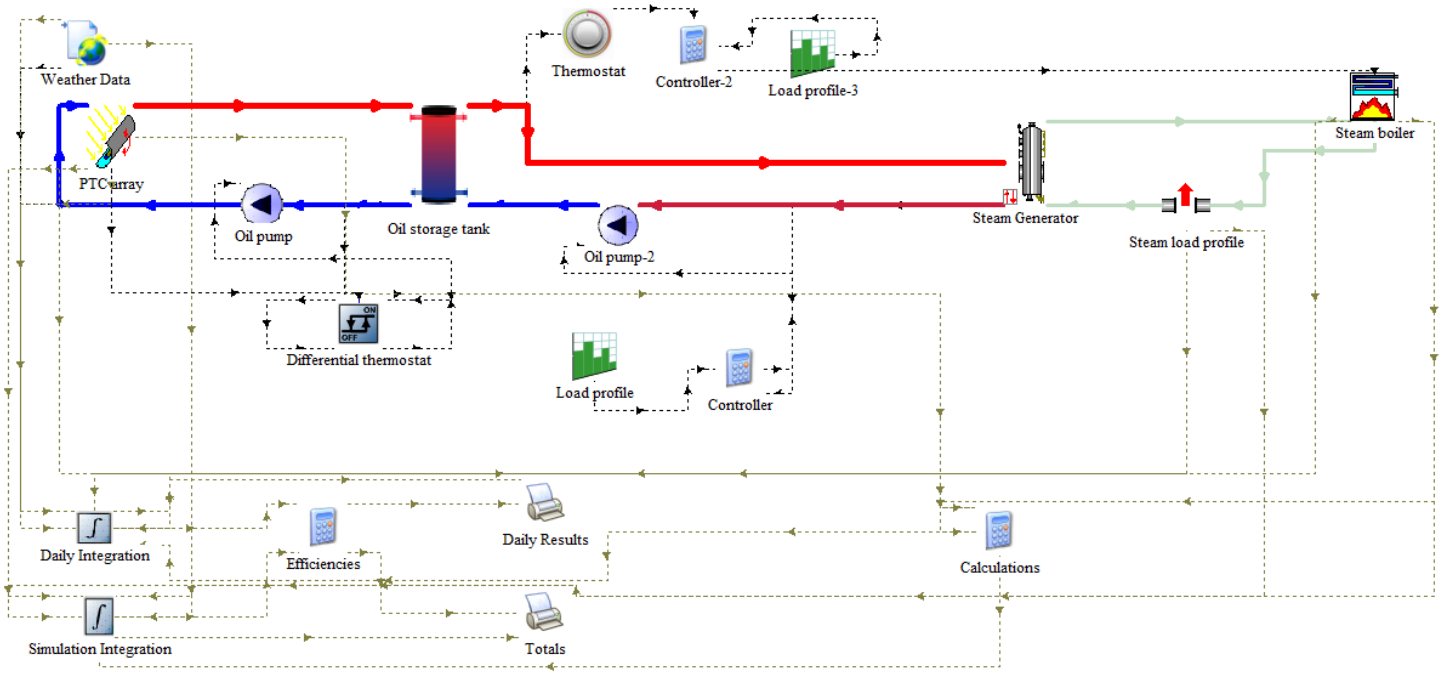

Figure 5. TRNSYS simulation model of an industrial PTC system.

6 RESULTS FROM ENERGY SIMULATION AND COST ANALYSIS

The investigated parameters mentioned in the previous section, together with the solar fraction obtained for each case and the present worth of solar savings are shown in Table 2. The optimum solar system will have the higher solar fraction with the lower payback period. A summary of the best cases is presented in Table 3. As the basic criterion is the maximum solar fraction with the higher 1st year solar savings, the best option is the installation of 120 PTC with 11,25 m^2 each with 30m^3 storage tank. This is done in order to avoid performing an economic life cycle analysis for all the cases.

Table 2. The investigated cases to define the optimum number of PTC and oil storage tank volume.

Number of PTC	Case 1 Storage tank: 15m^3		Case 2 Storage tank: 20m^3		Case 3 Storage tank: 25m^3		Case 4 Storage tank: 30m^3		Case 5 Storage tank: 35m^3	
	Solar fraction	Present worth of solar savings 1st year	Solar fraction	Present worth of solar savings 1st year	Solar fraction	Present worth of solar savings 1st year	Solar fraction	Present worth of solar savings 1st year	Solar fraction	Present worth of solar savings 1st year
100	0,511	16140,52	0,511	15909,33	0,508	15309,73	0,503	14478,12	0,499	13714,92
110	0,547	16430,62	0,549	16445,03	0,549	16213,84	0,547	15750,64	0,544	15110,24
120	0,574	15615,48	0,58	16121,11	0,582	16135,53	**0,583**	**16040,74**	0,581	15523,14
130	0,597	14309,13	0,604	14937,56	0,609	15320,39	0,611	15348,41	0,611	15076,42
140	0,615	12388,75	0,624	13262,80	0,63	13768,43	0,633	13919,25	0,635	13892,87
150	0,631	10222,78	0,642	11342,43	0,648	11848,06	0,653	12244,48	0,655	12218,10
160	0,645	7811,19	0,657	9053,64	0,664	9682,08	0,669	10078,50	0,672	10174,93

Table 3. The optimum values of cost, present worth value and solar fraction for the best cases.

No of collectors	Storage tank volume m^3	Overall cost €	Present worth value 1st year €	Solar fraction
110	15	373125	16430,62	0,55
110	20	374825	16445,03	0,55
110	25	376525	16213,84	0,55
120	**30**	**408500**	**16040,74**	**0,58**
120	35	410500	15523,14	0,58

In order to predict the payback time, the F-chart method is used. The cost of the various parts of the system are set as follows:

- Collector: 270 €/m^2
- Steam generator, steam boiler, control system, pipes and pumps: €34000
- 30m^3 storage tank: €10000
- Fuel: 20 €/GJ (+1% cost added per year)
- Maintenance cost: 7% (+1% cost added per year)

Consequently, a PTC system for the soft and drink industry with an annual thermal load of 659 GJ (500 kW_{th}) will have the following characteristics:

- Cost €408500
- Aperture collector area of 1350 m^2 (mounted on the roof or in the land)
- Payback period from 5 to 6 years

The overall savings from the solar energy is expected to be €142690 by the end of the cycle system life as shown in Figure 6. The model estimates the annual thermal production to be 742 GJ from which the 470 GJ are provided by the PTC system and the 272 GJ from the auxiliary steam boiler.

Additionally, the annual fuel savings are presented in Figure 7 and are estimated to be €92548,64. It is considered that the industry uses the light fuel oil (LFO) as the conventional fuel to cover the thermal needs.

Finally, the carbon emissions savings for a time period of 20 years are presented in Figure 8. The cost of auxiliary energy is 20€/GJ (+1% added every year) and the emissions of LFO are 77,4 $kgCO_2/GJ$.

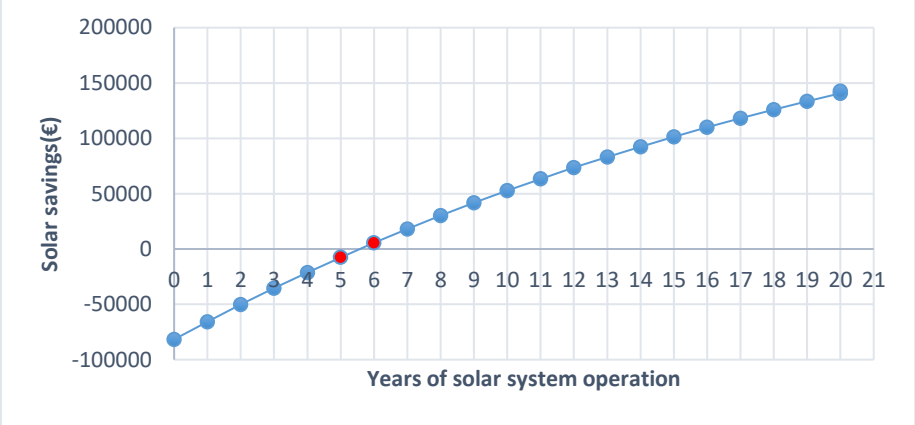

Figure 6: Yearly savings from solar energy.

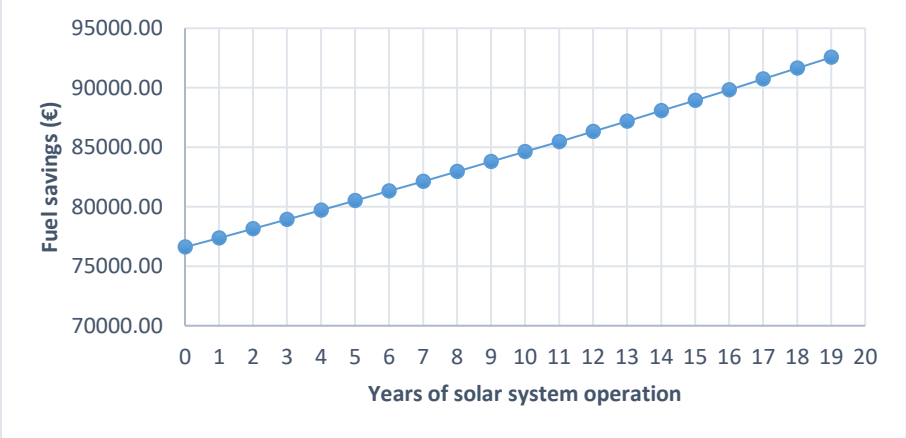

Figure 7: Fuel savings.

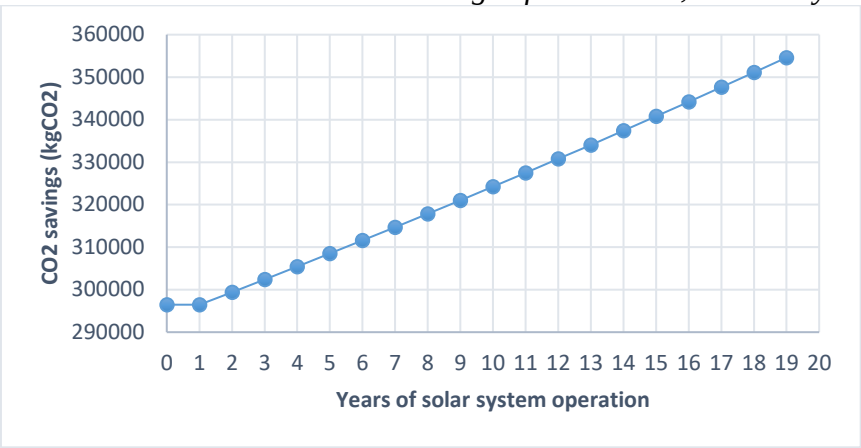

Figure 8: CO_2 savings.

7 CONCLUSIONS

The industrial sector is among the highest energy consumers in Cyprus from which the non-metallic mineral sector and the food and beverages sector are the biggest consumers. Thus, it is important to implement renewable energy systems to support the energy use of those industries.

Here in this study, attention is paid to the food and beverages industry, in order to examine the feasibility of using PTC systems to cover the thermal energy needs of the industry or to support the loads in order to eliminate the use of fossil fuels, support the CO_2 emissions reduction and increase the energy efficiency of the island. PTC systems are examined instead of flat plate collector (FPC) systems due to the highest required temperature range used by these industries.

A dynamic simulation is performed to demonstrate the use of a PTC system to supply the thermal energy needs of a soft drink factory in Limassol, Cyprus, in order to examine the feasibility of the use of these systems widely in Cyprus.

The most important outcomes from this study are summarized below:

- From the performance characteristics presented it is proved that the climate of Cyprus has a great potential for solar energy systems.
- The investigation of the various configuration and sizing parameters resulted to the ideal sizing of the system based on the solar fraction and the present worth of solar savings.
- The final system has 120 PTC 11,25 m^2 each and 30m^3 oil storage tank used to cover the thermal needs of a factory of 500kW_{th} steam.
- The performance of the examined system is very high, and the payback period is acceptable.
- The 58% of the thermal load is covered by the solar system with the fuel savings is estimated to be €92548,6.
- The overall solar savings by the end of the system's life cycle is estimated to be €142690,24.
- The reduction of CO_2 emissions is estimated to be 354617,05 kg.

NOMENCLATURE

DISS	DIrect Solar Steam
EU	European Union
FPC	flat plate collector
HTF	heat transfer fluid

PTC	parabolic trough collector
TMY	typical meteorological year

ACKNOWLEDGEMENTS

The work is supported by the project 'Evaluation of the Dispatchability of a Parabolic Trough Collector System with Concrete Storage' with acronym 'EDITOR' from technological development and innovation 2009-2010, KOINA/SOLAR-ERA.NET/0114, which is co-financed by the European Development Fund, and the Research Promotion Foundation of the Republic of Cyprus.

REFERENCES

[1] European Council, "4th National Energy Efficiency Action Plan," Nicosia, 2017.

[2] The European Union, "Cyprus Energy efficiency report," no. January, pp. 1–6, 2013.

[3] europa.eu, "2020 Energy Strategy," 2016. [Online]. Available: https://ec.europa.eu/energy/en/topics/energy-strategy-and-energy-union/2020-energy-strategy.

[4] F. Mauthner, W. Weiss, and M. Spork-Dur, "Solar Heat Worldwide: Markets and Contribution to the Energy Supply 2013," 2015.

[5] International Energy Agency, "Cyprus: Balances for 2015," 2017. .

[6] G. Kumaresan, R. Sridhar, and R. Velraj, "Performance studies of a solar parabolic trough collector with a thermal energy storage system," *Energy*, vol. 47, pp. 395–402, 2012.

[7] F. Wang, H. Feng, J. Zhao, W. Li, F. Zhang, and R. Liu, "ScienceDirect Performance assessment of solar assisted absorption heat pump system with parabolic trough collectors," *Energy Procedia*, vol. 70, no. 70, pp. 529–536, 2015.

[8] R. Silva, M. Pérez, and A. Fernández-Garcia, "Modeling and co-simulation of a parabolic trough solar plant for industrial process heat," *Appl. Energy*, vol. 106, pp. 287–300, Jun. 2013.

[9] R. Silva, M. Berenguel, M. Pérez, and A. Fernández-Garcia, "Thermo-economic design optimization of parabolic trough solar plants for industrial process heat applications with memetic algorithms," *Appl. Energy*, vol. 113, pp. 603–614, 2014.

[10] M. Cotrado, A. Dalibard, R. Söll, and D. Pietruschka, "Design, control and first monitoring data of a large scale solar plant at the meat factory Berger, Austria," *Energy Procedia*, vol. 48, pp. 1144–1151, 2014.

[11] M. Biencinto, L. González, and L. Valenzuela, "A quasi-dynamic simulation model for direct steam generation in parabolic troughs using TRNSYS," *Appl. Energy*, vol. 161, pp. 133–142, Jan. 2016.

[12] E. Zarza, L. Valenzuela, J. León, K. Hennecke, M. Eck, H.-D. Weyers, and M. Eickhoff, "Direct steam generation in parabolic troughs: Final results and conclusions of the DISS project," *Energy*, vol. 29, no. 5–6, pp. 635–644, Apr. 2004.

[13] R. Cundapí, S. L. Moya, and L. Valenzuela, "Approaches to modelling a solar field for direct generation of industrial steam," *Renew. Energy*, vol. 103, pp. 666–681, 2017.

[14] M. Eck, E. Zarza, M. Eickhoff, J. Rheinländer, and L. Valenzuela, "Applied research concerning the direct steam generation in parabolic troughs," *Sol. Energy*, vol. 74, no. 4, pp. 341–351, Apr. 2003.

[15] B. El Ghazzani, D. Martinez Plaza, R. Ait El Cadi, A. Ihlal, B. Abnay, and K. Bouabid, "Thermal plant based on parabolic trough collectors for industrial process heat generation in Morocco," *Renew. Energy*, vol. 113, pp. 1261–1275, Dec. 2017.

[16] S. A. Kalogirou, “Parabolic trough collectors for industrial process heat in Cyprus,” *Energy*, vol. 27, no. 9, pp. 813–830, Sep. 2002.

[17] Statistical Service, “Industrial Statistics 2011,” 2011.

[18] Statistical Service, “Industrial Statistics 2012,” 2012.

[19] Statistical Service, “Industrial Statistics 2013,” 2013.

[20] Statistical Service, “Industrial Statistics 2014,” 2014.

[21] Statistical Service, “Industrial Statistics 2015,” 2015.

ECONOMIC POTENTIAL TO DEVELOP CONCENTRATING SOLAR POWER IN CHINA: A PROVINCIAL ASSESSMENT

Hua Tang[1], Junping Ji[2], Xiaoming Ma[3]

1. Engineering Laboratory of Energy Conservation and Emission Reduction Data and Modeling, School of Environment and Energy, Peking University Shenzhen Graduate School, Shenzhen 518055, China; email: tanghua@pku.edu.cn
2. Engineering Laboratory of Energy Conservation and Emission Reduction Data and Modeling, School of Environment and Energy, Peking University Shenzhen Graduate School, Shenzhen 518055, China; Energy Analysis and Environmental Impacts Division, Lawrence Berkeley National Laboratory, One Cyclotron Road, MS90R2121, Berkeley, CA 94720, USA; email: jackyji@pku.edu.cn
3. Engineering Laboratory of Energy Conservation and Emission Reduction Data and Modeling, School of Environment and Energy, Peking University Shenzhen Graduate School, Shenzhen 518055, China; email: maxm@pkusz.edu.cn

ABSTRACT

Concentrating solar power (CSP) is a promising renewable energy technology that needs policy support in its initial deployment. Accurately forecasting the economic potential of CSP can be used as a basis for energy policy implementation. This study proposes a model based on meteorological data from China Integrated Meteorological Information Service System (CIMISS) to calculate the levelized cost of electricity(LCOE) in 32 provinces or cities in China. By considering the independent variables, including land occupation, concessionary loan, and technology mode, the LCOE is estimated to be 1.29 to 2.00 CNY/kWh in the regions with the DNI above 1500 kW/m^2 under current condition. It lays a solid foundation for forecasting power generation and selecting the economically feasible sites. Then the study analyses the learning curves of CSP conforming to technological advance trends and scale expansion. With the proper optimization of technology mode, it is reasonable to expect a significant LCOE reduction and reach grid parity in certain areas. By comparing the current policies, it provides a reference for the Chinese government to formulate the subsidy policies to make CSP more competitive.

Keywords: Concentrating solar power; Levelized cost of electricity; Learning curve.

1 INTRODUCTION

Energy is a strategic resource of the modern world concerning global and national security. During the last decades, global energy demand has been increasing at a high speed. However, the growth in the demand for electricity consumption has been relatively higher than that for total primary energy from 1974 to 2015. To satisfy the needs, the global electricity generating capacity increased by 191.52% over the period. Globally, over three-fifths of electricity and heat are generated from fossil fuels, mainly from coal (39.33%) and natural gas (22.85%) in 2015[1]. The factors that may influence energy consumption have been extensively explored, including economic level, industrial structure, demographic change, urbanization process and technological progress[2-4].

China has experienced a noticeable increase in electricity demand over the recent decades, requiring rapid and comprehensive development in the power sector. Energy production totals at 3.6 billion tce (ton standard equivalent) in 2015 while total energy consumption is 4.3 billion tce, its primary electricity production accounting for 14.5% with an increasing trend from 2011 [5].Without decisive action, energy-related emissions of CO_2 will more than double by 2050[6]. Slightly more than 40% of the global energy-related carbon dioxide emissions are attributable to emissions from electricity and heat production [7]. The 1% increase in non-fossil fuel electricity generation reduces CO_2 emissions by 0.82%[8].

At the global level, renewables represent reliable means to reduce CO_2 emissions, address climate change and satisfy the energy requirements. Concentrating solar plants, as one of the effective ways of solar energy utilization, generate solar thermal electricity while producing no greenhouse gas emissions, and the flexibility of concentrating solar plants enhances energy security [9]. In addition, concentrating solar plants combined with thermal storage systems can cope with diurnal rhythm, and can be a cost option. Thus, concentrating solar power (CSP) could be a vital technology for mitigating climate change, especially to achieve the goal of limiting the global mean temperature increase to 2 ℃.

Compared to PV market, CSP market seems to be mini-size. In 2013, the CSP capacity in European Union ranked first at 2.31GW, followed by the United States at 1.3GW. In the hi-Ren Scenario, solar-thermal electricity is expected to represent 11% of global electricity with a capacity increase of 27 GW per year on average, and it peaks at 40 GW per year from 2040 to 2045[9].
China's share of CSP installations is quite modest, ranked 10th in the world at the end of 2016[10]. The cumulative electricity generation rose to 8.983GWh in 2015 compared to that of solar photovoltaic at 69737GWh. The country has reached the cumulative capacity at 13.88 MW in 2013 and kept in the level until 2016, with the goal of installing 5 GW of CSP by 2020 [11]. In November 2017, China announced the capacity of 1089MW in development and 250MW under construction[12]. In the hi-Ren Scenario of CSP roadmap, it can be expected to deploy the capacity of 118 GW in 2050.
In general, CSP is classified as parabolic though collector (PTC), linear Fresnel collector (LFC), central receiver system (CRS), and parabolic dish system (PDS) by the way they concentrate the sun's rays. PTCs and CRSs are preferred in utility applications and widely deployed around the world.
The study aims to estimate the economic potential of concentrating solar power and is set out as follows, firstly, the paper estimate the annual power generation of CSP technology with the database of 32 provinces or cities in China provided by CIMISS. Then the study calculates the LCOE of different technology modes to assess the economic potential provincially. Finally, the influence of technology advance and scale expansion is analyzed with policy implication.

2 METHODOLOGY AND DATA

2.1 Calculation Methods

To assess the cost-effectiveness of CSP, we calculate the LCOE with the net present value (NPV) method. Firstly, we take weather condition and technology parameters into account to calculate the electricity generation of different geographic locations on the revenue side. Among them, peak solar-to-electric efficiency is influenced by factors such as the ratio of gross to net conversion, cycle conversion, and system availability.

$$EG = e_{s-e} * d_i * area \quad (1)$$

Where *EG* is the electricity generation, $e_{s\text{-}e}$ represents the transfer efficiency of solar irradiation to electricity; d_i indicates local DNI; *area* is the capture area.
When NPV=0 (break-even point, performing a discount cash flow), the LCOE is the internal price, equal to the lifecycle cost divided by lifetime energy generation[13]. The lifecycle cost can be classified into the initial investment and annual cost (operation and maintenance cost, insurance cost, tax).

$$LCOE = (I + \sum_{n=0}^{N} (O\&M_n + T_n)(1+r)^{-n}) / \sum_{n=0}^{N} (EG_n(1+r)^{-n}) \quad (2)$$

Where EG_n is the electricity generation in year *n* with the unit of kWh, *LCOE* represents the price of electricity at the break-even point; $(1+r)^{-n}$ indicates the discount factor of year *n*; *I* is the initial investment cost; $O\&M_n$ stands for the operation and maintenance cost and insurance cost in year *n*; T_n denotes the tax cost in year *n*. *N* represents the lifespan of a power plant with the unit of year; *n* represents the *n* year in life-cycle for a power plant. The discount rate *r*, usually assumed as the weighted average cost of capital(WACC), has an influence on the LCOE. In the section, the LCOE estimates are assumed as a 25-year economic life and a WACC of 7.5% in China[14-16].
Among them, investment cost is the initial construction investment, generating from factory gate equipment and on-site equipment[13]. The former includes transport cost, import levies, and relative taxes, while the later comprises project development, site preparation, auxiliary equipment and contingency payments. Operation and maintenance costs include the cost of alternative materials, mirror washing and plant insurance[14]. Taxes are comprised of the land-use tax and the value-added tax with tax-cut policy.
When considering the future evolution of CSPs, Several studies the technological change in cost by learning curves with learning rates range between 10% and 20%[15, 17-19]. Where $I(t)$ is the initial investment in the future year *t*, $C(t)$ represents the cumulative installed capacity at the moment *t*, *LR* denotes the learning rate in the period. Therefore, the investment cost of the new plants installed in the future year *t*, $I(t)$ and, relatively $LCOE(t)$ will be given as follows.

$$I(t) = I(0)(\frac{C(t)}{C(0)})^{\log(1-LR)/\log(2)} \quad (3)$$

$$LCOE(t) = (I(t) + \sum_{n=0}^{N}(O\&M_n(t) + T_n)(1+r)^{-n}) / \sum_{n=0}^{N}(EG_n(1+r)^{-n}) \quad (4)$$

2.2 Data and assumptions

Solar resource is the main factor of economic potential assessment. In order to identify an appropriate site, information on spatial distributions of direct normal irradiation (DNI) is normally required. The meteorological data is collected from China Integrated Meteorological Information Service System (CIMISS) to estimate the annual power generation of CSP technology in 32 provinces or cities in China. Considering the annual irradiation is relatively stable, the study selects the data of DNI in 2016.

Table 1 presents the main technical and economic parameters with their relative assumptions for different technology modes.

Table 1. Main technical & economic parameters and assumptions of CSP systems

Parameters	Units	PTCs	LFRs	CRSs	PDSs	Parameters	Unit	value
Capacity	MW	50	10	50	100	O&M cost	CNY/KW	186
Life span	Year	25	25	25	25	Loan	%	60
absorber's area	m^2	621,300	80,940	516,000	900,000	Discount rate	%	7.5
Solar-to-electric efficiency	%	10-20	10-18.5	8-24	16-29	Interest rate on loan	%	4.9
Initial Investment	CNY/KW	34182	-	30400	-	Value-added Tax rate	%	8.5
Share of Storage cost	%	15	-	10	-	Tax on land-use	CNY/m2/y	1

Note: The parameters and assumptions come from the information of the first 20 demonstration projects [20], and works [16], [21].

3 RESULTS

The cost of electricity generated by a power plant constructed in a certain year is determined by the initial investment cost, the discount rate, the variable costs, the level of solar irradiation and the efficiency. Analysis has been performed for plants of 4 scenarios in different geographical locations. The meteorological data is collected from China Integrated Meteorological Information Service System (CIMISS) to estimate the annual power generation of CSP technology in 32 provinces or cities in China. According to the meteorological data, there are obvious regional differences of solar resource, and relatively, the economic potential of CSP plants. Two types of CSP plant, PTC and CRS account for over 90% of the industry, with LFRs adding a little percent to global capacity[21]. Considering the data limit, we mainly analyse the LCOE of PTCs and CRSs.

Table 2 presents the levelized cost of electricity generated from the PTC plants and CRS plants, with and without thermal storage. The regions presented in table 2 is with the DNI above 1500 kW/m^2.

Table 2. LCOE of PTC & CRS in the region (CNY/kWh, DNI>1500kW/m^2)

province	CRS		PTC	
scenario	without storage	with storage	without storage	with storage
Shanxi	2.55	1.65	2.63	2.00
Tianjin	2.54	1.64	2.61	1.99
Guangxi	2.51	1.62	2.58	1.96
Shanxi	2.42	1.56	2.50	1.90
Hainan	2.39	1.54	2.46	1.87
Xinjiang	2.38	1.54	2.45	1.86
Ningxia	2.36	1.52	2.43	1.85
Inner Mongolia	2.34	1.51	2.41	1.83

Yunnan	2.31	1.49	2.37	1.80
Gansu	2.18	1.41	2.25	1.71
Qinghai	2.15	1.39	2.22	1.68
Tibet	2.01	1.29	2.07	1.57

As already shown in table 2, the sensitivity of LCOE partly results from technology modes and plant sites with different solar resources.

When dividing the regions into three different direct normal irradiance (DNI) levels, below 1500, 1500-1800 and above 1800 kWh/m ², it's clear to explore the output and the LCOE of different meteorological conditions. Table 2 displays LCOE ranges of 2 scenarios (without storage and with thermal storage), the former between 1.29 CNY/kWh (CRS, at the highest DNI) and 1.65 CNY/kWh (CRS, at the lowest DNI). Compared to the condition that DNI between1500 kWh/m^{2}and 1800 kWh/m^2, the LCOE of CRSs is 15.55% lower under higher irradiation condition. A similar relationship to variations in DNI is observed for PTCs. Owing to the project differences, the LCOE of PTC plants with thermal storage is much higher than that of CRS plants in table 2. CSP plants with thermal energy storage tend to have higher investment costs as shown in table 1, but they allow higher capacity factors, schedulability, and typically lower LCOEs, especially for CRSs, at nearly 35.48%. The LCOE of PTCs presents a similar relationship between two scenarios.

4 DISCUSSIONS

In the promoting process of CSP, assessments should take the site selection, technological advance, and capacity expansion into account.

4.1 Site selection

In the assessment of CSP promotion, we should select the sites with high solar resources and ample land & water availability gain momentum in terms of deployments.

In China, the solar thermal demonstration projects published in 2016 are mainly located in Qinghai, Gansu, Hebei, Xinjiang and the Inner Mongolia Autonomous Region with DNI above 1600 kW/m^2. Most adequate plant sites are located at high latitudes and altitudes, far away from power grids, water sources, and gas pipelines, which will increase initial investment. Besides, there is more wind (average wind power density $\geqslant$ 150W/m^2) and sand; thus, the projects demand a higher level of the wind resistance. More trickily, the average annual temperature in China is relatively low with regions with higher DNI at or below 10℃. Especially in winter, intensification of convective heat loss in the plants weakens the power generation efficiency and the total time of power generation, thus, increases the absorber's area and investment. It can partly explain the higher LCOE of China than that of other countries.

4.2 Technology advance and capacity expansion

As the estimated technology trend of storage, storage of variable renewable electricity will play a more important role in the future [21]. There will be a switchover to molten salt as the thermal storage media instead of thermal oil, which is predicted to reduce 50% of the storage cost [22]. Assuming the trend, recalculation of LCOE in the scenario will reduce by 5.7% of PTCs and 6.1% of CRSs on the basis of table 2.

Moreover, the aperture widths of trough collectors in the future will increases by 33.33%, which will decrease the number of collectors, thus, reducing the initial investments.

China's expansion is regarded in the third phrase of CSP industry when the perspective is more attractive than before[17].Under the high cost pressure and industry continuity, we assume the learning rate of 20% for CSP systems as work. Figure 1 shows the development of investment cost for CRSs with storage in the future year recalculated by the equation 3, and figure2 indicates the relatively LCOE of projects constructed in that period, which is calculated by the equation 4.

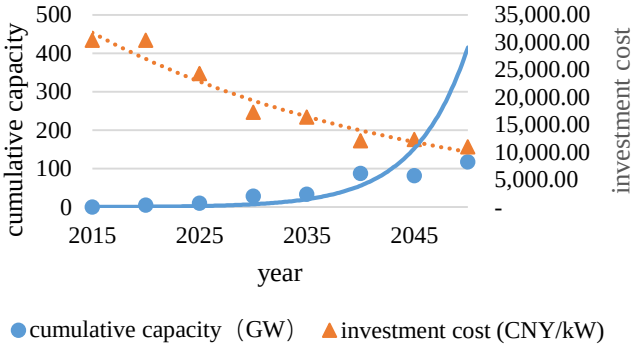

Figure 1. Objective and relatively investment cost

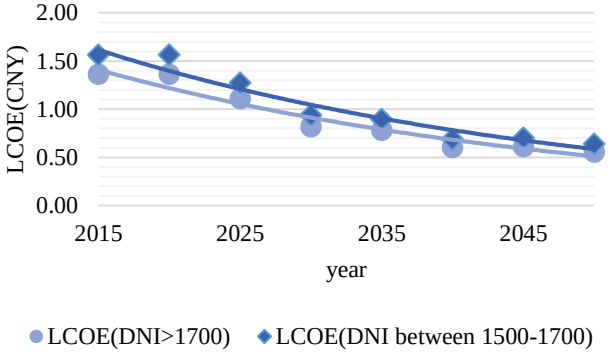

Figure 2. LCOE evolution for CSP

With larger-scale deployment, cost reduction potential can be seen in figure 2, and the LCOE of recalculation range between 1.05 CNY/kWh and 1.37 CNY/kWh for CPSs in 2025, and reach the lowest range between 0.53CNY/kWh and 0.63CNY/kWh in 2050.

4.3 Subsidies through the Feed-in-tariffs System

To promote the healthy development of solar thermal power generation industry, China emphasize the supportive policies at the national, provincial and municipal level. National Development and Reform Commission (NDFC) announced the Feed-in-tariffs of solar thermal power generation projects with more-than-4-hour storage. The example tariff determined by NDFC is same provincially, at1.15CNY/kWh including tax[23]. Moreover, policies are put forward by local departments, including tax relief, financial subsidies, green credit and land concessions.

In the earlier promotion period, the tariff seems inferior to the LCOE results calculated in the paper and the offer price of subjects [20]. Comparing the current benchmark price of coal desulfurization, an additional subsidy will be recommended to range between 0.1 CNY/kWh and 0.5 CNY/kWh on the basis of example tariff varying regionally. With the Under relatively favourable conditions and for the two scenarios considered in the study, the time when CSP electricity costs will reach grid parity is expected to be ahead of schedule when considering the CO_2 emission transaction.

5 CONCLUSION AND POLICY IMPLICATIONS

Renewable energy is the main solution of energy deficit and environmental pollution. The study, firstly, estimates the annual electricity generation of CSP technology based on the data of 32 provinces or cities in China. Then the study calculates the LCOE of CSP projects based on PTC and CRS regionally. The results indicate that LCOE of CRSs with storage ranges from 1.29 to 2.62 CNY/kWh, nearly 35.43% less than that without storage. The LCOE of PTCs with storage ranges from 2.07 to 3.18 CNY/kWh, nearly 31.63% less than that without storage. When selecting the areas with DNI above 1500 kW/h, the LCOE is below 1.65 and 2.00 CNY/kWh for CPS and PTC respectively. In the process of promotion, criteria of the resource limit, like minimum DNI, should be set in a reasonable range. Moreover, with the technological advance and scale development, projects in the regions with DNI above 1500 kW/m^2 will be more economically feasible in the learning curve analysis. In the long term, the subsidy should take the electricity demand and pollution treatment cost into account and pay more attention to the regional difference.

Supportive policies include policy-related loans, subsidized loans, tax deductions and exemptions and direct subsidies[13]. The cost of CSP projects is higher than the conventional ones, even other renewable energy generation projects. The initial investment of CSP is up to billions, varying from different projects owing to the geographic conditions and technology modes. Also, the tariff announced by NDFC is 1.15 CNY/kWh, equal among provinces and less than the LCOE results. It’s worthwhile to expand the capacity scale with relative methods, for the reduction in investment cost put the LCOE of CSP in a more competitive position. In terms of tax policy, 50% of the value-added tax from the solar-energy projects is deducted in China.

In the long run, governments are supposed to put forward timely and differentiated promoting policies by stages. And the long-term developments cannot rely absolutely on the subsidies from government, but the spontaneous growth. It’s vital to overcome the institutional barriers in order to build a competitive electricity market.

REFERENCES

[1] IEA, *Electricity Information 2017*, International Energy Agency, 2017.

[2] Liddle, B., Impact of population, age structure, and urbanization on carbon emissions/energy consumption: evidence from macro-level, cross-country analyses. *Population and Environment*, Vol. 35(3), pp. 286-304, 2014.

[3] Sadorsky, P., The Effect of Urbanization and Industrialization on Energy Use in Emerging Economies: Implications for Sustainable Development. A*merican Journal of Economics & Sociology*, Vol. 73(2), pp. 392--409, 2014.

[4] Yuan, X., et al., Forecasting China's regional energy demand by 2030: A Bayesian approach. *Resources, Conservation and Recycling*, Vol. 127, pp. 85-95, 2017.

[5] DES, *China Energy Statistical Yearbook 2016*, China Statistics Press, 2016.

[6] IEA, *Technology Roadmap：Concentrating Solar Power*, International Energy Agency, 2010.

[7] Ang, B.W. and B. Su, Carbon emission intensity in electricity production: A global analysis. *Energy Policy*, Vol. 94, pp. 56-63, 2016.

[8] Liddle, B. and P. Sadorsky, How much does increasing non-fossil fuels in electricity generation reduce carbon dioxide emissions? *Applied Energy*, Vol. 197, pp. 212-221, 2017.

[9] IEA, *technology road map：solar thermal electricity_2014 edition*, International Energy Agency, 2014.

[10] IRENA, *Renewable Capacity Statistics 2017*, International Renewable Energy Agency, 2018.

[11] IRENA, *Solar Energy Data*, pp. www.irena.org/solar, 2018.

[12] SolarPages, *CSP-MAP*, pp. www.nrel.gov/csp/solarpaces/, 2017.

[13] Ouyang, X. and B. Lin, Levelized cost of electricity (LCOE) of renewable energies and required subsidies in China. *Energy Policy*, Vol. 70, pp. 64-73, 2014.

[14] IRENA, *Renewable Power Generation Costs in 2017*, International Renewable Energy Agency, 2018.

[15] Hernández-Moro, J. and J.M. Martínez-Duart, Analytical model for solar PV and CSP electricity costs: Present LCOE values and their future evolution. *Renewable and Sustainable Energy Reviews*, Vol. 20, pp. 119-132, 2013.

[16] Purohit, I. and P. Purohit, Technical and economic potential of concentrating solar thermal power generation in India. *Renewable and Sustainable Energy Reviews*, Vol. 78, pp. 648-667, 2017.

[17] Lilliestam, J., et al., Empirically observed learning rates for concentrating solar power and their responses to regime change. *Nature Energy*, Vol. 2(7), pp. 17094(1-6), 2017.

[18] Shouman, E.R. and N.M. Khattab, Future economic of concentrating solar power (CSP) for electricity generation in Egypt. *Renewable and Sustainable Energy Reviews*, Vol. 41, pp. 1119-1127, 2015.

[19] Neij, L., et al., *Experience curves: A tool for energy policy assessment*, Lund University, Department of Technology and Society, Environmental and Energy Systems Studies, 2003

[20] NDFC, *Notice of National Energy Administration on Constructing Solar Thermal Power Demonstration Project*, pp. http://zfxxgk.nea.gov.cn/auto87/201609/t20160914_2298.htm, 2016.

[21] IRENA, *Electricity Storage and Renewables: Costs and Markets to 2030*, International Renewable Energy Agency, 2017.

[22] IRENA, *The Power to Change: Solar and Wind Cost Reduction Potential to 2025*, International Renewable Energy Agency, 2016.

[23] NDFC, *Notice of the policy on the electricity price of the solar power generation projects from the National Development and Reform Commission*, pp. http://www.ndrc.gov.cn/zcfb/zcfbtz/201609/t20160902_817573.html, 2016.

A HYBRID SPATIO-TEMPORAL FORECASTING OF SOLAR GENERATING RESOURCES FOR GRID INTEGRATION

Jin HUR[1*] and SeungBeom NAM[2]

1. Department of Electrical Engineering, Sangmyung University, Seoul, Republic of Korea; email: jinhur@smu.ac.kr
2. Department of Electrical Engineering, Sangmyung University, Seoul, Republic of Korea; email: 201731122@sangmyung.kr

ABSTRACT

Recently, the installed solar generating resources have been increasing rapidly. Consequently, forecasting for solar generating resources are becoming an important work to integrate utility-scale solar generating resources into power systems. As solar generating resources are variable, uncontrollable, and uncertain, accurate prediction enables higher penetrations of solar generating resources to be deployed on the electrical power grid. The accurate prediction of solar resources contributes to evaluation of system reserves over large geographic area and to transmission system planning. To increase the penetration of solar generating resources on the electric power grid, the accurate power prediction of geographically distributed solar generating resources is needed. In this paper, we propose a hybrid spatio-temporal forecasting of solar generating resources based on the naïve Bayesian classifier approach and spatial modelling approach. To validate our forecasting model, we use the empirical data from the practical solar farms in South Korea.

Keywords: solar generating resources, hybrid spatio-temporal forecasting, kriging, Naïve Bayes Classifier

1 INTRODUCTION

Solar generating resources are a hot issue in the electric power field around the world, and expected to play major role in future energy. As solar generating resources grow rapidly, global power companies such as ISO and TSO, are planning and establishing systems accordingly. Overseas, New York's ISO is going to increase the capacity of solar generating resources to 2.5 GW by 2027 [1]. In addition, PJM will supply 13% of the total loads through renewable energy by 2031, via solar generating resources and will expand its capacity to 8.1 GW by 2027 [2]. Currently, in the Republic of Korea, coal-fired and nuclear power plants account for about 70% of all power plants, but the country's goal is for renewable energy to account for 20% by 2030. As of 2016, in South Korea, newly installed solar generating resources have a capacity of 904.1 MW and a cumulative installation capacity of 4519.4 MW. Additionally, renewable energy capacity has increased by 1,835MW from 2014 to 2015, at which time solar generating resources were capable of 1,076 MW and had a rate of increase of 42.3% [3].

However, the expansion of solar energy resources makes planning and operation of the power system difficult. Since it is essentially dependent on spatial and meteorological characteristics. In particular, solar generating resources have high variability and uncertainty because it is dependent on weather conditions, such as cloud cover. Since more volatile power sources are integrated to the system, the more problematic the power system may be, the more essential that various solutions are to maintaining its reliability. They are proposed and implemented to overcome the variability and uncertainty of solar generating resources. Advanced countries, such as the United States, Canada, and European nations want to create a stable power grid through accurate predictions of renewable energy outputs [4].

Various studies are being conducted on forecasting techniques of solar generating resources. At UC San Diego, solar irradiance is predicted by estimating the movement and position of the clouds using the Total Sky Imager device. The Sky Imager taken every 30 s were processed to determine sky cover using a clear sky library, and cloud locations up to 5 minutes ahead were forecasted by the advection of the two-dimensional cloud map [5,6]. A study in Denmark performed short-term online solar generating resources forecasting using the clear-sky model [7]. Additionally, in the United States, reference [8] presents a set of empirical models that quantify the short-term variability of the solar resources based upon site/time specific satellite-derived hourly irradiance data. In addition, a review of the recent forecasting method as related to solar generating resources is shown in [9]. Most solar generating resources forecasting methods are not only complex but also difficult due their requirements, such as satellite images and sky imagers. Thus, in this paper, we propose using the Naïve Bayes Classifier (NBC) technique, a simple and promising method, to

probabilistically express the uncertainty in solar generating resources. In addition, we attempt to improve the accuracy of the solar output forecasting by applying spatial modelling to the weather data provided by the Korea Meteorological Administration (KMA). In the paper, we first discuss the probabilistic approach NBC method and the Bayes rules that are based on this technique. Furthermore, we apply a type of spatial interpolation, called kriging to estimate accurate weather information on the solar farms, and the weather and location data measured by the KMA and the location data of solar generation complexes were applied to the plugging. Finally, the actual output data from the solar generation complex was used to provide reliable results, and then the output predictions from the simulations were compared to the actual output values.

2 HYBRID SPATIAL-TEMPORAL FORECASTING METHOD

Since solar generating resources have a high variability and uncertainty, it is useful to apply a probabilistic method to forecast its output. Spatial interpolation was applied to estimate weather information on the exact solar location, considering of the differences between the locations of solar generation and MET towers. We propose a hybrid spatial-temporal forecasting method that combines two techniques so both temporal and spatial characteristics are considered. Figure 1 shows a flowchart of the proposed technique.

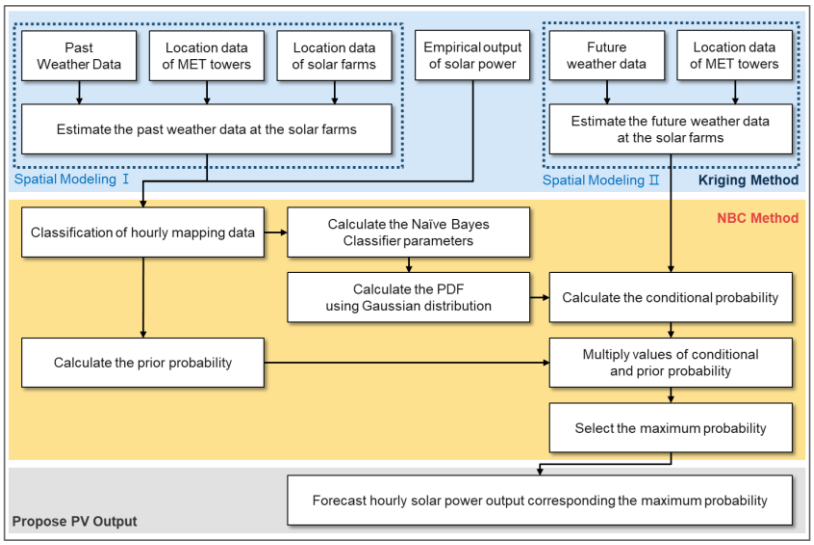

Figure 1. Hybrid Spatial-Temporal Forecasting Algorithm

2.1 Probabilistic Forecasting Method: NBC

Naïve Bayes Classifier is a machine-running technique based on the Bayes probabilistic rule. It is known to create a simple and efficient model in the fields of document taxonomy and disease prediction [10,11]. Bayes' rule states that when we learn new information from conditional probabilities, the probability improves. It consists of a classification variable Y_i, which represents the classes, and a variable value X_k, which is expressed in the Equation (1) [12,13].

$$P(Y_k \mid X_i) = \frac{P(X_i \mid Y_k) \cdot P(Y_k)}{P(X_i)} \quad \begin{cases} i = 1, 2, \cdots, n \\ k = 1, 2, \cdots, m \end{cases} \qquad (1)$$

The "Naïve" qualifier makes it possible to assume that the variables make up the dataset are independent. The independence of the variables means that they do not affect each other. The NBC method may not be independent in practice, but even under unrealistic circumstances, it tends to obtain good results. It is feasible to compute the conditional probability simply as shown in Equation (2) because of an independent assumption, thus avoiding complex calculation [14,15].

$$P(X_i \mid Y_k) = P(X_1 \mid Y_k) \cdot P(X_2 \mid Y_k) \cdot \ldots \cdot P(X_i \mid Y_k) = \prod_{i=1}^{n} P(X_i \mid Y_k) \qquad (2)$$

In this paper, conditional probability is the possibility that the meteorological factors will occur given the output value of solar generating resources. First, we calculate the mean and variance of the solar irradiance, humidity and temperature given all output values, and then we work out the conditional probability by applying Gaussian distribution as shown in Equation (3).

$$P(X_{new} \mid Y_k) = \frac{1}{\sqrt{2\sigma_{X_i Y_k}}} e^{-\frac{\left(x_{new} - \mu_{X_i Y_k}\right)^2}{2\sigma^2_{X_i Y_k}}} \qquad (3)$$

Prior probability refers to the ratio of each output value for solar generating resources to the total number of solar output data based on historical data, and can be as shown in Equation (4).

$$probability_{prior} = \frac{n(Y_i)}{\sum n(Y_k)} \qquad \begin{cases} i = 1, 2, \cdots, n \\ k = 1, 2, \cdots, m \end{cases} \qquad (4)$$

2.2 Spatial Interpolation for a Weather Data Set

Spatial modelling is a technique in which disparate data can be defined through its correlation with distance. This technique allows the value of an location of interest to be estimated regardless of historical data and is primarily used in GIS (Geographic Information System). Kriging is a type of the spatial interpolation based on the regression of values at the peripheral points depending on the specific weight of the spatial variance. The general formula for the ordinary kriging is shown in Equation (5).

$$\begin{aligned} \alpha^* &= \sum_{i=1}^{n} \lambda_i \alpha_i \\ s.t \sum_{i=1}^{n} \lambda_i &= 1 \end{aligned} \qquad (5)$$

where α is the estimated value of the point of interest, n is the number of neighbor data points, and λ represents the weight associated with the spatial distances between the two points. In kriging, the sum of all weights should be one to avoid biased models. This can be expressed as shown in Figure 2 below.

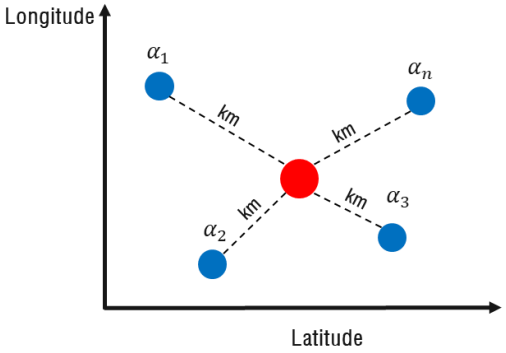

Figure 2. Graphical Expression of Kriging Method

3 SIMULATION CASE: PROBABILISTIC FORECASTING OF SOLAR GENERATING RESOURCES IN KOREA

3.1 Estimation of Weather Data Using Kriging

In this case study, to apply the kriging technique, we used weather and location information from South Korea. Before applying the kriging technique, we collected latitude and longitude data for 30 meteorological

towers (MET towers) and 10 solar farms as shown in Figure 3. We used the weather information measured by the 30 MET towers in South Korea, which consisted of irradiance, humidity and temperature, the factors mainly responsible for solar generating resources.

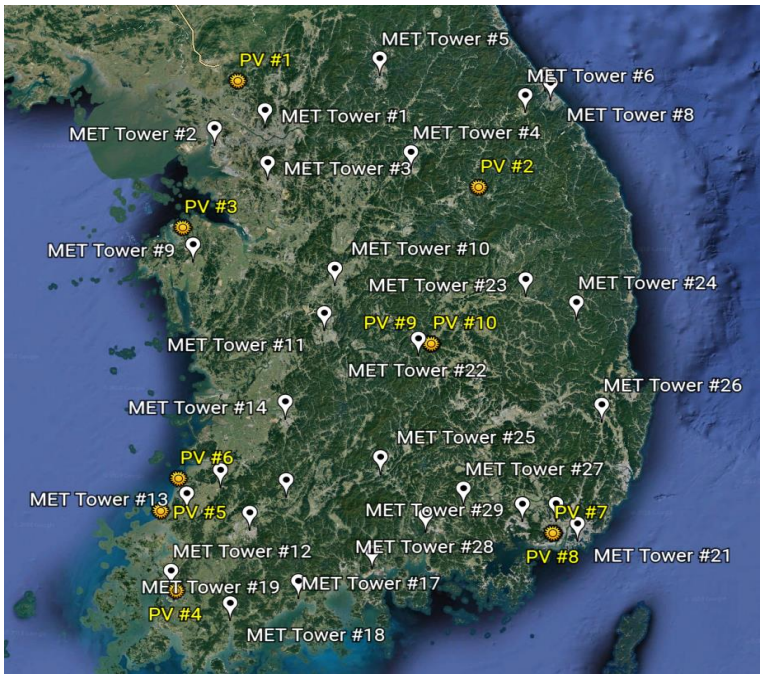

Figure 3. Locational Information of the PV farms and MET Towers

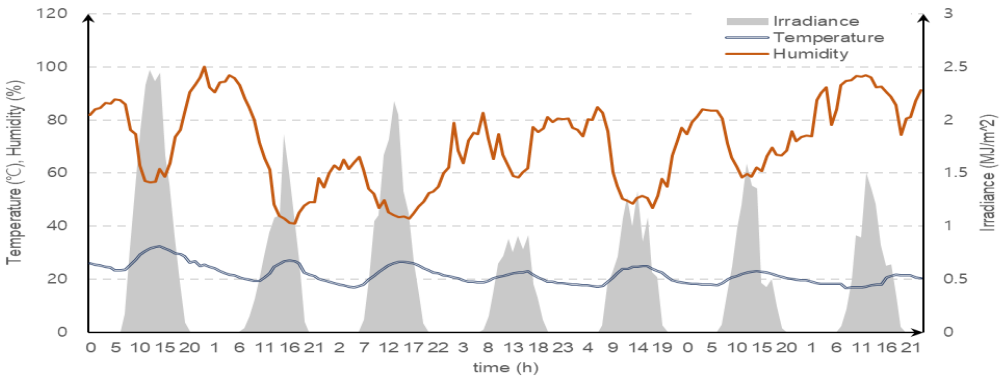

Figure 4. Estimated Weather Data Using the Spatial Modeling

Weather information was measured at the MET towers from January 1, 2015 to December 30, 2016 in hourly intervals, and Figure 4 shows the coordinate data of PV#1 from August 25 to 31, 2016 used in this paper. We forecast the solar generating resources within a day, over the duration of 2016.

3.2 Probabilistic Forecasting of solar generating resources using NBC method

Before applying the NBC method, we need to map previously the estimated weather data and the output value of solar generating resources based on one-hour intervals. To determine the probability of the output of solar generating resources using the Equation (1), prior and conditional probability is required for Equation (3) and (4). Only one case was selected because it was difficult to show the probabilities for all 8760 hours. Figure 5 shows the prior probability according to the output of solar generating resources. It is important to utilize Laplacian correction to avoid these problems since there is zero probability that outputs that do not exist in the past will be produced. This assumes that the dataset is large enough that there is little difference in the estimated probability even if one set is added.

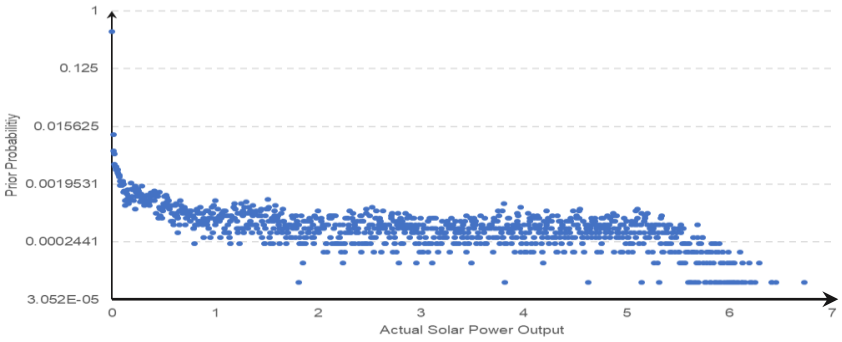

Figure 5. Prior Probability of Solar generating resource #1

Solar generating resources typically produces an output during the day, and since the output is zero at night, Figure 5 implies that the output has the most frequent probability of being zero.
Figure 6 shows NBC parameters that consist of the average and variance of the solar irradiance, humidity and temperature, given all output values. We calculated the conditional probability using the future weather data.

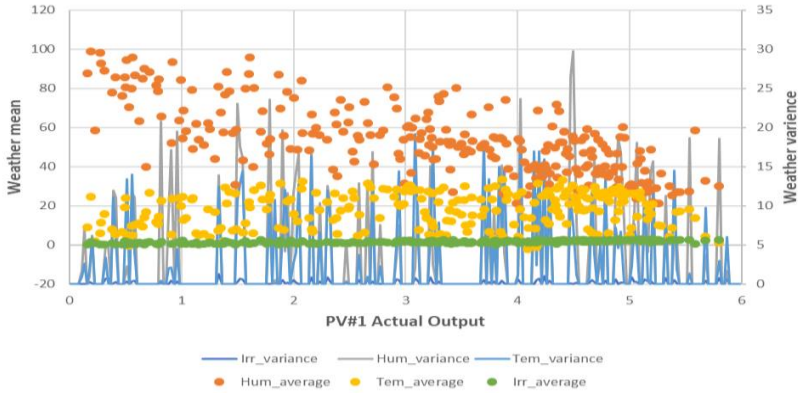

Figure 6. Distribution Chart of Weather Information for PV Generation #1 on 7 January 2016

By utilizing Equation (1), it was possible to draw the probability for solar generating resources by multiplying the prior and conditional probability calculated above. Finally, of the various models depending on the output value for solar generating resources, we selected a model that has the maximum probability. As a result, the output value for solar generating resources corresponding to the model with the highest probability over time was available. The results are shown in Figure 7. In this paper, errors with actual solar generating resources were calculated to determine the accuracy of the forecasting output values for solar generating resources. Errors were measured using the RMBE error rate shown in Table 1 below.

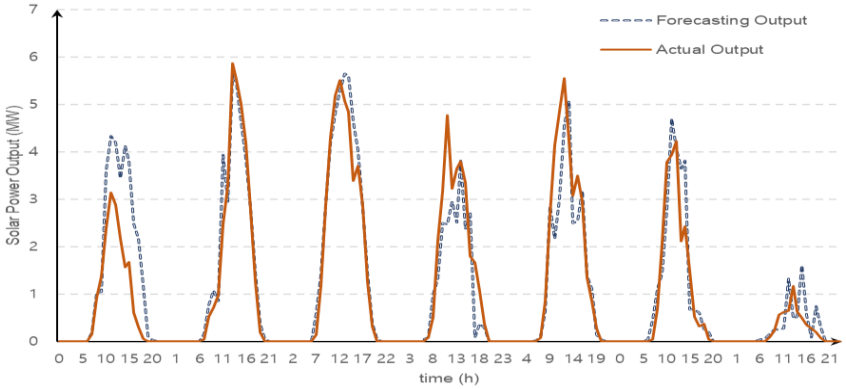

Figure 7. Solar Generating Resource #1 for August 25 to 31 2016

Table 1. Monthly RMBE Error rate in 2016

Month	RMBE [%]	Month	RMBE [%]	Month	RMBE [%]
January	19.447	May	5.520	September	6.836
February	2.940	June	-3.178	October	-1.670
March	-2.478	July	-20.766	November	23.952
April	3.566	August	1.360	December	8.858

4 CONCLUSION AND FUTURE WORK

Solar generating resources are rapidly growing all over the world, and with numerous solar generation connected to the system in the future, solar generating resources should be precisely forecasted to maintain power supply balance.

In this paper, hybrid spatial-temporal forecasting was performed. First, to carry out the forecasting of accurate points, a spatial modelling method called kriging was used to estimate the location of the tower in the 30 MET tower points. After mapping the weather data using kriging and solar output data measured in Korea over time, the NBC method, a probabilistic forecasting technique, was applied. The proposed techniques are types of simple machine running techniques that derive post probability from the prior probability based on the Bayes rule. Solar output values with a maximum probability over time are extracted, and in this paper, forecasting error is shown to average at 15 % per year.

Probabilistic forecasting is considered to be a very important approach since it can represent uncertainties in solar generation when intermittent solar generating resources are connected to the system. In future, reliable weather factors and optimized probability functions should be considered for more accurate forecasting.

REFERENCES

[1] NYISO, Power Trends – New York's Evolving Electric Grid 2017, 2017

[2] PJM, PJM's Evolving Resource Mix and System Reliability, 2017.3

[3] J.H. Seo, Energy Balancing Brief, Korea Photovoltaic Industry Association, 2017.5.

[4] NYISO, Solar Impact on Grid Operations – An Initial Assessment, 2016.6.

[5] C.W. Chow and B. Urquhart, M. Lave, A. Dominguez, J. Kleissl, J. Shields, B. Washom, Intra-hour Forecasting with a Total Sky Imager at the UC San Diego Solar Energy Testbed, Solar Energy, 2011.9.

[6] H. Yang, B. Kurtz, D. Nguyen, B. Urquhart, C.W. Chow, M. Ghonima, J. Kleissl, Solar Irradiance Forecasting using a Ground-based Sky Imager Developed at UC San Diego, Solar Energy, 2014.3.

[7] P. Bacher, H. Madsen, H.A. Nielsen, Online Short-term Solar Power Forecasting, Solar Energy, 2009.7.

[8] R. Perez, S. Kivalov, J. Schlemmer, K. Hemker, T. Hoff, Parameterization of Site-specific Short-term Irradiance Variability, Solar Energy, 2011.4.

[9] R.H. Inman, Hugo T.C. Pedro, Carlos F.M. Coimbra, Solar Forecasting Methods for Renewable Energy Integration, Progress in Energy and Combustion Science, 2013.

[10] S. Khan, M.R. Ghalib, A naïve-bayes approach for disease diagnosis with analysis of disease type and symptoms, IJAER, 2015.1.

[11] S.B. Kim, K.S. Soo, H.C. Rim, and S.H. Myaeng, IEEE, Some Effective Techniques for Naïve Bayes Text Classification, Vol. 18, NO.11, 2006.

[12] T.Davig, A.S. Hall, Recession Forecasting Using Bayesian Classification, The Federal Reserve Bank of Kansas City Research Working Papers, 2017.2.

[13] Y.T. Quek, W.L. Woo, T. Logenthiran, SEES, A Naïve Bayes Classification Approach for Short-Term Forecast of a Photovoltaic System, 2017.3.

[14] R.D. Visscher, V. Delouille, P. Dupont, C.A. Deledalle, SWSC, Supervised Classification of Solar Features using Prior Information, DOI: 10.1051/swsc/2015033, 2015.8.

[15] A. Bracale, P. Caramia, G. Carpinelli, Anna Rita Di Fazio, G. Ferruzzi, energies, A Bayesian Method for Short-Term Probabilistic Forecasting of Photovoltaic Generation in Smart Grid Operation and Control, DOI: 10.3390/en/6020733, 2013.6.

SEEP Conference 2018

University of the West of Scotland, Paisley Campus
Tuesday 8 – Friday 11 May 2018

UWS UNIVERSITY OF THE WEST of SCOTLAND

Institute of Engineering and Energy Technologies

RENEWABLE AND SUSTAINABLE ENERGY DEVELOPMENTS BEYOND 2030

VOLUME 2

ISBN: 978-1-903978-61-0